

Turkish Journal of

Analytical Chemistry

Volume 7
Issue 2
May 2025

<https://dergipark.org.tr/tr/pub/turkjac>

Turkish Journal of
**Analytical
Chemistry**
TurkJAC

Volume 7

Issue 2

May 2025

Publication Type: Peer-reviewed scientific journal

Publication Date: May 31, 2025

Publication Language: English

Published three times a year (January, May, September)

Owner

Prof. Miraç Ocak

Karadeniz Technical University, Faculty of Sciences, Department of Chemistry

Executive Editor

Prof. Ümmühan Ocak

Karadeniz Technical University, Faculty of Sciences, Department of Chemistry

Co-Editor

Ender Çekirge

Karadeniz Technical University, Institute of Forensic Sciences

Layout Editor

Ender Çekirge

Karadeniz Technical University, Institute of Forensic Sciences

Editorial Secretary

Ender Çekirge

Karadeniz Technical University, Institute of Forensic Sciences

Language Editors

Nurhayat Özbek

Karadeniz Technical University, Faculty of Sciences, Department of Chemistry

Aslıhan Yılmaz Çamoğlu

Karadeniz Technical University, Faculty of Sciences, Department of Chemistry

Copyeditors

Nurhayat Özbek

Karadeniz Technical University, Faculty of Sciences, Department of Chemistry

Aslıhan Yılmaz Çamoğlu

Karadeniz Technical University, Faculty of Sciences, Department of Chemistry

Proofreader

Merve Sarıcaoğlu

Karadeniz Technical University, Institute of Forensic Sciences

Editors

Prof. Ümmühan Ocak

Karadeniz Technical University, Faculty of Sciences, Department of Chemistry

Prof. Miraç Ocak

Karadeniz Technical University, Faculty of Sciences, Department of Chemistry

Prof. Ali Gündoğdu

Karadeniz Technical University, Maçka Vocational School, Department of Pharmacy Services

Prof. Selehattin Yılmaz

Çanakkale Onsekiz Mart University, Faculty of Science and Literature, Department of Chemistry

Prof. Duygu Özdeş

Gümüşhane University, Gümüşhane Vocational School, Department of Chemistry and Chemical Processing Technologies

Section Editors

Prof. Ali Gündoğdu

Karadeniz Technical University, Maçka Vocational School, Department of Pharmacy Services

Asst. Prof. Zafer Ocak

Kafkas University, Education Faculty, Mathematics and Science Education

Prof. Zehra Can

Bayburt University, Faculty of Applied Sciences, Department of Emergency Aid and Disaster Management

Prof. Olcay Bekircan

Karadeniz Technical University, Faculty of Sciences, Department of Chemistry

Asst. Prof. Bülent Akar

Gümüşhane University, Faculty of Engineering and Natural Sciences, Department of Food Engineering, Department of Food Science

Editor Board

Prof. Selehattin Yılmaz

Çanakkale Onsekiz Mart University, Faculty of Science and Literature, Department of Chemistry

Prof. Ali Gündoğdu

Karadeniz Technical University, Maçka Vocational School, Department of Pharmacy Services

Prof. Hakan Alp

Karadeniz Technical University, Faculty of Sciences, Department of Chemistry

Prof. Volkan Numan Bulut

Karadeniz Technical University, Maçka Vocational School, Department of Chemistry and Chemical Processing Technologies

Prof. Celal Duran

Karadeniz Technical University, Faculty of Sciences, Department of Chemistry

Asst. Prof. Aysel Başoğlu

Gümüşhane University, Faculty of Health Sciences, Department of Occupational Health and Safety

Prof. Ayşegül İyidoğan

Gaziantep University, Faculty of Science and Literature, Department of Chemistry

Prof. Sevgi Kolaylı

Karadeniz Technical University, Faculty of Sciences, Department of Chemistry

Prof. Hüseyin Serencam

Trabzon University, College of Applied Sciences, Department of Gastronomy and culinary arts

Assoc. Prof. Fatma Ağın

Karadeniz Technical University, Faculty of Pharmacy, Department of Basic Pharmaceutical Sciences

Prof. Duygu Özdeş

Gümüşhane University, Gümüşhane Vocational School, Department of Chemistry and Chemical Processing Technologies

Dr. Mustafa Z. Özel

University of York, Department of Chemistry

Prof. Małgorzata Wiśniewska	University of Maria Curie- Sklodowska, Faculty of Chemistry, Institute of Chemical Sciences, Department of Radiochemistry and Environmental Chemistry
Prof. Dilek Kul	Karadeniz Technical University, Faculty of Pharmacy, Department of Basic Pharmaceutical Sciences
Prof. Sławomira Skrzypek	University of Lodz, Faculty of Chemistry, Department of Inorganic and Analytical Chemistry
Prof. Fatih İslamoğlu	Recep Tayyip Erdoğan University, Faculty of Science and Literature, Department of Chemistry
Asst. Prof. Zekeriyya Bahadır	Giresun University, Faculty of Science and Literature, Department of Chemistry
Asst. Prof. Yasemin Çağlar	Giresun University, Faculty of Engineering, Department of Genetic and Bioengineering
Prof. Agnieszka Nosal-Wiercińska	University of Maria Curie- Sklodowska, Faculty of Chemistry, Institute of Chemical Sciences, Department of Analytical Chemistry
Assoc. Prof. Dr. Halit Arslan	Gazi University, Faculty of Science, Department of Chemistry
Assoc. Prof. Cemalettin Baltacı	Gümüşhane University, Faculty of Engineering and Natural Sciences, Department of Food Engineering
Asst. Prof. Zafer Ocak	Kafkas University, Education Faculty, Mathematics and Science Education
Prof. Mustafa İmamoğlu	Sakarya Univer.sity, Faculty of Science and Literature, Department of Chemistry
Assoc. Prof. Esra Bağda	Sivas Cumhuriyet University, Faculty of Pharmacy, Department of Basic Pharmaceutical Sciences, Analytical Chemistry Division
Assoc. Prof. Hüseyin Altundağ	Sakarya University, Faculty of Science and Literature, Department of Chemistry
Asst. Prof. Mehmet Başoğlu	Gümüşhane University, Faculty of Engineering and Natural Sciences, Department of Energy Systems Engineering

Publishing Board

Prof. Latif Elçi	Pamukkale University, Faculty of Science and Literature, Department of Chemistry
Prof. Münevver Sökmen	Konya Food and Agriculture University, Faculty of Engineering and Architecture, Department of Bioengineering
Prof. Atalay Sökmen	Konya Food and Agriculture University, Faculty of Engineering and Architecture, Department of Bioengineering
Prof. Kamil Kaygusuz	Karadeniz Technical University, Faculty of Sciences, Department of Chemistry
Prof. Yaşar Gök	Pamukkale University, Faculty of Science and Literature, Department of Chemistry

Prof. Ayşegül Gölcü	İstanbul Technical University, Faculty of Science and Literature, Department of Chemistry
Prof. Mustafa Tüzen	Gaziosmanpaşa University, Faculty of Science and Literature, Department of Chemistry
Prof. Mustafa Soylak	Erciyes University, Faculty of Sciences, Department of Chemistry
Prof. Fikret Karadeniz	Kafkas University, Faculty of Science and Literature, Department of Chemistry
Prof. Mehmet Yaman	Fırat University, Faculty of Sciences, Department of Chemistry
Prof. Halit Kantekin	Karadeniz Technical University, Faculty of Sciences, Department of Chemistry
Prof. Esin Canel	Ankara University, Faculty of Sciences, Department of Chemistry
Prof. Dilek Ak	Anadolu University, Faculty of Pharmacy, Department of Basic Pharmaceutical Sciences
Prof. Mustafa Küçükislamoğlu	Sakarya University, Faculty of Science and Literature, Department of Chemistry
Prof. Salih Zeki Yıldız	Sakarya University, Faculty of Science and Literature, Department of Chemistry
Prof. Recai İnam	Gazi University, Faculty of Sciences, Department of Chemistry
Prof. Dr. Durişehvar Ünal	İstanbul University, Faculty of Pharmacy, Department of Basic Pharmaceutical Sciences
Prof. Mehmet Tüfekçi	Avrasya University, Faculty of Science and Literature, Department of Biochemistry
Prof. Hüseyin Kara	Selçuk University, Faculty of Sciences, Department of Chemistry
Prof. Sezgin Bakirdere	Yıldız Technical University, Faculty of Science and Literature, Department of Chemistry
Prof. Hasan Basri Şentürk	Karadeniz Technical University, Faculty of Sciences, Department of Chemistry
Prof. Yusuf Atalay	Sakarya University, Faculty of Science and Literature, Department of Physics
Prof. Salih Zeki Yıldız	Sakarya University, Faculty of Science and Literature, Department of Chemistry

Authorship, Originality, and Plagiarism: The authors accept that the work is completely original and that the works of others have been appropriately cited or quoted in the text with the necessary permissions. The authors should avoid plagiarism. It is recommended that they check the article using appropriate software such as Ithenticate and CrossCheck. The responsibility for this matter rests entirely with the authors. All authors will be notified when the manuscript is submitted. If a change of author is needed, the reason for the change should be indicated. Once the manuscript is accepted, no author changes can be made.

Aims and Scope

“Turkish Journal of Analytical Chemistry” publishes original full-text research articles and reviews covering a variety of topics in analytical chemistry. Original research articles may be improved versions of known analytical methods. However, studies involving new and innovative methods are preferred. Topics covered include:

- Analytical materials
- Atomic methods
- Biochemical methods
- Chromatographic methods
- Electrochemical methods
- Environmental analysis
- Food analysis
- Forensic analysis
- Optical methods
- Pharmaceutical analysis
- Plant analysis
- Theoretical calculations
- Nanostructures for analytical purposes
- Chemometric methods
- Energy

ETHICAL GUIDELINES

TurkJAC follows ethical tasks and responsibilities are defined by the Committee on Publication Ethics (COPE) in publication procedure. Based on this guide, the rules regarding publication ethics are presented in the following sections.

Ethical Approval

Ethics committee approval must be obtained for studies on clinical and experimental regarding human and animals that require an ethical committee decision, this approval must be stated in the article and documented in the submission. In such articles, the statement that research and publication ethics are complied with should include. Information about the approval such as committee name, date, and number should be included in the method section and also on the first/last page of the article.

Editors

1. In the preliminary evaluation of a submission, the editor of the journal evaluates the article's suitability for the purpose and scope of the journal, whether it is similar to other articles in the literature, and whether it meets the expectations regarding the language of writing. When it meets the mentioned criteria, the scientific evaluation process is started by assigning a section editor if necessary.
2. A peer-reviewed publication policy is employed in all original studies, taking into full account of possible problems due to related or conflicting interests.

3. Section editors work on the articles with a specific subject and their suggestion is effective in the journal editor's decision about acceptance or rejection of the article.
4. No section editor contacts anyone except the authors, reviewers, and the journal editor about articles in the continued evaluation process.
5. In the journal editor's decision to accept or reject an article, in the addition of section editor's suggestion in consequence of scientific reviewing, the importance of the article, clarity and originality are decisive. The final decision, in this case, belongs to the journal editor.

Authors

1. The authors should actively contribute to the design and execution of the work. Authorship should not be given to a person who does not have at least one specific task in the study.
2. Normally all authors are responsible for the content of the article. However, in interdisciplinary studies with many authors, the part that each author is responsible for should be explained in the cover letter.
3. Before the start of the study, it would be better to determine the authors, contributors, and who will be acknowledged in order to avoid conflict in academic credits.
4. The corresponding author is one of the authors of the article submitted to the journal for publication. All communications will be conducted with this person until the publication of the article. The copyright form will be signed by the corresponding author on all the authors' behalf.
5. It is unacceptable to submit an article that has already been published entirely or partly in other publication media. In such situation, the responsibility lies with all authors. It is also unacceptable that the same article has been sent to TurkJAC and another journal simultaneously for publication. Authors should pay attention to this situation in terms of publication ethics.
6. Plagiarism from others' publications or their own publications and slicing of the same study is not acceptable.
7. All authors agree that the data presented in the article are real and original. In case of an error in the data presented, the authors have to be involved in the withdraw and correction process.
8. All authors must contribute to the peer-reviewed procedure.

Reviewers

1. Peer reviewers worked voluntarily are external experts assigned by editors to improve the submitted article.
2. It is extremely important that the referee performs the review on time so that the process does not prolong. Therefore, when the invitation is agreed upon, the reviewer is expected to do this on time. Also, the reviewer agrees that there are no conflicts of interest regarding the research, the authors, and/or the research funders.
3. Reviewers are expected not to share the articles reviewed with other people. The review process should be done securely.
4. Reviewers are scored according to criteria such as responding to the invitations, whether their evaluations are comprehensive and acting in accordance with deadlines, and the article submissions that they can make to TurkJAC are handled with priority.

Turkish Journal of Analytical Chemistry

2025

Volume: 7

Issue: 2

Contents

Research Articles

- Thermodynamic studies of Co(II) complexation with Schiff base ligands in different nonaqueous solvents 71–78
Khaled Muftah Elsheri, Abdulfattah Mohammed Alkherraz, Awatif Al-Arbash, Salima Abajja, Hana Bashir Shawish*
- Synthesis and characterization of biocopolymer kappa-Carrageenan(κ -C)-g-polyacrylamide/activated bentonite composite** 79–84
Kamel Ismet Benabadji, Tayeb Hocine, Oussama Bouras, Bouras Brahim, Noussaiba Kheir*
- Evaluation of antioxidant, antimicrobial, and α -amylase enzyme inhibition properties of *Rosa canina* seed extracts prepared with different solvents using maceration and ultrasound-assisted extraction methods 85–96
Kağan Kiliç, İmdat Aygül, Osman Akmeşe, Cemalettin Baltacı, Mohammed Abdulsamad Hafedh*
- Removal of anionic and cationic dyes from aqueous solutions using drinking water treatment plant sludge (DWTS): Equilibrium and kinetic evaluation** 97–107
*Fatma Asya Turfan, Neslihan Kılıç, Fatma Yaltrık, Duygu Özdes, Celal Duran**
- Advanced interpretation of kinetics and equilibrium data obtained from adsorption of Pb²⁺ ions from aqueous solution onto pine bark (*Pinus brutia* Ten.) using non-linear regression: A practical approach with Microsoft Excel Solver** 108–131
Ali Gundogdu, Volkan N. Bulut*
- Validation of stability-indicating high-performance liquid chromatography method for the determination of thymol in gelatin-based hydrogels 132–139
Onur Demir, Mehlika Pulat, Ali Bilgili*
- Hydrometallurgy of lithium: Selective separation from geothermal brines using chitosan-lithium ion sieve composite** 140–153
*Yaşar Kemal Recepoğlu, Aslı Yüksel**
- Microwave hydrodistillation of *Poncirus trifoliata* (L.) Raf. peels and essential oil profile: Greenness assessment 154–161
Yusuf Can Gerçek
- The accurate and reliable HPLC-UV based method for detecting the active ingredient hexaflumuron in some plant protection products 162–167
Ismail M. Elkamhawvy, Mostafa G. Emara, Alaa E. Ali, Mohamed A. Khashaba*
- Assessment of antioxidant, antimicrobial, antibiofilm, carbonic anhydrase, and α -glucosidase inhibitory activities of *Alchemilla vulgaris* L. extracts 168–175
Uğur Kardil, Zeynep Akar, Azer Özad Düzgün*

*Author of correspondence:

** [The paper was presented at the 6th International Environmental Chemistry Congress, EnviroChem 05-08 November 2024, Trabzon Türkiye.](#)

Synthesis, characterization and antioxidant activity of sulfonyl-1H-1,2,3-triazoles <i>Fatih Çelik</i>	176–181
Comparison of some mineral and trace-heavy metal contents of blossom honey samples from Yamadağ and Battalgazi regions, Malatya, Türkiye <i>Semiramis Karlıdağ*, Sevgi Kolaylı</i>	182–190
New 1H-1,2,3-triazol derivatives: Synthesis, characterization and antioxidant activity <i>Fatih Çelik</i>	191–194
Comparative analysis of phenolic compounds, volatile components, and antioxidant capacity in leaf and flower parts of <i>Aster caucasicus</i> <i>Abidin Gümrükçüoğlu</i>	195–208
Green synthesis of fluorescent carbon quantum dots from field horsetail <i>Equisetum Arvense</i> L and fluorimetric detection of Pd ²⁺ ions <i>Aysel Başoğlu</i>	209–219
Treatment of Silicate Ion with <i>Bacillus subtilis</i> Bacteria in Demineralization-Water/Steam Cycles in Power Plants <i>Deniz Bozkur, Aslıhan Dalmaz, Sefa Durmuş*</i>	220–227
Eco-friendly spectrofluorimetric determination of Hg ²⁺ using green-synthesized carbon nanodots from apricot kernel shells <i>Najlaa Ayad Salahaldeen, Nurhayat Özbek, Miraç Ocak*, Ümmühan Turgut Ocak</i>	228–236

*Author of correspondence:

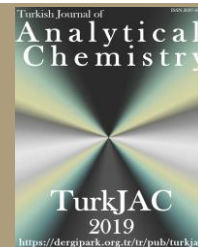
** [The paper was presented at the 6th International Environmental Chemistry Congress, EnviroChem 05-08 November 2024, Trabzon Türkiye.](#)



TurkJAC

Turkish Journal of

Analytical Chemistry

<https://dergipark.org.tr/tr/pub/turkjac>

Thermodynamic studies of Co(II) complexation with Schiff base ligands in different nonaqueous solvents

Khaled Muftah Elsherif^{1*} , Abdulfattah Mohammed Alkherraz² , Awatif Al-Arbash² ,
Salima Abajja² , Hana Bashir Shawish²

¹ Libyan Authority for Scientific Research, 80045, Tripoli, Libya

² Misurata University, Faculty of Science, Chemistry Department, 2478, Misurata, Libya

Abstract

This study explores the synthesis and characterization of two novel Schiff base ligands, N,N'-Bis(2-hydroxybenzylidene)ethylenediamine (L1) and N,N'-Bis(2,4-dihydroxybenzylidene)ethylenediamine (L2), and their complexation behavior with Co(II) ions in non-aqueous media. Ligand L1 was synthesized from o-hydroxyacetophenone and salicylaldehyde with ethylenediamine, while L2 was derived from 2,4-dihydroxybenzaldehyde and ethylenediamine. Stability constants of the Co(II) complexes were determined using conductometric measurements in ethanol, acetonitrile, and a 1:1 mixture of these solvents at 25 °C–40 °C. The results showed distinct temperature-dependent trends. L1 complexes exhibited decreased in stability with increasing temperature in all solvents, indicating exothermic reactions. In contrast, L2 complexes displayed varied behavior, suggesting endothermic reactions in acetonitrile and the mixed solvent. Solvent type significantly influenced stability, with acetonitrile yielding the highest stability constants, followed by the 1:1 mixture and ethanol. L2 complexes were more stable than those of L1, attributed to additional hydroxyl groups in L2 enhancing Lewis basicity, while the methyl group in L1 introduced steric hindrance, reducing stability. Thermodynamic analysis indicated spontaneity for all reactions, as evidenced by negative ΔG° values (-27.9 to -32.1 kJ/mol). Enthalpy changes (ΔH°) varied, with negative values (-27.6 to -195 kJ/mol) for exothermic and positive values (7.37 and 42.3 kJ/mol) for endothermic reactions. Entropy changes (ΔS°) reflected differences in molecular organization and solvent-ligand interactions. This study provides valuable insights into metal-ligand complexation in non-aqueous environments, aiding the design of coordination compounds for diverse chemical applications.

Keywords: Conductometry, Schiff bases, cobalt complexes, stability constants, nonaqueous solutions, thermodynamic parameters

1. Introduction

Stability constants are paramount in various scientific fields, including analytical, industrial, and environmental chemistry, as well as medicinal chemistry, for comprehending chemical equilibria in solutions. Due to their extensive applications, such as pollution remediation, drug development, and catalysis, metal-ligand complexation processes are of particular significance. By determining the stability constants of metal complexes, researchers can gain crucial insights into the strength and specificity of metal-ligand interactions. These findings are indispensable for addressing environmental challenges and advancing coordination chemistry [1–3].

A variety of techniques, including conductometry, spectrophotometric methods, and potentiometric

titration, can be employed to determine stability constants [4–6]. Spectrophotometric techniques are particularly valuable owing to their high sensitivity and adaptability across diverse experimental conditions [7]. However, conductometric techniques stand out for their ease of use, precision, and ability to quantify ionic interactions in solution without the need for sophisticated instrumentation. Conductometry is particularly useful when studying systems where variations in ionic conductivity reflect the extent of complex formation. This technique is also advantageous when working with non-absorbing species or in situations where optical methods are limited. Conductometric measurements can be performed in a wide range of solvent systems and concentrations,

Citation: K.M Elsherif, A.M. Alkherraz, A. Al-Arbash, S. Abajja, Hana B. Shawish, Thermodynamic studies of Co(II) complexation with Schiff base ligands in different nonaqueous solvents, Turk J Anal Chem, 7(2), 2025, 71-78.

*** Author of correspondence:** elsherif27@yahoo.com

Tel: +218 (92) 058 82 04

Fax: +218 (21) 360 5038

Received: December 24, 2024

Accepted: February 7, 2025

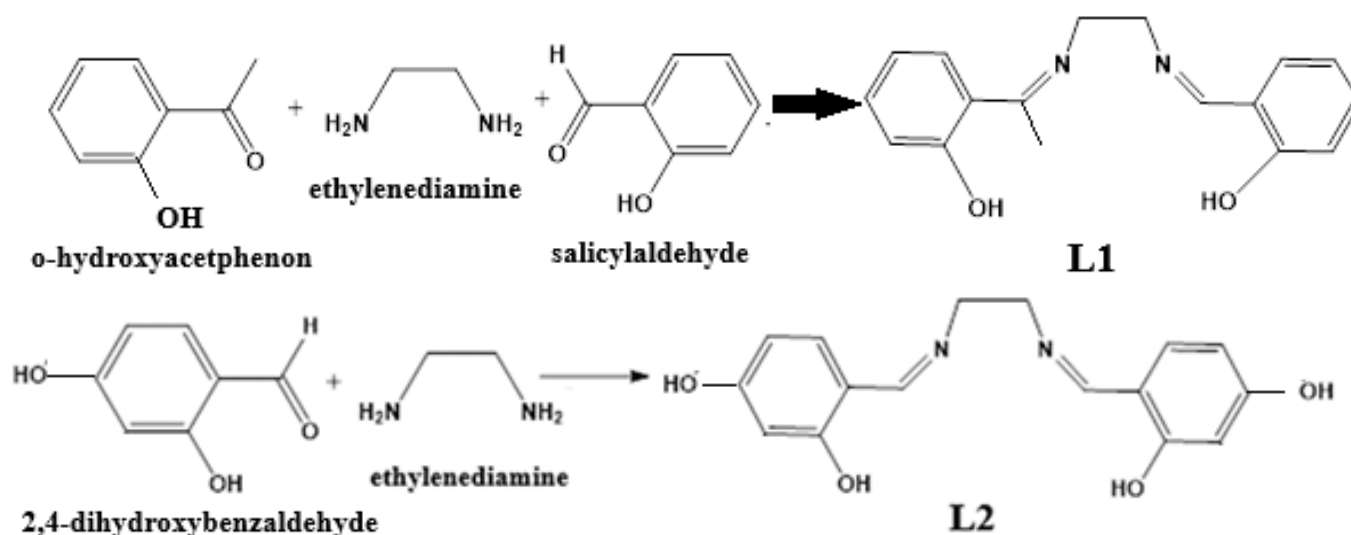
<https://doi.org/10.51435/turkjac.1606841>

making it a versatile and reliable method for determining stability constants [8–10].

The investigation of complexation processes involving oxygen and nitrogen donor ligands in non-aqueous environments is crucial for developing sophisticated analytical systems. These include solid-phase and cloud-point extraction methods, optical sensors, bulk and supported liquid membrane transport systems, and potentiometric sensors [11]. Such investigations are equally essential in biochemistry, where understanding ligand behavior leads to broader applications. Analyzing the complexation reactions of these ligands with metal ions provides valuable insights into ligand selectivity towards different metal cations, in addition to offering a comprehensive understanding of the complex formation process [12–14].

Schiff bases, named after Hugo Schiff, are a prominent class of ligands formed by the condensation of an amine and an aldehyde. Their structural diversity, ease of synthesis, and unique properties—such as thermal stability, versatile coordination abilities, and biological and catalytic activities—have made them highly attractive in various fields [15]. These ligands are particularly valued for their ability to coordinate with metal ions through the imine nitrogen atom and additional donor groups, often derived from the aldehyde component, stabilizing metals in different oxidation states [16,17]. The tunability of their electronic and steric properties, along with their straightforward synthesis, enhances their versatility. Furthermore, Schiff bases incorporating donor atoms like sulfur, oxygen, or nitrogen exhibit significant biological activity, which can be amplified through metal ion interactions. These features make them promising candidates for applications in catalysis, medicinal chemistry, and coordination chemistry [18].

Several studies have investigated the synthesis, stability, and characterization of metal complexes containing Schiff base ligands, demonstrating the diverse applications of these complexes in biological activity and coordination chemistry. Kalshetty et al. [19] investigated the solution stability constants of Cu(II), Zn(II), Ni(II), Co(II), Cd(II), and Mg(II) complexes using Schiff bases derived from 5-aldehydosalicylic acid and aniline. The study revealed that Cu(II) complexes exhibited higher stability compared to Zn(II) and Ni(II) complexes, attributed to their square planar geometry in contrast to the tetrahedral or octahedral geometry of Zn(II) and Ni(II) complexes. Jadhav et al. [5] investigated Schiff base complexes with Mn(II), Co(II), Ni(II), Cu(II), and Zn(II) using potentiometric methods. The order of stability constants was found to be $\text{Cu} > \text{Ni} > \text{Zn} > \text{Mn} > \text{Co}$, consistent with the Irving-Williams series. Esmailzadeh and Mashhadiagha [16] investigated the thermodynamic characteristics and formation constants of complexes of Co(II), Ni(II), Cu(II), and Zn(II) using methyl-2-amino-1-cyclopentenedithiocarboxylate as a Schiff base ligand. Spectrophotometric methods employed in the study indicated that the complexation process is spontaneous and exothermic, with the stability order $\text{CoL} > \text{CuL} > \text{NiL} > \text{ZnL}$. Density functional theory (DFT) calculations were also utilized in their study to validate experimental results. Muthal [17] synthesized a series of Schiff bases and associated transition metal complexes (CoII, NiII, CuII, and ZnII) using UV-Vis, IR, magnetic susceptibility, and conductivity studies. The complexes exhibited antibacterial, antifungal, and pesticidal activity, and thermodynamic data indicated that they were exothermic and entropically favorable. Farhan [20] synthesized Schiff base-azo ligands to study the Co(II), Cu(II), and Ni(II) complexes of imidazole derivatives. The complexes exhibited excellent stability due to the



Scheme 1. Preparation of Schiff base ligands (L1 & L2)

chelation effect, and negative thermodynamic functions confirmed their spontaneous origin. Jha [21] investigated the stability constants of transition metal complexes, such as Cu(II), Ni(II), Co(II), and Zn(II), using Schiff base ligands derived from β -naphthaldehyde and 7-hydroxy naphthalene 2-amine. The stability constant order, determined to be Cu(II) > Ni(II) > Co(II) > Zn(II), highlighted the significant coordination ability of Schiff bases with Cu(II).

This research aims to synthesize and characterize two Schiff base ligands, N,N'-Bis(2-hydroxybenzylidene)ethylenediamine (L1) and N,N'-Bis(2,4-dihydroxybenzylidene)ethylenediamine (L2), and to investigate their complexation behavior with Co²⁺ ions in non-aqueous solutions. Ligand L1 was prepared by condensing o-hydroxyacetophenone and salicylaldehyde with ethylenediamine, while L2 was synthesized using 2,4-dihydroxybenzaldehyde and ethylenediamine. Conductometric measurements were employed to investigate the complexation process of these ligands with Co²⁺ ions in three solvent systems: ethanol, acetonitrile, and a 1:1 mixture of the two. Experiments were conducted at four distinct temperatures (25 °C, 30 °C, 35 °C, and 40 °C) to determine the stability constants of the resulting complexes. Thermodynamic parameters, such as enthalpy change (ΔH°), entropy change (ΔS°), and Gibbs free energy change (ΔG°), were estimated to provide insights into the thermodynamic stability and spontaneity of the complexation processes.

2. Material and methods

2.1. Materials and equipment:

Salicylaldehyde (2-hydroxybenzaldehyde, $\geq 98\%$, Sigma-Aldrich) and 2,4-dihydroxybenzaldehyde ($\geq 97\%$, Sigma-Aldrich) were used for the synthesis of Schiff base ligands L1 and L2, respectively. Ethylenediamine ($\geq 99\%$, Sigma-Aldrich) served as the amine component for both ligands. Nickel(II) chloride hexahydrate (NiCl₂·6H₂O, $\geq 98\%$), copper(II) chloride dihydrate (CuCl₂·2H₂O, $\geq 99\%$), and cobalt(II) chloride hexahydrate (CoCl₂·6H₂O, $\geq 98\%$) (all from Sigma-Aldrich) were used as metal salts for complexation studies. Ethanol (absolute, $\geq 99.8\%$, Sigma-Aldrich) and acetonitrile ($\geq 99.9\%$, Sigma-Aldrich) were employed as nonaqueous solvents for the thermodynamic studies of complex formation. Conductometric measurements were performed using a Jenway 4510 conductometer (Cole-Parmer, UK) equipped with a Julabo ED circulator (Julabo GmbH, Germany) and a water bath for temperature control.

2.2. Synthesis of ligands

The two Schiff base ligands N,N'-Bis(2-hydroxybenzylidene)ethylenediamine (L1) and N,N'-Bis(2,4-dihydroxybenzylidene)ethylenediamine (L2) were synthesized through standard condensation reactions following established protocols [22,23]. Scheme 1 illustrates the synthetic pathway for the preparation of the two ligands. A solution of ethylenediamine (10 mmol) in ethanol was combined with the aldehyde or ketone (20 mmol) in ethanol (50 mL). The mixture was stirred using a magnetic stirrer, and within a few minutes, a thick yellow precipitate formed. Heating the mixture at 60°C for approximately 120 min produced a clear yellow solution. After cooling overnight, fine crystals were obtained, which were then isolated by filtration, washed with acetone, and dried under vacuum over silica gel. Salicylaldehyde, 2,4-dihydroxybenzaldehyde, and o-hydroxyacetophenone were employed as precursors for the synthesis of the Schiff base ligands.

2.3. Conductometric measurements

In a typical procedure, a double-walled conductometer glass cell was filled with 20.0 mL of a metal ion solution (1.0×10^{-4} mol/L) in the chosen test solvent (ethanol, acetonitrile, or a 1:1 mixture). The initial conductance of the solution was recorded. Subsequently, a Hamilton syringe was used to incrementally introduce 200 μ L aliquots of ligand solution (L1 or L2) at a concentration of 1.0×10^{-3} mol/L. After each addition, the conductance of the solution was measured. This process of ligand addition and conductance measurement was repeated until the desired ligand-to-metal ion mole ratio was attained. These measurements were carried out at various temperatures, specifically 25, 30, 35, and 40°C.

2.4. Determination of stability constants

The stability constants of the nickel complexes with the investigated Schiff bases (L1 and L2) in the three solvents were determined using conductivity measurement. A graphical representation was prepared to depict the relationship between conductivity changes and the molar ratio of the ligand to the metal ion. The stability constants (K_{stab}) at the investigated temperatures were calculated using the Simplex program.

2.5. Thermodynamic parameters determination

To thoroughly understand the thermodynamics of the complexation reactions between the Schiff base ligands and Co²⁺ ions in the investigated solvents, it is essential to analyze both the enthalpic and entropic contributions. The enthalpy change (ΔH° , kJ/mol) and entropy change (ΔS° , J/mol.K) for these reactions were determined using the Van't Hoff equation. This analysis requires the

stability constants of the complexes at various temperatures.

The Van't Hoff equation is expressed as:

$$\ln K_{\text{stab}} = \frac{\Delta S^\circ}{R} - \frac{\Delta H^\circ}{RT} \quad (1)$$

Where: K_{stab} : stability constant, R : gas constant (8.314 J/mol.K), T : absolute temperature (K).

By plotting $\ln K_{\text{stab}}$ versus $1/T$, the slope of the resulting line corresponds to $-\Delta H^\circ/R$, and the y-intercept corresponds to $\Delta S^\circ/R$. Furthermore, the Gibbs free energy change (ΔG° , kJ/mol) for the reactions was calculated using the following equation:

$$\Delta G^\circ = \Delta H^\circ - T \Delta S^\circ \quad (2)$$

3. Results and discussion

3.1. Temperature effect profile

The conductometric measurements revealed significant insights into the formation of the Co^{2+} complexes with Schiff bases L1 and L2 in three non-aqueous solvents: acetonitrile, ethanol, and a 1:1 mixture of the two. The stability of the complexes was observed to vary with temperatures (25, 30, 35, and 40 °C). Fig. 1 and Fig. 2 depict the variation in molar conductivity (Λ_m) as a function of the ligand-to-cobalt ion molar ratio ($[\text{L}]_t/[\text{Co(II)}]_t$), where $[\text{L}]_t$ and $[\text{Co(II)}]_t$ represent the total concentrations of the ligand and the cobalt ion, respectively. As illustrated in the figures, the addition of ligands (L1 and L2) leads to an increase in molar conductivity, indicating that the mobility of the formed complexes surpasses that of the solvated metal ions. The data further showed that transition metal ions tend to form coordination complexes with solvent molecules like water, ethanol, or acetonitrile [11,13], which restricts their mobility and reduces conductivity. Upon complex formation with Schiff bases, the ligands displace the coordinated solvent molecules, diminishing the attractive forces between the cation and its coordinated entities. This substitution resulted in a decrease in resistance to movement, thereby enhancing the overall conductivity of the solution [24].

The conductivity values of the complexes in the three solvents followed the order: mixture > acetonitrile > ethanol. This trend, observed for single-component solvents, correlates with the solvating ability of the solvents, as expressed by their Gutmann donor numbers [12]. A higher donor number reflects a greater tendency of the solvent to coordinate with the metal ion, thereby reducing the ability of the ligands to displace solvent molecules and, consequently, decreasing the solution's conductivity [25]. This observation is consistent with previous studies [25–27].

Furthermore, Fig. 1 and Fig. 2 reveal a linear increase in conductivity with the addition of ligand. A noticeable change in the slope of the curve occurs at a molar ratio of 1:1, indicating the formation of a 1:1 (ML) complex between Co^{2+} and the Schiff bases. A significant increase in molar conductivity is also observed with rising temperature, which can be attributed to enhanced ion mobility and faster complex formation at higher temperatures. Elevated temperatures reduce solvent viscosity, facilitating the movement of free ions and complexes. Additionally, the increased kinetic energy at higher temperatures accelerates ligand-metal interactions, thereby promoting the formation of ionic complexes [28,29].

3.2. Determination of stability constants (K_{stab})

The stability constants of cobalt complexes with Schiff bases L1 and L2 were determined in three non-aqueous solvents at various temperatures. This was accomplished by graphically analyzing the changes in molar conductivity as a function of the ligand-to-metal ion molar ratio and utilizing the statistical program Simplex [9]. The calculated stability constants are summarized in Table 1.

For L1 complexes, stability constants decreased with increasing temperature, indicating exothermic complex formation reactions. In contrast, L2 complexes exhibited a more complex behavior: stability constants decreased with temperature in ethanol but increased in acetonitrile and the mixed solvent. This suggests that the reactions are endothermic in the latter solvents. This observation aligns with Le Chatelier's principle, which predicts that increasing the temperature shifts the equilibrium of exothermic reactions towards the reactants, thereby decreasing the stability of the complexes.

The solvent environment significantly influenced the stability of the cobalt complexes, with the following trend observed: acetonitrile > mixture > ethanol. This trend correlates with the donor number (DN) of the solvents. Acetonitrile (DN = 14.1) has a lower donor number than ethanol (DN = 19.7), indicating weaker interactions between acetonitrile molecules and metal ions. The donor number reflects the solvent's Lewis basicity. Solvent with higher donor numbers indicate stronger interactions with metal ions, increasing competition with ligand molecules and reducing the stability of the complexes [30]. These findings are consistent with previous studies on solvent effects on the stability of transition metal complexes [31,32].

Finally, the stability constants of the cobalt complexes with L2 were generally higher than those with L1. This difference can be attributed to the additional donor groups (hydroxyl groups) in L2, which enhance its Lewis basicity. In contrast, the presence of a methyl group in L1 introduces steric hindrance, reducing the stability of its complexes [32,33].

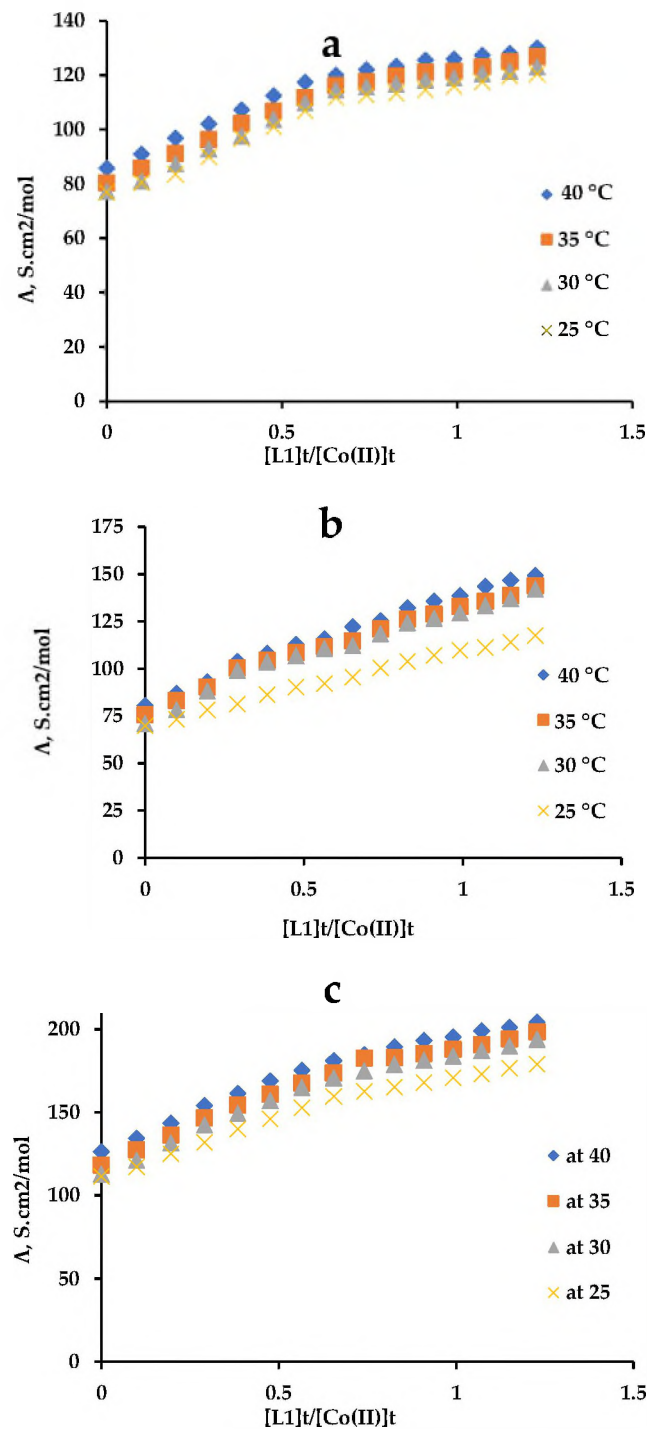


Figure 1. Molar ratio vs molar conductivity plots of Co-L1 complexes at different temperatures in various solvents: **a)** acetonitrile, **b)** ethanol, **c)** mixed solvent

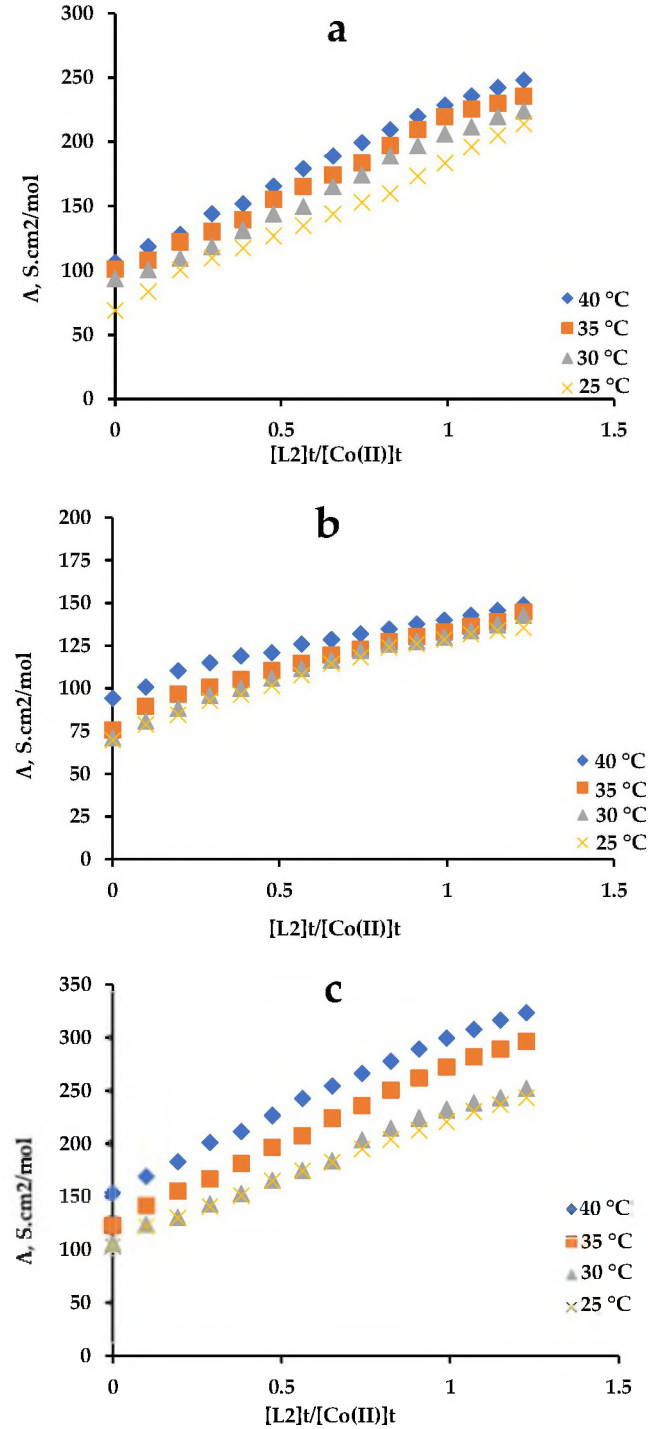


Figure 2. Molar ratio vs molar conductivity plots of Co-L2 complexes at different temperatures in various solvents: **a)** acetonitrile, **b)** ethanol, **c)** mixed solvent

Table 1. Values of stability constant ($\text{Log}K_{\text{stab}}$) in various solvents at different temperatures

Co-L1			Co-L2			T (°C)
AN	EtOH	1:1	AN	EtOH	1:1	
5.032	5.490	4.950	5.297	4.96	5.631	25
4.964	4.429	4.854	5.536	4.600	5.647	30
4.840	4.113	4.756	5.592	4.400	5.672	35
4.817	3.775	4.642	5.675	4.350	5.692	40

AN: Acetonitrile, EtOH: Ethanol, 1:1: mixed solvent

Table 2. Thermodynamic parameters for Co(II) complexes in various solvents

T (°C)	Co-L1			Co-L2		
	ΔG^a kJ/mol	ΔS^a kJ/mol.K	ΔH^a kJ/mol	ΔG^a kJ/mol	ΔS^a kJ/mol.K	ΔH^a kJ/mol
AN	-28.7	0.004	-27.6	-30.5	0.245	42.3
EtOH	-30.0	-0.552	-195	-27.9	-0.149	-72.4
1:1	-28.3	-0.027	-36.4	-32.1	0.132	7.37

AN: Acetonitrile, EtOH: Ethanol, 1:1: mixed solvent

3.3. Thermodynamic parameters

The thermodynamic parameters (enthalpy, ΔH^0 , and entropy, ΔS^0) for the complexation reactions of cobalt with Schiff bases in the studied non-aqueous solvents were determined using the linear form of the Van't Hoff equation, as depicted in Fig. 3a and Fig. 3b. The enthalpy change (ΔH^0) was calculated from the slope of the fitted line, while the entropy change (ΔS^0) was derived from the y-intercept. Using these values, the Gibbs free energy change (ΔG^0) was also computed. The thermodynamic constants are summarized in Table 2.

The results demonstrate that all ΔH^0 values for L1 complex formation are negative, confirming the exothermic nature of these reactions. In contrast, the formation of L2 complexes exhibited a mixed trend: exothermic in ethanol and endothermic in acetonitrile and the mixed solvent. The energy released during complexation was more significant in ethanol, with values of 195 kJ/mol for L1 and 72.4 kJ/mol for L2, suggesting stronger ligand-metal ion interactions in this solvent [16,20]. Exothermic reactions generally enhance the stability of complexes at lower temperatures, but their favorability decreases as the temperature rises, consistent with the observed results [34].

The ΔG^0 values for all reactions were negative, indicating that the complexation processes occurred spontaneously under the experimental conditions. In solution, metal ions are typically solvated, surrounded by a stabilizing shell of solvent molecules due to electrostatic interactions between the positively charged ions and the polar solvent molecules. Upon the introduction of ligands, they displace some of these solvent molecules and coordinate with the metal ions via Lewis acid-base interactions. These coordination bonds are strong, contributing significantly to the stabilization of the complexes in solution [34].

Entropy changes (ΔS^0) associated with the complexation varied, ranging from slightly positive to slightly negative. Positive ΔS^0 values, observed for L2 complexes in acetonitrile and the mixed solvent, as well as for L1 complexes in acetonitrile, suggest a slight increase in molecular disorder and greater freedom of movement within the solution. Conversely, negative ΔS^0 values, identified for L1 complexes in ethanol and the mixed solvent, as well as for L2 complexes in ethanol, indicate increased order and structural organization within the system. This observation correlates with the higher energy release (ΔH^0) during complexation in ethanol. This trend can be attributed to the formation of strong coordination bonds and the structured arrangement of solvent molecules around the complexes [27,35].

4. Conclusion

This study successfully synthesized two Schiff base ligands (L1 and L2) and investigated their complexation with Co(II) ions in non-aqueous solvents using conductometric methods. The stability constants of the complexes revealed distinct thermodynamic behaviors: L1 complexes exhibited a consistent decrease in stability with increasing temperature, confirming exothermic reactions. In contrast, L2 complexes displayed solvent-dependent behavior, with exothermic reactions in ethanol and endothermic reactions in acetonitrile and the mixed solvent.

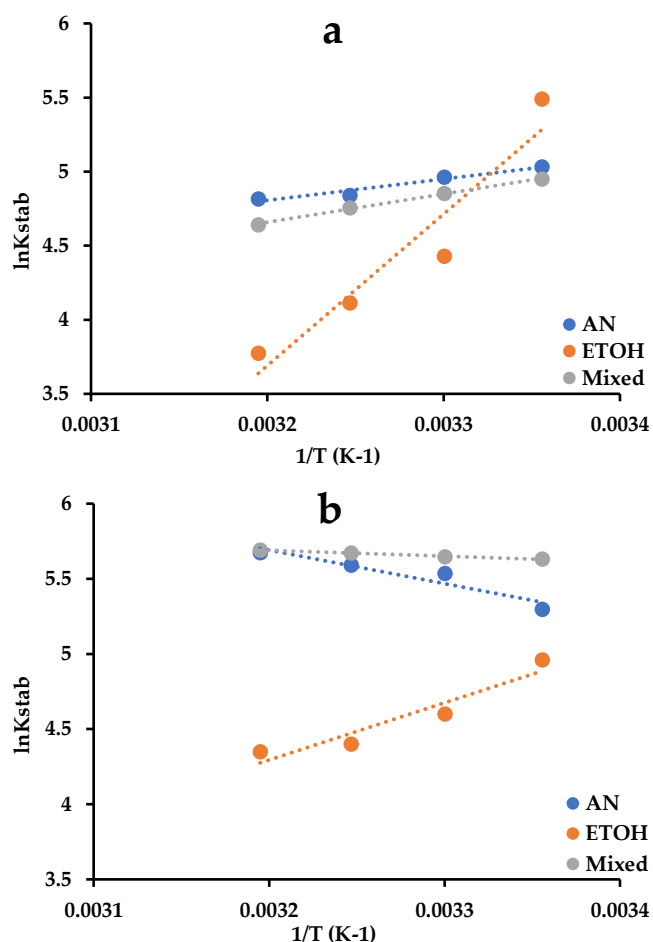


Figure 3. Van't Hoff plots of Co(II) complexes in various solvents: a) with L1 b) with L2

Among the tested solvents, acetonitrile facilitated higher complex stability, attributed to its moderate donor number and solvent-ligand competition. Additionally, L2 complexes demonstrated greater stability compared to L1, likely due to the presence of hydroxyl donor groups, which enhance ligand basicity and reduce steric hindrance around the metal ion. Thermodynamic analysis supported these findings, with negative ΔG values indicating spontaneous reactions and entropy changes reflecting variations in molecular organization within different solvent environments. These results highlight the critical role of solvent

properties, ligand structure, and thermodynamic parameters in determining the stability and behavior of metal-ligand complexes in non-aqueous media. The insights gained may contribute to the rational design of coordination complexes for applications in catalysis, materials science, and analytical chemistry.

Acknowledgements

The authors sincerely thank the Chemistry Department, Faculty of Science, Misurata University, for providing the essential facilities and support for this research. Their invaluable guidance and resources were crucial to completing this work.

Reference

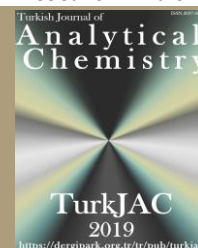
- [1] R. Golbedaghi, F. Khajavi, Investigation of formation constant of complex of a new synthesized tripodal ligand with Cu^{2+} using rank annihilation factor analysis in surfactant media, *Bull Chem Soc Ethiop*, 28(1), 2014, 1-8.
- [2] K.M. Elsherif, A. Zubi, A. Najar, H. Bin Ghashir, Determination of stoichiometry and stability constant of $\text{Cd}(\text{II})$ and $\text{Zn}(\text{II})$ complexes with pyrazole-based ligands in mixed solvent ($\text{EtOH-H}_2\text{O}$), *Sebha Univ J Pure Appl Sci*, 21(2), 2022, 128-134.
- [3] A.S. Alturiqi, E.S. Al-Farraj, M.M. Anazy, R.A. Ammar, Potentiometric determination of stability constants of binary and ternary complexes of L-tryptophan and anti-inflammatory drugs with $\text{Zn}(\text{II})$, *Int J Electrochem Sci*, 17, 2022, Article 220535.
- [4] K.M. Elsherif, Q. Hadidan, K. Alkariwi, Spectrophotometric determination of $\text{Zn}(\text{II})$ and $\text{Cu}(\text{II})$ in analytical samples using murexide reagent, *Prog Chem Biochem Res*, 5(3), 2022, 229-238.
- [5] S. Jadhav, M. Raia, R.K. Pardeshi, M. Farooqi, Determination of stability constant of metal-ligand equilibria with special reference to Schiff base and transition elements, *Der Pharm Lett*, 7(12), 2015, 316-320.
- [6] Z.Y. Alzalouk, K.M.M. Elsherif, A. Zubi, R.M. Atiya, S. Al-Darwish, Metal chelates of copper and nickel with murexide in mixed isopropanol: Water solvent: Spectrophotometric study, *Sci J Fac Sci Sirte Univ*, 3(1), 2023, 9-17.
- [7] K.M. Elsherif, A. Zubi, A. Najar, H. Bin Ghashir, Complexation of pyrazole-based ligands with $\text{Ag}(\text{I})$: Spectrophotometric studies in mixed solvents ($\text{EtOH-H}_2\text{O}$), *Arab J Chem Environ Res*, 5(2), 2021, 138-146.
- [8] A. Miličević, N. Raos, Stability prediction of Cu^{2+} , Ni^{2+} , and Zn^{2+} N-salicylidene-aminoacidato complexes by models based on connectivity index $3\chi_s$, *Cent Eur J Chem*, 12, 2014, 74-79.
- [9] H.B. Shawish, K.M. Elsherif, A.M. Alkheraz, H.I. Shuwat, E.B. Al-Melah, Investigation of substitution reaction kinetics and thermodynamics between salen and $[\text{Cu}(\text{PDTC})_2]$ complex, *J Appl Organomet Chem*, 4(1), 2024, 51-61.
- [10] P.M. Mishra, V. Mishra, Physico-chemical study of transition metal complexes with Schiff's base derived from naphthaldehyde and substituted aromatic amines, *Orient J Chem*, 32(5), 2016, 2745-55.
- [11] M. Payehghadr, H.H. Qezelje, F.M. Dosangani, A. Amiri, S. Hosseini, M.N. Hesarlo, et al., Solution complexation reaction studies of a pyrazoloisoindol derivative ligand by some metal ions in acetonitrile solution, *Orbital Electron J Chem*, 10(6), 2018, 430-434.
- [12] K.M. Elsherif, A. Zubi, H.B. Shawish, S.A. Abajja, E.B.M. Almelah, Complex formation of
- bis(salicylidene)ethylenediamine (Salen type ligand) with copper(II) ions in different solvents: Spectrophotometric and conductometric study, *Int J New Chem*, 7(1), 2020, 1-13.
- [13] M. Payehghadr, S.E. Hashemi, Solvent effect on complexation reactions, *J Inclusion Phenom Macrocycl Chem*, 89(1-2), 2017, 253-271.
- [14] K.M. Elsherif, A. Najar, H. Shuwat, Spectral study of 1,4-bis(3-(2-pyridyl)pyrazol-1-ylmethyl)benzene (PPB): UV-VIS absorption spectra investigation in single and binary solvents and spectrophotometric determination of the dissociation constant (pK_b), *Eurasian J Anal Chem*, 12(1), 2017, 12(1):67-82.
- [15] K.M. Elsherif, A. Zubi, H.B. Shawish, S.A. Abajja, E.B. Almelah, UV-VIS absorption spectral studies of N, N'-bis(salicylidene)ethylenediamine (Salen) in different solvents, *Iraqi J Sci*, 60(2), 2020, 204-210.
- [16] S. Esmailzadeh, G. Mashhadiagha, Formation constants and thermodynamic parameters of bivalent Co, Ni, Cu, and Zn complexes with Schiff base ligand: Experimental and DFT calculations, *Bull Chem Soc Ethiop*, 31(1), 2017, 159-170.
- [17] B.N. Muthal, Synthesis of new Schiff bases and their transition metal complexes ($\text{Co}(\text{II})$, $\text{Ni}(\text{II})$, $\text{Cu}(\text{II})$, & $\text{Zn}(\text{II})$) and their characterization, stability constant, and microbial activities, *Pharma Innov J*, 6(3), 2017, 72-76.
- [18] C. Boulechfar, H. Ferkous, A. Delimi, A. Djedouani, A. Kahlouche, A. Boublia, et al., Schiff bases and their metal complexes: A review on the history, synthesis, and applications, *Inorg Chem Commun*, 150, 2023, 110451.
- [19] B.M. Kalshetty, S.S. Suvarnakhandi, R.C. Sheth, P.S. Hiremath, M.B. Kalashetti, Temperature effect on solution stability constants of metal complexes with Schiff bases derived from 5-aldehydosalicylic acid - aniline and its related compounds, *Int J Appl Biol Pharm Technol*, 2(2), 2011, 88-93.
- [20] A. Farhan, Synthesis, identification of $\text{Co}(\text{II})$, $\text{Cu}(\text{II})$, and $\text{Ni}(\text{II})$ complexes with a Schiff base-azo ligand derived from imidazole derivatives, 4-aminoacetophenone, and 4-chloroaniline, and study of their physical properties and thermodynamic stabilities, *J Univ Babylon Pure Appl Sci*, 27(3), 2019, 406-419.
- [21] L.K. Jha, Study of transition metal complex with Schiff's base derived from naphthaldehyde, *Int J Adv Acad Stud*, 4(1), 2022, 48-51.
- [22] M. Nasir Uddin, D.A. Chowdhury, K. Hossain, Titanium(IV) complexes of unsymmetrical Schiff bases derived from ethylenediamine and o-hydroxyaldehyde/ketone and their antimicrobial evaluation, *J Chin Chem Soc*, 59(12), 2012, 1520-1527.
- [23] C. Demetgül, M. Karakaplan, S. Serin, Synthesis, Characterization and Thermal Properties of Oligo-N,N'-bis (2,4-dihydroxybenzylidene) ethylenediamine and Its Cobalt (II) and Manganese (II) Complexes, *Des Monomers Polym*, 11(6), 2008, 565-579.
- [24] M. Payehghadr, Synthesis and solution complexation studies of a new Schiff base ligand, *J Phys Theor Chem Islamic Azad Univ Iran*, 11(4), 2015, 165-175.
- [25] S. Ahmadzadeh, A. Kassim, M. Rezayi, Y. Abdollahi, G.H. Rounaghi, A conductometric study of complexation reaction between meso-octamethylcalix[4]pyrrole with titanium cation in acetonitrile-ethanol binary mixtures, *Int J Electrochem Sci*, 6, 2011, 4749-4759.
- [26] M. Rezayi, A. Kassim, S. Ahmadzadeh, N.A. Yusof, A. Naji, H. Abbastabar Ahangar, Conductometric determination of formation constants of tris(2-pyridyl)methylamine and titanium(III) in water-acetonitrile mixture, *Int J Electrochem Sci*, 6, 2011, 4378-4387.
- [27] E.R. Enemo, T.E. Ezenwa, E.C. Nleonu, Determination of formation constants and thermodynamic parameters of chromium(III) ions with some ligands by conductometry, *IOSR J Appl Chem*, 12(10), 2019, 54-58.
- [28] K.M. Elsherif, A. Zubi, Z.Y. Alzalouk, S.A. Al-Darwish, Investigation of murexide- $\text{Zn}(\text{II})$ complexes in water-

- isopropanol mixtures: Spectroscopic analysis and stability studies, *Sebha Univ J Pure Appl Sci*, 23(1), 2024, 84-89.
- [29] M. Joshaghani, M.B. Gholivand, F. Ahmadi, Spectrophotometric and conductometric study of complexation of salophen and some transition metal ions in nonaqueous polar solvents, *Spectrochim Acta A Mol Biomol Spectrosc*, 70(5), 2008, 1073-1078.
- [30] S.O. Mohod, D.T. Tayad, D.T. Tayade , To determine the stability constant of Cu(II) with substituted thiocarbamidophenol by spectrophotometric measurements, *Indo Am J Pharm Sci*, 4(2), 2017, 245-247.
- [31] P.R. Smirnov, Comparative characteristics of the nearest environment structures of metal ions in water and acetonitrile (A review), *Russ J Gen Chem*, 93(3), 2023, 575–585.
- [32] K.M. Elsherif, A. Zubi, A. Najar, E. Bazina, Complexation of 1,4-bis(3-(2-pyridyl)pyrazol-1-ylmethyl)benzene (1,4-PPB) with Cu(II), Co(II), and Ni(II): Spectrophotometric studies in mixed solvent (EtOH-H₂O), *To Chem*, 1(2), 2018, 214-223.
- [33] SA-S. Al-Darwish, K.M. Elsherif, A. Zubi, Z.Y. Alzalouk, R.M. Atiya, Study of absorption spectrum of murexide complex with cobalt ion in a water and 2-propanol solvent mixture, *Al-Mukhtar J Sci*, 38(2), 2023, 199-208.
- [34] S. Di Bella, Lewis acidic zinc(II) salen-type Schiff-base complexes: Sensing properties and responsive nanostructures, *Dalton Trans*, 50, 2021, 6050-6063.
- [35] N.O. Tapabashi, A.B. Dakeel, N.O. Tapabashi, Study of the kinetics and thermodynamic parameters of Schiff bases derived from 4-aminoantipyrin, *Cent Asian J Med Nat Sci*, 5(1), 2024, 573-588.



TurkJAC

Turkish Journal of Analytical Chemistry

<https://dergipark.org.tr/tr/pub/turkjac>


Synthesis and characterization of biocopolymer kappa-Carrageenan(κ -C)-g-polyacrylamide/activated bentonite composite*

Kamel Ismet Benabadji^{1**} , Tayeb Hocine¹ , Oussama Bouras¹ , Bouras Brahim¹ ,
Noussaiba Kheir¹

¹ University of Tlemcen, Faculty of Sciences, Department of Chemistry, Laboratory of Organic Electrolyte and Polyelectrolytes Application (LAEPO), BP 119, 13000, Tlemcen, Algeria

Abstract

In the last decade, there is an increased interest to use biodegradable materials. In the present study, new composites based on activated bentonite (BNA)/kappa-Carrageenan (κ -C)/acrylamide (AM) have been prepared by graft copolymerization of AM and kappa-Carrageenan (κ -C) in the presence of activated bentonite (BNA) clay powder, and ammonium persulfate (APS) as an initiator. Different component concentrations of AM and κ -C were used by maintaining 1 g of BNA in all types of composites.

We focused on the interactions between mineral clay structure and polymer matrices.

The structure and morphology of these materials were investigated by FT-IR and XRD, while the thermal properties were tested using TGA.

Evidence of grafting and BNA interaction was obtained by comparison of FTIR and TGA spectra of the initial substrates and the composites. The apparition of new absorption bands at 1256 cm⁻¹, 922 cm⁻¹, and 843 cm⁻¹ confirmed the presence of sulfate groups and correspond to the sulfonic acid group, C-O stretching band, 3, 6-anhydro-D-galactose and glycosidic linkages of κ -C backbone, in the composite structure. Electrostatic interactions and/or hydrogen bonds may have occurred between BNA and (κ -C/AM) copolymer.

TGA analysis showed the thermal stability improved by adding BNA clay particles.

The formation of intercalated nanocomposites in the case of C1 ((BNA/ κ -C/AM) (1/0.5/0.5)), C2 ((BNA/ κ -C/AM) (1/1/0.5)), C3 ((BNA/ κ -C/AM) (1/0.5/1)) and C4((BNA/ κ -C/AM) (1/1/1) samples was confirmed by XRD analysis. The shift of peak attributed to montmorillonite in the several composites except C4 to lower angles in XRD diffractometer suggests the formation of intercalated nanocomposites.

The absence of the basal peak corresponding to montmorillonite phase in the case of C4 composite suggests a high dispersion of clay platelets, named exfoliation in the nanocomposite material.

The obtained results from this study suggest that the prepared composites could be effectively applied for removing cationic dyes from aqueous solutions.

Keywords: Acrylamide, activated bentonite, carrageenan, composite

1. Introduction

The treatment of contaminated wastewater is one of the most serious environmental problems faced by chemical, pharmaceutical, textile, polymer, plastic, and leather industries. Recently, much attention has been focused on the use of a new generation of absorbent composites. These materials are essentially prepared by including inorganic clays into the polymeric matrix.

Due to their large surface area and high cation exchange capacity, clays such as montmorillonite [1,2] and bentonite [3], have been studied for potential applications as environmental remediation adsorbent

for heavy metals and organic compounds adsorption. The addition of these types of minerals in a composite mixture not only improves some properties such as swelling ability, gel strength, mechanical, and thermal stability but also significantly reduces production cost [4–6]. However, for extensive process utilization, most of these materials are not suitable. To resolve these issues, modification of conventional adsorbents by using a polysaccharide matrix is an ideal alternative.

Among the most abundant polysaccharides, carrageenans are soluble polysaccharides extracted from

Citation: K.I. Benabadji, T. Hocine, O. Bouras, B. Brahim, N. Kheir, Synthesis and characterization of biocopolymer kappa-Carrageenan(κ -C)-g-polyacrylamide/activated bentonite composite, Turk J Anal Chem, 7(2), 2025, 79–84.

****Author of correspondence:** bismetdz@yahoo.fr

Tel: +00213771872929

Fax: N/A

Received: December 30, 2024 **Accepted:** March 14, 2025

doi <https://doi.org/10.51435/turkjac.1610186>

*This paper was presented at the 6th International Environmental Chemistry Congress, EnviroChem 05-08 November 2024, Trabzon Türkiye.

red seaweeds. They have strong gel-forming ability and are biocompatible. They consist of long linear chains of D-anhydrogalactose and D-galactose with anionic sulfate groups ($-\text{OSO}_3^-$) [7]. There are three types of carrageenans: kappa (κ), iota (ι), and lambda (λ) which differ in sulfate ester and 3,6-anhydro- α -D-galactopyranosyl content. Their water solubility is strongly related to the content of sulfate groups and associated ions.

The structure of κ -carrageenan consists of the 4-sulfate-O- β -D-galactopyranosyl-(1,4)-3,6-anhydro- α -D-galactose units [8]. It is commonly used as a thickening and stabilizing agent in prepared foods, cosmetics, and pharmaceuticals. κ -Carrageenan has also been used to prepare biodegradable films for biomedical applications [9].

Due to their high biodegradability, biocompatibility, and nontoxicity, hydrogels based on carrageenans have been also used as potential adsorbents for eliminating pollution like dyes from aqueous solutions [10,11].

Moreover, the combination of diverse structures like bentonite nanoclay [12], montmorillonite clay [13] and other nanomaterials with carrageenan has paved the way for scientists to prepare new materials with interesting properties.

Including inorganic clays into a polymeric matrix improves some properties of plastics and gels [14]. A new generation of adsorbent composites was prepared by incorporating montmorillonite [15], attapulgite [16–18], kaolin [19–21], hydrotalcite [22,23], mica [24], bentonite [25,26] and laponite [27] into polymeric matrices. OH reactive groups contained on layered aluminosilicate surface are enabled to interact with reactive sites of natural polymers and monomers and lead to the formation of composites with high adsorption capacities.

The aim of this study was to develop new composites based on κ -carrageenan, acrylamide and activated bentonite.

2. Experimental

2.1. Materials and methods

Acrylamide (AM), ammonium persulfate [APS], and kappa-Carrageenan (κ -C) were supplied by Merck. In our earlier work, we prepared activated bentonite (BNA) by modifying raw clay (RC) particles [28]. The solid phase of RC was dispersed in a sodium chloride solution (1M). This operation was repeated three times. To remove excess salt, the resulting solid after saturation was washed with bidistilled water several times; the final product was BNA. The hexamminecobalt(III) chloride was used to determine the cation exchange capacity (CEC), which was found to be equal to 85 meq/g/100 g.

A series of BNA/ κ -C/AM with different contents of κ -C and AM was simply prepared. A constant mass weight of BNA was used (Table 1).

The κ -C solution has been prepared by slow addition of a weighted amount of κ -C powder to bidistilled water in a 100-mL three-necked flask equipped with a mechanical stirrer and a reflux condenser. The solution was heated to 65 °C. After complete dissolution of κ -C, APS initiator (0.1 g dissolved in 3 mL distilled water) was added and kept at 65 °C for 10 min to generate radicals. 1 g of BNA particles was dispersed separately in 12 mL of distilled water and 5 mL of monomer solution containing pre-weighted amount of AM was added. This mixture was poured into the flask containing κ -C radicals. The temperature was raised to 80 °C and maintained for 1 hour to complete the reaction.

After 24 hours, the obtained composite was precipitated by pouring it into the water/absolute ethanol mixture (ratio 1:5). The precipitate was filtered and subsequently dried in an oven at 75 °C for 24 hours.

The codes and the composition of composites are presented in Table 1.

Table 1. Sample codes and composition

Code	κ -Carrageenan mass (g)	Acrylamide mass (g)	BNA mass (g)
C1 (BNA/ κ -C/AM) (1/0.5/0.5)	0.5	0.5	1
C2 (BNA/ κ -C/AM) (1/1/0.5)	1	0.5	1
C3 (BNA/ κ -C/AM) (1/0.5/1)	0.5	1	1
C4 (BNA/ κ -C/AM) (1/1/1)	1	1	1

2.1.1. Fourier transform infrared spectroscopy (FTIR)

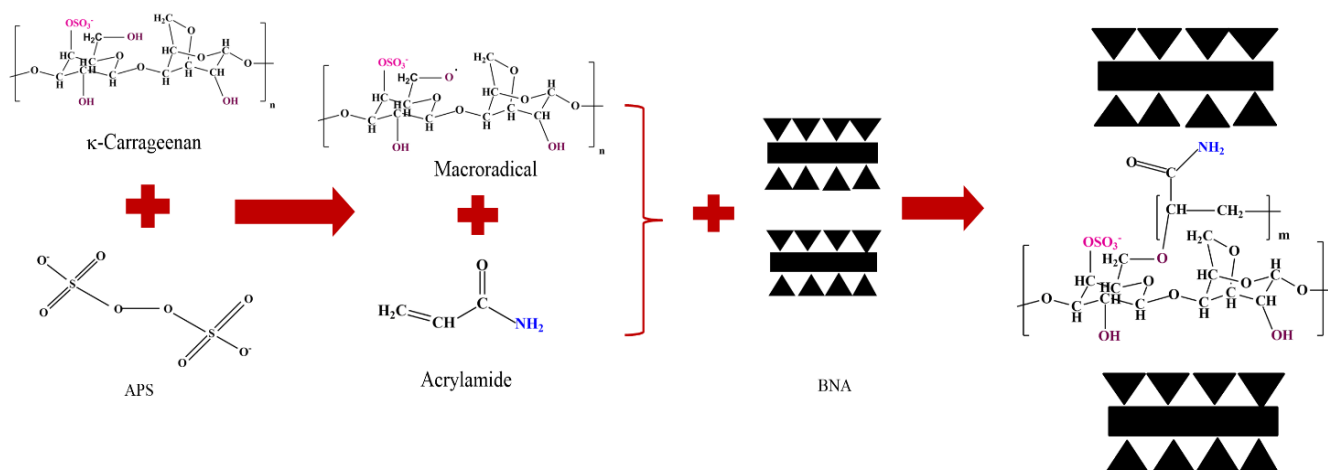
The ATR-FT-IR spectra of the samples were measured at 4 cm^{-1} resolution and a mirror velocity of 0.6329 cm/s in the 4000-500 cm^{-1} region, on an Agilent Cary 600 Series FTIR Spectrometer equipped with DRIFT (Diffuse Reflectance Infra-red Fourier Transform) accessories. Five recordings were performed for each sample, and the evaluations were made based on the average spectrum.

2.1.2. Thermogravimetric analysis measurements

Thermogravimetric analyses of the samples were performed by high-resolution TGA (TA Instruments Q Series Q600 SDT). 10 mg of finely ground sample was heated in an open platinum crucible with a heating rate of 10 °C min^{-1} and temperature from 50 to 800 °C under nitrogen atmosphere flow rate of 100 mL/min.

2.1.3. X-ray diffraction (XRD)

The measurements were performed on an X-ray diffractometer ULTIMA IV (Rigaku, Tokyo, Japan), using the $\text{CuK}\alpha$ radiation ($\lambda = 1.54 \text{ \AA}$) at 40 kV and 30 mA. All diffractograms were recorded in the 5-80 2θ degrees range at room temperature. A scan speed of 2°/min and a step size of 0.02° were considered to achieve measurements.



Scheme 1. BNA/κ-C/AM composite structure

3. Results and discussion

The composite was prepared by graft copolymerization of acrylamide onto κ-C in the presence of bentonite particles (Scheme 1).

Ammonium persulfate was used as an initiator. The persulfate is decomposed under heating and generates sulfate anion radicals that abstract hydrogen from OH groups of κ-C backbones. So, this persulfate-saccharide redox system results in active centers capable of radically initiating the polymerization of acrylamide, leading to a graft copolymer.

3.1. FTIR analysis

FTIR spectroscopy was used for identification of the composites. Fig. 1(a) and Fig. 1(b) represent the spectra of κ-carrageenan and the different BNA/κ-C/AM composites, respectively.

The spectra of κ-carrageenan showed a broad absorption at 3440 cm⁻¹ and 2954 cm⁻¹ due to the stretching frequency of the O-H and C-H. The bands at 1256 cm⁻¹, 922 cm⁻¹, and 843 cm⁻¹ are attributed to the presence of sulfate groups and correspond to the sulfonic acid group, C-O stretching band, 3, 6-anhydro-D-galactose and glycosidic linkages of κ-C backbone, respectively [29].

On IR spectra of BNA/κ-C/AM composites, it was observed that the signal hydroxyl peak between 3450 cm⁻¹ and 3627 cm⁻¹ became stronger, which could be explained by the superposition of the stretching vibration of O-H groups in all materials.

The intensities of those FTIR characteristic peaks corresponding to κ-C in various BNA/κ-C/AM composites increased with the increase in κ-C mass.

The presence of PAM polymer in different composites is also confirmed by the apparition of a new band at 3193 cm⁻¹ corresponding to νN-H (sym). This band is more pronounced in C3 and C4 composites. The bands at 1607 and 1453 cm⁻¹ are ascribed to δN-H (amide II) and νC-N (amide III), respectively [30]. These findings confirmed that BNA/κ-C/AM composites structure was prepared successfully.

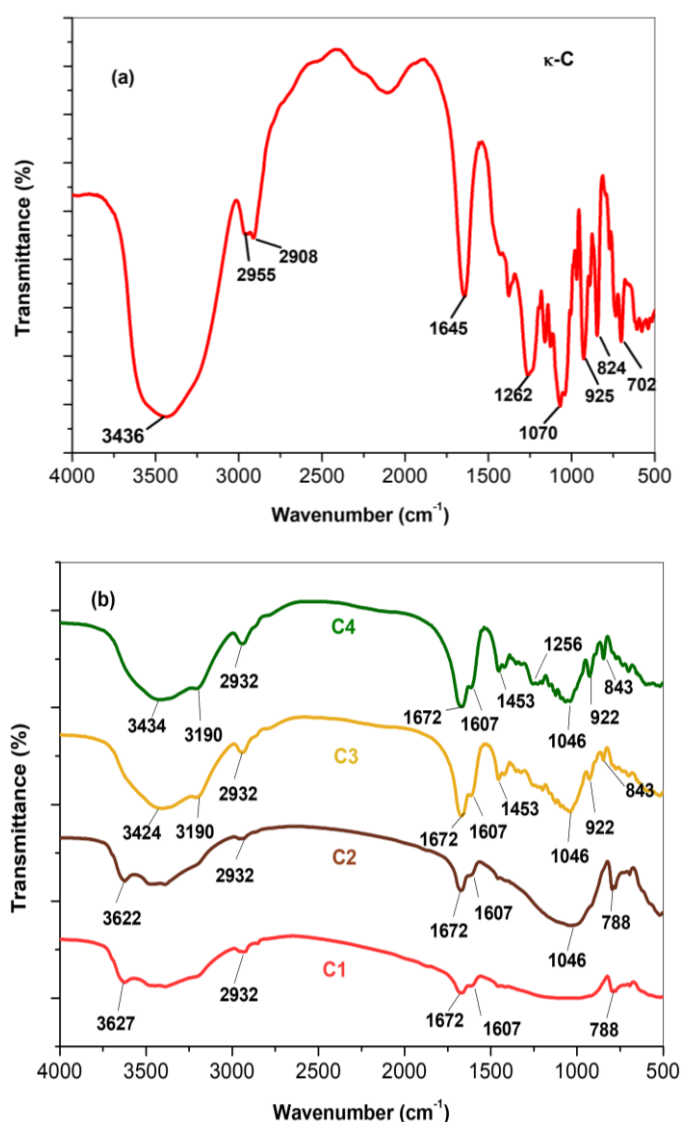


Figure 1. FTIR spectrum of κ-C (a), and BNA/κ-C/AM composites (b)

3.2. Thermogravimetric analysis

The thermal stabilities of κ-carrageenan and its various composites were analyzed using thermogravimetric analysis (TGA), and the obtained resulting TGA curves are presented in Fig. 2.

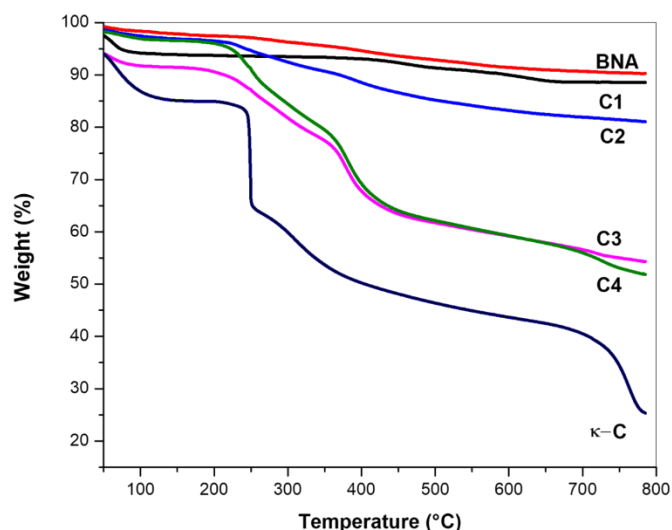


Figure 2. TGA curves of BNA, κ -C and BNA/ κ -C/AM composites

It is seen from the Fig. 2 that the weight loss of pure κ -carrageenan occurred in three different stages. The first one, located in the temperature range of 45–150 °C, was due to the adsorbed water by κ -carrageenan. The decomposition of κ -carrageenan started at 203 °C. For κ -carrageenan, the second weight loss of 21.04% in the temperature range of 209–262 °C and the third weight loss of 38.4% in the temperature range of 262–785 °C were observed. The residual weight observed in pure κ -carrageenan is 25.35%. A similar thermal decomposition behavior was previously reported [31].

For BNA/ κ -C/AM composites, the first degradation stage (50–150 °C) is also observed. This could be attributed to the loss of moisture content as hydrogen-bound water as well as the dehydration of BNA clay. With increasing temperature, both of the second and third degradation stages took place beyond 200 °C.

The second stage of decomposition occurred between 200 and 650 °C and corresponds to weight losses of 6.47, 6.64, 32.65, and 38.19% for C1 C2, C3, and C4 composites samples, respectively. These values are probably due to the degradations of κ -C and polyacrylamide. The random breaking chains of polysaccharide occur between 200 and 350 °C. In the range of temperature between 220 and 440 °C, the degradation is also due to both weight losses of NH_2 of amide side groups in ammonia form and to chain breakdown of polyacrylamide [32].

On the other hand, the different BNA/ κ -C/AM composites were found to be more thermally stable with increasing temperature than the pure polymer.

These observations could be related to the stability of BNA at higher temperatures since the dehydroxylation of the aluminosilicates within the BNA clay layers occurs at temperatures beyond 650 °C. As a result, BNA enhanced the stability of the developed composites and to the interaction between BNA particles and κ -C/AM mixture.

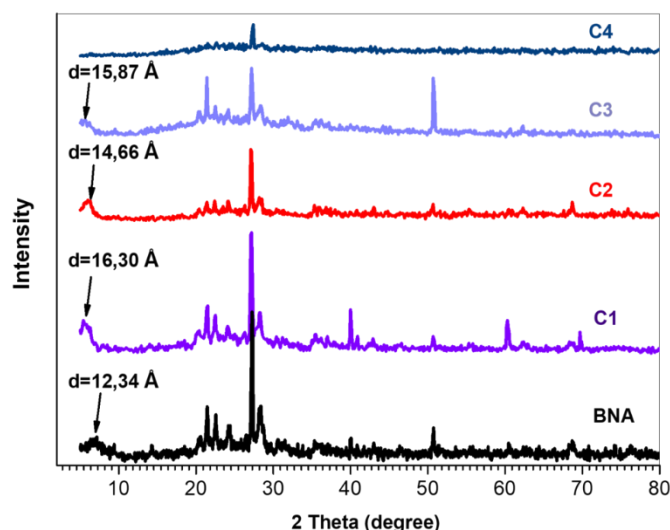


Figure 3. XRD patterns BNA and BNA/ κ -C/AM composites

The obtained results are consistent with other studies that focused on studying the effect of clay encapsulation on the thermal behavior of beads prepared from other natural polysaccharides [33,34].

3.3. X-ray diffraction analysis

To reveal the state of the BNA sheets in the prepared composites, XRD measurements were carried out on the dried materials with various κ -C and AM contents. The XRD patterns of the different BNA/ κ -C/AM composites with various weight ratios of κ -C and AM to BNA are shown in Fig. 3.

For κ -C, two signals were observed [35,36]: one at 4.5°, indicating the crystalline region, and a broad signal in the range of 12° to 25°, which reflects its semicrystalline nature.

The XRD of BNA contains a well-pronounced reflection at $2\theta = 7.15^\circ$ (d spacing of 12.34Å), corresponding to the spacing between BNA sheets.

With increasing κ -C and AM content, the diffraction signals were shifted to lower values corresponding to basal spacings from 12.34Å to 16.3Å, 14.66Å and 15.87Å for C1, C2, and C3 composites, respectively. These results suggest the intercalation of polymer chains between BNA sheets [37,38].

The absence of the basal peak corresponding to montmorillonite phase in the case of C4 composite suggests a high dispersion of clay platelets, named exfoliation in the nanocomposite material.

4. Conclusion

A new composite material was prepared by graft copolymerization of AM onto κ -C in the presence of ammonium persulfate as the initiator and BNA particles.

A series of composites were prepared by varying κ -C and AM amounts. The obtained materials were

evaluated for their thermal stability, structural features, and interactions.

Infrared spectroscopy showed the presence of interactions between κ -C, AM, and BNA, especially via electrostatic interactions and/or hydrogen bonding.

The thermal stability of the resultant composites was significantly improved by the presence of BNA. The moisture adsorption of the prepared composites was reduced. This behavior is probably attributed to the interfacial interaction between the κ -C/AM mixture matrix and BNA.

X-ray diffraction revealed that the incorporation of BNA into the κ -C and AM enhances the formation of an intercalated nanocomposite structure in the case of C1, C2, and C3 samples, where the polymer chains were intercalated between the clay sheets. The formation of exfoliated nanocomposite structure in the case of the C4 sample is clear when κ -C and AM amounts were 1 g for each component.

References

- [1] C. Erbil, D. Topuz, A. Gökçeören, B. Şenkal, Network parameters of poly(*N*-isopropylacrylamide)/montmorillonite hydrogels: effects of accelerator and clay content, *Polym Adv Technol*, 22, 2011, 1696-1704.
- [2] M. Ikeda, T. Yoshii, T. Matsui, T. Tanida, H. Komatsu, I. Hamachi, Montmorillonite-Supramolecular Hydrogel Hybrid for Fluorocolorimetric Sensing of Polyamines, *J Am Chem Soc*, 133, 2011, 1670-1673.
- [3] H. Kalaleh, M. Tally, Y. Atassi, Preparation of bentonite-g-poly(acrylate-co-acrylamide) superabsorbent polymer composite for agricultural applications: Optimization and characterization, *Polym Sci Ser B*, 57, 2015, 750-758.
- [4] W. Huang, J. Shen, N. Li, M. Ye, Study on a new polymer/graphene oxide/clay double network hydrogel with improved response rate and mechanical properties, *Polym Eng Sci*, 55, 2015, 1361-1366.
- [5] J. Du, P. Chen, A. Adalati, S. Xu, R. Wu, J. Wang, C. Zhang, Preparation and mechanical properties of a transparent ionic nanocomposite hydrogel, *J Polym Res*, 21, 2014, 1-6.
- [6] A. Rashidzadeh, A. Olad, D. Salari, A. Reyhanitabar, On the preparation and swelling properties of hydrogel nanocomposite based on Sodium alginate-g-Poly(acrylic acid-co acrylamide)/Clinoptilolite and its application as slow release fertilizer, *J Polym Res*, 21, 2014, 1-15.
- [7] A.A. Oun, J.W. Rhim, Carrageenan-based hydrogels and films: effect of ZnO and CuO nanoparticles on the physical, mechanical, and antimicrobial properties, *Food Hydrocoll*, 67, 2017, 45-53.
- [8] Z. Yao, F. Wang, Z. Gao, L. Jin, H. Wu, Characterization of a κ -Carrageenase from marine *Cellulophaga lytica* strain N5-2 and analysis of its degradation products, *Int J Mol Sci*, 14, 2013, 24592-24602.
- [9] G. Sun, T. Liang, W. Tan, L. Wang, Rheological behaviors and physical properties of plasticized hydrogel films developed from κ -carrageenan incorporating hydroxypropyl methylcellulose, *Food Hydrocoll*, 85, 2018, 61-68.
- [10] S. Lapwanit, T. Sooksimuang, T. Trakulsujaritchook, Adsorptive removal of cationic methylene blue dye by kappa-carrageenan/poly(glycidyl methacrylate) hydrogel beads: preparation and characterization, *J Environ Chem Eng*, 6, 2018, 6221-6230.
- [11] O. Levy-Ontman, C. Yanay, O. Paz-Tal, A. Wolfson, Iota-carrageenan as sustainable bio-adsorbent for the removal of europium ions from aqueous solutions, *Mater Today Commun*, 32, 2022, 104111.
- [12] B.I. Dogaru, B. Simionescu, M.C. Popescu, Synthesis and characterization of κ -carrageenan bio-nanocomposite films reinforced with bentonite nanoclay, *Int J Biologic Macromol*, 154, 2020, 9-17.
- [13] O. Goncharuk, O. Siryk, M. Frac, N. Guzenko, K. Samchenko, K. Terpilowski, K. Szewczuk-Karpisz, Synthesis, characterization and biocompatibility of hybrid hydrogels based on alginate, κ -carrageenan, and chitosan filled with montmorillonite clay, *Int J Biologic Macromol*, 278, 2024, 134703.
- [14] A. El Halah, J. Contreras, L. Rojas-Rojas, M. Rivas, M. Romero, F. López-Carrasquero, New superabsorbent hydrogels synthesized by copolymerization of acrylamide and *N*-2-hydroxyethyl acrylamide with itaconic acid or itaconates containing ethylene oxide units in the side chain, *J Polym Res*, 22, 2015, 1-10.
- [15] M. Ikeda, T. Yoshii, T. Matsui, T. Tanida, H. Komatsu, I. Hamachi, Rational Molecular Design of Stimulus-Responsive Supramolecular Hydrogels Based on Dipeptides, *J Am Chem Soc*, 133, 2011, 1670-1673.
- [16] J. Zhang, H. Chen, A. Wang, Study on superabsorbent composite-VII. Effects of organification of attapulgite on swelling behaviors of poly(acrylic acid-co-acrylamide)/sodium humate/organo-attapulgite composite, *Eur Polym J*, 42, 2006, 101-108.
- [17] X. Qi, M. Liu, Z. Chen, Study on swelling behavior of poly(sodium acrylate-co-2-acryloylamino-2-methyl-1-propanesulfonic acid)/attapulgite macroporous superabsorbent composite, *Polym Eng Sci*, 55, 2015, 681-687.
- [18] Q. Wang, W. Wang, J. Wu, A. Wang, Effect of Attapulgite Contents on Release Behaviors of a pH Sensitive Carboxymethyl Cellulose-g-Poly(acrylic acid)/ Attapulgite/Sodium Alginate Composite Hydrogel Bead Containing Diclofenac, *J Appl Polym Sci*, 124, 2012, 4424-4432.
- [19] A.K. Pradhan, P.K. Rana, P.K. Sahoo, Biodegradability and swelling capacity of kaolin based chitosan-g-PHEMA nanocomposite hydrogel, *Int J Biologic Macromol*, 74, 2015, 620-626.
- [20] X. Chen, J. Li, C. Mao, X. Jiao, Y. Liu, J. Gong, Y. Zhao, A Novel Superabsorbent Composite Based on Poly(Aspartic Acid) and Organo-Kaolin, *J Macromol Sci A*, 51, 2014, 799-804.
- [21] A. Pourjavadi, H. Ghasemzadeh, R. Soleyman, Synthesis, characterization, and swelling behavior of alginate-g-poly(sodium acrylate)/kaolin superabsorbent hydrogel composites, *Appl Polym Sci*, 105, 2007, 2631-2639.
- [22] Y.T. Zhang, L.H. Fan, T.T. Zhi, L. Zhang, H. Huang, H.L. Chen, Synthesis and characterization of poly(acrylic acid-co-acrylamide)/hydrotalcite nanocomposite hydrogels for carbonic anhydrase immobilization, *J Polym Sci A Polym Chem*, 47, 2009, 3232-3240.
- [23] W-F. Lee, Y-C. Chen, Effects of intercalated hydrotalcite on drug release behavior for poly(acrylic acid-co-*N*-isopropyl acrylamide)/intercalated hydrotalcite hydrogels, *Eur Polym J*, 42, 2006, 1634-1642.
- [24] N. Limparyoon, N. Seetapan, S. Kiatkamjornwong, Acrylamide/2-acrylamido-2-methylpropane sulfonic acid and associated sodium salt superabsorbent copolymer nanocomposites with mica as fire retardants, *Polym Degrad Stab*, 96, 2011, 1054-1063.
- [25] L.H. Fu, T.H. Cao, Z.W. Lei, H. Chen, Y.G. Shi, C. Xu, Biocompatible and biodegradable chitosan/sodium polyacrylate polyelectrolyte complex hydrogels with smart responsiveness, *Mater Des*, 94, 2016, 322-329.

- [26] H. Kalaleh, M. Tally, Y. Atassi, Preparation of bentonite-g-poly(acrylate-co-acrylamide) superabsorbent polymer composite for agricultural applications: Optimization and characterization, *Polym Sci Ser B*, 57, 2015, 750-758.
- [27] G.B. Marandi, M. Baharloui, M. Kurdtabar, Hydrogel with high laponite content as nanoclay: swelling and cationic dye adsorption properties, *Res Chem Intermed*, 41, 2015, 7043-7058.
- [28] S. Merad Boudia, K.I. Benabadji, B. Bouras, Graphene Oxide/Activated Clay/Gelatin Composites: Synthesis, Characterization and Properties, *Phys Chem Res*, 10, 2022, 143-150.
- [29] A.M. Salgueiro, A.L. Daniel-da-Silva, A.V. Girão, P.C. Pinheiro, T. Trindade, Unusual dye adsorption behavior of κ -carrageenan coated superparamagnetic nanoparticles, *Chemical Engineering Journal*, 229, 2013, 276-284.
- [30] R.M. Silverstein, G.C. Bassler, T.C. Morrill, *Spectrometric identification of organic compounds* (7. edition), 2013, New York, John Wiley & Sons.
- [31] O. Duman, T. Gürkan Polat, C. Özcan Diker, S. Tunç, Agar/ κ -carrageenan composite hydrogel adsorbent for the removal of Methylene Blue from water, *International Journal of Biological Macromolecules*, 160, 2020, 823-835.
- [32] H. Ferfera-Harrar, H. Aiouaz, N. Dairi, Synthesis and Properties of Chitosan-Graft Polyacrylamide/Gelatin Superabsorbent Composites for Wastewater Purification World Academy of Science, Engineering and Technology International Journal of Chemical and Molecular Engineering, 9:7, 2015, 849-856.
- [33] N. Belhouchat, H. Zaghoulane-Boudiaf, C. Viseras, Removal of anionic and cationic dyes from aqueous solution with activated organo-bentonite/sodium alginate encapsulated beads, *Appl Clay Sci*, 35, 2017, 9-15.
- [34] A. Ely, M. Baudu, J.P. Basly, M.O. Kankou, Copper and nitrophenol pollutants removal by Na-montmorillonite/alginate microcapsules, *J Hazard Mater*, 171, 2009, 405-409.
- [35] A.M. Ili Balqis, M.A.R. Nor Khaizura, A.R. Russly, Z.A. Nur Hanani, Effects of plasticizers on the physicochemical properties of kappa-carrageenan films extracted from *Eucommia cottonii*, *Int J Biol Macromol*, 103, 2017, 721-732.
- [36] S. Shankara, J.P. Reddy, J.-W. Rhima, H.-Y. Kim, Preparation, characterization, and antimicrobial activity of chitin nanofibrils reinforced carrageenan nanocomposite films, *Carbohydr. Polym.* 117, 2015, 468-475.
- [37] M.J. Sanchis, M. Carsía, M. Culebras, C.M. Gómez, S. Rodriguez, F.G. Torres, Molecular dynamics of carrageenan composites reinforced with cloisite Na⁺ montmorillonite nanoclay, *Carbohydr Polym*, 176, 2017, 117-126.
- [38] A. Pourjavadi, Z. Bassampour, H. Ghasemzadeh, M. Nazari, L. Zolghadr, S.H. Hosseini, Porous carrageenan-g-polyacrylamide/bentonite superabsorbent composites: swelling and dye adsorption behavior, *J Polym Res*, 23, 2016, 60.

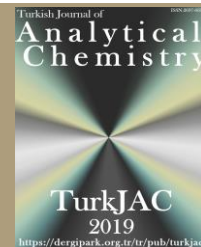


TurkJAC

Turkish Journal of

Analytical Chemistry

https://dergipark.org.tr/tr/pub/turkjac

TurkJAC
2019

https://dergipark.org.tr/tr/pub/turkjac

Evaluation of antioxidant, antimicrobial, and α -amylase enzyme inhibition properties of *Rosa canina* seed extracts prepared with different solvents using maceration and ultrasound-assisted extraction methods

Kağan Kiliç^{1*} , İmdat Aygöl² , Osman Akmeşe³ , Cemalettin Baltacı⁴ , Mohammed Abdulsamad Hafedh⁵

¹Gümüşhane University, Faculty of Engineering and Life Sciences, Department of Genetics and Bioengineering, 29100, Gümüşhane, Türkiye

²Gümüşhane University, Faculty of Health Sciences, Department of Nutrition and Dietetics, 29100, Gümüşhane, Türkiye

³Gümüşhane University, Central Research Laboratory Application and Research Center, 29000, Gümüşhane, Türkiye.

⁴Gümüşhane University, Faculty of Engineering and Life Sciences, Department of Food Engineering, 29100, Gümüşhane, Türkiye

⁵Gümüşhane University, Graduate Education Institute Department of Biotechnology, 29100, Gümüşhane Türkiye

Abstract

The efficient extraction of bioactive molecules from medicinal plants is strongly related to the solvents and methods used. This study evaluated the impact of solvent selection and extraction methods on the bioactive potential of *Rosa canina* seed extracts, focusing on antioxidant, antimicrobial, and α -amylase inhibitory activities. Four solvents —dimethyl sulfoxide (DMSO), ethanol-water (80:20), ethyl acetate, and acetonitrile— were paired with maceration and ultrasonic techniques to generate eight extracts (DMM, DMU, ESM, ESU, EAM, EAU, ACM, ACS). Antioxidant activity was assessed via total phenolic (TPC) and flavonoid (TFC) content, FRAP, DPPH, and ABTS assays. Antimicrobial efficacy was tested against seven microorganisms (Gram+, Gram-, and yeast) using well diffusion and MIC methods, while α -amylase inhibition was quantified via IC₅₀.

The ethyl acetate ultrasonic extract (EAU) exhibited the highest TPC (63.86 mg GAE/g) and TFC (210.23 mg QE/g), along with superior antioxidant activity across all assays ($P < 0.05$). Ethyl acetate maceration (EAM) ranked second, underscoring ethyl acetate's efficacy. Acetonitrile maceration (ACM) demonstrated the strongest α -amylase inhibition (IC₅₀ = 20.46 mg/mL). All extracts showed notable antimicrobial activity against *Aeromonas hydrophila* and *Klebsiella pneumoniae*, though efficacy varied for other strains. DMSO-based extracts (DMM/DMU) consistently underperformed. These findings highlight ethyl acetate (EAU/EAM) as optimal for antioxidant-rich extracts and ACM for enzyme inhibition, positioning *Rosa canina* seeds as a promising source of natural bioactive compounds for functional food and therapeutic applications.

Keywords: Antioxidant, antimicrobial, maceration, rosa canina seeds, solvent, ultrasonication

1. Introduction

There is an increasing interest in medicinal plant products today, and according to the World Health Organization (WHO), although there are differences between developed, underdeveloped, and developing countries, it has been reported that the global trust and usage rate of herbal products for therapeutic purposes has reached up to 80% [1]. During metabolic processes in plants, chemical reactions result in the formation of compounds known as primary and secondary metabolites, which are commonly used in various industrial fields, including agriculture, medicine, and

pharmaceuticals, to produce a wide range of products [2].

The genus *Rosa*, which belongs to the Rosaceae family, includes more than 100 species found in North America, Europe, Western Asia, and the Middle East [3, 4], and approximately 25% of these species are found in Türkiye [5]. *Rosa* species are widely used in traditional medicine. *Rosa canina*, commonly known as Rosehip, Dog Rose, Wild Rose, or Hip Rose, is a shrub that can grow at various altitudes [3]. With cultural diversity, rosehip is consumed in various forms such as herbal tea,

Citation: K. Kiliç, İ. Aygöl, O. Akmeşe, C. Baltacı, M.A. Hafedh, Evaluation of antioxidant, antimicrobial, and α -amylase enzyme inhibition properties of *Rosa canina* seed extracts prepared with different solvents using maceration and ultrasound-assisted extraction methods, Turk J Anal Chem, 7(2), 2025, 85–96.

*** Author of correspondence:** kagankilinc@yahoo.com

Tel: +90 (456) 233 10 00

Fax: +90 (456) 233 10 75

Received: February 20, 2025

Accepted: February 7, 2025

doi <https://doi.org/10.51435/turkjac.1643744>

marmalade, juice, jam, sweets, cakes, and even soup. Its maturation process lasts from the end of September until the beginning of November, and it is harvested during this period [6].

Rosa species are commonly used in traditional treatments for digestive disorders, colds, constipation, and some inflammatory diseases. The fruits of *Rosa canina* are especially consumed in the form of tea during the winter months. Various studies have demonstrated that the fleshy fruit, seeds, roots, flowers, and leaves of rosehip possess bioactive properties that can contribute to modern medicine, in addition to their traditional medicinal uses. These properties include anticancer, antimicrobial, anti-inflammatory, antidiabetic effects, and immune system enhancement [7–9]. It is stated that the therapeutic effects of rose hips are based on its high content of elements and compounds with antioxidant activity [9,10].

The main bioactive compounds in rosehip include amino acids, vitamin C, phenolic acids, flavonoids, carotenoids, anthocyanins, α - and β -tocopherols, tannins, pectins, essential and unsaturated oils, as well as magnesium and calcium [6–11]. Antioxidants neutralize free oxygen radicals, which are known to be effective in the development of various acute and chronic inflammatory diseases, cancer, cardiovascular diseases, and arthritis, thereby playing a protective role against these diseases [5,7]. There are several factors that determine the biological activity of phytochemicals. These factors include the plant part (flower, leaf, fruit, seed, root), maturation time, altitude, temperature, humidity, soil quality, climate-related factors, drying, storage, and preservation conditions, and the method of consumption (infusion, grinding, boiling, direct consumption, etc.) [12,13]. For this purpose, various techniques are employed to effectively utilize bioactive compounds in functional foods.

Rosehip seeds have a higher oil content compared to fruit skin and are considered a good source of unsaturated fatty acids, especially omega-3, oleic, linoleic, and linolenic acids [14,15]. Recently, the use of seed extracts, particularly in industries such as cosmetics, has gained attention, which in turn increases the significance of rosehip. This distinguishing feature of rosehip fruit and seeds may require the use of different extraction methods and solvents. Indeed, less polar or nonpolar solvents may be more effective in extracting the seed content compared to water, particularly for water-insoluble seed compounds.

2. Material and methods

2.1.2.1. Chemicals and equipment

In this study analytical or HPLC grade reagents and chemicals were used. Chemicals used in phenolic and flavonoid contents, (FRAP, DPPH, and ABTS reactives,

gallic acid, quercetin, trolox, Na_2CO_3 , AlCl_3 , NaOH , ascorbic acid, Folin-Ciocalteu reagent), and solvents (dimethyl sulfoxide, acetic acid, ethanol, ethyl acetate, and acetonitrile), Nutrient Broth and Mueller-Hinton Agar media used in antimicrobial activity analysis were purchased from Sigma-Aldrich and Merck (St. Louis and Burlington, MA USA). Instruments and other equipment used are mentioned in the text.

2.2. Plant material

Rosehip fruits were collected in early October 2024 from the Arzular Kabaköy district of Gümüşhane province (40°26'44.4" N - 39°44'40.4" E). The fruits, each weighing approximately 250 grams, were placed in airtight refrigerator bags and transported to the laboratory. The fresh fruit samples were dried at room temperature, away from direct sunlight. After washing, the fruits were further dried in an oven at 37 °C. The seeds were separated from their peels with a scalpel and the remaining fibers were removed with an air sprayer. Seeds were ground into a powder using a grinder (IKA A-10, Germany). The seed powders were aliquoted into 15 mL Falcon tubes and stored at -80 °C in a deep freezer (Thermo Scientific, USA) until further analysis.

2.3. Extraction of rosehip seeds

The extraction methods were partially modified from the method of Oz et al. [16]. Rosehip seed powders were weighed to 2 grams using a precision balance (KERN, Germany) and transferred into 100 mL capped glass bottles. To each seed powder sample, 40 mL of one of the following solvents was added: acidified dimethyl sulfoxide (DMSO, 1% acetic acid), ethanol-distilled water (80:20, v/v), ethyl acetate, or acetonitrile. After the bottles were thoroughly shaken, they were mixed for 30 minutes at room temperature on a magnetic stirrer at 250 rpm.

2.3.1. Maceration method

After magnetic stirring, the samples were incubated for 24 hours in a shaking incubator (Shel Lab, UK) at 37 °C and 150 rpm under dark conditions. Following incubation, the samples were sequentially filtered through coarse filter paper and a 0.45 μm membrane filter. The filtrates were then concentrated using a rotary evaporator (Heidolph, Germany) under reduced pressure (10 mbar) at 60 °C. Any remaining solvent was completely evaporated in a fanned and air-flow oven at 60 °C until dryness was achieved. The dried residues were subsequently dissolved in dimethyl sulfoxide (DMSO), and the final concentrations of the extracts were determined for further analysis (Table 1).

2.3.2. Ultrasonic-assisted extraction (UAE) method

For the ultrasonic-assisted extraction, the extraction procedure was identical to the maceration method up to

the shaking incubator stage. However, prior to the shaking incubator, the samples were treated in an ultrasonic water bath (cleaner ultrasonic bath Daihan Industries South Korea) for 45 minutes at 40 °C and 50% frequency intensity. Following this treatment, the samples were incubated in a shaking incubator, as described in the maceration method, at 37 °C and 150 rpm for 24 hours in a dark environment. After incubation, the samples were filtered as described above, evaporated in a rotary evaporator, and the residues were dissolved in DMSO, with final concentrations determined (Table 1). Samples obtained from both extraction methods were coded and aliquoted into small volumes, then stored at -20 °C until further analysis. Extract methods are shown in Fig. 1.

Extract methods were coded and grouped as follow: **DMM:** Dimethyl sulfoxide –maceration; **DMU:** Dimethyl sulfoxide-ultrasonic; **ESM:** Ethanol/water 80:20–maceration; **ESU:** Ethanol/water 80:20–ultrasonic; **EAM:** Ethyl acetate-maceration; **EAU:** Ethyl acetate-ultrasonic; **ACM:** Acetonitrile-maceration; **ACU:** Acetonitrile-ultrasonic.

Table 1. Final concentrations of *Rosa canina* seed extracts

Extracts	Concentration (mg/mL)
DMM.	38,48
DMU	32,14
ESM	28,42
ESU	30,68
EAM	24,02
EAU	22,97
ACM	20,48
ACU	25,02

2.4. Determination of antioxidant content and activities of seed powder extracts

In this study, the antioxidant content of rosehip seed extracts was evaluated using various solvents and extraction methods, including maceration and ultrasonic-assisted extraction. As antioxidant content and activity parameters, total phenolic content (TPC) total flavonoid content (TFC), ferric reducing antioxidant power (FRAP) assay, 2,2-diphenyl-1-picrylhydrazyl (DPPH) assay, and 2,2'-azino-bis 3-ethylbenzothiazolin-6-sulfonic acid scavenging activity (ABTS) assay, which are widely used in the literature of similar studies, were analyzed. In analyses, each sample and standard were run in 3 replicates.

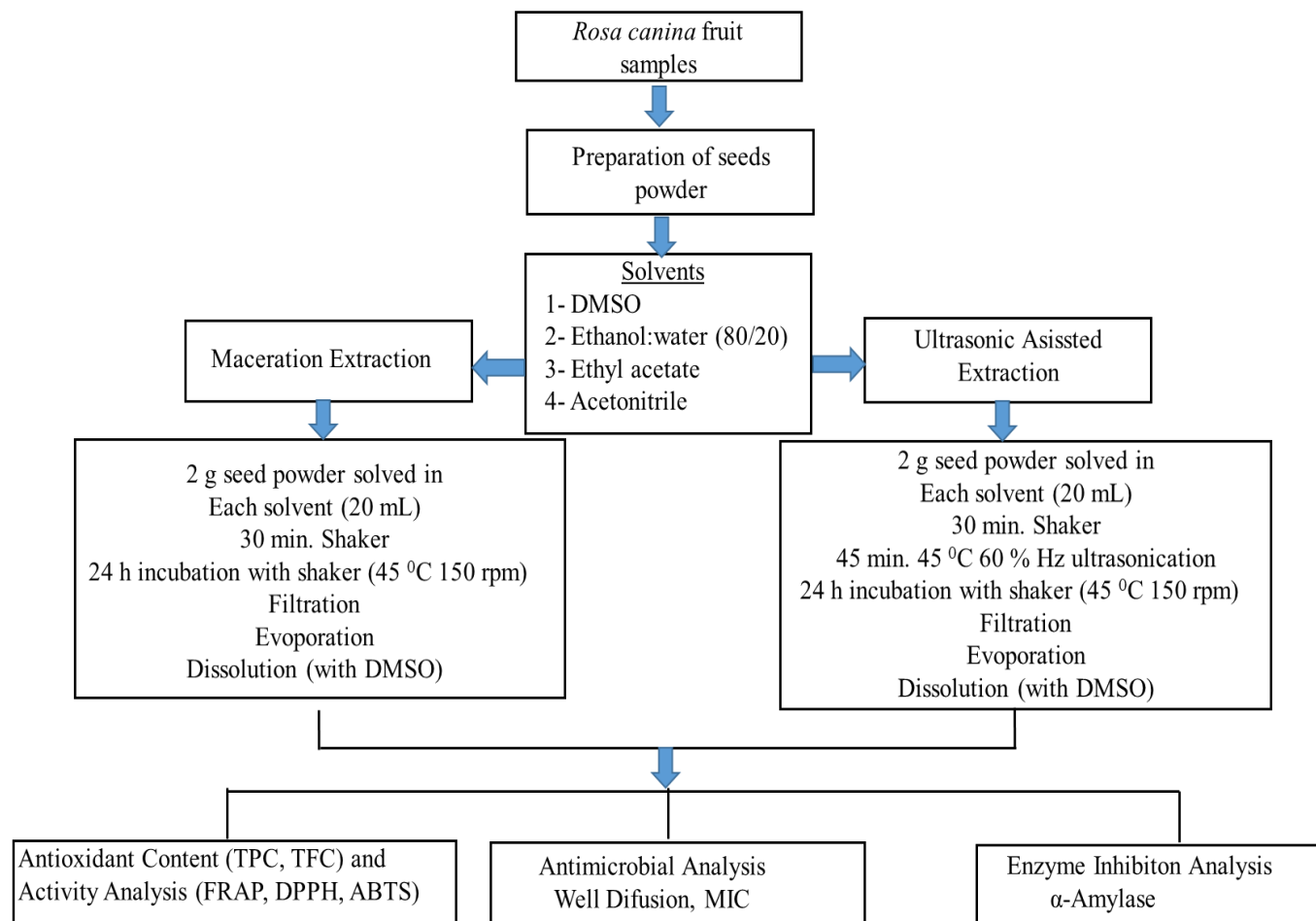


Figure 1. Figurative summary of extract methods and analyses parameters

2.4.1. Determination of total phenolic content (TPC)

Total phenolic content analysis was performed by Johnson et al. modified from the Folin-Ciocalteu procedure of Slinkard and Singleton adapted to microplate [17,18]. The method is based on the reduction of phosphotungstic acid to phosphotungstic blue in an alkaline environment. Gallic acid prepared in different concentrations was used as the standard in the study. Standard graphic equation is determined as $y = 0.00723461x + 0.0512804$ $R^2=0.999$. The extracts/standards were diluted as necessary and pipetted into the microplate in a volume of 25 μ L, followed by the addition of 10% (v/v) Folin-Ciocalteu reagent (125 μ L). 10% sodium carbonate (Na_2CO_3) (100 μ L) solution was added to the mixture, and the microplate was thoroughly shaken. The final volumes in the wells were 250 μ L. The plate was incubated at room temperature for 2 hours in the dark and read spectrophotometrically at 760 nm using a microplate reader (Thermo Fisher Sci. MultiScan Go Walham, Massachusetts USA). The results were expressed as mg/g of gallic acid equivalent (mg GAE /g extract).

2.4.2. Determination of total flavonoid content (TFC)

The total flavonoid assay will be performed according to the method adapted to a 96-well microplate, as described by Kamsi et al. [19] and based on the aluminum chloride colorimetric method by Beara et al. The procedure was carried out as follows: 50 μ L of sample/standard was pipetted into the microplate, followed by the addition of 30% methanol-water (120 μ L), 0.5 M 15 μ L sodium nitrite (NaNO_2), and 0.3 M 15 μ L aluminium chloride (AlCl_3) in sequence. After a 5-minute incubation, 1 M 100 μ L sodium hydroxide (NaOH) was added to the mixtures, and the final well volume was adjusted to 300 μ L. The mixtures were incubated in the dark at room temperature for 40 minutes. Absorbance values were measured spectrophotometrically at 406 nm against reagent and sample blanks using a microplate reader. Quercetin, prepared in five different concentrations, was used as the standard. The standard curve equation was determined as $y=0.000581872x+0.0183755$ with $R^2=0.998$. The total flavonoid content (TFC) of the extracts was expressed as quercetin equivalents (mg QE/g extract).

2.4.3. DPPH (1,1-Diphenyl-2-picrylhydrazyl) radical scavenging method

The DPPH radical scavenging method was adapted from the procedure used by Soler-Rivas et al. [20] for a 96-well microplate. In this method, 25 μ L of diluted extract/standard was pipetted into the microplate. Then, 100 μ M DPPH 185 μ L (1,1-diphenyl-2-picrylhydrazyl) and 90 μ L methanol were added in sequence. The final volume was adjusted to 300 μ L. After incubation for 30

minutes in the dark at room temperature, the absorbance was measured spectrophotometrically at 517 nm against blanks using a microplate reader. Trolox and ascorbic acid were used as standards. The results were expressed as trolox equivalent antioxidant capacity (TEAC) and ascorbic acid equivalent (AAE). The standard curve equations were determined as $y = -0.00433359x + 1.6969$ with $R^2=0.9946$ for Trolox and $y = -0.00368613x + 1.29333$ with $R^2=0.990$ for ascorbic acid.

2.4.4. Ferric reducing antioxidant power (FRAP) method

This method was modified from Benzie and Strainin's method to be applied to a 96-well microplate [21]. The principle of the method is based on the reduction of Fe^{3+} to Fe^{2+} in the presence of antioxidants. Standard solutions of Trolox and ascorbic acid were prepared in five different concentrations, and standard curves were generated. The standard curve equations were $y = 0.0110624x + 0.0412819$ with $R^2=0.999$ for Trolox and $y = 0.013392x + 0.127341$ with $R^2=0.995$ for ascorbic acid. In short, 25 μ L of extract/standard was pipetted into the microplate, and 275 μ L of FRAP reagent [300 mM acetate buffer + 10 mM 2,4,6-Tris(pyridyl)-S-triazine (TPTZ) solution + 20 mM FeCl_3 solution (10:1:1)] was added. The final volume was adjusted to 300 μ L. Absorbance values were measured spectrophotometrically at 593 nm against blanks using a microplate reader. Results were expressed as mg TEAC/g and mg AAE/g.

2.4.5. ABTS radical scavenging capacity

This method was modified from the procedure used by Silva et al. [22], which was adapted for a 96-well microplate from Re et al. [23]. Briefly, 25 μ L of sample/standard was pipetted into the microplate. ABTS (2,2'-azino-bis(3-ethylbenzothiazoline-6-sulfonic acid) radical solution, adjusted to an optical density of 0.7 with 7 mM ABTS + 2.45 mM potassium persulfate) was added to achieve a final volume of 200 μ L. After incubating at room temperature for 5-6 minutes, absorbance was measured spectrophotometrically at 734 nm using a microplate reader. Trolox and ascorbic acid solutions at five different concentrations were used as standards. The standard curve equations were determined as $y=-0.00766426x+2.0314$ with $R^2=0.999$ for Trolox and $y=-0.010095x+2.03325$ with $R^2=0.999$ for ascorbic acid. The analysis was performed in triplicates, and the results were expressed as mg TEAC/g and mg AAE/g.

2.5. Determination of antimicrobial activities

2.5.1. Agar well diffusion method

The antimicrobial activities of the 8 different rosehip extracts were determined using the well diffusion method with some modifications based on the CLSI (Clinical & Laboratory Standards Institute: CLSI

Guidelines [24]. The test organisms used were Gram-positive bacteria *Staphylococcus aureus* ATCC 25923 and *Bacillus cereus* ATCC 9634; Gram-negative bacteria *Pseudomonas aeruginosa* ATCC 27853, *Klebsiella pneumoniae* ATCC 13883, *Proteus vulgaris* ATCC 13315, *Aeromonas hydrophila* ATCC 35654 and fungi *Candida albicans* ATCC 18804. Fresh cultures of the microorganisms were prepared and diluted to a turbidity of 0.5 McFarland standard (1.5×10^8 microorganisms/mL) using sterile distilled water. The microorganisms were inoculated onto Müller-Hinton Agar petri dishes with the help of a sterile swab. Wells were created on the inoculated Petri dishes, and then 50 μ L of the extract solutions were pipetted into the wells. The plates were incubated at 4 °C for 2 hours to allow for diffusion of the extracts into the agar. Chloramphenicol was used as a positive control, and DMSO was used as a negative control. After incubation, the dishes were incubated at 37 °C for 24 hours for bacteria and at 28 °C for 48 hours for yeast. The inhibition zone diameters surrounding the wells were measured using a digital caliper. Analyses were run in 3 replicates.

2.5.2. Minimal inhibitory concentrations analysis of extracts

The minimum inhibitory concentration (MIC) values of the extracts were analyzed following the CLSI [24]. guidelines with some modifications. The method involved applying the broth dilution technique to 96-well sterile microplates with lids. Mueller-Hinton Broth was used as the culture medium. Unlike the other wells, the first wells received 100 μ L of the culture medium prepared at twice the concentration, while the other wells were inoculated with 100 μ L of the standard concentration medium. Then, 100 μ L of rosehip extract was pipetted into the first wells. Starting from an initial concentration of 2750.0 μ g/mL, a twofold serial dilution was performed to prepare 10 different concentrations, ranging down to 5.0 μ g/mL. Similarly, chloramphenicol was used at an initial concentration of 256 μ g/mL. Suspensions of standard microorganisms (at a 0.5 McFarland turbidity) were inoculated into the microplates. After incubation in an incubator at 37 °C for 24 hours for bacteria and 28 °C for 48 hours for yeast, microbial growth was observed using a microplate reader. The lowest concentrations of rosehip extracts and antibiotics that inhibited the growth of microorganisms were given as μ g/mL as MIC values.

2.6. Determination of α -amylase enzyme inhibitory effect of seeds extracts

The α -Amylase inhibitory activity of rosehip extracts was determined using the iodine/potassium iodide method, adapted from the method of Yang et al. [25].

Extract solutions were prepared at five different concentrations and pipetted into the wells of a microplate in 25 μ L volumes. Then, a 0.5 mg/mL α -amylase enzyme solution was prepared using phosphate buffer (pH 6.9, 6 mM sodium chloride) and 50 μ L of this solution was added to the wells. The samples in the microplate were incubated at 37 °C for 10 minutes. After the pre-incubation, 50 μ L of 0.1% starch solution was added to each well to initiate the reaction. The samples were incubated again at 37 °C for 10 minutes, after which 25 μ L of 1 M HCl was automatically added to stop the reaction. To observe the color change, 100 μ L of iodine-potassium iodide solution was added to the wells. The absorbances of the extracts and the control were spectrophotometrically measured in a microplate reader set to 630 nm wavelength. Acarbose was used as a standard at concentrations of 10, 25, 50, 100, and 200 μ g/mL. The α -amylase inhibitory activity results of the extracts and acarbose were presented as IC₅₀ (mg/mL) values.

2.7. Statistics

To compare the extracts with each other, ANOVA test was applied. ANOVA, Analysis of Variance, was conducted using Microsoft Excel with the help of XLSTAT (Addinsoft, 2024, XLSTAT statistical and data analysis solution, New York, USA). Results are given as mean \pm standard deviation. $P < 0.05$ was considered a statistically significant difference.

3. Results and discussion

3.1. Results of TPC TFC, and antioxidant activity

In this study, a total of 8 different extracts were obtained with 4 different solvents and 2 different extraction methods. TPC and TFC antioxidant activity results are shown in Table 2.

Total phenolic content (TPC) is an indicator of the antioxidant potential of medicinal plants because phenolic compounds are known for their ability to neutralize free radicals. Rosehip is known as an important source of antioxidants. As with many plants, the bioactive properties of rosehip fruits can vary depending on several factors such as ripening and harvesting time, storage, altitude, temperature, humidity, and climate [6]. Moreover, the effective extraction of the total phenolic content (TPC) and total flavonoid content (TFC) from rosehip fruits and seeds is influenced not only by the aforementioned conditions but also by solvents and extraction methods [11]. The polarity of the solvent is a significant parameter that affects the release of phytochemicals responsible for bioactive properties during the extraction process [26,27].

Table 2. Comparison of antioxidant content and activities of rosehip seed extracts prepared by maceration and ultrasonic assisted methods using different solvents

Extract	TPC mg GAE/g	TFC mg QE/g	DPPH mg TEAC/g	DPPH mg AAE/g	ABTS mg TEAC/g	ABTS mg AAE/g	FRAP mg TEAC/g	FRAP mg AAE/g
DMM	5.66 ±0.36 ^a	22.53 ±0.78 ^a	5.98 ±0.49 ^a	4.74 ±0.28 ^a	19.44 ±0.09 ^a	17.82 ±0.06 ^a	4.63 ±0.09 ^a	2.15 ±0.08 ^a
DMU	7.26 ±0.70 ^a	25.88 ±3.21 ^a	10.79 ±0.85 ^b	9.47 ±0.77 ^b	24.72 ±0.52 ^b	22.33 ±0.36 ^b	6.93 ±0.26 ^b	±3.73 ±0.21 ^a
ESM	47.31 ±3.29 ^d	133.04 ±3.25 ^e	57.37 ±2.85 ^d	39.13 ±2.17 ^d	59.26 ±2.50 ^e	46.90 ±1.73 ^e	50.63 ±2.48 ^f	39.56 ±2.05 ^e
ESU	41.10 ±0.77 ^c	107.22 ±2.81 ^d	63.51 ±1.30 ^e	38.79 ±1.85 ^d	54.74 ±2.97 ^d	43.34 ±2.05 ^d	46.79 ±0.72 ^e	36.55 ±0.59 ^d
EAM	60.53 ±3.14 ^e	189.90 ±3.12 ^f	115.34 ±2.53 ^f	107.57 ±1.93 ^f	84.07 ±1.83 ^f	64.61 ±1.97 ^f	63.88 ±1.07 ^h	49.18 ±2.30 ^g
EAU	63.86 ±3.11 ^e	210.23 ±3.61 ^g	117.43 ±2.49 ^f	91.08 ±2.39 ^e	97.52 ±2.16 ^g	73.65 ±2.67 ^g	59.40 ±1.09 ^g	45.56 ±1.94 ^f
ACM	16.00 ±1.13 ^b	31.09 ±2.13 ^b	17.40 ±1.53 ^c	14.37 ±0.33 ^c	26.59 ±2.01 ^b	26.60 ±1.39 ^c	±17.45 ±0.66 ^c	10.25 ±0.84 ^b
ACU	16.62 ±2.69 ^b	44.22 ±1.56 ^c	18.61 ±0.90 ^c	16.69 ±0.62 ^c	31.25 ±1.42 ^c	28.34 ±0.99 ^c	19.63 ±0.68 ^d	13.71 ±0.52 ^c

DMM: Dimethyl sulfoxide –maceration; **DMU:** Dimethyl sulfoxide-ultrasonic; **ESM:** Ethanol/water 80:20 –maceration; **ESU:** Ethanol/water 80:20–ultrasonic; **EAM:** Ethyl acetate-maceration; **EAU:** Ethyl acetate-ultrasonic; **ACM:** Acetonitrile-maceration; **ACU:** Acetonitrile-ultrasonic. Different letters (a-h) in the same column are significantly different ($p < 0.05$).

In our study, combinations of 4 solvents with varying polarities and extraction methods were employed.

Among the 4 solvents, EAU (Ethyl Acetate Ultrasonic) exhibited the highest TPC amounts (63.86 mg GAE/g) and significant differences from all other extracts (except EAM) demonstrating that ultrasonic-assisted extraction of the rosehip seeds with ethyl acetate was highly efficient for TPC ($p < 0.05$). EAM (Ethyl Acetate Maceration) had the second highest content (60.53 mg GAE/g) after EAU. However, there was no significant difference between these two extracts. It was observed that DMM (Dimethyl sulfoxide –Maceration) and DMU (Dimethyl sulfoxide –Ultrasonic) extracts had the lowest TPC values (5.66; 7.26 respectively). When the extracts are compared in terms of TPC content, the order EAU>EAM>ESM>ESU> ACU>ACM>DMU>DMM is seen. When TFC values were examined, it was observed that, similar to TPC, the highest level was in the EAU (210 mg QE/g) extract, followed by EAM (189.9 mg QE/g) and DMM (22.5 mg QE/g), and DMU (25.8 mg QE/g) had the lowest values, respectively. In TFC content comparison, extracts are listed as EAU>EAM>ESM>ESU>ACU>ACM>DMU>DMM. In this study, these findings suggest that ultrasonic-assisted extraction using ethyl acetate was again the most effective method for extracting phenolics and flavonoids from rose hip seeds.

The DPPH and ABTS assays are commonly used to assess the free radical scavenging ability of plant extracts. The FRAP assay evaluates the ability of extracts to reduce ferric ions, which is another important measure of antioxidant activity. In this study, these 3

commonly used antioxidant activity determination methods were preferred (Table 2).

It was determined that the ethyl acetate extracts (EAU and EAM) exhibited the highest values in all antioxidant activity analysis methods. Additionally, these values showed a significant difference compared to the values of other solvent extracts. However, when considering TEAC and AAE standards, the highest antioxidant activity values varied between EAU and EAM. For instance, in the DPPH assay, EAU had 117.43 mg TEAC/g, while EAM had 115.34 mg TEAC/g, and in terms of ascorbic acid standard, EAM was at 107.57 mg AAE/g, while EAU was at 91.08 mg AAE/g. Similarly, in the FRAP analysis, EAM was found to be significantly higher than EAU and all other extracts. Among the extracts, DMM and DMU showed the lowest values in terms of all three antioxidant activity methods.

In the literature, there are more studies on the antioxidant content and activity of rosehip fruit samples extracted with different methods and solvents compared to studies involving rosehip seeds. This could be due to the higher usage of the fruit compared to the seed. Montazari et al. used six different solvents (*n*-hexane, ethyl acetate, chloroform, acetone, water and methanol) to extract Iranian *Rosa canina* fruits using the maceration method and dissolved the residues in DMSO after evaporation. The researchers found that the four extracts with the highest TPC contents were ranked as methanol, acetone, water, and ethyl acetate (424.4, 295.8, 220.2, 173.3 mg GAE/g extract respectively). In terms of TFC, ethyl acetate performed better than water in the same ranking [28].

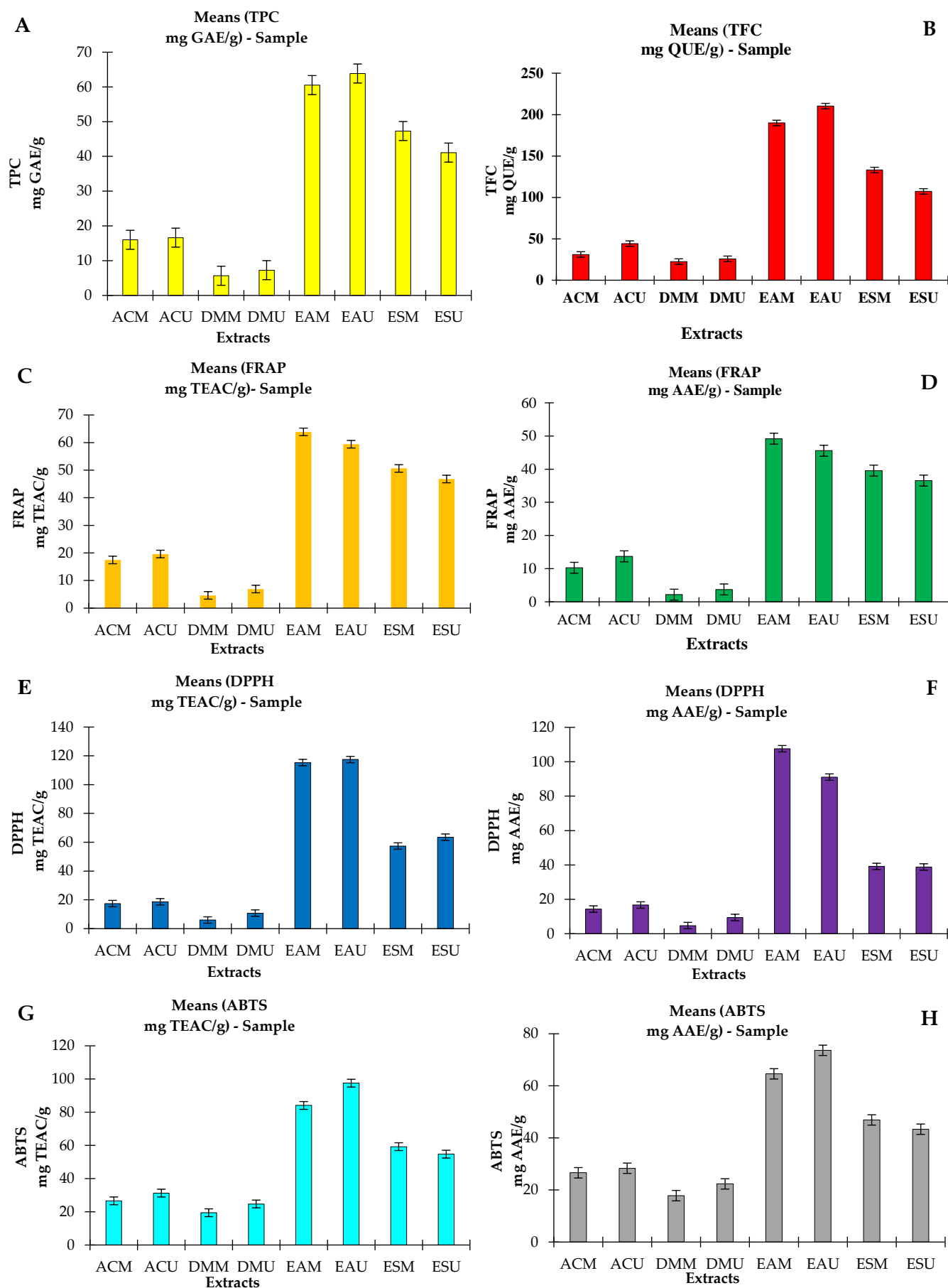


Figure 2. Graphical representations of solvent and methodological comparisons of phenolic and flavonoid contents and antioxidant activities of seed extracts. **A:** TPC (mg GAE/g); **B:** TFC (mg QUE/g); **C:** FRAP (mg TEAC/g); **D:** FRAP (mg AAE/g); **E:** DPPH (mg TEAC/g); **F:** DPPH (mg AAE/g); **G:** ABTS (mg TEAC/g); **H:** ABTS (mg AAE/g)

Graphical representations of solvent and methodological comparisons of phenolic and flavonoid contents and antioxidant activities of seed extracts are given in Fig 2.

In another study conducted in Turkey, the whole fruit (WF), pulp (P), and seeds (S) of *Rosa pimpinellifolia* (black rosehip) were analyzed for TPC, DPPH, ABTS, and CUPRAC (cupric reducing antioxidant capacity). It was determined that the seed TPC values were lower compared to those of WF and P; however, the seeds exhibited higher values in all three antioxidant activity assays than the other parts. The researchers, using an acidified ethanol-water mixture (50:50, v/v) as the solvent, employed the ultrasound-assisted extraction (UAE) method with three repetitions (30 minutes at temperatures ranging from 30 to 40 °C) for the extraction process [29].

TPC and TCF values in rosehip seeds may vary according to regional and methodological differences. In some studies conducted on *Rosa canina* seeds collected from Gümüşhane-Erzurum regions, TPC values were reported to be between 2.55 mg GAE/g and 52 mg GAE/g [30]. In a study using 80% methanol, 70% acetone and 60% ethanol as solvents by maceration method, ABTS values in rosehip seed powders were determined as approximately 2.5 mg TEAC/g for methanol and acetone, while ethanol was found to be lower, and TPC was determined as 2.55 mg GAE/g in the same study [31]. Çürük et al. determined DPPH value as 16.2 mg TEAC/g in rosehip seed powder obtained by supercritical carbon dioxide extraction method [32]. In another study, the DPPH value of 75% methanolic and 0.1% formic acid extract of dried and frozen rosehip seed powder in liquid nitrogen was found to be 5.38 mg TEAC/g. [30].

In recent years, the use of different extraction methods other than the traditional maceration-solvent extraction method, such as ultrasonic assisted extraction (UAE), microwave assisted extraction (MAE), and supercritical fluid extraction (SFE) has increased. UAE uses a combination of thermal and mechanical effects to elicit bioactive components and is generally effective at low frequencies of 20–100 kHz. Higher frequencies can do more harm than good [33,34].

In ultrasound-assisted extraction, several variables must be considered: sonication time, frequency, and temperature, along with the solvent/solute ratio, which are identified as the main variables [35]. In this study, both maceration and UAE methods were applied using the same solvents. When comparing the UAE and maceration methods, the highest values in terms of antioxidant activity, TPC, and TFC content were found in the EAM and EAU solutions. Among these, EAU exhibited statistically significantly higher TFC and ABTS

values (mg TEAC/g and mg AAE/g, respectively) than EAM ($P < 0.05$). Ultrasonic extracts of dimethyl sulfoxide and acetonitrile (DMU and ACU) had higher values for all antioxidant parameters compared to the extracts obtained by maceration (DMM and ACM). These increases were more distinctive in DMU. After ethyl acetate extracts, ESM and ESU extracts exhibited the highest antioxidant parameters, with the exception of DPPH (mg TEAC/g), where ESM showed higher values than ESU.

In general, it is reported that increasing the ultrasonication time will increase the mass transfer to the solvent and accordingly the amount of phenolic and flavonoid substances will increase, but the phenolic content may decrease due to the structural degradation of phenolic compounds as the ultrasonication time increases [36]. In a study, antioxidant activity and phenolic content were compared by ultrasonically assisted extraction of rosehip fruits using variable parameters consisting of 3, 6, 9, 12, and 15 minutes sonication time, 25, 50 and 100 % amplitude and 20, 30, and 50 °C temperature. It was shown that ultrasonication time and temperature increased the amount of phenolic matter, but amplitude was not effective [35].

3.2. Results of the antimicrobial activity of different rosehip extracts

3.2.1. Results of agar well diffusion method

Results of the antimicrobial activity of different rosehip extracts against 7 microorganisms were shown in Table 3.

In this study, all rosehip seed powder extracts showed significant antimicrobial activity against *A. hydrophila* and *K. pneumonia* strains. It was found that the highest activities were shown by DMU, ESU, and DMM extracts against *A. hydrophila* strain (24.43, 23.23, and 22.23 mm, respectively). No antimicrobial activity of any extract was detected against *E. faecalis*. Against *S. aureus*, activity was seen only in EAM and EAU. It was also determined that ACM and ACU only exhibited activity against *A. hydrophila* and *K. pneumoniae* strains. *Rosa canina* is a well-known and extensively studied medicinal plant for its antimicrobial activity. However, most studies on antimicrobial activity have focused primarily on the fruit and flowers. Extraction methods, solvents used, the time of fruit collection, and climatic conditions are influential factors in the expression of the plant's antimicrobial properties [13,37]. In a study with methods similar to ours, *Rosa pimpinellifolia* plant parts, including seeds, were extracted using UAE with a solvent consisting of an ethanol-water (50:50) mixture. In the antimicrobial activity analyses, it was observed that the seed extract was effective against *B. cereus* and *S. aureus*, but exhibited a lower effect compared to the whole fruit [31].

Table 3. Result of antimicrobial activity of different rosehip extracts (zone diameter mm)

Extracts	<i>S. aureus</i>	<i>E. faecialis</i>	<i>C. albicans</i>	<i>P. vulgaris</i>	<i>A. hydrophila</i>	<i>B. cereus</i>	<i>K. pneumoniae</i>
DMM	NI	NI	11.43 ±0.31	16.70 ±0.72	22.23 ±0.67	NI	17.53 ±0.67
DMU	NI	NI	NI	15.43 ±0.50	24.43 ±0.91	NI	17.70 ±0.72
ESM	NI	NI	15.50 ±0.66	15.40 ±0.46	23.23 ±0.70	12.57 ±0.68	15.33 ±0.35
ESU	NI	NI	14.63 ±0.40	15.63 ±0.55	20.60 ±0.46	12.10 ±0.36	15.03 ±0.61
EAM	15.70 ±0.46	NI	19.90 ±0.56	NI	19.33 ±0.38	10.70 ±0.44	16.90 ±0.56
EAU	15.60 ±0.36	NI	14.00 ±0.75	NI	20.73 ±0.68	10.67 ±0.25	17.57 ±0.47
ACM	NI	NI	NI	NI	21.40 ±0.89	NI	15.40 ±0.53
ACU	NI	NI	NI	NI	19.87 ±0.60	NI	16.73 ±0.60
CHL	26.63 ±0.31	25.73 ±0.51	30.10 ±0.80	30.63 ±0.86	25.10 ±0.62	22.93 ±0.74	30.40 ±0.85
DMSO	NI	NI	NI	NI	NI	NI	NI

CHL: Chloramphenicol; DMSO: as a negative control NI: No inhibition. Results were given mean ± Standard deviation (SD)

In a homogenization-based study, evaluating rosehip fruit samples from Samsun, T rkiye, where phosphate buffer was used as the solvent, it was observed that, in contrast to our study, *E. faecialis* and *S. aureus* strains were effectively inhibited by the rosehip fruits [37].

Phytochemical components of the extract may show different effects against different microorganisms. For example, citric acid has a pronounced antimicrobial effect against *Staphylococcus aureus* and *Klebsiella aerogenes*, and quinic acid against *S. aureus*. Researchers suggest that solvents may play an important role in antimicrobial activity in this case [28,38].

3.2.2. Results of minimal inhibitory concentrations of extracts

The minimal inhibitory concentration (MIC) values of the extracts obtained by maceration and UAE methods with different solvents against various microbial strains are given in Table 4.

In this context, a lower MIC value indicates a higher level of antimicrobial activity. When the extracts were evaluated in terms of both solvent and method, it was

determined that the minimum inhibitory concentrations (MICs) varied according to the microorganisms.

The lowest MIC values were observed against the Gram (-) bacteria *A. hydrophila* and *K. pneumoniae* in the EAU and EAM extracts (0.29 and 0.30 mg/mL, respectively). All other extracts had lower MIC values against these two strains compared to other microorganisms. The highest MIC values were observed against *E. faecialis*. DMM and DMU had the highest MIC values against *S. aureus*, *E. faecialis*, *A. hydrophila*, and *K. pneumoniae* compared to the other extracts. Extracts obtained by UAE and maceration exhibited similar MIC values for the same solvents, and these values varied depending on the microorganisms.

In antimicrobial activity analyses of *Rosa canina* fruit extracts prepared using the maceration method and six different solvents, it was observed that methanolic extracts showed the lowest MIC values against *C. albicans*, *B. cereus*, and *S. aureus* strains, followed by aqueous extracts. In this study, chloroform and n-hexane exhibited no activity, while ethyl acetate showed activity only against *S. aureus*, and acetone demonstrated activity against all strains except *B. cereus* [28].

Table 4. Results of minimal inhibitory concentrations (MIC) of seed extracts (mg/mL)

Extracts	<i>S. aureus</i>	<i>E. faecialis</i>	<i>C. albicans</i>	<i>P. vulgaris</i>	<i>A. hydrophila</i>	<i>B. cereus</i>	<i>K. pneumoniae</i>
DMM	3.85	3.85	1.92	0.96	0.48	3.85	0.48
DMU	3.21	3.21	3.21	0.80	0.40	1.61	0.40
ESM	2.84	2.84	0.71	0.71	0.36	0.71	0.36
ESU	3.07	3.07	0.77	0.77	0.38	0.77	0.38
EAM	0.60	2.40	0.60	2.40	0.30	1.20	0.30
EAU	0.57	2.30	0.57	2.30	0.29	1.15	0.29
ACM	2.05	2.05	2.05	2.05	0.26	2.05	0.26
ACU	2.50	2.50	2.50	2.50	0.31	2.50	0.31
CHL	0.02	0.01	0.001	0.001	0.02	0.01	0.01
DMSO	0.00	0.00	0.00	0.00	0.00	0.00	0.00

CHL: Chloramphenicol as antibiotic; DMSO: Dimethyl sulfoxide as negative control. The results are presented in mg/mL (mean ± Standard deviation (SD)).

3.3. Results of α -amylase enzyme inhibitory activity of extracts

Results of α -amylase enzyme inhibitory activity of extracts were given in Table 5. α -Glucosidase hydrolyzes starch and disaccharides in the intestine and ensures the absorption of glucose [39]. α -Amylase breaks down polysaccharides into maltose and glucose. Both of these enzymes have the effect of increasing glucose concentration in the blood, and inhibitors of these enzymes are used in diabetes treatments [40,41].

The IC_{50} values presented in the table reflect the inhibitory activity of various extracts on α -amylase enzyme activity, with lower IC_{50} values indicating greater enzyme inhibition. This analysis is crucial as α -amylase plays a significant role in carbohydrate metabolism, making its inhibition relevant for conditions such as diabetes and obesity [40].

In our study, ACM and EAU extracts had the highest inhibitory effect on α -amylase with the lowest IC_{50} values (20.48 and 22.97 mg/mL, respectively). In contrast, DMM (DMSO Mas) exhibited the least inhibition, with an IC_{50} of 38.48 mg/mL, indicating it is less effective compared to the other extracts. In general, the inhibitory effects of rosehip extracts on α -amylase enzyme were found to be weaker than acarbose, which is an α -amylase inhibitor. The effects of solvents on the bioactivity of extracts via phytochemicals may also apply to enzyme inhibition. Indeed, in a study conducted to determine the α -glucosidase enzyme inhibitory effect of rosehip fruits and using acetone, methanol, ethyl acetate, and *n*-hexane as solvents, it was reported that acetone extract had the strongest inhibitory effect, followed by methanol and ethyl acetate, while *n*-hexane showed a very low effect [42]. However, in a study showing the α -amylase inhibitory effect of rosehip fruit extract dissolved in liquid nitrogen and extracted with methanol, it was determined that the fruit extract showed 100% inhibitory effect at a concentration of 5.5 mg/mL. [43].

Table 5. Results of α -amylase enzyme inhibitory activity of extracts

Extracts	IC_{50} (mg/mL)
DMM	38.48 \pm 1.26 ^g
DMU	32.14 \pm 0.89 ^f
ESM	28.42 \pm 1.13 ^e
ESU	30.68 \pm 0.46 ^f
EAM	24.02 \pm 0.58 ^{cd}
EAU	22.97 \pm 1.23 ^c
ACM	20.48 \pm 1.47
ACU	25.02 \pm 0.56 ^d
Acarbose (μ g/mL)	123.750 \pm 2.01 ^a

Note: Results are presented as means \pm standard deviations. A variety of letters (a-g) in the same column indicate significant differences, attaining statistical significance at the 95% level ($P < 0.05$).

While their efficacy is lower than that of acarbose, their natural origin and potential for fewer side effects make them an attractive area of study. The role of solvents in enhancing bioactivity further underscores the importance of optimizing extraction methods to maximize the therapeutic potential of plant-based extracts.

4. Conclusion

This study demonstrates the critical role of solvent selection and extraction methodology in efficiently unlocking the bioactive potential of *Rosa canina* seeds. Ethyl acetate combined with ultrasound-assisted extraction (EAU) yielded extracts with the highest phenolic (63.86 mg GAE/g) and flavonoid (210.23 mg QE/g) content, alongside superior antioxidant activity in FRAP, DPPH, and ABTS assays. Ethyl acetate maceration (EAM) also showed exceptional performance, confirming the solvent's efficacy in enhancing bioactive compound recovery.

In particular, acetonitrile maceration (ACM) is thought to be used to control postprandial blood glucose levels in diabetes based on its concentration of α -amylase enzyme inhibition (IC_{50} = 20.46 mg/mL). Antimicrobial analysis revealed broad-spectrum efficacy against *Aeromonas hydrophila* and *Klebsiella pneumoniae*, though activity varied against other microbial strains. This finding highlights the potential for developing targeted antimicrobial formulations.

The aim of this study was to present feasible strategies to maximize the bioactivity of *Rosa canina* seeds by optimizing solvent polarity and extraction dynamics. The results are expected to bring new solutions and approaches in health and other plant-based industrial fields such as functional foods, natural preservatives and herbal therapeutic products.

References

- [1] D. Acıbuca, B. Budak, Dünya'da ve Türkiye'de tıbbi ve aromatik bitkilerin yeri ve önemi, Çukurova Tarım Gıda Bil Der, 33(1), 2018, 33–44.
- [2] H.S. Elshafiye, I. Camele, A.A. Mohamed, A Comprehensive review on the biological, agricultural and pharmaceutical properties of secondary metabolites based-plant origin, Int J Mol Sci, 24(4), 2023, 3266.
- [3] M. Oz, C. Baltacı, İ. Deniz, Gümüşhane yöresi kuşburnu (*Rosa canina* L.) ve siyah Kuşburnu (*Rosa pimpinellifolia* L.) meyvelerinin C vitamini ve şeker analizleri, Gümüşhane Üniv Fen Bilim Enst Derg, 2, 2018, 284–292.
- [4] I. Roman, A. Stănilă, S. Stănilă, Bioactive compounds and antioxidant activity of *Rosa canina* L. biotypes from spontaneous flora of Transylvania, Chem Cent J, 7(1), 2013, 73.
- [5] I. Turan, S. Demir, K. Kilinc, S.O. Yaman, S. Misir, H. Kara, B. Genç, A. Menteşe, Y. Aliyazıcıoğlu, O. Değer, Cytotoxic effect of *Rosa canina* extract on human colon cancer cells through

- repression of telomerase expression, *J Pharm Anal*, 8, 2018, 394–399.
- [6] M. Darak, K. Kılınç, Z. Akar, A.Ö. Düzgün, T. Acet, M.N. Ural, C. Baltacı, O. Akmeşe, Effect of different storage conditions and infusion times on antioxidant and antimicrobial activities and total phenolic content of rosehip fruits, *J Anatolian Env Anim Sci*, 9(4), 2024, 711–720.
 - [7] K. Kılınç, S. Demir, I. Turan, A. Menteşe, A. Orem, M. Sonmez, Y. Aliyazıcıoğlu, *Rosa canina* Extract has Antiproliferative and Proapoptotic Effects on Human Lung and Prostate Cancer Cells, *Nutr Cancer*, 72(2), 2019, 273–282.
 - [8] S. Patel, Rose hip as an underutilized functional food: Evidence-based review, *Trends Food Sci Technol*, 63, 2017, 29–38.
 - [9] I. Mármol, C. Sánchez-de-Diego, N. Jiménez-Moreno, C. Ancín-Azpilicueta, M.J. Rodríguez-Yoldi, Therapeutic applications of rosehips from different *Rosa* species, *Int J Mol Sci*, 18(6), 2017, 1137.
 - [10] A. Selahvarzian, A. Alizadeh, P.A. Baharvand, O.A. Eldahshan, B. Rasoulia, Medicinal properties of *Rosa canina* L., *Herbal Med J*, 3(2), 2018, 77–84.
 - [11] O.R. Negrean, A.C. Farcas, S.A. Nemes, D.E. Cic, S.A. Socaci, Recent advances and insights into the bioactive properties and applications of *Rosa canina* L. and its by-products, *Heliyon*, 10(9), 2024, e30816.
 - [12] G. Toydemir, B.G. Subasi, R.D. Hall, J. Beekwilder, D. Boyacıoğlu, E. Capanoglu, Effect of food processing on antioxidants, their bioavailability and potential relevance to human health, *Food Chem X*, 14, 2022, 100334.
 - [13] M. Hacıoğlu, S. Dosler, T.A.S. Birteksoz, G. Otuk, Antimicrobial activities of widely consumed herbal teas, alone or in combination with antibiotics: an in vitro study, *PeerJ*, 5, 2017, e3467.
 - [14] Ş.Ö. Doğan, H. Özçelik, Chemical composition analyses of fruit Roses/Rosehips (*Rosa* spp.) of Türkiye, *Biol Divers Conserv*, 10(2), 2017, 122–140.
 - [15] S. Kazaz, S. Baydar, H. Erbaş, S. Variations in Chemical Compositions of *Rosa damascena* Mill. and *Rosa canina* L. Fruits, *Czech J Food Sci*, 27(3), 2009, 178–184.
 - [16] M. Öz, I. Deniz, O.T. Okan, C. Baltacı, S.M. Karatas, Determination of the Chemical Composition, Antioxidant and Antimicrobial Activities of Different Parts of *Rosa canina* L. and *Rosa pimpinellifolia* L. Essential Oils, *J Essent Oil Bear Plants*, 24(3), 2021, 519–537.
 - [17] J.B. Johnson, J.S. Mani, M. Naiker, Development and validation of a 96-well microplate assay for the measurement of total phenolic content in ginger extracts, *Food Anal Methods*, 15(2), 2022, 413–420.
 - [18] K. Slinkard, V.L. Singleton, Total Phenol Analysis: Automation and Comparison with Manual Methods, *Am J Enol Vitic*, 28, 1977, 49–55.
 - [19] Y.E. Kamaş, B. Akar, C. Baltacı, Determination of physical, chemical and antioxidant properties of pomegranate sauces sold in Turkish markets, *Turk J Anal Chem*, 4(2), 2022, 67–75.
 - [20] C. Soler-Rivas, J.C. Espín, H.J. Wichers, An easy and fast test to compare total free radical scavenger capacity of foodstuffs, *Phytochem Anal*, 11(5), 2000, 330–338.
 - [21] I.F. Benzie, J.J. Strain, The ferric reducing ability of plasma (FRAP) as a measure of "antioxidant power": the FRAP assay, *Anal Biochem*, 239(1), 1996, 70–76.
 - [22] E.M. Silva, J.N.S. Souza, H. Rogez, J.F. Rees, Y. Larondelle, Antioxidant activities and polyphenolic contents of fifteen selected plant species from the Amazonian region, *Food Chem*, 101(3), 2007, 1012–1018.
 - [23] R. Re, N. Pellegrini, A. Proteggente, A. Pannala, M. Yang, C. Rice-Evans, Antioxidant activity applying an improved ABTS radical cation decolorization assay, *Free Radic Biol Med*, 26(9-10), 1999, 1231–1237.
 - [24] CLSI (Clinical and Laboratory Standards), Performance standards for antimicrobial susceptibility testing, 17th Informational Supplement, M100–S17, 2007, 27:1.
 - [25] X.W. Yang, M.Z. Huang, Y.S. Jin, L.N. Sun, Y. Song, H.S. Chen, Phenolics from *Bidens bipinnata* and their amylase inhibitory properties, *Fitoterapia*, 83(7), 2012, 1169–1175.
 - [26] H. Nawaz, A.M. Shad, N. Rehman, H. Andaleeb, N. Ullah, Effect of solvent polarity on extraction yield and antioxidant properties of phytochemicals from bean (*Phaseolus vulgaris*) seeds, *Braz J Pharm Sci*, 56, 2020, e17129.
 - [27] F. Kılıç, Z. Akar, Determination of LC-MS/MS phenolic profile, antioxidant activity and α -glucosidase enzyme inhibition of *Linum mucronatum* Bertol. subsp. *armenum* (Bordz.) P.H. Davis, *Turk J Anal Chem*, 4(2), 2022, 123–131.
 - [28] N. Montazeri, E. Baher, F. Mirzajani, Z. Barami, S. Yousefian, Phytochemical contents and biological activities of *Rosa canina* fruit from Iran, *J Med Plants Res*, 5(18), 2011, 4584–4589.
 - [29] B.T. Findik, H. Yildiz, M. Akdeniz, I. Yener, M.A. Yilmaz, O. Cakir, A. Ertas, Phytochemical profile, enzyme inhibition, antioxidant, and antibacterial activity of *Rosa pimpinellifolia* L., *Food Chem*, 455, 2024, 139921.
 - [30] S. Bakır, The Phenolic content and antioxidant capacity of pumpkin, rosehip and pomegranate seeds, *Turk J Agric Food Sci Technol*, 12(s2), 2024, 2347–2354.
 - [31] H. Ilyasoğlu, Characterization of rosehip (*Rosa canina* L.) seed and seed oil, *Int J Food Prop*, 17(7), 2014, 1591–1598.
 - [32] S.G. Çürük, M. Nijar, D. Köseoğlu, A. Akdoğan, Mineral and bioactive component contents of rosehip (*Rosa canina* L.) seed powder, *Akademik Gıda*, 21(4), 2023, 323–332.
 - [33] L. Shen, S. Pang, M. Zhong, Y. Sun, A. Qayum, Y. Liu, A. Rashid, B. Xu, Q. Liang, H. Ma, X. Ren, A comprehensive review of ultrasonic assisted extraction (UAE) for bioactive components: Principles, advantages, equipment, and combined technologies, *Ultrason Sonochem*, 101, 2023, 106646.
 - [34] I.S. Arvanitoyannis, K.V. Kotsanopoulos, A.G. Savva, Use of ultrasounds in the food industry-Methods and effects on quality, safety, and organoleptic characteristics of foods: A review, *Crit Rev Food Sci*, 57, 2017, 109–128.
 - [35] S. Turan, D. Atalay, R. Solak, M. Özoğlu, M. Demirtaş, Ultrasonik destekli ekstraksiyon parametrelerinin kuşburnu (*Rosa canina*) meyvesinin toplam fenolik ve karotenoid miktarları ile antoksidan aktivitesi üzerine etkisi, *Gıda*, 46(3), 2021, 726–738.
 - [36] Ç. Poyraz, G. Küçükyıldız, Ş.İ. Kırbaslar, S. Cigeroğlu, S. Şahin, Valorization of Citrus unshiu biowastes to value-added products: an optimization of ultrasound-assisted extraction method using response surface methodology and particle swarm optimization, *Biomass Conv Bioref*, 13, 2023, 3719–3729.
 - [37] B. Eldaw, G. Çiftçi, Antioxidant Capacity and Antibacterial Potential of Rosehip (*Rosa canina*) Fruits Grown, *J Anatolian Env Anim Sci*, 8(1), 2023, 103–109.
 - [38] V.M. Miljković, L. Nikolić, J. Mrmošanin, I. Gajić, T. Mihajilov-Krstev, J. Zvezdanović, M. Miljković, Chemical Profile and Antioxidant and Antimicrobial Activity of *Rosa canina* L. Dried Fruit Commercially Available in Serbia, *Int J Mol Sci*, 25(5), 2024, 2518.
 - [39] S.L. Samson, A.J. Garber, Prevention of type 2 Diabetes Mellitus: Potential of pharmacological agents, *Best Pract Res Clin Endocrinol Metab*, 30(3), 2016, 357–371.
 - [40] N. Kaur, V. Kumar, S.K. Nayak, P. Wadhwa, P. Kaur, S.K. Sahu, Alpha-amylase as molecular target for treatment of diabetes mellitus: A comprehensive review, *Chem Biol Drug Des*, 98(4), 2021, 539–560.
 - [41] Y. Tao, Y.F. Zhang, Y.Y. Cheng, Y. Wang, Rapid screening and identification of alpha-glucosidase inhibitors from mulberry leaves using enzyme-immobilized magnetic beads coupled with HPLC/MS and NMR, *Biomed Chromatogr*, 27, 2013, 148–155.

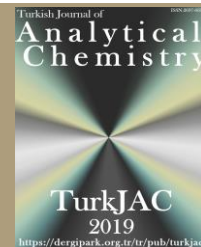
- [42] B. Asghari, P. Salehi, M.M. Farimani, S.N. Ebrahimi, α -Glucosidase inhibitors from fruits of *Rosa canina* L., *Rec Nat Prod*, 9(3), 2015, 276–283.
- [43] H.B. Jemaa, A.B. Jemia, S. Khlifi, H.B. Ahmed, F.B. Slama, A. Benzarti, J. Elati, A. Aouidet, Antioxidant activity and α -amylase inhibitory potential of *Rosa canina* L., *Afr J Tradit Complement Altern Med*, 14(2), 2017, 1–8.



TurkJAC

Turkish Journal of

Analytical Chemistry

<https://dergipark.org.tr/tr/pub/turkjac>TurkJAC
2019<https://dergipark.org.tr/tr/pub/turkjac>

Removal of anionic and cationic dyes from aqueous solutions using drinking water treatment plant sludge (DWTS): Equilibrium and kinetic evaluation*

Fatma Asya Turfan¹, Neslihan Kılıç¹, Fatma Yaltırık¹, Duygu Ozdes²,
Celal Duran^{1**}

¹ Karadeniz Technical University, Faculty of Science, Department of Chemistry, 61080, Trabzon, Türkiye

² Gümüşhane University, Gümüşhane Vocational School, Department of Chemical and Chemical Processing Technologies, 29100, Gümüşhane, Türkiye

Abstract

The present research investigates the removal of Brilliant Green (BG) and Remazol Brilliant Blue R (RBBR) dyes by an adsorption system utilizing drinking water treatment sludge (DWTS) as an adsorbent for the first time in the literature. It aims to contribute to sustainable treatment methods by evaluating waste sludge as a low-cost and environmentally friendly adsorbent. In the study, the significant parameters affecting the adsorption process were systematically investigated. During the experiments, the effects of factors such as initial pH of the solution, equilibrium time, adsorbent amount, and initial dye concentration on the adsorption efficiency were evaluated. The obtained data were tested with Langmuir and Freundlich isotherm models, and it was determined that adsorption occurred on both homogeneous and heterogeneous surfaces. The maximum adsorption capacity of DWTS was calculated as 100.0 mg/g and 38.9 mg/g for BG and RBBR, respectively. Kinetic analyses were performed to understand the dynamics of the adsorption process. Pseudo-first order and Pseudo-second order kinetic models were evaluated and it was noticed that the pseudo-second order model explained the adsorption data better. As a result, DWTS has been proven to be an effective adsorbent in the removal of BG and RBBR. The findings indicated that DWTS has significant potential for evaluation in advanced treatment processes in terms of environmental sustainability.

Keywords: Adsorption, brilliant green, drinking water treatment sludge, dye, Remazol Brilliant Blue R

1. Introduction

With the industrial revolution, rapidly increasing human activities have brought about various types of environmental pollution, and among these, water pollution has posed major threats to the ecosystem and human health [1]. Since water resources are indispensable for human survival, water pollution constitutes the most critical factor among environmental problems. Water pollutants can be divided into two main categories: organic and inorganic pollutants. Inorganic pollutants include toxic metals and metalloids; organic pollutants include surfactants, phenolic compounds, and anionic and cationic dyes, especially those originating from the textile, chemical, or food industries. These pollutants, which reach the environment, especially water resources, as a result of industrial activities, cause irreversible damage to the

ecosystem and threaten the health of living beings [2,3]. In this context, it is necessary to develop economical and efficient treatment processes in order to effectively treat polluted water.

Dyes are considered to be among the most dangerous pollutants due to their chemically stable structure, resistance to degradation and potential carcinogenic properties [4–6]. In addition to these harmful effects, the contamination of natural waters with dyes reduces the rate of light penetration and affects the ecosystem by degrading the overall water quality. In addition, bacteria in the water consume dissolved oxygen to break down the dyes, further degrading the quality of the water [7]. Dyes that pass into human metabolism through the food chain can have serious adverse effects on human health. These include acute health problems such as allergic

Citation: F.A. Turfan, N. Kılıç, F. Yaltırık, D. Ozdes, C. Duran, Removal of anionic and cationic dyes from aqueous solutions using drinking water treatment plant sludge (DWTS): Equilibrium and kinetic evaluation, Turk J Anal Chem, 7(2), 2025, 97–107.

****Author of correspondence:** cduran@ktu.edu.tr

Tel: +90 (462) 377 42 10

Fax: N/A

Received: December 31, 2024

Accepted: March 13, 2025

doi <https://doi.org/10.51435/turkjac.1609671>

*This paper was presented at the 6th International Environmental Chemistry Congress, EnviroChem 05-08 November 2024, Trabzon Türkiye.

reactions, skin rashes, dermatitis, digestive system disorders, headaches, nausea, vomiting, as well as serious disorders such as reproductive problems, developmental disorders and liver failure [8,9]. Therefore, it is of great importance that dyes in industrial wastewater are effectively treated before they are released into the natural environment. For this purpose, methods such as liquid-liquid extraction [10], ion exchange [11], advanced oxidation [12], coagulation [13], flocculation [14] and adsorption [15] have been developed. The adsorption technique offers high efficiency in removing pollutants from water, air and soil. It has important advantages such as being applicable to different pollutant types and concentrations, providing a wide range of applications, generally not being operationally complex and consuming less energy compared to some other treatment methods. In addition, by selecting the appropriate adsorbent, it can focus on specific pollutants and offers an effective solution for the separation of certain substances in industrial applications [16,17]. Adsorption, which is an environmentally friendly method with low chemical use, also stands out in terms of sustainability with the fact that some adsorbents can be recycled in an environmentally friendly way. However, the high cost of adsorbents to be used in the adsorption process can reduce the interest of wastewater producing factories in the treatment process [18]. For this reason, it is of great importance to develop low-cost, easily available and high adsorption capacity adsorbents for use in wastewater treatment. For this purpose, adsorbents such as acid and base activated *Symplocos racemosa* agro-waste [19], H_3PO_4 -functionalized bagasse [20], okara [21], used-tea powder [22], *Ficus benghalensis* tree leaves [23], fava bean peels [24], and watermelon and corn peels [25] have previously been tested by various researchers for the removal of dyes from water. Such adsorbents will both contribute to environmental sustainability and help industrial applications become more widespread [26,27]. In recent years, the usage of drinking water treatment sludge (DWTS) as an adsorbent has also attracted the interest of researchers [28,29].

DWTS is the solid waste generated during processes such as coagulation, flocculation, sedimentation, and filtration, which are used to treat water and make it suitable for drinking water standards. Some chemicals added during water treatment cause the sedimentation of suspended solids and these sediments accumulate as waste sludge over time. The disposal of this waste sludge is challenging and is primarily carried out through storage. Alternatively, under specific conditions, it can be used as a soil improver in agriculture and as a road filler or cement additive in the

construction sector. As a result, the proper management of DWTS is very important in terms of both environmental sustainability and economic benefit. Today, various studies are being conducted on the recycling of this sludge and its use in alternative areas [30]. In this context, in the present research, a cheap and effective adsorption method was developed by using DWTS as an adsorbent for the removal of cationic Brilliant Green (BG) and anionic Remazol Brilliant Blue R (RBBR) dyes from aqueous solutions.

2. Materials and methods

2.1. Preparation and characterization of adsorbent

In this study, drinking water treatment sludge (DWTS) used as adsorbent was supplied from a water treatment plant in Trabzon. The samples were homogeneously collected from a mixed sludge reservoir using sterile 500 mL containers. After the DWTS was collected, it was dried without any chemical or physical activation process, then ground to $<180\ \mu\text{m}$ and stored in petri dishes.

Scanning Electron Microscope (ZIESS EvoLs10) and Fourier Transform Infrared Spectrometer (Perkin Elmer Spectrum One) were used to elucidate the morphological structure of DWTS and to obtain information about the surface functional groups. The crystal structure of DWTS was investigated by X-Ray Diffraction (XRD) measurements (Rigaku TTR III) with $\text{Cu K}\alpha$ radiation ($\lambda = 1.5406\ \text{\AA}$) in the 2θ range of $5\text{--}80^\circ$.

2.2. Chemicals and instruments

All chemicals used in the study were of analytical grade and were supplied by Fluka (Buch, Switzerland) or Merck (Darmstadt, Germany). To prepare stock BG and RBBR solutions at a concentration of 5000 mg/L, 1.250 g of solid dyes were weighed and dissolved, and the final volume was completed to 250 mL with distilled water. Calibration and working solutions were obtained by diluting these stock solutions. Na_2CO_3 and Na_3PO_4 were used to evaluate the effects of salts on dye adsorption. Perkin Elmer Lambda 25 model UV-Vis spectrophotometer was used to determine the dye concentration in the solution medium before and after adsorption, Hanna pH-2221 model desktop pH meter was used to prepare solutions at desired pHs and to determine the pH values of the solutions, BOECO PSU-15i model mechanical shaker was used for adsorption experiments, BOECO S-8 model centrifuge was used to separate the adsorbent from the solution, Sartorius BP1106 model analytical balance was used for weighing the adsorbent and other chemicals.

2.3. Batch adsorption experiments

Adsorption experiments were carried out by batch method. For this purpose, certain amounts of DWTS (1.0-

20.0 g/L for BG and 1.0-15.0 g/L for RBBR) were weighed into 15 mL polypropylene centrifuge tubes. Then 10 mL each of BG solutions with an initial concentration range of 10-750 mg/L (at its natural pH) and a series of RBBR solutions with a concentration range of 10-600 mg/L (adjusted to an initial pH of 2.0) were added to the tubes and the resulting mixtures were shaken at 300 rpm on a mechanical shaker for 1-120 min. At the end of the determined periods, the adsorbate solutions were separated from the adsorbent by centrifuging at 3500 rpm for 5 min. The concentration of the dye remaining unadsorbed in the solution was determined by analyzing with a UV-Vis Spectrophotometer at 625 and 592 nm wavelengths for BG and RBBR, respectively. The amount of dye adsorbed by 1 g of DWTS was calculated as mg g^{-1} using Eq. 1.

$$q_e = \frac{(C_o - C_e) \times V}{m} \quad (1)$$

Here, q_e (mg g^{-1}) represents the amount of BG or RBBR retained by 1 g of DWTS, C_o (mg/L) is the initial concentration of BG or RBBR, C_e (mg/L) is the concentration of each dye remaining in the aqueous solution at equilibrium because of not being adsorbed by the DWTS, V (L) is the volume of dye solution added on the DWTS, and m (g) is the mass of DWTS.

3. Results and discussion

3.1. Characterization of DWTS

To identify the functional groups responsible for the adsorption of dyes on the surface of DWTS, the FTIR spectrum of DWTS was analyzed. According to the spectrum shown in Fig. 1, the peaks at 990 cm^{-1} and 694 cm^{-1} are attributed to Si-O groups, the peak at 3385 cm^{-1} is associated with O-H, and the peak at 1635 cm^{-1} is attributed to C=C stretching vibrations [30].

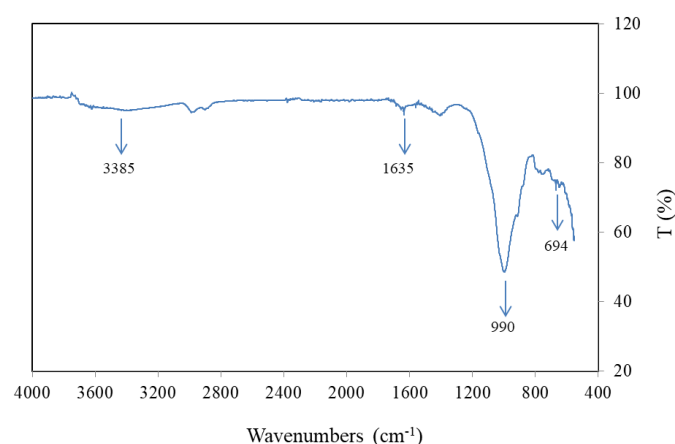


Figure 1. FTIR Spectrum of DWTS

SEM images, obtained at different magnifications (5000x and 10000x), were used to investigate the surface

morphology of the DWTS (Fig. 2). These images reveal that the DWTS surface is relatively rough with indentations and lacks significant porous structures or channels. There are agglomerated particles of varying sizes observed in the structure suggesting a non-uniform texture. This structure of the surface may affect the adsorption capacity of dyestuffs. In addition, according to EDX data, it is noticed that there is a significant amount of Si (52%) and Al (18%) in the DWTS structure.

XRD spectrum was obtained to get an idea about the crystal structure of DWTS (Fig. 3). In spectrum, characteristic peaks of kaolinite, quartz, muscovite and calcite minerals were observed at specific 2θ angles. As a result of the analysis, intense diffraction peaks were determined at 24.9° for kaolinite (JCPDS No: 01-078-1996), 26.6° for quartz (JCPDS No: 01-085-0795), 29.5° for muscovite (JCPDS No: 01-076-0663) and 23° for calcite (JCPDS No: 01-072-1652). These peaks were verified by comparing them with standard patterns registered in the JCPDS (ICDD) database. Based on these comparisons, it can be stated that DWTS is primarily composed of kaolinite, quartz, muscovite and calcite minerals [30].

3.2. Influences of initial pH

In the adsorption of anionic and cationic dyes, pH is a critical parameter to optimize as it influences both the chemical structure of the dye and the surface properties of the adsorbent [31]. The effect of pH on the adsorption of BG and RBBR was tested in the range of pH 2.0-8.0 using 5.0 g/L DWTS at an initial dye concentration of 100 mg/L. The adsorption efficiency of BG, a cationic dye, is low at low pH values but increases with rising pH, reaching an optimum at pH 5.0, beyond which no significant changes are observed. While the adsorption efficiency of RBBR, which is an anionic dye, is 6.49 mg/g at pH 2.0, it decreases to 0.30 mg/g at pH 8.0. The effect of pH on the adsorption of dyes can be explained by considering the pH_{pzc} value of DWTS. The pH_{pzc} value for DWTS is calculated as 8.4. At low pH values ($\text{pH} < \text{pH}_{\text{pzc}}$), the surface of the adsorbent is generally protonated and carries a positive charge, while at high pH values, the protons on the surface are separated and the adsorbent surface becomes negatively charged ($\text{pH} > \text{pH}_{\text{pzc}}$). Since BG is positively charged in aqueous solution, it creates a stronger electrostatic attraction with the negatively charged adsorbent surface at high pH values and the adsorption efficiency increases. However, since RBBR is negatively charged in aqueous solution, it shows a weak adsorption efficiency due to the repulsive forces with the negatively charged adsorbent surface at low pH values. However, at low pH values, when the surface is positively charged, electrostatic attractive forces increase RBBR adsorption [32]. The pH of the aqueous solution affects not only electrostatic interactions but also van der Waals forces, hydrogen bonds and hydrophobic interactions.

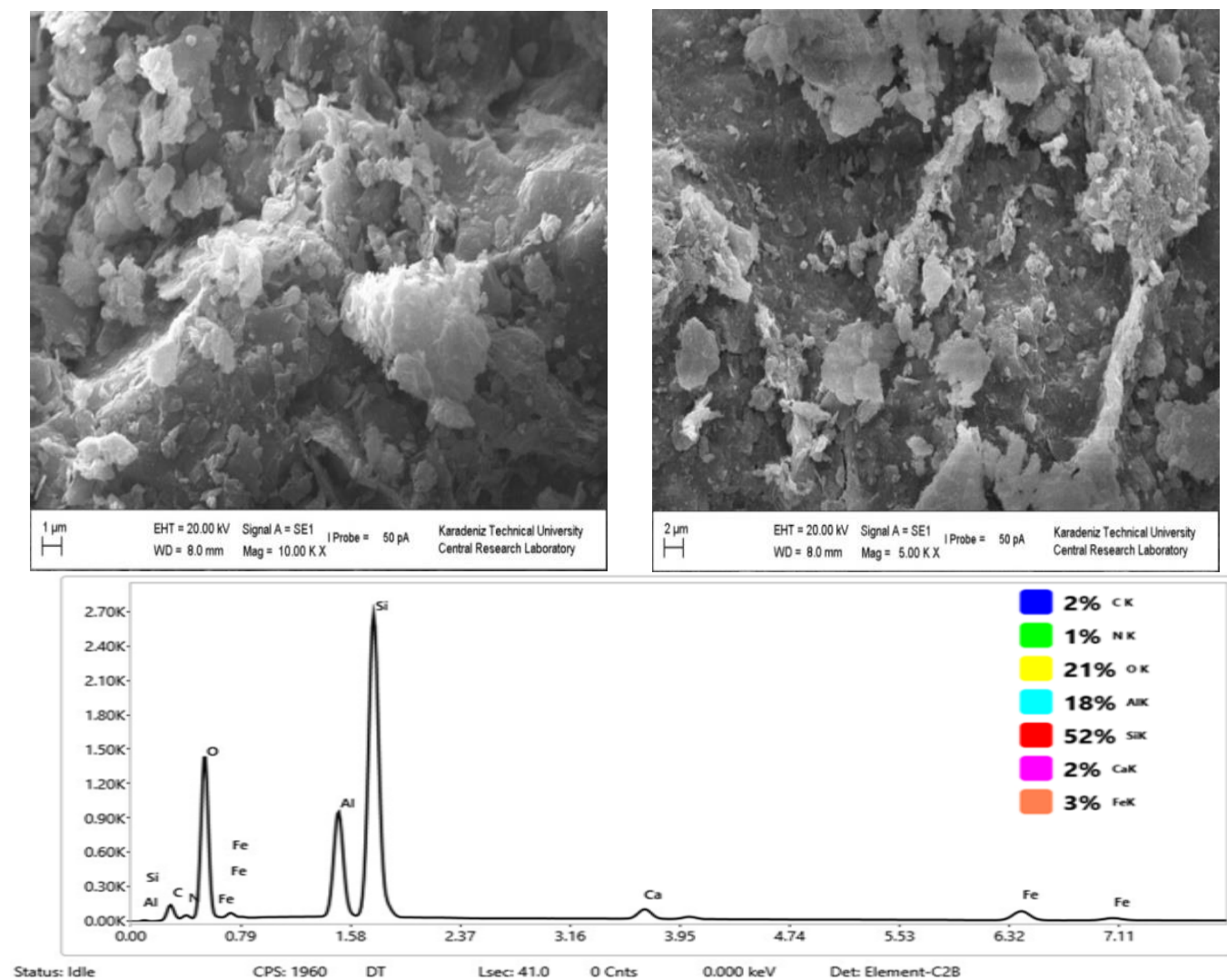


Figure 2. SEM-EDX images of DWTS

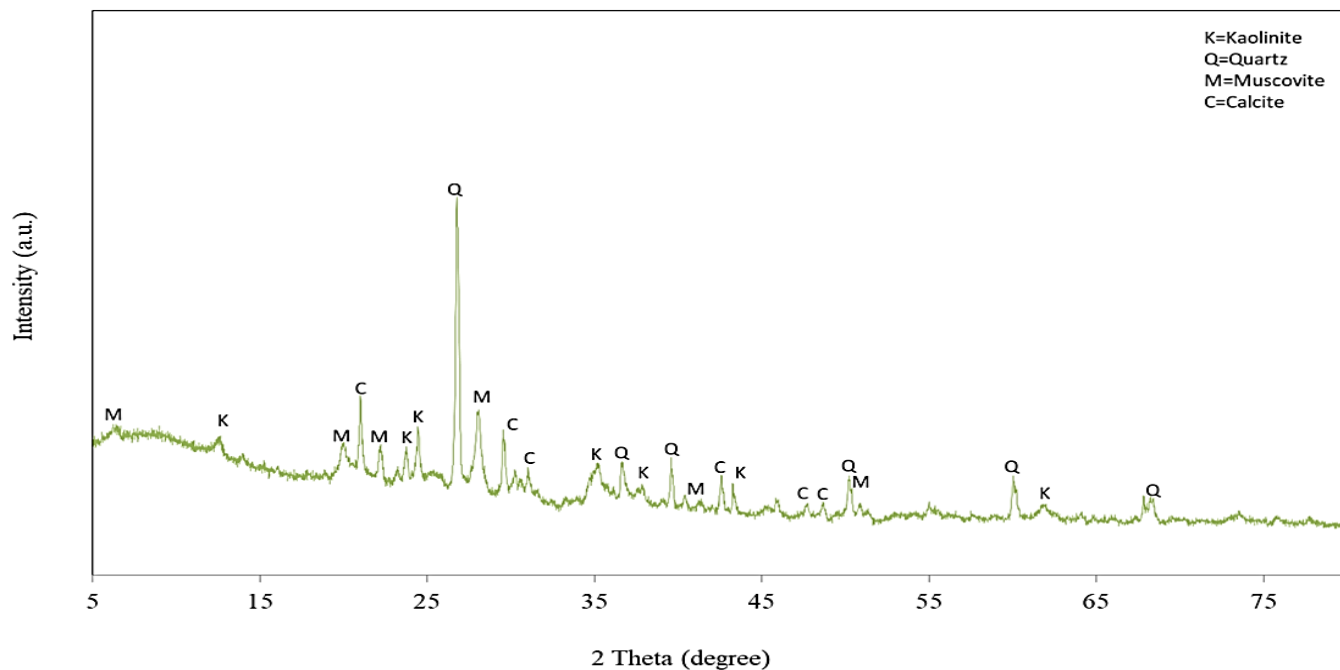


Figure 3. XRD Spectrum of DWTS

Therefore, the optimal pH range in each system must be determined experimentally. In general, lower pH values enhance the adsorption efficiency of anionic dyes ($\text{pH} < \text{pH}_{\text{pzc}}$), while higher pH values ($\text{pH} > \text{pH}_{\text{pzc}}$) improve the adsorption efficiency of cationic dyes. As a result, further studies on the adsorption of BG onto DWTS were carried out at the natural pH value of the dye, while the optimum pH for RBBR was determined as 2.0.

3.3. Influences of contact time and the kinetic studies

The equilibrium time plays a crucial role in ensuring the effective completion of the developed adsorption process. Data obtained from the equilibrium time study help to interpret the rate control mechanism of adsorption such as film diffusion, intraparticle diffusion or chemical bonding. In industrial applications, systems with short equilibrium times are preferred both to save time and to be more economical. However, the equilibrium time of the adsorption system is significantly affected by the surface area and pore structure of the adsorbent, the molecular size and concentration of the adsorbate, and the properties of the medium such as temperature and pH. In this study, the effect of equilibrium time for BG and RBBR adsorption on DWTS was investigated in detail. For this purpose, 10 mg of DWTS for BG and 50 mg of DWTS for RBBR were weighed separately and then 10 mL of BG (100 mg/L) at natural pH value and RBBR (100 mg/L) solution adjusted to pH 2.0 were added to them. After shaking at different time intervals, the adsorbate and adsorbent mixtures were separated from each other by centrifugation and the dye concentrations remaining unadsorbed in the solution were determined by UV-Vis Spectrophotometer and then the amount of dye (q_t) adsorbed by 1 g DWTS at different time intervals were calculated. In the initial stages of both BG and RBBR adsorption (1–5 min time interval), the adsorption rate is high due to the presence of many active binding sites on DWTS. In the initial stages, the active binding sites that are empty on DWTS promote rapid diffusion. After the 5 min, the adsorption rate decreases as the active sites on the DWTS surface begin to be filled with BG and RBBR molecules. Intraparticle diffusion is effective at this stage. After the 90 min for BG and the 60 min for RBBR, an equilibrium occurs between the dye concentration in the solution and the adsorbed amount on DWTS, and after this stage, no significant change occurs in the adsorption amount [33]. Therefore, in subsequent studies for BG and RBBR, the equilibrium time of 90 and 60 min was accepted as optimum, respectively (Fig. 4).

Kinetic models are essential for understanding the adsorption rate, mechanism, and controlling steps of BG and RBBR on DWTS. The experimental data obtained from kinetic studies were analyzed using the pseudo-first order (PFO) and pseudo-second order (PSO) models.

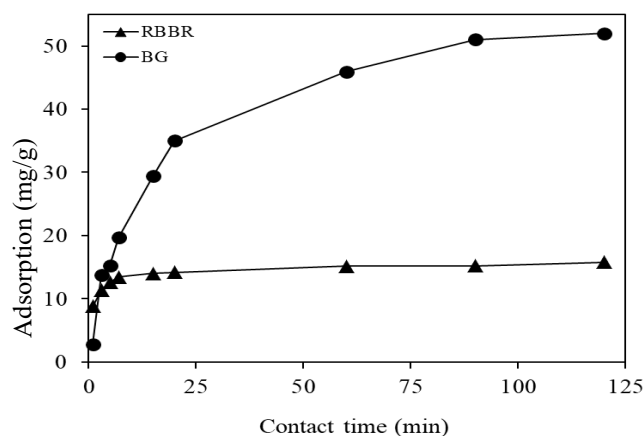


Figure 4. Effect of contact time on the adsorption of RBBR and BG onto DWTS

The PFO model is used to describe cases where adsorption is controlled by physical processes, while the PSO model is more appropriate for situations where chemical adsorption dominates.

The linear equations for the PFO [34] and PSO [35] models are given in Eq. 2 and Eq. 3, respectively.

$$\ln(q_e - q_t) = \ln q_e - k_1 t \quad (2)$$

$$\frac{t}{q_t} = \frac{1}{k_2 q_e^2} + \frac{t}{q_e} \quad (3)$$

In the equations, q_e (mg g^{-1}) and q_t (mg g^{-1}) are the amounts of BG and RBBR adsorbed on the DWTS at equilibrium and at any time t (min), respectively. k_1 (min^{-1}) and k_2 ($\text{g mg}^{-1} \text{min}^{-1}$) are the rate constants of the PFO and PSO models, respectively. According to the PFO kinetic model, k_1 and q_e values are obtained from the slope and intercept of the $\ln(q_e - q_t)$ graph against t , respectively. Considering the PSO kinetic model, q_e and k_2 values are calculated from the slope and intercept of the figure plotted between $t/q_t - t$, respectively. The constants obtained for each kinetic model, together with the relevant correlation coefficients (R^2), are shown in Table 1.

Table 1. Kinetic parameters in the adsorption of RBBR and BG onto DWTS

Kinetic models	Adsorbate	
	RBBR	BG
$q_{e \text{ exp}}$ (mg/g)	15.8	52.0
PFO		
k_1 (min^{-1})	-0.024	-0.040
$q_{e \text{ cal}}$ (mg/g)	3.64	44.6
R^2	0.7968	0.9780
PSO		
k_2 ($\text{g mg}^{-1} \text{min}^{-1}$)	0.041	0.012
$q_{e \text{ cal}}$ (mg/g)	15.8	58.5
R^2	0.9994	0.9962

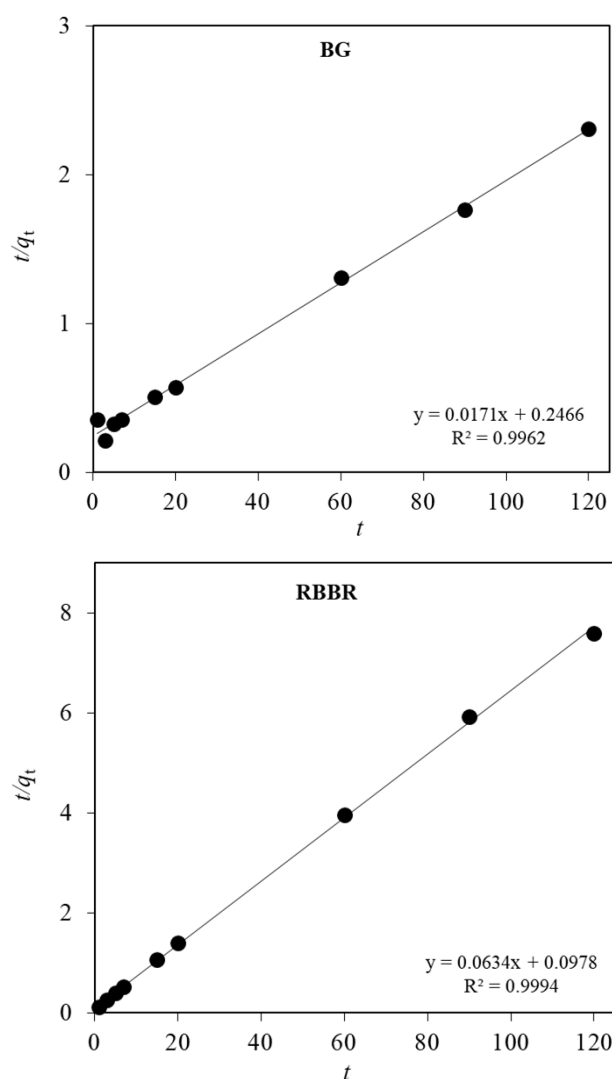


Figure 5. Pseudo-second order kinetics model

The $q_{e,exp}$ values for BG and RBBR were calculated as 52.0 mg/g and 15.8 mg/g, respectively. After applying the PFO kinetic model to the experimental data, the $q_{e,cal}$ values for BG and RBBR were determined to be 44.6 mg/g and 3.64 mg/g, respectively, with R^2 values of 0.978 and 0.797, respectively. By applying the PSO kinetic model, the $q_{e,cal}$ values for BG and RBBR were found to be 58.5 mg/g and 15.8 mg/g, respectively, with R^2 values exceeding 0.995 for both adsorbates (Fig. 5). Considering these data, it is noticed that the PSO kinetic model is dominant in the adsorption mechanism of both BG and RBBR on DWTS, as the experimentally calculated q_e values are close to the q_e values observed by applying the model. On the other hand, higher R^2 values were also obtained by applying the PSO kinetic model. This result indicates that chemisorption plays a significant role in the adsorption mechanism.

3.4. Influences of initial dye concentration and adsorption isotherms

The efficiency of the adsorption process and the adsorbent capacity are significantly affected by the

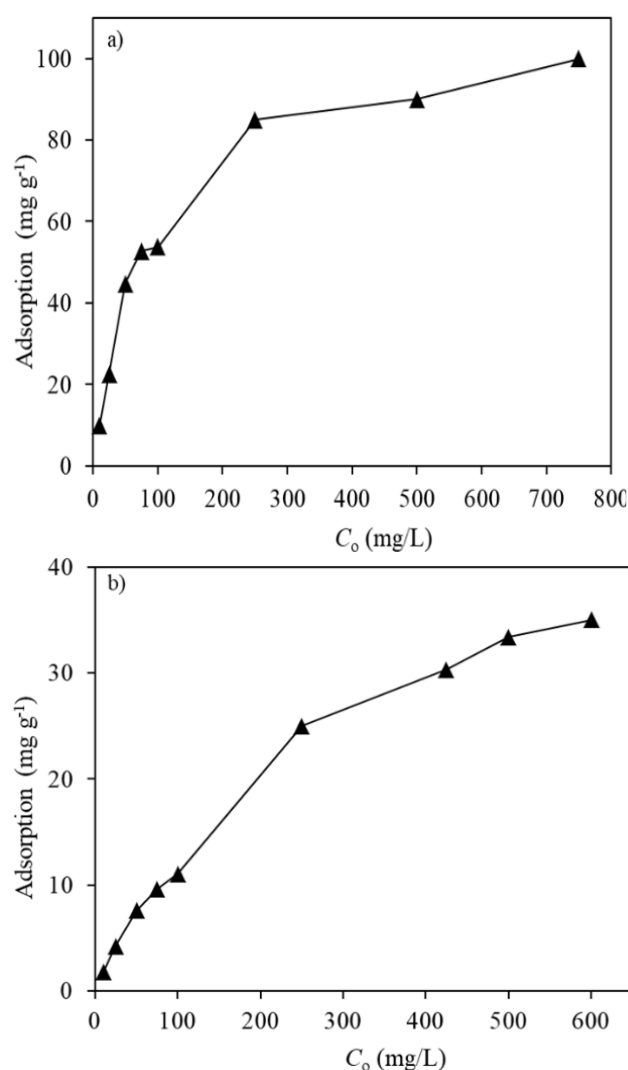


Figure 6. Effect of initial dye concentration on the adsorption efficiency of a) BG b) RBBR

initial dye concentration. As the initial concentration of dye molecules in solution increases, a concentration gradient is formed between the molecules in the solution and the DWTS surface, which increases the rate of dye molecules moving to the adsorbent surface. However, the active sites on the adsorbent surface are rapidly saturated at high dye concentrations. The initial concentration also influences the amount of dye adsorbed per unit of adsorbent (q_e). Generally, as the initial concentration increases, q_e increases because more dye molecules are adsorbed onto the adsorbent surface; however, after a certain stage, q_e remains constant because the surface reaches saturation [36].

In order to evaluate the effect of initial dye concentration on the adsorption efficiency of BG and RBBR on DWTS and to obtain the adsorption isotherm data, adsorption studies were carried out with dye solutions with initial concentrations ranging from 10 to 750 mg/L for BG and 10 to 600 mg/L for RBBR. The results obtained from the experimental studies showed that with the increase of BG concentration from 10 mg/L to 750 mg/L and RBBR concentration from 10 mg/L to 600 mg/L, the adsorbed dye amount increased from 10.0

mg/g to 100.0 mg/g (Fig. 6a) and from 1.78 mg/g to 35.0 mg/g (Fig. 6b), respectively.

The Langmuir [37] and Freundlich [38] isotherm models, based on different assumptions, were applied to the experimental data to mathematically represent the adsorption process and interpret its mechanism. The Langmuir isotherm model is based on the assumption that adsorption occurs in a single layer on the adsorbent surface, that all active sites on the adsorbent surface have equal energy, and that there is no interaction between molecules adsorbed on the surface. According to the Freundlich isotherm model developed to explain the adsorption processes occurring in multilayers on heterogeneous surfaces, the active sites on the adsorbent surface have different binding energies. The linear equations of these isotherm models are given in Eq. 4 and Eq. 5, respectively.

$$\frac{C_e}{q_e} = \frac{C_e}{q_{\text{maks}}} + \frac{1}{b q_{\text{maks}}} \quad (4)$$

$$\ln q_e = \ln K_f + \frac{1}{n} \ln C_e \quad (5)$$

In these equations, q_e (mg g⁻¹); is the amount of BG or RBBR adsorbed per unit DWTS mass, C_e (mg L⁻¹); is the dye concentration in the aqueous solution at equilibrium, b (L mg⁻¹); is the free energy of adsorption, q_{maks} (mg g⁻¹); is the maximum monolayer adsorption capacity, K_f (mg g⁻¹); is the adsorption capacity, and n is a unitless constant representing the adsorption density. In addition, the applicability of an adsorption process is estimated by evaluating the R_L parameter calculated with the help of Eq. 6. R_L values between 0 and 1 reveal suitable adsorption.

$$R_L = \frac{1}{1 + b \cdot C_0} \quad (6)$$

C_e/q_e versus C_e plots (for Langmuir isotherm) and $\ln q_e$ versus $\ln C_e$ plots (for Freundlich isotherm) for BG and RBBR are given in Fig. 7 and Fig. 8, respectively. The constants for both isotherm models were calculated from the slope of the plots and the point where they intersect the ordinate axis, and the values are provided in Table 2. When the data obtained for BG and RBBR adsorption were evaluated, the R^2 values obtained from both the Langmuir and Freundlich isotherm models were higher than 0.95, providing an idea that the DWTS surface exhibits both homogeneous and heterogeneous properties in its adsorption behavior. This indicates that the DWTS surface has a complex structure and contains active sites with different binding energies. It also

indicates that DWTS can support both monolayer and multilayer adsorption processes. The DWTS surface exhibiting both homogeneous and heterogeneous properties can be attributed to several factors. DWTS generally contains various inorganic and organic components. The presence of clay minerals, metal oxides (such as Fe and Al oxides), and organic matter can contribute to both homogeneous and heterogeneous characteristics of the surface. On the other hand, the DWTS surface may contain various functional groups responsible for adsorption. The irregular distribution of these groups can lead to homogeneous adsorption in some regions, while causing heterogeneous adsorption in others. Using the Langmuir isotherm model, the maximum adsorption capacities of DWTS for BG and RBBR were calculated as 100.0 mg/g and 38.9 mg/g, respectively. The proposed adsorbent exhibits a higher adsorption capacity than many of the adsorbents listed in Table 3 [19–25]. The R_L values obtained from the Langmuir isotherm model were in the range of 0.645–0.024 for BG concentrations of 10–750 mg/L and in the range of 0.862–0.094 for RBBR concentrations of 10–600 mg/L, supporting that the adsorption process was suitable under the studied conditions [39]. In addition, the n value obtained from the Freundlich isotherm model also gives an idea about the suitability of the adsorption process. The fact that this value is in the range of 1–10 indicates the suitability of the adsorption process [40]. The n values for BG and RBBR were calculated as 4.20 and 2.02, respectively, and this result supports the interpretation made for R_L .

3.5. Influences of adsorbent amount

During the adsorption process, the amount of DWTS directly influences the number of active sites available for binding with BG and RBBR molecules in the solution, making it one of the key parameters that determine the adsorption efficiency. The increase in the amount of adsorbent increases the number of active sites, which can lead to an increase in adsorption capacity. However, this increase continues up to a certain point; after this point, the adsorption process may reach saturation, and further increases in the amount of adsorbent do not provide a significant change in adsorption efficiency [41]. The effects of DWTS amount on the removal efficiency of BG and RBBR from aqueous media were evaluated for DWTS amounts in the range of 1.0–20.0 g/L and 1.0–15.0 g/L, respectively. The equilibrium BG and RBBR amounts and dye removal efficiency percentages are plotted against DWTS amounts in Fig. 9a and Fig. 9b, respectively. The increase in the amount of DWTS caused an increase in the active adsorption sites, and the

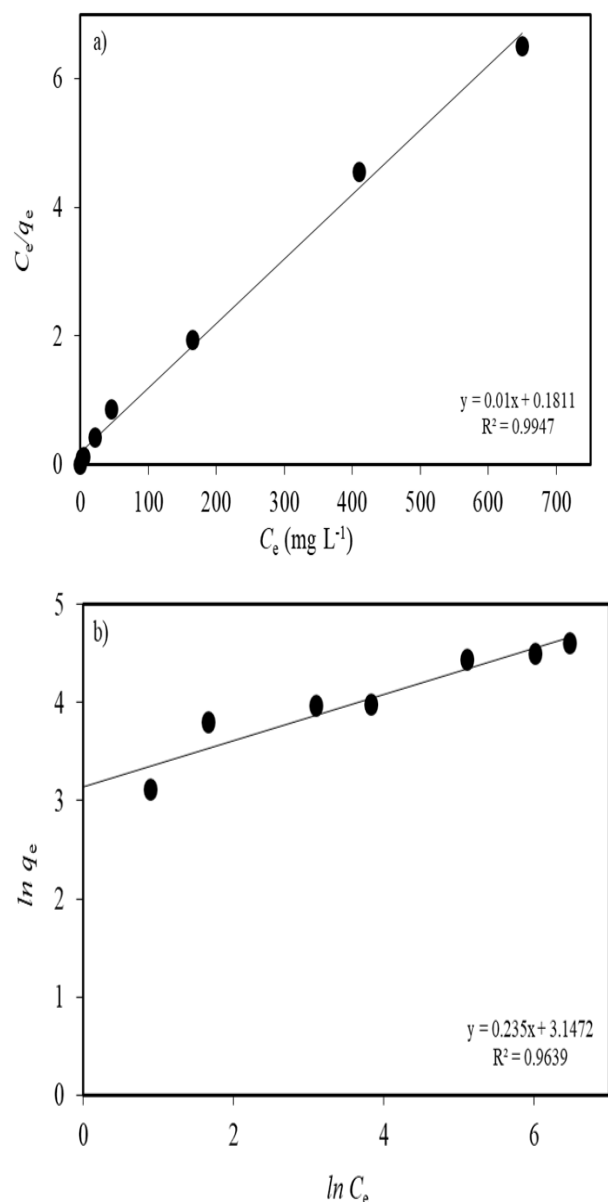


Figure 7. a) Langmuir isotherm model b) Freundlich isotherm model for the adsorption of BG

adsorption percentage increased from 20.1% to 97.4% and from 36.8% to 79.8% for BG and RBBR, respectively. However, since the excess amount of DWTS caused the formation and agglomeration of unsaturated adsorption surfaces, the amount of BG and RBBR adsorbed per gram of adsorbent decreased from 100.6 mg/g to 24.4 mg/g and from 73.5 mg/g to 10.6 mg/g, respectively.

3.6. Influences of foreign ions

During the adsorption process, the salts present in the solution can affect the electrostatic interactions between the adsorbent and the adsorbate, which can increase or decrease the adsorption efficiency. Therefore, the effects of various salts containing ions that can be commonly found in wastewater on the adsorption efficiency of BG and RBBR on DWTS were tested. Na_2CO_3 and Na_3PO_4 were used as model salts.

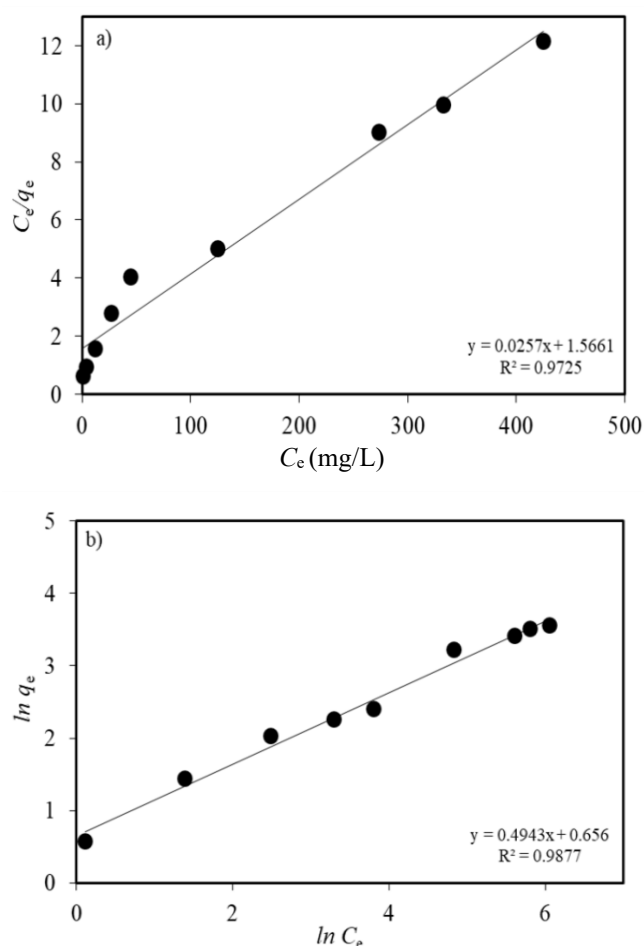


Figure 8. a) Langmuir isotherm model b) Freundlich isotherm model for the adsorption of RBBR

Table 2. Isotherm parameters for the adsorption of RBBR and BG

	RBBR	BG
Langmuir isotherm model		
q_{\max} (mg/g)	38.9	100.0
b (L mg ⁻¹)	0.016	0.055
R^2	0.9725	0.9947
Freundlich isotherm model		
K_f (mg/g)	1.93	23.3
n	2.02	4.2
R^2	0.9877	0.9639

Table 3. Comparison of the maximum dye adsorption capacities of various adsorbents

Adsorbent	Dye	q_{\max} (mg/g)	Reference
Acid activated <i>Symplocos racemosa</i> agro-waste	BG	62.9	[19]
Base activated <i>Symplocos racemosa</i> agro-waste	BG	71.0	[19]
H_3PO_4 -functionalized bagasse	BG	139	[20]
Okara	BG	64.33	[21]
Used tea leaves	BG	101.01	[22]
<i>Ficus benghalensis</i> Tree Leaves	BG	19.5	[23]
Fava bean peels	BG	28.14	[24]
Watermelon peel	RBBR	1.046	[25]
Corn peel	RBBR	0.047	[25]
DWTS	BG	100.0	This Study
DWTS	RBBR	38.9	This Study

In order to investigate the effect of salts on BG adsorption, BG solutions containing 10 mg DWTS at a concentration of 150 mg/L and salt solutions with a concentration of 0.01–0.10 M (at natural pH value) were treated separately for 90 min. In order to investigate the effect of salts on RBBR adsorption, RBBR solutions containing 50 mg DWTS at a concentration of 50 mg/L and adjusted to pH 2.0 and salt solutions with a concentration of 0.01–0.10 M were treated separately for 60 min. After determining the concentration of BG and RBBR remaining unadsorbed in the solution, the amount of BG and RBBR adsorbed per gram of DWTS (q_e) was plotted against the concentration of salts with the obtained data (Fig. 10a and Fig. 10b). No significant change was observed in the adsorption efficiency by increasing the concentrations of Na_2CO_3 and Na_3PO_4 from 0.01 M to 0.10 M for both dyes. This shows that the developed adsorption process will be effectively applied to wastewaters containing high concentrations of salt.

4. Conclusions

In the present study, drinking water treatment sludge (DWTS) has been utilized as a low-cost and effective adsorbent for the removal of Brilliant Green (BG) and Remazol Brilliant Blue R (RBBR) dyes from waters and wastewaters. This study is an original research in which DWTS is used as an adsorbent for the first time in the removal of BG and RBBR dyes. In this context, DWTS, which has no economic value and is formed as a waste, has been functionalized as an adsorbent in this study and has been created as an alternative to other adsorbents that are generally high cost and require the use of chemicals. This approach not only contributes to the solution of an environmental problem but also offers a sustainable waste management strategy.

In batch adsorption experiments, the adsorption of BG onto DWTS was found to be most efficient at the

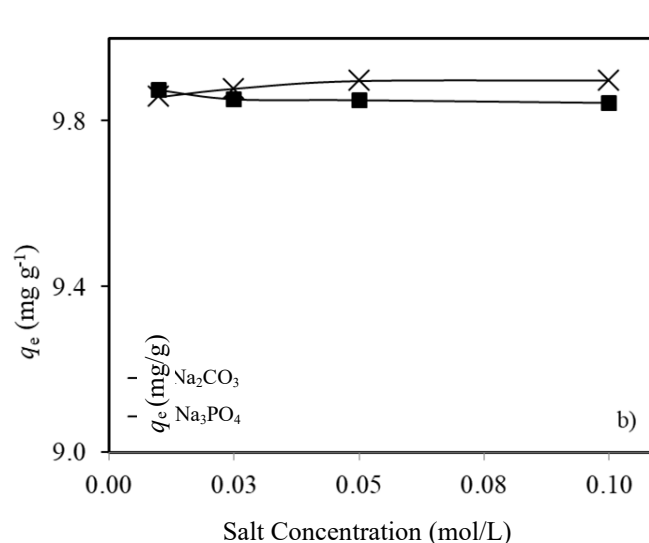
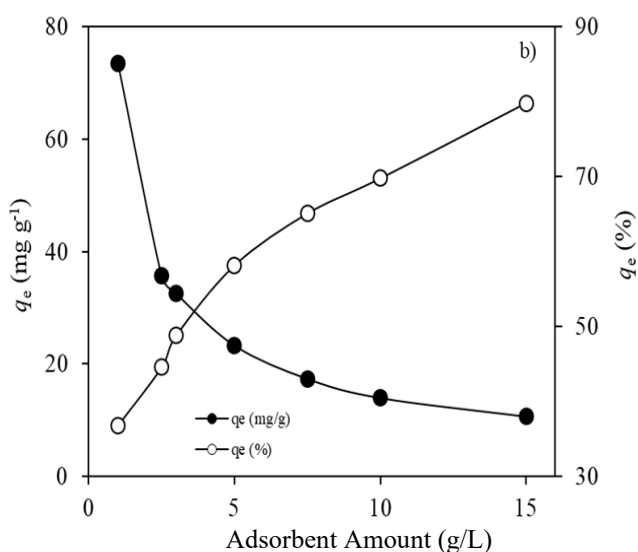
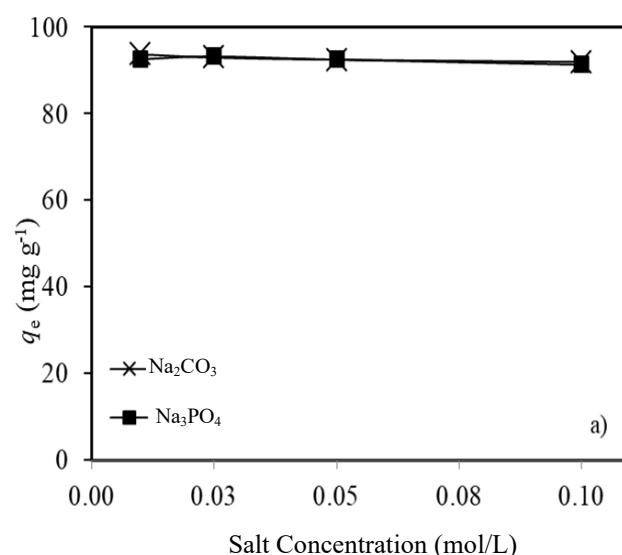
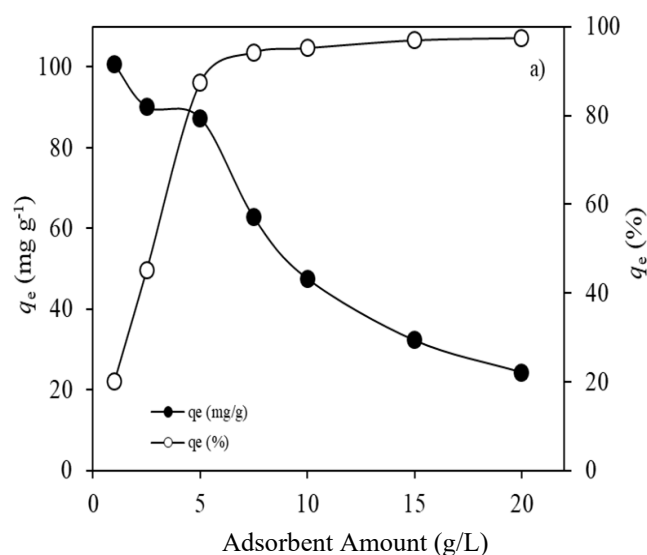


Figure 9. Influences of adsorbent dosage on the adsorption of a) BG b) RBBR

Figure 10. Effect of foreign salts on the adsorption efficiency of DWTS in the adsorption of a) BG b) RBBR

dye's natural pH, whereas the optimum pH for RBBR was determined to be 2.0. The equilibrium time for the most efficient adsorption of BG and RBBR was optimized as 90 min and 60 min, respectively. Using the Langmuir isotherm model, the maximum adsorption capacity of DWTS was obtained as 100 mg/g for BG and 38.9 mg/g for RBBR. This adsorption capacity is observed to be higher than many difficult-to-prepare adsorbents reported in the literature.

In further studies, it is suggested to investigate the potential of DWTS not only for the removal of other dyes but also for the removal of inorganic pollutants. Such studies may offer new opportunities for the development of environmentally friendly and economical adsorbents.

Acknowledgement

The financial support from the TUBİTAK 2209-A-Research Project Support Programme for Undergraduate Students (Project No. 1919B012305540) is gratefully acknowledged.

References

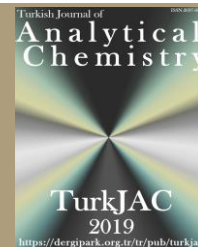
- [1] F.N. Chaudhry, M.F. Malik, Factors Affecting Water Pollution: A Review, *J Ecosyst Ecography*, 7, 2017, 225.
- [2] S. Rezaia, M. Ponraj, A. Talaiekhosani, S.E. Mohamad, M.F. Md Din, S.M. Taib, F. Sabbagh, F. Md Sairan, Perspectives of phytoremediation using water hyacinth for removal of heavy metals, organic and inorganic pollutants in wastewater, *J Environ Manag*, 163, 2015, 125-133.
- [3] S. Mishra, A. Maiti, The efficiency of *Eichhornia crassipes* in the removal of organic and inorganic pollutants from wastewater: a review, *Environ Sci Pollut Res*, 24, 2017, 7921–7937.
- [4] R. Jamee, R. Siddique, Biodegradation of synthetic dyes of textile effluent by microorganisms: an environmentally and economically sustainable approach, *Eur J Microbiol Immunol (Bp)*, 9, 2019, 114-118.
- [5] M. Umar, H. Khan, F. Akbal, M. Usama, R. Tariq, S. Hussain, S.U. Zaman, H.A. Eroğlu, E.N. Kadioğlu, Highly selective and reusable nanoadsorbent based on Fe₃O₄-embedded sodium alginate-based hydrogel for cationic dye adsorption: Adsorption interpretation using multiscale modeling, *Int J Biol Macromol*, 289, 2025, 138694.
- [6] A. Tkaczyk, K. Mitrowska, A. Posyniak, Synthetic organic dyes as contaminants of the aquatic environment and their implications for ecosystems: A review, *Sci Total Environ*, 717, 2020, 137222.
- [7] H.M. Solayman, M.A. Hossen, A. Abd Aziz, N.Y. Yahya, K.H. Leong, L.C. Sim, K.D. Zoh, Performance evaluation of dye wastewater treatment technologies: a review, *J Environ Chem Eng*, 11 (3), 2023, 109610.
- [8] M. Shahid, S. Islam, F. Mohammad, Recent advancements in natural dye applications: a review, *J Clean Prod*, 53, 2013, 310-331.
- [9] A. El Jery, H.S. Alawamleh, M.H. Sami, H.A. Abbas, S. Sammen, A. Ahsan, M.A. Imteaz, A. Shanableh, Md. Shafiquzzaman, H. Osman, N. Al-Ansari, Isotherms, kinetics and thermodynamic mechanism of methylene blue dye adsorption on synthesized activated carbon, *Sci Rep*, 14, 2024, 970.
- [10] K. Sahoo, U.S. Behera, S. Poddar, H.-S. Byun, Revolutionizing Dye Removal: Unleashing the Power of Liquid-Liquid Extraction Batch Process, *Korean J Chem Eng*, 41, 2024, 2621–2638.
- [11] D. Yanardağ, S. Edebali, Adsorptive removal of malachite green dye from aqueous solution by ion exchange resins, *Biomass Conv Bioref*, 14, 2024, 5699–5710.
- [12] A. Ahmad, S.N.A.M. Jamil, T.S.Y. Choong, A.H. Abdullah, N.H. Faujan, A.A. Adeyi, R. Daik, N. Othman, Removal of Cationic Dyes by Iron Modified Silica/Polyurethane Composite: Kinetic, Isotherm and Thermodynamic Analyses, and Regeneration via Advanced Oxidation Process, *Polymers*, 14(24), 2022, 5416.
- [13] H. Eslami, T. Zarei Mahmoudabadi, Modified coagulation processes using polyferric chloride and polytitanium tetrachloride for the removal of anionic dye from aqueous solution, *Int J Environ Sci Technol*, 19, 2022, 1811–1818.
- [14] S. Ihaddaden, D. Aberkane, A. Boukerroui, D. Robert, Removal of methylene blue (basic dye) by coagulation-flocculation with biomaterials (bentonite and *Opuntia ficus indica*), *J Water Process Eng*, 49, 2022, 102952.
- [15] M.R. Popaliya, M. Mishra, A. Mishra, Removal of cationic dyes onto java plum leaves ash: adsorption isotherms, kinetics, thermodynamic and characterizations, *Chem Pap*, 77, 2023, 7881–7901.
- [16] D.F. Katowah, H.K. Alzahrani, A new ternary nanocomposites-based cellulose derivatives-CuFe₂O₄-zeolite with ultra-high adsorption capacity for Brilliant Green dye treatment and removal from the aquatic environment, *J Saudi Chem Soc*, 27(6), 2023, 101764.
- [17] A.P.N. De Souza, D.R. Sánchez, M. Alzamora, M.V. Colaço, M.A.V. de Souza, J.S. De Gois, J.D. Senra, N.M.F. Carvalho, Outstanding adsorption capacity of iron oxide synthesized with extract of açai berry residue: kinetic, isotherm, and thermodynamic study for dye removal, *Environ Sci Pollut Res*, 30, 2023, 109423–109437.
- [18] J.-X. Yang, G.-B. Hong, Adsorption behavior of modified *Glossogyne tenuifolia* leaves as a potential biosorbent for the removal of dyes, *J Mol Liq*, 252, 2018, 289-295.
- [19] M. Rashid, R. Rehman, M.E. Al-Hazemi, M.M. Jahangir, Z.T. Althagafi, R.I. Alsantali, M. Akram, Process optimization of adsorptive phytoremediation of mutagenic brilliant green dye for health risk management using chemically activated *Symplocos racemosa* agro-waste, *Int J Phytoremediation*, 26(5), 2023, 626–638.
- [20] K. Singh, U. Dixit, M. Lata, Surface activity, kinetics, thermodynamics and comparative study of adsorption of selected cationic and anionic dyes onto H₃PO₄-functionalized bagasse from aqueous stream, *Environ Sci Pollut Res* 30, 2023, 105927–105943.
- [21] H.T.A. Nguyen, T.T. Pham, Brilliant Green Biosorption from Aqueous Solutions on Okara: Equilibrium, Kinetic and Thermodynamic Studies, *J Water Environ Technol*, 21 (1), 2023, 30-40.
- [22] S. Vithalkar, R.M. Jugade, D. Saravanan, Adsorption of brilliant green dye by used-tea-powder: equilibrium, kinetics and thermodynamics studies, *Aqua Water Infrastruct Ecosyst Soc*, 71 (10), 2022, 1148–1158.
- [23] S. Gul, A. Gul, H. Gul, R. Khattak, M. Ismail, S.U. Khan, M.S. Khan, H.A. Aouissi, A. Krauklis, Removal of Brilliant Green Dye from Water Using *Ficus benghalensis* Tree Leaves as an Efficient Biosorbent, *Materials*, 16 (2), 2023, 521.
- [24] L. Nahali, Y. Miyah, F. Mejbar, M. Benjelloun, O. Assila, Y. Fahoul, V. Nenov, F. Zerrouq, Assessment of Brilliant Green and Eriochrome Black T dyes adsorption onto fava bean peels: kinetics, isotherms and regeneration study, *Desalin Water Treat*, 245, 2022, 255-269.
- [25] S. Kanthasamy, T. Hadibarata, T. Hidayat, S.A. Alamri, A.A. Al-Ghamdi, Adsorption of azo and anthraquinone dye by using watermelon peel powder and corn peel powder: equilibrium and

- kinetic studies, *Biointerface Res Appl Chem*, 10 (1), 2020, 4706 – 4713.
- [26] D. Ozdes, C. Duran, H. B. Senturk, H. Avan, B. Bicer, Kinetics, Thermodynamics and Equilibrium Evaluation of Adsorptive Removal of Methylene Blue onto Natural Illitic Clay Mineral, *Desalin Water Treat*, 52, 2014, 208–218.
- [27] C. Duran, D. Ozdes, A. Gundogdu, H.B. Senturk, Kinetics and Isotherm Analysis of Basic Dyes Adsorption onto Almond Shell (*Prunus dulcis*) as a Low Cost Adsorbent, *J Chem Eng Data*, 56, 2011, 2136–2147.
- [28] N. Öztürk, M. Yazar, A. Gündoğdu, C. Duran, H.B. Senturk, M. Soylak, Application of cherry laurel seeds activated carbon as a new adsorbent for Cr(VI) removal, *Membr Water Treat*, 12 (1), 2021, 11–21.
- [29] N. Öztürk, H.B. Senturk, A. Gündoğdu, C. Duran, Modeling of Co(II) adsorption by artificial bee colony and genetic algorithm, *Membr Water Treat*, 9 (5), 2018, 363–371.
- [30] N. Öztürk, İçme Suyu Arıtma Tesisi Atık Çamurunun Sulu Çözültiden Bazı Kirlenici Türlerin Adsorpsiyonla Gideriminde Kullanılabilirliğinin Araştırılması ve Yapay Sinir Ağları ile Modellenmesi, Karadeniz Teknik Üniversitesi Fen Bilimleri Enstitüsü Kimya Anabilim Dalı, Doktora tezi, Trabzon, 2014.
- [31] E. Altıntig, A. Alsancak, H. Karaca, D. Angın, H. Altundag, The comparison of natural and magnetically modified zeolites as an adsorbent in methyl violet removal from aqueous solutions, *Chem Eng Commun*, 209 (4), 2022, 555–569.
- [32] F. Zhang, Y. Yin, C. Qiao, Y. Luan, M. Guo, Y. Xiao, C. Liu, Anionic Dye Removal by Polypyrrole-Modified Red Mud and Its Application to a Lab-Scale Column: Adsorption Performance and Phytotoxicity Assessment, *Adsorpt Sci Technol*, 2021, 2021, 1–13.
- [33] G.M. Ratnamala, S.K. Vidya, G. Srinikethan, Isotherm, kinetics, and process optimization for removal of Remazol Brilliant Blue dye from contaminated water using adsorption on acid-treated red mud, *Desalin Water Treat*, 57(24), 2016, 11361–11374.
- [34] S. Lagergren, About the theory of so-called adsorption of soluble substance, *Kungl Svenska Vetenskapsakad Handl*, 24, 1898, 1–39.
- [35] Y.S. Ho, G. McKay, Kinetic models for the sorption of dye from aqueous solution by wood, *Process Saf Environ Prot* 76, 1998, 183–191.
- [36] Z. Jing, Y. Li, Y. Zhang, M. Wang, Y. Sun, K. Chen, B. Chen, S. Zhao, Y. Jin, Q. Du, X. Pi, Y. Wang, Enhanced methylene blue adsorption using zirconate alginate/graphene oxide UiO-67 aerogel spheres: Synthesis, characterization, kinetic studies, and adsorption mechanisms, *Int J Biol Macromol*, 238, 2023, 124044.
- [37] I. Langmuir, The adsorption of gases on plane surfaces of glass, mica and platinum, *J Am Chem Soc*, 40, 1918, 1361–1403.
- [38] H.M.F. Freundlich, Über Die Adsorption in Lösungen, *Z fur Phys Chem*, 57, 1906, 385–470.
- [39] K.R. Hall, L.C. Eagleton, A. Acrivos, T. Vermeulen, Pore and Solid Diffusion Kinetics in Fixed Bed Adsorption under Constant Pattern Conditions, *Ind Eng Chem*, 5, 1966, 212–223.
- [40] F. Rozada, L.F. Calvo, A.I. García, J. Martín-Villacorta, M. Otero, Dye adsorption by sewage sludge-based activated carbons in batch and fixed-bed systems, *Bioresour Technol*, 87 (3), 2003, 221–230.
- [41] Z. Liu, B. Gao, J. Qin, H. Liu, H. Han, H. Fu, X. Lan, A.R. Kamali, Corn stalk decorated with magnetic graphene oxide as an efficient adsorbent for the removal of cationic dye from wastewater, *Sep Purif Technol*, 356, 2025, 129937.



TurkJAC

Turkish Journal of Analytical Chemistry

<https://dergipark.org.tr/tr/pub/turkjac>
TurkJAC
2019
<https://dergipark.org.tr/tr/pub/turkjac>

Advanced interpretation of kinetics and equilibrium data obtained from adsorption of Pb²⁺ ions from aqueous solution onto pine bark (*Pinus brutia* Ten.) using non-linear regression: A practical approach with Microsoft Excel Solver*

Ali Gundogdu^{1**} , Volkan N. Bulut² 

¹ Karadeniz Technical University, Maçka Vocational School, Department of Pharmacy Services, 61750, Maçka, Trabzon, Türkiye

² Karadeniz Technical University, Maçka Vocational School, Department of Chemistry and Chemical Processing Technologies, 61750, Maçka, Trabzon, Türkiye

Abstract

This study investigates the adsorption of Pb²⁺ ions from aqueous solutions onto pine bark (*Pinus brutia* Ten.) using non-linear regression analysis to evaluate kinetic and equilibrium data. Adsorption experiments were conducted over a range of initial concentrations, and the equilibrium data were fitted to various two-parameter isotherm models, including Langmuir, Freundlich, Temkin, Dubinin-Radushkevich (D-R), and Jovanovic, as well as advanced three-parameter models like Dubinin-Astakhov (D-A), Tóth, Sips, Redlich-Peterson (R-P), and Brouers-Sotolongo (B-S). Kinetic data were analyzed using pseudo-first order (PFO), pseudo-second order (PSO), Elovich, Avrami, and Brouers-Sotolongo (B-S) models. Non-linear regression was performed using Microsoft Excel Solver, a readily accessible tool that eliminates the need for expensive software. Model parameters were optimized, and the goodness of fit was evaluated using multiple error functions, including SSE, ARE, HYBRID, MPSD, and MAE.

Results indicate that the Brouers-Sotolongo (B-S) model provided the best fit for both kinetic and isotherm data, reflecting the heterogeneous surface characteristics of the adsorbent. The adsorption process was found to involve a combination of physical and chemical interactions, as evidenced by the B-S kinetic constants (α_{BS} and n_{BS}) and the half-reaction time ($\tau_{1/2}$). Among the equilibrium models, three-parameter isotherms, particularly the B-S, Tóth, and Sips models, showed superior performance over two-parameter models, highlighting the complex nature of adsorption mechanisms in this system.

This study underscores the efficacy of pine bark as a low-cost and eco-friendly adsorbent for heavy metal removal and demonstrates the utility of non-linear regression and advanced error analysis in adsorption studies. This approach is thought to improve the precision of model selection and the understanding of adsorption mechanisms, contributing to the literature.

Keywords: Adsorption, error function, excel solver, isotherm, kinetics and equilibrium data, non-linear regression

1. Introduction

The process of adsorption is a cornerstone of environmental protection technologies, particularly for the removal of pollutants from aqueous environments. It is a versatile and efficient technique employed in wastewater treatment, heavy metal recovery, and the purification of drinking water. As the demand for cleaner water and more sustainable industrial practices grows, optimizing adsorption processes becomes increasingly important. The accurate interpretation of adsorption equilibrium and kinetic data is essential for designing efficient adsorbents and scaling up industrial

applications. While traditional models provide foundational insights, recent advancements in computational techniques and error analysis have significantly enhanced the accuracy and predictive power of adsorption studies [1–3].

Adsorption equilibrium data, typically analyzed through isotherm models like Langmuir, Freundlich, Temkin, and Dubinin-Radushkevich, describe the relationship between the adsorbate concentration in the solution and the amount adsorbed onto the surface of the adsorbent. These models provide essential information

Citation: A. Gundogdu, V.N. Bulut, Advanced interpretation of kinetics and equilibrium data obtained from adsorption of Pb²⁺ ions from aqueous solution onto pine bark (*Pinus brutia* ten) using nonlinear regression: A Practical Approach with Microsoft Excel Solver, Turk J Anal Chem, 7(2), 2025, 108–131.

****Author of correspondence:** a.ramazan.gundogdu@gmail.com

Tel: +90 (462) 512 3535

Fax: +90 (462) 512 3552

Received: January 25, 2025

Accepted: March 31, 2025

 <https://doi.org/10.51435/turkjac.1626570>

*This paper was presented at the 6th International Environmental Chemistry Congress, EnviroChem 05-08 November 2024, Trabzon Türkiye.

about the adsorption capacity, surface heterogeneity, and the affinity of the adsorbate towards the adsorbent. However, the fitting of experimental data to these models can sometimes yield large deviations, especially when dealing with complex systems or heterogeneous adsorbents [4]. Researchers have therefore employed advanced techniques, including non-linear regression and error analysis, to enhance the reliability of adsorption isotherm model fitting. This is crucial because the accuracy of model predictions directly impacts the effectiveness of the adsorbent in real-world applications [4–6].

Non-linear regression, particularly when implemented through accessible tools like Microsoft Excel Solver, enables more precise fitting of data to isotherm models by minimizing the residuals (sum of squared errors). This approach reduces systematic bias often encountered with linearized versions of the models, where data transformations can distort the relationships between variables [7,8]. The use of error metrics such as the root mean square error (RMSE), coefficient of determination (R^2), and adjusted R^2 can further guide the selection of the most appropriate model, ensuring that it best describes the experimental data [9,10].

Adsorption kinetics studies the time-dependent behavior of adsorbate molecules on adsorbent surfaces. Traditional models, such as the pseudo-first order and pseudo-second order kinetic models, are commonly used to describe the rate of adsorption. However, these models often assume simple, linear adsorption mechanisms and do not always capture the complexities of real systems, where multiple factors (e.g., diffusion limitations, surface heterogeneity, chemical interactions) may influence the adsorption rate [11]. Recent studies have proposed hybrid kinetic models that combine multiple rate-limiting steps to better represent complex adsorption systems [12]. In these models, non-linear regression is again critical for fitting experimental data, as it provides a direct way to optimize parameters without introducing biases that can arise from linearization [13]. Non-linear regression methods, on the other hand, provide a more accurate and robust approach for fitting adsorption data, especially when dealing with complex adsorption behaviors [5].

Error analysis is particularly important when interpreting kinetic data. One key aspect is the propagation of error through model parameters. For example, when fitting experimental data to kinetic models, small measurement errors or uncertainties in the initial concentration of adsorbates can lead to significant discrepancies in the estimated rate constants [14]. To mitigate these issues, researchers often use methods such as bootstrapping or Monte Carlo simulations to

assess the robustness of their kinetic models and quantify the uncertainty in parameter estimates. These approaches allow for a more comprehensive understanding of how errors in the experimental setup may influence the interpretation of adsorption dynamics [15].

While traditional methods of data analysis remain valuable, the increasing complexity of adsorption systems has driven the adoption of advanced computational tools. Non-linear regression, enabled by software like Microsoft Excel Solver, is one such tool that offers a more accessible and cost-effective alternative to more specialized programs like MATLAB, OriginPro, or Python. Solver works by adjusting the parameters of a predefined model to minimize the error between predicted and experimental data. This optimization approach eliminates the need for data transformations and offers a more direct way to assess model fit. Moreover, recent studies have shown that Solver, when combined with error analysis techniques, can achieve results that are comparable to those obtained with more advanced software packages, making it an attractive option for researchers in the field of adsorption [10,16].

In this study, the adsorption data of Pb^{2+} ions from aqueous solution onto pine bark (*Pinus brutia* Ten.) [17] were analyzed using non-linear regression models. The primary objective is to compare and interpret the kinetic and equilibrium data obtained from experiments by fitting them to widely used adsorption models, including pseudo-first order, pseudo-second order, Elovich, Avrami, and Brouers-Sotolongo (B-S) for kinetic analysis, and Langmuir, Freundlich, Temkin, Dubinin-Radushkevich (D-R), Jovanovic, Dubinin-Astakhov (D-A), Redlich-Peterson (R-P), Sips, Toth, and Brouers-Sotolongo (B-S) models for adsorption equilibrium. To evaluate the goodness of fit, several error functions were applied, including sum of squared errors (SSE), average relative error (ARE), hybrid fractional error (HYBRID), Marquardt's percent standard deviation (MPSD), and mean absolute error (MAE). The use of Microsoft Excel Solver for non-linear regression fitting is demonstrated, emphasizing its simplicity, accessibility, and cost-effectiveness, especially when compared to other more complex and expensive software options.

Through this study, the goal is not only to provide a comprehensive comparison of these adsorption models but also to address some of the inconsistencies and inaccuracies found in the literature regarding the application of adsorption models. A significant issue in the literature is the frequent misapplication and misinterpretation of mathematical models, which can lead to misleading conclusions. By employing non-linear regression and performing error analysis, this study aims to provide more accurate and reliable results, contributing to a better understanding of Pb^{2+} adsorption processes and advancing the knowledge in this area.

Another aim of this study is to facilitate data analysis by enabling the Solver add-in in the low-cost and readily available Microsoft Excel and to propose it as a strong alternative to expensive software used for this purpose.

2. Material and method

2.1. Materials used and calculations

The preparation and characterization of the adsorbent, pine bark (*Pinus brutia* Ten.), are detailed in the literature [17]. The chemicals, materials, apparatus, and solutions employed in the adsorption tests are also described in the same reference.

The Pb^{2+} concentrations adsorbed onto the pine bark (q_e or q_t , mg/g) were calculated using the equation in **Formula (1)**, based on the difference between the initial (C_o , mg/L) and residual (C_e , mg/L) Pb^{2+} concentrations in the solution.

$$q_e \text{ or } q_t = \frac{(C_o - C_e) \cdot V}{m} \quad (1)$$

Where q_e represents the amount of Pb^{2+} adsorbed per unit mass of adsorbent at equilibrium (mg/g), q_t denotes the amount of Pb^{2+} adsorbed per unit mass of adsorbent at a specific time (mg/g), V is the solution volume (L), and m is the mass of the adsorbent (g).

2.2. Statistical evaluation

Each adsorption test was performed at least three times, and the average values were used. Microsoft Office 365 Excel was employed for data analysis and error function evaluations, while the Excel Solver add-in was utilized for non-linear regression analyses.

3. Theory

In this study, Pb^{2+} adsorption onto pine bark was investigated through equilibrium and kinetic analyses using non-linear regression methods. For the kinetic evaluation, the mathematical equations of the pseudo-first order (PFO), pseudo-second order (PSO), Elovich, Avrami, and Brouers-Sotolongo (B-S) models were applied. The adsorption equilibrium was analyzed using the mathematical equations of isotherm models, including Langmuir, Freundlich, Temkin, Dubinin-Radushkevich (D-R), Jovanovic, Dubinin-Astakhov (D-A), Redlich-Peterson (R-P), Sips, Toth, and Brouers-Sotolongo (B-S).

3.1. Adsorption kinetics models

3.1.1. Pseudo-first order (PFO) kinetic model

PFO kinetic model, proposed by Lagergren (1898), describes the adsorption rate based on the assumption

that the rate of change in adsorption capacity is proportional to the difference between the adsorption capacity at equilibrium and the amount of adsorbed solute at any given time [18].

The equation for this model is:

$$q_t = q_e(1 - e^{-k_1 t}) \quad (2)$$

where:

- q_t is the amount of solute adsorbed at time t (mg/g),
- q_e is the amount of solute adsorbed at equilibrium (mg/g),
- k_1 is the rate constant of the pseudo-first order kinetic (1/min).

3.1.2. Pseudo-second order (PSO) kinetic model

The PSO model, proposed by Ho (2006), assumes that the rate of adsorption is proportional to the square of the difference between the equilibrium adsorption capacity and the amount of solute adsorbed at any given time. This model is widely used for its accuracy in modeling the adsorption of pollutants in aqueous solutions [19].

The equation for this model is:

$$q_t = \frac{q_e^2 k_2 t}{q_e k_2 t + 1} \quad (3)$$

where k_2 is the rate constant of the pseudo-second order kinetic (g/mg·min).

This model often fits well with adsorption data from aqueous solutions, especially for systems where the adsorption process is dominated by chemisorption [19].

3.1.3. Elovich kinetic model

The Elovich adsorption kinetic model is an empirical rate equation that shows adsorption energy grows linearly with surface coverage. This model holds that adsorption occurs at specified places, adsorbed ions interact, and the adsorbate concentration remains constant. It is suitable for both gas adsorption and wastewater treatment [20].

The equation for this model is:

$$q_t = \frac{1}{\beta_E} \ln(1 + \alpha_E \beta_E t) \quad (4)$$

where:

- α_E is the initial adsorption rate (mg/g·min),
- β_E is related to the adsorption capacity (g/mg),

3.1.4. Avrami kinetic model

The primary goal of the Avrami model is to understand the rate and mechanism of crystallization or reaction processes. The Avrami kinetic model is also widely used in the processes of pollutant removal from aqueous environments through adsorption. Adsorption refers to the transition of pollutants from the liquid phase to a solid adsorbent surface. This process typically exhibits kinetic characteristics similar to crystallization and other physical-chemical reactions, which is why the Avrami model is suitable for understanding the rate and mechanism of adsorption reactions [21–23].

The Avrami equation is:

$$q_t = q_e [1 - \exp(-k_A t^{n_A})] \quad (5)$$

where k_A is the rate constant, and n_A is the Avrami exponent, a parameter that determines the adsorption mechanism and geometry. The unit of the rate constant k_A depends on the time unit (t) used. $k_A \approx t^{-n_A}$

- $n = 1$: One-dimensional adsorption on the surface or edge.
- $n = 2$: Two-dimensional adsorption (e.g., on planar surfaces).
- $n = 3$: Three-dimensional adsorption (e.g., in porous structures).
- $n = 4$: Three-dimensional adsorption with continuous nucleation (e.g., continuous formation of new adsorption sites) [23].

3.1.5. Brouers-Sotolongo (B-S) kinetic model

This model goes beyond traditional first and second-order kinetic models by including a fractal time parameter and a fractional order parameter. It provides better data fitting and helps in understanding the nature of processes. This model is especially useful for better understanding complex reactions and adsorption processes.

The Brouers-Sotolongo (B-S) kinetic model is represented by the following equation:

$$q_{n,\alpha}(t) = q_e \left[1 - \left(1 + (n_{BS} - 1) \left(\frac{t}{\tau_C} \right)^{\alpha_{BS}} \right)^{\frac{-1}{(n_{BS}-1)}} \right] \quad (6)$$

Where $q_{n,\alpha}(t)$ is the amount of substance adsorbed at time (t). q_e is the equilibrium adsorption capacity. n_{BS} is the fractional order parameter. α_{BS} is the fractal time parameter, and τ_C is the characteristic time constant.

The parameter n_{BS} allows the model to interpolate between different kinetic orders, providing flexibility in describing various kinetic processes. The parameter α_{BS}

accounts for the complexity and irregularity of the kinetic process over time. τ_C , this is a scaling factor that adjusts the time scale of the process.

The half-reaction time, denoted as $\tau_{1/2}$, represents the duration required to absorb half of the equilibrium amount. It is calculated using the following equation:

$$\left[1 + (n_{BS} - 1) \left(\frac{t}{\tau_C} \right)^{\alpha_{BS}} \right]^{\frac{-1}{(n_{BS}-1)}} = \frac{1}{2} \quad (7)$$

which gives

$$\tau_{1/2} = \tau_C \left[\frac{2^{(n_{BS}-1)} - 1}{n_{BS} - 1} \right]^{\frac{1}{\alpha}} \quad (8)$$

$\tau_{1/2}$ represents the half-life time, which is the time required for the quantity of the substance to reduce to half of its initial value.

The B-S model is particularly useful in describing complex adsorption processes and drug release kinetics, offering a more accurate fit to experimental data compared to traditional kinetic models [24–27].

3.2. Adsorption isotherm models

3.2.1. Two-parameter isotherms

3.2.1.1. Langmuir adsorption isotherm:

The Langmuir adsorption isotherm assumes that adsorption occurs on a homogeneous surface with a finite number of identical sites. Each site can hold only one molecule, and the adsorption process is reversible. It is one of the most commonly used models for describing monolayer adsorption [28,29].

The non-linear Langmuir equation is:

$$q_e = \frac{q_m K_L C_e}{1 + K_L C_e} \quad (9)$$

where:

- q_e is the amount adsorbed at equilibrium (mg/g),
- q_m is the maximum adsorption capacity (mg/g),
- K_L is the Langmuir constant related to adsorption enthalpy (L/mg),
- C_e is the equilibrium concentration of solute (mg/L).

3.2.1.2. Freundlich adsorption isotherm:

The Freundlich model is an empirical model that describes adsorption on heterogeneous surfaces. Unlike Langmuir, it does not assume uniform adsorption sites, adsorption is more favorable at lower concentrations, and Freundlich allows for multilayer adsorption. It is applicable to systems with a wide range of energy.

The non-linear equation is:

$$q_e = K_F C_e^{\frac{1}{n_F}} \quad (10)$$

where K_F is the Freundlich constant related to adsorption capacity (L/g), and $1/n_F$ is an empirical constant representing the intensity or heterogeneity of adsorption. If $(1/n_F) < 1$, adsorption is favorable, and $(1/n_F) > 1$, adsorption is less effective. This model is widely used in environmental chemistry for predicting the adsorption behavior of various solutes [4,30].

Linear adsorption ($n_F=1$): The adsorption follows a simple linear relationship, indicating no cooperative or competitive effects.

Chemical interaction ($n_F < 1$): Adsorption involves strong chemical interactions between the adsorbate and the surface.

Physical interaction ($n_F > 1$): The adsorption process is dominated by weaker physical forces, such as van der Waals interactions [4].

3.2.1.3. Temkin adsorption isotherm:

The Temkin adsorption isotherm considers the interactions between the adsorbent (surface) and the adsorbate (molecule). This isotherm assumes that the heat of adsorption decreases linearly with increasing coverage of the surface. It is particularly useful for describing adsorption processes at low to moderate concentrations [31]. The model takes into account the non-uniform energy distribution on the surface and performs particularly well in the medium concentration range.

The Temkin isotherm equation is expressed as:

$$q_e = \frac{RT}{b_M} \ln(K_M C_e) \quad (11)$$

where R is the universal gas constant with a value of 8.314 J/(mol·K). T represents the temperature in Kelvin. b_M is the Temkin constant related to the heat of sorption, measured in J/mg, and K_M is the Temkin isotherm constant, measured in L/g [32].

3.2.1.4. Dubinin-Radushkevich (D-R) adsorption isotherm:

The D-R isotherm is used to describe adsorption on microporous materials and is often applied to study the adsorption of gases and small molecules. Unlike Langmuir, it does not assume monolayer adsorption. It is based on the potential energy distribution on the surface of the adsorbent [32].

The non-linear equation for the D-R model is:

$$q_e = q_m \exp(-K_{DR} \varepsilon^2) \quad (12)$$

$$\varepsilon = RT \ln \left(1 + \frac{1}{C_e} \right) \quad (13)$$

where:

- K_{DR} is a constant related to the adsorption energy (mol^2/kJ^2),
- ε is the Polanyi potential (kJ/mol),
- R is the universal gas constant,
- T is the temperature (K).

This model is particularly useful for describing the adsorption of small molecules on solid adsorbents, especially in low-concentration regimes [33].

3.2.1.5. Jovanovic adsorption isotherm:

The Jovanovic adsorption isotherm is an extension of the Langmuir model, focusing on monolayer adsorption without lateral interactions between adsorbed molecules. It considers mechanical contact between adsorbing and desorbing molecules, making it suitable for systems involving localized adsorption. The isotherm can describe both physical and chemical adsorption processes and transitions to Henry's Law at low concentrations [32].

Jovanovic's mathematical equation is:

$$q_e = q_m (1 - e^{-K_J C_e}) \quad (14)$$

where K_J is the Jovanovic constant in L/mg [34]. The mathematical equation of the Jovanovic isotherm model shows significant similarity to the equation of the pseudo-first order kinetic model (Eq. 2).

3.2.2. Three-parameter isotherms

3.2.2.1. Dubinin-Astakhov (D-A) adsorption isotherm:

The D-A adsorption isotherm is a widely used model for describing adsorption in microporous materials, such as activated carbon and zeolites. It is an extension of the D-R isotherm, incorporating energy heterogeneity of the adsorbent surface. This model is commonly applied to describe the adsorption of organic or inorganic compounds from aqueous solutions [35].

The isotherm is mathematically expressed as:

$$q_e = q_m \exp \left[- \left(\frac{\varepsilon}{\sqrt{2E}} \right)^{n_{DA}} \right] \quad (15)$$

Where ε is the Polanyi potential in kJ/mol (see Eq. (13)), as in the D-R equation. E is the characteristic adsorption energy (kJ/mol), indicating the energy barrier of the adsorption process, and n_{DA} is the exponent reflecting the heterogeneity of the adsorbent surface [36].

In the D-A adsorption isotherm, the n_{DA} parameter is known as a heterogeneity factor that expresses the surface heterogeneity of the adsorbent. This parameter reflects the homogeneity or heterogeneity of the pore distribution on the surface where adsorption occurs. The n_{DA} value indicates how diverse the pore sizes on the surface are; higher n_{DA} values indicate a wider pore size distribution. The n_{DA} value typically ranges between 2 and 10. This range can vary depending on the surface heterogeneity and pore structure of the adsorbent.

A high E value suggests chemisorption, while a low E value is indicative of physisorption [37].

3.2.2.2. Redlich-Peterson (R-P) adsorption isotherm:

The R-P adsorption isotherm is a hybrid model that combines features of the Langmuir and Freundlich isotherms. It is designed to describe adsorption on both homogeneous and heterogeneous surfaces and is particularly effective for systems operating over a wide concentration range.

The isotherm is mathematically expressed as:

$$q_e = \frac{K_{RP}C_e}{1 + \alpha_{RP}C_e^{\beta_{RP}}} \quad (16)$$

where K_{RP} and α_{RP} are the R-P constant (L/g) and R-P energy constant (L/mg or L/mmol), respectively. β_{RP} is the empirical parameter ($0 < \beta_{RP} \leq 1$), reflecting the heterogeneity of the adsorbent surface. When $\beta_{RP}=1$, the isotherm reduces to the Langmuir model. When $\beta_{RP} < 1$, the isotherm resembles the Freundlich model. Lower β_{RP} values indicate greater surface heterogeneity.

The isotherm can describe adsorption on both homogeneous and heterogeneous surfaces and fits experimental data over a wide concentration range. The R-P isotherm is widely used in liquid-phase adsorption systems, particularly for modeling the adsorption of heavy metal ions, organic pollutants, and other contaminants from aqueous solutions [4,38,39].

3.2.2.3. Sips adsorption isotherm:

The Langmuir and Freundlich isotherms are undoubtedly the most recognized models in adsorption studies. The Sips isotherm integrates features of both models. It was introduced to overcome the limitations of the Freundlich model at higher adsorbate concentrations and to describe adsorption behavior in heterogeneous systems. At low concentrations, the Sips isotherm behaves similarly to the Freundlich model, while at high concentrations, it approaches the Langmuir isotherm.

The mathematical equation of the Sips adsorption isotherm is given in Eq. (17).

$$q_e = \frac{q_m K_S C_e^{\beta_S}}{1 + K_S C_e^{\beta_S}} \quad (17)$$

where K_S is Sips equilibrium constant (L/mg), and β_S is Sips model exponent [32,39].

3.2.2.4. Tóth adsorption isotherm:

In 1971, József Tóth proposed an isotherm model to provide both experimental and mathematical insights into gas adsorption. The Tóth model gained widespread recognition due to its accurate description of adsorption across the entire pressure range, effective parameter interpretation, and its ability to serve as a basis for deriving other isotherm equations [34,40].

The three-parameter Tóth isotherm, an empirical extension of the Langmuir model, was developed to improve alignment with experimental data. It effectively describes adsorption on heterogeneous surfaces at both low and high concentration extremes [4].

While originally formulated for gas adsorption, the Tóth isotherm has also proven applicable to adsorption phenomena in solution [41]. The mathematical expression for the Tóth isotherm is provided in Eq. (18).

$$q_e = \frac{q_m K_T C_e}{[1 + (K_T C_e)^{n_T}]^{\frac{1}{n_T}}} \quad (18)$$

where K_T is the Tóth equilibrium isotherm constant (L/mg), and n_T is a dimensionless parameter. The model simplifies to the Langmuir isotherm when $n_T=1$. Thus, n_T serves as an indicator of the system's heterogeneity; as n_T deviates from 1, the degree of heterogeneity in the adsorption system increases.

3.2.2.5. Brouers-Sotolongo (B-S) isotherm model:

This isotherm is constructed as a modified exponential function to describe adsorption on heterogeneous surfaces, inspired by Langmuir's suggestion to adapt his isotherm for nonuniform adsorbent surfaces. The model assumes that the adsorbent's surface is divided into distinct patches, each containing active sites with identical energy levels. The B-S equation is specifically designed to account for these features, making it suitable for complex adsorption scenarios involving surface heterogeneity.

The mathematical equation of the B-S isotherm model is:

$$q_e = q_m \left[1 - e^{(-K_{BS} C_e^{\alpha_{BS}})} \right] \quad (19)$$

where the parameter K_{BS} ensures that the exponential term is dimensionless. Therefore, the unit of K_{BS} must cancel out the unit of $C_e^{\alpha_{BS}}$. If q_e and q_m are expressed in

mg/g, and C_e is in mg/L, then the unit of K_{BS} can be determined as $\left(\frac{L}{mg}\right)^{\alpha_{BS}}$.

The parameter α_{BS} represents the distribution of adsorption energy and reflects the degree of heterogeneity of the adsorbent surface at a specific temperature. It characterizes how adsorption energy varies across different active sites, providing insights into the energy profile and structural diversity of the adsorbent [42,43].

3.3. Error function

Error analysis plays a crucial role in comparing experimental data with theoretical results, as it helps assess the accuracy and reliability of the model. In experimental fields such as adsorption studies, error analyses are used not only to evaluate how well the data fit the model but also to test the accuracy and validity of the model. The choice of error analysis method depends on the nature of the data and the complexity of the model. Generally, a combination of different error analysis methods is preferred to ensure reliable results and to prevent misinterpretations of model performance.

The following section outlines several common error analysis methods, providing concise definitions and their associated formulas [4,16,34,44–49]. The symbols used in these formulas and their meanings are as follows:

- $q_{e,exp,i}$: Experimental adsorption capacity at equilibrium for the i -th data point (mg/g).
- $q_{e,cal,i}$: Calculated adsorption capacity at equilibrium for the i -th data point based on the model (mg/g)
- $\bar{q}_{e,exp}$: Mean of experimental data (mg/g)
- $\bar{q}_{e,cal}$: Mean of calculated data (mg/g)
- N : Total number of experimental data points.
- p : Number of independent variables in the model.
- R^2 : Coefficient of determination, representing the proportion of variance explained by the model.

3.3.1. Sum of squared errors (SSE)

The sum of squared errors (SSE) provides the total of the squared differences between calculated and experimental data. SSE is used to determine how close the model is to the experimental data. This method minimizes the sum of squared errors to optimize the model parameters.

$$SSE = \sum_{i=1}^N (q_{e,exp,i} - q_{e,cal,i})^2 \quad (20)$$

SSE is simple to compute and interpret, and SSE offers a clear sense of the total error in the model. However, large errors are disproportionately penalized due to the squaring of the differences by SSE. In addition, SSE should be used in conjunction with other methods for a more comprehensive assessment.

3.3.2. Average relative error (ARE)

ARE is a measure of how well a model predicts experimental data, expressed in terms of the relative error between calculated and experimental values. It evaluates the percentage deviation of calculated values from experimental ones, averaged across all data points.

$$ARE = \frac{1}{N} \sum_{i=1}^N \left| \frac{q_{e,exp,i} - q_{e,cal,i}}{q_{e,exp,i}} \right| \times 100 \quad (21)$$

ARE represents the error in percentage form, making it suitable for comparing datasets with different units or scales. It is easy to interpret, as it provides a clear measure of percentage deviation. Unlike RMSE or SSE, ARE does not excessively penalize large errors due to the absence of squaring. However, when $q_{e,exp,i}$ values are small, ARE can become disproportionately large or even undefined. Additionally, larger deviations in $q_{e,exp,i}$ are weighted more heavily due to their relative nature. ARE is also sensitive to outliers and noise in experimental data.

3.3.3. Hybrid fractional error (HYBRID)

The HYBRID function is an error function used to evaluate the accuracy of a model by combining both absolute and fractional errors. It is commonly used in adsorption tests to assess the differences between experimental and calculated values.

$$HYBRID = \frac{1}{N-p} \sum_{i=1}^N \left[\frac{(q_{e,exp,i} - q_{e,cal,i})^2}{q_{e,exp,i}} \right] \times 100 \quad (22)$$

The HYBRID function combines both absolute and fractional errors, providing a more accurate measure of model performance. It is suitable for datasets with varying magnitudes and scales, and helps penalize errors relative to the experimental values, offering a more balanced evaluation. However, it is sensitive to small or zero values in the experimental data, which can result in inflated error values. Additionally, it can be more complex to interpret compared to simpler metrics like MAE or RMSE.

3.3.4. Marquardt's percent standard deviation (MPSD)

Marquardt's Percent Standard Deviation (MPSD) is an error analysis metric used to evaluate the fit of a model to experimental data. It is particularly useful in adsorption studies, where it helps quantify the deviation between experimental and calculated values in terms of a percentage. MPSD is similar to RMSE but is normalized by the experimental values, making it less sensitive to large magnitudes in the data.

$$MPSD = 100 \times \sqrt{\frac{1}{N-p} \sum_{i=1}^N \left(\frac{q_{e,exp,i} - q_{e,cal,i}}{q_{e,exp,i}} \right)^2} \quad (23)$$

MPSD expresses error as a percentage, making it easily interpretable and comparable across different datasets. By accounting for variations in the magnitude of experimental values, it reduces bias from large datasets. MPSD is particularly effective for comparing different models or adsorption isotherms to identify the best fit. However, similar to ARE, MPSD can be disproportionately influenced when $q_{e,exp,i}$ values are small, potentially leading to large errors or undefined values. Additionally, MPSD requires knowledge of the number of parameters (p), making it less straightforward than simpler metrics such as SSE or RMSE. MPSD can also be sensitive to outliers in experimental data.

3.3.5. Mean absolute error (MAE)

MAE calculates the average of the absolute errors between experimental and calculated values. It directly quantifies the magnitude of errors without considering their direction.

$$MAE = \frac{1}{N} \sum_{i=1}^N |q_{e,exp,i} - q_{e,cal,i}| \quad (24)$$

MAE directly represents the magnitude of errors and does not excessively penalize larger errors, offering a balanced approach. However, it does not differentiate between large and small errors in terms of their impact. Additionally, MAE lacks sensitivity to variations in error size across different parts of the data.

3.3.6. Coefficient of determination (R^2)

R^2 measures how well the model explains the variance in the data. A value close to 1 indicates a good fit, while values near 0 suggest poor model performance. The coefficient of determination (R^2) is also equal to the square of the correlation coefficient (R).

$$R^2 = \left[\frac{\sum (q_{e,exp,i} - \bar{q}_{e,exp})(q_{e,cal,i} - \bar{q}_{e,cal})}{\sqrt{\sum (q_{e,exp,i} - \bar{q}_{e,exp})^2 \sum (q_{e,cal,i} - \bar{q}_{e,cal})^2}} \right]^2 \quad (25)$$

R^2 provides a quick measure of model accuracy and is both widely used and easily interpretable. However, it can be misleading for non-linear data or when the model is poorly specified. A high R^2 value does not necessarily guarantee accurate predictions, particularly for non-linear models.

3.3.7. Adjusted R -squared (Adjusted R^2 or R^2 -adj)

The Adjusted R^2 statistic is used to evaluate the goodness of fit of a model (e.g., isotherm or kinetic model) to the experimental q_e data. It adjusts for the number of parameters in the model, providing a more accurate assessment of how well the model describes the adsorption process while penalizing unnecessary complexity.

$$R^2\text{-adj} = 1 - \left[\frac{(1 - R^2)(N - 1)}{N - p - 1} \right] \quad (26)$$

Adjusted R^2 prevents overfitting by accounting for the number of parameters, allows for better comparison between different adsorption models, and provides a more reliable measure of model fit. However, Adjusted R^2 is still sensitive to outliers, does not imply causality, and can be difficult to interpret in complex models.

4. Results and discussions

4.1. Minimization process with Excel Solver

Fig. 1 and Fig. 2 illustrate the minimization process for non-linear regression solutions in Excel Solver. Fig. 1 demonstrates the minimization/optimization process in the Solver using the HYBRID function for the two-parameter Langmuir isotherm. Fig. 2 illustrates the process for the three-parameter Redlich-Peterson (R-P) model using the SSE function.

In the Excel sheet, follow the sequence: **File – More options – Options – Add-ins – Solver Add-in** to add the Solver command to the menus. Then, navigate to the **Data** tab and run the Solver command.

In columns A and B in Fig. 1 and Fig. 2, the experimental C_e ($C_{e,exp}$) and corresponding experimental q_e values ($q_{e,exp}$) are placed. Column C represents the q_e values ($q_{e,cal}$) calculated by the model at the end of the process. Columns D and E contain the calculations for the error function, which minimizes the differences between $q_{e,exp}$ and $q_{e,cal}$.

In Fig. 1, Cells A14 and B14 contain the Langmuir model constants (K_L and q_m). The primary objective of the minimization process is to estimate these constants with the highest accuracy. To achieve this, the error function seeks to minimize the differences between $q_{e,exp}$ and $q_{e,cal}$. In other words, K_L and q_m values must be assigned to cells A14 and B14 such that the error function value in cell E14 is minimized.

Before running Solver, it is necessary to assign initial estimates to cells A14 and B14. (A14, B14, and C14 in Fig. 2) This is because Solver cannot operate if these cells are empty, as the calculated $q_{e,cal}$ values (C3–C11) would be undefined. Once initial estimates are assigned, Solver will use a trial-and-error method to minimize the differences between $q_{e,exp}$ and $q_{e,cal}$ through the selected error function, ultimately determining the most accurate values for K_L and q_m (K_{RP} , α_{RP} , and β_{RP} for R-P isotherm in Fig. 2).

Once the necessary cells are filled, Solver is run, and the “**Solver Parameters**” dialog box appears on the screen, as shown in Fig. 1 and Fig. 2. Click the arrow button next to the “**Set Objective**” bar and select the cell containing the value of the error function to be minimized (E14) as the target. Since error functions perform minimization, select the “**Min**” option in the dialog box.

Next, click the arrow button to the right of the “**By Changing Variable Cells**” bar and select the model parameters cells (A14:B14 for the Langmuir model, A14:C14 for the R-P model). If there are any constraints related to the model, as in the R-P model shown in Fig. 2, click “**Add**” under the “**Subject to the Constraints**” section and enter the necessary constraints in the window that appears. The constraints will be displayed in the dialog box (Fig. 2).

Since a non-linear solution is being performed, select “**GRG Nonlinear**” from the list under “**Select a Solving Method**” in the dialog box. Finally, click the “**Solve**” button to allow Solver to perform the minimization and estimate the $q_{e,cal}$ values and the model parameters.

Similar steps are, of course, applied to kinetic data as well. In this case, experimental t (min) values are entered into cells A3–A11, and experimental $q_{t,exp}$ values are entered into cells B3–B11. The remaining steps are carried out as described above.

4.2. Error function analysis for the kinetics models

Error functions are tools that help accurately estimate model parameters. These functions work to minimize the difference between experimental data and data calculated from the model as much as possible.

In this study, five different error functions were employed for data minimization: SSE, ARE, HYBRID, MPD, and MAE. Table 1 presents the results of minimization performed using these five error functions with Solver for each kinetic model. The rows detail the parameter values obtained for each kinetic model using the respective error function. For example, when minimization for the PFO kinetic model was conducted with SSE in Solver, the q_t value was 10.15784 mg/g, while it was 10.41159 mg/g with ARE, 9.89718 mg/g with HYBRID, 9.35466 mg/g with MPD, and 10.41206 mg/g with MAE.

In the respective tables, error function values are also provided both vertically and horizontally. When the same error function is aligned vertically and horizontally in these tables, the value read in the intersecting cell represents the result obtained when the solution is performed under that error function. For instance, in Table 1, when the horizontal SSE is aligned with the vertical SSE, the intersecting cell value is 5.61275. However, when the horizontal SSE aligns with the vertical ARE, the intersecting cell value becomes 9.41517. This value (9.41517) represents the ARE calculated under SSE minimization conditions, where the $q_{e,cal}$ values estimated via SSE are substituted into the mathematical equation for ARE. This approach was used to generate the values in Table 1, Table 3, and Table 4. As shown, each function provides the lowest minimization under its specific conditions.

At the end of Table 1, Table 3, and Table 4, SNE (Sum of Normalized Errors) values are provided for each model. SNE is a normalization process that identifies which error function minimizes the differences between $q_{e,exp}$ and $q_{e,cal}$ the most. Thus, SNE helps determine the most appropriate error function for a given model and allows for a more accurate prediction of the compatibility of experimental data with the model.

An example of SNE calculation from Table 1 is as follows: The error function values in each row are divided by the largest value in that row, resulting in five different normalized values (note that one of these values will always equal 1). The same process is repeated for the other four rows. Finally, the SNE value for each error function is obtained by summing up the normalized values for each column.

The error function with the relatively smallest SNE value is the one that should be preferred for the minimization of the corresponding model in Solver.

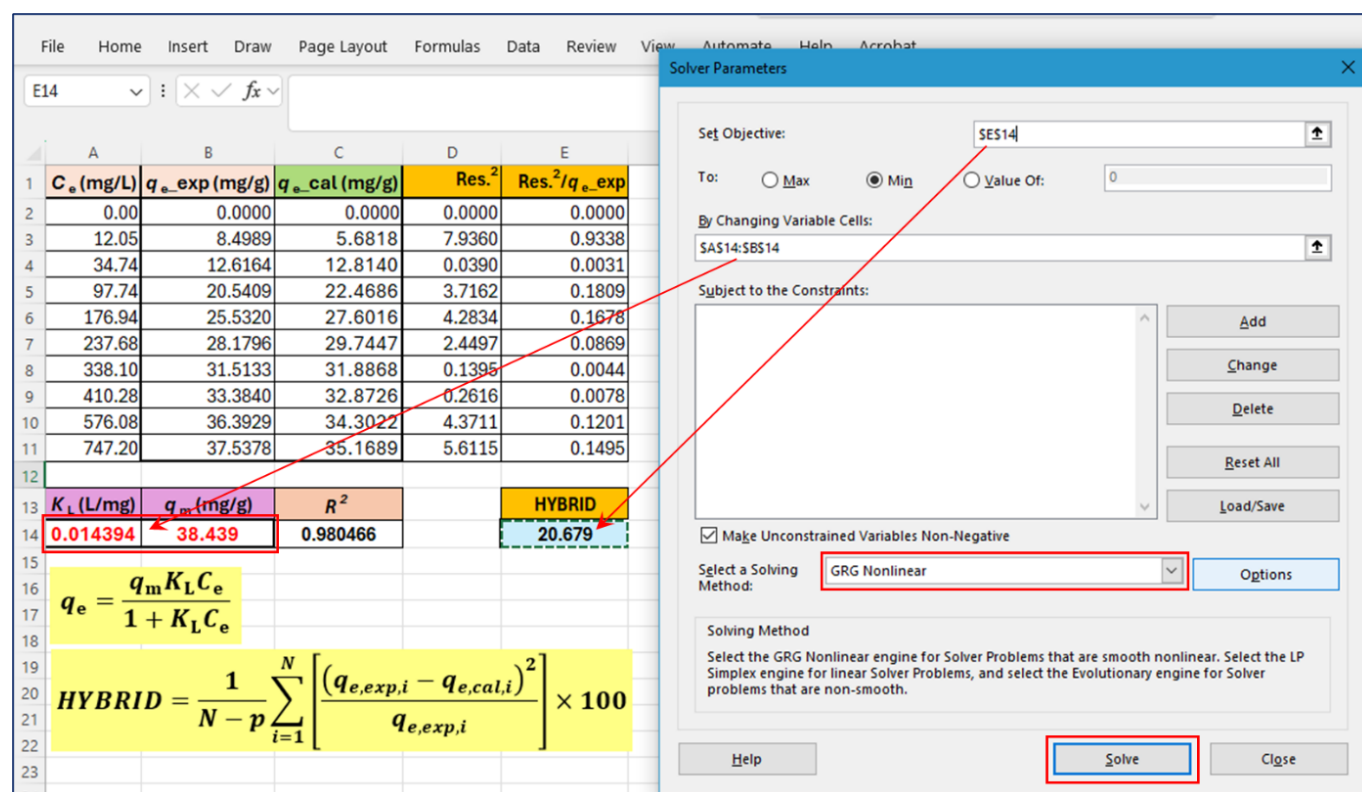


Figure 1. Optimization and solution of the two-parameter Langmuir isotherm model using the HYBRID error function in Excel Solver

- The $q_{e,cal}$ values in cells C3–C11 are calculated in Excel using the Langmuir equation as follows: $=($B$14*$A$14*$A3)/(1+A14*$A3)$, $=($B$14*$A$14*$A4)/(1+A14*$A4)$, ...
- In cells D3–D11, the squares of the differences (Res.²) between $q_{e,exp}$ and $q_{e,cal}$ are calculated (e.g., $=(B3-C3)^2$, $=(B4-C4)^2$, ..., $=(B11-C11)^2$). In cells E3–E11, the values in D3–D11 are divided by the $q_{e,exp}$ values in B3–B11 (e.g., $=D3/B3$, $=D4/B4$, ..., $=D11/B11$); $HYBRID=SUM(E3:E11)$.
- Coefficient of determination, $R^2=RSQ(B2:B11;C2:C11)$

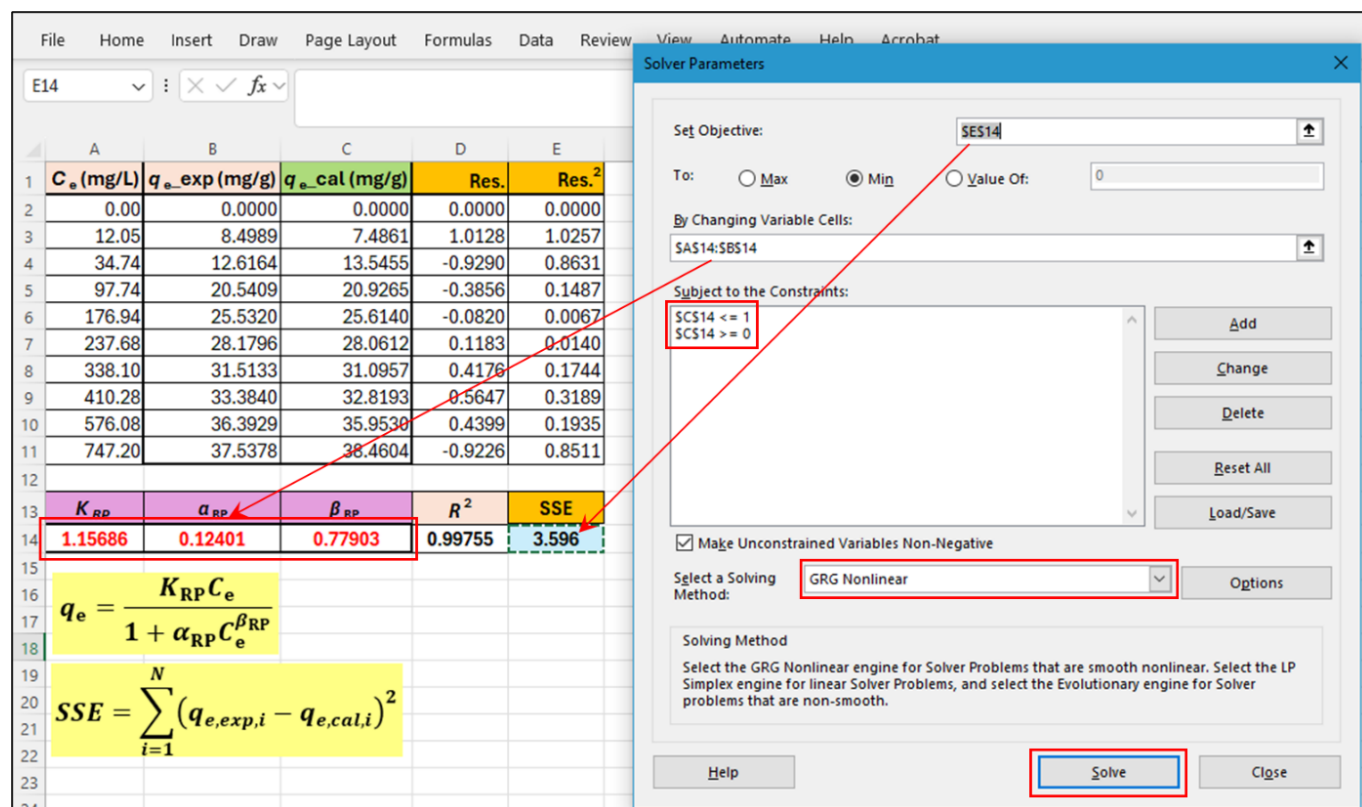


Figure 2. Optimization and solution of the three-parameter Redlich-Peterson (R-P) isotherm model using the SSE error function in Excel Solver

- The $q_{e,cal}$ values in cells C3–C11 are calculated in Excel using the Redlich-Peterson equation as follows: $=($A$14*$A3)/(1+B14*(A3*C14))$, $=($A$14*$A4)/(1+B14*(A4*C14))$, ...
- Res. (Residuals) are calculated as the differences between $q_{e,exp}$ and $q_{e,cal}$ (e.g., $=B3-C3$, $=B4-C4$, ..., $=B11-C11$). Then, the squares of these differences are calculated in cells E3–E11 (e.g., $=D3^2$, $D4^2$, ..., $D11^2$). SSE is ultimately the sum of the squares of these differences; $SSE=SUM(E3:E11)$.
- Determination coefficient, $R^2=RSQ(B2:B11;C2:C11)$

Table 1. Kinetic model constants with five different error analysis in Microsoft Excel Solver

Kinetic models	SSE	ARE	HYBRID	MPSD	MAE
<i>Pseudo-first order (PFO)</i>					
q_t (mg/g)	10.15784	10.41159	9.89718	9.35466	10.41206
k_1 (1/min)	0.07023	0.09935	0.09186	0.13775	0.06720
R^2	0.96996	0.95218	0.95737	0.92437	0.97119
R^2 -Adj	0.96138	0.93851	0.94519	0.90276	0.96295
SSE	5.61275	9.41517	6.62396	11.79655	5.98032
ARE	13.35946	12.29921	13.02401	14.70117	13.18084
HYBRID	17.16781	19.09022	15.13926	19.54712	18.12834
MPSD	25.19315	21.47662	21.60214	19.18431	25.66247
MAE	0.63672	0.70318	0.73162	1.00242	0.59712
SNE	3.87970	4.14975	3.79357	4.74756	3.92664
<i>Pseudo-second order (PSO)</i>					
q_t (mg/g)	10.78276	10.89592	10.57112	10.16293	10.91555
k_2 (g/mg·min)	0.01020	0.01097	0.01250	0.01689	0.01052
R^2	0.99369	0.99236	0.98997	0.97969	0.99307
R^2 -Adj	0.99188	0.99018	0.98710	0.97389	0.99109
SSE	1.15192	1.49209	1.49687	3.29579	1.38196
ARE	6.75051	6.23831	6.76816	8.41013	6.39992
HYBRID	5.14998	4.89708	4.34811	5.97884	5.01204
MPSD	15.58695	14.10526	12.88466	11.20023	14.69183
MAE	0.27226	0.27191	0.34589	0.54170	0.26400
SNE	3.51614	3.42046	3.45134	4.71856	3.44851
<i>Elovich</i>					
α_E (mg/g·min)	5.81997	3.30410	4.19424	3.57695	7.57775
β_E (g/mg)	0.64626	0.55775	0.60294	0.57811	0.65356
R^2	0.98244	0.97774	0.98081	0.97905	0.98223
R^2 -Adj	0.97743	0.97138	0.97533	0.97306	0.97715
SSE	2.59144	4.14707	2.92915	3.43097	3.62022
ARE	8.07160	5.31391	6.43614	5.67360	9.49963
HYBRID	5.49977	5.34174	4.30429	4.62875	9.80496
MPSD	12.44534	7.54710	7.98919	7.27624	18.55071
MAE	0.46489	0.48227	0.47149	0.47828	0.45524
SNE	3.67031	3.51102	3.23113	3.28062	4.81691
<i>Avrami</i>					
k_A (min^{-n_A})	0.20583	0.19139	0.19721	0.19300	0.19618
n_A	0.54050	0.56350	0.55483	0.56390	0.55076
R^2	0.99906	0.99887	0.99899	0.99891	0.99889
R^2 -Adj	0.99880	0.99854	0.99870	0.99860	0.99858
SSE	0.14050	0.18638	0.15811	0.18733	0.16781
ARE	1.70353	1.04928	1.27732	1.19222	1.16089
HYBRID	0.33165	0.29921	0.27052	0.28954	0.30130
MPSD	3.04051	1.99572	2.09374	1.93974	2.18486
MAE	0.08498	0.08555	0.08379	0.09397	0.07696
SNE	4.65432	4.07985	3.98981	4.21085	4.02343
<i>Brouers-Sotolongo (B-S)</i>					
q_t (mg/g)	11.07665	11.06952	11.09914	11.14210	11.07287
τ_c (min)	13.22303	13.21365	13.17745	13.04019	13.22493
α_{BS}	0.64608	0.63511	0.64283	0.63573	0.64583
n_{BS}	1.47640	1.48059	1.47811	1.46878	1.47454
$\tau_{1/2}$ (min)	9.74988	9.71516	9.71075	9.52562	9.73986
R^2	0.99958	0.99955	0.99957	0.99954	0.99956
R^2 -Adj	0.99915	0.99910	0.99914	0.99907	0.99912
SSE	0.06234	0.07943	0.06296	0.06825	0.07532
ARE	1.11769	0.90266	1.06123	0.96652	1.09833
HYBRID	0.12815	0.15190	0.12697	0.13233	0.15316
MPSD	1.63236	1.63037	1.57112	1.52857	1.84393
MAE	0.06708	0.06209	0.06576	0.06344	0.06150
SNE	4.50677	4.60932	4.40352	4.36279	4.84779

Accordingly, based on the SNE data in Table 1 and Table 2, the HYBRID error function provides the best minimization for all kinetic models except for PSO and B-S. For PSO and B-S, the most suitable minimizations are achieved using ARE and MPSPD, respectively. Based on the SNE values of the kinetic models presented in Table 1, the ranking of error functions from best to worst can be determined as follows: for PFO, HYBRID > SSE > MAE > ARE > MPSPD; for PSO, ARE > MAE > HYBRID > SSE > MPSPD; for Elovich, HYBRID > MPSPD > ARE > SSE > MAE; for Avrami, HYBRID > MAE > ARE > MPSPD > SSE; and for B-S, MPSPD > SSE > HYBRID > ARE > MAE.

Fig. 3 illustrates the $t-q_t$ plots obtained for each model when analyzed separately in Solver using five different error functions. As illustrated in Fig. 3, for PFO and PSO kinetic models, MPSPD is not regarded as a suitable minimization function in Excel Solver when compared to other error functions. Table 1 also demonstrates that the SNE values for MPSPD in PFO and PSO kinetic models are significantly higher relative to the other error functions. Notably, the Avrami and B-S kinetic models exhibit consistent trends across all error functions. In particular, for the B-S kinetic model, the $q_{t,cal}$ values obtained from each error function are remarkably close to each other, with their respective curves nearly overlapping entirely.

Consequently, it is evident that selecting an appropriate error function is crucial for non-linear solutions of the PFO kinetic model, as well as for the PSO and Elovich kinetic models. However, this choice is less critical for the Avrami and B-S kinetic models.

Another noteworthy point in Table 1 is that all error function values for the B-S model are the lowest among all models. Relatively low error function values indicate that the $q_{t,exp}$ and $q_{t,cal}$ values are very close to each other, signifying that the corresponding model represents the experimental data exceptionally well.

As seen in Fig. 3, the experimental data is best represented by the B-S model, followed by the Avrami model. Fig. 4 further supports this conclusion, providing a visual representation of the $t-q_t$ plots drawn using the error functions with the lowest relative SNE values (Table 2). As illustrated in Fig. 4, the kinetic models that best represent the experimental data are, in order, the B-S and Avrami kinetic models. The PSO kinetic model, on the other hand, ranks as the third most suitable model in this analysis. However, it can also be stated that both the Elovich and PFO kinetic models fail to adequately represent the experimental data.

Fig. 5 presents the detailed version of Fig. 4, showing the results for each model individually. As is evident from the figure, the two models that best represent the data are the B-S and Avrami models. Likewise, Fig. 5 suggests that the PSO kinetic model can be considered a

suitable model for adequately representing the experimental data.

In conclusion, based on the relevant tables and graphs, the kinetic model that best describes the adsorption of Pb^{2+} onto pine bark is the Brouers-Sotolongo (B-S) model, while the least representative model is the pseudo-first order (PFO) kinetic model.

4.3. Analysis of the kinetics model constants

In Section 3.1.5, it was stated that the 4-parameter B-S kinetic model provides a more precise and accurate description of the adsorption kinetics process compared to the classical PFO and PSO models, owing to its consideration of additional factors such as a fractal time parameter (α_{BS}) and a fractional order parameter (n_{BS}).

In this study, based on the data presented in Table 1, the α_{BS} value for the B-S kinetic model is 0.63573 (obtained through MPSPD minimization). This value ($\alpha_{BS} < 1$) indicates that the system is significantly heterogeneous, reflecting the heterogeneity of the pine bark surface. Additionally, the n_{BS} value derived from Table 1 is 1.46878. When $n_{BS} = 1$, the system follows PFO kinetics, whereas $n_{BS} = 2$ indicates PSO kinetics. Given that $1 < n_{BS} < 2$ for this study, it can be concluded that a mixed kinetic mechanism is at play, where adsorption occurs as a combination of physical and chemical interactions. On the other hand, for $0 < n_{BS} < 1$, adsorption proceeds predominantly through physical mechanisms. Consequently, the reaction order and pathway can be determined with greater precision using the B-S kinetic model.

$\tau_{1/2}$ represents the time required for half of the total adsorbed adsorbate ions/molecules to be adsorbed during the adsorption process. For this study, this duration is $\tau_{1/2} = 9.74988$ minutes (Table 1).

For the Avrami kinetic model, which was determined to be consistent with the experimental data, an examination of the model constants in Table 1 reveals that the n_A exponent, which provides information about the adsorption mechanism and geometry, is 0.55483 (obtained through minimization using the HYBRID error function). When $0 < n_A < 1$, it indicates that adsorption progresses through physical pathways on heterogeneous surfaces with limited and weak interactions.

Another parameter of the Avrami model, k_A , being less than 1 (in this study, $k_A \approx 0.2$) suggests that the adsorption process has relatively slow kinetics, with a low adsorption rate, or that one or more steps in the process are rate-limiting.

Unlike PFO, what perhaps makes the PSO kinetic model more appealing in many studies is the overlap between $q_{t,exp}$ and the $q_{t,cal}$ values. It should be noted,

however, that the choice of the error function type is crucial when performing analyses with PFO and PSO. When Fig. 3 is carefully examined, it becomes evident that the selection of the error function for PFO is critical. In Fig. 3, when MPSD is chosen as the error function for both PFO and PSO, neither model yields particularly reliable results. Therefore, identifying the error function that provides the most accurate results is essential. This study focuses specifically on this objective. However, when ARE or MAE is preferred for both models, the difference between $q_{t,\text{exp}}$ and the $q_{t,\text{cal}}$ values becomes significantly smaller (Table 1, Fig. 3). Nevertheless, in Table 1 and Table 2, the most optimal error function for PFO is found to be HYBRID. This is due to the sharper inflection point of the t - q_t curve in ARE and MAE, as well as the experimental data in this region being farther from the curve (Fig. 3). It can be observed from Fig. 3 that the Elovich kinetic model does not align well with the data, particularly near equilibrium. Although the Elovich model does not represent the experimental data in a fully satisfactory manner, certain interpretations can still be derived from the model constant values. Based on the values obtained using HYBRID minimization in Table 1, the α_E value for the Elovich model is 4.19424, and the β_E value is 0.60294. When $\alpha_E > 1$, it indicates that adsorption is quite rapid at the initial stages, suggesting strong interactions between the adsorbent and the adsorbate. Additionally, when $\beta_E > 0.5$, a more pronounced slowing of the adsorption rate is observed, indicating that active sites are filling up quickly.

4.4. Error function analysis for the isotherm models

A similar evaluation to the one conducted for kinetic models can undoubtedly be performed for isotherm models as well. Table 3 lists the minimization results obtained using five different error functions in Excel Solver for two-parameter isotherms, while Table 4 provides the corresponding results for three-parameter isotherms.

When evaluating the SNE values collectively presented in Table 5, it can be observed that many two- and three-parameter isotherm models are better minimized using the HYBRID error function. For the Temkin model, SSE; for the D-R model, ARE and SSE; and for the Jovanovic and D-A models, ARE provided better minimization results. In contrast, for the remaining models, the HYBRID function yielded the best minimization results. Overall, for both kinetic and isotherm models, the HYBRID error function generally offered superior minimization performance.

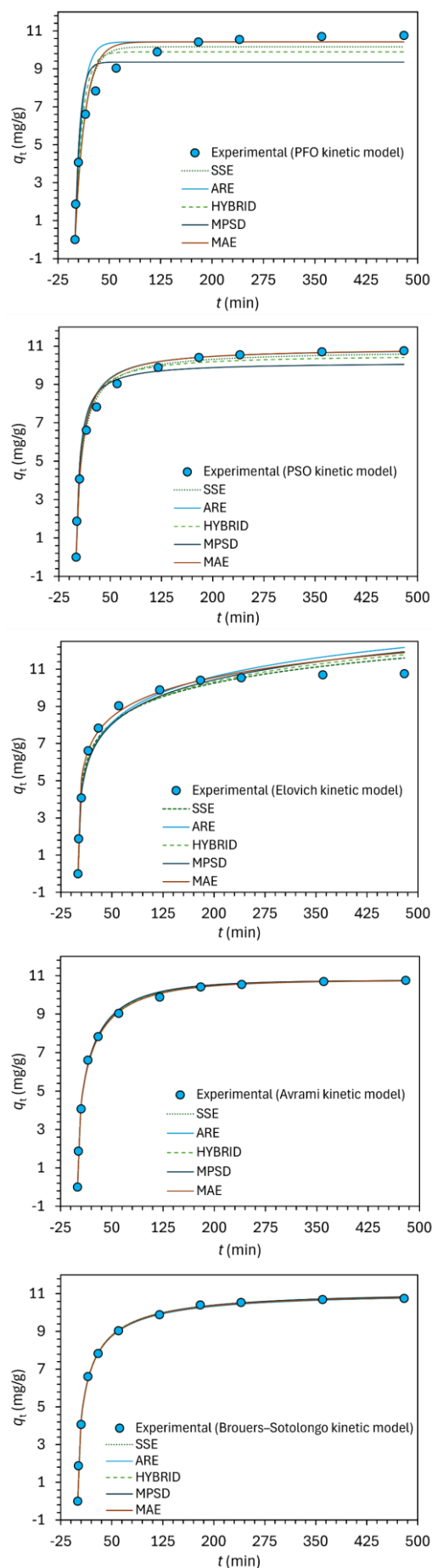


Figure 1. Comparison of experimental and model-predicted kinetic data using five different error functions (SSE, ARE, HYBRID, MPSD, and MAE) in Excel Solver for various kinetic models

Table 2. SNE values of the error functions for the kinetic models

Kinetic models	SNE values of the error functions				
	SSE	ARE	HYBRID	MPSD	MAE
Pseudo-first order (PFO)	3.87970	4.14975	3.79357	4.74756	3.92664
Pseudo-second order (PSO)	3.51614	3.42046	3.45134	4.71856	3.44851
Elovich	3.67031	3.51102	3.23113	3.28062	4.81691
Avrami	4.65432	4.07985	3.98981	4.21085	4.02343
Brouers-Sotolongo (B-S)	4.50677	4.60932	4.40352	4.36279	4.84779

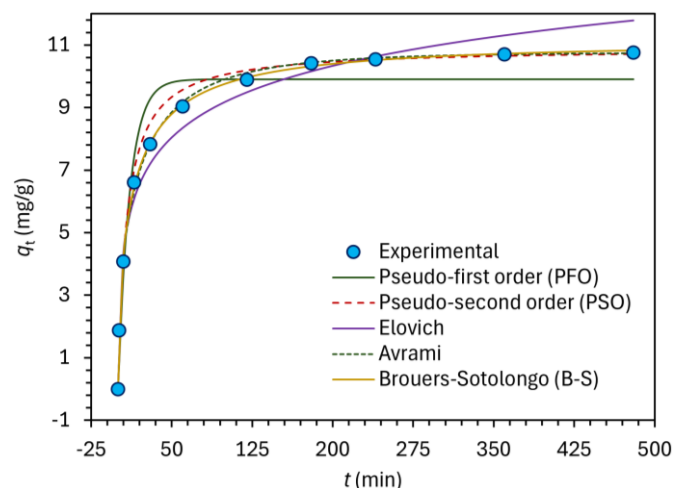
**Figure 2.** Comparison of the kinetic models optimized in Excel Solver

Fig. 6 and Fig. 7 illustrate the C_e - q_e plots for each isotherm model, generated by minimizing the differences between $q_{e,exp}$ and $q_{e,cal}$ using five error functions in Solver. In Fig. 6, except for the D-R and Jovanovic models, the C_e - q_e graphs generated for the other two-parameter isotherms after minimization with the five error functions are quite similar to each other. However, as with the kinetic models, the MPSD function provided poorer minimization results compared to the others. Similarly, in Fig. 7, for the four isotherms other than the D-A isotherm, the results obtained from the five error functions were closely aligned.

From the SNE data in Table 3, Table 4, and Table 5, the error functions providing the best minimization results are as follows: for the Temkin model, SSE; for the D-R, Jovanovic, and D-A models, ARE; and for all other isotherms, the HYBRID function. Additionally, the same tables reveal that MPSD yielded the highest SNE values for the Freundlich and Temkin isotherms.

Unlike the two-parameter isotherms, the three-parameter isotherms produced more consistent results across the five error functions, as illustrated in Fig. 7. For the three-parameter isotherms other than D-A, the five error functions provided nearly identical results, with all C_e - q_e graphs almost entirely overlapping. Therefore, the choice of error function for minimizing these three-parameter isotherms, excluding D-A, is not critical.

To ensure more accurate parameter estimation and, consequently, a better understanding of the adsorption process, it is essential to select the error function with the smallest SNE value for minimizing each isotherm model, as summarized in Table 5.

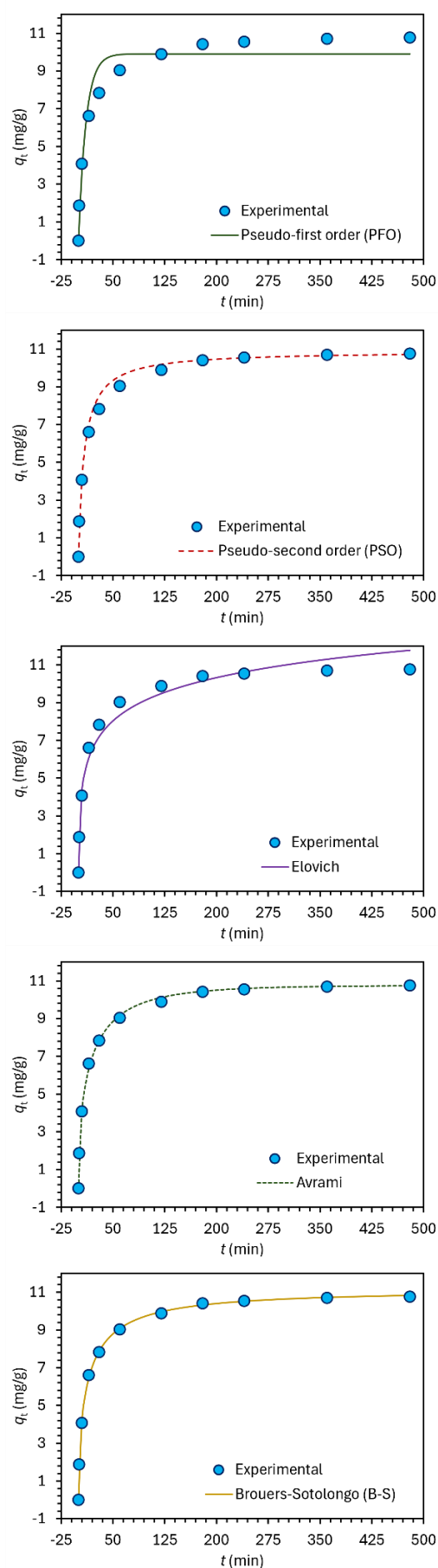
**Figure 3.** Single representations of the kinetic models optimized in Excel Solver

Table 3. Two-parameter isotherms constants with five different error analysis in Microsoft Excel Solver

	SSE	ARE	HYBRID	MPSD	MAE
<i>Langmuir</i>					
K_L (L/mg)	0.01116	0.01428	0.01439	0.01863	0.01003
q_m , (mg/g)	40.69627	38.04907	38.43876	35.98128	41.49816
R^2	0.98715	0.98075	0.98047	0.96900	0.98859
R^2 -Adj	0.98286	0.97433	0.97396	0.95866	0.98478
SSE	22.87550	30.00669	28.80803	49.32668	24.09545
ARE	7.57277	7.00233	7.25302	8.60763	7.70209
HYBRID	24.73757	21.10073	20.67920	25.11808	29.12894
MPSD	16.05378	13.26780	13.04970	11.87321	17.72985
MAE	1.15155	1.35836	1.39217	1.88286	1.04587
SNE	3.70984	3.61598	3.61199	4.53198	3.93875
<i>Freundlich</i>					
K_F (L/mg)	4.33510	3.23827	3.81191	3.48659	4.35667
n_F (mg/g)	2.98694	2.57897	2.80287	2.68231	2.95498
R^2	0.99068	0.98454	0.98910	0.98704	0.99053
R^2 -Adj	0.98758	0.97939	0.98547	0.98272	0.98738
SSE	13.85285	29.56261	16.12031	20.74284	18.78967
ARE	5.19552	3.67535	4.55495	4.11212	4.95398
HYBRID	9.23253	10.93279	7.42953	8.27996	11.56317
MPSD	8.29636	5.82268	5.94497	5.40667	9.16491
MAE	0.97761	1.10162	1.04825	1.08950	0.89804
SNE	4.05970	4.28821	3.66474	3.78812	4.40430
<i>Temkin</i>					
K_M (L/mg)	0.19314	0.29209	0.22476	0.25643	0.13608
b_M (mg/g)	331.07572	367.02597	346.77202	364.91014	305.20117
R^2	0.99150	0.98840	0.99105	0.99000	0.98883
R^2 -Adj	0.98866	0.98453	0.98807	0.98666	0.98510
SSE	12.37752	20.91711	14.16483	21.68239	22.03380
ARE	5.74074	5.29550	5.59892	5.72607	6.25771
HYBRID	12.03239	14.54045	10.56052	12.12317	30.31467
MPSD	10.62228	9.68113	8.93485	8.43623	18.71355
MAE	0.89423	1.11944	1.01901	1.23140	0.74194
SNE	3.16987	3.70161	3.19093	3.74981	4.60252
<i>Dubinin-Radushkevich (D-R)</i>					
q_m (mg/g)	31.87089	31.83077	30.76107	29.51396	31.83077
K_{DR} (mol ² /kJ ²)	0.00025	0.00019	0.00020	0.00018	0.00019
R^2	0.87572	0.86254	0.86704	0.85890	0.86254
R^2 -Adj	0.83429	0.81672	0.82272	0.81186	0.81672
SSE	217.06002	225.37728	225.17758	250.99127	225.37728
ARE	22.04778	20.17248	21.05657	20.48773	20.17248
HYBRID	178.33015	178.75627	173.45011	177.60889	178.75627
MPSD	39.65376	39.23137	38.80529	38.59592	39.23137
MAE	3.83446	3.65788	3.87830	3.97469	3.65788
SNE	4.82714	4.72253	4.77686	4.89615	4.72253
<i>Jovanovic</i>					
K_J (L/mg)	0.00853	0.00944	0.01170	0.01692	0.00849
q_m (mg/g)	35.14928	34.09320	33.21288	30.80221	34.44130
R^2	0.97164	0.96662	0.95154	0.91493	0.97183
R^2 -Adj	0.96219	0.95550	0.93539	0.88657	0.96244
SSE	59.50168	62.20115	75.24534	130.46033	62.53696
ARE	12.49796	11.75927	12.01660	12.85726	12.47312
HYBRID	59.03252	55.01072	50.27353	61.79123	61.59891
MPSD	23.95852	22.67810	19.79322	17.73674	24.47825
MAE	1.98414	1.94592	2.32689	2.98063	1.93578
SNE	4.02794	3.86097	3.91426	4.72459	4.09582

Table 4. Three-parameter isotherms constants with five different error analysis in Microsoft Excel Solver

	SSE	ARE	HYBRID	MPSD	MAE
<u>Dubinin-Astakhov (D-A)</u>					
q_m (mg/g)	36.28594	35.04878	33.01061	29.89269	35.04883
E (J/mol)	1740.32884	2370.09386	4451.71100	8034.88356	2370.07518
n_{DA}	1.00000	1.00000	1.00000	1.00000	1.00000
R^2	0.94460	0.93697	0.91760	0.89393	0.93697
R^2 -Adj	0.91136	0.89915	0.86815	0.83030	0.89915
SSE	97.34395	100.55178	124.23476	204.90305	100.55154
ARE	15.25030	13.82581	15.44667	15.65526	13.82583
HYBRID	112.40611	100.25168	89.25787	107.71588	100.25194
MPSD	33.73092	30.76576	25.23452	22.75592	30.76584
MAE	2.43443	2.41772	3.04288	3.66897	2.41772
SNE	4.11272	3.83680	3.96452	4.63291	3.83680
<u>Redlich-Peterson (R-P)</u>					
K_{RP} (L/g)	1.15686	1.83274	1.50019	2.05691	1.06898
α_{RP} (L/mg)	0.12401	0.25510	0.19890	0.34257	0.11967
β_{RP}	0.77903	0.73916	0.74688	0.71147	0.76908
R^2	0.99755	0.99674	0.99711	0.99558	0.99734
R^2 -Adj	0.99608	0.99478	0.99538	0.99292	0.99574
SSE	3.59616	5.46455	4.21248	6.55358	4.89234
ARE	2.85815	2.15054	2.58705	2.63208	2.69613
HYBRID	3.43104	3.83036	2.90971	3.45425	4.56374
MPSD	5.50514	4.88051	4.39294	4.03415	6.56932
MAE	0.48725	0.45206	0.51910	0.61325	0.42101
SNE	3.93307	3.90563	3.70067	4.29188	4.37635
<u>Sips</u>					
q_m (mg/g)	59.29319	72.03273	64.01559	71.94951	63.07625
K_s (L/mg)	0.03439	0.03615	0.03531	0.03444	0.03298
β_s	0.59838	0.52561	0.56595	0.53194	0.58558
R^2	0.99897	0.99838	0.99884	0.99831	0.99886
R^2 -Adj	0.99836	0.99740	0.99814	0.99730	0.99817
SSE	1.50396	2.81605	1.68900	2.46553	2.12054
ARE	1.78491	1.32273	1.63663	1.79113	1.61391
HYBRID	1.42883	1.84973	1.27027	1.46051	1.60914
MPSD	3.55774	3.32658	3.02625	2.84654	3.58978
MAE	0.30239	0.28083	0.31194	0.39150	0.26307
SNE	4.06653	4.38250	3.84006	4.45807	4.19596
<u>Tóth</u>					
q_m (mg/g)	78.99030	87.54891	99.49835	149.45298	84.73605
K_T (L/mg)	0.31601	0.32634	0.42686	0.57620	0.30829
n_T	0.35793	0.34153	0.29781	0.23384	0.35192
R^2	0.99853	0.99836	0.99831	0.99747	0.99837
R^2 -Adj	0.99765	0.99738	0.99730	0.99594	0.99740
SSE	2.15017	2.91173	2.46090	3.71978	2.95932
ARE	2.16364	1.96322	1.99460	2.10850	2.00727
HYBRID	2.05032	2.47813	1.79285	2.09525	2.66427
MPSD	4.25420	4.68729	3.53843	3.29990	4.95859
MAE	0.36618	0.30745	0.38921	0.47329	0.30643
SNE	3.97924	4.21515	3.79232	4.42643	4.37074
<u>Brouers-Sotolongo (B-S)</u>					
q_m (mg/g)	45.03682	51.10940	46.66169	49.60118	49.25654
K_{BS} [(L/mg) ^a]	0.04954	0.05273	0.05101	0.05113	0.05077
α_{BS}	0.54724	0.49742	0.52976	0.50955	0.51526
R^2	0.99930	0.99871	0.99922	0.99887	0.99897
R^2 -Adj	0.99888	0.99794	0.99875	0.99819	0.99835
SSE	1.02876	2.28147	1.13739	1.64635	1.83074
ARE	1.49086	1.13223	1.39978	1.56782	1.24023
HYBRID	1.04753	1.52039	0.95228	1.08274	1.18017
MPSD	3.10315	3.03517	2.72203	2.58492	2.70323
MAE	0.24226	0.23513	0.24984	0.32666	0.22761
SNE	3.83243	4.42005	3.65970	4.26676	3.93762

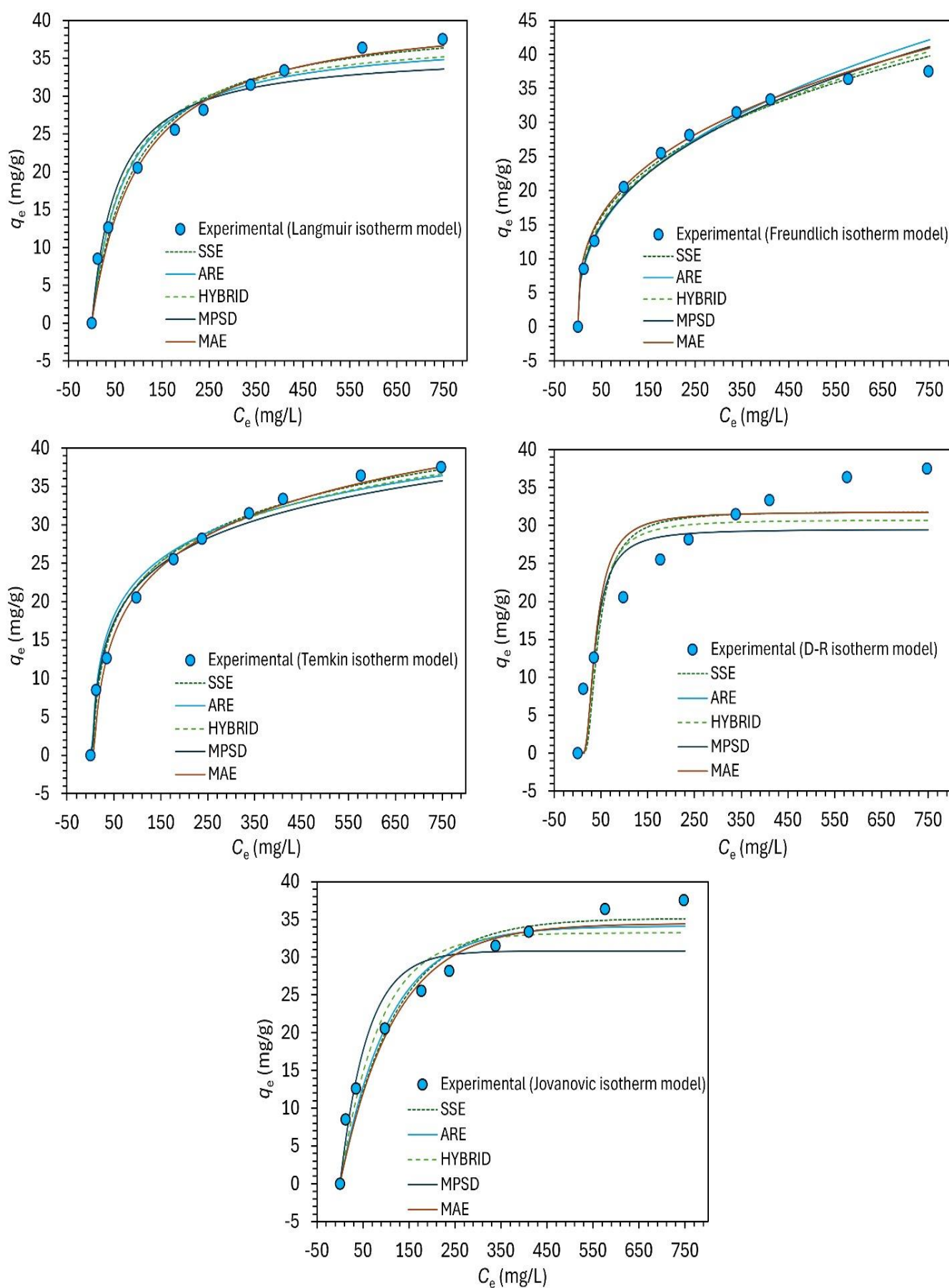


Figure 4. Comparison of experimental and model-predicted adsorption isotherm data using five different error functions (SSE, ARE, HYBRID, MPSD, and MAE) in Excel Solver for two-parameter isotherm models

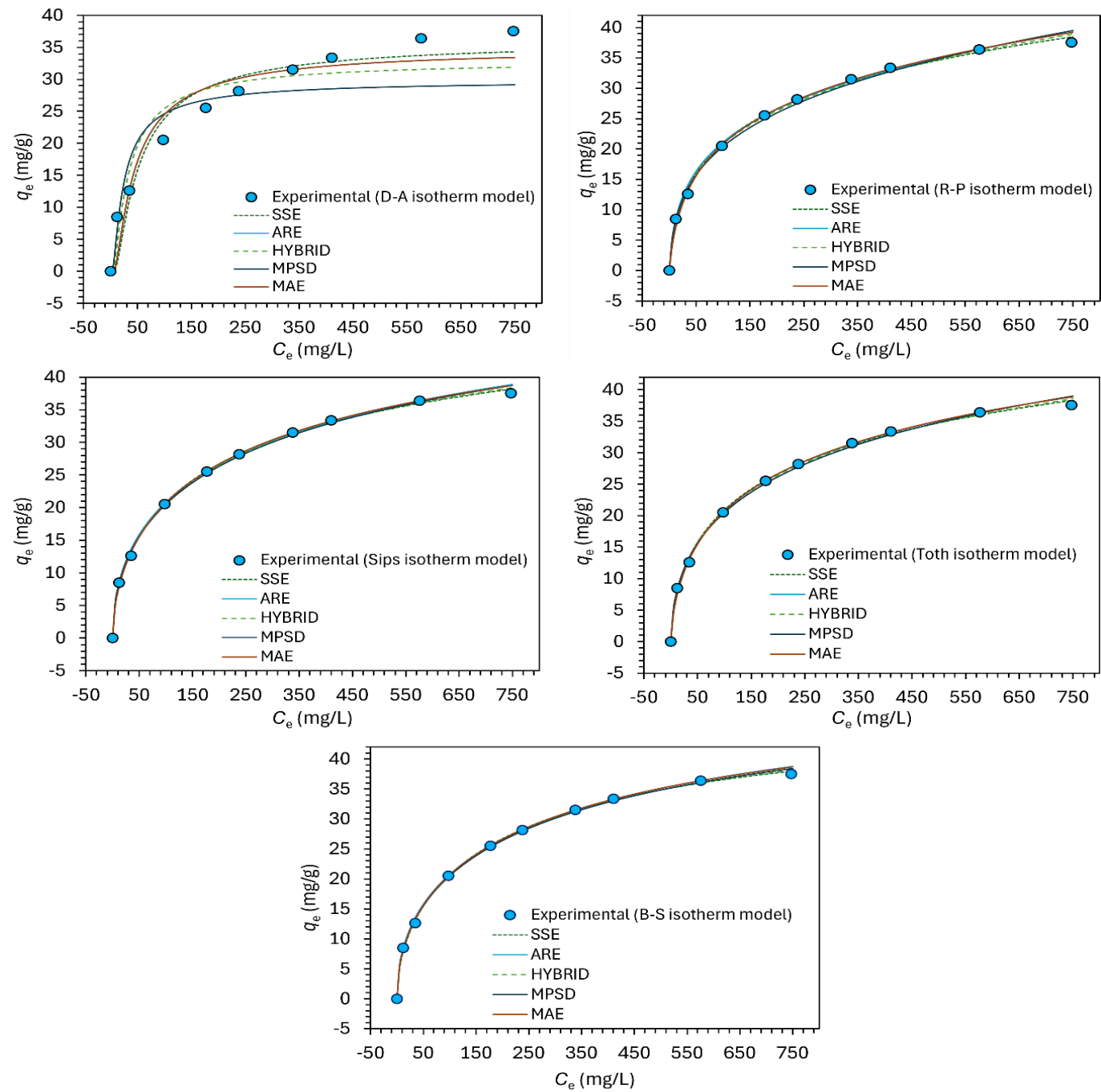


Figure 5. Comparison of experimental and model-predicted adsorption isotherm data using five different error functions (SSE, ARE, HYBRID, MPSD, and MAE) in Excel Solver for three-parameter isotherm models

Table 5. SNE values of the error functions for each isotherm model

Isotherm models	SNE values of the error functions				
	SSE	ARE	HYBRID	MPSD	MAE
<i>Two-parameter isotherms</i>					
Langmuir	3.70984	3.61598	3.61199	4.53198	3.93875
Freundlich	4.05970	4.28821	3.66474	3.78812	4.40430
Temkin	3.16987	3.70161	3.19093	3.74981	4.60252
Dubinin-Radushkevich (D-R)	4.82714	4.72253	4.77686	4.89615	4.72253
Jovanovic	4.02794	3.86097	3.91426	4.72459	4.09582
<i>Three-parameter isotherms</i>					
Dubinin-Astakhov (D-A)	4.11272	3.83680	3.96452	4.63291	3.83680
Redlich-Peterson (R-P)	3.93307	3.90563	3.70067	4.29188	4.37635
Sips	4.06653	4.38250	3.84006	4.45807	4.19596
Tóth	3.97924	4.21515	3.79232	4.42643	4.37074
Brouers-Sotolongo (B-S)	3.83243	4.42005	3.65970	4.26676	3.93762

Fig. 8 collectively illustrates the C_e-q_e plots drawn for each model based on the error functions with the lowest SNE values. Fig. 9 provides this representation individually. From these graphs, the model that best represents (or describes/explains) the experimental data can be selected.

When examining Fig. 8, and especially Fig. 9 and Fig. 10, it becomes evident that the isotherms that least represent the experimental data are D-R and D-A. Except for D-A, all three-parameter isotherms represent the experimental data very well. In Fig. 8 and Fig. 10, distinguishing between the R-P, Sips, Toth, and B-S isotherms is particularly challenging. All these isotherms were best minimized using the HYBRID error function. Therefore, a ranking among the models can be made using the HYBRID error function values in Table 4. According to this, the ranking for best representation of the experimental data is as follows: B-S > Sips > Toth > R-P.

These four isotherms are followed by Freundlich > Temkin > Langmuir > Jovanovic > D-A > D-R. From these results, it can be concluded that D-A and D-R fail to represent the experimental data, whereas the others represent it to some extent. Let us now analyze the isotherms that best represent the experimental data in order.

In this study, the Brouers–Sotolongo (B-S) isotherm model undoubtedly provides the best representation of Pb^{2+} adsorption onto pine bark from aqueous solutions. The B-S parameters (constants) determined in this study are $K_{BS} = 0.05101$ and $\alpha_{BS} = 0.52976$. The K_{BS} value indicates that the binding energy between the adsorbent and adsorbate is low to moderate. This suggests that the adsorption process does not require high binding energy and that the energy levels of the adsorption sites on the surface are limited. The α_{BS} parameter typically ranges between 0 and 1. An α_{BS} value of approximately 0.5 reflects a heterogeneous surface structure, indicating that the adsorption sites on the surface exhibit varying energy levels. The B-S isotherm can be considered a hybrid model, essentially an adaptation of the Langmuir isotherm for heterogeneous surfaces. The perfect fit of the experimental data to this model indicates that the material possesses a structure that combines both homogeneous and heterogeneous surface characteristics.

The experimental data also show excellent compatibility with other three-parameter isotherms, such as the R-P, Sips, and Tóth models, similar to the B-S model. Three-parameter isotherm models are designed to describe more complex adsorption mechanisms that two-parameter models, like Langmuir and Freundlich, fail to explain adequately. The compatibility of the data with these models suggests that the adsorption process

involves a more intricate nature, encompassing both homogeneous and heterogeneous surface characteristics with diverse energetic and structural features.

The Tóth isotherm is an empirical extension of the Langmuir model; however, by incorporating the dimensionless parameter n_T in its mathematical expression, it accounts for surface heterogeneity, which is neglected in the Langmuir model. As will be evident from the results obtained in this study, this adjustment enhances its fit with experimental data. In Table 4, the n_T parameter for the Tóth isotherm is approximately 0.30 (as determined by HYBRID minimization). The fact that $n_T < 1$ indicates that the adsorbent surface possesses a relatively heterogeneous structure.

A similar approach can also be applied to the Sips isotherm, which presents a hybrid model by combining the characteristics of both the Langmuir and Freundlich isotherms. The critical parameter in this model is β_s . In this study, the calculated β_s value is approximately 0.57 (Table 4). The dimensionless heterogeneity parameter β_s reflects surface homogeneity and the degree of deviation in adsorption. A $\beta_s < 1$ value indicates that the adsorbent surface is heterogeneous and contains adsorption regions with varying energy levels.

Another isotherm model with a similar approach and mathematical expression is the Redlich–Peterson (R-P) model. The mathematical expression of the R-P model is given in Eq. (16), where the parameter β_{RP} takes values between 0 and 1. As β_{RP} approaches 1, the model reduces to the Langmuir isotherm, while as β_{RP} approaches 0, it resembles the Freundlich isotherm. The values of β_{RP} between 0 and 1 characterize the heterogeneity of the adsorbent surface. In this study, β_{RP} is approximately 0.75 (Table 4). Consequently, most of the three-parameter isotherms share similarities with one another.

In this study, the models that least represent the experimental data, or perhaps do not represent them at all, are primarily the two-parameter Dubinin–Radushkevich (D-R) isotherm, followed by the three-parameter Dubinin–Astakhov (D-A) isotherm. The D-R isotherm is more suitable for describing adsorption behavior occurring on microporous, homogeneous surfaces with uniform adsorption energies. However, the pine bark used in this study was employed in its original, untreated form, characterized by a limited pore structure, low surface area, and heterogeneous surface properties. Therefore, it is unsurprising that the adsorption of Pb^{2+} does not fit this model.

The D-A model, another isotherm model that struggles to represent experimental data, is actually an extended version of the D-R model. In the D-A model, the n_{DA} parameter (Eq. (15)) ensures that the model has three parameters, providing information about the heterogeneity of the adsorbent and allowing its

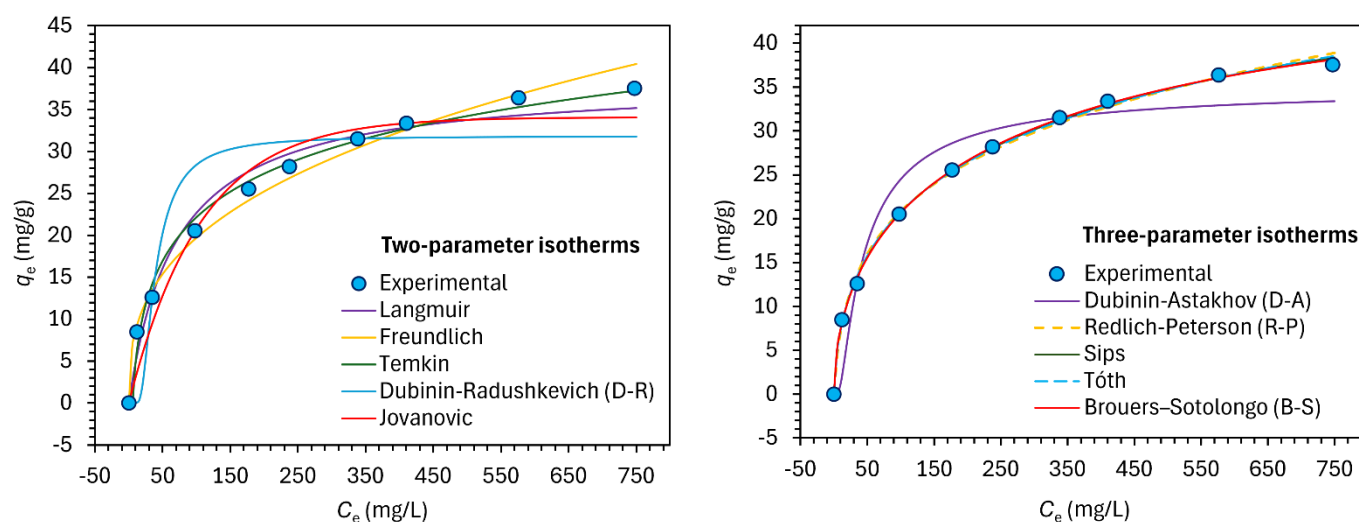


Figure 6. Comparison of two- and three-parameter isotherms optimized in Excel Solver

application to adsorbents on heterogeneous surfaces. The E constant in Eq. (15) characterizes the adsorption energy. When the E value is below 8 kJ/mol, adsorption generally proceeds through physical interactions. In this study, it is observed from Table 4 that the E value is 2.37 kJ/mol (determined by ARE minimization). In Table 4, the n_A values for this model are exactly 1. The $n_A = 1$ condition indicates that adsorption occurs on homogeneous surfaces. However, other isotherms suggest that the adsorbent surface is more heterogeneous. Since experimental data do not strongly support the D-A model, it may be more appropriate to disregard this result.

Among the commonly used two-parameter isotherms, the Langmuir and Freundlich models are the most well-known. The Langmuir isotherm, which is highly successful in describing monolayer adsorption processes on homogeneous surfaces, fails to fully describe the adsorption of Pb^{2+} onto red pine bark, which is determined to have a heterogeneous structure, as shown in Fig. 8 and Fig. 9. Specifically, experimental data deviate from the Langmuir model beyond the inflection point of the curve, as observed in Fig. 9.

On heterogeneous surfaces, the presence of regions with varying energy levels causes a delay in reaching equilibrium after the inflection point of the adsorption curve. In contrast, the Langmuir model assumes that the adsorption sites on the surface have uniform energy, resulting in a rapid attainment of equilibrium and the formation of a flat plateau beyond the inflection point. This behavior highlights the limitations of the Langmuir isotherm in describing adsorption on heterogeneous surfaces.

On the other hand, as evidenced by Fig. 8 and particularly Fig. 9, the experimental data are better represented by the Freundlich isotherm. This observation is further supported by the data presented in Table 3. The coefficient of determination (R^2) values, which indicate the degree of fit between the models and

the experimental data, are $R^2 = 0.98047$ for the Langmuir model and $R^2 = 0.98910$ for the Freundlich model. These results demonstrate that the Freundlich isotherm provides a more accurate representation of adsorption processes on heterogeneous surfaces.

Compared to these two well-known models, it is observed that the Temkin isotherm better represents the experimental data (Fig. 9). The R^2 value for the Temkin isotherm is 0.99150 (Table 3). As noted in Section 3.2.1, the Temkin isotherm accounts for the non-uniform energy distribution on the adsorbent surface. Therefore, the high degree of representation of the data by the Temkin isotherm is a reasonable outcome.

The Jovanovic isotherm is the third least representative model for the experimental data. In Table 3, the Jovanovic parameters are reported as $K_J = 0.00944$ L/mg, $q_m \approx 34$ mg/g, and $R^2 = 0.96662$. These results indicate that the Jovanovic model weakly explains the adsorption process in the system. Similar to the Langmuir model, the Jovanovic isotherm focuses on homogeneous surfaces and monolayer adsorption processes. Therefore, such a result is not surprising.

5. Conclusions

This study provides a comprehensive evaluation of Pb^{2+} ion adsorption onto pine bark, emphasizing the use of advanced modeling and error analysis techniques to enhance the reliability of kinetic and equilibrium data interpretation. Key findings are as follows:

Pine bark demonstrated moderate to high adsorption capacity, making it a viable, low-cost material for heavy metal removal from aqueous solutions.

The Brouers-Sotolongo (B-S) kinetic model best described the adsorption kinetics, indicating a mixed mechanism involving both physical and chemical interactions. The half-reaction time ($\tau_{1/2} = 10.99$ min) and fractal time parameter ($\alpha_{BS} = 0.64329$) highlighted the system's heterogeneity.

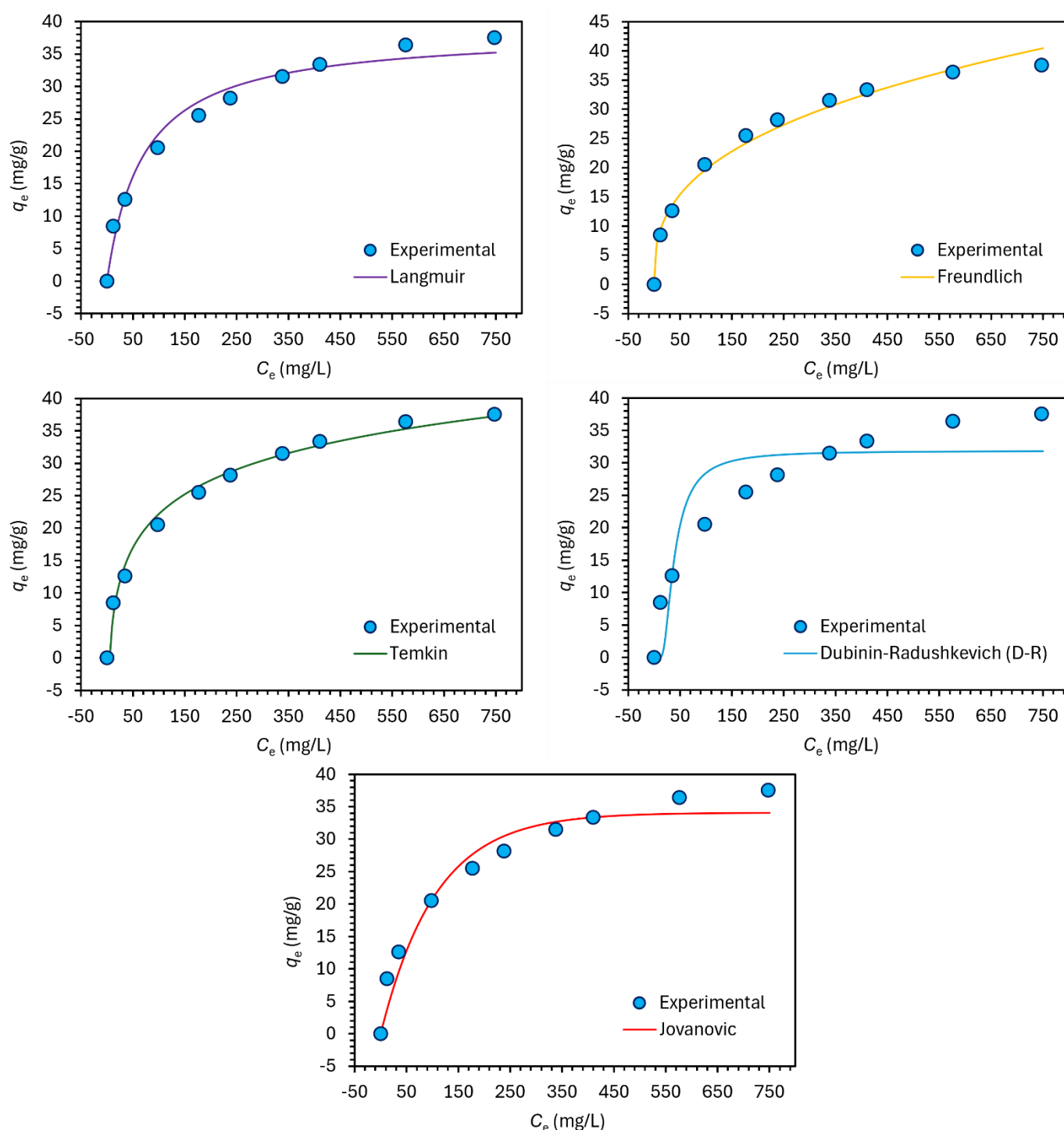


Figure 7. Single representations of two-parameter isotherms optimized in Excel Solver

Three-parameter isotherms, particularly the B-S, Tóth, and Sips models, provided the most accurate representation of experimental data. These models effectively captured the complexity of the adsorption process, including surface heterogeneity and variable energy distributions.

Non-linear regression using Microsoft Excel Solver proved to be an accessible and effective tool for optimizing adsorption model parameters. The HYBRID error function was identified as the most robust method for evaluating model performance.

The results reinforce the potential of using pine bark as an environmentally friendly adsorbent in wastewater treatment applications. Furthermore, this study highlights the importance of selecting appropriate models and error functions to ensure accurate data interpretation, particularly for systems with complex adsorption mechanisms.

In conclusion, this research contributes to the understanding of Pb^{2+} adsorption processes and demonstrates the practical application of advanced modeling techniques in environmental remediation studies. This study also contributes to the literature by

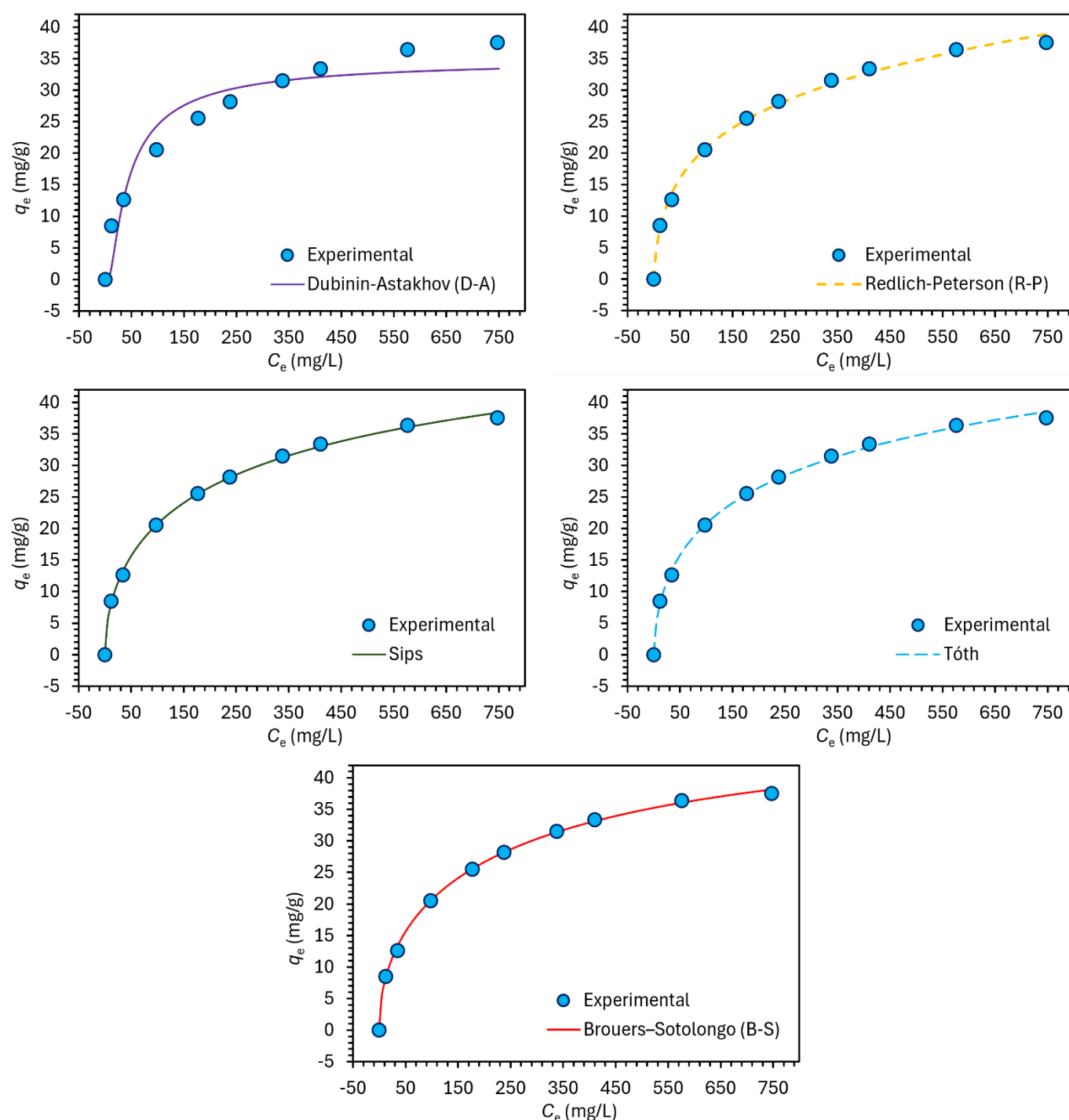


Figure 8. Single representations of three-parameter isotherms optimized in Excel Solver

demonstrating how the minimization of error functions using Microsoft Excel Solver enables more accurate interpretation and representation of equilibrium and kinetic data. This approach facilitates the selection of purpose-specific adsorbents and provides a deeper understanding of adsorption mechanisms. In addition, it is suggested that the selected method in this study can help eliminate the complexities and confusions found in the literature regarding this topic. It has been concluded that using Excel Solver with a non-linear approach allows for more accurate processing of adsorption data and better reflects the adsorption mechanism of the selected adsorbent.

References

- [1] A.M. Badran, U. Utra, N.S. Yussof, M.J.K. Bashir, *Advancements in adsorption techniques for sustainable water purification: A focus on lead removal*, *Separations* 10(11), 2023, 565.
- [2] N.e. Hira, S.S.M. Lock, N.F. Shoparwe, I.S.M. Lock, L.G. Lim, C.L. Yüin, Y.H. Chan, M. Hassam, *Review of Adsorption Studies for Contaminant Removal from Wastewater Using Molecular Simulation*, *Sustainability*, 15(2), 2023, 1510.
- [3] U.A. Edet, A.O. Ifeiebuegu, *Kinetics, isotherms, and thermodynamic modeling of the adsorption of phosphates from model wastewater using recycled brick waste*, *Processes*, 8(6), 2020, 665.
- [4] K.Y. Foo, B.H. Hameed, *Insights into the modeling of adsorption isotherm systems*, *Chem Eng J*, 156(1), 2010, 2–10.

- [5] H.R. Ghaffari, H. Pasalari, A. Tajvar, K. Dindarloo, B. Goudarzi, V. Alipour, A. Ghanbarnejad, Linear and nonlinear two-parameter adsorption isotherm modeling: A case-study, *Int J Eng Sci*, 6(9), 2017, 1–11.
- [6] L.S. Chan, W.H. Cheung, S.J. Allen, G. McKay, Error analysis of adsorption isotherm models for acid dyes onto bamboo derived activated carbon, *Chinese J Chem Eng*, 20(3), 2012, 535–542.
- [7] K. Suwannahong, S. Wongcharee, T. Kreetachart, C. Sirilamduan, J. Rioyo, A. Wongphat, Evaluation of the Microsoft Excel Solver spreadsheet-based program for nonlinear expressions of adsorption isotherm models onto magnetic nanosorbent, *Appl Sci*, 11(16), 2021, 7432.
- [8] E.A. Adekunbi, J.O. Babajide, H.O. Oloyede, J.S. Amoko, O.A. Obijole, I.A. Oke, Evaluation of Microsoft Excel Solver as a tool for adsorption kinetics determination, *Ife J Sci*, 21(3), 2019, 169–183.
- [9] J. Sreńscek-Nazzal, U. Narkiewicz, A.W. Morawski, R.J. Wróbel, B. Michalkiewicz, Comparison of optimized isotherm models and error functions for carbon dioxide adsorption on activated carbon, *J Chem Eng Data*, 60(11), 2015, 3148–3158.
- [10] Md A. Hossain, H.H. Ngo, W. Guo, Introductory of Microsoft Excel Solver function – spreadsheet method for isotherm and kinetics modelling of metals biosorption in water and wastewater, *J Water Sustain*, 3(4), 2013, 223–237.
- [11] Y.S. Ho, G. McKay, Sorption of dye from aqueous solution by peat, *Chem Eng J*, 70(2), 1998, 115–124.
- [12] Sahmoune Mohamed Nasser, Moussa Abbas, Mohamed Trari, Understanding the rate-limiting step adsorption kinetics onto biomaterials for mechanism adsorption control, *Prog React Kinet Mec*, 49, 2024, 1–26.
- [13] B. Mehdinejadiani, S.M. Amininasab, L. Manhooei, Linear and non-linear methods for estimating isotherm parameters of nitrate adsorption, Water resources and wetlands, 4th International Conference Water resources and wetlands, 5-9 September 2018, Tulcea (Romania), p.312.
- [14] G.W. Kajumba, S. Emik, A. Öngen, H.K. Özcan, S. Aydın, Modelling of Adsorption Kinetic Processes—Errors, Theory and Application. In *Advanced Sorption Process Applications*. Edited by Serpil Edebali, Published: 05 November 2018, IntechOpen.
- [15] J.-C. Liu, P. A. Monson, Monte Carlo simulation study of water adsorption in activated carbon, *Ind Eng Chem Res*, 45(16), 2006, 5649–5656.
- [16] A. Wongphat, S. Wongcharee, N. Chaiduangsi, K. Suwannahong, T. Kreetachart, S. Imman, N. Suriyachai, S. Hongthong, P. Phadee, P. Thanarat, J. Rioyo, Using Excel Solver's parameter function in predicting and interpretation for kinetic adsorption model via batch sorption: Selection and statistical analysis for basic dye removal onto a novel magnetic nanosorbent, *Chem Eng*, 8(3), 2024, 58.
- [17] A. Gundogdu, D. Ozdes, C. Duran, V.N. Bulut, M. Soylak, H.B. Senturk, Biosorption of Pb(II) ions from aqueous solution by pine bark (*Pinus brutia* Ten.) *Chem Eng J*, 153(1-3), 2009, 62–69.
- [18] S. Lagergren, About the theory of so-called adsorption of soluble substances. *Kungliga Svenska Vetenskapsakademiens Handlingar*, 24(4), 1898, 1–39.
- [19] Y.S. Ho, Review of second-order models for adsorption systems. *J Hazard Mater*, 136(3), 2006, 681–689.
- [20] L. Largitte, R. Pasquier, A review of the kinetics adsorption models and their application to the adsorption of lead by an activated carbon, *Chem Eng Res Design*, 109, 2016, 495–504.
- [21] M. Avrami, Kinetics of phase change. I. General theory. *J Chem Phys*, 7(12), 1939, 1103–1112.
- [22] R. George, S. Sugunan, Kinetics of adsorption of lipase onto different mesoporous materials: Evaluation of Avrami model and leaching studies, *J Mol Catal B-Enzymatic*, 2014, 105, 26–32.
- [23] A.G. Marangoni, Kinetics of crystal growth using the Avrami model and the chemical potential approach. In: *Kinetic analysis of food systems*, 2017, Springer, Cham.
- [24] F. Brouers, The fractal (BSf) kinetics equation and its approximations. *J Mod Phys*, 5(16), 2014, 1594–1601.
- [25] F. Brouers, T.J. Al-Musawi, The use of the Brouers–Sotolongo fractal kinetic equation for the study of drug release. *Adsorption*, 26, 2020, 843–853.
- [26] S. Karoui, R.B. Arfi1, M.J. Fernández-Sanjurjo, A. Nuñez-Delgado, A. Ghorbal1, E. Álvarez-Rodríguez, Optimization of synergistic biosorption of oxytetracycline and cadmium from binary mixtures on reed-based beads: modeling study using Brouers-Sotolongo models, *Environ Sci Pollut R*, 28, 2021, 46431–46447.
- [27] A.M.B. Hamissa, F. Brouers, M.C. Ncibi, M. Seffen, Kinetic modeling study on methylene blue sorption onto agave americana fibers: Fractal kinetics and regeneration studies, *Sep Sci Technol*, 48(18), 2013, 2834–2842.
- [28] I. Langmuir, The adsorption of gases on plane surfaces of glass, mica, and platinum, *J Am Chem Soc*, 40(9), 1918, 1361–1403.
- [29] A. Saha, D. Bhaduri, A. Pipariya, R.K. Ghosh, Linear and nonlinear sorption modelling for adsorption of atrazine onto activated peanut husk, *Environ Prog Sustain*, 36(2), 2017, 348–358.
- [30] H. Freundlich, Over the adsorption in solution. *Journal of Physical Chemistry*, 57, 1906, 385–471.
- [31] M.J. Temkin and V. Pyzhev, Recent modifications to Langmuir isotherms, *Acta Physiochim. USSR*, 12 (1940) 217–222.
- [32] M.M. Majd, V. Kordzadeh-Kermani, V. Ghalandari, A. Askari, M. Sillanpää, Adsorption isotherm models: A comprehensive and systematic review (2010–2020), *Sci Tot Environ*, 812, 2022, 151334.
- [33] N.D. Hutson, R.T. Yang, Theoretical basis for the Dubinin-Radushkevitch (D-R) adsorption isotherm equation, *Adsorption*, 3, 1997, 189–195.
- [34] R. Saadi, Z. Saadi, R. Fazaeli, N.E. Fard, Monolayer and multilayer adsorption isotherm models for sorption from aqueous media, *Korean J. Chem. Eng.*, 32(5), 2015, 787–799.
- [35] M.M. Dubinin, V.A. Astakhov, Development of the concepts of volume filling of micropores in the adsorption of gases and vapors by microporous adsorbents, *Russ Chem Bull*, 20, 1971, 3–7.
- [36] G.J. Millar, S.J. Couperthwaite, M. de Bruyn, C.W. Leung, Ion exchange treatment of saline solutions using Lanxess S108H strong acid cation resin, *Chem Eng J*, 280, 2015, 525–535.
- [37] V.J. Inglezakis, Solubility-normalized Dubinin–Astakhov adsorption isotherm for ion-exchange systems, *Micropor Mesopor Mat*, 103(1-3), 2007, 72–81.
- [38] O. Redlich, D.L. Peterson, A useful adsorption isotherm, *J Phys Chem*, 63(6), 1959, 1024–1024.
- [39] S. Kalam, S.A. Abu-Khamsin, M.S. Kamal, S. Patil, Surfactant adsorption isotherms: A review, *ACS Omega*, 6(48), 2021, 32342–32348.
- [40] J. Toth, State equations of the solid gas interface layer, *Acta Chem Acad Hung*, 69 (1971) 311–317.
- [41] L. Bokányi, Some applications of Tóth-isotherm in mineral processing, XXVI International Mineral Processing Congress (IMPC) 2012 Proceedings, New Delhi, India, 24–28 September 2012.
- [42] R. Ramadoss, D. Subramaniam, Removal of divalent nickel from aqueous solution using blue-green marine algae: adsorption modeling and applicability of various isotherm models, *Sep Sci Technol*, 54(6), 2019, 943–961.
- [43] F. Brouers, O. Sotolongo, F. Marquez, J.P. Pirard, Microporous and heterogeneous surface adsorption isotherms arising from Levy distributions. *Physica A*, 349(1-2), 2005, 271–282.
- [44] F. Gimbert, N. Morin-Crini, F. Renault, P.-M. Badot, G. Crini, Adsorption isotherm models for dye removal by cationized starch-based material in a single component system: Error analysis, *J Hazard Mater*, 157(1), 2008, 34–46.

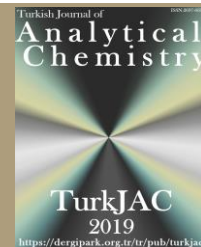
- [45] N. Sivarajasekar, R. Baskar, Adsorption of Basic Magenta II onto H₂SO₄ activated immature *Gossypium hirsutum* seeds: Kinetics, isotherms, mass transfer, thermodynamics and process design, *Arab J Chem*, 12(7), 2019, 1322–1337.
- [46] C.J. Willmott, K. Matsuura, Advantages of the mean absolute error (MAE) over the root mean square error (RMSE) in assessing average model performance, *Clim Res*, 30, 2005, 79–82.
- [47] N.R. Draper, H. Smith, *Applied Regression Analysis*. 3th Edition, 1998, Wiley, New York.
- [48] R.J. Hyndman, A.B. Koehler, Another look at measures of forecast accuracy, *Int J Forecasting*, 22(4), 2006, 679–688.
- [49] W.H. Press, S.A. Teukolsky, W.T. Vetterling, B.P. Flannery, *Numerical recipes: The art of scientific computing* (3rd ed.), 2007, Cambridge University Press.



TurkJAC

Turkish Journal of

Analytical Chemistry

<https://dergipark.org.tr/tr/pub/turkjac>TurkJAC
2019<https://dergipark.org.tr/tr/pub/turkjac>

Validation of stability-indicating high-performance liquid chromatography method for the determination of thymol in gelatin-based hydrogels

Onur Demir^{1,2*} , Mehlika Pulat³ , Ali Bilgili⁴ ¹ Republic of Turkey Ministry of Agriculture and Forestry, Pendik Veterinary Control Institute, Pharmaceutical Quality Control Laboratory, 34890, Istanbul, Türkiye² Ankara University, Graduate School of Health Sciences, 06110, Ankara, Türkiye³ Gazi University, Faculty of Science, Department of Chemistry, 06560, Ankara, Türkiye⁴ Ankara University, Faculty of Veterinary Medicine, Department of Pharmacology and Toxicology, 06070, Ankara, Türkiye

Abstract

The aim of this study was to develop an analytical method to determine the amount of thymol loaded into the structure of a gelatin hydrogel developed to struggle varroosis infestation of honey bees and released into a model release system. Chromatographic separation was achieved using a high-performance liquid chromatograph, C18 column, and acetonitrile:water (75:25) mobile phase with an isocratic flow rate of 1 mL/min. To validate the method, specificity, precision, linearity, detection and measurement limit, accuracy, robustness, solution stability, and system suitability parameters were studied. Hydrolytic, thermal, oxidative, and photolytic degradation studies were performed for stress testing. The method is linear in the range of 0.25-15 µg/mL ($R^2 = 0.999$). LOD was calculated as 6.22 ng/mL and LOQ as 18.84 ng/mL. Intra-day and inter-day precision study %RSD values were $\leq 2\%$. The average recovery for the hydrogel was 100.3% (± 2.12) and for the air sample was 99.9% (± 3.14). The analytical method proved to be specific, linear, precise, and robust. This study presents a sensitive, convenient, and practical method for the detection of thymol in gelatin-based hydrogel structure and model release atmosphere.

Keywords: Controlled release, HPLC, hydrogel, thymol, validation, varroosis

1. Introduction

Thymol (known as 2-isopropyl-5-methylphenol) is a phenolic compound found in the extract and essential oil of *Thymus vulgaris* L. [1,2]. The utilization of thymol has been sanctioned for the management of pests encompassing bacteria, fungi, viruses, and parasites in both indoor and outdoor environments. [3]. Since the 1980s, thymol has been utilized in the management of varroosis, an infestation characterized by the proliferation of the mite *Varroa destructor* (Anderson and Trueman), which inflicts considerable damage on honey bee colonies [4,5]. When thymol is applied to the hive, it sublimates and diffuses into the hive atmosphere. In mites exposed to thymol vapour, GABA-gated chloride channels are blocked, resulting in excitation and convulsions in the central nervous system, leading to acaricidal effects [6]. However, when thymol is applied to colonies, acaricidal activity efficiency may vary because of environmental factors [7]. It is known that

thymol has a highly volatile nature due to its structure and may decompose and cause loss in the environmental conditions in which it is applied [2,8–10]. Consequently, a hydrogel system was developed using gelatin polymer and thymol, hypothesizing that it could limit the volatility and degradation of thymol and enable its controlled release [11]. The development and validation of analytical methods to quantify active substances in such studies (e.g., loading efficiency and release tests) are crucial for the advancement of controlled release systems research and development [12,13] and for the quantification of thymol in air [14–17].

Qualitative and quantitative determination of thymol active substance can be done by chromatographic techniques such as high performance liquid chromatography (HPLC) systems equipped with UV (ultraviolet) or DAD (diode array detector).

Citation: O. Demir, M. Pulat, A. Bilgili, Validation of stability-indicating high-performance liquid chromatography method for the determination of thymol in gelatin-based hydrogels, Turk J Anal Chem, 7(2), 2025, 132–139.

***Author of correspondence:** demir.onur@tarimorman.gov.tr

Tel: +90 (216) 390 12 80

Fax: +90 (216) 354 76 92

Received: December 20, 2024

Accepted: March 07, 2025

doi <https://doi.org/10.51435/turkjac.1604250>

Quantification of thymol in the animal skin matrix was performed by the HPLC-UV system at 278 nm in a method using an RP-C18 column and a mobile phase containing acetonitrile:water (35:65 v/v) [18].

In another study, determination of thymol in aromatic juice of *Origanum onites* L. was carried out using an HPLC-UV system at 254 nm and 273 nm using an XBridge C18 column and mobile phase containing acetonitrile:water (42:58 v/v) [19].

A method for the measurement of thymol in a tincture prepared with thymol, glycerol, ethyl alcohol, and purified water using a Microsob Varian C18 (4.6 × 250 mm, 5 µm) column and HPLC-UV system at 274 nm using a mobile phase containing acetonitrile:water (50:50 v/v) is reported [20].

It has been reported that the determination of thymol in a controlled release system in the form of a nanocapsule developed using Poly D, L-lactide-co-glycolide and Poly(ethylene glycol)-block-poly(propylene glycol)-block-poly(ethylene glycol) was performed by an HPLC-DAD system with an ODS Hypersil C18 (250 mm × 4.6 mm, 5 µm) column, acetonitrile:water (78:22 v/v) mobile phase, and a detection wavelength of 278 nm [21].

The migration amount of thymol loaded into polypropylene packaging films [12] and the release of thymol in films formed using silver nanoparticles and polylactic acid [13] were measured at 274 nm using an HPLC-UV system, acetonitrile:water (40:60 v/v) mobile phase, LiChrospher 100 RP18 column (250 mm × 5 mm × 5 µm, Agilent Technologies).

It was reported that the amount of thymol in swab samples taken from a cultural heritage mask exhibited in a museum was measured using a Jones C18 column (4 µm, 4.6 × 250 mm), acetonitrile:water (90:10 v/v) mobile phase, and HPLC-UV system at 225 nm [16].

In a study, the stability of thymol in *Nigella sativa* oil contained in gelatin capsules was investigated by HPLC-UV under different stress conditions. Inertsil ODS-3v C18 (250 mm × 4.6 mm 5-µm) column, 0.1 % aqueous formic acid:methanol (40:60 v/v) mobile phase, and measurements were made at 254 nm wavelength [22].

Although there are differences between studies in terms of analytical method components with placebo or matrix in which the amount of thymol is investigated, it is seen that methods are generally established with isocratic flow of acetonitrile, methanol and water or aqueous formic, C18 column and UV, DAD detectors in the wavelength range of 225-278 nm.

However, no published study was found for the determination of thymol in the developed CRS using gelatin polymer, glutaraldehyde crosslinker, sunflower oil, and thymol. For this reason, it was necessary to

develop an analytical method to perform quantitative determination analyses for the gelatin based CRS.

The present study aims to develop and validate a stable HPLC-DAD method for the determination of thymol in a gelatin-based hydrogel and model release system atmosphere [11].

2. Material and methods

2.1. Reagents, solvents and materials

The hydrogel production materials included powdered bovine gelatin (Alfasol, s-Hertogenbosch, the Netherlands), glutaraldehyde (25%, Merck, Darmstadt, Germany), sunflower oil (Yudum, Ayvalık, Türkiye), thymol (99% purity, Sigma-Aldrich, St. Louis, MO, USA), and distilled water. For chromatographic analyses, a thymol reference standard (99.6% purity, Dr. Ehrenstorfer, Teddington, UK), a *p*-cumenol reference standard (99.6% purity, Dr. Ehrenstorfer, Augsburg, Germany), N-methyl-2-pyrrolidone (BASF Ludwigshafen, Germany), hydrochloric acid (%37, Scharlau, Sentmenat, Spain) sodium hydroxide (Sigma-Aldrich, St. Louis, MO, USA), Hydrogen peroxide (%30, (Sigma-Aldrich, St. Louis, MO, USA), acetonitrile (HPLC grade, Sigma-Aldrich, Darmstadt, Germany), and distilled water were used.

2.2. Instrumentation and analytical conditions

All chromatographic analyses were performed on an RP-HPLC-DAD (Dionex Ultimate 3000, Thermo Scientific, Waltham, Massachusetts, USA) using Chromeleon 7.2.9 chromatography software (Thermo Scientific, Waltham, Massachusetts, USA). Analytical separation was performed on an ACE 5 C18, 250x4.60 5 µm column (Advanced Chromatography Technologies Ltd, Aberdeen, Scotland). A PTFE 0.45 µm syringe tip filter (Isolab) was also used for sample preparation.

The mobile phase was adjusted isocratically at a flow rate of 1 mL/min in a ratio of 75 % acetonitrile and 25 % water from different lines. The detection wavelength was set to 277 nm, the column oven temperature to 25°C, the sample injection volume to 20 µL, and the analysis time to 7 min. Acetonitrile was used as the solvent, and acetonitrile:water (80:20) was used for diluent.

2.2.1. Preparation of standard solutions

p-Cumenol and thymol standards were first prepared with acetonitrile at 1000 µg/mL. Stock solutions of *p*-cumenol 10 µg/mL, thymol 100 µg/mL, and thymol 10 µg/mL were then prepared by dilution with diluent. All solutions were placed in an ultrasonic bath for 20 min to ensure complete dissolution. All standards were filtered through a 0.45 µm PTFE (Isolab) syringe tip filter into glass vials prior to analysis by HPLC-DAD.

2.2.2. Preparation of blank, placebo and spike samples

For the hydrogel placebo sample, thymol-free sunflower oil was added to the centrifuge tubes. For the 80%, 100 %, and 120 % accuracy samples, a thymol/sunflower oil solution with a concentration of 500 mg/mL was added to the tubes. All tubes were then cross-linked by adding 10 % gelatin solution and 12.5 % glutaraldehyde solution prepared with water, respectively. After one night, the hydrogels were removed from the tubes, cut into 0.5 cm thick discs, and left to dry. The hydrogel discs containing 20, 25, 30 wt % thymol were cut into smaller pieces with the help of a scalpel and extracted with acetonitrile in a water bath at 70°C for 1 hour [11]. The resulting solutions passed through a 0.45 µm filter. After dilution with diluent, the solutions were analysed by HPLC-DAD.

For the preparation of air spike and blank samples, *p*-cumenol solution with a concentration of 10 µg/mL was added to the centrifuge tubes as an internal standard. Then, a thymol solution with a concentration of 100 µg/mL was added to the spike sample tubes with a final concentration of 0.25, 0.5, 1, 5, 10, and 15 µg/mL. All tubes were filled to volume with 10% N-methyl-2-pyrrolidone solution prepared with water. All solutions were kept in an ultrasonic bath for 20 min for complete dissolution. As a result, a blank sample with a *p*-cumenol concentration of 2 µg/mL and air spike samples with concentrations of 0.25, 0.5, 1, 5, 10, 15 µg/mL were prepared. The solutions were filtered through a 0.45 µm PTFE filter into glass vials and analysed by HPLC-DAD.

2.3. Validation of the HPLC method

The parameters of specificity, accuracy, precision, limit of detection, quantitative limit, linearity, robustness and system suitability [23,24], solution stability [23,25] were studied for the validation of the analytical method. The results were statistically analysed using Excel® (2010 version, Microsoft, Washington-USA).

2.3.1. Specificity:

The chemicals used in the analytical method, excipients used in the hydrogel, and structurally closely related substances such as *p*-cumenol were compared with the active substance thymol. The relevant chemical and excipient samples were injected into the HPLC-DAD system, and their interaction status was analysed in terms of retention times.

In addition, the thymol standard was subjected to hydrolytic, oxidative, thermal, and photolytic forced degradation conditions by stress test to investigate possible degradation product formation and interference [22]. For hydrolytic degradation, 2 mL of thymol solution with a concentration of 100 µg/mL was placed separately in 10 mL balloon jugs lined with aluminum foil. Then 2 mL each of 2 mol/L HCl or 1 mol/L

NaOH solutions were added to the flasks. The flasks were sealed and kept at room temperature for one month. At the end of the period, the solutions were neutralised with 2 mol/L NaOH or 1 mol/L HCl. For oxidative degradation; 2 mL of thymol solution with a concentration of 100 µg/mL was placed separately in 10 mL flasks lined with aluminium foil. Then 0.5 mL of hydrogen peroxide solution (30%, v/v) was added to the flasks. The flasks were sealed and stored at room temperature for one month. For photodegradation, a 100 µg/mL concentration of thymol solution was placed in a 10 mL transparent flask and exposed to direct sunlight for 6 hours. For thermal degradation, thymol solution with a concentration of 100 µg/mL was placed in a 10 mL flask covered with aluminium foil and placed in a water bath set at 85 °C for 2 hours. All degradation studies were performed in triplicate. Degradation solutions were diluted with diluent to a thymol concentration of 10 µg/mL before analyses. All samples were filtered through a 0.45 µm filter and transferred to glass vials. They were then injected into the HPLC-DAD system.

2.3.2. Precision:

For intraday precision, 6 samples of thymol standard solution with a concentration of 10 µg/mL, hydrogel, and air spike samples were prepared, and 3 injections of each were made. At the end of this study, the %RSD value calculated according to the peak areas corresponding to each injection should be ≤ 3 [26]. For interday precision, samples of thymol standard solution with a concentration of 10 µg/mL, hydrogel and air spike samples prepared by different analysts were analyzed on 2 different days with 2 different HPLC devices. The %RSD value of the analysis results should be ≤ 2 [27].

2.3.3. Linearity, limit of detection (LOD) and limit of quantification (LOQ):

Solutions were prepared from thymol standard at concentrations of 0.25, 0.5, 1, 2.5, 5, 10, and 15 µg/mL. Samples were injected into the HPLC-DAD system 3 times [24]. The correlation coefficient calculated by plotting the concentration pilot curve against the peak areas should be at least 0.995 [26]. LOD is defined as the lowest amount of analyte that can be detected in a sample but does not need to be measured quantitatively under the specified experimental conditions, and LOQ is defined as the lowest amount of analyte in a sample that can be determined quantitatively with appropriate precision and accuracy [23]. These values can be calculated theoretically by regression of the calibration curve data [28]. For the verification of the theoretical limits, the standard prepared at the calculated LOQ level was injected into the HPLC-DAD system 6 times. The suitability was evaluated according to the criterion that

the RSD value between the measured field values was not more than 10% [20]. LOD was calculated with Equation 1, LOQ with Equation 2. (σ = standard deviation of the response, S = slope of the calibration curve)

$$\text{LOD} = 3.3 \sigma/S \quad (1)$$

$$\text{LOQ} = 10 \sigma/S \quad (2)$$

2.3.4. Accuracy

The recovery study was performed on hydrogel prepared with 80%, 100% and 120% concentration and air spike samples prepared with 0, 0.25, 0.5, 1, 2.5, 5, 10, and 15 $\mu\text{g/mL}$ concentration for linearity study [29,30]. The recovery rate for hydrogel should be in the range of 95-105% [6] and the recovery for air should be in the range of 80-110% [5]. The percentage recovery rate was calculated separately for each concentration level with Equation 3.

$$\text{Recovery (\%)} = \frac{\text{Concentration of analysis results}}{\text{Theoretical concentration}} \times 100 \quad (3)$$

2.3.5. Robustness

In order to test the robustness of the analytical method, it is recommended to evaluate the potential effects of changes to be made in at least 3 of the method components with factorial design on the analysis results [31]. For the robustness study, the test was carried out with changes made in the mobile phase flow rate, organic solvent ratio in the mobile phase and column temperature components presented in Table 3 [18]. The %RSD between the results obtained under normal conditions and the results obtained with the changes should be <2.0 [32].

2.3.6. Solution stability:

In order to evaluate the stability of analytical solutions, injections of *p*-cumenol and thymol standard solutions at a concentration of 10 $\mu\text{g/mL}$, which were kept at room and refrigerator conditions, were carried out into the HPLC DAD system at certain intervals. The difference between the peak areas obtained for the injections was calculated. The difference should be $\leq 2\%$ for stability acceptance [23,25].

2.3.7. System suitability:

Six injections of 10 $\mu\text{g/mL}$ concentration thymol solution were performed. After the analysis, the retention times and peak areas obtained were calculated for repeatability, and the theoretical plate number, resolution, peak symmetry parameters were calculated to evaluate the suitability in terms of pharmacopoeia limits [33,34].

3. Results and discussion

3.1. Results of HPLC method validation

3.1.1. Specificity

The chemicals used in the analytical method and the excipients used in the hydrogel not caused any interference in the retention time of thymol (Fig. 1 and Fig. 2). In the oxidative degradation experiment, thymol interacted with the free oxygen groups provided by hydrogen peroxide and almost completely degraded. This is expected in terms of the reported antioxidant properties of thymol [9,10]. In acidic degradation experiments, an average of 47% of thymol degraded, and in alkaline degradation experiments, 37%. Although degradation is also expected in acidic and basic conditions low levels [2], in present study, the degradation probably occurred at a high level due to long-term exposure. There was no significant change in the amount of thymol in photolytic and thermal degradation experiments. No interference was observed in the retention time of thymol with the formed degradation products (Fig. 3). The findings prove that the analytical method is stability-indicating.

3.1.2. Precision:

intraday and interday precision results are within the acceptance limits as presented in Table 1.

Table 1. Precision standard solution, hydrogel, and air spike samples (10 $\mu\text{g/mL}$)

	intra-day precision		inter-day precision	
	SD	% RSD	SD	% RSD
Thymol standard sol.	0.0175	0.17%	0.127	1.29%
Hydrogel	0.0333	0.33%	0.166	1.66%
Air Spike	0.0399	0.40%	0.174	1.74%

3.1.3. Linearity, LOD and LOQ:

It was calculated that the correlation coefficient (R^2) values calculated by plotting the concentration pilot curve against the peak areas were greater than or equal to 0.995 and that the method was linear in the concentration range studied (Fig. 4). Then, regression analysis was performed on the linearity graph data with Excel® package program (2010 version, Microsoft, Washington, USA) at a 95 % confidence level [28]. The remaining standard error of the y-axis data was calculated with the regression analysis. With the help of formulas, LOD was determined as 6.2261 ng/mL and LOQ as 18.866 ng/mL. The standard prepared at the LOQ level was injected into the HPLC-DAD system 6 times, and %RSD was calculated as 1.64. As a result of the evaluation, the detection limit was confirmed as 18.866 ng/mL [27].

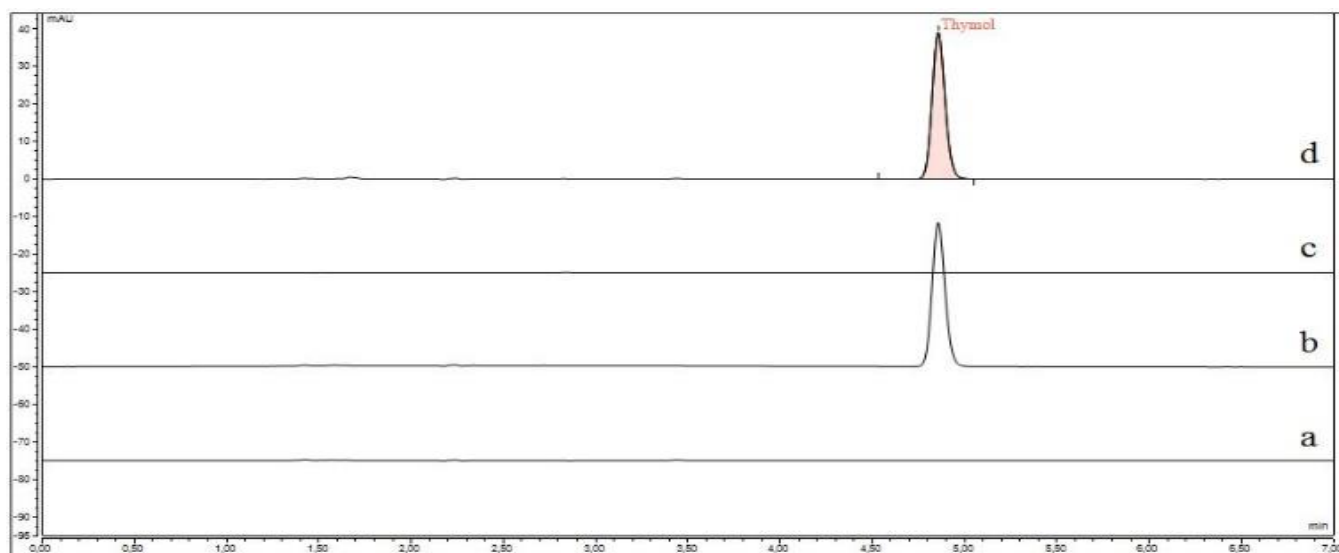


Figure 1. HPLC chromatograms of a) mobil phase, b) standard thymol solution (10 $\mu\text{g/mL}$), c) hydrogel placebo, d) hydrogel sample (10 $\mu\text{g/mL}$ thymol)

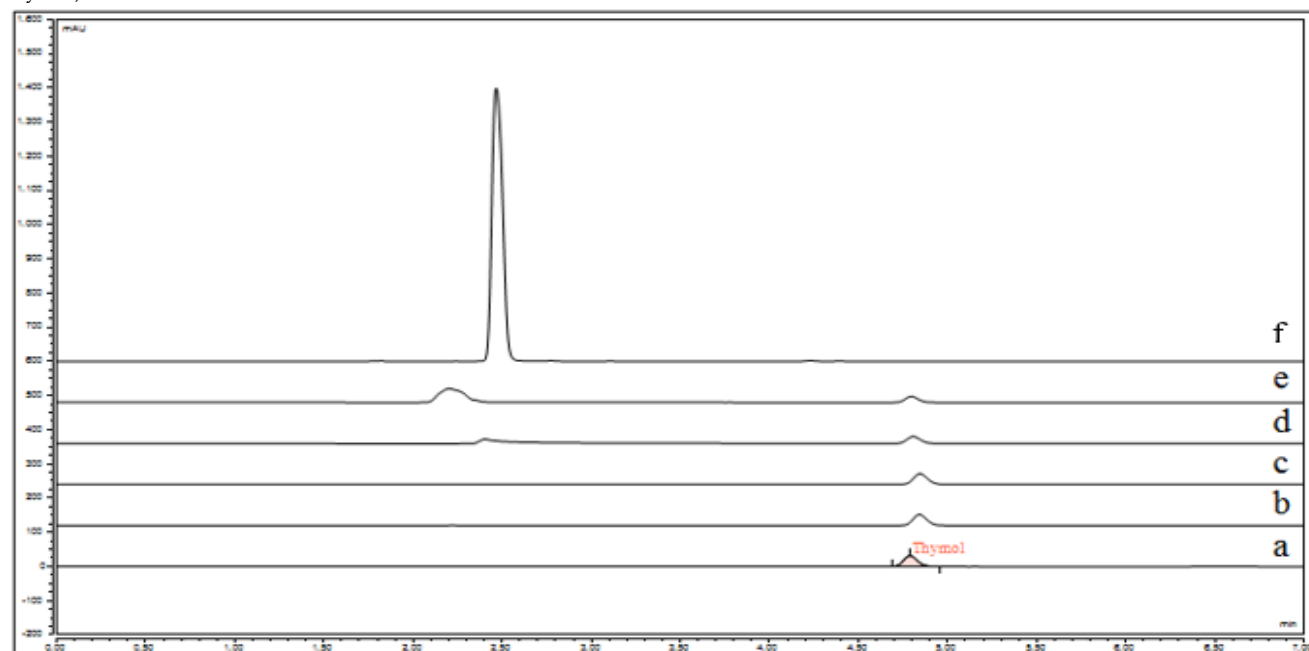


Figure 2. HPLC chromatograms of a) mobil phase, b) air blank sample (2 $\mu\text{g/mL}$ *p*-cumenol) and c) air spike sample (2 $\mu\text{g/mL}$ *p*-cumenol, 10 $\mu\text{g/mL}$ thymol)

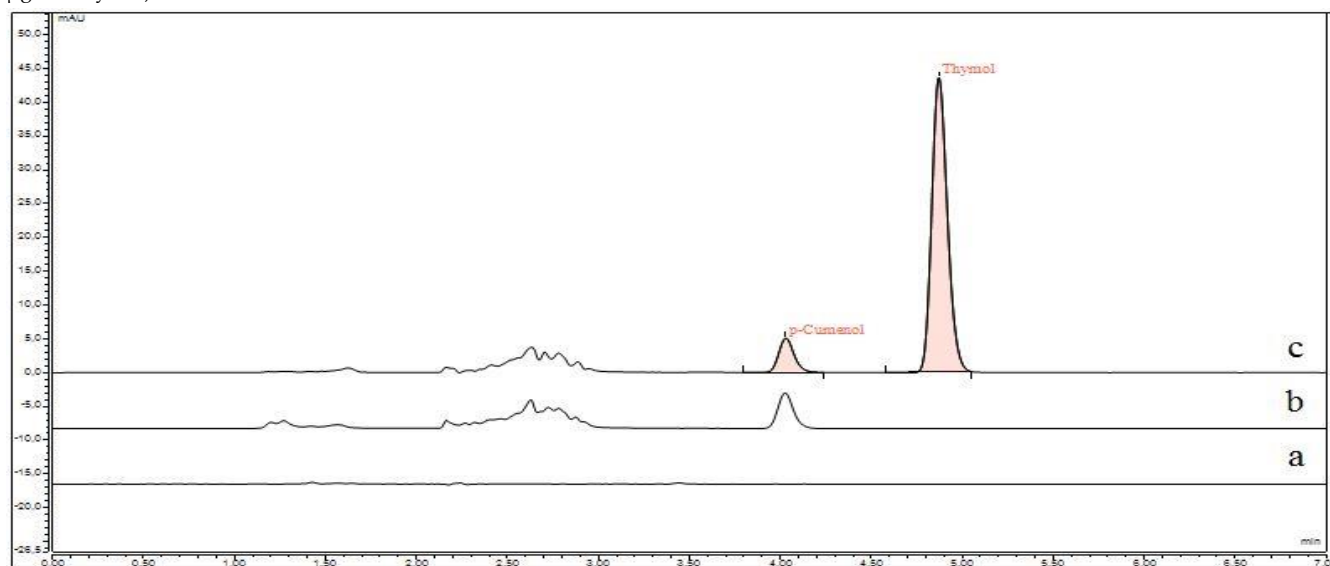


Figure 3. HPLC chromatograms of a) thymol standard solution, b) acid, c) base, d) oxidative, e) light and f) thermal induced forced degradation of thymol

3.1.4. Accuracy:

The mean recovery was calculated as 100.3% (± 2.12) for hydrogel spike samples and 99.9% (± 3.14) for air spike samples. The results are within the acceptance limits [26,30].

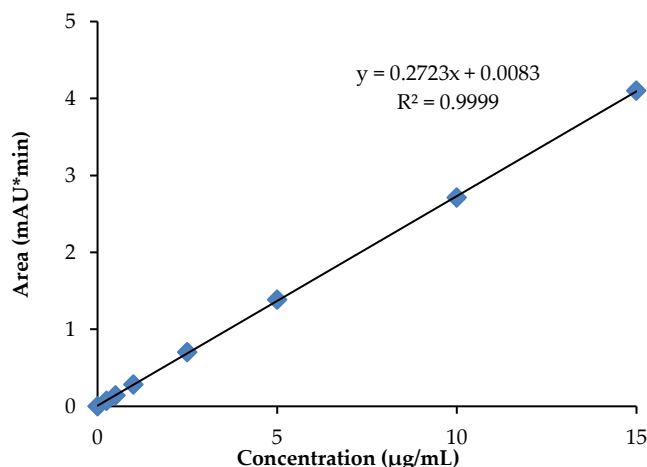


Figure 4. Linearity plot of thymol standard solutions (0-0.25-0.5-1-5-10-15 µg/mL)

Table 2. Robustness study results of thymol standard solution (10 µg/mL)

Mobil phase (acetonitril/water)	Column Temperature (°C)	Flow (mL/min)	Difference (%)
74-26 %	23	0.9	0.099
74-26 %	23	1.1	0.100
76-24 %	23	0.9	0.101
76-24 %	23	1.1	0.098
76-24 %	27	0.9	0.098
76-24 %	27	1.1	0.100
74-26 %	27	0.9	0.099
74-26 %	27	1.1	0.100

Table 3. System suitability test for thymol standard solution (10 µg/mL)

Parameter	Thymol	Acceptance limits
Hydrogel		
Repeatability – Retention time	0.08%	%RSD < 1%
Repeatability – Peak areas	0.18%	%RSD < 1%
Theoretical plates (N)	22597	N ≥ 2000
Resolution	7.06	≥ 2.0
Peak symmetry	1.1	0.8–1.8

3.1.5. Robustness:

As presented in Table 2, the difference in the comparison between the areas obtained with the changes made in the method and the areas obtained under normal conditions is less than 2%. The analytical method is successful in the robustness test against small changes [32].

3.1.6. Solution stability;

Thymol and *p*-cumenol standard solutions are stable for 42 hours at room temperature and 90 days under refrigerator conditions.

3.1.7. System suitability:

As shown in Table 3, the results obtained for thymol standard solution 10 µg/mL meet the acceptance criteria [27,33,34].

In the present study, similar to previous studies, acetonitrile and water were preferred as HPLC system, DAD detector and mobile phase components [12,13,16,19–21]. The ideal ratio of mobile phase, acetonitrile, and water was determined as 75:25 (v/v), which provided ideal separation between the internal standard *p*-cumenol and thymol. In addition, no interference was observed between thymol peaks and chemicals used in the analytical method and excipients used in hydrogel production. Ideal resolution and peak symmetry values were obtained in the system suitability test using the ACE 5 C18 column, which has a similar structure to the columns used in previous studies. In the selection of reference wavelength, investigations were performed in the range of 225–278 nm, and optimum intensity and baseline appearance were obtained at the 277 nm wavelength.

Acetonitrile was successful in the dissolution of thymol and *p*-cumenol when used in standard solution and hydrogel extraction. However, it tended to volatilise when used in the model release system. For this reason, a 10 % N-methyl-2-pyrrolidone solution was tried in the model release medium. 10% N-methyl-2-pyrrolidone solution showed a successful performance in terms of recovery and stability of gaseous thymol.

Only one of the previous studies [22], which included methods for the determination of thymol, included a stress test for selectivity. In the present study, a stress test was performed under the specified conditions. As a result of thymol degradation in the oxidative degradation experiment, peaks of degradation products could be observed in the chromatogram. These peaks, which did not interfere with the thymol standard peak, could not be observed in the previous study [22]. This is thought to be due to the difference in the selectivity of the columns used in the methods.

In addition, an average of 47% of thymol was degraded in acidic degradation and 37% in alkaline degradation experiments. In a previous study, thymol was expected to show low levels of degradation under acidic and basic conditions [2], whereas in the present study, degradation was observed at high levels. This is probably due to the difference between the application times of acidic and basic conditions between the two methods.

In terms of peak retention time and analysis times, this method provides the advantage of faster thymol determination compared to previous studies [18–21].

When the LOD and LOQ values were compared with a reported study [18], it was determined that the LOD

and LOQ values of this study were at similar levels. For these reasons, it is thought that a rapid and sensitive method has been developed.

4. Conclusion

In this study, the analytical method required for the determination of thymol in gelatin-based controlled release system development stages was developed using HPLC-DAD. In order to ensure that the measurements made with the analytical method are consistently accurate and sensitive, the analytical method was tested and validated in terms of specificity, accuracy, precision, LOD, LOQ, linearity, robustness, system suitability and solution stability parameters determined for quantitative determination by HPLC. In addition, thymol degradation products were detected by stress test study. In conclusion, it is thought that this rapid and sensitive analytical method with stability indicator for thymol determination in gelatin-based hydrogel will contribute to the development of controlled release systems.

Acknowledgments

This study is derived from the first author's PhD thesis titled "Development of a Controlled Thymol Release System for Varroosis Control and Investigation of its Effectiveness" (PhD Thesis, Ankara University, Ankara, Turkey, 2022). We would like to thank the T.C. Ministry of Agricultural and Forestry, General Directorate of Agricultural Research and Policies (TAGEM) (project no: TAGEM/HSGYAD/A/20/A5/P6/1943, Project Start-End date: 01.01.2020-01.01.2022)) for their contribution to the financial support for this study.

Conflict of interest

The authors declare that there are no conflicts of interest.

Author Contributions

The first, second, and third authors designed and planned the experiments. The first and second authors performed the experiments and contributed to the interpretation of the results. All the authors provided critical feedback and helped to analyze the research and shape the manuscript.

Availability of Data

The data supporting the findings of this study are available from the corresponding author upon reasonable request.

Ethical Statement

This study was carried out after animal experiments were approved by the Local Ethics Committee of Pendik Veterinary Control Institute (decision number: 202-17/2018).

References

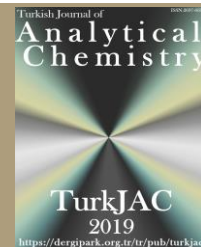
- [1] ICH, Validation of Analytical Procedures: Text and Methodology Q2(R1), International Conference on Harmonisation of Technical Requirements for Registration of Pharmaceuticals for Human Use (ICH), 2005.
- [2] VICH, Topic GL2 (Validation: Methodology), Guideline on Validation of Analytical Procedures: Methodology, International Cooperation on Harmonisation of Technical Requirements for Registration of Veterinary Medicinal Products (VICH) 1999.
- [3] FDA, Analytical Procedures and Methods Validation for Drugs and Biologics, Guidance for Industry, U.S. Department of Health and Human Services Food and Drug Administration (FDA), 2015.
- [4] HSE, Volatile organic compounds in air Laboratory method using sorbent tubes, solvent desorption or thermal desorption and gas chromatography, Methods for the Determination of Hazardous Substances 104, The Health and Safety Executive (HSE), 2016.
- [5] AOAC, Guidelines for Standard Method Performance Requirements, Appendix F, Association of Official Agricultural Chemists (AOAC), 2016.
- [6] ORA, Methods, Method Verification and Validation, Manual Volume II, Food and Drug Administration Office of Regulatory Affairs (ORA) Laboratory, 2020.
- [7] USP, General Chapter, 621-Chromatography, System Suitability, United States Pharmacopeia (USP) 40–NF 35:621, 2022, 16–18.
- [8] EP, System Suitability, 2.2.46. Chromatographic Separation Techniques, European Pharmacopeia (EP) 11.0: 2022, 91–92.
- [9] M. Ramos, A. Beltrán, M. Peltzer, A.J.M. Valente, M.D.C. Garrigós, Release and antioxidant activity of carvacrol and thymol from polypropylene active packaging films, LWT - Food Science and Technology, 58(2): 2014, 470–477.
- [10] M. Ramos, A. Beltran, E. Fortunati, M. Peltzer, F. Cristofaro, L. Visai, A.J.M. Valente, A. Jiménez, J.M. Kenny, M.C. Garrigós, Controlled Release of Thymol from Poly(Lactic Acid)-Based Silver Nanocomposite Films with Antibacterial and Antioxidant Activity, Antioxidants, 9(5):2020, 395.
- [11] A. Imdorf, V. Kilchenmann, C. Maquelin, S. Bogdanov, Optimierung der Anwendung von 'Apilife VAR' zur Bekämpfung von Varroa jacobsoni Oud in Bienenvölkern, Apidologie, 25: 1994, 49–60.
- [12] A. Imdorf, V. Kilchenmann, C. Maquelin, S. Bogdanov, B. Bachofen, C. Beretta Toxizität von Thymol, Campher, Menthol und Eucalyptol auf Varroa jacobsoni Oud und Apis mellifera L im Labortest, Apidologie, 26: 1995, 27–31.
- [13] I.D. Rushworth, C. Higgitt, M.J. Smith, L.T. Gibson, Non-invasive multiresidue screening methods for the determination of pesticides in heritage collections, Heritage Science, 2:3, 2014, 2–8.
- [14] K. Xie, D.P. Tashkin, M.Z. Luo, J.Y. Zhang, Chronic toxicity of inhaled thymol in lungs and respiratory tracts in mouse model, Pharmacol Res Perspect, 27:7(5), 2019, 1–10.
- [15] T. Angelo, F.Q. Pires, G.M. Gelfuso, J.K.R. Da Silva, T. Gratieri, M.S.S. Cunha-Filho, Development and validation of a selective HPLC-UV method for thymol determination in skin permeation experiments, J Chromatogr B Analyt Technol Biomed Life Sci, 1;1022: 2016, 81–86.

- [16] B.O. Louchard, L.C. Costa, A.R.A. Silva, L.K.A.M. Leal, Validation of a High Performance Liquid Chromatography Method to Quantify Thymol in Nanocapsules of Bioactive Essential Oil from *Lippia Sidoides*, *Int J Complement Alt Med*, 10(2):2017, 902–907.
- [17] Ö. Aybastier, C. Demir, Antioxidant Activity Assay of Phenolic Compounds Isolated from *Origanum Onites* L. Aromatic Water by High Performance Liquid Chromatography, *Ann Nutr Disord & Ther*, 4(3): 2017, 1–4.
- [18] M. Dedić, E. Bečić, B. Imamović, N.B. Žiga, S.C. Medanhodžić-Vuk, M. Šober, HPLC method for determination the content of thymol and carvacrol in Thyme tincture, *Bulletin of the Chemists and Technologists of B&H*, 50, 2018, 1–6.
- [19] H. Paithankar, Hplc Method Validation for Pharmaceuticals: A Review, *IJUPBS*, 2, 2013, 229–240.
- [20] G. Shabir, Step-by-step analytical methods validation and protocol in the quality system compliance industry, *JVT*, 10, 2004, 314–324.
- [21] V.Y. Heyden, A. Nijhuis, J. Smeyers-Verbeke, B.G. Vandeginste, D.L. Massart, Guidance for robustness/ruggedness tests in method validation, *JPBA*, 24(5-6), 2001, 723–753.
- [22] A. Shrivastava, V.B. Gupta, Methods for the determination of limit of detection and limit of quantitation of the analytical Methods, *Chron Young Sci*, 2, 2011, 21–25.
- [23] R.M. Soliman, R.A. Abdel Salam, B.G. Eid, A.N. Khayyat, T.A. Neamatallah, M.K. Mesbah, G.M. Hadad, Stability study of thymoquinone, carvacrol and thymol using HPLC-UV and LC-ESI-MS, *Acta Pharm*, 70, 2020, 325–342.
- [24] D. Hu, J. Coats, Evaluation of the environmental fate of thymol and phenethyl propionate in the Laboratory, *Pest Manag Sci*, 64(7), 2008, 775–779.
- [25] J.L. De Oliveira, E.V. Campos, M. Bakshi, P.C. Abhilash, L.F. Fraceto, Application of nanotechnology for the encapsulation of botanical insecticides for sustainable agriculture: prospects and promises, *Biotechnol Adv*, 32(8), 2014 1550–1561.
- [26] EPA, Registration Eligibility Decision (RED): Thymol United States Environmental Protection Agency (EPA) Office of Prevention, Pesticides And Toxic Substances (7508W) -738-F-93-010, 1993.
- [27] R.R.L. Martins, M.G.P.M.S. Neves, A.J.D. Silvestre, A.M.S. Silva, J.A.S. Cavaleiro, Oxidation of aromatic monoterpenes with hydrogen peroxide catalysed by Mn(III) porphyrin complexes, *J Mol Catal A Chem*, 137: 1–3, 1999, 41–47.
- [28] Z. Wei, Z. Yun, L. Ruyi, P. Shengfeng, R. Roger, L. Wei, Fabrication of Caseinate Stabilized Thymol Nanosuspensions via the pH-Driven Method: Enhancement in Water Solubility of Thymol, *Foods*, 10(5):1074, 2021, 1–13.
- [29] A. Esmaeili, A.A. Khodadadi, Antioxidant Activity of a Solution of Thymol in Ethanol, *ZJRMS*, 14, 2012, 14–18.
- [30] FAO, Varroa mites (Varroaosis or Varroosis), Food and Agriculture Organization (FAO), 8416, 2015, 1–5.
- [31] Tihelka, Effects of synthetic and organic acaricides on honey bee health, *Slov Vet Res*, 55, 2018, 119–140.
- [32] D. Bisrat, C. Jung, Insecticidal Toxicities of Three Main Constituents Derived from *Trachyspermum ammi* (L.) *Sprague ex Turrill* Fruits Against the Small Hive Beetles, *Aethina tumida* Murray, *Molecules*, 25, 2020, 1100.
- [33] B. Emsen, A. Dodoloğlu, Efficacy of Different Organic Compounds Against Bee Mite (*Varroa destructor* Anderson and Trueman) in Honey Bee (*Apis mellifera* L.) Colonies, *AJAVA*, 10, 2011, 802–805.
- [34] O. Demir, M. Pulat, and A. Bilgili, Evaluation of the preparation, characterisation, and release properties of thymol-containing gelatin-based hydrogels for varroosis control, *Ankara Univ Vet Fak Derg*, 71,: 4, 2024, 407–416.





TurkJAC

Turkish Journal of Analytical Chemistry

<https://dergipark.org.tr/tr/pub/turkjac>TurkJAC
2019<https://dergipark.org.tr/tr/pub/turkjac>

Hydrometallurgy of lithium: Selective separation from geothermal brines using chitosan-lithium ion sieve composite*

Yaşar Kemal Recepoğlu¹ , Aslı Yüksel^{1**} ¹ Izmir Institute of Technology, Department of Chemical Engineering, 35430, Urla, Izmir, Türkiye

Abstract

This study investigates the selective recovery of lithium (Li) from geothermal brines using a chitosan-coated lithium manganese oxide composite (CTS/LMO). Geothermal brines from Germencik and Tuzla in Türkiye, characterized by distinct physicochemical properties, were used to evaluate adsorption performance. This study introduces a novel application of CTS/HMO adsorbent for selective lithium separation from real geothermal water samples from the Germencik and Tuzla regions, marking the first such investigation. The Freundlich isotherm provided the best fit for the adsorption data, indicating heterogeneous and multilayer adsorption, with maximum adsorption capacities of 3.622 mg/g for Germencik and 3.556 mg/g for Tuzla derived from the Langmuir isotherm. Kinetic studies revealed that lithium adsorption followed a pseudo-first-order model for Germencik ($R^2 = 0.992$) and a pseudo-second-order model for Tuzla ($R^2 = 0.914$). The intraparticle diffusion model identified boundary layer diffusion as a significant rate-limiting step, with diffusion rate constants of 0.365 mg/g·h^{0.5} for Germencik and 0.588 mg/g·h^{0.5} for Tuzla. Mechanistic studies demonstrated ion exchange as the dominant adsorption mechanism, supported by adsorption energy values of 8.64 kJ/mol for Germencik and 9.13 kJ/mol for Tuzla. Optimal conditions yielded lithium recovery efficiencies of 95% for Germencik and 80% for Tuzla, with the differences attributed to variations in salinity and ionic composition. CTS/LMO effectively retained Li up to 241 BV with 69.03% efficiency, while desorption peaked at 43 mg/L at 9 BV, achieving 76% elution efficiency in column operation with a model solution. These findings demonstrate the potential of CTS/LMO as an efficient and sustainable adsorbent for Li recovery from geothermal brines, contributing to the growing demand for Li in renewable energy applications.

Keywords: Adsorption, geothermal water, lithium, selective separation

1. Introduction

Lithium (Li) naturally occurs in various Earth environments, including igneous, volcanic, and sedimentary rocks, with concentrations ranging from 20 to 60 mg/kg [1]. It is also found in seawater at approximately 0.18 ppm, brines and salt marshes (sabkhas) at around 1000 ppm, and thermal fluids ranging from 15 to 350 ppm [2]. The high volatile content in late-stage magmatic fluids, combined with slow magma cooling, promotes the formation of Li-rich minerals in larger structures like pegmatites. These pegmatites often contain minerals such as phlogopite, tourmaline, spodumene (LiAlSi₃O₆), and zinwaldite (a Li-bearing mica found in certain granites). Globally, an estimated 31.1 million tons of Li are available from natural sources, with the largest reserves in brines (21.6 million tons), followed by pegmatites (3.9 million tons)

[3,4]. Deposits of hectorite and jadarite account for about 3.4 million tons, while geothermal fluids contribute to 2 million tons [5]. Despite lower Li concentrations in geothermal waters than in brines, they still represent a significant source. Li concentrations in geothermal waters vary by region [6–9]. In Türkiye, sediments associated with thermal springs also have elevated Li concentrations [10–13]. The rising demand for electric vehicles has notably increased the need for Li, with about 8 kg required for a 60 kWh Li-ion battery. Global Li consumption, 280,000 tons in 2018, is expected to rise significantly to 1.2–1.6 million tons by 2030. Given the growing economic importance of Li, extracting valuable metals from geothermal fluids has become crucial for environmental and economic reasons [14–16].

Citation: Y.K. Recepoğlu, A. Yüksel, Hydrometallurgy of lithium: Selective separation from geothermal brines using chitosan-lithium ion sieve composite, Turk J Anal Chem, 7(2), 2025, 140–153.

****Author of correspondence:** asliyuksele@iyte.edu.tr**Tel:** +90 (232) 750 66 09**Fax:** +90 (232) 750 66 45**Received:** January 30, 2024**Accepted:** March 23, 2025**doi** <https://doi.org/10.51435/turkjac.1629713>

*This paper was presented at the 6th International Environmental Chemistry Congress, EnviroChem 05-08 November 2024, Trabzon Türkiye.

Extracting Li from brines remains one of the most cost-effective methods and has been utilized for a long time. Various techniques can be employed to recover Li from aqueous sources. Namely, the precipitation of Li as Li-aluminate has been documented, and the highest yield was achieved at room temperature [17]. Traditional liquid-liquid extraction methods, such as the beta-diketone/trioctylphosphine oxide process and more recent ionic liquid-based techniques, have also been employed [18]. Membrane technologies, such as electrodialysis with bipolar membranes and membrane electrolysis, have proven effective for Li recovery [19,20]. In addition, membranes containing (2-ethylhexyl)-diphenyl phosphate selectively separate Li^+ ions from Mg^{2+} and Ca^{2+} , while reverse osmosis and nanofiltration processes have shown 85% efficiency in separating Mg from Li in brines [21]. On the other hand, adsorption/ion exchange is emerging as a promising, environmentally friendly method for Li extraction from brines, geothermal water, and seawater, offering rapid recovery despite the need for large volumes of eluent and freshwater [22]. However, a major challenge in adsorption lies in the lack of suitable adsorbents for large-scale industrial applications, which limits its effectiveness in practical settings. As a mostly studied adsorbent type, Li-ion sieves (LISs) exhibit excellent Li screening capabilities due to their stable molecular framework, enabling efficient Li recovery from brines with high rates and selectivity [23]. LISs are classified into manganese-based (Mn-LIS) and titanium-based (Ti-LIS) types [24]. Mn-LISs are popular for their higher Li adsorption capacity, although they suffer from manganese loss, which may affect their cycling performance [25,26]. Xiao et al. synthesized a spinel-type $\text{Li}_4\text{Mn}_5\text{O}_{12}$ through a solid-phase reaction, achieving a Li adsorption capacity of 39.62 mg/g at pH 10.1 using a LiCl-based model solution. Except for Mg^{2+} , almost all competitor ions were fully rejected. After 55 adsorption-desorption cycles, the adsorption capacity remained at 2.78 mg/g [27]. In another study, $\text{Li}_{1.6}\text{Mn}_{1.6}\text{O}_4$ was synthesized, resulting in a Li adsorption capacity of 42.1 mg/g at pH 10.1. After six cycles, the adsorption capacity decreased by 11.33%, from 28.36 mg/g to 25.15 mg/g, while maintaining high Li selectivity [28]. Zhang et al. synthesized LiMn_2O_4 , which exhibited a Li adsorption capacity of 16.9 mg/g at pH 9.19, with high selectivity for Li^+ , followed by divalent ions (Ca^{2+} , Mg^{2+}), and then monovalent ions (K^+ , Na^+) [29]. Moreover, spinel-type $\lambda\text{-MnO}_2$ was used to recover Li from the Balçova geothermal water sample resourced from İzmir province, Türkiye, by adsorption and adsorption/ultrafiltration (UF) hybrid methods. The maximum Li sorption capacity was reported to be powdery and granulated $\lambda\text{-MnO}_2$ at 31.55 and 30.42 mg/g, respectively. Also, the adsorption-UF hybrid

system efficiently handled fine particles, making it a favorable process for Li separation from geothermal water [30–32]. As LISs are in powder form, their practical use is limited due to poor fluidity, low permeability, and high energy consumption from pressure drops [22,23]. To overcome this, methods like foaming [33], fiber formation [34], and granulation [35,36] are employed, with granulation being the most promising nanoparticle modification. Granulated LISs offer high water permeability and mechanical and chemical stability. Chitosan, a hydrophilic and stable binder, improves adsorption capacity and reduces dissolution loss, making it widely used in the granulation of LMOs (LiMn_2O_4 , $\text{Li}_4\text{Mn}_5\text{O}_{12}$, and $\text{Li}_{1.66}\text{Mn}_{1.66}\text{O}_4$) [37].

This study presents the application of chitosan-coated hydrometallurgically synthesized LMO (CTS/ LiMn_2O_4) as an innovative adsorbent for Li extraction using geothermal brines from Germencik and Tuzla Geothermal Energy Power Plants located in the western Anatolia region of Türkiye coupling enhanced ease of operation due to the chitosan coating. This study also presents a novel approach by applying a previously developed CTS/HMO adsorbent to real geothermal water samples with varying characteristics from the Germencik (Aydın) and Tuzla (Çanakkale) regions for selective lithium separation—marking the first such application in the literature. While the experimental framework follows a classical approach, its implementation in actual geothermal brine systems yields significant and novel insights from an engineering perspective. The findings provide valuable implications for practical applications, particularly in advancing lithium recovery strategies. Furthermore, using a column method enhances the study's relevance for industrial-scale applications, reinforcing its potential for large-scale implementation.

2. Experimental

2.1. Materials

CTS/ LiMn_2O_4 (CTS/LMO) adsorbent was synthesized, and the CTS/ HMn_2O_4 (CTS/HMO) form of the adsorbent was prepared using the same method described in the literature [38]. A 1.0 mol/L manganese (II) nitrate ($\text{Mn}(\text{NO}_3)_2$) solution (100 mL) was prepared by dissolving 28.7 g of manganese (II) nitrate hexahydrate ($\text{Mn}(\text{NO}_3)_2 \cdot 6\text{H}_2\text{O}$) in deionized water, while 11.4 g of ammonium peroxodisulfide ($(\text{NH}_4)_2\text{S}_2\text{O}_8$) and 8.4 g of lithium hydroxide monohydrate ($\text{LiOH} \cdot \text{H}_2\text{O}$) were used to prepare 0.5 mol/L $(\text{NH}_4)_2\text{S}_2\text{O}_8$ and 2.0 mol/L LiOH solutions, respectively. The LiOH solution was gradually added to the $\text{Mn}(\text{NO}_3)_2$ solution with vigorous mixing, followed by 42.0 g of $\text{LiOH} \cdot \text{H}_2\text{O}$ until a white precipitate formed. The mixture was left at 25°C for 2 h,

then heated to 80°C before (NH₄)₂S₂O₈ was added dropwise over 10 h. The black precipitate was filtered, washed, dried under vacuum at 120°C for 12 h, and sintered at 600°C for 24 h. Finally, the Li_{1.6}Mn_{1.6}O₄ (LMO) powder was ground.

To form the granulated adsorbent, 3 g of chitosan was dissolved in 97 mL of 2% glacial acetic acid at room temperature. After achieving a uniform solution, 2 g of LMO was added and thoroughly mixed until a consistent black mixture was obtained. This mixture was then dispensed into a 1 mol/L NaOH solution using a needle-tipped syringe, resulting in spherical CTS/LMO granules. The granules were rinsed with deionized water until the pH stabilized at 7 and then dried at 60°C for 12 h.

To modify the adsorbent, 5 g of CTS/LMO was mixed with 75 mL of deionized water containing 0.075 g of NaCl and 0.35 mL of epichlorohydrin. After adding 0.3 g of KOH (dissolved in 2 mL of water) dropwise for 15 min, the mixture was stirred at 25°C for 16 h. The resulting solid was filtered, washed with distilled water, and dried overnight at 70°C.

CTS/HMO was prepared by shaking CTS/LMO in 0.25 M HCl for 12 h, replacing Li⁺ with H⁺ ions. This process caused the adsorbent to develop a slightly dark red/brown hue due to its manganese content. The mixture was then filtered, rinsed with deionized water until the pH stabilized at 4–5, and dried at 60°C for 12 h. The final adsorbent exhibited a uniform spherical shape with a diameter of approximately 1–2 mm.

Geothermal water samples with different physicochemical properties were collected from two locations in the geothermal-rich western Anatolia region of Türkiye: Germencik (Aydın) and Tuzla (Çanakkale) Geothermal Energy Power Plants. These water samples were characterized using various analytical methods, with detailed analysis results in Table 1.

2.2. Methods

2.2.1. Investigation of the effect of adsorbent dosage on Li recovery from geothermal waters

The effect of CTS/HMO composite adsorbent dosage on Li recovery was investigated using water samples collected from the Germencik and Tuzla geothermal fields. Various amounts of adsorbent (0.05 g, 0.1 g, 0.2 g, 0.3 g, 0.4 g, and 0.5 g) were contacted with 25 mL geothermal water samples at 25°C in a water bath shaker operating at 180 rpm for 24 h. After 24 h, the adsorbent was filtered out, and the concentrations of Li were measured in the remaining solution using the ICP-OES instrument. Li recovery or separation efficiency percentages were calculated for each adsorbent dosage, and the optimal adsorbent amount was determined. The % Li separation efficiency was calculated using the following equation:

$$Li\ Recovery\ (\%) = [(C_0 - C_e)/C_0] \times 100 \quad (1)$$

where C_0 represents the initial Li concentration in the geothermal water (mg/L), and C_e denotes the equilibrium Li concentration after adsorption (mg/L).

The Li adsorption capacity (q_e , mg/g) is calculated using the equation:

$$q_e = [(C_0 - C_e) \times V]/m \quad (2)$$

where V is the volume of the solution (L), and m is the amount of adsorbent used (g).

Moreover, the findings obtained from these studies were further analyzed using adsorption isotherms such as Langmuir, Freundlich, and Dubinin-Radushkevich (D-R), providing a theoretical explanation of the adsorption behavior.

Table 1. The physicochemical properties of the geothermal water sample collected from Germencik (Aydın) and Tuzla (Çanakkale) Geothermal Energy Power Plants

Cation species	Concentration (mg/L)		Anion species	Concentration (mg/L)	
	Germencik	Tuzla		Germencik	Tuzla
^e Li ⁺	6.56	32.27	^b HCO ₃ ⁻	1264.10	132.19
^e Na ⁺	1178.95	16920.53	^a Cl ⁻	1254.99	35170
^e K ⁺	80.24	2121.71	^a F ⁻	9.37	4.05
^e Ca ²⁺	14.75	2737.53	^a NO ₃ ⁻	*N.D.	4.64
^e Mg ²⁺	3.15	134.14	^a SO ₄ ²⁻	36.43	205.43
^a NH ₄ ⁺	*N.D.	105.19	^a PO ₄ ³⁻	*N.D.	*N.D.
			Germencik	Tuzla	
			^c pH	8.94	6.71
			^d Conductivity (mS/cm)	2.79	83.4
			^d Salinity (ppt)	1.50	58.6
			^b Total alkalinity (mg/L as CaCO ₃)	1036.15	108.36
			^e B (mg/L)	39.48	24.56
			^e As (µg/L)	110	37.11
			^f SiO ₂ (mg/L)	152	230

^aIon chromatography (Thermo Scientific Dionex ICS-5000), ^bTitrimetric method, ^cpH meter (Thermo, Orion Star A111), ^dMultimeter (YSI Model 30M), ^eICP-OES (Agilent Technologies, 5110), ^fSpectrophotometer (Hach-DR5000), *not determined (below the detection limit)

The Langmuir model postulates that adsorption occurs at distinct, homogeneous sites within the adsorbent, where each site can accommodate only a single Li^+ ion. Once occupied, no further adsorption can occur at that site. Additionally, the model assumes the absence of lateral movement of adsorbed species across the surface, leading to uniform adsorption energies [39,40]. The Langmuir isotherm model is given in Eq. (3), and to evaluate the favorability of adsorption for the Langmuir isotherm, the effect of the adsorption isotherm shape, was investigated using the dimensionless constant ' R_L ', also known as the separation factor or equilibrium parameter. The ' R_L ' value was calculated using Eq. (4) provided below, and if the value is between 0 and 1, the adsorption is favorable.

$$q_e = [(q_{\max} K_L C_e) / (1 + K_L C_e)] \quad (3)$$

$$R_L = 1 / (1 + K_L C_0) \quad (4)$$

where q_{\max} (mg/g) is the maximum adsorption capacity and K_L (L/mg) is the Langmuir constant related to the affinity of the binding sites.

The Freundlich model is an empirical equation describing adsorption as an exponential function, where the adsorbate concentration on the adsorbent surface increases with rising bulk-phase concentration. This model suggests that adsorption initially occurs at the highest-affinity binding sites, with subsequent occupation of weaker sites as adsorption progresses. It characterizes sorption on heterogeneous surfaces or surfaces with sites of varying binding strengths [41]. The Freundlich isotherm is described in Eq. (5) as follows:

$$q_e = K_F C_e^{1/n} \quad (5)$$

where K_F (L/g) and n are Freundlich constants for the adsorption capacity and adsorption intensity of the adsorbent, respectively. The value of n also describes the adsorption characteristics so that if $n > 1$, the adsorption is favorable.

The D-R isotherm [42], as given in Equations 6, 7, and 8, allows for determining the nature of the adsorption process (physical or chemical) occurring on the surface of the adsorbent and can be used to calculate the mean free energy of adsorption (E). The value of this parameter helps determine the adsorption mechanism. If $E < 8$ kJ/mol, the process is physical adsorption; if $8 < E < 16$ kJ/mol, the process is driven by ion exchange; and if $16 < E < 40$ kJ/mol, chemical adsorption occurs.

$$q_e = q_s \exp(-\beta \varepsilon^2) \quad (6)$$

$$\varepsilon = [RT \ln(1 + 1/C_e)] \quad (7)$$

$$E = 1 / (2\beta)^{0.5} \quad (8)$$

where β is the model constant (mol^2/kJ^2), and ε is the Polanyi potential (kJ/mol). T is the absolute temperature (K), and R (8.314 J/mol.K) is the related universal gas constant.

2.2.2. Investigation of the effect of contact time on Li recovery from geothermal waters and adsorption kinetics

The effect of contact time on Li recovery from geothermal waters and adsorption kinetics was studied by adding 3 g of adsorbent to 750 mL of geothermal water (4 g/L) and continuously stirring at 250 rpm. Samples of 5 mL were taken from the solution at specific time intervals (0, 5, 10, 15, 20, 30, 45, 60, 90, 120, 180, 240, 360, 480, and 1440 minutes) to evaluate the adsorption process.

The results obtained from the kinetic studies were evaluated using pseudo-first-order, pseudo-second-order, and intra-particle diffusion kinetic models.

The pseudo-first-order kinetic model [43] is given in Eq. (9):

$$\ln(q_e - q_t) = \ln q_e - k_1 t \quad (9)$$

where q_e is the adsorption capacity at equilibrium (mg/g), q_t is the adsorption capacity (mg/g) at time t (h), and k_1 is the rate constant of the pseudo-first-order model (1/h).

The pseudo-second-order kinetic model related to equilibrium adsorption [44,45] is expressed in Eq. (10):

$$t/q_t = 1 / (k_2 q_e^2) + t/q_e \quad (10)$$

where k_2 is the rate constant of the pseudo-second-order model (g/mg.h).

Since the kinetic models above cannot describe the diffusion mechanism, the intra-particle diffusion model, proposed by Weber and Morris [46], is an empirically derived functional relationship based on the theory expressed in Eq. (11):

$$q_t = k_{id} t^{0.5} + C_i \quad (11)$$

where k_{id} is the intra-particle diffusion rate constant ($\text{mg/g} \cdot \text{h}^{0.5}$), and C_i is a constant related to the thickness of the boundary layer (mg/g).

2.2.3. Adsorption selectivity of the CTS/HMO in geothermal waters

The selectivity of the adsorbent to Li^+ , Na^+ , K^+ , Ca^{2+} , and Mg^{2+} was investigated from the experiment where 0.5 g of the CTS/HMO was contacted in 25 mL geothermal water samples at room temperature for 24 h. The distribution coefficient (K_d), separation factor (α_{Me}^{Li}), and concentration factor (CF) were calculated considering C_0 , C_e , and q_e through Eq.'s 12 – 14 [28]:

$$K_d = (C_0 - C_e)V/(C_eV) \quad (12)$$

$$\alpha_{Me}^{Li} = K_{d_{Li}}/K_{d_{Me}} \quad (13)$$

$$CF = Q_{e_{Me}}/C_{0_{Me}} \quad (14)$$

2.2.4. Li recovery studies in a continuous-flow dynamic packed column system using a model solution

A glass column with a diameter of 0.7 cm and a height of 12 cm, packed with CTS/HMO, was used for the chromatographic separation of Li from an aqueous solution. A continuous-flow packed column system was employed to investigate Li sorption using a solution with an initial Li concentration of 10 mg/L. The solution was fed from top to bottom at a flow rate of 0.25 mL/min through a column with a bed height of 1.5 cm. Li sorption experiments were conducted using a peristaltic pump (SHENCHEN model) and a fraction collector (BÜCHI C-660), with 3 mL fractions collected, as illustrated in Fig. 1. Li desorption experiments were performed using a 5% (v/v) H₂SO₄ solution at a flow rate of 0.12 mL/min, with 2 mL fractions collected. The Li concentration in the samples was also determined using an ICP-OES instrument (Agilent Technologies, 5110).

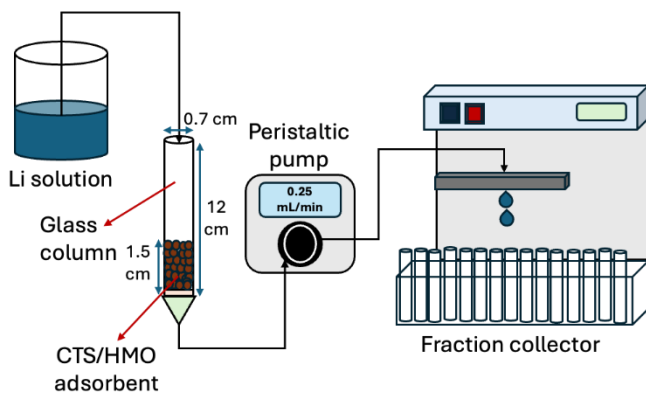


Figure 1. Schematic illustration of chromatographic separation set-up

The breakthrough curves representing the performance of fixed-bed column sorption were plotted as normalized concentration (C/C_0), defined as the ratio of the effluent Li concentration (C , mg/L) to the influent Li concentration (C_0 , mg/L), against the bed volume. The bed volume (BV, mL solution/mL adsorbent) was calculated using Eq. (15) [47]:

$$BV = Q \cdot t/V \quad (15)$$

where Q represents the feed solution flow rate (mL/min), t is the operation time (min), and V is the wet volume of the adsorbent (mL).

The breakthrough time (t_b) and breakthrough capacity are critical parameters in column adsorption processes, where the breakthrough time represents the

operational lifespan of the adsorbent in a single adsorption cycle. Typically, the breakthrough time is defined based on the ratio of the effluent concentration to the influent concentration. For example, the breakthrough time is commonly taken in heavy metal removal when the effluent concentration reaches 5% of the feed concentration ($C/C_0 = 0.05$). However, since this study focuses on recovering a valuable metal, t_b is defined based on the Li extraction efficiency, following literature recommendations [48]. Specifically, the t_b is taken as the time required for the Li extraction efficiency to decrease to 60%, corresponding to an effluent concentration of approximately 4 mg/L from an initial feed concentration of 10 mg/L.

The total or stoichiometric capacity of the bed and the usable capacity of the bed up to the break-point (breakthrough) time t_b of the bed are calculated by Eq. (16) and Eq. (17), respectively [49]:

$$t_t = \int_0^\infty (1 - C/C_0) dt \quad (16)$$

$$t_u = \int_0^{t_b} (1 - C/C_0) dt \quad (17)$$

where t_t is the time equivalent to the total or stoichiometric capacity, and t_u is the time equivalent to the usable capacity or when the effluent concentration reaches its maximum permissible level. The value of t_u is usually very close to that of t_b . Numerical integration of Eqs. (16) and (17) was done using a spreadsheet.

The scale-up design method was applied to estimate the length of bed used up to the breakpoint, H_B (Eq. (18)), and the length of unused bed, H_{UNB} (Eq. (19)), for a total bed length of H_T (Eq. (20)), simulating a full-scale packed-bed tower [49].

$$H_B = (t_u/t_t)H_T \quad (18)$$

$$H_{UNB} = (1 - t_u/t_t)H_T \quad (19)$$

$$H_T = H_B + H_{UNB} \quad (20)$$

The H_{UNB} represents the mass transfer zone (MTZ), primarily influenced by fluid velocity rather than the total column length. To determine H_{UNB} , experiments can be conducted in a small-diameter laboratory column packed with the chosen adsorbent at the design velocity. When scaling up to a full-scale adsorption system, the total bed height (H_T) is calculated by adding the H_{UNB} to the bed height required to achieve the desired adsorption capacity at the breakpoint (H_B). This approach allows for an efficient transition from laboratory-scale testing to industrial-scale application [49].

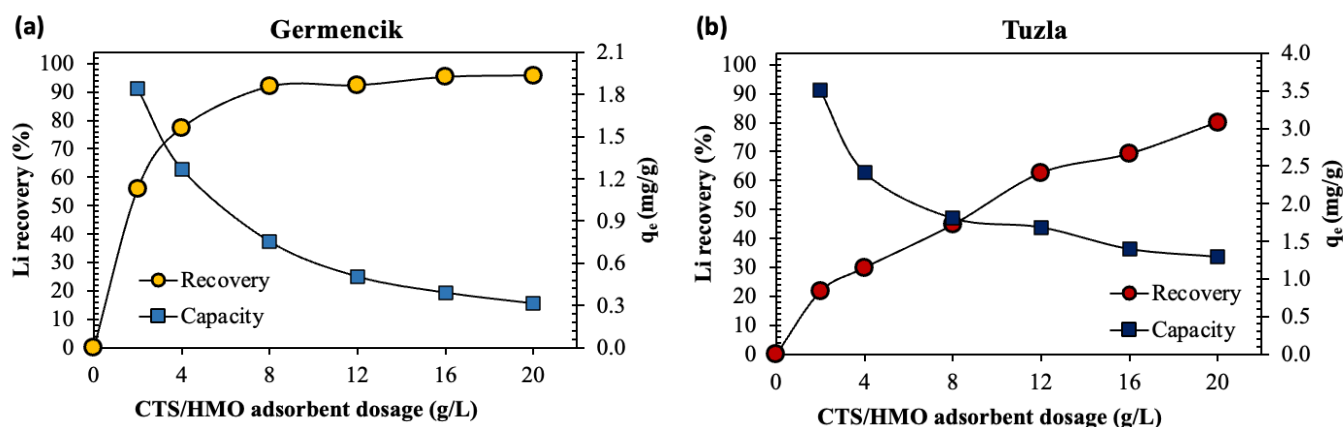


Figure 2. The effect of CTS/HMO adsorbent dose on Li recovery and the adsorption capacity using (a) Germencik and (b) Tuzla geothermal waters

3. Result and discussion

3.1. Characteristics of the adsorbent

As we reported previously, the characteristics of the synthesized adsorbent were discussed in detail [38]. For example, EDX integrated with SEM analysis of CTS/HMO confirmed the presence of C and O from the raw chitosan structure and the uniform incorporation of Mn into both CTS/LMO and the final CTS/HMO product. The even distribution of Mn indicated a homogeneous functional structure throughout the composite. Additionally, the elemental composition—31.22% C, 44.36% O, and 15.62% Mn—validated the successful synthesis.

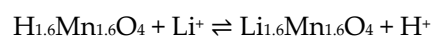
The FTIR spectrum of chitosan showed O–H and N–H stretching ($3250\text{--}3500\text{ cm}^{-1}$) and peaks for --NH_2 deformation (1650 cm^{-1}) and C–N stretching (1380 cm^{-1}). LMO exhibited a Li–O absorption band at 530 cm^{-1} , with MnO_6 and LiO_6 groups shifting the Mn–O peak from 633 cm^{-1} to 901 cm^{-1} . In CTS/LMO and CTS/HMO, reduced peak intensity confirmed successful cross-linking. The absence of Li–O vibrations ($500\text{--}550\text{ cm}^{-1}$) in CTS/HMO indicated Li^+ to H^+ conversion. Lithium removal caused spectral changes, producing peaks at 520, 495, 605, and 325 cm^{-1} , while cubic symmetry was maintained.

The XRD diffractogram of chitosan displayed broad peaks at $2\theta = 10^\circ$ and 20° , but in CTS/LMO and CTS/HMO, the 10° peak disappeared, and the 20° peak weakened, confirming chitosan's compatibility with LMO. Diffractograms matched standard references, verifying successful LMO synthesis. Characteristic peaks at $2\theta = 18.69^\circ, 36.40^\circ, 38.10^\circ, 44.29^\circ, 48.66^\circ, 58.73^\circ, 64.55^\circ$, and 67.83° corresponded to $\text{Li}_{1.6}\text{Mn}_{1.6}\text{O}_4$ crystal planes. Cross-linking with epichlorohydrin reduced peak intensities due to increased amorphicity, though LMO spinel peaks remained. Acid-treated CTS/HMO showed further intensity reduction, indicating successful chitosan coating on LMO.

The specific surface area of LMO was measured by BET analysis at $8.410\text{ m}^2/\text{g}$. In contrast, the surface area

of CTS/HMO significantly dropped to $0.185\text{ m}^2/\text{g}$ due to increased particle size from LMO granulation with cross-linked chitosan. This decrease is likely due to reduced porosity caused by chitosan covering the lattice and collapsing pores.

The adsorption mechanism of the CTS/HMO depends on the Li^+/H^+ ion exchange and it is provided in the chemical equation below:



3.2. Determination of optimum adsorbent dose and adsorption isotherms

The comparative graph of the Li recovery efficiency and the static adsorption capacity against the adsorbent dose for both Germencik and Tuzla geothermal waters is shown in Fig. 2(a) and Fig 2(b), respectively. As the adsorbent amount increased, the number of functional groups available for Li adsorption also increased, resulting in an enhanced Li recovery rate. For Germencik, the Li recovery rapidly increased with the rise in adsorbent dose, reaching over 90% recovery at a dose of 8 g/L. However, with further increases beyond 8 g/L, the recovery rate slowed, and after 12 g/L, it plateaued at around 95%. This indicates that adding more adsorbent does not yield further benefits. Therefore, the optimum adsorbent dose for effective Li recovery from Germencik geothermal water was 0.2 g/25 mL of geothermal water (8 g/L). For Tuzla, Li recovery started at lower levels and reached approximately 65% at a dose of 12 g/L. After 12 g/L, the recovery rate increased more slowly and approached 80% at a dose of 20 g/L. This indicates that more adsorbent is required for Li recovery from Tuzla water. This is because, while Germencik geothermal water contains 6.56 mg/L of Li, Tuzla geothermal water has a higher Li concentration of 32.27 mg/L and a more saline characteristic than Germencik. On the other hand, despite Germencik having nearly one-fifth less Li, its softer characteristics

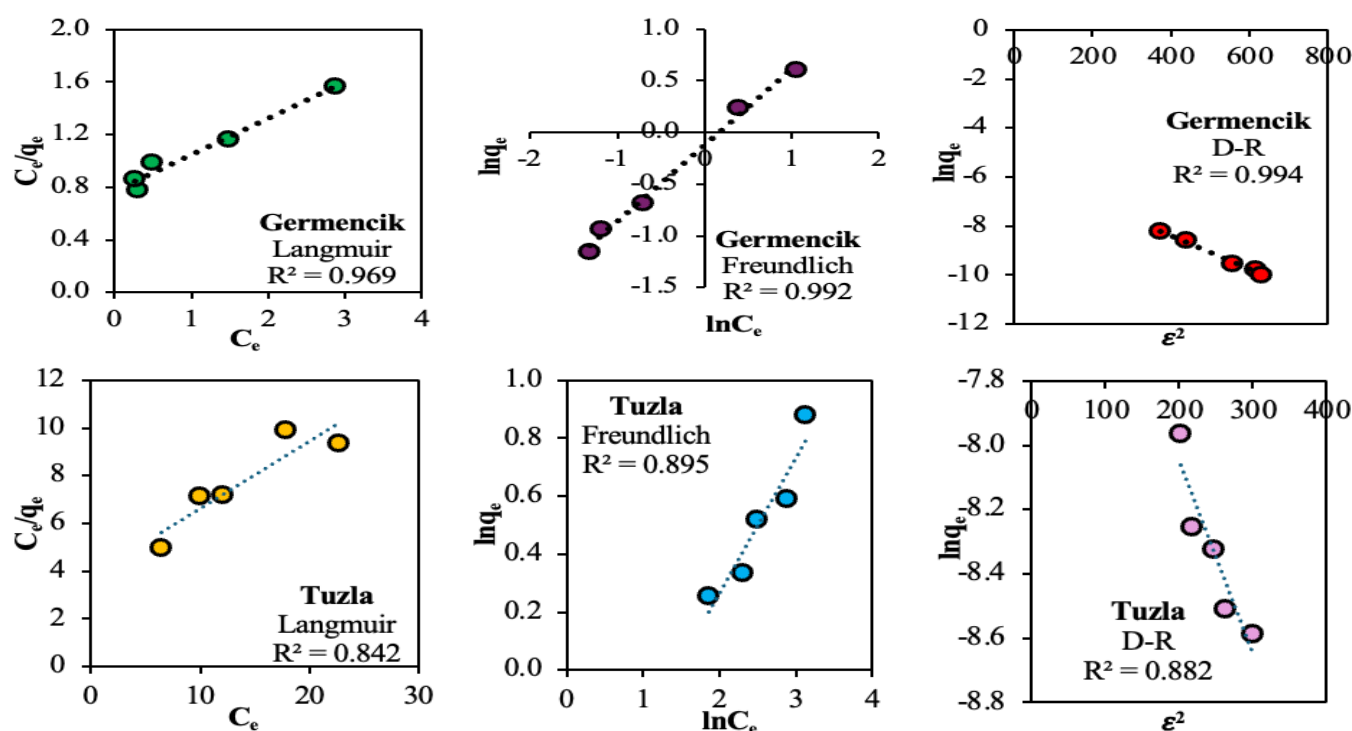


Figure 3. The trend lines of the experimental data for the adsorption behavior of Li from Germencik and Tuzla geothermal water onto CTS/HMO using Langmuir, Freundlich, and Dubinin-Radushkevich (D-R) type isotherms

allow for a higher Li recovery of 95%, while the aforementioned factors can explain the lower recovery rate for Tuzla geothermal water. Furthermore, the maximum static adsorption of lithium onto CTS/HMO adsorbent was achieved for an adsorbent-to-solution ratio of 2.0 g/L, as expected. It was found to be 1.84 mg/g for Germencik geothermal water, while it was 3.51 mg/g for Tuzla geothermal water.

Furthermore, the adsorption equilibrium is typically characterized by an isotherm equation that describes the affinity and surface properties of the adsorbent under specific pH and temperature conditions. These equations establish the relationship between the amount of adsorbate bound to the adsorbent and the concentration

of the dissolved adsorbate in the liquid phase, which are referred to as adsorption isotherms.

Adsorption isotherms help characterize any pollutant removal or valuable metal recovery process using an adsorbent and distinguish between physical/chemical phenomena, favorable adsorption, adsorption energy, and single-layer versus multi-layer adsorption scenarios. These equations are generally used to describe experimental isotherms and were developed by Freundlich, Langmuir, and Dubinin-Radushkevich (D-R).

Fig. 3 shows the linear fitting of isotherm models with experimental data for Germencik and Tuzla geothermal waters, providing information on the adsorption

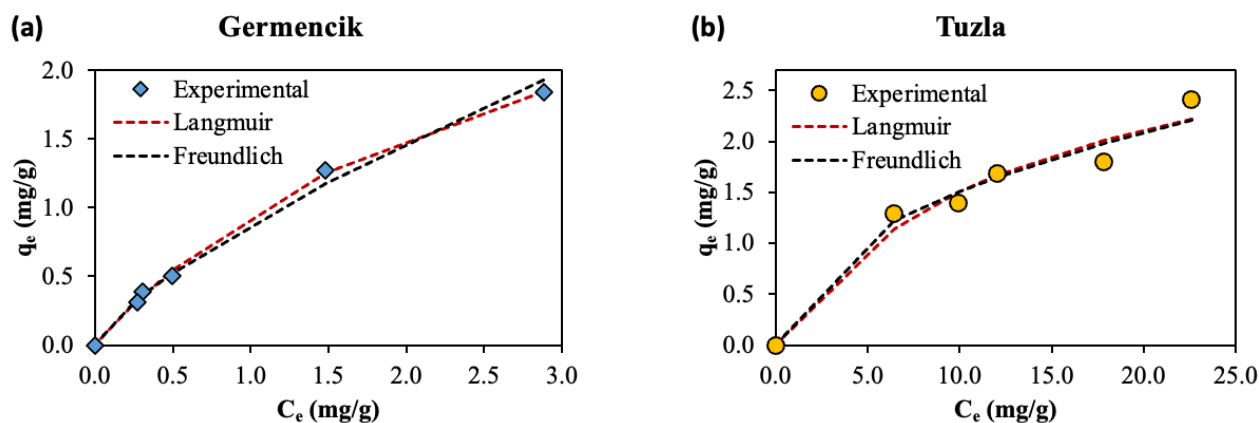


Figure 4. Comparison of lithium adsorption isotherm fitting and experimental data using CTS/HMO for (a) Germencik and (b) Tuzla geothermal waters

behavior of Li^+ ions with CTS/HMO. Fig. 4(a) and Fig. 4(b) are q_e vs. C_e plots for the experimental and theoretical data reproduced by Langmuir and Freundlich isotherms for lithium recovery from Germencik and Tuzla geothermal waters, respectively, using CTS/HMO adsorbent. Table 2 includes the isotherm model equations, associated parameters, and their values.

Table 2. The values of the isotherm models and associated parameters for Li adsorption from Germencik and Tuzla geothermal waters using the CTS/HMO adsorbent

Isotherm model	Linear form	Parameters	Values	
			Germencik	Tuzla
Langmuir	$\frac{C_e}{q_e} = \frac{1}{q_{\max}} C_e + \frac{1}{K_L q_{\max}}$	q_{\max} (mg g ⁻¹)	3.622	3.556
		K_L (L mg ⁻¹)	0.358	0.073
		R^2	0.969	0.842
Freundlich	$\ln q_e = \frac{1}{n} \ln C_e + \ln K_F$	K_F (L/g)	0.881	0.510
		n	1.350	2.128
		R^2	0.992	0.895
D-R	$\ln q_e = -\beta \epsilon^2 + \ln q_s$	β (mol ² kJ ⁻²)	0.0067	0.0060
		E (kJ mol ⁻¹)	8.64	9.13
		q_s (mg g ⁻¹)	22.88	7.33
		R^2	0.994	0.882

The experimental dataset shows strong compatibility with the Langmuir model, but due to the higher correlation coefficient of the graph plotted between $\ln q_e$ and $\ln C_e$, it can be concluded that CTS/HMO adsorbent exhibits Freundlich-type adsorption behavior for Li in both Germencik ($R^2 = 0.992$) and Tuzla ($R^2 = 0.895$) geothermal waters. The Freundlich constants, n , and K_F , were found to be 1.350 and 0.881 for Germencik geothermal water and 2.128 and 0.510 for Tuzla geothermal water, respectively. n values greater than 1 suggest that Li^+ ions are favorably adsorbed by the adsorbent, and the adherence to the Freundlich isotherm indicates that the adsorbent may have a heterogeneous structure.

The C_e/q_e vs. C_e graphs showing the adsorption of Li^+ ions onto CTS/HMO adsorbent displayed linear relationships with high correlation coefficients, confirming that the

Langmuir model applies to the current study. The monolayer maximum adsorption capacity (q_{\max}) and Langmuir constant (K_L) values were found to be 3.622 mg/g and 0.358 for Germencik geothermal water and 3.556 mg/g and 0.0073 for Tuzla geothermal water, respectively. Compared to the experimental equilibrium capacity (q_e) values (1.571 mg/g and 2.073 mg/g) under specific conditions, the q_{\max} values from the Langmuir isotherm did not match closely. These findings suggest that instead of Li^+ ions adsorbing in a monolayer homogeneous configuration, a multilayer heterogeneous adsorption process occurs on the CTS/HMO surface, validating the Freundlich-type adsorption behavior. Additionally, the effect of the isotherm shape on the feasibility of adsorption was investigated for the Langmuir isotherm. On the other hand, the obtained R_L values, which range between 0 and 1, confirm that the adsorption process is favorable for both Germencik and Tuzla geothermal waters. This result is also strongly supported by the $1/n$ values obtained from the Freundlich isotherm.

According to the D-R isotherm model, the E value for Li adsorption from Germencik geothermal water was determined to be 8.64 kJ/mol, and for Tuzla geothermal water, it was 9.13 kJ/mol. This suggests that ion exchange governs the adsorption mechanism of Li^+ ions onto the CTS/HMO adsorbent. The value of the q_s parameter in the model (22.88 mg/g for Germencik and 7.33 mg/g for Tuzla) reflects the porosity of the adsorbent: the larger this value compared to the equilibrium capacity, the more developed the active binding sites are.

3.3. The effect of contact time and adsorption kinetics

The Li recovery efficiency from Germencik and Tuzla geothermal water over time is illustrated in Fig. 5(a) as a C/C_0 vs. time graph and in Fig. 5(b) as a q_e vs. time graph. The adsorption kinetics for both geothermal waters showed an initially rapid Li recovery rate, gradually slowing down before reaching equilibrium for Li adsorption onto the CTS/HMO adsorbent. With a 4 g/L

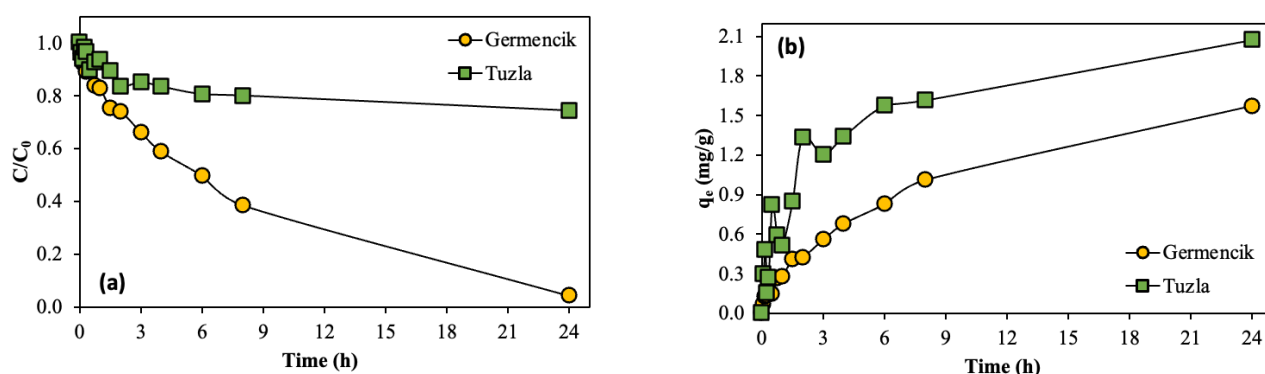


Figure 5. The effect of contact time on Li recovery from Germencik and Tuzla geothermal waters in terms of (a) normalized concentration (C/C_0) vs. time and (b) adsorption capacity (q_e , mg/g) vs. time

adsorbent dose, equilibrium was achieved after 24 h, with approximately 95% Li recovery efficiency from Germencik geothermal water and about 25% from Tuzla geothermal water. Despite a lower Li recovery percentage for Tuzla water due to its high salt content, the increased mass transfer caused by a stronger concentration polarization effect resulted in a Li adsorption capacity of 2.073 mg/g. In comparison, the adsorption capacity for Germencik geothermal water was determined to be 1.571 mg/g under given conditions.

Table 3. The calculated parameters and correlation coefficients of the kinetic models for Li recovery from Germencik and Tuzla geothermal waters using the CTS/HMO adsorbent

Kinetic model		Germencik	Tuzla
Pseudo-first order	R^2	0.992	0.875
	$q_e, \text{theo (mg/g)}$	1.460	1.638
	$k_1 \text{ (h}^{-1}\text{)}$	0.119	0.185
	$q_e, \text{exp (mg/g)}$	1.571	2.073
	R^2	0.898	0.914
Pseudo-second order	$q_e, \text{theo (mg/g)}$	1.201	1.914
	$k_2 \text{ (g mg}^{-1} \text{ h}^{-1}\text{)}$	0.321	0.342
	$q_e, \text{exp (mg/g)}$	1.571	2.073
	R^2	0.991	0.868
Intraparticle diffusion	R^2	0.991	0.868
	$k_i \text{ (g mg}^{-1} \text{ h}^{0.5}\text{)}$	0.365	0.588

Moreover, Fig. 6 presents the linear graphs of the three kinetic models, as the pseudo-first-order, pseudo-second-order, and intraparticle diffusion models, illustrating their alignment with the experimental data for both Germencik and Tuzla geothermal waters. The linear equations and correlation coefficients (R^2) demonstrate the compatibility. When the correlation coefficients of the pseudo-first-order and pseudo-second-order kinetic models evaluated separately for the CTS/HMO adsorbent in Table 3 are compared, it was determined that Li adsorption from Germencik geothermal water fits the pseudo-first-order kinetic model. In contrast, Li adsorption from Tuzla geothermal water fits the pseudo-second-order model, as the coefficients are higher. Additionally, the kinetic parameters for each model were calculated. Furthermore, when the theoretical adsorption capacity (q_e , theoretical, mg/g) was compared with the experimentally determined adsorption capacity, it was observed that the deviation was smaller for the kinetic model, showing better agreement. The rate constants for adsorption kinetics were calculated as 0.119 h⁻¹ and 0.342 g mg⁻¹ h⁻¹ for Germencik and Tuzla geothermal waters, respectively.

When interpreting experimental kinetic data, determining the rate-limiting step is crucial from a mechanistic perspective. The transport of the adsorbate to the adsorbent surface involves multiple stages. For instance, in Li adsorption, three main steps are typically

observed: transport of Li to the surface (film diffusion), transport within the pores of the adsorbent (particle diffusion), and adsorption onto the inner surfaces of the pores. The final step is generally rapid and does not determine the overall rate. The slowest step, which could be either film diffusion or pore diffusion, dictates the overall adsorption rate. However, the controlling step can vary depending on the external mass transfer and intraparticle diffusion mechanisms. External mass transfer dominates in systems with poor mixing, low adsorbate concentrations, small adsorbent particle sizes, and high adsorbate affinity for the adsorbent. Conversely, intraparticle diffusion becomes significant in well-mixed systems with larger adsorbent particle sizes, higher adsorbate concentrations, and lower adsorbate affinity for the adsorbent.

The most common method for distinguishing adsorption mechanisms is fitting experimental data to the intraparticle diffusion model proposed by Weber and Morris in 1962 (Eq. (11)). In many cases documented in the literature, multiple linearities have been observed in the q_t versus $t^{0.5}$ plot. However, as shown in Fig. 6, the adsorption data of Li onto CTS/HMO for Tuzla geothermal water, despite some deviations, was represented by a single straight line. This suggests the dominance of external diffusion (boundary layer diffusion). Nevertheless, the data points do not intercept the origin, indicating that boundary layer diffusion is not the sole limiting mechanism and that other factors, such as repulsive forces between Li⁺ ions and the adsorbent (due to concentration gradients), also significantly contribute. The intercept, C_i , provides information about the boundary layer thickness: a higher intercept indicates a more pronounced boundary layer effect. The C_i value was found to be 0.13 mg/g. Moreover, the intraparticle diffusion rate constant, derived from the slope of the q_t versus $t^{0.5}$ plot, was determined to be 0.365 mg/g h^{0.5} for Germencik geothermal water and 0.588 mg/g h^{0.5} for Tuzla geothermal water.

So far, the adsorption of Li from reverse osmosis (RO) concentrate of geothermal water has been studied using powdered and granulated forms of Li-selective spinel-type manganese oxide (λ -MnO₂) adsorbents. The interaction between Li⁺ ions and λ -MnO₂ was examined through equilibrium and kinetic studies, focusing on adsorption capacity and uptake rate. The Langmuir isotherm model effectively described the adsorption of Li⁺ ions (q_{max} : 33.44 mg/g and 27.40 mg/g), and the pseudo-second-order kinetic model (k_2 : 0.2912 g/mg.min and 0.0030 g/mg.min) best represented the lithium uptake process by both forms of λ -MnO₂ [50].

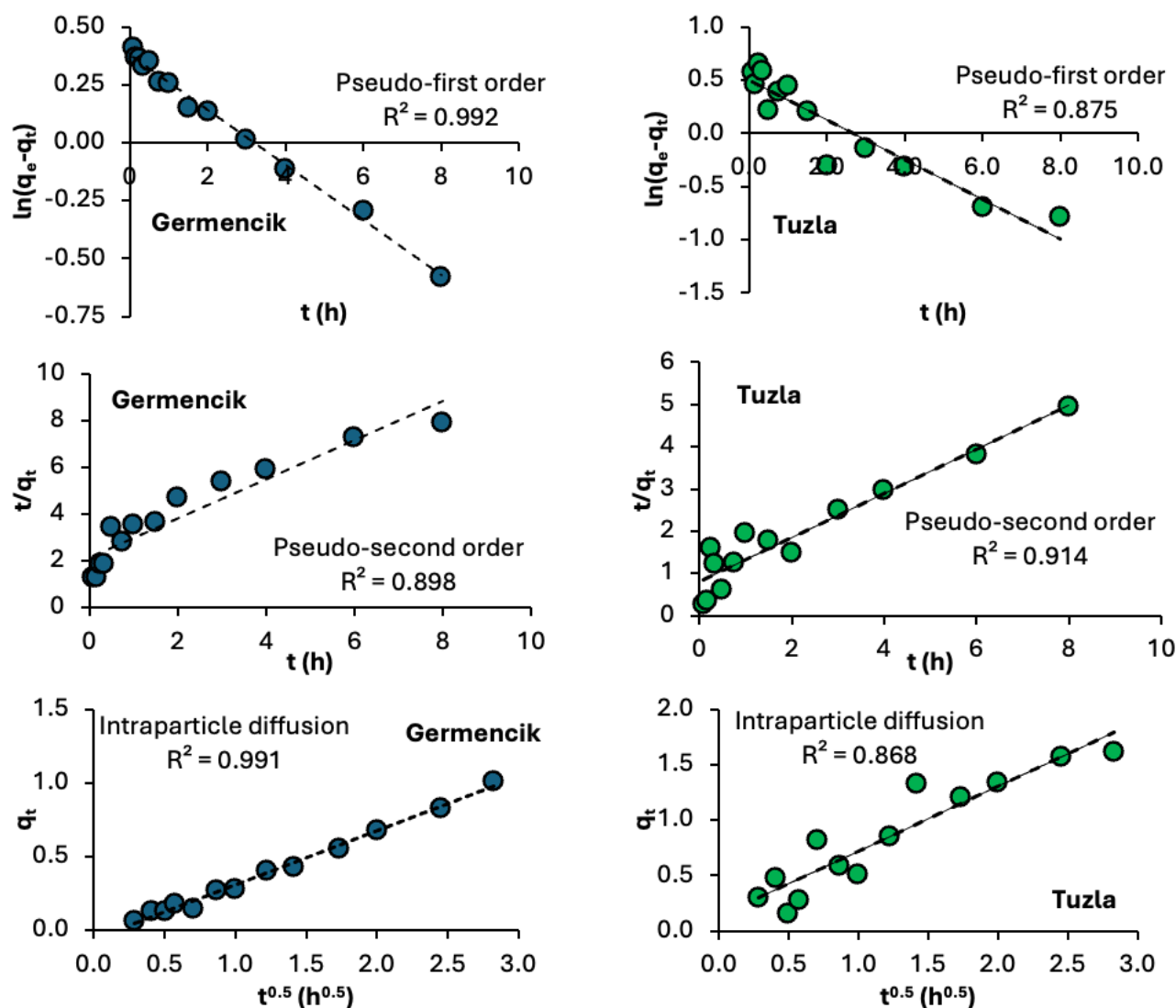


Figure 6. The trend lines of experimental data for Germencik and Tuzla geothermal waters, investigating the adsorption behavior of Li onto CTS/HMO, were analyzed using pseudo-first-order, pseudo-second-order, and intraparticle diffusion kinetic models

3.4. Selectivity of the CTS/HMO adsorbent

The selectivity of the adsorbent toward Li^+ relative to competing cations can be assessed by examining the distribution coefficient (K_d) and selectivity coefficient (α_{Me}^{Li}), while the concentration factor (CF) provides a measure of Li enrichment efficiency and the obtained results are given in Table 4. In the Germencik geothermal water, the K_d value for Li^+ (1.166 mL/g) is substantially higher than those of Na^+ (0.001 mL/g), K^+ (0.001 mL/g), Ca^{2+} (0.002 mL/g), and Mg^{2+} (0.003 mL/g), reflecting strong preferential adsorption of Li^+ over these competing ions. This is further supported by the high $\text{Mg}^{2+}/\text{Li}^+$ selectivity coefficient ($\alpha_{Mg^{2+}}^{Li^+} = 380.66$),

underscoring the minimal interference of Mg^{2+} in lithium uptake.

In contrast, the Tuzla geothermal water exhibits a notably lower K_d for Li^+ (0.201 mL/g), with comparable values for competing cations. Yet, the $\text{Mg}^{2+}/\text{Li}^+$ selectivity coefficient significantly declines to 58.88, indicating a reduced capacity of the adsorbent to distinguish between these ions under the given conditions. The CF further substantiates these findings, with Germencik exhibiting a higher lithium enrichment efficiency ($\text{CF} = 47.943 \text{ L/g} \times 10^{-3}$) than Tuzla ($\text{CF} = 40.037 \text{ L/g} \times 10^{-3}$). The relatively lower CF values for competing cations, particularly Na^+ ($0.610 \text{ L/g} \times 10^{-3}$) and Mg^{2+} ($2.885 \text{ L/g} \times$

Table 4. Adsorption selectivity of the CTS/HMO in Germencik and Tuzla geothermal water

Ion	C_0 (mg/L)		C_e (mg/L)		q_e (mg/g)		CF ($\text{L/g} \times 10^{-3}$)		K_d (mL/g)		α_{Me}^{Li}	
	Germencik	Tuzla	Germencik	Tuzla	Germencik	Tuzla	Germencik	Tuzla	Germencik	Tuzla	Germencik	Tuzla
Li^+	6.56	32.27	0.270	6.430	0.315	1.292	47.94	40.037	1.166	0.201	1.00	1.00
Na^+	1178.95	16920.53	1164.57	15977.4	0.719	47.156	0.610	2.787	0.001	0.003	1887.33	68.08
K^+	80.24	2121.71	79.134	2060.53	0.055	3.059	0.686	1.442	0.001	0.001	1675.48	135.35
Ca^{2+}	14.75	2737.53	14.079	2573.7	0.034	8.1915	2.281	2.992	0.002	0.003	487.66	63.13
Mg^{2+}	3.15	134.14	2.972	125.570	0.009	0.4285	2.885	3.194	0.003	0.003	380.66	58.88

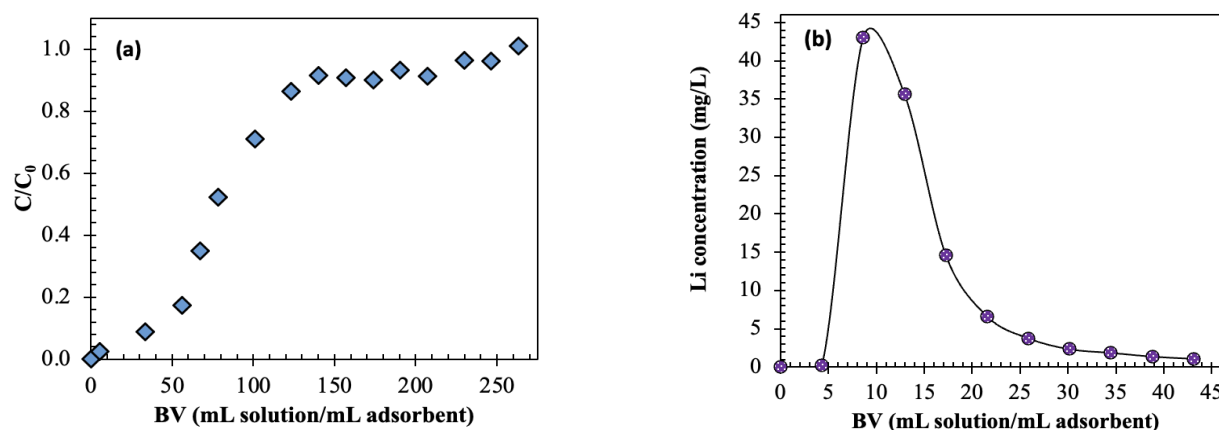


Figure 7. Concentration profiles for the packed bed column by CTS/HMO for Li (a) breakthrough curve ($C_0=10$ mg/L, $pH_{initial}=12$, $T=25^\circ\text{C}$, bed height=1.5 cm, $\Phi=0.25$ mL/min) and (b) elution curve (5% H_2SO_4 , $\Phi=0.12$ mL/min, $T=25^\circ\text{C}$)

10^{-3}) in Germencik, suggest that the adsorbent operates with greater specificity in this system. Conversely, in Tuzla, the increased CF values for Na^+ ($2.787 \text{ L/g} \times 10^{-3}$), Mg^{2+} ($3.194 \text{ L/g} \times 10^{-3}$), and other cations point to a more competitive adsorption environment, which may be attributed to the elevated ionic strength and complex geochemical composition of this geothermal brine. Overall, the results demonstrate that while the adsorbent exhibits a strong affinity for lithium in both geothermal sources, its performance is significantly influenced by the competing ion matrix, with Germencik offering a more favorable environment for selective lithium recovery.

3.5. Fixed-bed adsorption/desorption concentration profiles and capacity of the column

The chromatographic separation of Li from aqueous solution using CTS/HMO adsorbent was demonstrated through breakthrough and desorption curves, as shown in Fig. 7(a) and Fig. 7(b). During adsorption, the initial C/C_0 value was close to zero, indicating effective Li uptake. As BV increased, C/C_0 gradually rose, reaching approximately 0.9 at 140 BV, signifying near-saturation of the adsorbent. At 241 BV, C/C_0 reached 1.0, confirming complete saturation. The breakthrough point, defined as the time when lithium extraction efficiency dropped to 60%, resulted in a breakthrough capacity of 0.435 mg Li/mL adsorbent at 67 BV. At saturation, the total capacity was determined as 0.63 mg Li/mL adsorbent at 241 BV, with a column utilization efficiency of 69.03%.

A sharp peak of approximately 43 mg/L was observed during the desorption phase at 9 BV, indicating rapid and efficient Li desorption. The concentration then declined swiftly, falling below 10 mg/L at 22 BV and approaching 1 mg/L after 43 BV. These results demonstrate that the CTS/HMO adsorbent can effectively retain Li up to 241 BV and subsequently release it in a concentrated form. The majority of Li was recovered within the first 17 BV of the elution solution, with an elution efficiency of 76%. 0.25 M HCl could be

used instead of 5% H_2SO_4 in batch desorption and conditioning processes to enhance this efficiency.

On the other hand, the time equivalent to the usable capacity was found to be 144 min, and the length of the used bed was 1.02 cm. The total saturation time was 212 min, resulting in 0.48 cm of unused bed. Mass transfer limitations, including film and pore diffusion, slowed adsorption, leading to a gradual increase in C/C_0 rather than a sharp transition. The particle size-to-column diameter ratio also influenced bed porosity, further impacting breakthrough curve behavior. Enhancing adsorption efficiency in dynamic column operations requires optimization of key parameters such as column configuration, flow rate, pH, and temperature. Adjusting the height-to-diameter ratio and adsorbent packing density increases residence time, ensuring effective interaction between the solution and adsorbent. Pulsed or variable flow regimes optimize Li uptake by extending residence time, while precise pH control enhances Li selectivity [51]. Sustainable adsorption-regeneration cycles and real-time monitoring improve process efficiency and ensure consistent Li recovery under varying operational conditions.

Table 5 summarizes key findings from this study, including adsorption capacity, desorption efficiency, and degree of column utilization (breakthrough capacity/total capacity) under the investigated conditions using CTS/HMO.

Table 5. Fixed bed column operation results for Li recovery using CTS/HMO adsorbent

Breakthrough capacity, mg Li/mL adsorbent	0.435
Breakpoint time, t_b , min	144
BV at breakthrough capacity, mL solution/mL adsorbent	67
Total capacity, mg Li/mL adsorbent	0.630
Total saturation time, t_s , min	212
BV at total capacity, mL solution/mL adsorbent	241
Degree of column utilization, %	69.03
Elution efficiency, %	75.72
Used bed length, H_B , cm	1.02
Unused bed length, H_{UNB} , cm	0.48

Recently, electrolytic manganese dioxide (γ -MnO₂) powder was tested as a sorbent for Li recovery from geothermal water obtained from the Tuzla Geothermal Power Plant (GPP). The sorption and desorption behavior of γ -MnO₂ was evaluated under various conditions, including sorption at 360 K and 2 bars. The highest sorption efficiency was achieved after 1 h of treatment with Tuzla GPP brine. For desorption, acidic solutions were used, and the average concentration of Li in the desorption solution was 25 mg/L when 10 g of γ -MnO₂ was added to 30 mL of the acidic solution. After four cycles, the desorption process was repeated using the same solution for cumulative Li recovery, reaching a Li concentration of 230 mg/L [52]. Table 6 also compares some adsorbents available in the literature regarding Li source and adsorption capacity.

Table 6. Comparison of some adsorbents available in the literature regarding lithium source and their maximum adsorption capacity

Adsorbent	Li source	q _{max} (mg/g)	Ref.
Li _{1.6} Mn _{1.6} O ₄	Seawater	40	[53]
Powder λ -MnO ₂	RO concentrate of geothermal	33.44	[50]
Granulated λ -MnO ₂	water	27.40	
Powder λ -MnO ₂	Balçova geothermal water	31.55	[30]
Granulated λ -MnO ₂		30.42	
HZn _{0.5} Mn _{1.5} O ₄	Artificial seawater	33.1	[54]
Li _{1.6} Mn _{1.6} O ₄	Qarhan Salt Lake brine	26.93	[55]
Li _{1.6} Mn _{1.6} Cr _{0.4} O ₄	Lop Nor Salt Lake	25.5	[56]
Lewatit TP-260 ion exchange resin	Germencik geothermal water	4.31	[4]
CTS/HMO	Model Li solution (C ₀ =10 mg/L)	4.94	[38]
CTS/HMO	Germencik geothermal water	3.62	This study
	Tuzla geothermal water	3.56	

4. Conclusions

The study demonstrated the efficacy of the CTS/HMO composite as a promising adsorbent for Li recovery from geothermal brines, leveraging the distinctive physicochemical properties of geothermal waters from Germencik and Tuzla in the western region of Türkiye. The adsorption process, underpinned by Freundlich-type multilayer and heterogeneous adsorption behavior, showcased the versatility of the material in accommodating variable ionic compositions. Notably, the kinetic studies revealed a distinct dependence of adsorption dynamics on the brine source, with Li adsorption aligning with pseudo-first-order kinetics for Germencik geothermal water and pseudo-second-order kinetics for Tuzla geothermal water. These differences highlight the critical role of geothermal water characteristics, such as salinity and Li concentration, in influencing adsorption mechanisms. The D-R model provided insights into adsorption behavior, suggesting ion exchange as the dominant mechanism, with calculated energy values (E) between 8.64–9.13 kJ/mol. The intraparticle diffusion model further elucidated the

rate-limiting steps, identifying boundary layer diffusion as a significant factor, especially in the case of Tuzla water. The results also underscore the importance of optimizing adsorbent dosage to balance recovery efficiency and operational feasibility, with recovery efficiencies reaching 95% for Germencik and 80% for Tuzla under optimal conditions. An effective chromatographic separation of Li using CTS/HMO adsorbent was achieved with a total adsorption capacity of 0.63 mg Li/mL adsorbent and a column utilization efficiency of 69.03% for a model Li solution. The desorption process was highly efficient, with a peak Li concentration of 43 mg/L at 9 BV and an elution efficiency of 76%. This work developed the potential of CTS/HMO composites as efficient, eco-friendly solutions for Li recovery, paving the way for their application in industrial-scale operations. Future research focusing on regenerability, economic feasibility, and the environmental impact of this adsorbent can further enhance its practical utility, especially in the context of rising Li demands driven by the global transition to renewable energy and electric vehicles.

Acknowledgment

This study was financially supported by the Research Universities Support Program of the Higher Education Council of Türkiye (Grant No: 2022IYTE-2-0009). We acknowledge “The Environmental Research and Development Center” for ICP-OES analyses at the Izmir Institute of Technology Integrated Research Center.

References

- [1] N. Bolan, S.A. Hoang, M. Tanveer, L. Wang, S. Bolan, P. Sooriyakumar, B. Robinson, H. Wijesekara, M. Wijesooriya, S. Keerthanan, From mine to mind and mobiles–Lithium contamination and its risk management, *Environ Pollut*, 290 (2021) 118067.
- [2] D. Chandrasekharam, M.F. Şener, Y.K. Recepoğlu, T. Isık, M.M. Demir, A. Baba, Lithium: An energy transition element, its role in the future energy demand and carbon emissions mitigation strategy, *Geothermics* 119 (2024) 102959.
- [3] G. Calvo, A. Valero, A. Valero, Assessing maximum production peak and resource availability of non-fuel mineral resources: Analyzing the influence of extractable global resources, *Resour Conserv Recycl* 125 (2017) 208–217.
- [4] Y.K. Recepoğlu, Optimized Lithium (I) Recovery from Geothermal Brine of Germencik, Türkiye, Utilizing an Aminomethyl phosphonic Acid Chelating Resin, *Solvent Extr Ion Exch*, (2024) 1–22.
- [5] P. Christmann, E. Gloaguen, J.-F. Labbé, J. Melleton, P. Piantone, Global lithium resources and sustainability issues, in: *Lithium Process Chemistry*, Elsevier, 2015: pp. 1–40.
- [6] R. Millot, A. Hegan, P. Négrel, Geothermal waters from the Taupo volcanic zone, New Zealand: Li, B and Sr isotopes characterization, *Appl Geochem*, 27 (2012) 677–688.
- [7] Z. Qin, L. He, J. Duo, M. Li, Y. Li, Q. Du, G. Zhang, G. Wu, G. Liu, Origin and evolution of Li-rich geothermal waters from the

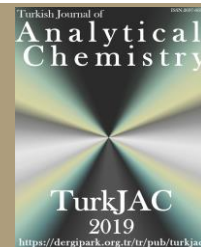
- Kawu geothermal system, Himalayas: based on hydrochemistry and HO, Li isotopes, *Int Geol Rev* 66 (2024) 1519–1534.
- [8] B. Sanjuan, B. Gourcerol, R. Millot, D. Rettenmaier, E. Jeandel, A. Rombaut, Lithium-rich geothermal brines in Europe: An up-date about geochemical characteristics and implications for potential Li resources, *Geothermics* 101 (2022) 102385.
- [9] J. Li, X. Wang, C. Ruan, G. Sagoe, J. Li, Enrichment mechanisms of lithium for the geothermal springs in the southern Tibet, China, *J Hydrol (Amst)* 612 (2022) 128022.
- [10] A. Gökgöz, G. Tarcan, Mineral equilibria and geothermometry of the Dalaman–Köyceğiz thermal springs, southern Turkey, *Appl Geochem*, 21 (2006) 253–268.
- [11] A. Vengosh, C. Helvacı, İ.H. Karamanderesi, Geochemical constraints for the origin of thermal waters from western Turkey, *Appl Geochem*, 17 (2002) 163–183.
- [12] S. Pasvanoğlu, Geochemistry and conceptual model of thermal waters from Erciş-Zilan Valley, Eastern Turkey, *Geothermics* 86 (2020) 101803.
- [13] E.H. Temizel, F. Gültekin, A.F. Ersoy, R.K. Gülbay, Multi-isotopic (O, H, C, S, Sr, B, Li) characterization of waters in a low-enthalpy geothermal system in Havza (Samsun), Turkey, *Geothermics* 97 (2021) 102240.
- [14] S. S. Rangarajan, S.P. Sunddararaj, A.V. V Sudhakar, C.K. Shiva, U. Subramaniam, E.R. Collins, T. Senjyu, Lithium-ion batteries—The crux of electric vehicles with opportunities and challenges, *Clean Technol*, 4 (2022) 908–930.
- [15] Y. Miao, P. Hynan, A. Von Jouanne, A. Yokochi, Current Li-ion battery technologies in electric vehicles and opportunities for advancements, *Energies (Basel)* 12 (2019) 1074.
- [16] Y. Ding, Z.P. Cano, A. Yu, J. Lu, Z. Chen, Automotive Li-ion batteries: current status and future perspectives, *Electrochem Energy Rev*, 2 (2019) 1–28.
- [17] A. Khalil, S. Mohammed, R. Hashaikeh, N. Hilal, Lithium recovery from brine: Recent developments and challenges, *Desalination* 528 (2022) 115611.
- [18] S. Sahu, A. Mohanty, N. Devi, Application of various extractants for liquid-liquid extraction of lithium, *Mater Today Proc* 76 (2023) 190–193.
- [19] J. Zhu, A. Asadi, D. Kang, J.C.-Y. Jung, P.-Y.A. Chuang, P.-C. Sui, Bipolar membranes electrodialysis of lithium sulfate solutions from hydrometallurgical recycling of spent lithium-ion batteries, *Sep Purif Technol* 354 (2025) 128715.
- [20] X. Chen, X. Ruan, S.E. Kentish, G.K. Li, T. Xu, G.Q. Chen, Production of lithium hydroxide by electrodialysis with bipolar membranes, *Sep Purif Technol* 274 (2021) 119026.
- [21] B. Swain, Separation and purification of lithium by solvent extraction and supported liquid membrane, analysis of their mechanism: a review, *J Chem Technol Biotechnol*, 91 (2016) 2549–2562.
- [22] M.R. Mojidi, K.J. Lee, J. You, A review on advances in direct lithium extraction from continental brines: Ion-sieve adsorption and electrochemical methods for varied Mg/Li ratios, *Sustain Mater Technol*, (2024) e00923.
- [23] S. Ye, C. Yang, Y. Sun, C. Guo, J. Wang, Y. Chen, C. Zhong, T. Qiu, Application and Mechanism of Lithium-ion Sieves in the Recovery of Lithium-Containing Wastewater: a Review, *Water Air Soil Pollut* 235 (2024) 272.
- [24] S. Chen, Z. Chen, Z. Wei, J. Hu, Y. Guo, T. Deng, Titanium-based ion sieve with enhanced post-separation ability for high performance lithium recovery from geothermal water, *Chem Eng J*, 410 (2021) 128320.
- [25] X. Xu, Y. Chen, P. Wan, K. Gasem, K. Wang, T. He, H. Adidharma, M. Fan, Extraction of lithium with functionalized lithium ion-sieves, *Prog Mater Sci* 84 (2016) 276–313.
- [26] Y. Orooji, Z. Nezafat, M. Nasrollahzadeh, N. Shafiei, M. Afsari, K. Pakzad, A. Razmjou, Recent advances in nanomaterial development for lithium ion-sieving technologies, *Desalination* 529 (2022) 115624.
- [27] J. Xiao, X. Nie, S. Sun, X. Song, P. Li, J. Yu, Lithium ion adsorption-desorption properties on spinel $\text{Li}_4\text{Mn}_5\text{O}_{12}$ and pH-dependent ion-exchange model, *Adv Powder Technol*, 26 (2015) 589–594.
- [28] J.-L. Xiao, S.-Y. Sun, J. Wang, P. Li, J.-G. Yu, Synthesis and adsorption properties of $\text{Li}_1.6\text{Mn}_1.6\text{O}_4$ spinel, *Ind Eng Chem Res* 52 (2013) 11967–11973.
- [29] Q.-H. Zhang, S. Sun, S. Li, H. Jiang, J.-G. Yu, Adsorption of lithium ions on novel nanocrystal MnO_2 , *Chem Eng Sci* 62 (2007) 4869–4874.
- [30] Y.K. Recepoğlu, N. Kabay, İ. Yılmaz-Ipek, M. Arda, K. Yoshizuka, S. Nishihama, M. Yüksel, Equilibrium and Kinetic Studies on Lithium Adsorption from Geothermal Water by $\lambda\text{-MnO}_2$, *Solvent Extr Ion Exch*, 35 (2017) 221–231.
- [31] Y.K. Recepoğlu, N. Kabay, K. Yoshizuka, S. Nishihama, İ. Yılmaz-Ipek, M. Arda, M. Yüksel, Effect of Operational Conditions on Separation of Lithium from Geothermal Water by $\lambda\text{-MnO}_2$ Using Ion Exchange–Membrane Filtration Hybrid Process, *Solvent Extr Ion Exch*, 36 (2018) 499–512.
- [32] Y.K. Recepoğlu, N. Kabay, İ. Yılmaz-Ipek, M. Arda, M. Yüksel, K. Yoshizuka, S. Nishihama, Elimination of boron and lithium coexisting in geothermal water by adsorption-membrane filtration hybrid process, *Sep Sci Technol (Philadelphia)* 53 (2018) 856–862.
- [33] G.M. Nisola, L.A. Limjuco, E.L. Vivas, C.P. Lawagon, M.J. Park, H.K. Shon, N. Mittal, I.W. Nah, H. Kim, W.-J. Chung, Macroporous flexible polyvinyl alcohol lithium adsorbent foam composite prepared via surfactant blending and cryo-desiccation, *Chem Eng J*, 280 (2015) 536–548.
- [34] S. Wei, Y. Wei, T. Chen, C. Liu, Y. Tang, Porous lithium ion sieves nanofibers: General synthesis strategy and highly selective recovery of lithium from brine water, *Chem Eng J*, 379 (2020) 122407.
- [35] G. Zhang, C. Hai, Y. Zhou, J. Zhang, Y. Liu, J. Zeng, Y. Shen, X. Li, Y. Sun, Z. Wu, Synthesis and performance estimation of a granulated PVC/PAN-lithium ion-sieve for Li^+ recovery from brine, *Sep Purif Technol* 305 (2023) 122431.
- [36] J.-L. Xiao, S.-Y. Sun, X. Song, P. Li, J.-G. Yu, Lithium ion recovery from brine using granulated polyacrylamide– MnO_2 ion-sieve, *Chem Eng J*, 279 (2015) 659–666.
- [37] I.A. Udoetok, A.H. Karoyo, E.E. Ubuo, E.D. Asuquo, Granulation of Lithium-Ion Sieves Using Biopolymers: A Review, *Polymers (Basel)* 16 (2024) 1520.
- [38] Y.K. Recepoğlu, B. Arabacı, A. Kahvecioğlu, A. Yüksel, Granulation of hydrometallurgically synthesized spinel lithium manganese oxide using cross-linked chitosan for lithium adsorption from water, *J Chromatogr A* (2024) 464712.
- [39] I. Langmuir, The constitution and fundamental properties of solids and liquids. Part II.-Liquids, *J Franklin Inst* 184 (1917) 721.
- [40] I. Langmuir, The constitution and fundamental properties of solids and liquids. Part I. Solids., *J Am Chem Soc* 38 (1916) 2221–2295.
- [41] H. Freundlich, Über die adsorption in lösungen, *Z Phys Chem*, 57 (1907) 385–470.
- [42] C. Nguyen, D.D. Do, The Dubinin–Radushkevich equation and the underlying microscopic adsorption description, *Carbon*, 39 (2001) 1327–1336.
- [43] E.D. Revellame, D.L. Fortela, W. Sharp, R. Hernandez, M.E. Zappi, Adsorption kinetic modeling using pseudo-first order and pseudo-second order rate laws: A review, *Clean Eng Technol* 1 (2020) 100032.
- [44] Y.-S. Ho, Review of second-order models for adsorption systems, *J Hazard Mater* 136 (2006) 681–689.
- [45] Y.-S. Ho, Second-order kinetic model for the sorption of cadmium onto tree fern: a comparison of linear and non-linear methods, *Water Res* 40 (2006) 119–125.
- [46] W.J. Weber, J.C. Morris, Kinetics of adsorption on carbon from solution, *J Sanit Eng Div ASCE*, 89 (1963) 31–60.

- [47] Y.K. Recepoglu, A. Yüksel, Cross-Linked Phosphorylated Cellulose as a Potential Sorbent for Lithium Extraction from Water: Dynamic Column Studies and Modeling, *ACS Omega* 7 (2022) 38957–38968.
- [48] H. Jiang, Y. Yang, J. Yu, Application of concentration-dependent HSDM to the lithium adsorption from brine in fixed bed columns, *Sep Purif Technol* 241 (2020) 116682.
- [49] C. Geankoplis, Transport processes and separation process principles (includes unit operations), Prentice Hall Press, 2003.
- [50] B. Sever, E. Altıok, Y. Abdullahi Jarma, K. Bostancı, N. Kabay, M. Arda, S. Nishihama, K. Yoshizuka, Lithium Recovery from Reverse Osmosis Concentrate of Geothermal Water by Spinel Type λ -MnO₂-Batch Tests, *Solvent Extr Ion Exch* (2025) 1–20.
- [51] H. Patel, Fixed-bed column adsorption study: a comprehensive review, *Appl Water Sci* 9 (2019) 45.
- [52] S. Toprak, Ç. Öncel, S. Yılmaz, A. Baba, G.A. Koç, M.M. Demir, Lithium extraction from geothermal brine using γ -MnO₂: A case study for Tuzla geothermal power plant, *Heliyon* 10 (2024).
- [53] R. Chitrakar, H. Kanoh, Y. Miyai, K. Ooi, Recovery of lithium from seawater using manganese oxide adsorbent (H_{1.6}Mn_{1.6}O₄) derived from Li_{1.6}Mn_{1.6}O₄, *Ind Eng Chem Res* 40 (2001) 2054–2058.
- [54] K.S. Chung, M.A. Kim, H. Lee, Y.J. Suh, D.S. Kil, B.C. Dave, J.C. Lee, Preparation of ion-sieve type (H)[M_{0.5}Mn_{1.5}]O₄ (M= Mg, Zn) and their lithium adsorption properties in seawater, *Solid State Phenom* 124 (2007) 739–742.
- [55] S.-Y. Sun, J.-L. Xiao, J. Wang, X. Song, J.-G. Yu, Synthesis and adsorption properties of Li_{1.6}Mn_{1.6}O₄ by a combination of redox precipitation and solid-phase reaction, *Ind Eng Chem Res* 53 (2014) 15517–15521.
- [56] G. Cao, X. Yang, Z. Yin, Y. Lei, H. Wang, J. Li, Synthesis, adsorption properties and stability of Cr-doped lithium ion sieve in salt lake brine, *Bull Chem Soc Jpn* 92 (2019) 1205–1210.



TurkJAC

Turkish Journal of Analytical Chemistry

<https://dergipark.org.tr/tr/pub/turkjac>TurkJAC
2019<https://dergipark.org.tr/tr/pub/turkjac>

Microwave hydrodistillation of *Poncirus trifoliata* (L.) Raf. peels and essential oil profile: Greenness assessment

Yusuf Can Gerçek 

Istanbul University, Faculty of Science, Department of Biology, 3116 Beyazıt, Istanbul, Türkiye

Abstract

The aim of the study was to determine the profile of essential oils obtained from *Poncirus trifoliata* (L.) Raf. fruit peels by hydrodistillation (MHD) and classical steam distillation (SD) methods and the bioactive potential of the wastewater from this process. The chemical composition of the essential oils was analyzed by Gas Chromatography-Mass Spectrometry (GC-MS), while the total phenolic content (TPC), total flavonoid content (TFC), total proanthocyanidin (TPA), and total antioxidant capacity of the wastewater (aqueous phase) after distillation were determined by spectrophotometric methods. GC-MS analysis revealed that the main component of the essential oils obtained by both methods was limonene, but there were significant differences in the relative proportions of the components. The SD method yielded a higher proportion of monoterpene hydrocarbons (70.27%) and esters (8.59%), while the MHD method was more efficient in sesquiterpene hydrocarbons (14.06%) and oxygenated monoterpenes (2.10%). In wastewater analysis, the wastewater obtained by the SD method showed higher antioxidant capacity (with CUPRAC and CERAC) and higher TPC and TFC values compared to MHD. In addition, MHD (0.53 points) was found to be slightly more environmentally friendly than SD (0.49 points) in terms of energy consumption and sample size in the greenness assessment using the AGREEprep tool. In conclusion, it can be concluded that post-distillation wastewater is also a valuable source of bioactive compounds, and the choice of method should be based on the targeted compound profile and the requirements of the application.

Keywords: *P. trifoliata*, wastewater, antioxidant, essential oil

1. Introduction

Poncirus trifoliata (L.) Raf., also known as three-leaved orange, is a deciduous shrub or small tree belonging to the family Rutaceae, widely distributed in East Asia. This plant has historically been used in traditional Chinese and Korean medicine for the treatment of gastrointestinal disorders, inflammation, and allergic reactions due to its rich phytochemical composition [1]. Recently, there has been increased interest in the potential of *P. trifoliata* as a source of high-value bioactive compounds, especially in fruit peels containing essential oils, flavonoids, limonoids, coumarins, and phenolic acids [2].

Essential oils from *P. trifoliata* exhibit various biological activities, such as anti-inflammatory, antimicrobial, and antioxidant properties. These bioactivities are primarily attributed to the volatile terpenes, aldehydes, ketones and oxygenated compounds present in high concentrations in the peel [3]. However, efficient recovery of these essential oils

requires careful consideration of extraction techniques that can preserve the chemical integrity of the sensitive compounds. The first step of extraction is to extract bioactive materials from the plant, and various methods have been used to extract these compounds from peel residues. These methods include conventional solvent extraction, alkaline extraction [4], microwave-assisted extraction [5], resin-based extraction [6], enzyme-assisted extraction [7], subcritical water extraction [8], and supercritical fluid extraction [9]. Extraction techniques primarily target plant-derived compounds. These plants are rich in bioactive substances, including a variety of lipids, fragrances, flavors, phytochemicals, and pigments, which are extensively utilized in the pharmaceutical, food, and cosmetic sectors [10]. The growing interest in these compounds has spurred a demand for improved extraction methods that can yield a higher quantity of bioactive ingredients in less time and at a reduced cost [11].

Citation: Yusuf Can Gerçek, Microwave hydrodistillation of *Poncirus trifoliata* (L.) Raf. peels and essential oil profile: Greenness assessment, Turk J Anal Chem, 7(2), 2025, 154–161.

****Author of correspondence:** yusuf.gercek@istanbul.edu.tr

Tel: +90 (212) 440 00 00 → 20343 **Fax:** N/A

Received: April 14, 2025

Accepted: April 24, 2025

doi <https://doi.org/10.51435/turkjac.1675694>

With the development of the concept of "Green Chemistry" in recent years, environmentally friendly techniques have become increasingly attractive. In this context, researchers aim to optimize the most environmentally friendly extraction method [12]. Microwave-assisted extraction (MHD) has emerged as a sustainable and innovative alternative to traditional hydro-distillation and solvent-based methods. Utilizing microwave energy to rapidly heat the moisture in plant cells, MHD facilitates cell disruption and improves the release of essential oils while significantly reducing extraction time, solvent use, and energy consumption [13]. Furthermore, MHD has been shown to enhance the recovery of thermolabile and low abundance components, making it a highly suitable method for essential oil extraction from citrus and Rutaceae family plants [14]. However, the aqueous phase remaining after MHD, which is usually discarded as waste, contains a significant amount of water-soluble bioactive compounds, including phenolics and flavonoids. These compounds play a key role in scavenging free radicals and protecting biological systems from oxidative stress [15].

The primary objective of this study was to characterize the essential oil profile of *Poncirus trifoliata* (L.) Raf. fruit peels using two distinct extraction techniques: microwave hydrodistillation (MHD) and conventional steam distillation (SD). Additionally, the study aimed to evaluate the bioactive potential of the residual aqueous phase (wastewater) generated from both extraction methods. The essential oils obtained were analyzed by Gas Chromatography-Mass Spectrometry (GC-MS) to identify and quantify their chemical constituents, with particular emphasis on variations in the levels of limonene—the major component—as well as other monoterpene and sesquiterpene hydrocarbons. Furthermore, the total phenolic content (TPC), total flavonoid content (TFC), total proanthocyanidin content (TPA), and total antioxidant capacity of the wastewater were determined using spectrophotometric assays. The environmental sustainability (greenness) of the MHD and SD techniques was also assessed using the AGREEprep tool, which considers criteria such as energy efficiency and sample throughput. This comparative evaluation aimed to identify the more environmentally sustainable extraction method.

2. Materials and methods

2.1. Chemicals

Folin-Ciocalteu phenol reagent, sodium carbonate, Trolox, gallic acid, 2,2-Azino-bis(3-ethylbenzothiazoline-6-sulfonic acid), quercetin, and

gallic acid were obtained from Sigma-Aldrich. Cu(II) chloride, neocuproin, ammonium acetate, aluminum chloride, cerium sulfate, sodium hydroxide, sodium nitrite, ethanol, methanol, hexane were obtained from Merck. All chemicals used in the experiments were of analytical purity.

2.2. Plant material

Poncirus trifoliata was obtained from Istanbul University Faculty of Science Botanical Garden. In this study, approximately 500 g of *P. trifoliata* fruits were collected, and the skins were removed. Fresh plant material was used in the study, and an experimental design with three replications was applied.

2.3. Microwave hydrodistillation (MHD) and steam distillation (SD) of essential oils

Microwave hydrodistillation (MHD) and steam distillation (SD) were performed using Milestone Ethos X (Bergamo, Italy) and ISOLAB brand steam distillation systems, respectively. This system is a 2.45 GHz multimode microwave reactor providing variable maximum power up to 1000 W in 10 W increments. The temperature was monitored with an external infrared (IR) sensor. In a typical MHD procedure performed under atmospheric pressure, 150 g of fresh plant material was heated with constant power application for 15 min with the addition of 100 mL of distilled water. In the steam distillation procedure, 1000 mL of distilled water was added to 200 g of fresh plant material, and essential oil separation was carried out using a Clevenger apparatus with a heater at 110°C for 4 h.

2.4. Gas Chromatography-Mass Spectrometry (GC-MS) analysis of essential oils

The analysis of essential oil composition was performed using gas chromatography-mass spectrometry (GC-MS), following a modified procedure by Fan et al. [16]. An Agilent 7890A gas chromatograph coupled to a 5975C mass spectrometer was used for the analysis. A fused silica HP-5 capillary column (30 m × 0.25 mm i.d., 0.25 µm film thickness) facilitated the separation of volatile compounds. Injection and detector temperatures were both set at 210 °C. The temperature gradient initiated at 40 °C (held for 4 min), increased at 4 °C/min to 90 °C (held for 4 min), then at 3 °C/min to 115 °C (held for 8 min), followed by a ramp of 2 °C/min to 140 °C (held for 10 min), and finally increased to 220 °C at 3 °C/min (held for 10 min). Helium, at a constant flow rate, was employed as the carrier gas. Mass spectrometric detection was operated in electron ionization mode at 70 eV, scanning a mass range between 45 and 550 atomic mass units (AMU) with a scan interval of 0.3 seconds. Compound identification was carried out by matching

mass spectra with those in the WILEY and NIST spectral libraries. The relative abundance of each component was quantified using peak area normalization.

2.5. Total phenolic content (TPC)

The total phenolic content of the samples was determined through the Folin–Ciocalteu colorimetric assay, using gallic acid as a calibration standard, in accordance with the method described by Magalhaes et al. [17], with slight modifications. Briefly, 50 μ L of the wastewater sample was mixed with 50 μ L of Folin–Ciocalteu reagent, followed by the addition of 100 μ L of 0.35 M sodium hydroxide solution, resulting in a final reaction volume of 200 μ L per well. After an incubation period of three minutes, the absorbance of the solution was read at 760 nm. The phenolic content was quantified and expressed as milligrams of gallic acid equivalents (mg GAE/g) based on a gallic acid calibration curve.

2.6. Total flavonoid content (TFC)

The quantification of total flavonoid content in the wastewater samples was performed according to a modified colorimetric method based on the procedure described by Zhishen et al. [18]. The reaction mixture, with a final volume of 6 mL, was prepared in glass tubes by sequentially adding 1 mL of the sample, 0.3 mL of 5% sodium nitrite (NaNO_2), 0.3 mL of 10% aluminum chloride hexahydrate ($\text{AlCl}_3 \cdot 6\text{H}_2\text{O}$), 2 mL of 1 M sodium hydroxide (NaOH), and finally 2.4 mL of distilled water. After thorough mixing, the absorbance of the mixture was measured at 510 nm using a microplate reader (BioTek Instruments, Inc., P). Flavonoid concentration was calculated and expressed as milligrams of quercetin equivalents per gram of sample (mg QE/g).

2.7. Total proanthocyanidin assay (TPA)

Total proanthocyanidin levels were determined using the vanillin-hydrochloric acid (vanillin-HCl) assay, based on the method outlined by Zurita et al. [19], with slight adaptations. For each measurement, 200 μ L of the wastewater sample was mixed with 800 μ L of freshly prepared vanillin reagent to achieve a final volume of 1 mL. The resulting mixture was incubated, and its absorbance was recorded at 500 nm using a microplate reader. The concentration of proanthocyanidins was calculated and presented as milligrams of catechin equivalents per gram of dry weight (mg CAE/g DW).

2.8. Cupric reducing antioxidant capacity (CUPRAC) assay

To determine antioxidant capacity, a reaction system was prepared in a test tube by sequentially combining 1 mL of copper (II) chloride solution, 1 mL of neocuproine

reagent, and 1 mL of ammonium acetate buffer. Following this, 1.1 mL of the wastewater sample was added, yielding a final volume of 4.1 mL. The resulting solution was incubated at ambient temperature for 30 minutes. Absorbance readings were then recorded at 450 nm using a spectrophotometer. Results were expressed in terms of Trolox equivalents (mg TE/g) [20].

2.9. Cerium (IV)-based antioxidant capacity (CERAC) assay

The Cerium (IV) assay, as outlined by Özyurt et al. [21], was employed to assess the total antioxidant capacity (TAC) of the samples. A mixture was prepared by combining wastewater, diluted with distilled water to reach a final volume of 9 mL, with 1 mL of $\text{Ce}(\text{SO}_4)_2$, resulting in a total volume of 10 mL. This reaction mixture was then left to incubate at room temperature for 30 minutes. The absorbance was recorded at 320 nm, and the findings were reported in terms of trolox equivalents (mg TE/g).

2.10. 2,2'-azinobis-(3-ethylbenzothiazoline-6-sulfonic acid) (ABTS) assay

A reaction system with a total volume of 4 mL was prepared by mixing 1 mL of wastewater, 1 mL of ABTS solution, and 2 mL of methanol in a reaction tube. The tubes were then sealed and allowed to stand at room temperature for six hours. Following incubation, absorbance was recorded at 734 nm using a spectrophotometric method as described in a previous study [22]. Antioxidant capacity was expressed as milligrams of Trolox equivalents per gram (mg TE/g).

2.11. Statistical analysis

All experiments were conducted in triplicate. The results are expressed as mean \pm standard deviation (SD). Data analysis was performed using GraphPad Prism version 8 (San Diego, CA, USA).

3. Results and discussion

The fruits of *Poncirus trifoliata* cultivated in Alfred Heilbronn Botanical Garden of Istanbul University Faculty of Science were collected, washed with pure water, and then peeled with a knife (Fig 1).

In this study, the chemical compositions of the essential oils obtained from *P. trifoliata* fruit peel using two different extraction methods, MHD and SD, were determined, and the results obtained were evaluated comparatively. Compound classification based on GC-MS analysis revealed that there were significant quantitative differences between the essential oils obtained using different extraction methods (Table 1, Table 2).



Figure 1. *Poncirus trifoliata* fruits

Monoterpene hydrocarbons were the most dominant class among the essential oils isolated by both methods. While 70.27% monoterpene hydrocarbons were obtained by the SD method, this rate was 58.39% by MHD. Especially D-limonene was isolated by SD with a rate of 36.66%, while this rate was 30.07% by the MHD method. This may be attributed to the high temperature and prolonged distillation conditions of SD, which increase the release of volatile monoterpenes [23,24]. Similarly, other volatile hydrocarbons such as β -myrcene, β -pinene, and α -pinene were obtained with similar profiles in both methods, but method-induced variations in concentration levels were observed.

Table 1. Profile of the essential oil obtained by steam distillation

Peak number	Retention time	Compound	Retention index	Relative amount (%)
1	7.925	Alpha-pinene, (-)-	939	1.07
2	9.643	Sabinene	975	1.11
3	9.781	Beta-pinene	979	4.64
4	10.636	Beta-myrcene	991	16.46
5	10.823	Butanoic acid, butyl ester	985	3.25
6	11.032	Hexanoic acid, ethyl ester	1010	3.53
7	11.168	l-Phellandrene	1005	3.36
8	11.337	3-Hexen-1-ol, acetate, (Z)	1006	0.13
9	11.696	Acetic acid, hexyl ester	1015	1.28
10	12.630	D-Limonene	1031	36.66
11	13.175	Benzeneacetaldehyde	1049	0.08
12	13.606	Beta-ocimene	1049	6.35
13	14.029	Gamma-Terpinene	1059	0.37
14	14.762	1-Octanol	1080	0.19
15	15.683	Alpha-terpinolene	1089	0.12
16	16.474	Linalool	1100	1.09
21	21.494	Benzeneacetonitrile	1172	0.2
22	21.570	Cryptone	1240	0.17
25	24.525	Beta-citronellol	1238	0.58
26	27.157	Phellandral	1259	0.1
27	27.327	1-Decanol	1275	0.31
28	31.251	Alpha-terpinene	1015	0.14
29	33.190	Neryl acetate	1370	0.13
30	34.416	Geranyl acetate	1388	0.13
31	34.653	Beta elemene	1390	0.46
32	35.198	Decanoic acid, ethyl ester	1400	0.14
33	35.861	Dodecanal	1200	0.05
34	36.237	Caryophyllene	1418	5.58
35	37.164	Gamma-elemene	1430	0.21
36	38.197	Alpha-humulene	1455	0.3
37	38.809	trans-beta-farnesene	1456	0.82
38	39.934	Germacrene D	1480	1.78
39	40.816	bicyclogermacrene	1502	0.24
40	41.892	E,E-.alpha-farnesene	1456	1.77
41	42.589	beta-sesquiphellandrene	1505	0.11
42	42.849	Oxacyclotridec-10-en-2-one	1975	0.45
43	44.276	Germacrene B	1560	1.34
44	45.696	Caryophyllene oxide	1418	0.31
45	80.578	Tricosane	2300	0.1
46	88.462	Eicosane	2000	0.13
47	95.783	Docosane	2200	0.15
<i>Alcohols</i>				0.5
<i>Aldehydes</i>				0.13
<i>Esters</i>				8.59
<i>Monoterpene hydrocarbons</i>				70.27
<i>Oxygenated monoterpenes</i>				1.42
<i>Sesquiterpene hydrocarbons</i>				12.81
<i>Others</i>				1.42
Total				95.14

Table 2. Profile of essential oil obtained by microwave distillation

Peak number	Retention time	Compound	Retention index	Relative amount (%)
1	7.943	Alpha-pinene, (-)-	939	1.39
2	9.881	Beta-pinene	979	6.56
3	11.005	Beta-myrcene	991	16.86
4	11.341	Hexanoic acid, ethyl ester	1010	4.06
5	11.478	l-Phellandrene	1005	2.73
6	11.903	Acetic acid, hexyl ester	1015	1.68
7	13.220	D-Limonene	1031	30.07
8	13.317	trans-beta-ocimene	1049	0.16
9	13.475	Benzeneacetaldehyde	1049	0.22
10	14.004	1,3,7-Octatriene, 3,7-dimethyl-	1054	6.7
11	14.311	Gamma-terpinene	1059	0.44
12	14.934	1-Octanol	1080	0.22
13	15.797	Alpha-terpinolene	1089	0.15
14	16.681	Linalool	1100	1.35
18	19.754	Citronella	1228	0.05
19	21.282	Terpinen-4-ol	1177	1.58
20	21.620	Benzeneacetonitrile	1172	0.3
21	21.717	Cryptone	1240	0.15
24	24.679	Beta-citronellol	1238	0.65
25	27.202	Phellandral	1259	0.14
26	27.438	1-Decanol	1275	0.35
27	31.285	Delta-elemene	1389	0.2
28	32.526	Alpha-Terpinene	1015	0.05
29	33.236	Neryl acetate	1370	0.14
30	34.512	Geranyl acetate	1388	0.19
31	34.696	Beta-elemene	1390	0.35
32	34.817	Butyl caprylate	1260	0.18
33	35.334	Decanoic acid, ethyl ester	1200	0.16
34	35.982	Dodecanal	1200	0.06
35	36.467	Caryophyllene	1418	5.92
36	37.221	Gamma-elemene	1430	0.24
37	38.265	Alpha-humulene	1455	0.34
38	38.654	trans-beta-farnesene	1456	0.97
39	40.111	Germacrene D	1480	1.97
40	40.890	bicyclogermacrene	1502	0.3
41	42.081	E,E-.alpha-farnesene	1456	1.97
42	42.681	Beta-sesquiphellandrene	1505	0.13
43	42.962	Oxacyclotridec-10-en-2-one	1975	0.48
44	44.448	Germacrene B	1560	1.45
45	45.016	d-Nerolidol	1545	0.1
46	45.784	Caryophyllene oxide	1418	0.35
47	80.596	Tricosane	2300	0.12
48	88.490	Heneicosane	2100	0.15
49	95.816	Tetracosane	2400	0.18
<i>Alcohols</i>				0.57
<i>Aldehydes</i>				0.28
<i>Esters</i>				6.22
<i>Monoterpene hydrocarbons</i>				58.39
<i>Oxygenated monoterpenes</i>				2.1
<i>Sesquiterpene hydrocarbons</i>				14.06
<i>Others</i>				10.18
Total				91.8

β -myrcene was detected at 16.46% in SD and 16.86% in MHD. Sesquiterpene hydrocarbons were 14.06% in the essential oil obtained with MHD and 12.81% in the essential oil obtained with SD. Among the prominent compounds, caryophyllene was 5.92% in MHD and 5.58% in SD; germacrene D was 1.97% in MHD and 1.78% in SD. These results indicate that the MHD method provides higher efficiency on sesquiterpene structures. In terms of oxygenated monoterpenes, the MHD method (2.10%) provided higher yields compared

to SD (1.67%). In particular, linalool was determined to as 1.35% in MHD and 1.09% in SD. This result can be attributed to the fact that MHD is a method with shorter duration, intrinsic moisture, and rapid heat transfer [25,26].

In addition, microwave energy increases the release of compounds by breaking down cell walls, contributing to the preservation of a wider phytochemical diversity [27,28].

Table 3. Phytochemical analysis from *Poncirus trifoliata* peels wastewater

	CUPRAC (mg TE/g)	CERAC (mg TE/g)	ABTS (mg TE/g)	TF (mg QE/g)	TP (mg GAE/g)	TPA (mg CAE/g)
MHD	11.06±0.98	15.37±1.1	13.24±9.87	2.63±0.04	7.26±0.42	1.02±0.08
SD	13.27±1.24	19.98±1.84	13.50±1.43	2.84±0.21	7.67±0.65	0.99±0.08

Ester compounds were obtained at a significantly higher rate (8.59% vs. 6.23%) in the SD method compared to MHD. In particular, ethyl hexanoate was 3.53% by SD and 4.06% by MHD; acetic acid, hexyl ester was 1.28% by SD and 1.68% by MHD. Excluding the alcohol (0.50-0.57%) and aldehyde (0.13-0.28%) classes, which were obtained in lower proportions, the differences in the basic structure groups reveal the method-specific chemical selectivity effect. Sesquiterpene hydrocarbons such as germacrene B/D, caryophyllene, farnesene, and their oxygenated derivatives were more stable in oils obtained by MHD. These compounds are important phytochemicals, especially for their antimicrobial, anti-inflammatory, and aromatic functions [29]. As a matter of fact, in some studies, it was reported that *P. trifoliata* essential oils showed inhibitory effects on foodborne pathogens, and this was especially associated with sesquiterpenes [29]. Again, in essential oils obtained by MHD, the possibility of detecting rare aromatic compounds containing sulfur, such as 3-sulfanylbutyl alkanoates increases, which can provide differentiation, especially for the aroma industry [30]. MHD offers advantages not only in terms of chemical profile but also in environmental and economic aspects. Compared to conventional distillation techniques: energy consumption is lower, time saving, reduced water use, low risk of thermal degradation, high purity, and biologically active fractions are obtained [31,32]. In these aspects, it offers a more sustainable alternative in the production of functional food

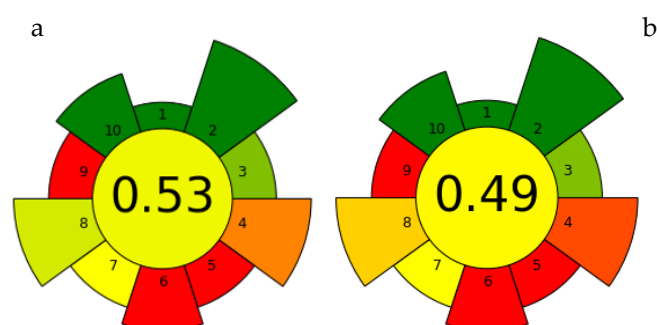
additives, natural preservatives, cosmetic formulations, and pharmaceutical ingredients.

In this study, in addition to the chemical profile of the essential oil obtained from *P. trifoliata* fruit peels by MHD and SD methods, the antioxidant capacity and phenolic compound contents of the wastewater obtained during the processing process were compared. The antioxidant capacity of the wastewater was evaluated by various spectrophotometric methods such as CUPRAC, CERAC, and ABTS, and the TFC, TPC, and TPA contents were also analyzed (Table 3).

When evaluated in terms of antioxidant capacity, the antioxidant activity values of the wastewater obtained with SD (in all three antioxidant methods) were higher than MHD. While the antioxidant activity value of MHD wastewater was determined as 11.06 ± 0.98 mg TE/g by CUPRAC method, this value increased to 13.27 ± 1.24 mg TE/g in SD. Similarly, in CERAC analysis, 15.37 ± 1.1 mg TE/g for MHD and 19.98 ± 1.84 mg TE/g for SD. In the ABTS radical scavenging capacity test, similar results

were obtained in both methods (MHD: 13.24 ± 9.87 mg TE/g, SD: 13.50 ± 1.43 mg TE/g). When the antioxidant activity results obtained are evaluated, especially the methods based on metal ion reduction such as CERAC and CUPRAC, they reveal a stronger electron transfer capacity in the wastewater obtained with SD.

When the data on the phenolic compound content of the wastewater obtained during different processes were evaluated, the TFC was determined as 2.84 ± 0.21 mg QE/g for the wastewater obtained during the SD process and 2.63 ± 0.04 mg QE/g for the wastewater obtained during the MHD process. Furthermore, the TPC of the wastewater was determined as 7.67 ± 0.65 mg GAE/g in the SD process and 7.26 ± 0.42 mg GAE/g in the MHD process. In addition, the TPA of wastewater was found to be quite similar in both methods (MHD: 1.02 ± 0.08 mg CAE/g, SD: 0.99 ± 0.08 mg CAE/g). The findings indicate that the SD method promotes the transition of hydrophilic and heat-stable compounds, especially polyphenols, to the wastewater more. Similarly, in different studies reported in the literature, it has been reported that wastewater obtained during distillation processes contains significant amounts of soluble phenolic compounds and has antioxidant activity [23,24]. When these results obtained for different extraction methods are evaluated, this study once again supports that the wastewater obtained after distillation is not waste but a potential source of antioxidants and phenolic compounds.

**Figure 2.** AGREEprep assessment scores a) for MHD method b) for SD method

Finally, the greenness assessment of the sample preparation procedure for essential oil extraction was carried out in this study. At this stage, in recent years, several tools have been developed to assess the greenness of analytical procedures, and one of the most widely used in sample preparation is the AGREEprep

tool [33]. The assessment criteria are grounded in ten principles of green sample preparation, including the selection of solvents, materials, and reagents; the volume of waste produced; energy usage; and the quantity and yield of samples. AGREEprep pictograms illustrate varying degrees of environmental sustainability. The central score of these pictograms is 0.53 in the microwave-assisted technique (Fig. 2a) and 0.49 in the steam distillation method (Fig. 2b), this discrepancy is attributed to the differences in energy consumption and sample amount.

4. Conclusion

This study compares MHD and SD methods to extract essential oil from fruit peels of *P. trifoliata* (three-leaved orange). When the chemical composition of the obtained essential oils was compared by GC-MS, it was observed that the essential oils isolated by both methods contained similar major components, but there were marked differences in the relative abundance and distribution of these components. While the MHD method offered advantages in terms of speed, energy efficiency, and certain compound groups (oxygenated monoterpenes and sesquiterpenes), the SD method provided higher yields for monoterpene hydrocarbons and esters. However, it was determined that MHD has the potential to diversify the composition of essential oils obtained from *P. trifoliata* peels and increase some bioactive components. Therefore, the MHD method can be recommended as a more efficient and environmentally friendly alternative in the production of essential oils to be used for food, cosmetic, or pharmaceutical purposes. In addition, the composition of the wastewater obtained during the essential oil extraction reveals that this product should be evaluated in terms of functional content and may serve as an additional source of bioactive components in food, cosmetic, or pharmaceutical products.

Acknowledgements

The author wishes to acknowledge the technical support of Istanbul University Science Faculty Alfred Heilbronn Botanical Garden and Food, Environmental and Instrumental Analysis Laboratory for the sample's analysis (<https://cealab-fen.istanbul.edu.tr>).

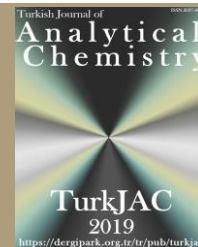
Funding

No funding was provided.

References

- [1] H.Y. Lee, S. W. Kim, Y.K. Kim, S.Y. Lee, M.Y. Yoon, Protective effect of Poncirus trifoliata fruit extracts against gastric ulcer in rats, *Food Sci Biotechnol*, 20, 2011 1097–1102.
- [2] Y. Zhang, Y. Li, Y. Wang, X. Zhang, H. Zhang, Chemical constituents and pharmacological activities of Poncirus trifoliata (L.) Raf.: A review. *Phytochem. Rev.*, 19, 2020, 97–119.
- [3] H.J. Kim, J.H. Kim, H.Y. Park, J.Y. Kim, H.J. Lee, Antioxidant and antimicrobial activities of extracts from Poncirus trifoliata fruit, *Korean J Food Sci Technol*, 46, 2014, 351–357.
- [4] A. Bocco, M. E. Cuvelier, H. Richard, C. Berset, Antioxidant activity and phenolic composition of citrus peel and seed extracts. *J Agric Food Chem*, 46, 1998, 2123–2129.
- [5] Z. Wang, Q. Shang, W. Wang, X. Feng, Microwave-assisted extraction and liquid chromatography/mass spectrometry analysis of flavonoids from grapefruit peel. *J Food Process Eng*, 34, 2011, 844–859.
- [6] A. Di Mauro, B. Fallico, A. Passerini, E. Maccarone, Waste water from citrus processing as a source of hesperidin by concentration on styrene–divinylbenzene resin. *J Agric Food Chem*, 48, 2000, 2291–2295.
- [7] B.B. Li, B. Smith, M.M. Hossain, Extraction of phenolics from citrus peels: I. Solvent extraction method, *Sep Purif Technol*, 48, 2006, 182–188.
- [8] M. J. Ko, C. I. Cheigh, M. S. Chung, Relationship analysis between flavonoids structure and subcritical water extraction (SWE). *Food Chem*, 143, 2014, 147–155.
- [9] A.N. Giannuzzo, H. J. Boggetti, M. A. Nazareno, H. T. Mishima, Supercritical fluid extraction of naringin from the peel of Citrus paradisi. *Phytochem Anal*, 14, 2003, 221–223.
- [10] P.A. Uwineza, A. Waśkiewicz, Recent advances in supercritical fluid extraction of natural bioactive compounds from natural plant materials, *Molecules* 2020, 25(17), 3847.
- [11] A. Krakowska-Sieprawska, A. Kielbasa, K. Rafińska, M. Ligor, B. Buszewski, Modern methods of pre-treatment of plant material for the extraction of bioactive compounds, *Molecules*, 27, 2022, 730.
- [12] M. Boukroufa, C. Boutekedjiret, L. Petigny, N. Rakotomanomana, F. Chemat, Bio-refinery of orange peels waste: A new concept based on integrated green and solvent free extraction processes using ultrasound and microwave techniques to obtain essential oil, polyphenols and pectin. *Ultrason. Sonochem.*, 24, 2015, 72–79.
- [13] W. Routray, V. Orsat, Microwave-assisted extraction of flavonoids: A review. *Food Bioproc. Tech.*, 5, 2012, 409–424.
- [14] F. Chemat, N. Rombaut, A. G. Sicaire, A. Meullemiestre, A. S. Fabiano-Tixier, M. Abert-Vian, Ultrasound assisted extraction of food and natural products. Mechanisms, techniques, combinations, protocols and applications. A review. *Ultrason. Sonochem.*, 34, 2017, 540–560.
- [15] J. Dai, R. J. Mumper, Plant phenolics: Extraction, analysis and their antioxidant and anticancer properties. *Molecules*, 15, 2010, 7313–7352.
- [16] S. Fan, J. Chang, Y. Zong, G. Hu, J. Jia, GC-MS analysis of the composition of the essential oil from *Dendranthema indicum* Var. *Aromaticum* using three extraction methods and two columns. *Molecules*, 23, 2018, 576.
- [17] L.M. Magalhães, F. Santos, M. A. Segundo, S. Reis, J.L. Lima, Rapid microplate high-throughput methodology for assessment of Folin-Ciocalteu reducing capacity. *Talanta*, 83, 2010, 441–447.
- [18] J. Zhishen, T. Mengcheng, W. Jianming, The determination of flavonoid contents in mulberry and their scavenging effects on superoxide radicals. *Food Chem*, 64, 1999, 555–559.
- [19] J. Zurita, M. E. Diaz-Rubio, F. Saura-Calixto, Improved procedure to determine non-extractable polymeric proanthocyanidins in plant foods. *Int J Food Sci Nutr* 63, 2012, 936–939.

- [20] R. Apak, K. Güçlü, B. Demirata, M. Özyürek, S. Çelik, B. Bektaşoğlu, D. Özyurt, Comparative evaluation of various total antioxidant capacity assays applied to phenolic compounds with the CUPRAC assay. *Molecules*, 12, 2007, 1496-1547.
- [21] D. Ozyurt, B. Demirata, R. Apak, Modified cerium (IV)-based antioxidant capacity (CERAC) assay with selectivity over citric acid and simple sugars. *J. Food Compos. Anal.*, 23, 2010, 282-288.
- [22] R. Re, N. Pellegrini, A. Proteggente, A. Pannala, M. Yang, C. Rice-Evans, Antioxidant activity applying an improved ABTS radical cation decolorization assay. *Free Radic. Biol. Med.*, 26, 1999, 1231-1237.
- [23] Y. Zhang, X. Zhao, Q. Yang, Li, Y., X. Liu, M. Huang, Recovery and utilization of phenolic compounds from distillation wastewater of essential oil plants: A review. *Ind Crops Prod*, 170, 2021, 113753.
- [24] Y.J. Fu, Y.G. Zu, L.Y. Chen, X.H. Shi, Z. Wang, S. Sun, T. Efferth, (2010). Antioxidant properties of waste residues from vine tea (*Ampelopsis grossedentata*) extraction. *Afr. J. Biotechnol.*, 9, 2010, 7248–7253.
- [25] Y. Liu, Z. Liu, C. Wang, Q. Zha, C. Lu, Z. Song,... A. Lu, Study on essential oils from four species of Zhishi with gas chromatography–mass spectrometry. *Chem. Cent. J.*, 8, 2014, 22.
- [26] F. Papa, F. Maggi, K. Cianfaglione, G. Sagratini, G. Caprioli, S. Vittori, Volatile profiles of flavedo, pulp and seeds in *Poncirus trifoliata* fruits. *J Sci Food Agric* 94, 2014, 2874–2887.
- [27] M. E. Lucchesi, F. Chemat, J. Smadja, Solvent-free microwave extraction of essential oil from aromatic herbs: Comparison with conventional hydro-distillation. *J. Chromatogr. A*, 1043, 2004, 323–327. H
- [28] V. Mandal, Y. Mohan, S. Hemalatha, Microwave assisted extraction – an innovative and promising extraction tool for medicinal plant research. *Phcog Rev*, 5, 2011, 7.
- [29] A. Rahman, S. M. Al-Reza, J. I. Yoon, S. C. Kang, In vitro inhibition of foodborne pathogens by volatile oil and organic extracts of *Poncirus trifoliata* seeds, *J Sci Food Agric*, 89, 2009, 876–881.
- [30] C. Starkenmann, Y. Niclass, S. Escher, Volatile organic sulfur-containing constituents in *Poncirus trifoliata* fruit peel. *J Agric Food Chem*, 55, 2007, 4511–4517.
- [31] K. Boztaş, Y. C. Gerçek, G. Türer, D. Canlı, S. Bayram, S. Çelik,... N. Ecem Bayram, Microwave hydrodistillation of Pelargonium graveolens L'Her leaves: Essential oil profile, phytochemical composition of wastewater, histo-anatomical structure. *J. Essent. Oil-Bear. Plants*, 27, 2024, 659-677.
- [32] L. Zhang, W. Bai, L. Zhou, C. Li, Comparative evaluation of extraction technologies on the chemical composition and antioxidant activity of essential oils from citrus peels. *Ind Crops Prod*, 191, 2023, 116066.
- [33] W. Wojnowski, M. Tobiszewski, F. Pena-Pereira, E. Psillakis, AGREEp–analytical greenness metric for sample preparation. *TrAC Trends Anal. Chem.* 149, 2022, 116553



The accurate and reliable HPLC-UV based method for detecting the active ingredient hexaflumuron in some plant protection products

Ismael M. Elkamhawy^{1,2*} , Mostafa G. Emara² , Alaa E. Ali¹ , Mohamed A. Khashaba³ 

¹ Damanhour University, Faculty of Science, Chemistry Department, Damanhour, 22511, Egypt

² Chromatographic Analysis Laboratory, KZ for Pesticides and Chemicals Company, Nubaria City, Egypt

³ Alexandria University, Faculty of Science, Chemistry Department, Alexandria, Egypt

Abstract

The main objective of this study was to present a new selective, sensitive, and validated RP-HPLC analytical method for measuring the concentrations of hexaflumuron (HFM), which is a well-known active ingredient that is widely used as an insecticide to protect crops, especially fruits and vegetables. Quantification was carried out using a reversed phase HPLC system that was equipped with a UV detector. The development of the novel method was performed on a reversed-phase C-18 (stainless steel, 5 μ m, 250 \times 4.6 mm) column at a constant temperature of 30°C. The mobile phase consists of acetonitrile and distilled water in a volumetric ratio of 85:15, a flow rate of 1 mL/min, and the detection wavelength at 220 nm. Retention time of separation at 3.84 min. The method was validated by testing specificity, linearity, precision, recovery, LOD, LOQ, and accuracy according to the CIPAC (Collaborative International Pesticides Analytical Council) and complies with the guidelines of SANCO/3030/99 rev.5. guidelines. The method revealed an acceptable linearity regression R^2 (0.9974). The method was found to be accurate from concentration levels 50–250 μ g/mL with high accuracy (99.3–100.7%). The method's validation results make it suitable for use as a standardization tool in the evaluation of Emulsion Concentrate formulations containing this active ingredient.

Keywords: Hexaflumuron, HPLC analysis, method validation, precision, accuracy

1. Introduction

Hexaflumuron (HFM) is one of the widely used insecticides since its registration in the Environmental Protection Agency (US EPA) in 1994 [1]. HFM chemical name is [1-(3,5-dichloro-4-(1,1,2,2-tetrafluoroethoxy)phenyl)-3-(2,6-difluorobenzoyl)urea] and its chemical structure is indicated in Fig. 1. HFM is a white crystal or powder with the melting point range between “202 °C – 205 °C” and its molar mass of 461.1 g/mol. It is insoluble in water (27 μ g/l), soluble in methanol and xylene 11.3 and 5.2 (gm/l), respectively [2,3]. HFM chemically belongs to the class of benzoylphenylureas, a significant group of potent insect growth regulators (IGRs). HFM action's mode through the inhibition of chitin synthesis in the cuticle of insects that cause disrupt hormonal balance with exchanging in molting process and makes it also effective in controlling immature stages of insects. Benzoylphenylureas including HFM have been used to control a wide range of agricultural pests worldwide due

to their high selectivity, insecticidal activity, and low acute toxicity to mammals [4–6].

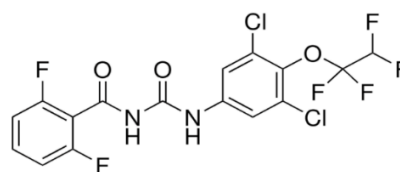


Figure 1. Hexaflumuron structural diagram, $C_{16}H_8Cl_2F_6N_2O_3$

Chromatographic separation techniques are one of the most important, straightforward, and effective methods for both qualitative and quantitative analysis. At the moment, high performance liquid chromatography (HPLC) is used for carrying out structural and functional analysis, and purification of a wide range of molecules within a short time, that makes it the most effective technique for achieving a superior and ideal separation in all applied fields. HPLC is

Citation: I.M. Elkamhawy, M.G. Emara, A.E. Ali, M.A. Khashaba, The accurate and reliable HPLC-UV based method for detecting the active ingredient hexaflumuron in some plant protection products, Turk J Anal Chem, 7(2), 2025, 162-167.

***Author of correspondence:** Ismael.elkamhawy@sci.dmu.edu.eg
Ismaelkamhawy@yahoo.com

Tel: +20 106 2515962

Fax: N/A

Received: January 30, 2024

Accepted: March 23, 2025

doi <https://doi.org/10.51435/turkjac.1651242>

accurate, simple to use, and produces fast results [7,8]. The literature survey has only reported a limited number of methods [9–11] using different techniques or detector types other than used in this article. HPLC can be used successfully in pesticide analysis, which is the main topic in our article. We here aimed to report a new validated method for determining the concentration of hexaflumuron active ingredients in some EC products such as SCORCH 10% EC®. Our new applicable method addresses researchers and chemists who need these types of methods for essential purposes such as generating data for authorization, stability studies, post-registration control, and quality control monitoring.

2.2. Materials and methods

2.1. Chemicals and Reagents

Hexaflumuron analytical standard was supplied by Shandong Luba Chemical Co., Ltd., China, as a gift sample from Kafr El-Zayat for Pesticides and Chemicals Company, Egypt, with a known purity $\geq 95\%$ w/w. Acetonitrile with a pure HPLC grade was purchased from Scharlab, Spain. MS® 0.45 μm nylon membrane filters were purchased from Membrane Solutions, LLC., Seattle, USA.

2.2. Instrumentation and chromatographic conditions

The HPLC system consisted of a Series 200 liquid chromatograph, a Series 200 UV/vis spectrophotometric detector with a range of 190 to 700 nm, and the pump can

generate pressure up to 6100 psi. Brownlee™ C-18 reversed phase column with definite specifications (stainless steel, 250×4.6 mm i.d., 5 μm particle size) was procured from PerkinElmer Instruments, LLC, USA. The Merit Water still instrument model W4000 was used to obtain the distilled water. The mobile phase was prepared by mixing 850 mL acetonitrile and 150 mL distilled water to prepare a 1 L solution. The mobile phase was filtered through a 0.45 μm membrane filter and then degassed before use by using an Elmasonic S40H ultrasonic bath (220–240 V~). The pump flow rate reached 1 mL/min with UV/vis detection at 220 nm. The column oven was adjusted to 30° C with an injection volume of 20 μL . The retention time of HFM was about 3.84 min (Fig. 2).

2.3. Preparation of standard solution

The stock solution (1000 ppm) was prepared by weighing accurately about 26.3 mg of hexaflumuron analytical standard and then diluting it to 25 mL by using acetonitrile. After that, 100 $\mu\text{g/mL}$ is prepared for injection by taking 1 mL from the standard stock solution, and the volume is completed to 10 mL using acetonitrile.

2.4. Method validation parameters

CIPAC document 3807 [12] and the document SANCO/3030/99 rev.5 [13] outlines the validation requirements for analytical methods used for the quality analysis of technical aspects and commercial formulations of plant protection products.

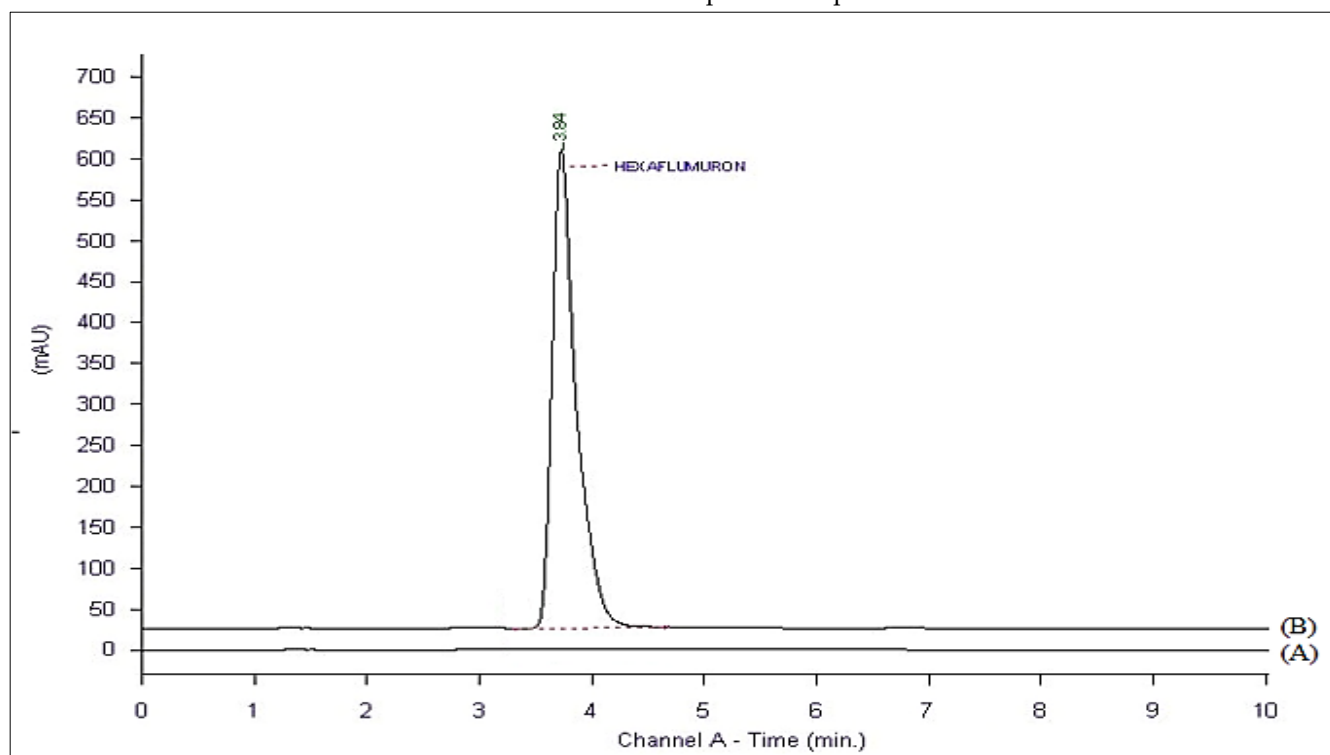


Figure 2. (A) Represents the HPLC-UV baseline of the blank sample, and (B) illustrates the chromatogram of the HFM analytical standard analyzed in this study.

Validation is required for specific and non-standardized analytical methods used in plant protection product formulations. This includes calculating and discussing the specificity, linearity, recovery, accuracy, LOD, LOQ, and precision of the method.

2.4.1. System suitability

As usual, the instrument's performance and the system's adaptability have been confirmed. After that, chromatography was performed first to ensure that there were no interfering peaks in any of the sample solutions that were established.

2.4.2. Specificity

When a method provides a result for just one analyte, it is referred to as specific [14]. The specificity has been investigated by injecting the excipients to ensure that there are no interferences from other peaks or distortions with the target peak.

2.4.3. Linearity and range

Linearity is evaluated by calculating the correlation coefficient, R^2 , which must be ≥ 0.99 [14]. The regression linearity equation (1):

$$Y = aX \pm b \quad (1)$$

Where (Y) represents the response of the average peak area, (X) represents the claimed working concentration in ppm, (a) represents the slope, and (b) is the intercept of the calibration curve. The recommended procedure for determining linearity is by preparing the stock solution of higher concentration and then diluting it to at least five different concentrations. The working range is the range where the matrix gives results with acceptable uncertainty that is determined by observing the concentrations between the minimum and the maximum concentration in the linearity test [15,16].

Linearity was performed by preparing 5 different concentrations (50, 100, 150, 200, and 250 ppm) of HFM analytical standard. The stock solution (10000 ppm) was prepared by weighing accurately 250 mg of HFM analytical standard and dissolving it in 25 mL of acetonitrile in a calibrated volumetric flask. Then, serial dilutions were prepared by taking (0.25 mL, 0.5 mL, 0.75 mL, 1 mL, and 1.25 mL) from the stock solution, respectively, and completing to 50 mL with acetonitrile, and then each concentration was injected in triplicate.

2.4.4. Limit of detection (LOD) and limit of quantification (LOQ)

LOD is the lowest concentration in a sample that can be detected but not necessarily quantified under the stated experimental conditions. LOQ is the lowest

concentration of analyte that can be determined with acceptable precision and accuracy [17]. From the linearity of the calibration, LOD and LOQ could be estimated according to the following equations;

$$LOD = 3.3\sigma/S \quad (2)$$

$$LOQ = 10\sigma/S \quad (3)$$

where (σ) is the standard deviation of response (peak area) and (S) represents the slope of the linearity calibration curve.

2.4.5. Repeatability and Precision

The precision of an analytical method represents the closeness among repeatable measurements acquired through a method under normal conditions. The analytical variation and a measure of the test method's precision are provided by the replicates' relative standard deviation (RSD), which $\leq 1.5\%$ is accepted [15,18]. The following formula (4) can be used to estimate the RSD% of this method:

$$RSD (\%) = \frac{\sigma}{\bar{x}} \times 100 \quad (4)$$

Precision was determined in the current new method by triplicate analyses at a concentrations of 50 $\mu\text{g/mL}$, 100 $\mu\text{g/mL}$, 150 $\mu\text{g/mL}$, 200 $\mu\text{g/mL}$, and 250 $\mu\text{g/mL}$ of standard HFM solution using the developed method.

2.4.6. Accuracy and recovery

Accuracy is the parameter responsible for evaluating the degree of agreement between the value that is identified as true or as a reference and the result obtained by the method being evaluated [18]. It is determined by assessing the analyte recovery percentage (R%) according to equation (5). The new test method's accuracy was evaluated in triplicate at three different concentration levels 50% (0.05 mg/mL), 100% (0.1 mg/mL), and 150% (0.15 mg/mL). Three sets were prepared and injected in triplicate at each concentration. The calculated R% for each level should be between 98.0% and 102.0% [19,20].

$$R\% = \frac{\text{Actual Conc.} (\%)}{\text{Theoretical Conc.} (\%)} \times 100 \quad (5)$$

2.5. Preparation of sample solution

Weigh about 250 mg from the product under study (SCORCH 10% EC[®]), then dilute to 25 mL with acetonitrile in a 25 mL volumetric flask. After that, prepare the injected solution by taking 1 mL from the previous flask, and the volume is completed to 10 mL using acetonitrile.

3. Results and discussion

3.1. Method development

HPLC-UV was used to develop a new analytical technique for determining the active ingredient hexaflumuron in the pesticide formulation SCORCH 10% EC®, using the Brownlee™ C-18 reversed phase column (250 × 4.6 mm, 5 μm), which is made for successfully separating the analyte with high efficiency and excellent peak shape with all pesticide sample types. It was found that the mobile phase, which included acetonitrile/water (85/15, v/v), isocratic elution with a flow rate of 1.0 mL/min, constant column temperature at 30 °C, and UV detection at 220 nm, produced the best separation and symmetrical peak shape of the pesticide under investigation. In these chromatographic conditions, a zero-response baseline was obtained, and the chromatographic peak of HFM was clear, narrow, and symmetrical, as shown in Fig. 2. The optimized chromatographic parameters for the developed HPLC-UV method are illustrated in Table 1.

Table 1. Optimized chromatographic conditions for the hexaflumuron reversed phase HPLC-UV developed method

No.	Parameter	Condition
1	Column	Brownlee™ C-18 reversed phase column (250 × 4.6 mm, 5 μm)
2	Mobile phase	Acetonitrile: distilled water (85%:15%) (v/v)
3	Flow rate	1 mL/min
4	Injection Volume	20 μL
5	Wavelength	220 nm
6	Column temperature	30°C
7	Mode of separation	Isocratic
8	Run time	10 min.
9	Retention time	Hexaflumuron: 3.845 min.

3.2. Method validation

3.2.1. Method suitability

A reverse phase high-performance liquid chromatography (RP-HPLC) method was designed with consideration of system suitability factors, including tailing factor (T), number of theoretical plates (N), runtime, and cost-effectiveness. System suitability tests are essential in method development and are employed to verify the correct operation of the chromatographic system. The advanced method produced the elution of HFM at 3.845 min, where the total run time is 10 minutes, as shown in Fig. 2. Retention time, number of theoretical plates, and peak tailing factor (T) were assessed for six replicate injections of the standard at working concentration. The final results are given in Table 2.

Table 2. System suitability results of Hexaflumuron

Parameters	Hexaflumuron (HFM)
Retention time (min)	3.845
Number of theoretical plates (N)	4823
Tailing Factor (T)	1.15

3.2.2. Specificity

The analyte was identified by comparing its retention time with that of the sample and the standard solution that was completely identical. Moreover, the positioned peak of the pure analytical standard of HFM was used to corroborate the identification. As can be seen from the chromatograms in Figure 2, there were no other coeluted peaks that interfered with the HFM peak when a blank sample was injected.

3.2.3. Linearity and range

As can be easily seen by reviewing the data in Figure 3, the calibration data don't show any non-linear trends or outliers. According to Table 3, the calibration range was 0.05 mg/mL to 0.25 mg/mL, and linearity was evaluated using the correlation coefficient (R^2). The slope value was $y = 4 \times 10^7 x + 174405$ and appeared high linearity with $R^2 = 0.9974$.

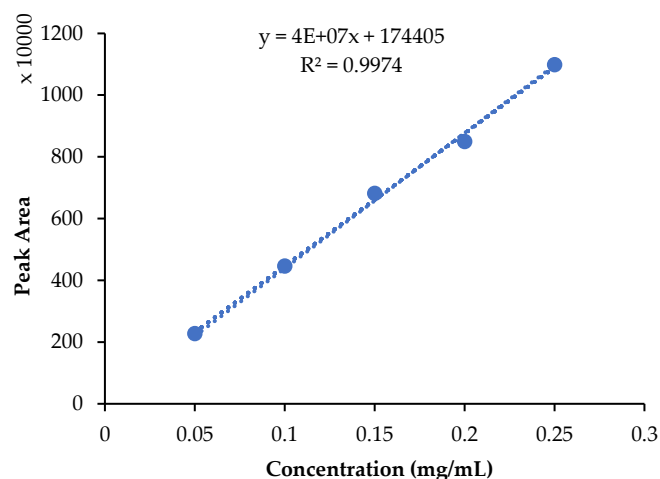


Figure 3. The linear response of peak area against hexaflumuron concentration.

3.2.4. LOD & LOQ

The linearity calibration data of HFM could be used for easily determining the LOD and LOQ limitations. The results showed that the LOQ was 41.6 μg/mL and the LOD was 13.7 μg/mL.

3.2.5. Repeatability and precision

As shown in Table 3, triplicate injections of HFM standard solutions with five concentrations of 50 μg/mL, 100 μg/mL, 150 μg/mL, 200 μg/mL, and 250 μg/mL were used to assess the analyte's repeatability using the RSD% of peak areas. The results were found to be below the 1.5% acceptability threshold. These findings demonstrate the repeatability of the existing HFM determination method.

Table 3. Results of the linearity study of the HPLC-UV method

Conc. (mg/mL)	Rep.	Peak Area	Average	STDEV	RSD%
0.05	R ₁	2253316.25	2282300.03	29813.53	1.31
	R ₂	2280704.60			
	R ₃	2312879.25			
0.1	R ₁	4425770.96	4462113.24	31742.17	0.71
	R ₂	4484406.82			
	R ₃	4476161.95			
0.15	R ₁	6892058.69	6822192.34	69631.53	1.02
	R ₂	6821720.31			
	R ₃	6752798.04			
0.2	R ₁	8448178.54	8498632.79	45345.77	0.53
	R ₂	8511734.95			
	R ₃	8535984.89			
0.25	R ₁	10996251.52	10992666.12	56672.10	0.52
	R ₂	11047460.39			
	R ₃	10934286.44			

Conc: Concentration, Rep.: Replicates

3.2.6. Accuracy and recovery

The accuracy results of the tested range (50% -150%) of the target concentration of 100% (100 µg/mL) were found to be within the range of acceptable criteria levels (98–102%), as demonstrated in Table 4.

3.3. Method application

In order to verify the applicability of the new validated method to a commercial formulation, SCORCH 10% EC® was analyzed at working concentration, and it is shown in Fig. 4. The sample peak was first identified by comparing the retention time with the analytical standard of HFM. System suitability parameters fell within the acceptance ranges. Integration of separated peak area was done, and product concentration was determined by triplicate injection and then using the average peak area concentration relationship obtained in the standardization step. These good results that are shown in Table 5 revealed that the validated method was

Table 4. Accuracy and recovery results

Theoretical Conc. (%)	Rep.	Peak Area	Actual Conc. (%)	Mean Actual Conc. (%)	R(%)
50	R ₁	2319572.20	50.39	50.35	100.70
	R ₂	2365003.87	51.38		
	R ₃	2268531.62	49.28		
100	R ₁	4502659.95	97.82	98.48	98.48
	R ₂	4575316.55	99.40		
	R ₃	4521545.61	98.23		
150	R ₁	6811329.70	147.97	148.99	99.32
	R ₂	6960648.22	151.22		
	R ₃	6802656.43	147.79		

Conc: Concentration, Rep.: Replicates

found to be resolute, selective, and specific for the HFM peak. Also, these results are compatible with the acceptable limit provided by the manufacturer.

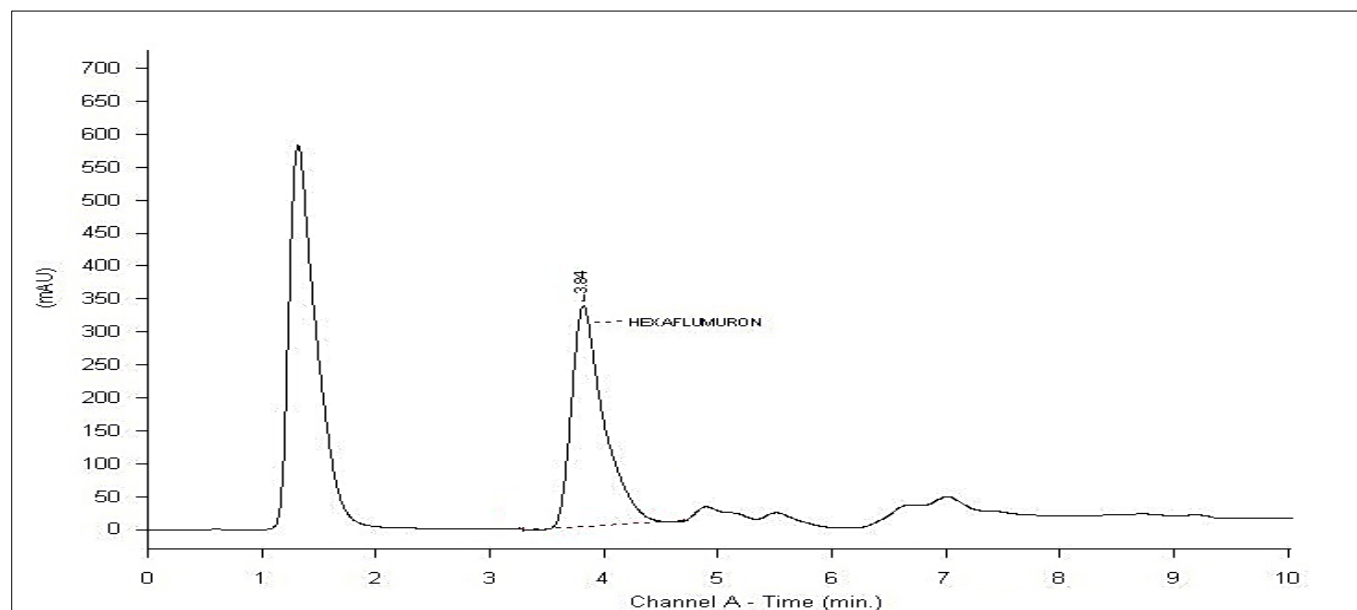
Table 5. The values of hexaflumuron in commercial sample that determined by the new method

Product Name	Replicates	Peak Area	Actual Conc. (%)	Mean Actual Conc. (%)
SCORCH® 10% EC	R ₁	4407754.93	9.72	9.79
	R ₂	4459302.19	9.83	
	R ₃	4468061.92	9.85	

4. Conclusion

This stated method can be used effectively to determine the amount of hexaflumuron in some pesticide products while simultaneously obtaining precise chromatographic profiles for chemometric analysis.

The new method showed good linear regression, $R^2 > 0.99$. The method was reliable and stable, with RSDs

**Figure 4.** The chromatogram of the commercial formulation containing HFM pesticide

between 0.52 and 1.31 %. These validation results were excellent compared to other methods reported in literature, making our new method widely applicable. The retention time of HFM was about 3.84 min with run time of the analysis was about 10 min. This analysis requires a small amount of organic solvent, as indicated by the justified run time, making this method both economical and environmentally benign. The appropriate quantification limit and reliable results proved the method's ability to be used routinely in the chemical analysis laboratories.

Acknowledgements

The corresponding author gratefully acknowledges KZ for Pesticides and Chemicals Company, Nubaria City, Egypt, for its valuable support.

Data availability statement

The data that support the findings of this study are available from the corresponding author upon reasonable request.

References

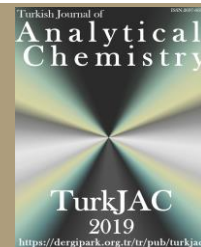
- [1] C. Lu, X. Yin, X. Liu, M. Wang, Study of the photodegradation kinetics and pathways of hexaflumuron in liquid media, *Photochem. Photobiol.*, 90, 2014, 1219-1223.
- [2] A.A. Mohamed, G. S. Refae, Effect of Hexaflumuron on Some Biological Aspects of The Predator Mite Eusebius Hutu (Pritchard & Baker), *Egypt J. Agric Res*, 91, 2013, 111-118.
- [3] C. Tomlin, The pesticide manual: a world compendium, incorporating the agrochemicals handbook (10th edition), 1994, UK, British Crop Protection Council Publications.
- [4] M. Mahmoudvand, H. Abbasipour, A.S. Garjan, A.R. Bandani, Sublethal effects of hexaflumuron on development and reproduction of the diamondback moth, *Plutella xylostella* (Lepidoptera: Yponomeutidae), *Insect Sci*, 18, 2011, 689-696.
- [5] C. Yu, M. Fu, R. Lin, Y. Zhang, L. Yongquan, H. Jiang, T.C. Brock, Toxic effects of hexaflumuron on the development of *Coccinella septempunctata*, *Environ Sci Pollut Res*, 21, 2014, 1418-1424.
- [6] S. Khajepour, H. Izadi, M. J. Asari, N. Liu, Evaluation of two formulated chitin synthesis inhibitors, hexaflumuron and lufenuron against the raisin moth, *Ephestia figulilella*, *J insect sci*, 12, 2012, 102.
- [7] M.F. Al-Hakkani, N. Ahmed, M. H. Hassan, Rapidly, sensitive quantitative assessment of thiopental via forced stability indicating validated RP-HPLC method and its in-use stability activities, *Sci Rep*, 13, 2023, 10294.
- [8] O. Coskun, Separation techniques: chromatography, *North Clin Istanbul*, 3, 2016, 156-160.
- [9] J.H. Kim, J.S. Seo, J.K. Moon, J.H. Kim, Multi-residue method development of 8 benzoylurea insecticides in mandarin and apple using high performance liquid chromatography and liquid chromatography-tandem mass spectrometry, *J Korean Soc Appl. Biol Chem*, 56, 2013, 47-54.
- [10] L. Chen, J. Chen, Y. Guo, J. Li, Y. Yang, L. Xu, F. Fu, Study on the simultaneous determination of seven benzoylurea pesticides in Oolong tea and their leaching characteristics during infusing process by HPLC-MS/MS, *Food Chem*, 143, 2014, 405-410.
- [11] C.H. Wang, X.X. Ma, C. Wang, Q.H. Wu, Z. Wang, Poly (vinylidene fluoride) membrane based thin film microextraction for enrichment of benzoylurea insecticides from water samples followed by their determination with HPLC, *Chin Chem Lett*, 25, 2014, 1625-1629.
- [12] CIPAC (Collaborative International Pesticide Analytical Council), Guidelines on method validation to be performed in support of analytical methods for agrochemical formulations, Document no 3807, July 2003.
- [13] European Commission (Directorate General Health and Consumer Protection), Technical Active Substance and Plant protection products: guidance for generating and reporting methods of analysis in support of pre-and post-registration data requirements for Annex (Section 4) of Regulation (EU) No 283/2013 and Annex (Section 5) of Regulation (EU) No 284/2013, SANCO/3030/99 rev.5, March 2019.
- [14] M. Yuwono, G. Indrayanto, Validation of chromatographic methods of analysis, *Profiles Drug Subst Excip Relat Methodol*, 32, 2005, 243-259.
- [15] I.M. Elkamhawy, A new Validated Method for Rapid Determination of Commercial Formulations Containing Quinalofop-P-Ethyl by Reversed-Phase Liquid Chromatography, *SciRad*, 3, 2024, 254-265.
- [16] A. Sharma, J. K. Dubey, S. Katna, D. Shandil, G. S. Brar, S. Singh, Validation of analytical methods used for pesticide residue detection in fruits and vegetables, *Food Anal Methods*, 14, 2021, 1919-1926.
- [17] B.T. Alquadeib, Development and validation of a new HPLC analytical method for the determination of diclofenac in tablets, *Saudi Pharm J*, 27, 2019, 66-70.
- [18] L. Velkoska-Markovska, J. Davitkova, M. S. Jankulovska, HPLC Method For Determination of Active Ingredients in Pesticide Formulation SWITCH 62,5 WG, *J Agric Food Environ Sci*, 75, 2021, 11-18.
- [19] B.M. Marson, V. Concentino, A.M. Junkert, M.M. Fachi, R.O. Vilhena, R. Pontarolo, Validation of analytical methods in a pharmaceutical quality system: an overview focused on HPLC methods, *Quim Nova*, 43, 2020, 1190-1203.
- [20] I.M. Elkamhawy, Development and validation of an innovative HPLC-UV method for determination of Metalaxyl-M in flowable suspension fungicide formulas, *Curr Chem Lett*, in press, 2025.



TurkJAC

Turkish Journal of

Analytical Chemistry

<https://dergipark.org.tr/tr/pub/turkjac>TurkJAC
2019<https://dergipark.org.tr/tr/pub/turkjac>

Assessment of antioxidant, antimicrobial, antibiofilm, carbonic anhydrase, and α -glucosidase inhibitory activities of *Alchemilla vulgaris* L. extracts

Uğur Kardil^{1*} , Zeynep Akar² , Azer Özad Düzgün³ ¹ Gümüşhane University, Department of Medical Services and Techniques, Gümüşhane University Vocational School of Health Services, 29000, Gümüşhane, Türkiye² Gümüşhane University, Chemistry and Chemical Processing Technologies Department, Gümüşhane Vocational School, 29000, Gümüşhane, Türkiye³ Gümüşhane University, Department of Occupational Health and Safety, Faculty of Health Sciences, 29000, Gümüşhane, Türkiye

Abstract

This study was to investigate the biological properties (antioxidant, enzyme inhibitory, and antimicrobial activity) of water extract (WE), 50:50% water:ethanol extract (WEE), and ethanol extract (EE) of aerial parts of *Alchemilla vulgaris* L. which was traditionally used to alleviate and treat many diseases. The WEE extract exhibited the highest total phenolic content (TPC), with a value of 612 μg GAE/mL, while the EE extract demonstrated the highest total flavonoid content (TFC), with a value of 86.3 μg QE/mL. The data showed that the WEE extract exhibited the highest radical scavenging capacities with SC_{50} values of 0.0056 and 0.0028 mg/mL as determined by the DPPH and ABTS assays, respectively. The WEE extract also showed the highest antioxidant activities with 267 and 0.081 μM TEAC as determined by FRAP and CUPRAC assays, respectively. Furthermore, with IC_{50} values of 0.0628 and 0.0535 mg/mL, WEE extract was found to be an effective inhibitor of bovine carbonic anhydrase (BCA) and α -glucosidase. The EE extract showed activity against both Gram-negative and Gram-positive bacteria used in the study. EE extract has the highest activity against *Yersinia pseudotuberculosis* and the lowest activity against *Streptococcus pyogenes*. Moreover, the extracts significantly reduced the biofilm ability of the *Acinetobacter baumannii* isolate. EE and WE reduced the biofilm formation capacity of the strain to a weak level, while WEE extract reduced it to a moderate level. The results suggest that EE has a significant effect in combating antibiotic resistance, while WEE has high antioxidant activity and a good inhibitory effect against BCA and α -glucosidase enzymes. In addition, the results revealed that solvent extracts with different solvent compositions and polarities may have different effects on diverse bioactivity tests.

Keywords: Antibiofilm, antioxidant activity, *Alchemilla vulgaris* L., carbonic anhydrase, α -glucosidase

1. Introduction

Throughout history, the utilization of medicinal plants has been documented as an alternative therapeutic tool for the treatment of numerous diseases. [1]. The medicinal plants have been known to contain a variety of secondary metabolites, including phenolic acids, flavonoids, anthocyanins, lignans, and coumarins [2]. These secondary metabolites have been demonstrated to exhibit various biological activities, including antioxidant, antimicrobial, antidiabetic, and anticancer properties [3]. A considerable number of plant species have been found to possess the ability to scavenge and hinder the process of free radical formation, which is known to induce oxidative damage in biomolecules. The presence of antioxidant activity in these secondary

metabolites has been identified as a key factor in their function [4]. Moreover, plant based natural antioxidants are favored over synthetic ones due to their safety profiles [5]. Therefore, there is considerable interest in scientific research that focuses on the bioactivity of natural products.

Alchemilla is commonly referred to as "Lady's Mantle" or "Lion's Foot", and species belonging to this genus are predominantly distributed across Europe and Asia, being found in northeastern Anatolia (Türkiye), northern Iraq, and northwestern Iran [6]. A wide range of biological activities has been attributed to various species of *Alchemilla*, including antioxidant, anticancer, antidiabetic, and antimicrobial properties [1,7,8].

Citation: U. Kardil, Z. Akar, A.Ö. Düzgün, Assessment of antioxidant, antimicrobial, antibiofilm, carbonic anhydrase, and α -glucosidase inhibitory activities of *Alchemilla vulgaris* L. extracts, Turk J Anal Chem, 7(2), 2025, 168–175.

****Author of correspondence:** ugurkardil_61@hotmail.com

Tel: 0 (456) 233 11 49

Fax: 0 (456) 233 11 56

Received: March 26, 2025

Accepted: April 16, 2025

doi <https://doi.org/10.51435/turkjac.1666390>

The genus *Alchemilla vulgaris* L., an herbaceous perennial plant in the family Rosaceae, is widely used in folk medicine throughout the world, and in traditional medicine, the plant is commonly used for the treatment of ulcers, wounds, eczema, and digestive problems [7]. *A. vulgaris* has been characterized by strong antioxidant activity due to the presence of phenolic constituents and large quantities of tannins, flavonoids, and phenolic carboxylic acids [9]. The aerial parts of the plant are used in the treatment of gastrointestinal diseases and for the acceleration of wound healing, a consequence of their potent antimicrobial and anti-inflammatory properties [1].

Reactive oxygen species (ROS), which have been identified as agents of a range of diseases, including oxidative stress, cancer, Alzheimer's, diabetes, and aging, have been shown to induce oxidative damage to biomolecules [10]. Antioxidants have been shown to inhibit or delay the oxidation process by obstructing the initiation or propagation of oxidizing chain reactions [11].

The carbonic anhydrase (CA) enzyme is of pivotal importance in a multitude of physiological processes [12]. Carbonic anhydrase inhibitors (CAIs) are employed in clinical settings as diuretics, anti-glaucoma, anti-obesity, and antineoplastic agents [13]. Consequently, there is a scientific imperative to explore novel natural CA inhibitors.

Diabetes mellitus (DM) is a prevalent metabolic disorder, characterized by elevated blood glucose levels, triggered by the development of either insulin deficiency or resistance. The α -glucosidase enzyme plays a crucial role in regulating the process of carbohydrate digestion [14]. Inhibition of the activity of the α -glucosidase enzyme can delay the absorption of glucose by the body. Thus, there is a significant need to identify novel natural α -glucosidase inhibitors for the management of diabetes.

A major global public health challenge is represented by the alarming prevalence of Gram-negative bacteria that exhibit high levels of antibiotic resistance. The morbidity and mortality rates associated with these infections are high, largely due to a paucity of effective treatment options [15]. Research and development are vital to determine more effective natural antibacterials to combat bacterial infections.

The literature contains various studies investigating such as the phenolic composition, antimicrobial, and antioxidant properties of *A. vulgaris*, with a particular focus on the biological activities [1,6,7,8,16]. A review of the literature revealed that no study had been conducted to evaluate the antibiofilm and carbonic anhydrase inhibition activities of *A. vulgaris*. The objective of the present study was to evaluate the antibiofilm, antioxidant, and antimicrobial activity and carbonic

anhydrase and α -glucosidase inhibition abilities of aerial parts of *A. vulgaris* extracts.

2. Materials and methods

2.1. Chemicals and reagents

Trolox (6-hydroxy-2,5,7,8-tetramethylchroman-2-carboxylic acid), methanol, acetic acid, gallic acid, quercetin, ammonium acetate, ammonium nitrate, ethanol, NaOH, CuCl₂, NaCl, HCl, Na₂CO₃, CH₃COONH₄, neocuproine (2,9-Dimethyl-1,10-phenanthroline), DPPH• (2,2-diphenyl-1-picrylhydrazyl), ABTS (2,2'-azino-bis(3-ethylbenzothiazoline-6-sulfonic acid)), FeCl₃.6H₂O, α -glucosidase (*Saccharomyces cerevisiae*, lyophilized powder, ≥ 10 units/mg protein), 4-nitrophenyl- α -D-glucopyranoside, sulfanilamide (4-aminobenzenesulfonamide), Folin-Ciocalteu's, phenol reagent, and yeast extract were purchased from Sigma Aldrich (St. Louis, MO, USA). TPTZ (2,4,6-tris(2-pyridyl)-s-triazine), bovine carbonic anhydrase (BCA, lyophilized powder, ≥ 2000 W-A units/mg protein), tryptone, and crystal violet were purchased from Merck (Darmstadt, Germany). 4-nitrophenyl acetate was purchased from BLDpharm (Shanghai, China).

2.2. Plant material and sample preparation

The dried aerial parts of *A. vulgaris* were obtained from an herbalist in Trabzon in February 2025. The dried aerial parts were pulverized using a grinder. Three different solvents, water, 50:50% water:ethanol, and ethanol were utilized for the extraction process. The water, 50:50% water:ethanol, and ethanol extracts are coded WE, WEE, and EE, respectively.

The dried and powdered aerial parts (10 g) of *A. vulgaris* were subjected to solvent (100 mL) extraction for a period of 2 hours, employing continuous stirring at ambient temperature. The quantity of the extracts was determined subsequent to filtration through 0.45 μ m syringe filters (Whatman) and concentrating under reduced pressure. The process of dissolution was carried out for each extract in its own solvent, with the objective of achieving the desired concentration. The extracts were then maintained at a temperature of 4°C until further utilization in subsequent experiments.

2.3. Determination of total phenolic and flavonoid contents

2.3.1. Total phenolic content (TPC)

The total phenolic content of the aerial parts of *A. vulgaris* extracts was determined using the Folin-Ciocalteu reagent method, as described by Slinkard and Singleton [17]. 50 μ L of the sample solution was mixed with 250 μ L of 0.2 N Folin-Ciocalteu reagent. Then 750 μ L of Na₂CO₃

(7.5%) was added to the mixtures, and the reaction solutions were incubated for 2 hours. Following the conclusion of the incubation period, the absorbances were determined spectrophotometrically at a wavelength of 765 nm. The standard calibration graph of gallic acid was prepared and the amount of phenolic compound in the samples was calculated as gallic acid equivalent ($\mu\text{g GAE/mL}$).

2.3.2. Total flavonoid content (TFC)

The total flavonoid content of the extracts obtained from the aerial parts of *A. vulgaris* was determined in accordance with the method established by Fukumoto and Mazza [18]. Following the addition of the sample solutions to the test tubes, 1 M ammonium acetate ($\text{CH}_3\text{COONH}_4$) and 10% aluminum nitrate ($\text{Al}(\text{NO}_3)_3 \cdot 9\text{H}_2\text{O}$) were introduced to the tubes in the prescribed manner. Following the conclusion of the incubation period (40-minutes), the absorbances were measured at a wavelength of 415 nm. The standard calibration graph of quercetin was prepared and the amount of flavonoid compound in the samples was calculated as quercetin equivalent (mg QE/mL).

2.4. Determination of antioxidant activities

2.4.1. DPPH • radical scavenging activity

The DPPH radical scavenging activities of extracts obtained from the aerial parts of *A. vulgaris* were examined by employing the method that had been described by Brand-Williams et al. [19]. The testing concentrations of extracts from the aerial parts of *A. vulgaris* were adjusted with the objective of yielding results indicative of scavenging activity. The methodology comprised the mixing of the extracts with a DPPH solution, with the mixture then being maintained at ambient temperature and in the absence of light for a period of 50 minutes. The absorbance of the solution treatment with standard and extracts was measured at a wavelength of 517 nanometers. A graph was generated based on the concentrations that corresponded to the values of the absorbances that had been determined. The quantity of sample necessary to reduce the DPPH concentration by 50% was determined in mg/mL , and this is represented in the graph as the SC_{50} (half of the maximal scavenging concentration) value. A comparison was made between the scavenging capacity of the extracts and that of the standard antioxidant, Trolox.

2.4.2. ABTS •• radical scavenging activity

The ABTS radical scavenging activities of extracts obtained from the aerial parts of *A. vulgaris* were examined by employing the method that had been described by Re et al. [20]. The preparation of the ABTS

stock solution involved the dissolution of ABTS, followed by its mixture with a potassium persulfate solution. Subsequently, the mixture was left at ambient temperature and in darkness for a period of 18 hours in order to obtain the ABTS radical cation ($\text{ABTS} \cdot^+$). At the end of this period, it was diluted to approximately 1/50 of its original concentration, and its absorbance was adjusted to 0.07 at 734 nm. Trolox was utilized as the antioxidant standard, and was studied in triplicate at six distinct concentrations. Following a 20-minute interval, the absorbances of each sample were measured at a wavelength of 734 nm. The quantity of sample required to reduce $\text{ABTS} \cdot^+$ concentration by 50% was calculated as mg/mL , with the results expressed as SC_{50} .

2.4.3. Ferric reducing antioxidant power (FRAP)

The FRAP effects of the extracts obtained from the aerial parts of *A. vulgaris* were evaluated in vitro according to the method described by Benzie and Strain [21]. Following a series of preliminary trials, it was established that all extracts should be diluted to a concentration of 0.1 mg/mL . Subsequently, 50 μL of each extract and standard solution were combined with 1.5 μL of freshly prepared FRAP reagent. Subsequent to a 20-minute incubation period, the absorption values were measured at a wavelength of 595 nm. The results were calculated in $\mu\text{M TEAC}$ (Trolox Equivalent Antioxidant Capacity) by employing a standard curve that had been prepared from Trolox solutions.

2.4.4. Cupric reducing antioxidant capacity (CUPRAC)

The original description of the CUPRAC assay was provided by Apak and colleagues [22]. This assay was modified and utilized for the analysis of the aerial parts of *A. vulgaris* extracts in the present study. Preliminary trials indicated that all extracts should be studied by dilution to a concentration of 0.1 mg/mL . In the initial phase of the experimental procedure, equal volumes of a Cu (II) chloride solution, a neocuproin solution, and an ammonium acetate buffer were added to test tubes, respectively. Then, the spectrophotometric measurement of the absorbance values was conducted at a wavelength of 450 nm. The antioxidant capacity of the extracts was calculated in $\mu\text{M TEAC}$, utilizing a standard antioxidant Trolox graph that had been studied at various concentrations.

2.5. Determination of enzyme inhibition

2.5.1. Carbonic anhydrase inhibitory activity

The aerial parts of *A. vulgaris* extracts were tested for carbonic anhydrase inhibitory (CAI) activity by using bovine carbonic anhydrase enzyme (BCA). The CA enzyme catalysis the hydrolysis of *p*-nitrophenyl acetate (PNPA) to *p*-nitrophenol and *p*-nitrophenolate ions. The

measurement of the absorbency at 348 nm, resulting from the formation of *p*-nitrophenol and *p*-nitrophenolate, is conducted at the conclusion of the reaction. In order to determine the inhibition activity of extracts, a series of reactions were conducted in test tubes. The reactions, comprised 150 μ L of enzyme, 50 μ L of inhibitor, 550 μ L of 0.05 M phosphate buffer (pH: 7.4) and 750 μ L of 3 mM substrate (*p*-nitrophenyl acetate). Inhibition activity is expressed in terms of IC₅₀ values, representing the concentration of the sample that yields 50% inhibition of enzyme activity [23]. Sulfanilamide was studied as a standard inhibitor. The IC₅₀ values of sulfanilamide and the samples were calculated in mg/mL.

2.5.2. α -Glucosidase inhibitory activity

The α -glucosidase enzyme activity of the aerial parts of *A. vulgaris* extracts was investigated through a modified approach [24]. A volume of 20 μ L of sample and 30 μ L of α -glucosidase enzyme (*Saccharomyces cerevisiae*, lyophilized powder, ≥ 10 units/mg protein) were added to 650 μ L of phosphate buffer (pH: 6.8 and 0.1 M). The mixture was then maintained at 37 °C for a period of 10 minutes. Subsequently, 75 μ L of substrate (4-nitrophenyl- α -D-glucopyranoside) was added to the tubes. The mixture was then maintained at the initial temperature for a further 20 minutes. Finally, 650 μ L of 1 M Na₂CO₃ was added to the tubes. Absorbance values were measured at 405 nm in a UV/VIS spectrophotometer. Acarbose (positive control) was studied as a standard inhibitor. The IC₅₀ values of acarbose and the samples were calculated in mg/mL.

2.6. Determination of antimicrobial activities

2.6.1. Agar diffusion assay

For the agar diffusion test, 6 different microorganisms were used (SA: *Staphylococcus aureus* ATCC 25923 and SP: *Streptococcus pyogenes* ATCC 19615, EC: *Escherichia coli* ATCC 25922, PA: *Pseudomonas aeruginosa* ATCC 43288, PV: *Proteus vulgaris* ATCC 13315, YP: *Yersinia pseudotuberculosis* ATCC 911). Holes were made in the agar using sterile hole punchers (diameter 6 mm), and extracts were added to each hole (50 μ L). Ampicillin was used as a positive control, and 50 μ L was loaded into the central hole. The prepared petri dishes were kept at room temperature for 2 hours and then incubated at 37°C for 24 hours, and the inhibition zone diameters were measured with a scale [25].

2.6.2. Minimum inhibitory concentrations (MIC)

Minimum inhibitory concentrations (MIC) of the aerial parts of *A. vulgaris* extracts were determined using the broth microdilution method. Initial concentrations of the extracts were used as 10 mg/mL. MIC values were

investigated against previously determined clinical antibiotic-resistant biofilm forming capacity of *A. baumannii* strains. The assays have been performed in 96 plates and in triplicate [25,26].

2.6.3. Antibiofilm properties

The 1/2 MIC values of the aerial parts of *A. vulgaris* extracts were used as a reference for the antibiofilm activity test against antibiotic-resistant *A. baumannii*, which has a strong biofilm formation capacity. After overnight incubation of *A. baumannii* in 3 mL LB medium, 1/100 dilutions were added to 96-well plates together with 1/2 MIC extracts. Plates were incubated at 37 °C for 24 hours. The suspension in the 96-well plate was then decanted, and the plate was washed three times with distilled water. 200 μ L of 1% crystal violet dye was added to each well and incubated for 20 minutes at ambient temperature. The crystal violet was removed from the plates, washed with distilled water, and allowed to dry for 15 minutes at ambient temperature. 200 μ L of 95% ethanol was added into the wells. Optical absorbance (A) was measured at 620 nm on a spectrometer. The experiment was carried out in triplicate. The evaluation was based on four different criteria [26].

2.7. Statistical evaluation

The measurements were made in triplicate, and the mean values are reported. Standard deviations were calculated in Microsoft Excel. The percentage relative standard deviations were in the range of 2-5%. The regression analyses were done by using Microsoft Excel with R² values over 0.98.

3. Results and discussions

3.1. Evaluation of total phenolic and flavonoid contents

Phenolic and flavonoid compounds represent a noteworthy group of antioxidants, which are present in significant concentrations within the plants.

In the present work, WEE had the highest total phenolic content, with 612 ± 1.92 μ g GAE/mL (Table 1). According to the literature, Vlasisavljević et al. [1] reported that the total phenolic contents of methanolic, ethanolic, ethyl acetate, and water extracts of *A. vulgaris* were 7.71, 7.40, 9.65, and 6.89 mg GAE per g of extract, respectively. Tasić-Kostov et al. [27] reported that the total polyphenol contents of ethanolic and water extracts of *A. vulgaris* were 110.80 and 82.16 μ g GA/mg, respectively. Jelača et al. [16] reported that the ethanolic extract of *A. vulgaris* L. represents a valuable source of bioactive compounds. They also reported that the total phenolic content of *A. vulgaris* extract was 7.55 ferulic acid equivalents per gram of dry weight.

The total flavonoid content of the WE, WEE, and EE extracts is shown in Table 1. The EE had the highest total flavonoid content, with a value of 86.3 ± 2.5 $\mu\text{g QE/mL}$, while the WE extract demonstrated the lowest total phenolic content, with a value of 43.8 ± 1.8 $\mu\text{g QE/mL}$. In the literature, Kanak et al. [6] reported that twenty flavonoids were detected in aqueous ethanol (80% v/v) obtained from the leaves of *A. vulgaris*. Jelača et al. [16] reported that the total flavonoids content of the *A. vulgaris* extract was 6.99 quercetin equivalents per gram of dry weight. Tasić-Kostov et al. [27] reported that the total flavonoid contents of ethanolic and water extracts of *A. vulgaris* were 128.09 and 52.29 $\mu\text{g rutin/mg}$, respectively.

Table 1. Total phenolic and flavonoid contents of the aerial parts of *A. vulgaris* extracts

Samples	Total phenolic content ($\mu\text{g GAE/mL}$)	Total flavonoid content ($\mu\text{g QE/mL}$)
WE	462 ± 1.67	43.8 ± 1.8
WEE	612 ± 1.92	54.5 ± 4.1
EE	423 ± 2.89	86.3 ± 2.5

3.2. Evaluation of antioxidant activity

The present study investigated the antioxidant activities of the WE, WEE, and EE extracts, as determined by the DPPH, ABTS, FRAP, and CUPRAC methods.

In the present work, the SC_{50} values of DPPH scavenging activities of standard and extracts are presented in Table 2. The DPPH radical scavenging assay showed that WEE had the highest antioxidant activity, with an SC_{50} value of 0.0056 ± 0.0002 mg/mL , whereas EE had the lowest activities, with an SC_{50} value of 0.0099 ± 0.0004 mg/mL . According to the literature, Boroja et al. [7] reported that the SC_{50} values of DPPH radical scavenging in methanolic extract of above ground parts of *A. vulgaris* was 0.0059 mg/mL . In another study, Tasić-Kostov et al. [27] reported that the SC_{50} values of DPPH radical scavenging activity in the aerial parts of ethanolic and water extracts of *A. vulgaris* with, 0.11 and 27.22 $\mu\text{g/mL}$, respectively.

The SC_{50} values of ABTS scavenging activities of standard and extracts are presented in Table 2. WEE had the highest reducing activities, with 0.0028 ± 0.0001 mg/mL , while WE and EE were exhibited values of 0.0048 ± 0.0002 , 0.0243 ± 0.0006 , and 0.0055 ± 0.0003 mg/mL , respectively. In the literature, Boroja et al. [7] reported that the SC_{50} values of ABTS radical scavenging in methanolic extract of aboveground parts of *A. vulgaris* was 0.0148 mg/mL . In another study, Vlaisavljević et al. [1] reported that the SC_{50} values of ABTS radical scavenging activity in the aerial parts of 70% ethanol and water extracts of *A. vulgaris* were 119.62 and 37.50 mg TE / g DE , respectively.

As demonstrated in Table 2, the results of the FRAP activities of the standard and the extracts are expressed in terms of $\mu\text{M TEAC}$. The WEE extract demonstrated the highest level of reducing activity, with a TEAC of 267 ± 1.39 μM , while the EE extract exhibited the lowest reducing activity, with a TEAC of 179 ± 3.42 μM . In the literature, Vlaisavljević et al. [1] reported that the FRAP values of the aerial parts of 70% ethanol and water extracts of *A. vulgaris* were 6405.75 and 3240.09 mg AAE / g DE , respectively.

The CUPRAC activities of the standard and the extracts are presented in Table 2, expressed as $\mu\text{M TEAC}$. WEE had the highest reducing activities, with 0.081 ± 0.003 $\mu\text{M TEAC}$, while WE and EE were exhibited values of 0.067 ± 0.002 and 0.064 ± 0.001 $\mu\text{M TEAC}$, respectively. Vlaisavljević et al. [1] reported that the CUPRAC values of the aerial parts of 70% ethanol and water extracts of *A. vulgaris* were 203.53 and 78.56 mg TE / g DE , respectively.

In this study, in accordance with the literature, it was determined that the WEE extract has a strong antioxidant capacity. Moreover, the results of the DPPH, ABTS, FRAP, and CUPRAC antioxidant activity tests exhibited positive correlation.

Table 2. DPPH and ABTS radical scavenging capacities, FRAP and CUPRAC antioxidant activities of the aerial parts of *A. vulgaris* extracts

Samples	DPPH (SC_{50} values mg/mL)	ABTS (SC_{50} values mg/mL)	FRAP ($\mu\text{M TEAC}$)	CUPRAC ($\mu\text{M TEAC}$)
WE	0.0077 ± 0.0003	0.0048 ± 0.0002	206 ± 3.15	0.067 ± 0.002
WEE	0.0056 ± 0.0002	0.0028 ± 0.0001	267 ± 1.39	0.081 ± 0.003
EE	0.0099 ± 0.0004	0.0055 ± 0.0003	179 ± 3.42	0.064 ± 0.001
Trolox	0.0020 ± 0.0001	0.0026 ± 0.0001	—	—

3.3. Evaluation of enzyme inhibition

CAIs are valuable for their use in many medical conditions including diuretic, anti-glaucoma, anti-epileptic, anti-obesity, and anti-cancer [13]. A considerable number of phenolic compounds with antioxidant properties have been documented to possess CA inhibition capabilities [28]. In addition, newly synthesized compounds are being evaluated for their carbonic anhydrase inhibitory activity [23]. In recent years, there has been an increase in the search for CAIs, whether synthetic or natural. Therefore, the aerial parts of *A. vulgaris* extracts were tested for CAI by using BCA. It was evident that all extracts exhibited significant inhibitory activity against BCA. The WEE extract demonstrated the most effective inhibitory activity, exhibiting low IC_{50} values of 0.0628 mg/mL (Table 3).

Table 3. IC₅₀ values of the aerial parts of *A. vulgaris* extracts in carbonic anhydrase inhibitory (CAI) activity test

Sample/Standard	IC ₅₀ Value (mg/mL)
Sulfanilamide	0.0004
WE	0.1748
WEE	0.0628
EE	0.0754

It has been established that the inhibition of the α -glucosidase enzyme is a pivotal strategy for the prevention of diabetes, which is a major public health concern. For the purpose of this study, the aerial parts of *A. vulgaris* extracts were examined as potential natural inhibitors of the α -glucosidase enzyme. The α -glucosidase enzyme activity of the WE, WEE, and EE extracts was measured as 0.1275, 0.0535, and 0.1623 mg/mL IC₅₀, respectively (Table 4). The highest α -glucosidase enzyme inhibition value of the plant was observed in the WEE, and the lowest in the EE. The present review demonstrated the findings from studies conducted in the literature on the α -glucosidase enzyme activity of different species belonging to the *Alchemilla* family. Methanol and pure water were utilized as solvents in the course of these studies. It was determined that the α -glucosidase enzyme activity of the methanol extract was higher than that of pure water [29,30]. In a study conducted with *A. vulgaris* L. species, different enzyme activities (lipase activity and α -amylase activity) were examined. In the study, leaf and flower parts of the plant were extracted using different solvents (MeOH, MeOH 70%, EtOH, EtOH 70%, Hexane and Chloroform). In the study conducted with these enzymes, it was observed that the ethanol-water mixture showed activity [31].

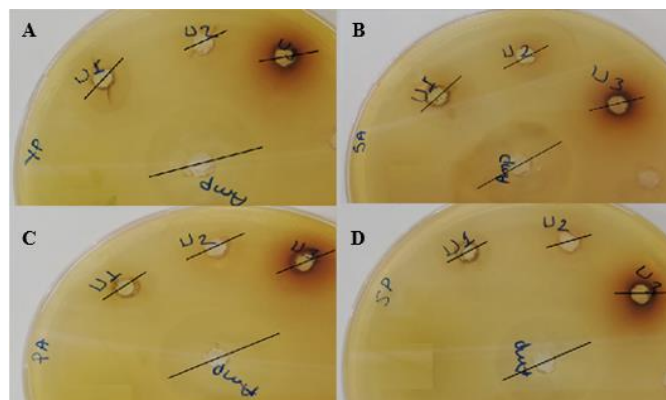
Table 4T. α -Glucosidase enzyme inhibition activities of the aerial parts of *A. vulgaris* extracts

Sample/Standard	IC ₅₀ Value (mg/mL)
Acarbose	0.0118
WE	0.1275
WEE	0.0535
EE	0.1623

3.4. Evaluation of antimicrobial activity

The activities of the WE, WEE, and EE extracts against standard bacteria were investigated by the agar diffusion method. The results obtained from the study indicated that the WE and WEE extracts demonstrated no effect against the six bacterial strains employed in the experiment. The investigation revealed that the EE extract exhibited activity against both Gram-negative and Gram-positive bacteria utilized in the study. Ampicillin was used as a control. Accordingly, it was observed that the EE extract exhibited the highest activity against YP and PV, with zone diameters of 18 and 17, respectively. It was also observed that EE extract exhibited the lowest activity against SP, with a zone

diameter of 12. In addition, EE extract was established that the same inhibitory effect (15 zone diameter) against SA, PA, and EC (Fig. 1).

**Figure 1.** Antimicrobial activity of the aerial parts of *A. vulgaris* extracts

A: YP (*Yersinia pseudotuberculosis* ATCC 911),

B: SA (*Staphylococcus aureus* ATCC 25923),

C: PA (*Pseudomonas aeruginosa* ATCC 43288),

D: SP (*Streptococcus pyogenes* ATCC 19615)

U1: EE (ethanol extract of aerial parts of *Alchemilla vulgaris* L.);

U2: WE (water extract of aerial parts of *Alchemilla vulgaris* L.);

U3: WEE (50:50% water:ethanol extract of aerial parts of *Alchemilla vulgaris* L.);

Amp: Ampicillin (control).

In a study investigating the antimicrobial activity of the lady's claw plant in 2022, it was seen that the extracts had MIC values of 2.5-5-10 mg/mL against different microorganisms [32]. Aerial parts of *Alchemilla alpina* L. were extracted using different solvents (methanol, ethanol, and chloroform), and their antimicrobial activity was determined by disk-disk diffusion method, and it was shown that these extracts inhibited the growth of some bacteria at different rates (8-23 mm) [33]. In a different report investigating the biological activity of the extract of the aerial part of *A. vulgaris*, it has antimicrobial activity against both bacteria and fungi [34]. In 2024, the antimicrobial activity of the plant *Alchemilla holotricha* Juz. was investigated, and the extract had the highest antibacterial activity against *E. coli* with a measurement of 17 mm and the lowest activity against *Bacillus subtilis* with a diameter of 8 mm [35]. In this study, it was observed that the plant has activity against both Gram-negative and Gram-positive bacteria. The findings will contribute to the foundation for more extensive and in-depth research on the potential effects of plant extracts [34].

A. baumannii is responsible for a variety of medical device-associated infections, urinary tract infections, meningitis, endocarditis, respiratory infections, wound infections, and bacteremia in hospitalized patients. All of these infections are associated with the formation of biofilms [36]. The MIC and antibiofilm effects of extracts

against antibiotic resistant clinical *A. baumannii* isolates were investigated. EE and WE extracts were found to have MIC values of 5 mg/mL, while WEE extract was found to have MIC value of 25 mg/mL against *A. baumannii*. After determining the MIC values, antibiofilm assay was performed using half MIC value and *E. coli* DH5 α isolate as a control strain. According to the data, *A. baumannii* has a strong biofilm formation capacity. When treated with extracts, it was observed that the biofilm formation capacity of the strain decreased. The EE and WE extracts reduced the biofilm formation capacity of the strain to a weak level, while WEE extract reduced it to a moderate level.

In a study conducted by Kardil et al. in 2024 investigating the effect of plant extract on the biofilm formation capacity of clinical antibiotic-resistant *A. baumannii* isolate, it was determined that methanol, water, and 50:50% methanol:water extracts reduced the biofilm formation capacity of *A. baumannii* isolate by approximately 1.7, 1.6, and 1.3 times, respectively [37]. In the same year, Kardil et al., in a study investigating the antibiofilm effect of the *Vaccinium arctostaphylos* L. leaf and fruit extracts against clinical antibiotic-resistant *A. baumannii* isolates, found that the plant's leaf extract significantly reduced the biofilm-forming capacity of the *A. baumannii* isolate compared to the fruit extract [38]. In a study carried out by Ouslimani et al., *A. verticillata* and *C. cassia* were found to possess the ability to inhibit the formation of biofilms, in addition to weakening and dissolving pre-formed biofilms. [39]. In this study, in accordance with the literature, the EE of the plant significantly reduced the biofilm formation capacity of the *A. baumannii* isolate, which has a strong biofilm formation capacity.

4. Conclusions

Medicinal plants represent a significant source of active biological compounds that have the potential for use in the development of new drugs. The choice of solvents and solvent compositions with differing polarities that are utilized in the extraction of plants has affected the type and amount of bioactive components extracted. In this study, the total phenolic and flavonoid contents and the antioxidant, carbonic anhydrase inhibitory, α -glucosidase inhibitory, antimicrobial, and antibiofilm activities of aerial parts of *A. vulgaris* L. were presented. The study showed that the use of diverse solvent compositions resulted in the extraction of different bioactive components, which led to remarkable differences in the biological activity. WEE, together with the highest total phenolic content, showed the highest antioxidant, carbonic anhydrase inhibition, and α -glucosidase inhibition activities. In addition, a good

correlation has been found between the antioxidant activity, the total phenolic content, and the enzyme inhibitory effects. In contrast, the findings demonstrate that the EE exhibited the most pronounced total flavonoid, antimicrobial, and antibiofilm activity. In this study it was shown for the first time that the aerial parts of *A. vulgaris* L. have both a carbonic anhydrase inhibitory activity and an antibiofilm effect. The findings of our investigation suggest that the WEE and EE may serve as promising candidates for the prevention and treatment of diseases associated with oxidative damage, cancer, diabetes, and bacterial infections. As a result, further research is needed to confirm these biological activities and to elucidate the underlying mechanisms of action.

Acknowledgments

—

Funding

None.

Conflicts of interest

The authors declare that they have no conflict of interest.

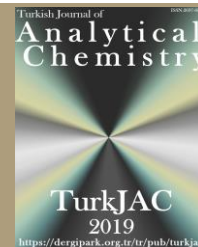
Authors' contribution:

UK: Conducted the extraction, antioxidant activity and enzyme activity experiments and wrote the article. ZA: Conducted the antioxidant activity and enzyme activity experiments. AÖD: Performed the antimicrobial, antibiofilm experiments. All authors contributed to the study conception and design. The authors read and approved the final manuscript.

References

- [1] S. Vlasisavljević, S. Jelača, G. Zengin, N. Mimica-Dukić, S. Berežni, M. Miljić, Z.D. Stevanović, *Alchemilla vulgaris* agg. (Lady's mantle) from central Balkan: antioxidant, anticancer and enzyme inhibition properties, RSC adv, 9(64), 2019, 37474-37483.
- [2] W. Sun, M.H. Shahrajabian, Therapeutic potential of phenolic compounds in medicinal plants—Natural health products for human health, *Molecules*, 28(4), 2023, 1845.
- [3] S. Vishwakarma, V. Chaudhry, S. Chand, K. Sagar, K.K. Gupta, N. Bhardwaj, R. Prasad, P. Kumar, H. Chandra, The potential of fungal endophytes in plants: sources of bioactive compounds, *Indian J Microbiol*, 2024, 1-15.
- [4] S.S. Pammi, B. Suresh, A. Giri, Antioxidant potential of medicinal plants, *Journal of Crop Science and Biotechnology*, 26(1), 2023, 13-26.
- [5] C. Nirmala, M.S. Bisht, H.K. Bajwa, O. Santosh, Bamboo: A rich source of natural antioxidants and its applications in the food

- and pharmaceutical industry, Trends Food Sci Tech, 77, 2018, 91-99.
- [6] S. Kanak, B. Krzemińska, R. Celiński, M. Bakalczuk, K. Dos Santos Szewczyk, Phenolic composition and antioxidant activity of *Alchemilla* species. Plants, 11(20), 2022, 2709.
 - [7] T. Boroja, V. Mihailović, J. Katanić, S.P. Pan, S. Nikles, P. Imbimbo, D.M. Monti, N. Stanković, M.S. Stanković, R. Bauer, The biological activities of roots and aerial parts of *Alchemilla vulgaris* L. S Afr J Bot, 116, 2018, 175-184.
 - [8] E. Neagu, G. Paun, C. Albu, G.L. Radu, Assessment of acetylcholinesterase and tyrosinase inhibitory and antioxidant activity of *Alchemilla vulgaris* and *Filipendula ulmaria* extracts, J Taiwan Inst Chem E, 52, 2015, 1-6.
 - [9] A.T. Mansour, H.H. Mahboub, G.E. Elshopakey, E.K. Aziz, A.H. Alhajji, G. Rayan, H.S. Ghazzawy, W. El-Houseiny, Physiological performance, antioxidant and immune status, columnaris resistance, and growth of Nile tilapia that received *Alchemilla vulgaris*-supplemented diets, Antioxidants, 11(8), 2022, 1494.
 - [10] A.A. Alfadda, R.M. Sallam, Reactive oxygen species in health and disease, BioMed research international, 2012(1), 2012, 936486.
 - [11] E. Choe, D.B. Min, Mechanisms of antioxidants in the oxidation of foods, Comp Rev Food Sci F, 8(4), 2009, 345-358.
 - [12] E. Kupriyanova, N. Pronina, D. Los, Carbonic Anhydrase-a Universal Enzyme of the Carbon-Based Life, Photosynthetica, 55(1), 2017, 3-19.
 - [13] C.T. Supuran, Structure-Based Drug Discovery of Carbonic Anhydrase Inhibitors, J Enzym Inhib Med Ch, 27, 2012, 759-772.
 - [14] M. Safithri, Y.P. Sari, Inhibition of α -glucosidase activity by ethanolic extract of *Melia azedarach* L. leaves, IOP Conference Series: Earth and Environmental Science, 31(1), 2016, 012025.
 - [15] R. Rangarajan, R. Venkataraman, Antibiotics targeting Gram-negative bacteria, In Drug Discovery Targeting Drug-Resistant Bacteria, Academic Press, 2020, 39-70.
 - [16] S. Jelača, Z. Dajić-Stevanović, N. Vuković, S. Kolašinac, A. Trendafilova, P. Nedialkov, M. Stankovic, N. Tanic, N.T. Tanic, A. Acovic, S. Mijatovic, D. Maksimović-Ivanić, Beyond traditional use of *Alchemilla vulgaris*: genoprotective and antitumor activity in vitro, Molecules, 27(23), 2022, 8113.
 - [17] K. Slinkard, V.L. Singleton, Total phenol analysis: Automation and comparison with manual methods, Am J Enol Viticult, 28, 1977, 49–55.
 - [18] L.R. Fukumoto, G. Mazza, Assessing antioxidant and prooxidant activities of phenolic compounds, J Agric Food Chem, 48 (8), 2000, 3597–3604.
 - [19] W. Brand-Williams, M.E. Cuvelier, C. Berset, Use of a free radical method to evaluate antioxidant activity, Lwt-Food Sci Technol, 28 (1), 1995, 25–30.
 - [20] R. Re, N. Pellegrini, A. Proteggente, A. Pannala, M. Yang, C. Rice-Evans, Antioxidant activity applying an improved ABTS radical cation decolorization assay, Free Radical Bio Med, 26 (9-10), 1999, 1231–1237.
 - [21] I.F.F. Benzie, J.J. Strain, The ferric reducing ability of plasma (FRAP) as a measure of "antioxidant power": the FRAP assay, Anal Biochem, 239 (1), 1996, 70–76.
 - [22] R. Apak, K. Güçlü, M. Özyürek, S.E. Karademir, Novel total antioxidant capacity index for dietary polyphenols and vitamins C and E, using their cupric ion reducing capability in the presence of neocuproine: CUPRAC method, J Agr Food Chem, 52(26), 2004, 7970-7981.
 - [23] E. Gültekin, U. Kardil, Y. Topaloğlu, M. Ocak, N. Yıldırım, S. Alkan, M. Küçük, H. Bektaş, O. Bekircan, Synthesis of some new 1, 2, 4-triazole derivatives, investigation of their fluorescence properties and biological activities, Karadeniz Chemical Science and Technology 1, 2017, 36-42.
 - [24] Z. Yu, Y. Yin, W. Zhao, J. Liu, F. Chen, Anti-diabetic activity peptides from albumin against α -glucosidase and α -amylase, Food Chem, 135, 2012, 2078–2085.
 - [25] O. Üçüncü, C. Baltacı, Z. Akar, A. Duzgun, M. Cuce, A. Kandemir, Biological activities and phytochemical screening of ethanol extracts from *Adonis paryadrica* (*Ranunculaceae*), Farmacia, 68(6), 2020, 1062-1068.
 - [26] M. Çimen, A.Ö. Düzgün, Antibiotic induced biofilm formation of novel multidrug resistant *Acinetobacter baumannii* ST2121 clone, Acta Microbiol Imm H, 68, 2020, 80–86.
 - [27] M. Tasić-Kostov, I. Arsić, D. Pavlović, S. Stojanović, S. Najman, S. Naumović, V. Tadić, Towards a modern approach to traditional use: in vitro and in vivo evaluation of *Alchemilla vulgaris* L. gel wound healing potential, J Ethnopharmacol, 238, 2019, 111789.
 - [28] M. Şentürk, İ. Gülçin, Ş. Beydemir, Ö.İ. Küfrevioğlu, C.T. Supuran, In vitro inhibition of human carbonic anhydrase I and II isozymes with natural phenolic compounds, Chem Biol Drug Des, 77(6), 2011, 494-499.
 - [29] L. Güven, A. Ertürk, M. Yılmaz, S. Alwasel, İ. Gülçin, *Alchemilla pseudocartalinica* Juz: phytochemical screening by UPLC-MS/MS, molecular docking, anti-oxidant, anti-diabetic, anti-glaucoma, and anti-Alzheimer effects, Rec Nat Prod, 18(2), 2024, 251-272.
 - [30] Ç. Uzunkaya, İ. Gökkaya, D. Akkaya, M. Şoral, G. Seyhan, B. Barut, M.A. Yılmaz, G. Renda, Phytochemical Analysis and Assessment of Antioxidant and Enzyme Inhibitory Activity of *Alchemilla pseudocartalinica* Juz., Chem Biodivers, e202401217.
 - [31] S. Samah, K. Abdullah, N. Ream, Phytochemical screening of *Alchemilla vulgaris*, *Sophora Japonica*, *Crataegus azarolus*, and their inhibitory activity on lipase and α -amylase. IJASR, 6, 2018, 01-21.
 - [32] E. Kurtul, M. Eryilmaz, S.Y. Sarialtin, M. Tekin, Ö.B. Acikara, T. Çoban, Bioactivities of *Alchemilla mollis*, *Alchemilla persica* and their active constituents, Braz J Pharm Sci, 58, 2022, e18373.
 - [33] Ş. İnci, A. Eren, S. Kirbağ, Determination of antimicrobial and antioxidant activity of *Alchemilla alpina* L., Türk J Agric-Food Sci Tech, 9(12), 2021, 2260-2264.
 - [34] O.H. Ibrahim, K.A. Abo-Elyousr, K.A. Asiry, N.A. Alhakamy, M.A. Mousa, Phytochemical characterization, antimicrobial activity and in vitro antiproliferative potential of *Alchemilla vulgaris* Auct root extract against prostate (PC-3), breast (MCF-7) and colorectal adenocarcinoma (Caco-2) cancer cell lines. Plants, 11(16), 2022, 2140.
 - [35] B. Kaya, Y. Artuvan, F. Caf, Y. Menemen, Investigation antioxidant, antimicrobial effect and phenolic compounds of *Alchemilla holotrichia* extracts in different polarities, Turkish Journal of Nature and Science, 13(3), 2024, 99-108.
 - [36] A. Gedefie, W. Demsis, M. Ashagrie, Y. Kassa, M. Tesfaye, M. Tilahun, H. Bisetegn, Z. Sahle, *Acinetobacter baumannii* Biofilm Formation and Its Role in Disease Pathogenesis: A Review, Infect Drug Resist, 10(14), 2021, 3711-3719.
 - [37] U. Kardil, Z. Akar, A. Özad Düzgün, Antibiofilm, Antidiabetic and Antioxidant Potentials of *Vitis labrusca* L. Skin Extracts, Journal of Anatolian Environmental and Animal Sciences, 9(4), 2024, 590-597.
 - [38] U. Kardil, Z. Akar, A. Özad Düzgün, Investigation of antibiofilm and biological activities of *Vaccinium arctostaphylos* L., Turkish Journal of Analytical Chemistry, 6(1), 2024, 25-31.
 - [39] S. Ouslimani, M. Bendahou, K. Abedelmounaim, F. Benbelaid, F. Mahdi, M. Yassine Benziane, J. Costa, Antibacterial and anti-biofilm efficiency of twenty algerian plants essential oils against resistant *Acinetobacter baumannii*, J Essent Oil Bear Pl, 26(1), 2023, 206-231.



Synthesis, characterization and antioxidant activity of sulfonyl-1H-1,2,3-triazoles

Fatih Çelik 

Karadeniz Technical University, Faculty of Sciences, Department of Chemistry, 61080 Trabzon, Türkiye

Abstract

The compounds were characterized by FT-IR (Fourier Transform Infrared Spectroscopy), ^1H -NMR (Proton Nuclear Magnetic Resonance Spectroscopy) and ^{13}C -NMR (Carbon Nuclear Magnetic Resonance Spectroscopy) methods. The antioxidant properties of the compounds were evaluated using two widely accepted methodologies assays DPPH (1,1-Diphenyl-2-picrylhydrazyl radical; $\text{C}_{18}\text{H}_{12}\text{N}_5\text{O}_6$) and FRAP (Determination of Ferric Reducing Antioxidant Power). Compounds **7** and **10** emerged as the most potent antioxidant candidates, displaying the strongest effects in both assays.

Keywords: 1,2,3-triazole, organic synthesis, antioxidant activity, FRAP assay

1. Introduction

Sulfonyl compounds and 1,2,3-triazoles are important and versatile structures in the field of organic chemistry, notable for their biological activities, chemical stability, and wide range of applications. These compounds are of great significance both in pharmaceutical research and industrial chemistry. Due to their unique structures, these two classes of compounds can undergo a variety of chemical reactions and interact with biological systems. The sulfonyl group refers to a structure in which a sulfur atom is bonded to two oxygen atoms and a carbon group. The compounds containing this group can be generally represented by the formula $\text{R-SO}_2\text{-}$. The sulfonyl group holds a significant place in organic chemistry due to its chemical bondability and reactivity. Sulfonyl compounds are widely used in many industrial products, such as pharmaceutical molecules, polymers, agricultural chemicals, detergents, dyes, and plastics. The biological effects of sulfonyl compounds are quite diverse. These compounds can exhibit antimicrobial, antitumor, anti-inflammatory, and analgesic properties. Especially in the pharmaceutical field, drugs containing sulfonyl groups are highlighted as effective therapeutic agents due to their high affinity for specific targets. Additionally, molecules containing sulfonyl groups are being researched as potential therapeutic agents for cancer, diabetes, and HIV treatment. The interaction of sulfonyl groups with biological systems often results in the

activation or inhibition of proteins, making them an important building block in drug design. Furthermore, sulfonyl compounds can also act as catalysts in chemical reactions because these compounds, with their electrophilic properties, can interact with different reactants to carry out various chemical transformations [1–12]. 1,2,3-Triazoles are known for their biological activities, with many triazole derivatives demonstrating antimicrobial, antifungal, antiviral, anticancer, and anti-inflammatory effects. 1,2,3-Triazoles are part of the most well-known class of antifungal drugs, azoles, and are thus used in the treatment of fungal infections. Moreover, numerous studies have explored the potential of triazole derivatives as therapeutic agents, particularly in the treatment of cancer and neurological diseases. Sulfonyl compounds and 1,2,3-triazoles are frequently studied in combination with one another in organic chemistry. The advantage of such combinations lies in the merging of the biological and chemical activities of both structures. These combinations can be used to create new strategies in molecular design. While the triazole ring facilitates binding to biological targets, the sulfonyl group enhances the reactivity and stability of the molecule, increasing its overall efficacy. The combination of triazole and sulfonyl compounds can also be useful in catalytic processes, as both groups serve as active building blocks for various chemical transformations [13–21].

Citation: F. Çelik, Synthesis, characterization and antioxidant activity of sulfonyl-1H-1,2,3-triazoles, Turk J Anal Chem, 7(2), 2025, 176–181.

Author of correspondence: fatih.celik502@gmail.com

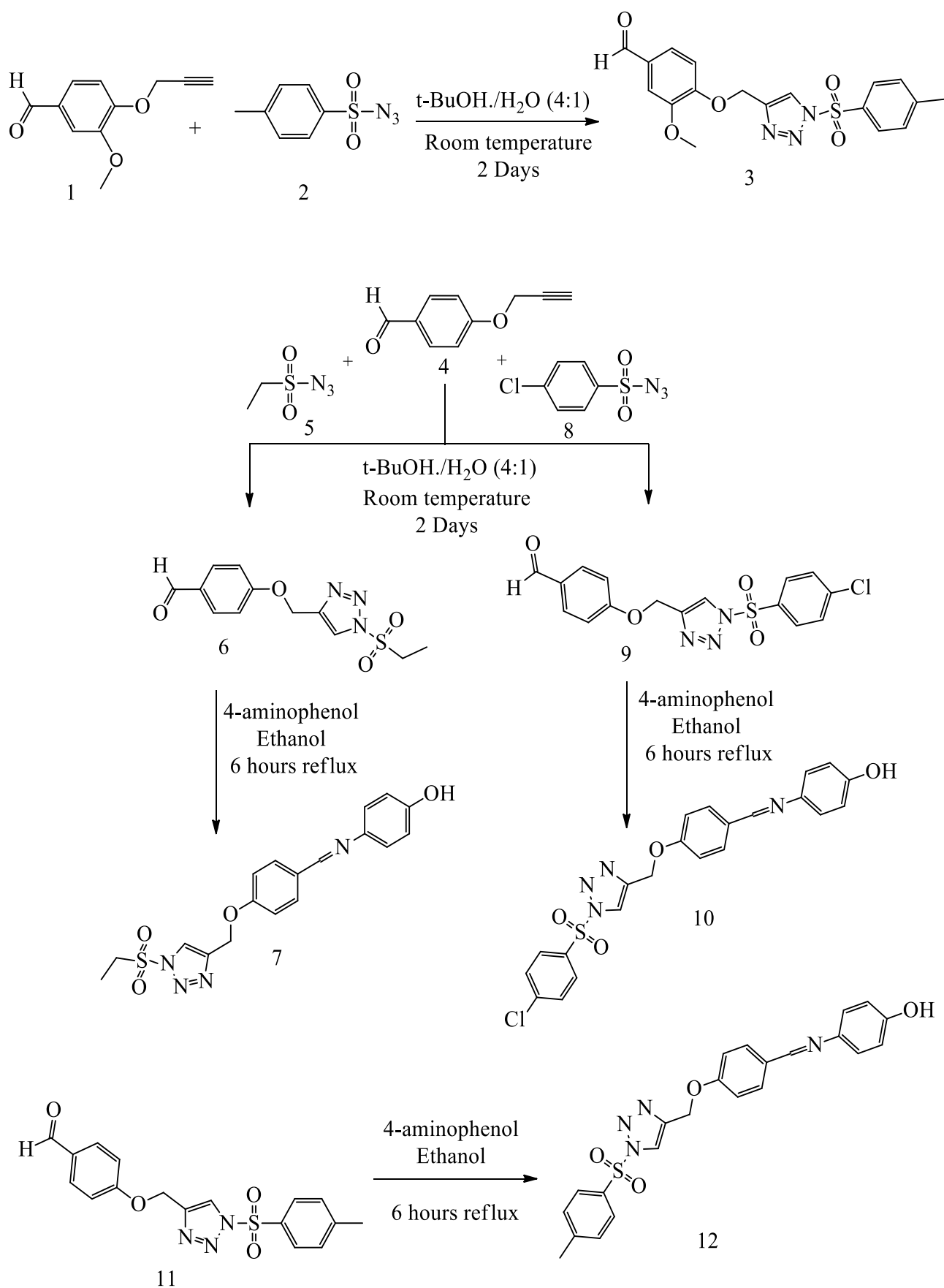
Tel: +90 (462) 377 25 25

Fax: +90 (462) 325 31 96

Received: March 26, 2025

Accepted: April 24, 2025

doi <https://doi.org/10.51435/turkjac.1665889>



Scheme 1. Synthetic pathway for the preparation of compounds 3,6,7,9,10,12

2. Experimental

2.1. Instrumentation

IR spectra of the synthesized compounds were taken on a Perkin Elmer FT-IR 1600 FT-IR (4000-400 cm^{-1}) spectrophotometer device, and ^1H -NMR, ^{13}C -NMR spectra were taken on a Bruker brand 400 MHz NMR device with DMSO- d_6 (Dimethyl sulfoxide- d_6) solvent. The solvents and chemicals used in synthesis and structure elucidation were obtained from Fluka, Merck and Aldrich companies, and all solvents were subjected to appropriate purification and drying processes. Compounds **1** and **2** were synthesized literature [22,23].

2.2. Synthesis of 3-methoxy-4-((1-tosyl-1H-1,2,3-triazol-4-yl)methoxy)benzaldehyde (3):

3-Methoxy-4-(prop-2-yn-1-yloxy)benzaldehyde (**1**) (1 mmol) and 4-methylbenzenesulfonyl azide (**2**) (1 mmol) was mixed in water/t-butanol (1:4) Then copper sulfate pentahydrate %98 (1/20 mol) and sodium ascorbate %98 (1/10 mol) were added to the reaction mixture. The reaction mixture was stirred at room temperature for 2 days. At the end of the reaction the contents of the flask were poured into the ice-water mixture, the resulting solid was filtered and washed with water, crystallized with N,N-Dimethylformamide (DMF)-water (Scheme 1).

Yield: 88.02%; m.p.170-172°C; IR (ν, cm^{-1}): 1742 (C=O), 1587 (C=C), 1265 (C-O), 1123 (C-SO₂); ^1H -NMR (δ ppm): 2.39 (s, 3H, CH₃), 3.78 (s, 3H, OCH₃), 4.20 (s, 2H, OCH₂), Arom. [7.12 (bs, 1H, CH), 7.40 (bs, 3H, CH), 7.50 (bs, 1H, CH), 7.80 (bs, 2H, CH)], 9.84 (s, 1H, 1,2,3-trz.CH), 12.26 (s, 1H, HC=O); ^{13}C -NMR (δ ppm): 21.53 (CH₃), 56.06 (OCH₃), 64.14 (OCH₂), Arom. C [110.39 (CH), 126.43 (CH), 127.98 (CH), 149.58(C), 153.56(C) 169.47(C) 4-CH₃-Ph C (122.73 (CH), 130.00 (CH), 136.89 (C), 144.71 (C)], 112.73 1,2,3-trz.(CH), 130.29 1,2,3-trz.(C), 191.87 (HC=O).

2.3. Synthesis of compounds (6,9)

Compound 4-(prop-2-yn-1-yloxy)benzaldehyde (**4**) (1 mmol) separately with ethanesulfonyl azide (**5**) and 4-chlorobenzenesulfonyl azide (**8**) (1 mmol) water/t-butanol (1: 4) mixed in. Then, copper sulfate pentahydrate %98 (1/20 mol) and sodium ascorbate %98 (1/10 mol) were added to the reaction mixture. The reaction mixture was stirred at room temperature for 2 days. At the end of the reaction, the contents of the flask were poured into the ice-water mixture, and the solid obtained was filtered and washed with water. It was crystallized with DMF-water.

2.3.1. 4-((1-(Ethylsulfonyl)-1H-1,2,3-triazol-4-yl)methoxy)benzaldehyde (6):

Yield: 89.08%; m.p.160-162°C; IR (ν, cm^{-1}): 1705 (C=O), 1600 (C=C), 1255 (C-O), 1130 (C-SO₂); ^1H -NMR (δ ppm):

1.20 (t, 3H, CH₃) 2.85 (q, 2H, SCH₂), 4.32 (s, 2H, OCH₂), Arom. [7.14 (d, 2H, CH), 7.88 (d, 2H, CH)], 9.88 (s, 1H, 1,2,3-trz.CH), 11.81 (s, 1H, HC=O); ^{13}C -NMR (δ ppm): 8.22 (CH₃), 47.01 (SCH₂), 63.98 (OCH₂), Arom. C [115,54 (CH), 132.31 (CH), 163.49 (C), 170.57(C)], 115.70 (1,2,3-trz.(CH)), 130.14 (1,2,3-trz.(C)), 191.88 (HC=O).

2.3.2. 4-((1-((4-Chlorophenyl)sulfonyl)-1H-1,2,3-triazol-4-yl)methoxy)benzaldehyde (9):

Yield: 90.12%; m.p.185-187°C; IR (ν, cm^{-1}): 1729 (C=O), 1604 (C=C), 1258 (C-O) 1130 (C-SO₂); ^1H -NMR (δ ppm): 4.22 (s, 2H, OCH₂), Arom. [7.01 (d, 2H, CH), 7.72 (d, 2H, CH), 7.85 (d, 2H, CH), 7.94 (d, 2H, CH)], 9.96 (s, 1H, 1,2,3-trz.CH), 12.14 (s, 1H, HC=O); ^{13}C -NMR (δ ppm): 63.83 (OCH₂), Arom. C [115,70 (CH), 129.79 (CH), 163.51 (C), 169.73(C), 4-Cl-Ph C (129.99 (CH), 132.22 (CH), 138.52 (C), 139.15 (C)], 115.70 (1,2,3-trz.(CH)), 130.20 (1,2,3-trz.(C)), 191.96 (HC=O).

2.4. Synthesis of compounds (7,10,12)

Compounds 7,10,12 (1 mmol) were mixed separately in 4-aminophenol and ethanol a round bottom flask and refluxed for 6 hours. At the end of the reaction, the contents of the balloon were kept in the refrigerator overnight. The solid formed as a result of standing was filtered, washed with water and crystallized with DMF-water and dried.

2.4.1. 4-((4-((1-(Ethylsulfonyl)-1H-1,2,3-triazol-4-yl)methoxy)benzylidene)amino)phenol (7):

Yield: 91.25%; m.p.180-182°C; IR (ν, cm^{-1}): 3221 (OH), 1577 (N=CH), 1606 (C=C), 1254 (C-O), 1138 (C-SO₂); ^1H -NMR (δ ppm): 1.20 (t, 3H, CH₃) 2.82 (q, 2H, SCH₂), 4.28 (s, 2H, OCH₂), Arom. [6.79 (d, 2H, CH), 7.04 (d, 2H, CH), 7.16 (d, 2H, CH), 7.84 (d, 2H, CH)], 8.52 (s, 1H, 1,2,3-trz.CH), 9.45 (s, 1H, N=CH), 11.63 (s, 1H, OH); ^{13}C -NMR (δ ppm): 8.24 (CH₃), 46.99 (SCH₂), 63.60 (OCH₂), Arom. C [115.12 (CH), 132.50 (CH), 156.00 (C), 160.00(C), 4-OH-Ph C (116.12 (CH), 130.45 (CH), 143.41 (C), 170.00(C)], 122.74 (1,2,3-trz.(CH)), 130.05 (1,2,3-trz.(C)), 157.00 (N=CH).

2.4.2. 4-((4-((1-((4-Chlorophenyl)sulfonyl)-1H-1,2,3-triazol-4-yl)methoxy)benzylidene)amino)phenol (10):

Yield: 93.32%; m.p.201-203°C; IR (ν, cm^{-1}): 3384 (OH), 1573 (N=CH), 1605 (C=C), 1241 (C-O), 1158 (C-SO₂); ^1H -NMR (δ ppm): 4.15 (s, 2H, OCH₂), Arom. [6.79 (d, 2H, CH), 6.92 (bs, 2H, CH), 7.14 (bs, 2H, CH), 7.72 (bs, 2H, CH) 7.79 (bs, 2H, CH), 7.94 (bs, 2H, CH)], 8.51 (s, 1H, 1,2,3-trz.CH), 9.45 (s, 1H, N=CH), 11.96 (s, 1H, OH); ^{13}C -NMR (δ ppm): 63.93 (OCH₂), Arom. C [115.07 (CH), 129.97 (CH), 156.37 (C), 160.77(C), 4-OH-Ph C (116.12 (CH), 130.38 (CH), 143.38 (C), 170.09(C)), 4-Cl-Ph

C(129.74 (CH), 132.23 (CH), 138.72(C), 139.01(C)), 122.74 (1,2,3-trz.(CH)), 138.72 (1,2,3-trz.(C)), 157.00 (N=CH).

2.4.3. 4-((4-((1-Tosyl-1H-1,2,3-triazol-4-yl) benzyldene)amino) phenol (12):

Yield: 95.41%; m.p.211-213°C; IR (ν ,cm⁻¹): 3383 (OH), 1574 (N=CH), 1605 (C=C), 1241 (C-O), 1156 (C-SO₂); ¹H-NMR (δ ppm): 2.39 (s, 3H, CH₃) 4.36 (s, 2H, OCH₂), Arom. [6.79 (d, 2H, CH), 6.93 (bs, 2H, CH), 7.15 (bs, 2H, CH), 7.42 (bs, 2H, CH) 7.81 (bs, 4H, CH)], 8.51 (s, 1H,1,2,3-trz.CH), 9.46 (s,1H, N=CH), 12.01 (s,1H, OH); ¹³C-NMR (δ ppm): 21.54 (CH₃), 63.57 (OCH₂), Arom. C [115.09 (CH), 128.00 (CH), 156.36 (C), 160.92(C), 4-OH-Ph C(116.12 (CH), 130.37 (CH), 144.24 (C), 169.70(C)), 4-CH₃-Ph C(129.99 (CH), 132.23 (CH), 137.20(C), 140.26(C)), 122.74 (1,2,3-trz.(CH)), 134.24 (1,2,3-trz.(C)), 157.01 (N=CH).

2.5. Antioxidant activity

The antioxidant properties of the compounds were evaluated using two widely accepted methodologies: the DPPH and FRAP assays, renowned for their effectiveness in gauging the antioxidant potential of diverse compounds. The DPPH assay, adapted from [24] measures the compounds' ability to scavenge the DPPH radical. This method relies on the decolorization of the purple DPPH solution (0.1 mM) upon interaction with antioxidants. Absorbance changes at 517 nm, recorded spectrophotometrically, indicate the degree of radical scavenging activity. Results, reported as SC₅₀ values (μ g of sample per mL), delineate the concentration required for a 50% reduction in the DPPH radical compared to the standard Trolox.

Concurrently, the antioxidant capacity was determined through the FRAP method, following the protocol described by [25]. This approach involves the reduction of the Fe³⁺-TPTZ complex to the Fe²⁺-TPTZ complex in the presence of antioxidants. Spectrophotometric readings at 593 nm after a 4-minute incubation period elucidate the compounds ability to reduce ferric ions. Results are expressed as μ M Trolox equivalent per milligram of compound, where higher Trolox equivalent values denote elevated FRAP and hence increased antioxidant efficacy.

Both assays serve as robust tools for assessing the antioxidant prowess of compounds, providing valuable insights into their capacity to neutralize free radicals and reduce ferric ions. These standardized methodologies offer a comparative analysis of diverse compounds, enabling a comprehensive evaluation of their antioxidant capabilities. All experiments were conducted in three independent repetitions.

3. Results and discussion

3.1. Synthesis

Sulfonyl-1H-1,2,3-triazoles (6,7,9,10,12) 3-methoxy-4-((1-tosyl-1H-1,2,3-triazol-4-yl)methoxy)benzaldehyde (3), 4-((1-(ethylsulfonyl)-1H-1,2,3-triazol-4-yl) methoxy) benzaldehyde (6), 4-((4-((1-(ethylsulfonyl)-1H-1,2,3-triazol-4-yl) methoxy) benzyldene) amino)phenol (7), 4-((1-((4-chloro phenyl) sulfonyl)-1H-1,2,3-triazol-4-yl) methoxy) benzaldehyde (9), 4-((4-((1-((4-chlorophenyl) sulfonyl)-1H-1,2,3-triazol-4-yl) methoxy) benzyldene) amino) phenol (10), 4-((4-((1-tosyl-1H-1,2,3-triazol-4-yl) methoxy) benzyldene)amino) phenol (12) were synthesized. The compounds were characterized by FTIR, ¹H-NMR and ¹³C-NMR spectroscopic methods. The most important evidence that the reaction took place is the proton and carbon data of the 1,2,3 triazole ring. C-H proton signal belonging to 1,2,3-triazole ring was seen at 8.51-9.88 ppm as a singlet in the ¹H NMR spectra of these compounds. Carbon peaks belonging to 1,2,3 triazole ring were observed at 115.70-138.72 ppm in the ¹³C- NMR spectra of these compounds. Other proton and carbon data belonging to the compounds also appeared in the desired regions.

3.2. Antioxidant activity

The antioxidant properties of the analyzed compounds were assessed using the DPPH radical scavenging assay and the FRAP (Ferric Reducing Antioxidant Power) assay. The obtained results highlight significant variability in antioxidant activities among the tested compounds.

Table 1. DPPH and FRAP activities of compounds 3, 6, 7, 9, 10 and 12

Compound	DPPH (IC ₅₀ : mg/mL)*	FRAP (μ M Trolox Equivalent/mg compound)*
3	2,452±0,029 ^d	79,51±0,42 ^c
6	1,44±0,031 ^b	35,34±0,82 ^c
7	0,022±0,002 ^a	6204,82±75,87 ^a
9	2,125±0,022 ^c	25,97±0,19 ^c
10	0,009±0,000 ^a	4933,99±35,68 ^b
12	3,475±0,003 ^e	16,38±0,65 ^c
Trolox	0,0074±0,000 ^a	Not tested

*Same letters in each column were not significantly different at P < 0.05 (Tukey's range test). The means of three replicates were given with \pm standard deviations.

The DPPH assay was employed to evaluate the free radical scavenging potential of the compounds, where a lower IC₅₀ value corresponds to a higher antioxidant capacity. Among the tested compounds, compound 10 exhibited the strongest radical scavenging activity (IC₅₀ = 0.009 mg/mL), followed by compound 7 (IC₅₀ = 0.022 mg/mL). Both demonstrated a considerably higher efficiency in scavenging free radicals than the reference antioxidant Trolox (IC₅₀ = 0.121 mg/mL).

Compound **6** ($IC_{50} = 1.44$ mg/mL) displayed relatively high scavenging activity, while compound **9** ($IC_{50} = 2.12$ mg/mL) and compound **3** ($IC_{50} = 2.45$ mg/mL) were in the moderate range. Compound **12** ($IC_{50} = 3.47$ mg/mL) was the least effective among the tested compounds in terms of radical scavenging.

The FRAP assay, which measures the capacity of compounds to reduce Fe^{3+} to Fe^{2+} , revealed that compound **7** (6204.82 μ M Trolox equivalent/mg compound) had the highest reducing power, followed by compound **10** (4933.99 μ M Trolox equivalent/mg compound). These results indicate that these two compounds possess strong electron-donating abilities. Compound **3** exhibited moderate reducing power (79.51 μ M Trolox equivalent/mg compound), whereas compound **6** (35.34 μ M), compound **9** (25.97 μ M), and compound **12** (16.38 μ M) demonstrated relatively weak activity.

Overall, compounds **7** and **10** emerged as the most potent antioxidant candidates, displaying the strongest effects in both assays. Compounds **6**, **9**, and **3** exhibited moderate antioxidant activity, while compound **12** had the weakest performance. The significantly higher antioxidant potential of compounds **7** and **10** compared to Trolox suggests that they may serve as promising antioxidant agents.

Acknowledgment

The author thanks Dr. Ersan Bektaş for antioxidant studies.

References

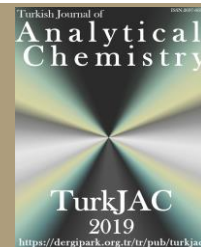
- [1] M. Feng, B. Tang, S.H. Liang, X. Jiang, Sulfur Containing Scaffolds in Drugs: Synthesis and Application in Medicinal Chemistry, *Curr Top Med Chem*, 16, 2016, 1200-1216.
- [2] P. Devendar, G.F. Yang, Sulfur-Containing Agrochemicals, *Curr Top Med Chem*, 82, 2017, 375-382.
- [3] S. Maker, T. Saha, S.K. Singh, Naphthalene, a versatile platform in medicinal chemistry: Sky-high perspective, *Eur J Med Chem*, 161, 2019, 252-276.
- [4] R.S. Burden, M.S. Kemp, (-)-7-Hydroxycalamenene, A Phytoalexin From *Tilia europaea*, *Phytochemistry*, 22, 1983, 1039-1040.
- [5] S. Rohrbach, A.J. Smith, J.H. Pang, D.L. Poole, T. Tuttle, S. Chiba, J.A. Murphy, Concerted Nucleophilic Aromatic Substitution Reactions, *Angew Chem Int Ed*, 58, 2019, 16368-16388.
- [6] V. Palani, M.A. Perea, R. Sarpong, Site-Selective Cross-Coupling of Polyhalogenated Arenes and Heteroarenes with Identical Halogen Groups, *Chem Rev*, 122, 2022, 10126-10169.
- [7] B. Swami, D. Yadav, R.S. Menon, Benzannulation and N-Annulation of β -Ketoenamines for Synthesizing Aniline and Pyridine Derivatives Using DMSO as a Methine Source, *Chem Rec*, 22, 2022, 3736-3742.
- [8] T. Bera, K. Pandey, R. Ali, The Dötz Benzannulation Reaction: A Booming Methodology for Natural Product Synthesis, *Chem Select*, 5, 2020, 5239-5267.
- [9] S.J. Hein, D. Lehnher, H. Arslan, F.J. Uribe-Romo, W.R. Dichtel, Alkyne Benzannulation Reactions for the Synthesis of Novel Aromatic Architectures, *Acc Chem Res*, 50, 2017, 2776-2788.
- [10] L.J. Wu, L.F. Yang, J.H. Li, Q.A. Wang, Dicarbonylative benzannulation of 3-acetoxy-1,4-enynes with CO and silylboranes by Pd and Cu cooperative catalysis: one-step access to 3-hydroxyarylacetylsilanes, *Chem Commun*, 56, 2020, 1669-1672.
- [11] T.N. Poudel, R.J.I. Tamargo, H. Cai, Y.R. Lee, Recent Progress in Transition-Metal-Free, Base-Mediated Benzannulation Reactions for the Synthesis of a Diverse Range of Aromatic and Heteroaromatic Compounds, *Asian J Org Chem*, 7, 2018, 985-1005.
- [12] J. Xue, E. Gao, X.N. Wang, J. Chang, Metal-Free Formal Inverse-Electron-Demand Diels–Alder Reaction of 1,2-Diazines with Ynamides, *Org Lett*, 20, 2018, 6055-6058.
- [13] D. Gonzaga, M.R. Senger, F.D.C. Da Silva, V.F. Ferreira, F.P. Silva, 1-Phenyl-1H- and 2-phenyl-2H-1,2,3-triazol derivatives: Design, synthesis and inhibitory effect on alpha-glycosidases, *Eur J Med Chem*, 74, 2014, 461-476.
- [14] P. Sambasiva Rao, C. Kurumurthy, B. Veeraswamy, G. Santhosh Kumar, Y. Poornachandra, C. Ganesh Kumar, S.B. Vasamsetti, S. Kotamraju, B. Narsaiah, Synthesis of novel 1,2,3-triazole substituted-N-alkyl/aryl nitron derivatives, their anti-inflammatory and anticancer activity, *Eur J Med Chem*, 80, 2014, 184-191.
- [15] S.B. Ferreira, M.S. Costa, N. Boechat, J.S.R. Bezerra, M.S. Genestra, M.M. Canto-Cavalheiro, W.B. Kover, V.F. Ferreira, Synthesis and evaluation of new difluoromethyl azoles as antileishmanial agents, *Eur J Med Chem*, 42, 2007, 1388-1395.
- [16] Z.Y. Sheng, T.X.Y. Tang, M. Shi, Unprecedented synthesis of aza-bridged benzodioxepine derivatives through a tandem Rh(ii)-catalyzed 1,3-rearrangement/[3+2] cycloaddition of carbonyltriazoles, *Chem Commun*, 50, 2014, 15971-15974.
- [17] M.S. Costa, N. Boechat, E.A. Rangel, F.C. Silva, A.M.T. Souza, C.R. Rodrigues, H.C. Castro, I.N. Junior, M.C.S. Lourenço, S.M.S.V. Wardell, V.F. Ferreira, Synthesis, tuberculosis inhibitory activity, and SAR study of N-substituted-phenyl-1,2,3-triazole derivatives, *Med Chem*, 14, 2006, 8644-8653.
- [18] M.M. Pisal, R.A. Annadate, M.C. Athalye, D. Kumar, S.P. Chavan, D. Sarkar, H.B. Borate, Synthesis and cell imaging applications of fluorescent mono/di/tri-heterocycl-2,6-dicyanoanilines, *Bioorg Med Chem Lett*, 27, 2017, 979-988.
- [19] H. Hagiwara, R. Minoura, S. Okada, Y. Sunatsuki, Synthesis, Structure, and Magnetic Property of a New Mononuclear Iron(II) Spin Crossover Complex with a Tripodal Ligand Containing Three 1,2,3-Triazole Groups, *Chem Lett*, 43, 2014, 950-952.
- [20] H. Hagiwara, S. Okada, A polymorphism-dependent T1/2 shift of 100 K in a hysteretic spin-crossover complex related to differences in intermolecular weak CH...X hydrogen bonds (X = S vs. S and N), *Chem Commun*, 52, 2016, 815-818.
- [21] H. Hagiwara, T. Tanaka, S. Hora, Synthesis, structure, and spin crossover above room temperature of a mononuclear and related dinuclear double helicate iron(ii) complexes, *Dalton Trans*, 45, 2016, 17132-17140.
- [22] H.S. Armiger, D.B. James, Preparation of Some Organic Diazides, Contribution from the Research Division of Abbott Laboratories, *J Org Chem*, 9, 1957, 3491-3492.
- [23] R.H. Hager, E.M. Green, C. Liu, P.S. Jurs, W. Baojie, G.F. Scott, G. Jiri, J.R. Philip, C. Kelly, Synthesis, antimalarial and antitubercular activity of acetylenic chalcones, *Bioorg Med Chem Lett*, 20, 2010, 942-944.
- [24] M. Cuendet, K. Hostettmann, O. Potterat, W. Dyatmiko, Iridoid Glucosides with Free Radical Scavenging Properties from *Fagraea blumei*, *Helv Chim Acta*, 80, 1997, 1144-1152.

- [25] I.F. Benzie, J.J. Strain, The ferric reducing ability of plasma (FRAP) as a measure of "antioxidant power": the FRAP assay, *Anal Biochem*, 239, 1996, 70-76.



TurkJAC

Turkish Journal of Analytical Chemistry

<https://dergipark.org.tr/tr/pub/turkjac>

Comparison of some mineral and trace-heavy metal contents of blossom honey samples from Yamadağ and Battalgazi regions, Malatya, Türkiye

Semiramis Karlıdağ^{1*} , Sevgi Kolaylı² 

¹ Malatya Turgut Ozal University, Battalgazi Vocational School, Plants and Animal Production Department, 44210, Malatya, Türkiye

² Karadeniz Technical University, Faculty of Sciences, Department of Chemistry, 61080, Trabzon, Türkiye

Abstract

Among bee products, honey is particularly valued for its nutritional profile, notably its content of essential macro- and microelements. The mineral composition of honey is shaped by the interplay of geographic origin, botanical source, and bee genotype. This study aimed to (i) characterize the trace element profiles of honey samples harvested from Yamadağ Mountain and the Battalgazi Plateau in Malatya Province, Türkiye, and (ii) assess the influence of two *Apis mellifera* genotypes; *A. m. caucasica* and *A. m. carnica*, on elemental composition.

Honey samples were digested and analyzed by inductively coupled plasma mass spectrometry (ICP-MS) for Fe, Cu, Zn, Se, Mn, Pb, Cd, Cr, Ni, As, Bi and Ag. Statistical analysis revealed that both geographic origin and bee genotype exert significant effects on mineral concentrations. Specifically, samples from Yamadağ Mountain exhibited lower total trace element levels compared to those from the Battalgazi Plateau, although concentrations of all measured heavy metals remained well below national and international safety thresholds. According to the obtained findings, the average values of trace elements iron, zinc, copper, selenium and manganese in Yamadağ Mountain honey samples were determined as 0.41 mg/kg, 0.62 mg/kg, 0.04 mg/kg, 0.17 mg/kg and 0.04 mg/kg, respectively. The average values of trace elements iron, zinc, copper and manganese in Battalgazi Plateau honey samples were found to be 7.55 mg/kg, 1.30 mg/kg, 0.18 mg/kg and 0.23 mg/kg, respectively. Selenium was not detected in Battalgazi Plateau honey samples. When the heavy metal contents of the honey samples were examined, silver was not detected in Yamadağ Mountain honey samples and silver, cadmium, arsenic and bismuth were not detected in Battalgazi Plateau honey samples. The average values of lead, cadmium, chromium, nickel, arsenic and bismuth in Yamadağ Mountain honey samples were found to be 0.10 mg/kg, 0.05 mg/kg, 0.46 mg/kg, 0.03 mg/kg, 0.12 mg/kg and 0.02 mg/kg, respectively. In Battalgazi honey samples, the average values of lead, chromium and nickel were found as 0.11 mg/kg, 0.21 mg/kg and 0.14 mg/kg, respectively.

These findings demonstrate that regional environmental factors and genetic variation within *Apis mellifera* colonies critically determine the mineral composition of honey. Accordingly, both geographic provenance and bee genotype should be considered in quality control protocols and in the development of region-specific standards for trace element content in honey.

Keywords: Honey, mineral composition, geographical variation, Malatya, Türkiye

1. Introduction

Minerals are essential inorganic nutrients required in small amounts for the maintenance of fundamental biochemical functions in the human body. In dietary supplements, they are commonly classified as macro minerals (e.g., calcium, magnesium, potassium) and trace minerals (e.g., iron, zinc, selenium), serving to correct deficiencies or support optimal health [1,2]. Minerals are essential inorganic nutrients required for human health and are naturally present in various foods. Dairy products serve as a primary source of calcium, while green leafy vegetables are rich in magnesium. Red

meat and organ meats provide significant amounts of iron, whereas seafood is abundant in iodine and zinc. Nuts, legumes, and whole grains contribute essential minerals such as potassium (K), phosphorus (P), and selenium (Se). A well-balanced diet ensures adequate mineral intake, supporting vital biological processes and overall physiological functions [3].

Various organisms have been used as an alternative tool to detect pollution using low-cost conventional methods. In recent years, honey bees and their products (e.g., honey and beeswax) have been used to monitor

Citation: S. Karlıdağ, S. Kolaylı, Comparison of some mineral and trace-heavy metal contents of blossom honey samples from Yamadağ and Battalgazi regions, Malatya, Türkiye, Turk J Anal Chem, 7(2), 2025, 182–190.

***Author of correspondence:** semiramis.karlidag@ozal.edu.tr

Tel: +90 (422) 846 12 55

Fax: +90 (422) 846 12 25

Received: March 6, 2025

Accepted: May 13, 2025

doi <https://doi.org/10.51435/turkjac.1652944>

pollutants, including heavy metals such as As, Pb, Cd, and Hg. Metals detected in bee products have been found to be correlated with atmospheric concentrations [4]. Honeybees produce honey by collecting nectar and other substances from plants contaminated by environmental pollution. Heavy metals are elements with high atomic mass and density that can exert toxic effects on biological systems. Environmental contaminants that contaminate honey; naturally present in soil, water, and air, these metals can also be introduced into the environment through anthropogenic activities such as industrial processes, mining, agriculture, and waste management. Lead (Pb), mercury (Hg), cadmium (Cd), and arsenic (As) are among the most concerning heavy metals, as they can cause severe health issues even at low concentrations through bioaccumulation and biomagnification. While some heavy metals, such as zinc (Zn), copper (Cu), and iron (Fe), are essential trace elements for living organisms, they can become toxic beyond certain thresholds. Therefore, monitoring heavy metal levels in food, water, and environmental samples is of critical importance. The elements found in honey can be beneficial or dangerous to health [5].

Honey is a natural bee product that serves as significant sources of essential minerals for human nutrition. Honey contains essential minerals such as sodium (Na), potassium, calcium (Ca), magnesium (Mg) and phosphorus, which support energy metabolism and are known as the macro elements of honey, as well as trace amounts of minerals such as iron, copper, zinc, and selenium [6,7]. These minerals play a crucial role in regulating cellular functions, enhancing immune system activity, and exerting antioxidant effects. As bioavailable and nutritionally valuable food sources, honey and pollen help address mineral deficiencies and positively impact. The mineral content of honey varies depending on geographical characteristics and floral composition. Among the richest honeys in terms of mineral content, chestnut honey stands out, while dark-colored forest honeys have been reported to contain higher ash content and, consequently, greater mineral concentrations [8,9].

This study aims to investigate the mineral composition of honey, considering the influence of geographical characteristics and floral composition. By analyzing the variations in mineral content among different honey types, particularly mountain and plateau honey samples, this research seeks to provide insights into their nutritional value and potential health benefits. Additionally, the study evaluates the bioavailability of essential minerals in honey, contributing to a better understanding of their role in human nutrition and dietary supplementation.

2. Materials and methods

2.1. Samples

Honey samples were obtained from two different locations in the Yamadağ Mountain and Battalgazi Plateau regions of Malatya province in the Eastern Anatolia Region of Türkiye, from two different *Apis mellifera* (A. m.) genotype bee races (Table 1). The Yamadağ Mountain massif, situated within the Sivas Province area and extending to the south and southeast, delineates the northern boundary of Malatya Province. Geologically, Yamadağ and its extensions exhibit a predominantly volcanic structure, attaining elevations above 1 500 m and forming a broad, high-relief plateau interspersed with distinct peaks [10]. The Battalgazi district spans a considerable altitudinal range and supports a rich assemblage of wild and cultivated flora, including solanaceous vegetables (tomato, pepper, cabbage), orchards (apricot, cherry, walnut, apple), vineyards, and ornamental nurseries [11].

The experimental trial was conducted at the Bee and Bee Products Development Application and Research Center apiary on the Battalgazi Campus of Malatya Turgut Özal University. In April, all colonies were equalized with respect to supplemental feeding and frame number. During the first week of June, forty colonies remained at the Battalgazi site, while a matched set of forty colonies was relocated to the Hekimhan–Yamadağ plateau. Twenty colonies were used in each group, and samples were harvested from these colonies. Honey was harvested in the second week of September; each honey frame was logged with hive identifier, bee genotype, and collection site, then filtered and transferred into amber glass jars for storage under dark, dry conditions until analysis.

2.2. Determination of metals by ICP-MS

Elemental analyses were performed using Inductively Coupled Plasma Mass Spectrometry (ICP-MS). The analyses were conducted with an Analytic Jena Plasma Quant MS instrument (Jena, Germany). Sample preparation involved acidic digestion using a microwave-assisted method (CEM - Mars 5, Matthews, North Carolina, USA), followed by measurement under the standard operating conditions of the instrument. Samples H1, H2, H3 and H4 were weighed in amounts of 0.4662 g, 0.7238 g, 0.6374 g and 0.5485 g, respectively, and placed in teflon tubes. The honey samples were digested in a microwave system using 2 mL of 37% hydrochloric acid (HCl) and 5 mL of 65% nitric acid (HNO₃). Following digestion, the final volume was adjusted to 10 mL with ultrapure water prior to analysis. A multi-element analysis was performed, and internal standards were used to enhance measurement accuracy. Calibration curves were constructed using certified reference materials, and the accuracy of the analytical results was verified with quality control samples (Table 2) [12].

Table 1. Regions where honey samples were collected

Region	Honey Code	Race	Coordinates/ Altitude (meter)
Yamadağ	H1	<i>A. m. caucasica</i>	38° 54' 41" N 38° 7' 55" E/2306
	H2	<i>A. m. carnica</i>	
Battalgazi	H3	<i>A. m. caucasica</i>	38°25'22"N 38°21'56"E/885
	H4	<i>A. m. carnica</i>	

Prior to each analysis, the ICP-MS instrument was calibrated according to the protocol outlined in Table 3. Reported elemental concentrations have been adjusted to account for the applied dilution factors. After the solutions were prepared, the device was calibrated before reading the heavy metal content of the solubilized samples. The calibration graphs drawn for the elements were used as an indicator of the accuracy of the prepared standards [12].

2.3. Statistics

All experiments were conducted in triplicate, and the results are expressed as mean \pm standard deviation (SD). Statistical analyses were performed using SPSS software (version 22). Pearson's correlation coefficient was calculated to assess relationships between the variables. ANOVA was used for statistical analysis of the means of the elements Fe, Zn, Cu, Mn, Pb, Cr and Ni, and T-test was used for statistical analysis of the means of the elements Se, Cd, As, Bi and Ag. Differences were considered statistically significant when $P < 0.05$.

Table 2. The properties of elemental analysis by inductively Coupled Plasma Mass Spectrometry (ICP-MS)

Parameter	Value
Flow Parameters (L/min)	
Plasma Flow	9.0
Auxiliary Flow	1.65
Sheath Gas	0.00
Nebulizer Flow	1.10
Torch Alignment (mm)	
Sampling Depth	7.0
Other	
RF Power (kW)	1.40
Pump Rate (rpm)	12
Stabilization delay (s)	10
Ion Optics (volts)	
First Extraction Lens	-46
Second Extraction Lens	-161
Third Extraction Lens	-246
Corner Lens	-194
Mirror Lens Left	23
Mirror Lens Right	32
Mirror Lens Bottom	39
Entrance Lens	-5
Entrance Plate	-68
Fringe Bias	-4.6
Pole bias	0.0
iCRC (mL/min)	
Skimmer Gas Source	H ₂
Skimmer Flow	60
Nitrox	
Flow (ml/min)	0.0

3. Results and discussions

LOD (limit of detection) can indicate the presence of a substance but cannot determine its exact amount. LOQ (limit of quantification) is the lowest level at which the amount of a substance can be measured accurately and reliably. LOD and LOQ values were determined for Fe, Zn, Cu, Se, Mn, Pb, Cd, Cr, Ni, As, Bi and Ag [12]. The calibration range, isotope of element, blank equivalent concentration, calibration equation, correlation coefficient, limit of detection, and limit of quantification of the calibration curves for determination of the element using inductively coupled plasma mass spectrometry are given in Table 3. Calibration curves showed very strong linearity. Values show that the device is quite sensitive. The correlation coefficients of all the calibration curves were equal to or greater than 0.9983 ($R^2 \geq 0.9983$). These correlation coefficients showed that there was a strong positive correlation and linear fit for the absorbance change with concentration. The calibration equation formulas of the elements are given in Table 3.

c/s: Signal ratio obtained from the device. It expresses how the measured concentration changes depending on the ratio of the internal standard.

conc: Analyt contraction

I/S: Internal standard ratio

LOD: The lowest concentration that the device can reliably detect.

LOQ: The lowest concentration at which the instrument can reliably quantify.

BEC: The equivalent concentration of the signal given when the blank sample is measured (Table 3).

Heavy metal concentrations in honey must remain below thresholds that could compromise human health. Accordingly, honey products within the scope of this standard shall conform to the maximum heavy metal limits established by the Codex Alimentarius Commission [13]. Under Article 8 "Contaminants" of the Honey Communique (22 April 2020, No. 31107), the provisions of the Turkish Food Codex Contaminants Regulation (Official Gazette No. 28157, 29 December 2011) are applied to covered products. Although the "Communique on Maximum Limits of Contaminants in Foodstuffs" [14] does not specify heavy metal limits for honey, metal residues in honey are monitored via the National Residue Control Plan [15]. Heavy metals, defined by a physical density exceeding 5 g cm^{-3} , comprise over 60 elements, notably lead, cadmium, chromium, iron, cobalt, copper, nickel, mercury, and zinc [12,16]. While the human body tolerates certain levels of dietary heavy metals, concentrations above specific thresholds induce toxicity.

Table 3. Analytical measurement parameters of the methods studied

Element	Calibration Range (ppb)	Mass	BEC (ppb)	Calibration Equation	Correlation Coefficient (R ²)	LOD (ppb)	LOQ (ppb)
Fe	5-10-50-100-200	57	5.94	$c/s = (788.3 + 334.4 + 132.4 \cdot \text{conc}) \cdot [I/S \text{ Ratio}]$	0.9993	1.55	5.15
Zn	5-10-50-100-200	64	2.85	$c/s = (282.4 + 232.9 + 99.41 \cdot \text{conc}) \cdot [I/S \text{ Ratio}]$	0.9991	1.57	5.23
Cu	0.5-1-5-10-20	65	0.13	$c/s = (21.7 + 2.742 + 167.2 \cdot \text{conc}) \cdot [I/S \text{ Ratio}]$	0.9999	0.14	0.45
Se	5-10-50-100-200	78	0.65	$c/s = (5.1 + 6.431 + 7.917 \cdot \text{conc}) \cdot [I/S \text{ Ratio}]$	0.9983	3.05	10.18
Mn	0.5-1-5-10-20	55	0.45	$c/s = (536.7 - 18.37 + 1214 \cdot \text{conc}) \cdot [I/S \text{ Ratio}]$	0.9996	0.05	0.17
Pb	0.5-1-5-10-20	207	0.21	$c/s = (7.0 + 5.277 + 32.68 \cdot \text{conc}) \cdot [I/S \text{ Ratio}]$	0.9998	0.49	1.62
Cd	0.5-1-5-10-20	112	0.12	$c/s = (8.2 - 0.365 + 67.24 \cdot \text{conc}) \cdot [I/S \text{ Ratio}]$	0.9999	0.05	0.16
Cr	0.5-1-5-10-20	52	0.08	$c/s = (48.3 - 3.845 + 612.4 \cdot \text{conc}) \cdot [I/S \text{ Ratio}]$	0.9995	0.06	0.21
Ni	0.5-1-5-10-20	58	-0.44	$c/s = (-66.0 - 22.49 + 150.2 \cdot \text{conc}) \cdot [I/S \text{ Ratio}]$	0.9997	0.55	1.83
As	5-10-50-100-200	75	-5.46	$c/s = (-83.2 - 29.59 + 15.57 \cdot \text{conc}) \cdot [I/S \text{ Ratio}]$	0.9991	4.62	15.41
Bi	0.5-1-5-10-20	209	0.07	$c/s = (8.7 + 0.043 + 121.4 \cdot \text{conc}) \cdot [I/S \text{ Ratio}]$	0.9988	0.1008	0.3359
Ag	0.5-1-5-10-20	107	0.21	$c/s = (80.0 + 8.323 + 391.9 \cdot \text{conc}) \cdot [I/S \text{ Ratio}]$	0.9996	0.1158	0.3861

R²: Determination coefficient; **BEC:** Blank equivalent concentration; **Mass:** Isotope of element; **LOD:** Limit of detection; **LOQ:** Limit of quantification

Maximum daily intake levels for cadmium, lead, zinc, and copper are 60 µg, 210 µg, 12–15 mg, and 30 mg, respectively [12], whereas the maximum permissible concentrations in food for tin and mercury are 50 mg kg⁻¹ and 1 mg kg⁻¹, respectively [14]. The U.S. Environmental Protection Agency has set a soil arsenic limit of 75 mg kg⁻¹, and both WHO and USEPA have reduced the permissible arsenic concentration in water from 50 µg L⁻¹ to 10 µg L⁻¹, a standard likewise adopted by the Turkish Standards Institute for drinking water [16].

In this study, some trace element and some heavy metal contents of honey from Yamadağ and Battalgazi regions, which are at two different altitudes with rich floral characteristics in terms of honey production, were compared. The values found are summarized in Table 4 and Table 5.

Among the five trace elements analyzed using ICP-MS (Fe, Cu, Zn, Se, and Mn), iron (Fe) was found to be the most abundant. Se, Fe, Mn, Cu, Zn and Ni at recommended doses have antioxidant properties, enzymatic activities and the ability to contribute to general human development. In contrast, Pb, As, Cr and Cd have no known benefits and may be toxic in relatively small amounts [5]. The average iron concentration was determined as 0.41 µg/g in Yamadağ honey and 7.55 mg/kg in Battalgazi honey. The approximately 20-fold higher iron content in Battalgazi honey compared to Yamadağ honey is particularly noteworthy.

Bees are exposed to chemicals in a variety of ways: by inhaling metals while flying and collecting them bound to particulate matter or soil particles on their hairy bodies; by ingesting metals from the water they carry; and by collecting pollen and nectar from plants that may be rich in bioavailable metals found in soil, water, and air, thus adding them to bee products. These interactions affect the quality of what honeybees produce, making honey a potentially valuable indicator of environmental pollution [4]. Honey serves as a bioindicator of environmental contamination, with its mineral profile reflecting not only the regional flora but also local soil, water, and climatic conditions. In Malatya Province, post-earthquake demolition, debris-removal operations, and reconstruction efforts have markedly increased atmospheric particulate levels, particularly in urban and district centers relative to highland plateaus. This anthropogenic pollution likely accounts for the elevated trace-element concentrations observed in Battalgazi honey versus Yamadağ Mountain samples. Statistical analysis demonstrated a strong positive correlation between manganese and iron concentrations ($R^2 = 0.993$, $p < 0.01$), indicative of co-accumulation or common environmental sources. In contrast, iron and arsenic exhibited a pronounced negative correlation ($R^2 = -0.992$, $p < 0.01$) (Table 6), consistent with the known adsorption of ionic arsenic species onto iron and aluminum oxides in acidic to neutral soils, which reduces arsenic bioavailability to plants [16].

Table 4. Trace elements of the honey samples (mg/kg)

Region	Honey Code	Fe	Zn	Cu	Se	Mn
Yamadağ	H1	0.32	1.10	0.05	0.34	0.05
	H2	0.49	0.13	0.03	ND	0.03
	Mean±SD	0.41±0.12	0.62±0.69	0.04±0.01	0.17±0.24	0.04±0.01
Battalgazi	H3	7.19	1.28	0.21	ND	0.23
	H4	7.91	1.31	0.15	ND	0.23
	Mean±SD	7.55±0.51	1.30±0.02	0.18±0.04	ND	0.23±0.00
Sig.		0.003*	0.296	0.047*		0.003*

ND: Not detected; **Mean±SD:** Arithmetic mean and standard deviation; *: $P < 0.05$

Table 5. Heavy metal amount of honey samples (mg/kg)

Region	Honey Code	Pb	Cd	Cr	Ni	As	Bi	Ag
Yamadağ	H1	0.17	0.10	0.84	0.04	0.13		ND
	H2	0.03	ND	0.07	0.01	0.11	ND	ND
	Mean±SD	0.10±0.10	0.05±0.07	0.46±.54	0.03±0.02	0.12±0.01	0.02±0.02	ND
Battalgazi	H3	0.08	ND	0.16	0.13	ND	ND	ND
	H4	0.13	ND	0.25	0.14	ND	ND	ND
	Mean±SD	0.11±0.04	ND	0.21±0.06	0.14±0.01	ND	ND	ND
Sig.		0.952		0.585	0.020*			

ND: Not detected; Mean±SD: Arithmetic mean and standard deviation; *: P<0.05

Similarly, the average zinc concentration in honey from the Yamadağ region was found to be 0.62 mg/kg, while in honey from the Battalgazi region, it was 1.30 mg/kg. This indicates that the zinc content in Battalgazi honey is approximately twice as high as that in Yamadağ honey. No significant differences were observed between different bee species in this context.

The amount of zinc in chestnut honey was reported to be 1.45 mg/kg [17]. According to Bengü and Kutlu [18], zinc and iron values are 5.00-12.0 mg/100g and 10.0-27.0 mg/100g, respectively. In honey samples from the Yamadağ region, the average copper concentration was found to be 0.04 mg/kg, whereas in the Battalgazi region, it was 0.18 mg/kg. When compared to existing literature, the copper levels in honeys from both regions are considerably low. In a study [18], the elements in honey samples were determined as chromium 2.51 ppb, copper 0.98 ppb, iron 28.84 ppb, manganese 3.93 ppb, nickel 2.02 ppb and zinc 9.71 ppb. In a study conducted on chestnut honey from the Kastamonu region, it was reported that the amount of iron mineral varied between 1.32 and 9.75 mg/kg [9]. In the same study, the average copper amount was found to be 0.07 mg/kg. The amount of copper in New Zealand Manuka honey was reported as 0.35 mg/kg [1] and in pine honey as 0.84 [19]. Pipoyan et al. [20] reported that copper concentrations in several samples of honey they examined were above the maximum allowable level. The concentrations of copper ranged from 9.00E-02 to 1.86E+00 mg/kg.

The amount of selenium element, known as an essential element and having an important role in antioxidant activity, was found to be 0.34 mg/kg. In a study conducted on many honey samples collected from different regions of Anatolia, it was reported that the amount of selenium varied between 0.42 and 19.9 mg (Kg) [21]. *A. m.* genotype from Yamadağ region but below the detection limits in *A. m. carnica* genotype. In the honeys of Battalgazi region, it was determined that the detection limits were at six, that is, at a very low level. In their study, Tuzen et al. [22] reported the amount of selenium as 38 to 112 mg/kg, while it was reported as 0.04 mg/kg in pine honey [19].

Manganese (Mn), which is a grayish metal in its pure form, is a hard and brittle substance. Manganese is found

in nature in the form of an oxide and has physical properties similar to iron. Manganese is naturally found in soil, water, and rocks, but it is not found as a base metal in nature. Ocean events that mobilize the earth's crust, earthquakes, volcanic events, fires and vegetation are also natural sources of manganese in the atmosphere [12,23]. The average manganese concentrations in honey samples from both regions were approximately 0.04 mg/kg, with no significant differences observed between the regions or among different genotypes. The results showed a strong positive correlation between manganese and nickel ($R^2= 0.991$, $p\leq 0.01$) (Table 6). In fact, in a study [24] it was observed that the adsorption for manganese (II) and nickel (II) increased as the pH increased. The results showed a strong negative correlation between manganese and arsenic ($R^2= -0.982$, $p\leq 0.01$) (Table 6). These manganese levels are relatively low compared to findings from other studies. For instance, research on honey samples from Türkiye reported manganese concentrations ranging from 0.096 to 29.496 µg/g, while another study found levels between 0.25 ± 0.24 mg/kg. These variations in Mn content are likely influenced by environmental factors, floral sources, and regional characteristics. In the study conducted on chestnut honey, Mn amounts were found to be 1.39 to 18.69 mg/kg [9], while it was reported as 28 mg/kg in Manuka honey [1], 1.1 to 4.2 mg/kg in Manuka honey [25] and 2.8 mg/kg in pine honey [19].

Heavy metals, the elements characterized by high atomic weight and density, are among the most persistent environmental pollutants and pose toxicological risks even at trace concentrations. These contaminants originate from both natural and anthropogenic sources, leading to deposition in air, soil, and water [5]. Plant uptake of heavy metals from contaminated soils results in bioaccumulation within floral tissues, which foraging honeybees (*Apis mellifera*) then transport to the hive. During nectar processing, bees incorporate these metals into honey, creating a route of dietary exposure for humans. Chronic consumption of heavy metal-contaminated honey can lead to progressive accumulation in human organs and tissues [18].

Unlike degradable organic pollutants, heavy metals remain chemically persistent and can cycle indefinitely

through environmental compartments. Principal soil contaminants include cationic species such as mercury (Hg), cadmium (Cd), lead (Pb), nickel (Ni), copper (Cu), zinc (Zn), chromium (Cr), and manganese (Mn), as well as oxyanionic forms of arsenic (As), molybdenum (Mo), and selenium (Se) [16]. Empirical studies have documented considerable variability in trace-metal concentrations across honey types. For instance, Rhododendron honeys analyzed by Silici et al. [26] contained Cu (9.75–35.8 µg/kg), Cd (0.28–2.37 µg/kg), Pb (1.51–55.3 µg/kg), Co (1.44–28.5 µg/kg), Cr (1.57–12.9 µg/kg), Ni (1.35–131 µg/kg), Al (47.8–644 µg/kg), and Se (14.1–323 µg/kg), exceeding levels typically observed in regional multifloral honeys. Meister et al. [25] reported Cr (0.02–0.03 mg/kg), Cu (0.13–0.30 mg/kg), Fe (0.72–1.20 mg/kg), and Zn (0.32–0.47 mg/kg) in Manuka honey. Aygün [27] detected Al, As, Cd, and Pb at 435.9, 4.8, 337.9, and 409.9 µg/kg, respectively, in Turkish honey samples, whereas Sobhanardakani and Kianpour [28] found mean Cd, Cr, Ni, and Zn levels of 63.18, 58.05, 56.15, and 684.43 µg/kg. Ligor et al. [29] identified As up to 0.49 µg/kg in polyfloral and linden honeys, Ni in excess of 400 µg/kg in samples from Lesser Poland, the highest Cr content (3.76 µg/kg) in buckwheat honey, and Mo (5.94 µg/kg) in dandelion honey.

Iron stands out among trace elements for its vital roles in living organisms: it is an essential component of hemoglobin, myoglobin, cytochromes, peroxidases, catalases, ferritin, and transferrin, and it participates in the biosynthesis of large biomolecules [30]. In contrast, nickel and certain nickel compounds are classified as carcinogenic; dietary Ni accumulates over time in pulmonary, gastrointestinal, and dermal tissues, contributing to chronic pulmonary fibrosis, cardiovascular disorders, and renal toxicity [12].

In the context of food biochemistry, iron, copper, zinc, and manganese are essential trace elements vital for various metabolic processes. However, at elevated concentrations, these elements can exhibit toxic effects and are thus categorized as heavy metals. Analyses of honey samples from Malatya's Yamadağ and Battalgazi regions have determined that the levels of these trace elements are well below toxic thresholds, indicating no significant health risk associated with their consumption. The results showed a strong positive correlation between selenium and cadmium ($R^2=1.000$, $p<0.01$), and selenium and bismuth ($R^2=1.000$, $p<0.01$) (Table 6). The positive increase relationships between them are thought to be due to factors related to agricultural fertilizers, agricultural pesticides and environmental pollution [5].

In the study, concentrations of seven different heavy metals, lead, cadmium, chromium, nickel, arsenic, and

silver, were measured in honey samples. The levels of these metals were found to be below the safe consumption limits. The results showed a strong positive correlation between bismuth and cadmium ($R^2=1.000$, $p<0.01$), and a strong negative correlation between nickel and arsenic ($R^2=-0.951$, $p<0.05$) (Table 6). In a study [4], a moderate correlation was found between nickel and cadmium in honey samples ($r=0.41$, $p>0.001$). In addition to environmental effects, weak but statistically significant correlations were reported between nickel and arsenic ($r=0.18$, $p=0.003$), cadmium and lead ($r=0.18$, $p=0.003$), and chromium and nickel ($r=0.14$, $p=0.02$). It was emphasized that the lack of significance or weak correlations between metal concentrations was due to the fact that the sources and magnitudes of metal pollution varied greatly between sample locations. In another study [20], concentrations of lead, cadmium, arsenic, and nickel ranged from $2.30\text{E-}03$ to $4.50\text{E-}02$ mg/kg, from $6.00\text{E-}04$ to $3.10\text{E-}03$ mg/kg, from $5.00\text{E-}03$ to $4.80\text{E-}02$ mg/kg, and from $2.40\text{E-}01$ to $8.49\text{E-}01$ mg/kg respectively. In a study, the amount of lead in some honey samples was found to be 0.08–0.44 mg/kg and the amount of selenium was found to be 2.20 to 12.13 mg/kg [5]. In addition to the botanical origin of honey, the density of flowers, the production period, and the amount of rainfall affect the composition of honey. In addition, the containers in which honey is stored and packaged after harvest can cause an increase in the amount of chromium in honey. Similarly, storing honey in galvanized or aluminum containers can cause zinc and aluminum contamination. On the other hand, the elements found in nectar also cause an increase in the element content of honey [26].

In a study [31], the amounts of mineral elements in *Ziziphus* spp. honey varied according to the honey bee species. The highest amounts of iron (33.54 mg/kg) and manganese (0.61 mg/kg) were found in honey produced by *A. florea*. The highest amounts of Mg (145.35 mg/kg), zinc (13.37 mg/kg) and copper (0.58 mg/kg) were obtained from honey harvested from *A. m. jemenitica* colonies. Highly significant positive correlations were found between all mineral elements determined in *Ziziphus* spp. honey produced by *A. florea* and *A. mellifera*.

Chromium is important for animals and humans. There are human and animal studies showing that chromium deficiency negatively affects lipid metabolism and causes atherosclerosis [12]. Manouchehri et al. [32] summarized studies reporting heavy metal levels in honey samples examined in different countries. In the studies conducted, it was emphasized that the rate of contamination of honey with heavy metals is directly related to the number of industrial centers and the pollution rate in the region. It was determined that the amounts of heavy metals (especially cadmium and mercury) in the examined honey samples were above the permitted rate.

Table 6. Pearson correlation matrix on the honey samples (n=4)

		Fe	Zn	Cu	Se	Mn	Pb	Cd	Cr	Ni	As	Bi
Fe	Pearson Correlation	1	0.692	0.928	-0.590	0.993**	0.055	-0.590	-0.421	0.979*	-0.992**	-0.590
	Sig. (2-tailed)		0.308	0.072	0.410	0.007	0.945	0.410	0.579	0.021	0.008	0.410
Zn	Pearson Correlation		1	0.732	0.173	0.755	0.709	0.173	0.352	0.825	-0.616	0.173
	Sig. (2-tailed)			0.268	0.827	0.245	0.291	0.827	0.648	0.175	0.384	0.827
Cu	Pearson Correlation			1	-0.471	0.957*	0.039	-0.471	-0.339	0.933	-0.935	-0.471
	Sig. (2-tailed)				0.529	0.043	0.961	0.529	0.661	0.067	0.065	0.529
Se	Pearson Correlation				1	-0.515	0.741	1.000**	0.977*	-0.411	0.669	1.000**
	Sig. (2-tailed)					0.485	0.259	0.000	0.023	0.589	0.331	0.000
Mn	Pearson Correlation					1	0.117	-0.515	-0.347	0.991**	-0.982*	-0.515
	Sig. (2-tailed)						0.883	0.485	0.653	0.009	0.018	0.485
Pb	Pearson Correlation						1	0.741	0.866	0.245	0.063	0.741
	Sig. (2-tailed)							0.259	0.134	0.755	0.937	0.259
Cd	Pearson Correlation							1	0.977*	-0.411	0.669	1.000**
	Sig. (2-tailed)								0.023	0.589	0.331	0.000
Cr	Pearson Correlation								1	-0.229	0.518	0.977*
	Sig. (2-tailed)									0.771	0.482	0.023
Ni	Pearson Correlation									1	-0.951*	-0.411
	Sig. (2-tailed)										0.049	0.589
As	Pearson Correlation										1	0.669
	Sig. (2-tailed)											0.331
Bi	Pearson Correlation											1
	Sig. (2-tailed)											

Correlation is significant at the 0.01 level (2-tailed). *. Correlation is significant at the 0.05 level (2-tailed).

Another study reported that honey samples from Türkiye, Argentina, Nigeria and Pakistan were contaminated with heavy metals such as cadmium and arsenic. It was stated that this pollution may be due to the presence of industrial areas in the region. The results of studies conducted in Croatia and Kosovo showed that the lead content in honey samples was higher than the amount reported in other European countries, and it was emphasized that this situation was alarming.

It was stated that these findings indicate that honey bee colonies should be placed in areas away from roads and railways. In the study conducted in Nigeria, it was found that the amount of iron, copper, manganese, and zinc in honey samples was higher than the maximum permissible concentration and average concentration determined by the World Health Organization (WHO) and the Food and Agriculture Organization (FAO). It was stated that the rate of heavy metals in industrial cities was higher than in rural areas.

According to the Turkish Food Codex Honey Communiqué, honey must not contain heavy metals in amounts that could pose a health risk (TSE) [15]. Therefore, the heavy metal concentrations in the analyzed honey samples are within acceptable levels as per current legal regulations and health standards.

The mineral content of honey varies not only with the flora of the region where it is produced but also with the conditions of the soil, water, and air. In areas with abundant vegetation, the mineral content of honey is

typically higher. The concentrations of heavy metals in honey serve as significant indicators of environmental pollution, reflecting the levels of contaminants present in the surrounding soil, water, and air. Honeybees, through their foraging activities, accumulate these pollutants from various environmental sources, including industrial emissions, agricultural runoff, and atmospheric deposition [4,32]. Consequently, the heavy metal content in honey mirrors the extent of environmental contamination in the area where it is produced. It is thought that the fact that Yamadağ honey samples have higher heavy metal content than the honey samples of Battalgazi district is due to Yamadağ being a volcanic mountain.

Studies have demonstrated that honey can effectively reflect the levels of heavy metals in the environment. For instance, research conducted in the Black Sea region of Türkiye analyzed honey samples from various locations to determine heavy metal concentrations. The findings indicated that the levels of heavy metals in honey varied depending on the proximity to pollution sources, such as industrial areas and urban centers. This variability underscores the role of honey as a bioindicator of environmental pollution [33].

Furthermore, the mineral content of honey is influenced by the flora of the region where it is produced, as well as the conditions of the soil, water, and air. In areas with abundant vegetation, the mineral content of honey is typically higher [26].

Therefore, analyzing the heavy metal content in honey provides valuable insights into the environmental quality of the region, highlighting the interconnectedness of air, water, and soil pollution [4].

4. Conclusion

In this study, some trace element and some heavy metal contents of honey from Yamadağ and Battalgazi regions, which are at two different altitudes with rich floral characteristics in terms of honey production were compared. The approximately 20-fold higher iron content in Battalgazi honey compared to Yamadağ honey is particularly noteworthy. Similarly, the average zinc concentration in honey from the Yamadağ Mountain was found to be 0.62 mg/kg, while in honey from the Battalgazi Plateau, it was 1.30 mg/kg. In honey samples from the Yamadağ Mountain, the average copper concentration was found to be 0.04 mg/kg, whereas in the Battalgazi Plateau, it was 0.18 mg/kg. *A. m.* genotype from Yamadağ Mountain but below the detection limits in *A. m. carnica* genotype. Analyses of honey samples from Malatya's Yamadağ and Battalgazi regions have determined that the levels of these trace elements are well below toxic thresholds, indicating no significant health risk associated with their consumption.

Funding

None

Declaration of competing interest

The authors declare no competing interest.

Ethical approval

This study did not involve animal or human subjects.

Author contributions

Semiramis Karlıdağ: Samples production, formol analyses, statistical analysis; Sevgi Kolaylı: Conception, writing.

References

- [1] L.P. Vanhanen, A. Emmertz, G.P. Savage, Mineral analysis of mono-floral New Zealand honey, *Food Chem*, 128(1), 2011, 236-240.
- [2] V. Nanda, B.C. Sarkar, H.K. Sharma, A.S. Bawa, Physico-chemical properties and estimation of mineral content in honey produced from different plants in Northern India, *Food Compos Anal*, 16(5), 2003, 613-619.
- [3] S. Dinç, M. Kara, Ç. Takma, Y. Kara, S. Kolaylı, Strawberries from Konya in the Central Anatolia Region of Türkiye: Phenolic Profile, Antioxidant Potential and Mineral Composition, *Applied Fruit Science*, 66(4), 2024, 1229-1240.
- [4] T.R. Godebo, H. Stoner, P. Taylor, M. Jeuland, Metals in honey from bees as a proxy for environmental contamination in the United States, *Environmental Pollution*, 364, 2025, 125221.
- [5] N.A. Obasi, C. Aloke, S.E. Obasi, A.C. Famurewa, P.N. Ogbu, G.N. Onyeji, Elemental composition and associated health risk of honey obtained from apiary farms in Southeast Nigeria, *Journal of Food Protection*, 83(10), 2020, 1745–1756.
- [6] M. Moniruzzaman, M.A.Z. Chowdhury, M.A. Rahman, S.A. Sulaiman, S.H. Gan, Determination of mineral, trace element, and pesticide levels in honey samples originating from different regions of Malaysia compared to Manuka honey, *Biomed Res Int*, 1, 2014, 359890.
- [7] S.P. Kek, N.L. Chin, S.W. Tan, Y.A. Yusof, L.S. Chua, classification of honey from its bee origin via chemical profiles and mineral content, *Food Anal Methods*, 10, 2017, 19–30.
- [8] M. Küçük, S. Kolaylı, Ş. Karaoğlu, E. Ulusoy, C. Baltacı, F. Candan, Biological activities and chemical composition of three honeys of different types from Anatolia, *Food Chem*, 100(2), 2007, 526–534.
- [9] U. Ertop, H. Şevik, M.H. Ertop, Mineral composition and heavy metal contents of chestnut honey collected from Kastamonu region, *Journal of Apitherapy and Nature*, 6(2), 2023, 73-87.
- [10] Anonymous, 2025, <http://www.malatya.gov.tr/cografi-konum>
- [11] S. Karlıdağ, A. Köseman, A. Akyol, G. Saatçioğlu, İ. Şeker, A. Uyumlu, M. Yilmaztekin, S. Erdoğan, The effects of different industrial sugars on royal jelly production, *Journal of the Hellenic Veterinary Medical Society*, 73(4), 2023, 4689–4696.
- [12] S. Bakırcı, Aydın İlinde Üretimi Yapılan Bazı Arı Ürünlerindeki Ağır Metal Düzeylerinin Karşılaştırılması, Yüksek lisans programı, Aydın Adnan Menderes Üniversitesi, Sağlık Bilimleri Enstitüsü Biyokimya (Veteriner), Aydın, 2019.
- [13] Codex Alimentarius international Food Standards, 2022, www.standartlar-codexalimentarius-fao-who
- [14] T.C. Resmi Gazete, 17 Mayıs 2008 Cumartesi, Sayı : 26879, Türk Gıda Kodeksi Gıda Maddelerindeki Bulaşanların Maksimum Limitleri Hakkında Tebliğ (Tebliğ No: 2008 / 26), Tarım ve Köyişleri Bakanlığı'ndan, 2008, <https://www.resmigazete.gov.tr/eskiler/2008/05/20080517-7.htm>
- [15] Türk Gıda Kodeksi Bal Tebliği (Tebliğ No: 2020/7), 2020, <https://www.resmigazete.gov.tr/eskiler/2020/04/20200422-13.htm>
- [16] T.D. Çiftçi, Investigation of arsenic, copper, iron, lead leaching to acidic and alkaline waters from soil, *Karaelmas Fen ve Müh Derg*, 8(1), 2018, 73-78.
- [17] S. Kolaylı, Z. Can, H.E. Çakır, O.T. Okan, O. Yıldız, An investigation on Trakya region Oak (*Quercus* spp.) honeys of Turkey: Their physico-chemical, antioxidant and phenolic compounds properties, *Turk J Biochem*, 43(4), 2018, 362-374.
- [18] A.Ş. Bengü, M. A. Kutlu, Analysis of some essential and toxic elements by ICP-MS in honey obtained from Bingöl, *U Bee J*, 20(1), 2020, 1-12.
- [19] I.K. Karabagias, A.P. Louppis, S. Kontakos, C. Papastefanou, M.G. Kontominas, Characterization and geographical discrimination of Greek pine and thyme honeys based on their mineral content, using chemometrics, *Eur Food Res Technol*, 243, 2017, 101-113.
- [20] D. Pipoyan, S. Stepanyan, M. Beglaryan, S. Stepanyan, S. Asmaryan, A. Hovsepyan, N. Merendino, Carcinogenic and non-carcinogenic risk assessment of trace elements and POPs in honey from Shirak and Syunik regions of Armenia, *Chemosphere*, 239, 2020, 124809.
- [21] S.S. Altunatmaz, D. Tarhan, F. Aksu, N.P. Ozsobaci, M.E. Or, U.B. Barutcu, Levels of chromium, copper, iron, magnesium, manganese, selenium, zinc, cadmium, lead and aluminium of

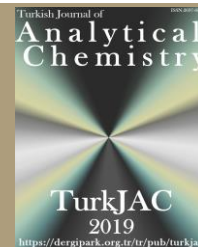
- honey varieties produced in Turkey, Food Sci Tech-Brazil, 39, 2018, 392-397.
- [22] M. Tuzen, S. Silici, D. Mendil, M. Soyak, Trace element levels in honeys from different regions of Turkey, Food Chem 103, 2007, 325–330.
<https://doi.org/10.1016/j.foodchem.2006.07.053>
- [23] WHO, Manganese and Its Compounds: Environmental Aspects, Geneva, 6-7, 2004,
- [24] E. Buldağ, Nikel(II) ve Mangan(II)'In Sulu Çözeltiden Klorit İhtiva Eden Killerle Uzaklaştırılması, Yüksek lisans tezi, Dicle Üniversitesi, Fen Bilimleri Enstitüsü, Diyarbakır, 2018.
- [25] A. Meister, M.J. Gutierrez-Gines, A. Maxfield, S. Gaw, N. Dickinson, J. Horswell, B. Robinson, Chemical elements and the quality of Manuka (*Leptospermum scoparium*) Honey, Foods, 10, 2021, 1670.
- [26] S. Silici, O.D. Uluozlu, M. Tuzen, M. Soyak, Assessment of trace element levels in rhododendron honeys of Black Sea, Region, Turkey, J Hazard Mater, 156, 2008, 612-618.
- [27] O. Aygün, Some toxic heavy metal levels of honeys produced in Elazığ, Fırat Üniversitesi Müh Bil Dergisi, 32(1), 2020, 119-125.
- [28] S. Sobhanardakani, M. Kianpour, Heavy metal levels and potential health risk assessment in honey consumed in the west of Iran, Avicenna, J Environ Health Eng, 3(2), 2016, e7795.
- [29] M. Ligor, T. Kowalkowski, B. Buszewski, Comparative study of the potentially toxic elements and essential microelements in honey depending on the geographic origin, Molecules, 27, 2022, 5474.
- [30] E.O. Çakır, Türkiye'nin Farklı Bölgelerinden Toplanan Süt Örneklerinde Bazı Metal Düzeyleri, Doktora Tezi, Ankara Üniversitesi, Sağlık Bilimleri Enstitüsü, Ankara, 2009.
- [31] El-K. A. Taha, S. Al-Kahtani, R. Taha, Comparison of pollen spectra and amount of mineral content in honey produced by *Apis florea* F. and *Apis mellifera* L., Journal Of The Kansas Entomological Society, 91(1), 2018, 1–7.
- [32] A. Manouchehri, M. Pirhadi, S. Shokri, G.J. Khaniki, S. Shamaei, M.H. Miranzadeh, The possible effects of heavy metals in honey as toxic and carcinogenic substances on human health: a systematic review (toksik ve kanserojen bir madde olarak baldaki ağır metallerin insan sağlığına olası etkileri; sistematik bir inceleme), Ari D/U Bee J, 21(2), 2021, 238-248.
- [33] L. Bezberdaya, O. Chernitsova, M. Lychagin, *et al*, Pollution of a Black Sea coastal city: potentially toxic elements in urban soils, road dust, and their PM10 fractions, J Soils Sediments, 24, 2024, 3485–3506.



TurkJAC

Turkish Journal of

Analytical Chemistry

<https://dergipark.org.tr/tr/pub/turkjac>

New 1H-1,2,3-triazol derivatives: Synthesis, characterization and antioxidant activity

Fatih Çelik 

Karadeniz Technical University, Faculty of Sciences, Department of Chemistry, 61080 Trabzon, Türkiye

Abstract

4-bromo-N-(4-((1-(4-bromobenzyl)-1H-1,2,3-triazol-4-yl)methoxy)-3-methoxy benzylidene) aniline (3), 2-((1-(3-(1,3-dioxoisindolin-2-yl) propyl)-1H-1,2,3-triazol-4-yl)methoxy) benzaldehyde (6), and 4-((1-(3-(1,3-dioxoisindolin-2-yl)propyl) -1H-1,2,3-triazol-4-yl)methoxy)-3-methoxybenzaldehyde (8) were synthesized. The compounds were characterized by FTIR, ¹H-NMR and ¹³C-NMR spectroscopic methods. The antioxidant properties of the compounds were evaluated using two widely accepted methodologies assays (DPPH and FRAP). Compound 3 has the highest antioxidant potential among the compounds.

Keywords: 1,2,3-triazole, organic synthesis, antioxidant activity, FRAP assay

1. Introduction

1,2,3-Triazoles are five-membered heterocyclic compounds containing three nitrogen atoms in the ring. These compounds have attracted significant interest due to their extraordinary stability, ease of synthesis, and various biological activities. The triazole ring, in particular, has been incorporated into many drug candidates because of its ability to interact with a variety of biological targets. 1,2,3-Triazoles exhibit antimicrobial, antifungal, anticancer, and anti-inflammatory activities, making them valuable in the development of new therapeutic agents [1–3]. The synthesis of 1,2,3-triazoles has been greatly facilitated with the advent of the concept of "click chemistry." This concept involves the copper(I)-catalyzed azide-alkyne cycloaddition (CuAAC) reaction, which efficiently and regioselectively forms 1,2,3-triazole rings, enabling the creation of complex molecules with high yields and minimal side products. Functionalizing the 1,2,3-triazole ring at different positions further enhances their appeal for use in drug design, materials science, and as ligands in coordination chemistry [4–7]. The combination of Schiff bases and 1,2,3-triazoles is an exciting area of research. By synthesizing hybrid molecules that incorporate both the imine group of Schiff bases and the triazole ring, the aim is to combine the distinctive

advantages of both structures. These hybrid compounds often exhibit improved biological and chemical properties compared to their individual components. Schiff base-triazole derivatives may demonstrate stronger antimicrobial activity, increased stability, or enhanced metal coordination ability, making them particularly useful in drug development and catalysis. Furthermore, the structural diversity of Schiff bases and the regioselectivity of 1,2,3-triazole formation offer a wide range of possibilities for the creation of compounds with new properties. This opens new avenues for the development of multifunctional agents that can be applied in various fields, such as medicinal chemistry, materials science, and beyond [8–11].

2. Experimental

2.1. Instrumentation

IR spectra of the synthesized compounds were taken on a Perkin Elmer FT-IR 1600 FT-IR (4000–400 cm⁻¹) spectrophotometer device, and ¹H-NMR, ¹³C-NMR spectra were taken on a Bruker brand 400 MHz NMR device with DMSO-d₆ solvent. Antioxidant measurements were made using a Buchi brand spectrophotometer. The solvents and chemicals used in

Citation: F. Çelik, New 1H-1,2,3-triazol derivatives: Synthesis, characterization and antioxidant activity, Turk J Anal Chem, 7(2), 2025, 191–194.

Author of correspondence: fatih.celik502@gmail.com

Tel: +90 (462) 377 25 25

Fax: +90 (462) 325 31 96

Received: April 22, 2025

Accepted: May 21, 2025

doi <https://doi.org/10.51435/turkjac.1681862>

synthesis and structure elucidation were obtained from Fluka, Merck and Aldrich companies, and all solvents were subjected to appropriate purification and drying processes.

2.2. Synthesis of 4-bromo-N-(4-((1-(4-bromobenzyl)-1H-1,2,3-triazol-4-yl)methoxy)-3-methoxybenzylidene)aniline (3)

Acetylene derivative 4-bromo-N-(3-nitro-4-(prop-2-yn-1-yloxy)benzylidene) aniline (1) (1 mmol) with 1-(azidomethyl)-4-bromobenzene (2) (1 mmol) was stirred in a water/acetone (1:4) mixture at room temperature in a 100 mL flask. Then, copper sulfate pentahydrate (1/20 mol) and sodium ascorbate (1/10 mol) were added to the reaction mixture in the specified proportions and refluxed for 18 hours. At the end of the reaction, the contents of the flask were poured into the ice-water mixture, and a solid was obtained, which was filtered and washed with water. It was crystallized with DMF-water and then dried over CaCl₂ in a desiccator (Scheme 1).

Yield: 96.72%; m.p.253-255°C; IR (ν,cm⁻¹): 1576 (CH=N), 1267 (C-O); ¹H-NMR (δ ppm): 3.81 (s, 3H, OCH₃), 5.27 (s, 2H, OCH₂), 5.63 (s, 2H, NCH₂), Arom. [7.22 (bs, 3H, CH), 7.31 (bs, 4H, CH), 7.59 (bs, 4H, CH)], 8.36 (s, 1H,1,2,3-trz.CH), 8.53 (s,1H, N=CH); ¹³C-NMR (δ ppm): 52.46 (OCH₂), 55.99 (OCH₃), 61.86 (NCH₂), Arom. C [113.04(CH), 113.28 (CH), 123.66 (CH), 129.55(C), 149.65(C), 153.23(C), 4-Br-Ph₁C (124.60(CH), 132.19(CH), 118.54 (C), 151.04(C)), 4-Br-Ph₂C C(130.74 (CH), 132.49 (CH), 122.06 (C), 135.69 (C)], 126.24 (1,2,3-trz.(CH)), 135.84 (1,2,3-trz.(C)), 161.54 (N=CH)

2.3. Synthesis of 1,2,3-triazole derivatives 6

Azide derivative 2-(3-azidopropyl)isoindoline-1,3-dione (4) compound (1 mmol) and acetylene derivative 2-(prop-2-yn-1-yloxy)benzaldehyde (5) and 3-methoxy-4-(prop-2-yn-1-yloxy)benzaldehyde (7) compounds (1 mmol) were mixed separately in water/acetone (1:4) in a 100 mL flask. Then, copper sulfate pentahydrate (1/20 mol) and sodium ascorbate (1/10 mol) were added to the reaction mixture in the specified proportions and refluxed for 18 hours. At the end of the reaction, the contents of the flask were poured into the ice-water mixture, and a solid was obtained, which was filtered and washed with water. It was crystallized with DMF-water and then dried over CaCl₂ in a desiccator (Scheme 1). Compounds 1,2, 5 and 7 were synthesized from literature [12,13].

2.3.1. 2-((1-(3-(1,3-dioxoisoindolin-2-yl)propyl)-1H-1,2,3-triazol-4-yl)methoxy)benzaldehyde (6):

Yield: 86.48%; m.p.184-186°C; IR (ν,cm⁻¹): 1719 (C=O), 1600 (C=C), 1242 (C-O) ; ¹H-NMR (δ ppm): 2.20 (bs, 2H,

CH₂), 3.63 (t, 2H, NCH₂), 4.44 (t, 2H, NCH₂), 5.32 (s, 2H, OCH₂), Arom. [7.12 (bs, 1H, CH), 7.44 (bs, 1H, CH), 7.68 (bs, 2H, CH), 7.84 (bs, 4H, CH)], 8.33 (s, 1H,1,2,3-trz.CH), 10.35 (s,1H, HC=O); ¹³C-NMR (δ ppm): 29.08 (CH₂), 35.33 (NCH₂), 47.80 (NCH₂), 62.72 (OCH₂), Arom. C [114.62(CH), 121.57 (CH), 134.75 (CH), 136.83(CH), 124.90©, 160.87©, 4-Br-Ph₁C (123.43(CH), 128.04(CH), 132.20 ©)], 125.24 (1,2,3-trz.(CH)), 132.20 (1,2,3-trz.(C)), 168.32 (C=O), 189.65 (HC=O).

2.4. Synthesis of new 1,2,3-triazole derivative compound 8

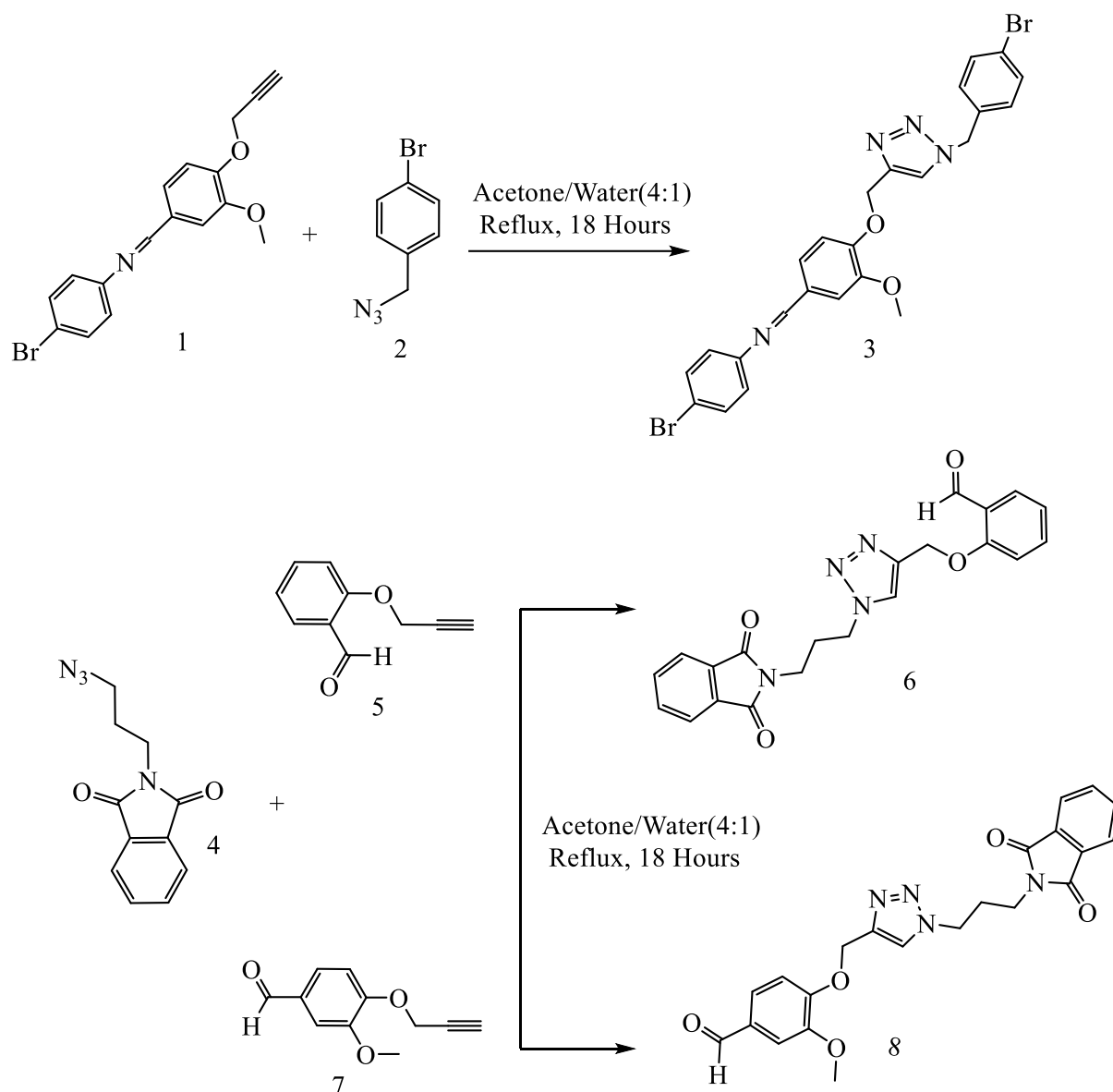
Azide derivative 2-(3-azidopropyl)isoindoline-1,3-dione (4) compound (1 mmol) and acetylene derivative 3-methoxy-4-(prop-2-yn-1-yloxy)benzaldehyde (7) compounds (1 mmol) were mixed separately in water/acetone (1:4) in a 100 mL flask. Then, copper sulfate pentahydrate (1/20 mol) and sodium ascorbate (1/10 mol) were added to the reaction mixture in the specified proportions and refluxed for 18 hours. At the end of the reaction, the contents of the flask were poured into the ice-water mixture, and a solid was obtained, which was filtered and washed with water. It was crystallized with DMF-water and then dried over CaCl₂ in a desiccator (Scheme 1). Compounds 1,2 and 7 were synthesized from literature [12,13].

2.4.1. 4-((1-(3-(1,3-dioxoisoindolin-2-yl)propyl)-1H-1,2,3-triazol-4-yl)methoxy)-3-methoxybenzaldehyde (8):

Yield: 93.20%; m.p.195-197°C; IR (ν,cm⁻¹): 1704 (C=O), 1587 (C=C), 1259 (C-O) ; ¹H-NMR (δ ppm): 2.21 (bs, 2H, CH₂), 3.64 (t, 2H, NCH₂), 4.48 (t, 2H, NCH₂), 3.81 (s, 3H, OCH₃), 5.25 (s, 2H, OCH₂), Arom. [7.40 (bs, 2H, CH), 7.55 (bs, 2H, CH), 7.86 (bs, 3H, CH)], 8.29 (s, 1H,1,2,3-trz.CH), 9.85 (s,1H, HC=O); ¹³C-NMR (δ ppm): 29.32 (CH₂), 35.18 (NCH₂), 47.78 (NCH₂), 55.91 (OCH₃), 62.19 (OCH₂), Arom. C [109.92(CH), 113.13 (CH), 123.46 (CH), 130.35(C), 149.89(C), 153.28(C), 4-Br-Ph₁C (126.38(CH), 134.94(CH), 142.02 (C)], 125.40 (1,2,3-trz.(CH)), 132.22 (1,2,3-trz.(C)), 168.46 (C=O), 192.04 (HC=O).

2.5. Antioxidant activity

The antioxidant properties of the compounds were evaluated using two widely accepted methodologies: the DPPH and FRAP assays, renowned for their effectiveness in gauging the antioxidant potential of diverse compounds. The DPPH assay, adapted from [14] measures the compounds' ability to scavenge the DPPH radical. This method relies on the decolorization of the purple DPPH solution upon interaction with antioxidants. Absorbance changes at 517 nm, recorded spectrophotometrically, indicate the degree of radical scavenging activity. Results, reported as SC₅₀ values (mg of sample per mL), delineate the concentration required for a 50% reduction in the DPPH radical compared to the standard Trolox.



Scheme 1. Synthetic pathway for the preparation of compounds 3,6 and 8

Concurrently, the antioxidant capacity was determined through the FRAP method, following the protocol described by [15]. This approach involves the reduction of the Fe^{3+} -TPTZ complex to the Fe^{2+} -TPTZ complex in the presence of antioxidants. Spectrophotometric readings at 593 nm after a 4-minute incubation period elucidate the compounds' ability to reduce ferric ions. Results are expressed as μM Trolox equivalent per milligram of compound, where higher Trolox equivalent values denote elevated FRAP and hence increased antioxidant efficacy.

Both assays serve as robust tools for assessing the antioxidant prowess of compounds, providing valuable insights into their capacity to neutralize free radicals and reduce ferric ions. These standardized methodologies offer a comparative analysis of diverse compounds, enabling a comprehensive evaluation of their antioxidant capabilities.

3. Results and discussion

3.1. Synthesis

Compounds 3, 6 and 8 were synthesized with click reaction in the ^1H NMR spectra of compounds 3, 6, and 8, C-H proton signal belonging to 1,2,3-triazole ring was seen at 8.29–8.36 ppm as a singlet. Carbon peaks belonging to 1,2,3 triazole rings were observed at 1326.24–135.84 ppm in the ^{13}C -NMR spectra of compounds 3, 6, and 8. ^1H -, ^{13}C -NMR data confirm the structures of the compounds. The spectral data obtained are in full compliance with the literature. [16].

3.2. Antioxidant activity

The antioxidant capacities of the F-series compounds were investigated using DPPH radical scavenging and FRAP reducing power assays. The results revealed substantial differences among the tested compounds (Table 1).

Table 1. DPPH and FRAP activities of compounds 3, 6 and 8

Compound	DPPH (SC ₅₀ : mg/mL)	FRAP (μM Trolox Equivalent/mg compound)
3	2.27±0.03 ^d	278.47±0.42 ^c
6	10.81±0.03 ^b	28.05±0.82 ^c
8	6.620±0.002 ^a	No activity
Trolox	0.121±0.000 ^a	Not tested

*Same letters in each column were not significantly different at $p < 0.05$ (Tukey's range test). The means of three replicates were given with \pm standard deviations.

In the DPPH assay, where lower SC₅₀ values indicate higher free radical scavenging activity, compound **3** exhibited the highest antioxidant potential (SC₅₀ = 2.27 mg/mL). Compound **8** (SC₅₀ = 6.62 mg/mL) showed moderate activity, whereas compound **6** (SC₅₀ = 10.81 mg/mL) had the weakest radical scavenging capacity. When compared to Trolox (SC₅₀ = 0.121 mg/mL), all tested compounds displayed significantly lower antioxidant efficiency.

The FRAP assay, which measures the ferric ion-reducing ability, showed that compound **3** had the highest reducing power (278.47 μM Trolox equivalent/mg compound), indicating strong electron donation potential. Compound **6** (28.05 μM Trolox equivalent/mg compound) exhibited a relatively weak reduction capacity. Furthermore, compound **8** did not show any detectable activity in the FRAP assay, suggesting its limited ability to reduce ferric ions.

These findings suggest that compound **3** has the highest antioxidant potential among the compounds, demonstrating superior performance in both radical scavenging and reducing power. Compound **8** exhibited moderate activity, while compound **6** had the weakest overall antioxidant efficacy.

Acknowledgment

The author thanks Dr. Ersan Bektaş for antioxidant studies.

References

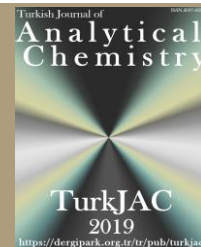
- [1] F. Çelik, Y. Ünver, B. Barut, A. Özel, K. Sancak, Synthesis, Characterization and Biological Activities of New Symmetric Bis-1,2,3-Triazoles with Click Chemistry, *Medicinal Chemistry*, 2018, 230-241.
- [2] E. Dügüdü, D. Ünlüer, F. Çelik, K. Sancak, Ş. A. Karaoğlu, A. Özel, Synthesis of Novel Symmetrical 1,4-Disubstituted 1,2,3-Bistriazole Derivatives via 'Click Chemistry' and Their Biological Evaluation, *Molecules*, 21, 2019, 659-672.
- [3] F. Çelik, F. Türkan, A. Aras, M. N. Atalar, H. S. Karaman, Y. Ünver, N. Kahrman, Synthesis of novel 1,2,3 Triazole Derivatives and Assessment of Their Potential Cholinesterases, Glutathione S-transferase Enzymes Inhibitory Properties: An in Vitro and in Silico Study, *Bioorganic Chemistry*, 107, 2021.
- [4] R. P. Frutos, S. Rodriguez, N. D. Patel, D. Reeves, T. Tampone, C.H. Senanayake, A General and Practical Synthesis of N-Aryl-3-4-(imidazol-4-yl)-1,2,3-triazol-1-yl benzamide Anti-Inflammatory Cytokine Inhibitors, *Asian Journal of Organic Chemistry*, 3, 2014, 769-772.
- [5] R. Jain, P. Gahlyan, S. Dwivedi, R. Konwar, S. Kumar, M. Bhandari, R. Arora, R. Kakkar, R. Kumar, A.K. Prasad, Design, Synthesis and Evaluation of 1H-1,2,3-Triazol-4-yl-methyl Tethered 3-Pyrrolylisatins as Potent Anti-Breast Cancer Agents, *Chemistry Select*, 19, 2018, 5263-5268.
- [6] D. L. Jardim, M. Schwaederle, D. S. Hong, R. Kurzrock, An appraisal of drug development timelines in the Era of precision oncology, *Oncotarget*, 7, 2016, 53037-53046.
- [7] V. Judge, B. Narasimhan, M. Ahuja, D. Sriram, P. Yogeeswari, Isonicotinic Acid Hydrazide Derivatives: Synthesis, Antimycobacterial, Antiviral, Antimicrobial Activity and QSAR Studies, *Letters in Drug Design & Discovery*, 8, 2011, 792-810.
- [8] V. Judge, B. Narasimhan, M. Ahuja, D. Sriram, P. Yogeeswari, E. De Clercq, C. Pannecouque, J. Balzarini, Isonicotinic acid hydrazide derivatives: synthesis, antimicrobial activity, and QSAR studies, *Medicinal Chemistry Research*, 21, 2012, 1451-1470.
- [9] D. Kumar, N.M. Kumar, S. Ghosh, K. Shah, Novel bis(indolyl)hydrazide-hydrazones as potent cytotoxic agents, *Bioorganic & Medicinal Chemistry Letters*, 22, 2012, 212-215.
- [10] K.S. Kumar, S. Mohanty, G.P. Reddy, V. Siddaiah, J.D. Lilakar, G.L. Goud, Synthesis and Antimicrobial Activity of 3-[2-(1-Aryl-1H-1,2,3-triazol-4-yl)methoxy -5-fluorophenyl]isoxazoles, *Russian Journal of General Chemistry*, 89, 2019, 1221-1224.
- [11] S. Kumar, B. Sharma, V. Mehra, V. Kumar, Recent accomplishments on the synthetic/biological facets of pharmacologically active 1H-1,2,3-triazoles, *European Journal of Medicinal Chemistry*, 212, 2021, 113069.
- [12] S. Gallagher, M. Hashemzadeh, L.R. Peyton, Triazole antifungals: A review. *Drugs Today*, 51, 2015, 705-718.
- [13] H. H. Renate, M. G. Eric, L. Carmen, J. S. Peter, W. Baojie, G. F. Scott, G. Jiri, J. R. Philip, C. Kelly, Synthesis, antimalarial and antitubercular activity of acetylenic chalcones, *Bioorganic & Medicinal Chemistry Letters*, 20, 2010, 942-944.
- [14] M. Cuendet, K. Hostettmann, O. Potterat, W. Dyatmiko, Iridoid Glucosides with Free Radical Scavenging Properties from *Fagraea blumei*, *Helv Chim Acta*, 80, 1997, 1144-1152.
- [15] I.F. Benzie, J.J. Strain, The ferric reducing ability of plasma (FRAP) as a measure of "antioxidant power": the FRAP assay, *Anal Biochem*, 239, 1996, 70-76.
- [16] F. Çelik, Y. Ünver, B. Barut, A. Özel, K. Sancak, Synthesis, Characterization and Biological Activities of New Symmetric Bis-1,2,3-Triazoles with Click Chemistry, *Medicinal Chemistry*, 14, 2018, 230-241.



TurkJAC

Turkish Journal of

Analytical Chemistry

<https://dergipark.org.tr/tr/pub/turkjac>TurkJAC
2019<https://dergipark.org.tr/tr/pub/turkjac>

Comparative analysis of phenolic compounds, volatile components, and antioxidant capacity in leaf and flower parts of *Aster caucasicus*

Abidin Gümrukçüoğlu 

Artvin Coruh University, Medicinal and Aromatic Plants Research and Application Center, 08000, Artvin, Türkiye

Abstract

The study presents a comprehensive phytochemical analysis of *A. caucasicus*, examining both the leaf and flower parts of this plant. The researchers investigated the phenolic compound profiles using HPLC-DAD methodology, volatile compounds via SPME-GC-MS technique, and antioxidant properties through multiple assays (total phenolic content, total flavonoid content, FRAP, and CUPRAC).

Results revealed significant differences between plant organs. The flower parts contained higher total phenolic content (25.57 mg GAE/g) compared to leaves (17.81 mg GAE/g), with notably higher concentrations of compounds like gallic acid, caffeic acid, rosmarinic acid, and quercetin. Conversely, leaves demonstrated higher total flavonoid content (5.02 mg QE/g vs. 3.99 mg QE/g in flowers) and greater antioxidant capacity in both FRAP and CUPRAC assays.

Volatile compound analysis identified several bioactive components, including monoterpenes (beta-pinene, D-limonene, alpha-pinene), terpenoids, sesquiterpenes, and oxygenated heterocyclic compounds. Beta-pinene dominated in flowers (52.26%), while D-limonene was highest in leaves (28.68%).

This research fills a knowledge gap regarding *A. caucasicus*, suggesting its potential applications in pharmaceutical and cosmetic products. The flower parts show promise for pharmaceutical applications due to their rich phenolic content, while the leaf parts, with their high flavonoid content and antioxidant capacity, could be valuable in cosmetic products, particularly for UV protection.

Keywords: *A. caucasicus*, antioxidant capacity, phenolics, volatile compound

1. Introduction

Phenolic compounds are a group of phytochemical substances found as secondary metabolites in various plants. These compounds have received great interest in the scientific world due to their diverse biological activities and positive effects on human health. Natural polyphenols are considered important compounds due to their antioxidant properties, antimutagenic and/or anticarcinogenic effects, anti-inflammatory properties, and neuroprotective effects [1–4]. Scientific studies reveal that these compounds can both function as protective antioxidants against oxidative degradation and act as pro-oxidants that damage biomolecules, causing cellular death [5–6].

The medicinal properties of plant species are largely attributed to their secondary metabolites, particularly compounds like phenolic acids and flavonoids [7–8]. Recent scientific interest has grown around plant

polyphenols due to their antioxidant properties and various health benefits, as well as their applications in industry. Beyond therapeutic uses, medicinal plants serve nutritional purposes globally and are often classified as food products under regulatory frameworks in numerous countries [8–10]. The significant therapeutic potential of these plants makes the identification and characterization of their phenolic constituents a priority in analytical science research [11–12].

Many research efforts have documented the presence of polyphenols in plant materials and sought to elucidate their therapeutic applications, nutritional value, and antioxidant capabilities [13]. Consequently, developing analytical methodologies to identify and characterize these compound classes has become essential in phytomedicine research. Analytical approaches such as

Citation: A. gümrukçüoğlu, Comparative Analysis of Phenolic Compounds, Volatile Components, and Antioxidant Capacity in Leaf and Flower Parts of *Aster caucasicus*, Turk J Anal Chem, 7(2), 2025, 195–208.

Author of correspondence: gumrukcuogluabidin@artvin.edu.tr

Tel: +90 (466) 215 1044

Fax: N/A

Received: April 10, 2025

Accepted: May 23, 2025

doi <https://doi.org/10.51435/turkjac.1673174>

gas chromatography [14], high-performance liquid chromatography [7,15], and capillary electrophoresis [15,16] have been employed for phenolic compound characterization. However, due to the high melting points and thermal instability of phenolic acids and flavonoids above 200°C, liquid chromatography-based separation techniques are generally preferred.

High-Performance Liquid Chromatography (HPLC) is the most widely used separation technique applied to detect and quantify phytochemicals in plants [17–20]. Different detection modes are used, such as on-line diode array detection (DAD) [21–22], ultraviolet detectors [23], or electrochemical detectors [24].

As a more economical alternative, HPLC-DAD systems simplify the analytical methodology and significantly reduce associated costs, thereby making them suitable for routine analyses in laboratories with limited financial resources. In contrast, the integration of more sophisticated techniques such as electrospray ionization (ESI), atmospheric pressure chemical ionization (APCI), negative or positive ion mode coupled with MS-MS (utilizing triple quadrupole) or theoretical MS_n (employing ion trap technology) provides confirmatory evidence for peak identification, yet simultaneously increases both the financial investment required and the methodological complexity [25–30].

The technique of headspace solid-phase microextraction (HS-SPME) is extensively employed for isolation and pre-concentration of volatile compounds prior to gas chromatography-mass spectrometry (GC-MS) analysis [31–34]. Compared to alternative sample preparation methodologies such as solid-phase extraction or liquid-liquid extraction, SPME offers distinct benefits, including solvent-free operation, automation capability, and minimal sample volume requirements [35]. These advantageous characteristics render SPME particularly valuable for research necessitating the examination of large sample quantities, exemplified by studies evaluating plant populations utilized by plant breeders investigating genetic foundations of specific traits [36,37]. Researchers have documented the mapping of genes or quantitative trait loci (QTLs) governing volatile production, including those contributing to aroma, across numerous plant species such as tomato [32], melon [38,39], apple [40,41], and grape [42–44]. For plant volatile phenotyping, GC-MS methodology is typically implemented for both focused analysis of select volatiles [45,46] and comprehensive profiling of numerous targeted or untargeted volatile compounds (referred to as "metabolomics") [31,32,38,39,40,47].

The genus *Aster* within the Asteraceae family comprises approximately 600 species that have adapted

to diverse ecological environments and demonstrate widespread natural distribution. Although many species and interspecific hybrids serve ornamental purposes or contribute to the cut flower industry, these plants are predominantly valued for their medicinal properties, which have been recognized since antiquity. Traditional Chinese medicine has utilized *Aster* species for treating conditions including cough, fever, and tonsillitis. Contemporary scientific investigations have indicated that these plants exhibit diuretic, anti-tumor, antibacterial, antiviral, and anti-ulcer activities [48].

The therapeutic properties of *Aster* species are attributed to their high content of antioxidant compounds such as polyphenols and ascorbic acid, which exhibit antibacterial, antiviral, anti-inflammatory, anti-allergic, antithrombotic, and vasodilator effects, and are beneficial in the treatment and prevention of arteriosclerosis, cancer, diabetes, neurodegenerative diseases, arthritis, and other pathologies [49–50]. The variability of antioxidant content in plants results from the fact that the synthesis and accumulation of these compounds are a direct consequence of plant-environment interaction.

In the present study, the phenolic compound profile of the methanolic extract of *A. caucasicus* leaves and flowers, the composition of volatile compounds using solid-phase microextraction (SPME) technique, and their antioxidant potential were comparatively examined. Although there are individual content analyses on similar species in the literature, HPLC-DAD methodology for the simultaneous analysis of phytochemicals with a wide range of chemical structures, such as phenolic acids and flavonoids in these plant extracts, and SPME-GC-MS technique for the characterization of volatile compounds have not been reported. In the current literature, there are only studies comparing the antioxidant properties of *A. caucasicus* and *Aster sedifolius* species grown under cell culture conditions. However, there is no comprehensive research that comparatively evaluates both the phenolic and volatile compound profiles and antioxidant capacities of *A. caucasicus* leaves and flowers. The primary objective of this research is to determine the phenolic compound profile of *A. caucasicus* species, which lacks detailed characterization in the literature, to characterize its volatile compound composition, and to evaluate its antioxidant capacity. The polyphenol content determined in this study was evaluated by comparison with compounds reported in the literature to be effective in the treatment of pathologies such as arteriosclerosis, cancer, diabetes, neurodegenerative diseases, and arthritis. These comprehensive phytochemical characterization results will provide a foundation for future in vitro and in vivo bioactivity

studies investigating the antibacterial, antiviral, anti-inflammatory, anti-allergic, and antithrombotic activities of *A. caucasicus*.

2. Materials and methods

2.1. Plant material and methanolic extraction of leaf and flower parts of *A. caucasicus* species

The taxon names of *A. caucasicus*, the place of collection of the plant, and the receipt number are indicated as shown in Table 1. Also, the habit of *A. caucasicus* is shown in Fig. 1. Following collection, the plant material was promptly moved to a well-ventilated drying room with moderate ambient light, ensuring it remained protected from direct sunlight. The leaves and flowers of *A. caucasicus* were kept at -20°C for antioxidant capacity, some phenolic and flavonoid compound contents, and volatile compound content. All experiments and analyses were carried out in triplicate.

Table 1. Collection data of the examined *A. caucasicus*

Taxon	Locality	Voucher*
<i>Aster caucasicus</i>	(Aksu 399) specimens were collected on 26 July 2022 from the roadside habitat along the Heba Plateau road in Borçka (Artvin Province, NE Türkiye), at an altitude of approximately 1600 m, growing among Rhododendron shrubs along the roadside.	Aksu 399



Figure 1. Habitat of *A. caucasicus* plant

2.2. Preparation of samples

The extraction method was used by revising the methods [51,52]. Here, leaf and flower samples consisting of 20 grams of dry powder were treated separately with 200 ml of methanol to increase the extraction of target compounds, and the mixtures were subjected to ultrasonication for 30 minutes. After

ultrasonication, the samples were transferred to a shaker and kept at room temperature in the dark for 24 hours for optimal extraction efficiency. Following the incubation period, regular filter paper was used to remove large particles from the extracts, followed by a second filtration process with a 0.45 µm syringe filter to remove smaller particles. This comprehensive extraction procedure, including ultrasonication, long-term incubation, and double filtration stages, was designed to ensure maximum transfer of compounds from the dry powder samples to the extraction solution, and the resulting clear filtrates were prepared for analysis [51,52].

2.3. Antioxidant capacity of *A. caucasicus* leaves and flowers

2.3.1. Reagents and materials

For the analysis of polyphenols, flavonoids, and antioxidant capacity, various analytical reagents were sourced as follows: Methanol, Trolox (6-hydroxy-2,5,7,8-tetramethylchroman-2-carboxylic acid), 2,4,6-tripyridyl-s-triazine (TPTZ), and Folin-Ciocalteu's phenol reagent were procured from Sigma Chemical Co. (St. Louis, MO, USA). Complementary reagents, including sodium carbonate, acetic acid, neocuproine (2,9-dimethyl-1,10-phenanthroline), aluminum nitrate nonahydrate, CuCl₂, FeSO₄·7H₂O and ammonium acetate were acquired from Merck Chemical Co. (Darmstadt, Germany). All chemical compounds utilized throughout the experimental procedures were of analytical grade purity.

2.3.2. Determination of total polyphenolic content

The quantification of total phenolic (TP) compounds was conducted using the Folin-Ciocalteu methodology [53]. A standard calibration curve was prepared using gallic acid at six different concentrations (1, 0.5, 0.25, 0.125, 0.0625, and 0.03125 mg/mL). The experimental protocol involved combining 20 µL of either standard solution or methanolic plant extract (1 mg/mL) with 400 µL of 0.5 N Folin-Ciocalteu reagent and 680 µL of distilled water. Following thorough mixing and a 3-minute reaction period, 400 µL of 10% Na₂CO₃ solution was introduced to the mixture. The reaction was allowed to develop for 2 hours at 25°C, after which absorbance measurements were recorded at 760 nm. The polyphenolic content was subsequently calculated and expressed as milligrams of gallic acid equivalents (GAE) per gram of plant dry weight.

2.3.3. Assessment of total flavonoid content

Total flavonoid (TF) (mg QE/g dry sample) quantification was performed according to a modified protocol from reference [54]. The analytical principle

exploits the characteristic of aluminum chloride to form coordination complexes with flavonoid compounds. Specifically, aluminum ions establish stable complexes with the C-4 keto group and either C-3 or C-5 hydroxyl groups present in flavones and flavonols, while forming fewer stable associations with ortho-dihydroxyl configurations in both A and B rings. For standardization purposes, quercetin solutions ranging from 0.03125 to 1.0 mg/mL were employed to generate a reference curve correlating absorbance measurements with known concentrations [54].

2.4. Ferric and copper reduction assays of antioxidant activity in *A. caucasicus* leaves and flowers

In the FRAP assay, total antioxidant potential was assessed through the conversion of a yellow Fe^{+3} -TPTZ (2, 4, 6-tripyridyl-s-triazine) complex into a blue Fe^{+2} -TPTZ complex when exposed to electron-donating compounds in acidic medium [55]. The protocol involved combining 3 mL of freshly prepared FRAP reagent with 100 μL of either experimental extract or control solvent in a test tube. Spectrophotometric measurements at 593 nm were recorded over a 4-minute interval at ambient temperature (25°C). The resulting absorbance values were quantified against an $\text{FeSO}_4 \cdot 7\text{H}_2\text{O}$ calibration curve (100-1000 $\mu\text{mol/L}$), with final results expressed as micromoles of ferrous sulfate heptahydrate equivalents per gram of plant dry matter.

The CUPRAC methodology involves the interaction of antioxidant compounds with a reaction mixture containing Cu^{2+} ions, neocuproine (alcoholic solution), and ammonium acetate buffer (pH 7). Following a 60-minute incubation period, optical density was determined at 450 nm. The experimental procedure entailed combining equal volumes (1 mL each) of copper(II) chloride (10 mM), neocuproine (7.5 mM), and ammonium acetate (1 M) with sample extract (0.2 mL) and deionized water (0.9 mL) to achieve a final reaction volume of 4.1 mL. Absorbance readings were obtained after a 60-minute reaction period, and antioxidant capacity was calculated in terms of Trolox® equivalent antioxidant capacity (TEAC) [56].

2.5. HPLC-DAD analysis of phenolic compounds in *A. caucasicus* leaves and flowers

2.5.1. Chemical reagents

The acetonitrile HPLC gradient was acquired from Sigma-Aldrich Co. (St. Louis, MO, USA), while the methanol HPLC gradient was obtained from Merck KGaA (Darmstadt, Germany). All phenolic reference compounds utilized in the analysis were procured from Sigma-Aldrich, an established vendor recognized for supplying research-grade chemicals and analytical standards.

2.5.2. Instrumental parameters

Protocol A: Advanced chromatographic methodology for the quantification of compounds numbered 1, 2, 3, 4, 6, 7, 8, 9, 14, 15, 16, 17, 18, and 19 isolated from the plant, as shown in Fig. 2. Compound isolation was performed with an ACE 5 C18 stationary phase (250 \times 4.6 mm, 5 μm particle size). The binary mobile phase consisted of (A) acetonitrile and (B) dilute acetic acid (1.5% v/v). The elution profile commenced with 15% component A and 85% component B, transitioning to 40% component A and 60% component B at 29 minutes. The instrumental configuration incorporated a 1260 DAD WR spectrophotometric detector (monitoring at 250, 270, and 320 nm), a 1260 Quaternary Pump (maintaining 0.7 mL/min volumetric flow), a 1260 Vial Sampler (delivering 10 μL injection volume), and a G7116A thermostatic column compartment (maintained at 35°C). Protocol B: Advanced chromatographic methodology for the quantification of compounds numbered 5, 10, 11, 12, 13, 20, 21, 22, 23, and 24 isolated from the plant, as shown in Fig. 2: Compound isolation was performed with an ACE 5 C18 stationary phase (250 \times 4.6 mm, 5 μm particle size). The binary mobile phase consisted of (A) methanol and (B) dilute acetic acid (1.5% v/v). The elution profile commenced with 10% component A and 90% component B, transitioning to 40% component A and 60% component B at 29 minutes, followed by 60% component A and 40% component B through 40 minutes, concluding with 90% component A and 10% component B from 40 to 53 minutes.

No	1	2	3	4	5	6	7	8	9	10	11	12	13	14	15	16	17	18	19	20	21	22	23	24
Compounds	Ascorbic acid	Galic acid	3-4-Hydroxybenzoic acid	Vanillic acid	Syringic acid	Cummaric acid	Caffeic acid	Ferulic acid	Rosmarinic acid	Protogallol	Chlorogenic acid	Resveratrol	Oleuropein	Catechin	Epicatechin	Rutin	Myricetin	Quercetin	Apigenin	Cyanidin chloride	Hesperitin	Kaempferol	Baicalin	Chrysin
	Vitamin	Phenolics											Flavonoids											

Figure 2. It lists the standards separated by the HPLC-DAD method

Table 2. Phytochemical compounds of *A. caucasicus* leaf

No	RT (min)	RI	Name of the compound	Content [%]
1	4.11	705	Furan, 2-ethyl-	7.08
2	6.16	802	Hexanal	9.62
3	7.29	834	Butanal, 2-ethyl-3-methyl-	1.29
4	7.86	850	2-Hexenal, (E)-	4.66
5	8.12	857	6,6-Dimethylhepta-2,4-diene	0.99
6	11.17	932	α -Pinene	4.21
7	12.17	953	2-Heptanone,6-methyl-	1.51
8	12.39	958	Benzaldehyde	2.37
9	13.19	975	β -Pinene	19.34
10	13.33	978	Sabinene	0.76
11	13.95	991	Furan, 2-pentyl	3.01
12	15.63	1023	p-Cymene	0.52
13	15.84	1027	D-Limonene	28.68
14	16.90	1047	β -Ocimene	0.90
15	17.49	1058	Isophorone	2.94
16	24.90	1195	Myrtenal	0.97
17	31.68	1323	Silphiperfol-5-ene	5.02
18	34.47	1378	Modephene	4.66
19	34.81	1385	α -Isocomene	1.25

RT: Retention times on an HP-5MS UI column, **RI:** Experimentally determined retention indices on an HP-5MS UI column

The instrumental configuration incorporated a 1260 DAD WR spectrophotometric detector (monitoring at 280, 290, 320, 370 and 535 nm), a 1260 Quaternary Pump (maintaining 0.7 mL/min volumetric flow), a 1260 Vial Sampler (delivering 10 μ L injection volume) and a G7116A thermostatic column compartment (maintained at 35°C).

2.5.3. Preparation of reference standard solutions

Quantitative determination of phenolic constituents was accomplished through external calibration curves using six serial dilutions of each reference standard at precisely defined concentrations: 25, 50, 75, 100, 200, and 300 μ g/mL. Subsequent to preparation, these calibration solutions were subjected to HPLC-DAD analysis under identical instrumental conditions as the experimental samples.

2.6. SPME-GC-MS analysis of volatile compounds in leaves and flowers of *A. caucasicus*

2.6.1. SPME absorption of volatile compounds

The fiber was conditioned as recommended by the manufacturer before use. The plant was thoroughly fragmented in a laboratory-type grinder. From the powdered sample, enough to fill one-third of a 20 mL vial was placed in a 20 mL bottle sealed with PTFE/silicone septa (Supelco). Each sample was heated at 45°C for 15 minutes. Then, a syringe with an appropriate fiber tip was immersed in the bottle and absorbed for 40 minutes. The compounds exposed to the fiber tip were injected into the injection block of the GC unit and held for 20 minutes for absorption.

Table 3. Phytochemical compounds of *A. caucasicus* flower

No	RT (min)	RI	Name of the compound	Content [%]
1	6.14	800	Hexanal	9.83
2	9.30	890	2-Heptanone	1.23
3	11.16	932	α -Pinene	6.19
4	12.39	958	Benzaldehyde	2.47
5	13.19	975	β -Pinene	52.26
6	13.74	986	Sulcatone	1.36
7	13.94	991	Furan, 2-pentyl	3.19
8	15.62	1023	p-Cymene	1.28
9	15.84	1027	D-Limonene	7.29
10	16.90	1047	β -cis-Ocimene	0.87
11	24.89	1195	cis-Myrtenal	1.28
12	25.09	1198	Dodecane	1.58
13	31.67	1223	Silphiperfol-5-ene	2.83
14	34.46	1278	Modephene	1.09
15	34.81	1285	(-)-Isocomene	0.55
16	35.45	1298	Tetradecane	1.31
17	36.44	1318	Caryophyllene	5.19

RT: Retention times on an HP-5MS UI column, **RI:** Experimentally determined retention indices on an HP-5MS UI column

2.6.2. Instrument conditions

GC-MS analysis will be performed using an Agilent (Agilent Technologies, Santa Clara, CA, USA) gas chromatograph and HP-5MS ultra inert capillary column (30 m \times 0.25 mm \times 0.25 μ m). High-purity helium (>99.99%) will be used as the mobile phase at a flow rate of 1.0 mL/min. The injector temperature was set to 250°C. The GC program maintained an initial temperature of 50°C for 2 minutes. It will be raised to 150°C at a rate of 2.5°C/min and held constant there for 5 minutes. Finally, it will be increased to 250°C at a rate of 6.5°C/min and held constant there for 1 minute. The MS operating parameters include an ionization energy of 70 eV, with a scanned mass range of 35-500 m/z [57].

3. Results and discussion

3.1. GC-MS analysis and photochemical profile of *A. caucasicus*

Various phytochemical compounds characterized by retention times ranging from 4 to 36 minutes and different indices varying between 700 and 1385 were detected in samples taken from the leaf and flower parts of *A. caucasicus*. As shown in Table 2 and Table 3, compounds found in high amounts in the flower and leaf parts of the plant include monoterpenes, terpenoids, sesquiterpenes, oxygenated heterocyclic compounds, and volatile organic compounds, and the proportions of these compounds vary according to plant parts.

In the research, beta-pinene, D-limonene, and alpha-pinene were identified as monoterpenes; silphiperfol-5-ene as a terpenoid; modephene as a sesquiterpene; Furan, 2-ethyl and Furan, 2-pentyl, as oxygenated heterocyclic compounds; and hexanal as a volatile organic compound. The distribution and concentrations

of these compounds in plant tissues provide significant contributions to understanding the phytochemical profile of *A. caucasicus*.

In the leaf part of the plant, the monoterpenes β -pinene (19.34%), D-limonene (28.68%), and α -pinene (4.21%); silphiperfol-5-ene (5.02%) as a terpenoid; modephene (4.66%) as a sesquiterpene; Furan, 2-ethyl (7.08%), and Furan, 2-pentyl (3.01%) as oxygenated heterocyclic compounds; and hexanal (9.62%) as a volatile organic compound were determined. In the flower part, the monoterpenes β -pinene (52.26%), D-limonene (7.29%), and α -pinene (6.19%); silphiperfol-5-ene (2.83%) as a terpenoid; modephene (1.09%) as a sesquiterpene; Furan, 2-pentyl (3.19%) as an oxygenated heterocyclic compound; and hexanal (9.83%) as a volatile organic compound were detected.

When examining the phytochemical profile of the *A. caucasicus* plant, notable differences were observed between the leaf and flower parts. β -pinene (52.26%) stands out as the dominant compound in the flower part, while D-limonene (28.68%) was found in the highest proportion in the leaf part. This difference reflects the different physiological functions and ecological roles of plant organs. The high presence of monoterpenes in both plant parts is one of the characteristic features of the Aster genus, particularly containing compounds such as beta-pinene, which has antispasmodic, anti-inflammatory [59], hypotensive [60], antimicrobial [61], anti-depressant, and sedative [58] effects, and D-limonene, which has antibacterial, anti-inflammatory, antiviral, antinociceptive, and antidiabetic effects [62]. The approximately 2.7 times higher proportion of beta-pinene in the flower part compared to the leaf part can be associated with the flowers' pollination process of attracting insects and their protective functions. In contrast, the approximately 4 times higher proportion of D-limonene in leaves compared to flowers can be considered as part of the leaves' defense mechanism against herbivores.

The detection of terpenoids and sesquiterpenes such as silphiperfol-5-ene and modephene in both parts, but their presence in higher concentrations in the leaf part, indicates that these compounds are more actively synthesized in the vegetative tissues of the plant. It is particularly noteworthy that modephene is approximately 4.3 times higher in the leaf part (4.66%) compared to the flower part (1.09%). When the distribution of oxygenated heterocyclic compounds is

examined, the detection of Furan, 2-ethyl compound only in the leaf part (7.08%) indicates the presence of a biosynthesis pathway specific to leaf tissue. Volatile organic compounds such as hexanal were found in similar proportions (9.62-9.83%) in both tissues.

These differences in the chemical composition of the leaf and flower parts of *A. caucasicus* demonstrate that different tissues of the plant possess different physiological functions and ecological roles. These findings are expected to make significant contributions to the evaluation of the plant's potential pharmacological and bioactive properties.

3.2. Total phenolic content and antioxidant properties of *A. caucasicus* extract

In this study, total phenolic, total flavonoid, FRAP, and CUPRAC contents of *A. caucasicus* flower and leaf extracts were determined spectrophotometrically (Table 4).

When examining the analysis results, it was observed that the total phenolic content among the plant organs varied between 17.81 and 25.57 mg GAE/g dry weight. While the total phenolic content of the leaf part of the plant was 17.81 ± 0.60 mg GAE/g, the flower part showed values of 25.57 ± 5.40 mg GAE/g. These results indicate that although there is not a very significant difference between the values of the leaf and flower parts, the total phenolic content of the flower part is slightly higher compared to the leaf part. The leaf parts of plants are exposed to higher rates of sunlight compared to other parts due to their large surface areas. For this reason, flavonoids accumulate more abundantly in leaves compared to other parts as the plant's mechanism to protect itself from UV radiation and reduce oxidative stress [63-65]. As shown in Table 4, the total flavonoid content varied between 5.02 and 3.99 mg QE/g dry weight. It was observed that the total flavonoid content of the plant's leaf part (5.02 ± 0.04 mg QE/g) was higher than the total flavonoid content of the flower part (3.99 ± 0.11 mg QE/g). Unlike total phenolics (TP), which show higher concentrations in flowers, total flavonoid (TF) content is typically more abundant in leaves. This finding aligns with established research demonstrating that flavonoids primarily accumulate in leaf tissue as a protective mechanism against UV radiation and oxidative stress [66].

FRAP and CUPRAC assays were independently applied to the flower and leaf extracts of the plant.

Table 4. The antioxidant properties of *A. caucasicus* extracts were investigated, including the total phenolic content, total flavonoid content, FRAP, and CUPRAC analyses.

Taxon	Used part	Total phenolic content (mg GAE/g dry sample)*	Total flavonoid content (mg QE/g dry sample)*	FRAP (μ mol FeSO ₄ .7H ₂ O/g sample)*	CUPRAC (mmol TEAC/g sample)*
<i>A. caucasicus</i>	Leaf	17.81 ± 0.60	5.02 ± 0.04	7.77 ± 0.18	0.32 ± 0.01
	Flower	25.57 ± 5.40	3.99 ± 0.11	7.53 ± 0.17	0.27 ± 0.01

According to these findings, FRAP results ranged between 7.77 and 7.53 $\mu\text{mol Fe}^{2+}/\text{g}$ dry weight, while CUPRAC values varied between 0.32 and 0.27 mmol TEAC/g dry weight. The FRAP activity in leaves ($7.77 \pm 0.18 \mu\text{mol Fe}^{2+}/\text{g}$) was slightly higher than in flowers ($7.53 \pm 0.17 \mu\text{mol Fe}^{2+}/\text{g}$). Similarly, the CUPRAC activity in leaves ($0.32 \pm 0.01 \text{ mmol TEAC}/\text{g}$) exceeded that observed in flowers ($0.27 \pm 0.01 \text{ mmol TEAC}/\text{g}$).

These results indicate that the higher total phenolic content in flowers compared to leaves demonstrates that flowers are richer in phenolic compounds, which is consistent with the overall findings. However, the lower total flavonoid content in flowers compared to leaves supports the premise that plant leaves accumulate flavonoids as a protective mechanism against UV radiation and to mitigate oxidative stress, resulting in a richer flavonoid profile than flowers.

Furthermore, the elevated FRAP and CUPRAC values observed in leaves suggest that flavonoids may contribute more significantly to total antioxidant capacity than other phenolic compounds present in flowers. This observation aligns with expectations given the powerful reducing properties characteristic of flavonoids.

When comparing our current research with similar studies in the literature, remarkably intriguing findings emerge. One study reported that the total phenolic content of 17 different species from the Asteraceae family, including *A. caucasicus*, varied between 2.65 and 13.34 mg GA/g [67]. In a 2021 investigation on *Cirsium englerianum*, the total flavonoid content of the methanolic extract was determined to be 5.88 ± 0.21 [68]. In comparison with these literature data, the total phenolic content of the plant in our study (17.81-25.57 mg GAE/g) is significantly higher than the values reported for other species in the Asteraceae family (2.65-13.34 mg GA/g). This suggests that our investigated plant is rich in phenolic compounds and may constitute a valuable resource for potential phytotherapeutic applications.

The total flavonoid content, meanwhile, is comparable to the value reported in the literature for *Cirsium englerianum*; particularly, the value in our leaf samples ($5.02 \pm 0.04 \text{ mg QE}/\text{g}$) approximates that of *Cirsium englerianum* (5.88 ± 0.21). Another study examined the time-dependent variations of leaf extracts from *Leuzea carthamoides*, another member of the same family. In this investigation, FRAP values were observed to range between 1.2 and 60 $\mu\text{mol Fe}^{2+}/\text{g}$ [69]. Hence, it is evident that the FRAP values of the plant in our study (7.53-7.77 $\mu\text{mol Fe}^{2+}/\text{g}$) are situated in the lower-middle

range of the broad spectrum of values for *Leuzea carthamoides*.

In conclusion, the compositional differences among plant parts analyzed in our study distinctly reflect the characteristic physiological functions and ecological roles of different plant organs. While flowers demonstrate superiority in total phenolic content, leaves exhibit higher flavonoid content and robust antioxidant capacity. These findings indicate a noteworthy phytochemical richness when compared with other members of the Asteraceae family and suggest that different parts of the plant could be evaluated as valuable natural resources for various purposes in pharmacological and therapeutic applications. Particularly, the antioxidant potential exhibited by leaf extracts suggests that they could be utilized as promising components in the development of protective and therapeutic formulations against various diseases associated with oxidative stress.

3.3. Quantification of phenolic and flavonoid compounds via HPLC analysis of *A. caucasicus* extract

In this study, ascorbic acid as a vitamin, along with various phenolic compounds and flavonoids, was examined in the leaf and flower parts of the *A. caucasicus* plant. The standard compounds used included 12 phenolic compounds such as gallic acid, 3,4-hydroxy benzoic acid, vanillic acid, syringic acid, coumaric acid, caffeic acid, rosmarinic acid, pyrogallol, chlorogenic acid, oleuropein, and resveratrol; additionally, there were 11 flavonoids, including catechin, epicatechin, rutin, myricetin, quercetin, apigenin, cyanidin chloride, hesperetin, kaempferol, baicalein, and chrysin.

The study employed two distinct methodologies. Advanced chromatographic techniques were developed to quantify compounds isolated from the plant, as detailed in Table 5. Protocol A was used to determine compounds 1, 2, 3, 4, 6, 7, 8, 9, 14, 15, 16, 17, 18, and 19, whereas Protocol B was specifically optimized for compounds 5, 10, 11, 12, 13, 20, 21, 22, 23, and 24. Fig. 3 and Fig.4 demonstrate the clear separation achieved between the various phenolic compounds.

In the study, both identification and quantification of a total of 24 phenolic compounds in the leaf and flower parts of the *A. caucasicus* plant were carried out by applying Protocol A and Protocol B (Table 5). Upon examination of the chromatograms obtained from the phytochemical analysis of *A. caucasicus*, the

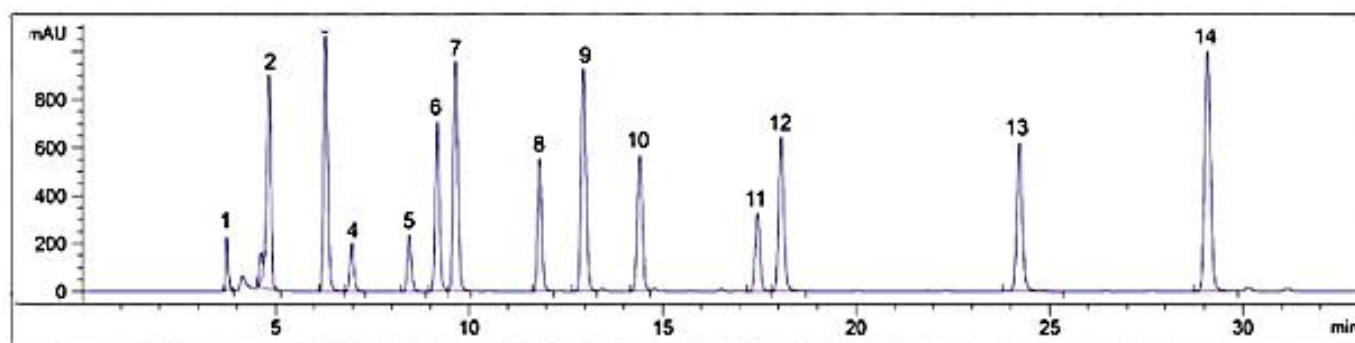


Figure 3. The HPLC Chromatograms of the Phenolic Standards (Protocol A). Their symbols and retention times are ascorbic acid (AsA) (1), gallic acid (2), 3-4 hydroxybenzoic acid (3), catechin (4), epicatechin (5), caffeic acid (6), vanillic acid (7), rutin (8), cumaric acid (9), ferrulic acid (10), rosmarinic acid (11), myricetin (12), quercetin (13), and apigenin (14)

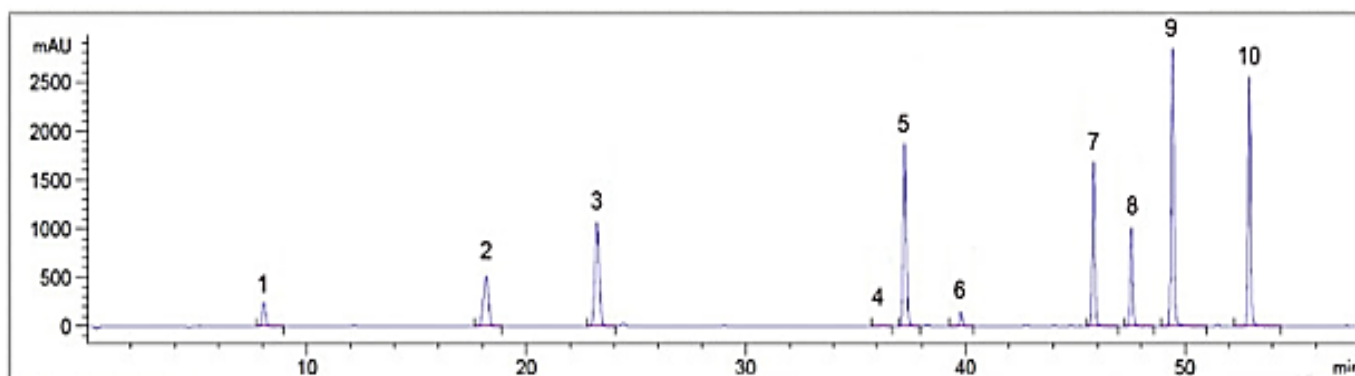


Figure 4. The HPLC Chromatograms of the Phenolic Standards (Protocol B.) Their symbols and retention times are pyrogallol (1), chlorogenic acid (2), syringic acid (3), cyanidin chloride (4), resveratrol (5), oleuropein (6), hesperitin (7), kaempferol (8), baicalein (9) and chrysin (10)

characteristic compounds of the flowers are presented in Fig. 5, while those of the leaves are presented in Fig. 6. Regarding ascorbic acid content, it was detected at a level of 178.3 mg/kg in the flower part but was not detected in the leaf part. This accumulation of ascorbic acid in flowers is attributed to increased metabolic activity and greater exposure to oxidative stress [70].

Phenolic compounds were predominantly concentrated in the flower part of the plant. Gallic acid (59.8 mg/kg) and 3,4-hydroxy benzoic acid (16.8 mg/kg) were detected in the flower part but not found in the leaf part. Caffeic acid was determined to be 15.5 mg/kg in flowers and 7.5 mg/kg in leaves. Although caffeic acid is present in both parts, it has approximately twice the concentration in the flower part compared to the leaf. Vanillic acid, however, is present in higher amounts in the leaf part (Table 5). These compounds are known for their properties to neutralize free radicals and protect against oxidative stress. The higher accumulation of these compounds in the flower part compared to the leaf part indicates that the flower part has a higher antioxidant potential than the leaf part.

Rosmarinic acid and *p*-coumaric acid, which have antioxidant and anti-inflammatory properties, were detected in both flower and leaf parts of the plant. The amounts of rosmarinic acid (131.6 mg/kg) and *p*-coumaric acid (141.9 mg/kg) in the flower part were higher than the amounts of rosmarinic acid (41.9 mg/kg) and *p*-coumaric

acid (119.2 mg/kg) in the leaf part. These results indicate that the flower part is more effective in terms of antioxidant activity.

Among flavonoids, Rutin, Quercetin, Apigenin, Hesperetin, Myricetin, and Chrysin were determined. Flavonoid compounds such as Apigenin (11.5 mg/kg), Hesperetin (321.5 mg/kg), Myricetin (4.7 mg/kg), and Chrysin (4.7 mg/kg) were detected in the flower part, while Quercetin was found to be 389.6 mg/kg in the flower part and 34.9 mg/kg in the leaf part. While Apigenin, Hesperetin, Myricetin, and Chrysin could not be detected at all in the leaf part, Quercetin was found in a much higher proportion in the flower part compared to the leaf part. This indicates that the immune-supporting, anti-inflammatory, and free radical scavenging properties [71] of flavonoid compounds are more prominent in the flower part compared to the leaf part. However, Rutin, which serves as a natural protection mechanism against harmful organisms and UV radiation, was found to be 1438.8 mg/kg in the leaf part and 315.2 mg/kg in the flower part, showing a significant difference in the leaf part of the plant.

Due to the limited studies on *A. caucasicus* in the literature, research on similar species has been examined. In one study [72], the phenolic content of 11 Aster species (*A. diplostephioides*, *A. souliei*, *A. himalaicus*, *A. flaccidus*, *A. farreri*, *A. sutschanensis*, *A. tongolensis*, *A.*

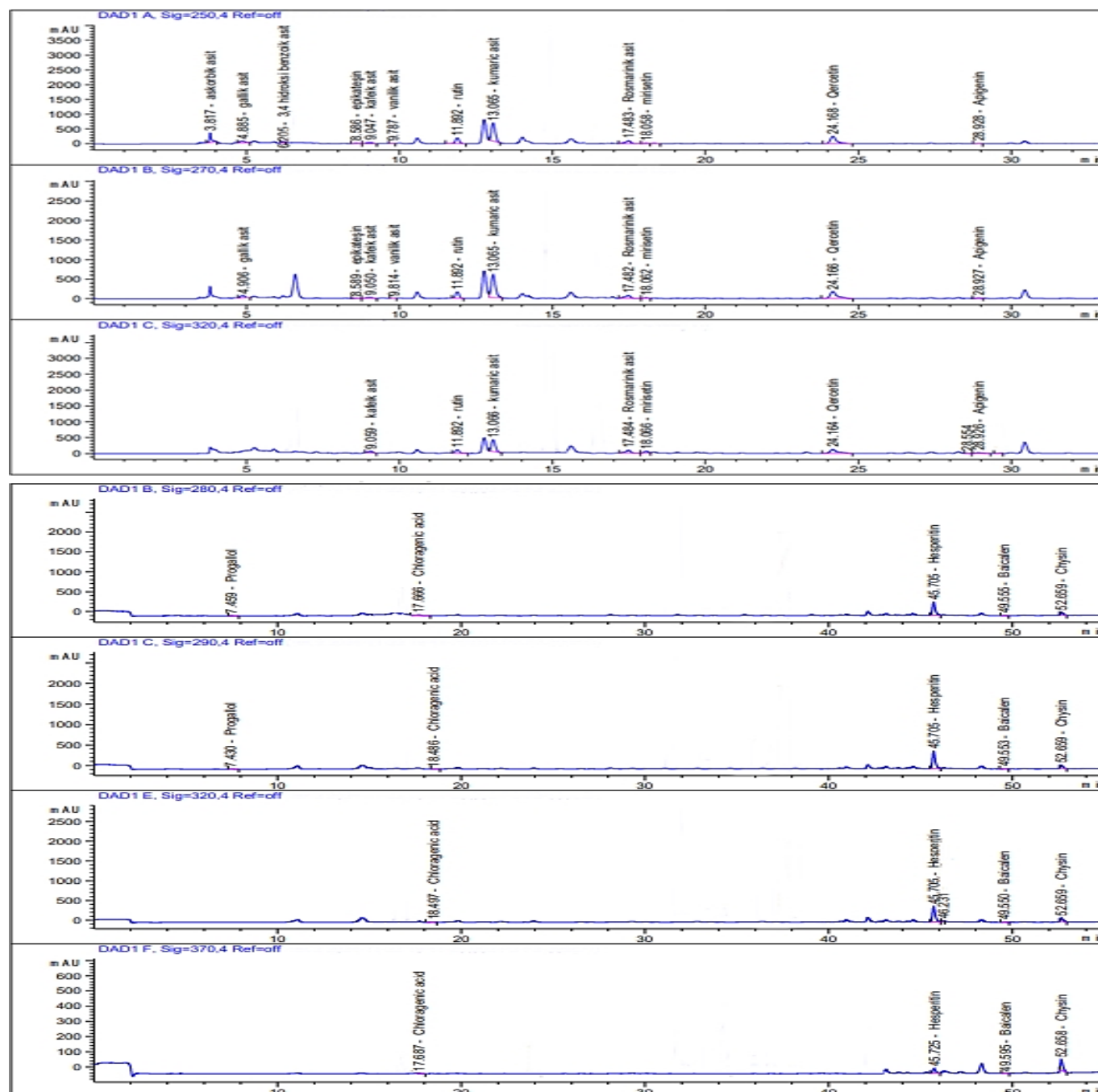
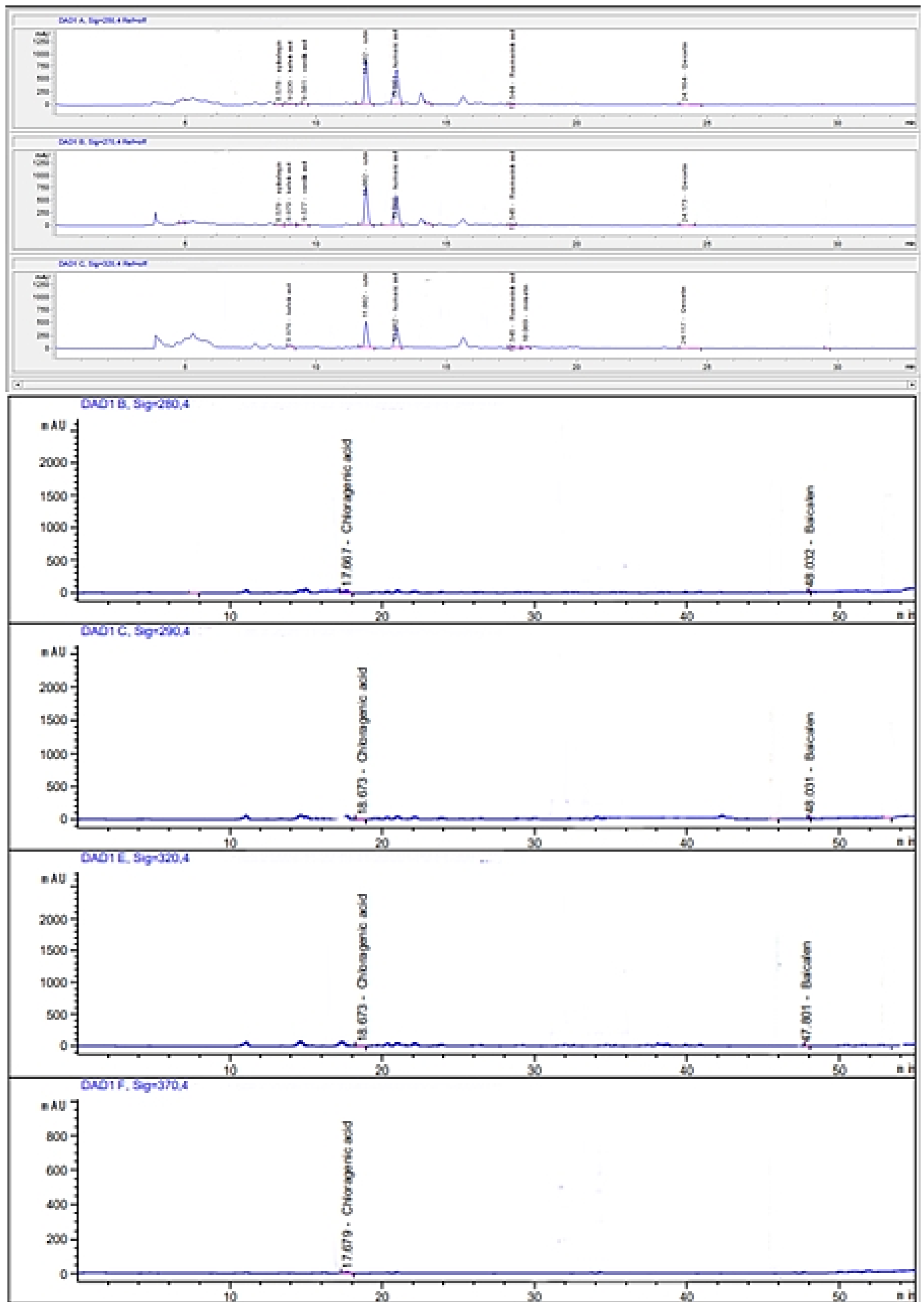


Figure 5. The chromatogram of the analysis results of *A. caucasicus* flowers

bietii, *A. yunnanensis*, *A. trinervius*, and *A. latibracteatus*) collected from different regions was compared. This study investigated the content of *chlorogenic acid* and its isomers, *rutin*, *isoquercitrin*, *3,5-dicaffeoylquinic acid*, *3,4-dicaffeoylquinic acid*, and *1,3-dicaffeoylquinic acid*. According to the results, *A. latibracteatus* and *A. trinervius* contained abundant amounts of *chlorogenic acid* and its isomers (23.5 ± 4.9 and 20.5 ± 5.8 mg/g, respectively), while these compounds were found in significantly lower quantities in samples of *A. latibracteatus* and *A. sutschanensis* (7.6 ± 0.55 and 9.5 ± 0.43 mg/g, respectively; $p < 0.01$). Several other *Aster* species (*A. souliei*, *A. bietii*, and *A. flaccidus*) also contained specific amounts of *chlorogenic acid* and its isomers (13.3 ± 5.1 , 14.3 ± 4.4 , and 15.2 ± 5.7 mg/g, respectively). In our current study, the

chlorogenic acid content in the leaves and flowers of *A. caucasicus* was determined to be approximately twice as high as the highest values reported in the literature, while the *rutin* content was approximately 10 times higher in leaves and more than 10 times higher in flowers. In another study from the literature [73], *quercetin* content was examined in the methanolic extract of *Aster spatulifolius* flowers but was not detected. In contrast, our current study identified high levels of *quercetin* in both the leaves and flowers of *A. caucasicus*. A subsequent study conducted in 2018 investigated the flavonoid content, including *apigenin*, *catechin*, *epicatechin*, *hesperidin*, *myricetin*, *quercetin*, and *rutin*, in the petals of various Chinese asters from the Asteraceae family (to which *A. caucasicus* also belongs), categorized



into seven groups based on flower colors [74]. According to this study, the highest apigenin value was reported as 266.1 ppm, while the lowest was 7.9 ppm; the highest catechin value was 284.3 ppm, while the lowest was 4 ppm. The *A. caucasicus* plant used in our current study demonstrated higher apigenin and catechin content in its flowers compared to most species examined. Furthermore, the content of other flavonoids such as epicatechin, hesperidin, quercetin, and rutin was found to be higher than all other species, while the myricetin content was higher than most species.

The results revealed that the diversity of phenolic compounds in the flower part was higher than in the leaf part. The presence of these compounds, which confer strong antioxidant and anti-inflammatory properties, in the flower part has shown that this part of the plant can be effectively included in pharmaceutical applications and can be a biological source for pharmaceutical products. Additionally, the very high amount of Rutin, which has natural protective properties against UV radiation, and Vanillic acid, which has antioxidant properties, in the leaf part compared to the other part has shown that the leaf parts can be included as an important biological source in cosmetic products.

4. Conclusions

In this study, a comprehensive analysis of *A. caucasicus*, a plant with limited and rare studies in the literature, was conducted. The phenolic and flavonoid contents, antioxidant capacities (total phenolic, total flavonoid, FRAP, and CUPRAC), and volatile compounds of the flower and leaf parts of the plant were examined in detail. This research has made a significant contribution to filling the knowledge gap in the literature regarding *A. caucasicus*.

The analysis results demonstrated that the leaf parts of the plant are rich in flavonoids to protect against UV radiation and reduce oxidative stress. The overall antioxidant capacity of the leaves was found to be higher compared to the flowers. On the other hand, flower parts were richer in phenolic compounds, and their antioxidant capacity was slightly lower than that of leaves.

In the chemical composition profile, beta-pinene (52.26%) stands out as the dominant compound in the flower part, while D-limonene (28.68%) was found in the highest proportion in the leaf part. This difference reflects the different physiological functions and ecological roles of plant organs. The high presence of monoterpenes in both plant parts is one of the characteristic features of the Aster genus.

The total phenolic content was higher in flower parts (25.57 mg GAE/g) compared to leaves (17.81 mg GAE/g),

Table 5. Contents of phenolic compounds in the leaves and flowers of *A. caucasicus*

No	Compounds	Flower (mg/L)	Leaf (mg/L)
Vitamin			
1	Ascorbic acid	178.3	N/D
Phenolics			
2	Gallic acid	59.8	N/D
3	3,4 hydroxy benzoic acid	16.8	N/D
4	Vanillic acid	1.0	20.5
5	Syringic acid	N/D	N/D
6	Coumaric Acid	141.9	119.2
7	Caffeic acid	15.5	7.5
8	Ferulic acid	N/D	N/D
9	Rosmarinic acid	131.6	41.9
10	Pyrogallol	46.7	84.6
11	Chlorogenic acid	51.2	54.5
12	Resveratrol	N/D	N/D
13	Oleuropein	N/D	N/D
Flavonoids			
14	Catechin	N/D	N/D
15	Epicatechin	54.8	39.4
16	Rutin	315.2	1438.8
17	Myricetin	4.7	N/D
18	Qercetin	389.6	34.9
19	Apigenin	11.5	N/D
20	Cyanidin chloride	N/D	N/D
21	Hesperitin	321.5	N/D
22	Kaempferol	N/D	N/D
23	Baicalein	10.5	11.6
24	Chrysin	4.7	N/D

N/D: Not Detected

while the leaves demonstrated higher total flavonoid content (5.02 mg QE/g) than flowers (3.99 mg QE/g). Furthermore, the leaves exhibited elevated FRAP (7.77 $\mu\text{mol Fe}^{2+}/\text{g}$) and CUPRAC (0.32 mmol TEAC/g) values, suggesting superior antioxidant capacity compared to the flower parts.

HPLC analyses revealed that phenolic compounds such as gallic acid (59.8 mg/kg), caffeic acid (15.5 mg/kg), rosmarinic acid (131.6 mg/kg), and quercetin (389.6 mg/kg) were present in higher concentrations in the flower parts compared to leaves, while rutin was detected at a significantly higher level in leaves (1438.8 mg/kg) than in flowers (315.2 mg/kg).

These findings highlight the potential of *A. caucasicus* flower and leaf parts in cosmetic and pharmaceutical applications and provide a solid foundation for future studies investigating the therapeutic applications of their bioactive properties. The flower parts, with their rich phenolic content, show promise for pharmaceutical applications, while the leaf parts, with their high flavonoid content and antioxidant capacity, could be valuable in cosmetic products, particularly for UV protection.

However, a significant limitation of the study is the lack of in vivo tests that would provide deeper insights into the bioavailability and therapeutic efficacy of these active compounds. Future research should address this

limitation by including in vivo studies to verify the current findings and further investigate the pharmacokinetics of the active components of the extract.

References

- [1] N. Kumar, V. Pruthi, Potential applications of ferulic acid from natural sources, *Biotechnol Rep*, 4, 2014, 86-93.
- [2] K.H. Kwon, A. Barve, S. Yu, M.T. Huang, A.N. Kong, Cancer chemoprevention by phytochemicals: potential molecular targets, biomarkers and animal models, *Acta Pharmacol Sin*, 28, 2007, 1409-1421.
- [3] J. Moore, M. Yousef, E. Tsiani, Anticancer effects of rosemary (*Rosmarinus officinalis* L.) extract and rosemary extract polyphenols, *Nutrients*, 8, 2016, 731.
- [4] A. Trivellini, M. Lucchesini, R. Maggini, H. Mosadegh, T.S.S. Villamarin, P. Vernieri, A. Mensuali-Sodi, A. Pardossi, Lamiaceae phenols as multifaceted compounds: bioactivity, industrial prospects and role of positive-stress, *Ind Crops Prod*, 83, 2016, 241-254.
- [5] Y. Sakihama, M.F. Cohen, S.C. Grace, H. Yamasaki, Plant phenolic antioxidant and prooxidant activities: phenolics-induced oxidative damage mediated by metals in plants, *Toxicology*, 177, 2002, 67-80.
- [6] W. Watjen, G. Michels, B. Steffan, P. Niering, Y. Chovolou, A. Kampkotter, Q.H. Tran-Thi, P. Proksch, R. Kahl, Low concentrations of flavonoids are protective in rat H4IIE cells whereas high concentrations cause DNA damage and apoptosis, *J Nutr*, 135, 2005, 525-531.
- [7] C.M. Ajila, S.K. Brar, M. Verma, R.D. Tyagi, S. Godbout, J.R. Valéro, Extraction and analysis of polyphenols: recent trends, *Crit Rev Biotechnol*, 31, 2011, 227-249.
- [8] L. Bravo, Polyphenols: chemistry, dietary sources, metabolism, and nutritional significance, *Nutr Rev*, 56, 1998, 317-333.
- [9] L.M. Carvalho, M. Martini, A.P.L. Moreira, A.P. de Lima, D. Correia, T. Falcão, S.C. Garcia, A.V. de Baires, P.C. do Nascimento, D. Bohrer, Presence of synthetic pharmaceuticals as adulterants in slimming phytotherapeutic formulations and their analytical determination, *Forensic Sci Int*, 204, 2010, 6-11.
- [10] L.M. Carvalho, A.P. Moreira, M. Martini, T. Falcão, The illegal use of synthetic pharmaceuticals in herbal formulations: an overview on the adulteration practice and analytical investigations, *Forensic Sci Rev*, 23, 2011, 73-90.
- [11] D. Krishnaiah, R. Sarbatly, R. Nithyanandam, A review of the antioxidant potential of medicinal plant species, *Food Bioprod Process*, 89, 2011, 217-233.
- [12] M.A.M. Maciel, A.C. Pinto, V.F. Veiga Jr, N.F. Grynberg, A. Echevarria, Plantas medicinais: a necessidade de estudos multidisciplinares, *Quím Nova*, 25, 2002, 429-438.
- [13] N. Balasundra, K. Sundram, S. Samman, Phenolic compounds in plants and agro-industrial by-products: antioxidant activity, occurrence, and potential uses, *Food Chem*, 99, 2006, 191-203.
- [14] C.D. Stalikas, Extraction, separation, and detection methods for phenolic acids and flavonoids, *J Sep Sci*, 30, 2007, 3268-3295.
- [15] I.G. Casella, C. Colonna, M. Contursi, Electroanalytical determination of some phenolic acids by high-performance liquid chromatography at gold electrodes, *Electroanalysis*, 19, 2007, 1503-1508.
- [16] R. Gotti, Capillary electrophoresis of phytochemical substances in herbal drugs and medicinal plants, *J Pharm Biomed Anal*, 55, 2011, 775-801.
- [17] D. Argyropoulos, J. Müller, Effect of convective-, vacuum- and freeze drying on sorption behaviour and bioactive compounds of lemon balm (*Melissa officinalis* L.), *J Appl Res Med Aromat Plants*, 1, 2014, 59-69.
- [18] V. Kumar, R.S. Chauhan, H. Sood, C. Tandon, Cost effective quantification of picrosides in *Picrorhiza kurroa* by employing response surface methodology using HPLC-UV, *J Plant Biochem Biotechnol*, 24, 2015, 376-384.
- [19] V. Kumar, H. Sood, R.S. Chauhan, Optimization of a preparative RP-HPLC method for isolation and purification of picrosides in *Picrorhiza kurroa*, *J Plant Biochem Biotechnol*, 25, 2016, 208-214.
- [20] A. Ray, S.D. Gupta, S. Ghosh, Isolation and characterization of potent bioactive fraction with antioxidant and UV absorbing activity from *Aloe barbadensis* Miller gel, *J Plant Biochem Biotechnol*, 22, 2013, 483-487.
- [21] M.N. Irakli, V.F. Samanidou, C.G. Biliaderis, I.N. Papadoyannis, Simultaneous determination of phenolic acids and flavonoids in rice using solid-phase extraction and RP-HPLC with photodiode array detection, *J Sep Sci*, 35, 2012, 1603-1611.
- [22] B. Shan, Y.Z. Cai, M. Sun, H. Corke, Antioxidant capacity of 26 spice extracts and characterization of their phenolic constituents, *J Agric Food Chem*, 53, 2005, 7749-7759.
- [23] S.T. Saito, A. Welzel, E.S. Suyenaga, F. Bueno, A method for fast determination of epigallocatechin gallate (EGCG), epicatechin (EC), catechin (C) and caffeine (CAF) in green tea using HPLC, *Food Sci Technol (Campinas)*, 26, 2006, 394-400.
- [24] A. Cantalapiedra, M.J. Gismera, M.T. Sevilla, J.R. Procopio, Sensitive and selective determination of phenolic compounds from aromatic plants using an electrochemical detection coupled with HPLC method, *Phytochem Anal*, 25, 2014, 247-254.
- [25] E. Barrajón-Catalán, S. Fernández-Arroyo, C. Roldán, E. Guillén, D. Saura, A. Segura-Carretero, V. Micó, A systematic study of the polyphenolic composition of aqueous extracts deriving from several *Cistus* genus species: evolutionary relationship, *Phytochem Anal*, 22, 2011, 303-312.
- [26] C.S. Harris, A.J. Burt, A. Saleem, P.M. Le, L.C. Martineau, P.S. Haddad, S.A. Bennett, J.T. Arnason, A single HPLC-PAD-APCI/MS method for the quantitative comparison of phenolic compounds found in leaf, stem, root and fruit extracts of *Vaccinium angustifolium*, *Phytochem Anal*, 18, 2007, 161-169.
- [27] K.M. Kalili, A. de Villiers, Recent developments in the HPLC separation of phenolic compounds, *J Sep Sci*, 34, 2011, 854-876.
- [28] A. Ribas-Agusti, M. Gratacos-Cubarsi, C. Sarraga, J.A. Garcia-Regueiro, M. Castellari, Analysis of eleven phenolic compounds including novel p-coumaroyl derivatives in lettuce (*Lactuca sativa* L.) by ultra-high-performance liquid chromatography with photodiode array and mass spectrometry detection, *Phytochem Anal*, 22, 2011, 555-563.
- [29] R. Rodríguez-Solana, J.M. Salgado, J.M. Domínguez, S. Cortes-Díez, Comparison of Soxhlet, accelerated solvent and supercritical fluid extraction techniques for volatile (GC-MS and GC/FID) and phenolic compounds (HPLC-ESI/MS/MS) from Lamiaceae species, *Phytochem Anal*, 26, 2015, 61-71.
- [30] C.D. Stalikas, Extraction, separation, and detection methods for phenolic acids and flavonoids, *J Sep Sci*, 30, 2007, 3268-3295.
- [31] J.L. Rambla, A. Trapero-Mozos, G. Diretto, A. Rubio-Moraga, A. Granell, L. Gómez-Gómez, O. Ahrazem, Gene-metabolite networks of volatile metabolism in Airen and Tempranillo grape cultivars revealed a distinct mechanism of aroma bouquet production, *Front Plant Sci*, 7, 2016, 1619.
- [32] J. Zhang, J. Zhao, Y. Xu, J. Liang, P. Chang, F. Yan, M. Li, Y. Liang, Z. Zou, Genome-wide association mapping for tomato volatiles positively contributing to tomato flavor, *Front Plant Sci*, 6, 2015, 1042.
- [33] A. Slegers, P. Angers, É. Ouellet, T. Truchon, K. Pedneault, Volatile compounds from grape skin, juice and wine from five interspecific hybrid grape cultivars grown in Québec (Canada) for wine production, *Molecules*, 20, 2015, 10980-11016.
- [34] X.W. Ma, M.Q. Su, H.X. Wu, Y.G. Zhou, S.B. Wang, Analysis of the volatile profile of core Chinese mango germplasm by headspace solid-phase microextraction coupled with gas chromatography-mass spectrometry, *Molecules*, 23, 2018, 1480.

- [35] R. Marsili, Flavor, Fragrance, and Odor Analysis, 2nd ed., 2012, Boca Raton, FL, CRC Press.
- [36] S. Van Nocker, S.E. Gardiner, Breeding better cultivars, faster: applications of new technologies for the rapid deployment of superior horticultural tree crops, *Hortic Res*, 1, 2014, 14022.
- [37] S. Yang, J. Fresnedo-Ramírez, M. Wang, L. Cote, P. Schweitzer, P. Barba, E.M. Takacs, M. Clark, J. Luby, D.C. Manns, et al., A next-generation marker genotyping platform (AmpSeq) in heterozygous crops: a case study for marker-assisted selection in grapevine, *Hortic Res*, 3, 2016, 16002.
- [38] L.A. Chaparro-Torres, M.C. Bueso, J.P. Fernández-Trujillo, Aroma volatiles obtained at harvest by HS-SPME/GC-MS and INDEX/MS-E-nose fingerprint discriminate climacteric behavior in melon fruit, *J Sci Food Agric*, 96, 2016, 2352-2365.
- [39] J.M. Obando-Ulloa, J. Ruiz, A.J. Monforte, J.P. Fernández-Trujillo, Aroma profile of a collection of near-isogenic lines of melon (*Cucumis melo* L.), *Food Chem*, 118, 2010, 815-822.
- [40] F. Dunemann, D. Ulrich, A. Boudichevskaia, C. Grafe, W.E. Weber, QTL mapping of aroma compounds analysed by headspace solid-phase microextraction gas chromatography in the apple progeny "Discovery" × "Prima", *Mol Breed*, 23, 2009, 501-521.
- [41] J. Vogt, D. Schiller, D. Ulrich, W. Schwab, F. Dunemann, Identification of lipoxygenase (LOX) genes putatively involved in fruit flavour formation in apple (*Malus* × *domestica*), *Tree Genet Genomes*, 9, 2013, 1493-1511.
- [42] J. Battilana, L. Costantini, F. Emanuelli, F. Sevinci, C. Segala, S. Moser, R. Velasco, G. Versini, M.S. Grando, The 1-deoxy-d-xylulose 5-phosphate synthase gene co-localizes with a major QTL affecting monoterpene content in grapevine, *Theor Appl Genet*, 118, 2009, 653-669.
- [43] A. Doligez, E. Audiot, R. Baumes, P. This, QTLs for muscat flavor and monoterpenic odorant content in grapevine (*Vitis vinifera* L.), *Mol Breed*, 18, 2006, 109-125.
- [44] S. Guillaumie, A. Ilg, S. Réty, M. Brette, C. Trossat-Magnin, S. Decroocq, C. Léon, C. Keime, T. Ye, R. Baltenweck-Guyot, et al., Genetic analysis of the biosynthesis of 2-methoxy-3-isobutylpyrazine, a major grape-derived aroma compound impacting wine quality, *Plant Physiol*, 162, 2013, 604-615.
- [45] Y. Bezman, F. Mayer, G.R. Takeoka, R.G. Buttery, G. Ben-oliel, H.D. Rabinowitch, M. Naim, Differential effects of tomato (*Lycopersicon esculentum* Mill) matrix on the volatility of important aroma compounds, *J Agric Food Chem*, 51, 2003, 722-726.
- [46] T. Vandendriessche, B.M. Nicolai, M.L.A.T.M. Hertog, Optimization of HS SPME fast GC-MS for high-throughput analysis of strawberry aroma, *Food Anal Methods*, 6, 2013, 512-520.
- [47] L. García-Vico, A. Belaj, A. Sánchez-Ortiz, J.M. Martínez-Rivas, A.G. Pérez, C. Sanz, Volatile compound profiling by HS-SPME/GC-MS-FID of a core olive cultivar collection as a tool for aroma improvement of virgin olive oil, *Molecules*, 22, 2017, 141.
- [48] T.B. Ng, L. Liu, Y. Lu, C.H.K. Cheng, Z. Wang, Antioxidant activity of compounds from the medicinal herb *Aster tataricus*, *Comp Biochem Physiol C Pharmacol Toxicol Endocrinol*, 136, 2003, 109-115.
- [49] A.K. Tiwari, Imbalance in antioxidant defence and human diseases: multiple approach of natural antioxidants therapy, *Curr Sci*, 81, 2001, 1179-1187.
- [50] F. Pourmorad, S.J. Hosseini-mehr, N. Shahabimajd, Antioxidant activity, phenol and flavonoid contents of some selected Iranian medicinal plants, *Afr J Biotechnol*, 5, 2006, 1142-1145.
- [51] A. Uysal, G. Zengin, Y. Durak, A. Aktumsek, Investigation of the antioxidant, antimutagenic properties and enzyme inhibition potential of *Centaurea pterocaula* extracts, *Marmara Pharm J*, 20, 2016, 232-242.
- [52] İ. Akbulut, E. Gürbüz, A.R. Ergün, T. Baysal, Drying of apricots treated with Ginkgo biloba plant extract and determination of the quality properties, *J Adv Res Nat Appl Sci*, 7, 2021, 145-159.
- [53] K. Slinkard, V.L. Singleton, Total phenol analysis: automation and comparison with manual methods, *Am J Enol Vitic*, 28, 1977, 49-55.
- [54] J. Zhishen, T. Mengcheng, W. Jianming, The determination of flavonoid contents in mulberry and their scavenging effects on superoxide radicals, *Food Chem*, 64, 1999, 555-559.
- [55] I.F.F. Benzie, Y.T. Szeto, Total antioxidant capacity of teas by the ferric reducing/antioxidant power assay, *J Agric Food Chem*, 47, 1999, 633-636.
- [56] R. Apak, K. Güçlü, M. Ozyürek, S.E. Karademir, Novel total antioxidant capacity index for dietary polyphenols and vitamins C and E, using their cupric ion reducing capability in the presence of neocuproine: CUPRAC method, *J Agric Food Chem*, 52, 2004, 7970-7981.
- [57] C. Altuntaş, A. Gümrükçüoğlu, N. Aksu Kalmuk, K.V. İmamoğlu, The bioactive potential of three different *Rumex* species: Antioxidant capacity, mineral composition and elemental status, *S Afr J Bot*, 180, 2025, 107-120.
- [58] S.L. Guzmán-Gutiérrez, R. Gómez-Cansino, J.C. García-Zebaúda, N.C. Jiménez-Pérez, R. Reyes-Chilpa, Antidepressant activity of *Litsea glaucescens* essential oil: identification of β -pinene and linalool as active principles, *J Ethnopharmacol*, 143, 2012, 673-679.
- [59] R.N. Almeida, S.C. Motta, J.R. Leite, Óleos essenciais com propriedades anticonvulsivantes, *Bol Latinoam Caribe Plant Med Aromát*, 2, 2003, 3-6.
- [60] I.A.C. Menezes, I.J.A. Moreira, J.W.A. De Paula, A.F. Blank, A.R. Antoniolli, L.J. Quintans-Júnior, M.R.V. Santos, Cardiovascular effects induced by *Cymbopogon winterianus* essential oil in rats: involvement of calcium channels and vagal pathway, *J Pharm Pharmacol*, 62, 2010, 215-221.
- [61] A.C.R. Silva, P.M. Lopes, M.M.B. Azevedo, D.C.M. Costa, C.S. Alviano, D.S. Alviano, Biological activities of α -pinene and β -pinene enantiomers, *Molecules*, 17, 2012, 6305-6316.
- [62] S.A. Mahdavi, R. Sadeghi, A. Faridi, S. Hedayati, R. Shaddel, C. Dima, S.M. Jafari, Nanodelivery systems for d-limonene; techniques and applications, *Food Chem*, 388, 2022, 132479.
- [63] M.A.K. Jansen, V. Gaba, B.M. Greenberg, Higher plants and UV-B radiation: balancing damage, repair and acclimation, *Trends Plant Sci*, 3, 1998, 131-135.
- [64] D. Treutter, Significance of flavonoids in plant resistance and enhancement of their biosynthesis, *Plant Biol*, 7, 2006, 581-591.
- [65] G. Agati, E. Azzarello, S. Pollastri, M. Tattini, Flavonoids as antioxidants in plants: location and functional significance, *Plant Sci*, 196, 2012, 67-76.
- [66] P. Feduraev, L. Skrypnik, S. Nebreeva, G. Dzhobadze, A. Vatagina, E. Kalinina, A. Pungin, P. Maslennikov, A. Riabova, O. Krol, G. Chupakhina, Variability of phenolic compound accumulation and antioxidant activity in wild plants of some *Rumex* species (Polygonaceae), *Antioxidants*, 11, 2022, 311.
- [67] A. Güneş, Ş. Kordali, M. Turan, A.U. Bozhüyük, Determination of antioxidant enzyme activity and phenolic contents of some species of the Asteraceae family from medicinal plants, *Ind Crops Prod*, 137, 2019, 208-213.
- [68] M. Bibiso, M. Anza, B. Alemayehu, Antibacterial and antioxidant activity of *Cirsium englerianum* (Asteraceae), an endemic plant to Ethiopia, *Res J Pharmacogn*, 8, 2021, 5-12.
- [69] V. Koleckar, L. Opletal, E. Brojerova, Z. Rehakova, F. Cervenka, K. Kubikova, K. Kuca, D. Jun, M. Polasek, J. Kunes, L. Jahodar, Evaluation of natural antioxidants of *Leuzea carthamoides* as a result of a screening study of 88 plant extracts from the European Asteraceae and Cichoriaceae, *J Enzyme Inhib Med Chem*, 23, 2008, 218-224.
- [70] A. Ortiz-Espín, A. Sanchez-Guerrero, F. Sevilla, A. Jimenez, The role of ascorbate in plant growth and development, *Ascorbic*

Acid in Plant Growth, Development and Stress Tolerance, Editors: M.A. Hossain, S. Munne-Bosch, D.J. Burritt, P. Diaz-Vivancos, M. Fujita, A. Lorence, 2017, Cham, Switzerland, Springer, 25-45.

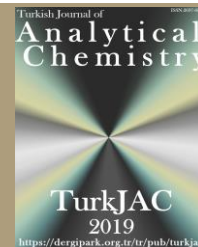
- [71] J.A. Ross, C.M. Kasum, Dietary flavonoids: bioavailability, metabolic effects, and safety, *Annu Rev Nutr*, 22, 2002, 19-34.
- [72] L. Li, L. He, X. Su, H. Amu, J. Li, Z. Zhang, Chemotaxonomy of Aster species from the Qinghai-Tibetan Plateau based on metabolomics, *Phytochem Anal*, 32, 2021, 890-901.
- [73] N.G. Quilantang, S.H. Ryu, S.H. Park, J.S. Byun, J.S. Chun, J.S. Lee, J.P. Rodriguez, Y.S. Yun, S.D. Jacinto, S. Lee, Inhibitory activity of methanol extracts from different colored flowers on aldose reductase and HPLC-UV analysis of quercetin, *Hortic Environ Biotechnol*, 59, 2018, 899-907.
- [74] V. Bhargav, R. Kumar, K.S. Shivashankara, T.M. Rao, M.V. Dhananjaya, A. Sane, T.U. Bharathi, R. Venugopalan, T.K. Roy, Diversity of flavonoids profile in China aster [*Callistephus chinensis* (L.) Nees.] genotypes, *Ind Crops Prod*, 111, 2018, 513-519.



TürkJAC

Turkish Journal of

Analytical Chemistry

<https://dergipark.org.tr/tr/pub/turkjac>

TürkJAC

2019

<https://dergipark.org.tr/tr/pub/turkjac>

Green synthesis of fluorescent carbon quantum dots from field horsetail *Equisetum Arvense* L and fluorimetric detection of Pd²⁺ ions

Aysel Başoğlu 

Gümüşhane University, Gümüşhane Vocational School, Chemistry and Chemical Processing Technologies, 29100, Gümüşhane, Türkiye

Abstract

The study presents a comprehensive phytochemical analysis of *A. caucasicus*, examining both the leaf and flower parts of this plant. The Fluorescent carbon quantum dots (CQDs) were synthesized via a hydrothermal method using field horsetail (*Equisetum arvense* L.) as a green carbon source at 180 °C. The resulting CQDs were characterized by various techniques, including UV-Vis absorption spectroscopy, fluorescence spectroscopy, fourier-transform infrared (FTIR) spectroscopy, and transmission electron microscopy (TEM). Under UV illumination at 365 nm, the CQDs displayed intense blue fluorescence. The effects of 32 different metal ions, including Li⁺, Na⁺, K⁺, Ag⁺, NH₄⁺, Tl⁺, Ba²⁺, Be²⁺, Ca²⁺, Cd²⁺, Co²⁺, Cu²⁺, Pb²⁺, Mg²⁺, Mn²⁺, Ni²⁺, Zn²⁺, Sr²⁺, Cr³⁺, Au³⁺, Y³⁺, Al³⁺, V³⁺, Bi³⁺, B³⁺, Sc³⁺, Sb³⁺, Ti⁴⁺, Se⁴⁺, Mo⁶⁺, W⁶⁺, and Pd²⁺, on the fluorescence properties of the CQDs were systematically investigated using fluorescence spectrophotometry. Among them, Pd²⁺ ions caused significant fluorescence quenching. Based on this response, a sensitive and straightforward fluorometric sensing strategy was developed for detecting Pd²⁺ in tap water. The method showed a good linearity over the concentration range of 0.5 to 15.0 μM, with a detection limit of 50.2 nM and a quantification limit of 150.6 nM. The applicability of the method was further validated through spiking experiments, yielding satisfactory recoveries at various concentrations. The approach also demonstrated excellent reproducibility, with a relative standard deviation (RSD) consistently below 2.3%.

Keywords: Pd²⁺ detection, fluorescent carbon quantum dots, hydrothermal-assisted synthesis, field horsetail (*Equisetum arvense* L.)

1. Introduction

Initially observed as a byproduct in 2004 [1], carbon dots were later recognized as a distinct class of nanomaterials through detailed characterization reported in 2006 [2]. Between 2007 and 2011, production strategies and structure-property relationships were investigated, followed by the development of practical applications and large-scale production methods from 2011 onwards. Due to their small size, rich functional groups, fluorescence properties, chemical stability, biocompatibility, good solvent dispersion, and non-toxicity, carbon dots are known as discrete, quasi-spherical particles that find applications in various fields such as sensors, energy storage, drug delivery, bioimaging, catalysis, and LEDs. These superior structural features have positioned carbon dots significantly in materials chemistry [2]. However, due to their extensive structural diversity, there remains a need for the development of more economical and efficient production methods. Carbon dots can be found in various structural forms, including graphene-based,

graphitic carbon nitride-based, polymer-derived, and classical carbon quantum dots and nanodots. The main difference between carbon quantum dots and carbon nanodots lies in their internal structure. Some researchers argue that carbon nanodots primarily exhibit an amorphous structure and lack a crystalline cage, whereas carbon quantum dots are emphasized to possess a crystalline structure [3,4]. This distinction becomes significant when considering the more pronounced crystallinity of carbon-based quantum dots. The microstructural properties of these dots can be adjusted to exhibit diverse characteristics. Quantum size is an important feature of carbon quantum dots and depends mainly on processing conditions such as precursor ratio [5], reaction time [6], temperature [7], and solvent [8].

Alternatively, key properties can be enhanced in carbon dots by employing strategies such as doping with heteroatoms, functionalizing the surface, or passivating the surface to alter their structural characteristics.

Citation: A. Başoğlu, Green synthesis of fluorescent carbon quantum dots from field horsetail *Equisetum Arvense* L and fluorimetric detection of Pd²⁺ ions, Turk J Anal Chem, 7(2), 2025, 209–219.

Author of correspondence: abasoglu@gumushane.edu.tr

Tel: +90 (456) 233 10 60

Fax: +90 (456) 233 10 67

Received: April 21, 2025

Accepted: May 22, 2025

doi <https://doi.org/10.51435/turkjac>.

Heteroatom doping [9], surface modification [9], and passivation techniques involve substituting carbon atoms with elements like N, B, S, and P, introducing functional groups to the carbon dot surface via covalent bonds, and applying passivation agents (e.g., polyethylene glycol, PEG) to coat the nanoparticles. The strategy used in material production is of critical importance in materials science. Carbon dot synthesis techniques are typically categorized into two primary strategies: 'top-down' and 'bottom-up' methods. In "top-down" strategies, carbon-based precursors (e.g. graphene and fullerenes) are broken down by exposure to harsh conditions. This approach is commonly used for synthesizing graphene quantum dots and carbon nanodots. In contrast, 'bottom-up' methods typically involve the polymerization and subsequent carbonization of small molecular precursors, such as citric acid and acetaldehyde, leading to the formation of carbon dots (e.g., carbon quantum dots – CQDs, carbon nanodots – CNDs, and carbon polymer dots – CPDs) with a lower degree of carbonation. Bottom-up approaches for preparing CDs generally include combustion/thermal and template strategies. Thermal or combustion-based approaches involve the rearrangement and carbonization of precursor materials through the application of heat. In principle, precursors that contain carbon—such as citric acid [10], acetaldehyde [11], and natural biomass [12]—can serve as the starting materials for CDs synthesis using thermal methods. Depending on the heating technique employed, these processes can be divided into categories such as direct pyrolysis, microwave-assisted, ultrasonic, and hydrothermal/solvothermal treatments. Applying green chemistry principles in the synthesis of carbon dots (CDs) offers numerous benefits, particularly in minimizing chemical hazards, improving cost-efficiency, ensuring the use of renewable resources, reducing environmental impact, and supporting scalable production. Importantly, the intrinsic composition of plant-derived carbon dots (CDs)—rich in carbohydrates, proteins, amino acids, and other biomolecules—obviates the need for external reagents for doping or surface functionalization. In the present study, CQDs were synthesized using field horsetail (*Equisetum arvense* L.), a naturally sourced biomass, as the carbon precursor, without the use of any additional chemicals for doping or surface modification. Horsetail (*Equisetum arvense*) served as a precursor for the microwave-assisted preparation of luminescent silicon nanoparticles (SiNPs), as reported in a study by Adinarayana and colleagues in 2020 [13]. The synthesized SiNPs were characterized and suggested as a luminescent probe for detecting Fe^{3+} ions; however, no real sample analysis was conducted in the study. In our study, fluorescent CQDs synthesized via a different method (hydrothermal)

enabled the selective detection of a different type of metal ion (Pd^{2+}) and were successfully applied to real water samples. These features highlight the potential of the study to make a significant contribution to the literature. The optical characteristics of the CQDs were assessed using UV-Vis and fluorescence spectroscopy, while their structural features were analyzed via TEM and FTIR. As is well known, CQDs have found applications in many fields, particularly in ion detection due to their wide range of properties. The synthesized CQDs were used for the determination of Pd^{2+} ions.

Palladium ions (Pd^{2+}) are known to pose serious health and environmental threats due to their high toxicity. Human exposure to Pd^{2+} ions has been linked to various health issues, including respiratory complications, skin irritation, and genotoxic effects. Pd^{2+} can interfere with DNA and cellular proteins, potentially leading to mutations and cell damage. Prolonged exposure has been shown to cause systemic toxicity, particularly affecting vital organs such as the kidneys and liver, which are especially more susceptible to heavy metal accumulation and associated toxic effects [14,15]. Environmentally, Pd^{2+} ions can accumulate in aquatic ecosystems, leading to bioaccumulation and disruption of aquatic species, which can ultimately affect the food chain and biodiversity [12]. Pd^{2+} ions are also difficult to remove from contaminated water due to their ability to form stable complexes, making remediation efforts more challenging. Moreover, soil contamination with Pd^{2+} can lead to long-term damage to plant growth, impacting the photosynthetic and enzymatic activities of various species [16]. Therefore, strict environmental monitoring and control are necessary to mitigate the harmful effects of Pd^{2+} pollution. Analytical methods such as spectrometry (Bazel' et al. 2021), colorimetry (Liu et al. 2019), and electrochemical processes (Velmurugan et al. 2017) have demonstrated trace-level detection capabilities for Pd^{2+} ions. The toxicity of heavy metals and their compounds is well established, with palladium (Pd^{2+}) being increasingly recognized for its potential health risks. Exposure to palladium, particularly via inhalation of particulate forms, has been associated with allergic reactions and other toxicological effects in humans [17]. Moreover, palladium is commonly released into the environment through industrial activities such as automotive catalytic converter manufacturing and electronic waste processing, leading to its accumulation in soil, water, and air [18]. Given its toxic, hazardous, and carcinogenic nature, the World Health Organization [19] has established a maximum allowable concentration for palladium (Pd^{2+}) ions in drinking water, set at 10 parts per billion, 6 ppb (56.4 nM). These factors underscore the pressing necessity for accurate and specific detection of trace amounts of Pd^{2+}

ions to mitigate public health risks. In this study, the limit of detection (LOD) was obtained as 50.2 nM which is well below the standard limits set by the WHO for Pd^{2+} ions in drinking water. Consequently, the synthesized CQDs were successfully applied to the determination of Pd^{2+} ions at different concentrations in tap water.

2. Materials and method

2.1. Chemicals and materials

The field horsetail (*Equisetum Arvense* L.) was collected from a rural area in Dipsizgöl Village of Bolu, Turkey. Standard stock solutions containing 1000 ppm of LiNO_3 , NaNO_3 , KNO_3 , AgNO_3 , NH_4Cl , TiNO_3 , $\text{Ba}(\text{NO}_3)_2$, $\text{Be}_4\text{O}(\text{C}_2\text{H}_2\text{O}_2)_6$, $\text{Ca}(\text{NO}_3)_2$, $\text{Cd}(\text{NO}_3)_2$, $\text{Co}(\text{NO}_3)_2$, $\text{Cu}(\text{NO}_3)_2$, $\text{Pb}(\text{NO}_3)_2$, $\text{Mg}(\text{NO}_3)_2$, $\text{Mn}(\text{NO}_3)_2$, $\text{Ni}(\text{NO}_3)_2$, $\text{Zn}(\text{NO}_3)_2$, $\text{Sr}(\text{NO}_3)_2$, $\text{Cr}(\text{NO}_3)_3$, HAuCl_4 , $\text{Y}(\text{NO}_3)_3$, $\text{Al}(\text{NO}_3)_3$, NH_4VO_3 , $\text{Bi}(\text{NO}_3)_3$, H_3BO_3 , Sc_2O_3 , Sb_2O_3 , $(\text{NH}_4)_2\text{TiF}_6$, SeO_2 , $(\text{NH}_4)_6\text{Mo}_7\text{O}_{24}$, $(\text{NH}_4)_2\text{WO}_4$, and $\text{Pd}(\text{NO}_3)_2$ were all procured from Merck Chemical Company (Darmstadt, Germany). All chemicals utilized in this study were of analytical reagent grade and were used as received without any further purification. The water employed in all experimental procedures was double-distilled (DD) water. The buffer solutions used in this study, supplied by Merck Certipur (AVS Titrimorm), included glycine buffer (pH 1.0), citrate buffer (2.0, 3.0, 5.0, 6.0, and 12.0), phthalate buffer (4.01), disodium hydrogen phosphate buffer (pH 7.0), and borate buffer (8.0 to 11.0).

2.2. Instruments

The collected plant material was ground into a fine powder using a blender (Arçelik, Turkey) prior to extraction. Fluorescence data were collected using a PTI QM-4 spectrofluorometer, with a 1.0 nm slit width, and recorded in a 1 cm quartz cuvette. The UV-Vis absorption spectra of the CQDs were recorded using a Specord 21 spectrophotometer from Analytik Jena (Jena, Germany). The morphological features of the CQDs were analyzed using a transmission electron microscope (TEM), specifically the FEI TALOS F200S TEM operating at 200 kV (Thermo Fisher Scientific, Waltham, MA, USA). FTIR analysis of the freeze-dried CQDs was carried out using a Perkin Elmer 1600 spectrophotometer (Perkin Elmer, Inc., Waltham, MA, USA).

2.3. Synthesis of CQDs

CQDs were synthesized utilizing *Equisetum arvense* (EA), a plant commonly known as horsetail, as an environmentally sustainable precursor. The EA was thoroughly washed using tap water and subsequently rinsed three times with ultrapure water. The washed plant was then left to dry completely in the shade for four weeks. After drying, the material was finely ground

to obtain a uniform powder. An amount of 8 grams of this powder was then mixed with 140 ml of ultrapure water. The mixture was subsequently placed in a 250 ml Teflon-lined autoclave, sealed securely, and heated in an oven at 180°C for 12 hours. Following the heating process, the autoclave was allowed to cool, and the resulting product was filtered using standard filter paper to separate larger particles. The filtrate was then passed through syringe filter membranes with pore sizes of 0.45 μm and 0.25 μm , respectively. The light brown dispersion of CQDs obtained was stored at 4°C in a refrigerator for future application in subsequent experiments. For fluorescence measurements, the working solution of CQDs was prepared by diluting 1:250 (v/v, 0.4%) with deionized water.

2.4. Fluorescence stability of the CQDs

The impact of pH on the fluorescence (FL) intensity was investigated for the synthesized CQDs across a pH range from 1.0 to 12.0. To perform this examination, the pH of aqueous solutions containing the synthesized CQDs (0.4%, v/v) was adjusted within the range of 1.0–12.0 using various aqueous buffer solutions. Subsequently, the FL intensities of the CQDs were measured at an excitation of 340 nm. Furthermore, the crucial aspect of optical stability for practical applications was investigated. The FL intensities of CQDs solutions were also monitored under daylight illumination for various durations (0–45 minutes). To assess the fluorescence stability of CQDs, fluorescence spectra were recorded by exciting the solutions at 340 nm under different ionic strengths, ranging from 0 to 2.0 M KCl.

2.5. Selectivity of the CQDs for metal ions

Initially, the fluorescence spectra of a solution containing 2 mL of CQDs and 2 mL of distilled water were recorded as baseline data. To investigate the impact of metal ions on the fluorescence emission properties of CQDs, 2 mL of a 100 μM metal ion solution was added to the CQDs solution prior to measurement. Fluorimetric titration was performed to explore the potential linear correlation between metal ion concentration and the fluorescence intensity of the CQDs. For this experiment, 2 mL of CQDs solution was added to each tube, followed by incremental additions of the metal ion solution, and the final volume was adjusted to 4 mL with distilled water. After a 6-minute incubation, the fluorescence spectra of the CQDs, both with and without the metal ions, were recorded at an excitation wavelength of 340 nm.

2.6. Standard procedure for detecting Pd^{2+}

The fluorescence quenching behavior of the CQDs in the presence of Pd^{2+} ions was evaluated using a standard addition protocol under ambient conditions [20]. In this procedure, 2 mL of the CQDs solution (0.4%, v/v) was distributed into a series of test tubes.

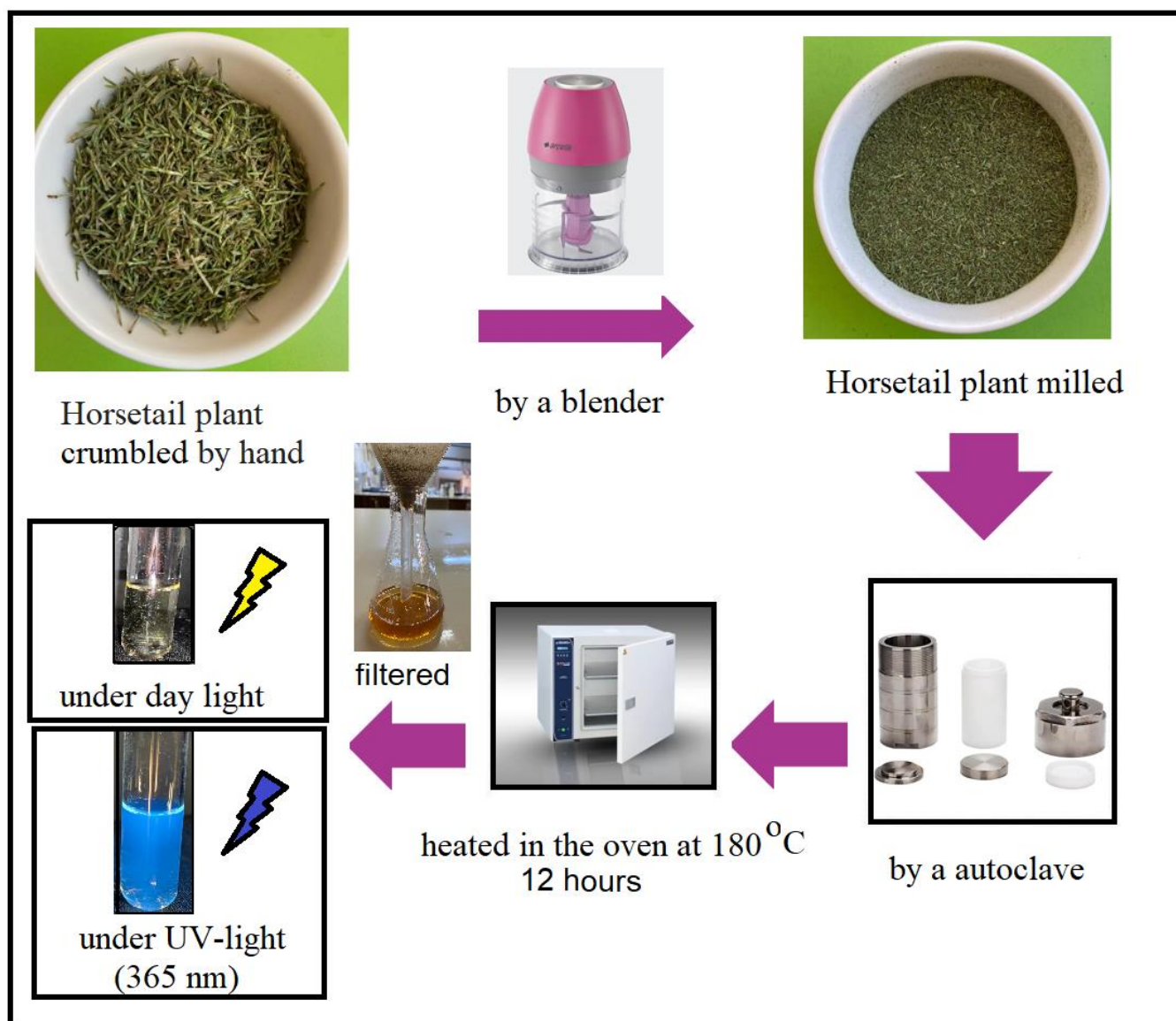


Figure 1. Synthesis of CQDs

Except for the first tube, each received a defined quantity of the sample matrix. To assess the concentration-dependent quenching effect, incremental volumes of Pd^{2+} solutions (1.5–15.0 μM) were added starting from the third tube in the sequence. The pH was adjusted to 7.0 using 0.5 mL of citrate buffer, and each solution was brought to a final volume of 4 mL with deionized water. The change in fluorescence intensity between the first and second tubes served as a reference for estimating the Pd^{2+} levels in tap water samples. A modified standard addition method [21], based on fluorescence quenching of the CQDs by Pd^{2+} ions, was employed under the optimized conditions (Table S1 in the Supplementary Information). A detailed description of the procedure is provided in the Supplementary Information (Scheme S1). The analytical method was validated according to commonly accepted parameters. Linearity was evaluated over a concentration range of 0.5 to 15.0 μM using the modified standard addition approach. The

limit of detection (LOD) and limit of quantification (LOQ) were determined following IUPAC recommendations, based on the standard deviation (Sd) of replicate blank measurements and the slope (m) of the calibration curve. These values were calculated using the formulas: $\text{LOD} = 3 \times \text{Sd} / m$ and $\text{LOQ} = 10 \times \text{Sd} / m$.

The method's accuracy was assessed through recovery studies. Tap water samples were spiked with Pd^{2+} at concentrations of 1.5, 1.75, 2.0, and 2.5 μM , and analyzed under identical conditions to evaluate the method's applicability and precision in real sample matrices.

For sensitivity evaluation, various Pd^{2+} concentrations within the same range were mixed with 2 mL of the CQDs solution. After adjusting the volume to 4.00 mL, the solutions were incubated for six minutes. The fluorescence spectra were then recorded at an excitation wavelength of 340 nm using a spectrofluorometer.

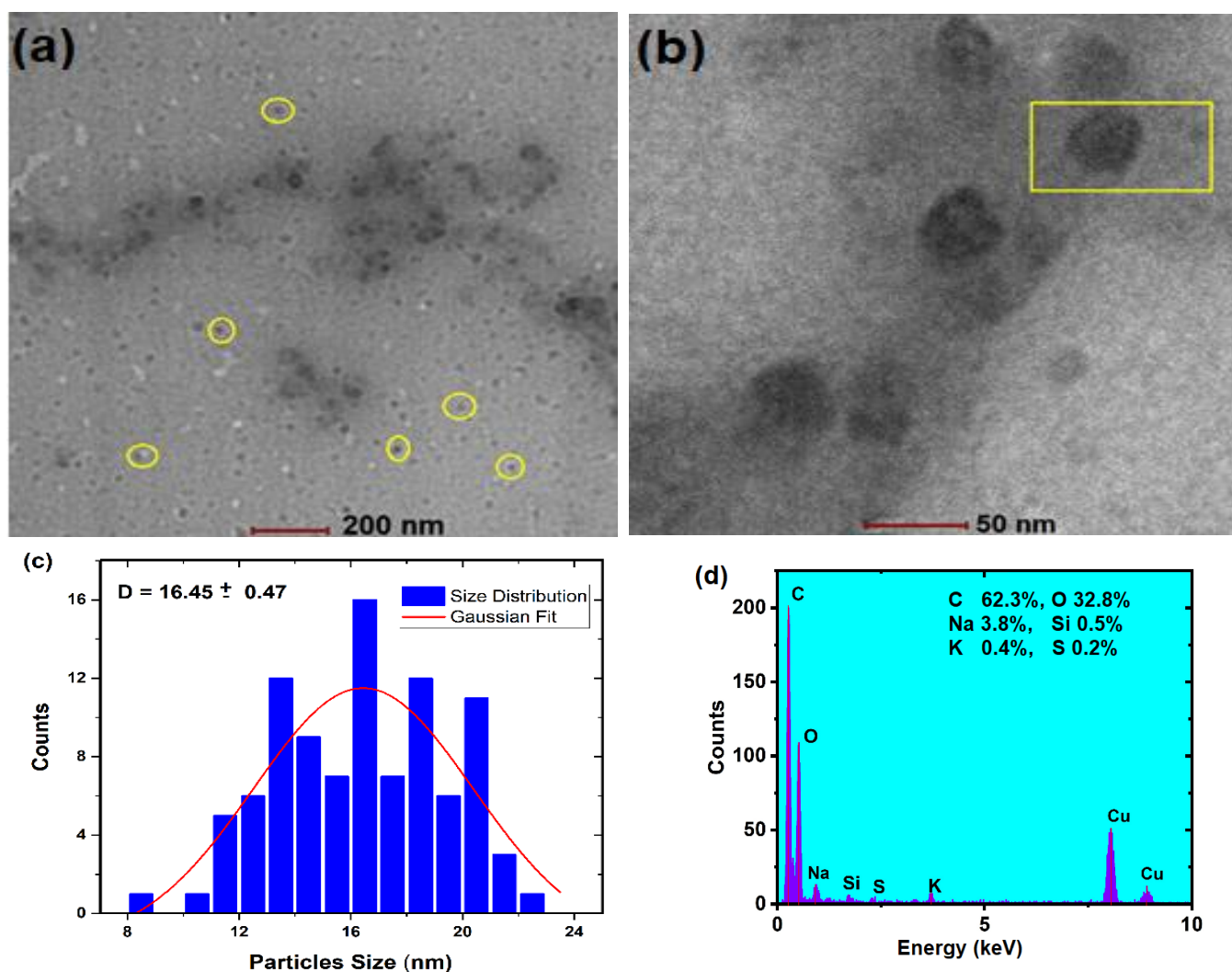


Figure 2. (a) TEM image of the prepared CQDs at a scale of 200 nm, (b) HRTEM image at a scale of 50 nm, (c) particle size distribution histogram based on the TEM image in (a), and (d) EDX spectrum showing the elemental composition of the CQDs

3. Results and discussion

3.1. Characterization of CQDs

To create CQDs in an autoclave, a one-step synthesis process utilizing the hydrothermal method at 180°C was carried out (Fig. 1). This synthesis method is straightforward and does not require the use of surface passivation agents or treatment with strong acids or bases.

The morphological characteristics and internal structure of the synthesized CQDs were examined through transmission electron microscopy (TEM), as presented in Fig. 2a and Fig. 2b. The TEM images revealed that the CQDs were uniformly distributed and exhibited predominantly spherical geometry in shape, with diameters ranging approximately from 11 nm to 21 nm. According to the size distribution histogram (Fig. 2c), the calculated average particle diameter was about 16.45 nm. This estimation was based on measurements from 94 individual particles using the ImageJ analysis software. Notably, no lattice fringes were observed in the

high-resolution TEM images, indicating the amorphous nature of the CQDs.

Elemental analysis was carried out via energy-dispersive X-ray spectroscopy (EDX), with the results presented in Fig. 2d. The CQDs mainly consisted of carbon (C) and oxygen (O), with weight percentages of 62.3% and 32.8%, respectively, confirming the carbonaceous nature of the nanostructures. Trace levels (each below 4%) of sodium (Na), silicon (Si), potassium (K), and sulfur (S) were also detected. The copper signal was excluded from the composition analysis, as it originated from the carbon-coated copper grid used during TEM sample preparation. It is worth noting that sodium and potassium are commonly present in many plant species, while silicon is especially abundant in *Equisetum arvense* L., the botanical source of the CQDs [13].

Fig. 3 presents the FT-IR spectrum used to identify the functional groups present on the surface of the synthesized CQDs, which influence their solubility, optical properties, and sensing capabilities. A broad absorption band observed between 3342 and 3225 cm⁻¹

is attributed to the stretching vibrations of hydroxyl (OH) and amine (N–H) groups [22,23], commonly found in CQDs synthesized via hydrothermal methods. Additionally, a weak band observed near 3062 cm^{-1} is likely associated with aromatic C–H stretching vibrations [24], suggesting the possible presence of graphitic or aromatic domains within the CQD structure. The absorption peaks at 2929 cm^{-1} and 2971 cm^{-1} are assigned to symmetric and asymmetric stretching vibrations of aliphatic $-\text{CH}_3$ and $-\text{CH}_2$ groups, respectively [25]. A sharp peak near 1669 cm^{-1} confirms the presence of carbonyl (C=O) groups [26], while a prominent band detected at 1575 cm^{-1} is attributed to the C=C stretching vibrations [27], indicative of conjugated or aromatic domains within the carbon framework. In addition, signals observed at 1397 cm^{-1} and 1442 cm^{-1} correspond to the symmetric stretching modes of carboxylate ($-\text{COO}^-$) groups [28]. Finally, the bands at 1045 cm^{-1} and 1084 cm^{-1} are attributed to C–O and C–N stretching vibrations [29], suggesting the presence of ether and amine functionalities. These surface groups contribute to the chemical reactivity and fluorescence behavior of CQDs.

3.2. Optical and fluorescence properties of CQDs

The optical properties of the synthesized CQDs were investigated using UV–Vis and fluorescence spectroscopic techniques. As shown in Fig. 4a, the UV–Vis spectrum of the CQDs displays a characteristic absorption profile extending from the UV region into the edge of the visible range. Although the diluted CQDs (1:250, v/v) show negligible absorbance within the visible window (400–700 nm), a pronounced absorption band is observed in the ultraviolet region. The absorption peak at 278 nm corresponds to $\pi-\pi^*$ transition of C=C bonds in an aromatic sp^2 structure, while the band at 326 nm is attributed to the $n-\pi^*$ transition [30].

The fluorescence emission of the CQDs exhibits a clear dependence on the excitation wavelength. Upon excitation with 365 nm UV light, CQDs emit strong blue fluorescence, as shown in Fig. 1. The CQDs are characterized by their distinct excitation-dependent emission behavior (Fig. 4b). It was found that when aqueous solutions of CQDs were excited within the wavelength range of 340 to 400 nm, the emission maxima shifted towards longer wavelengths, accompanied by a reduction in emission intensity. In contrast, excitation within the 300 to 330 nm range resulted in the maximum emission wavelength remaining near 400 nm. The excitation wavelength yielding the highest fluorescence intensity was found to be 340 nm. This behavior demonstrates the excitation wavelength-dependent fluorescence characteristics of the CQDs.

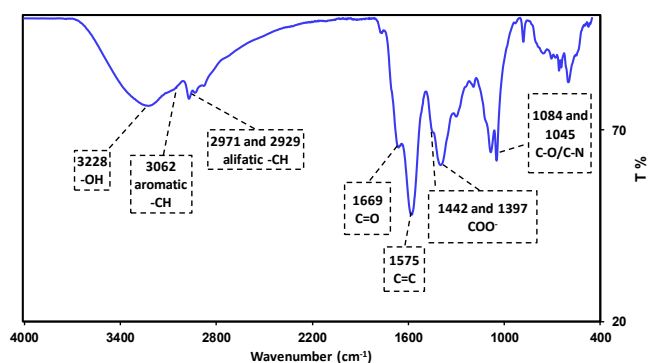


Figure 3. FTIR spectrum of CQDs

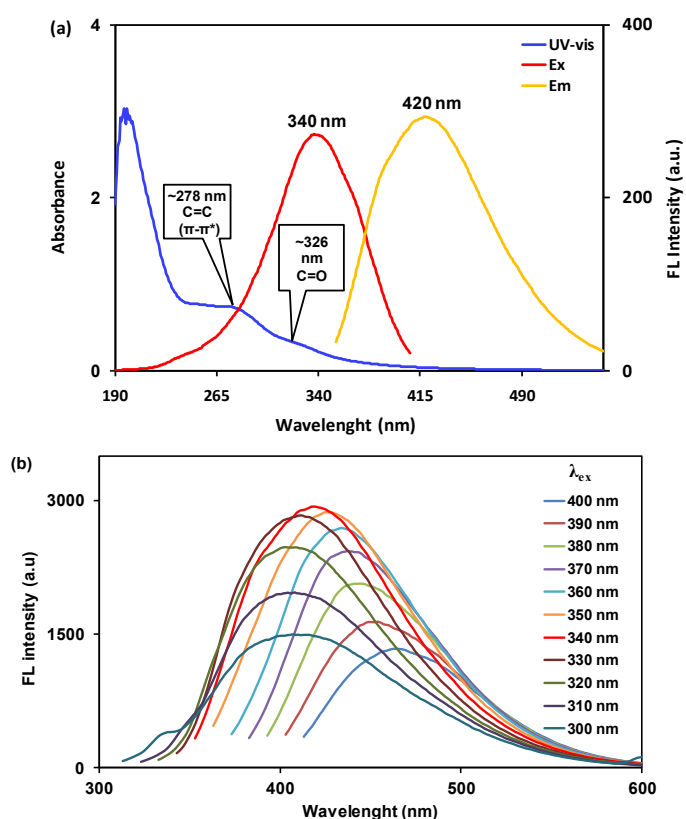


Figure 4. (a) UV–Vis absorbance spectrum, fluorescence excitation (Ex.) at 340 nm, and emission (Em.) at 420 nm for CQDs (0.4%, v/v) (b) Emission behavior as a function of excitation wavelength (300–400 nm)

3.3. Optimization of experimental parameters

Before conducting the quantitative analysis of Pd^{2+} ions using the proposed sensing system, the effects of pH, incubation time (0–45 min), and ionic strengths (0 to 2 M KCl) on fluorescence intensity were investigated to determine the optimal conditions for Pd^{2+} detection (Fig. 5).

Fig. 5a illustrates the fluorescence (FL) intensity of the CQDs measured under daylight conditions over a 45-minute period. The maximum decrease in FL intensity, calculated at the 45th, was 3.18%. The decrease was determined using the formula: $(F_0 - F_t) / F_t \times 100$, where F_0 and F_t represent the fluorescence intensities at time 0 and at the given time points, respectively.

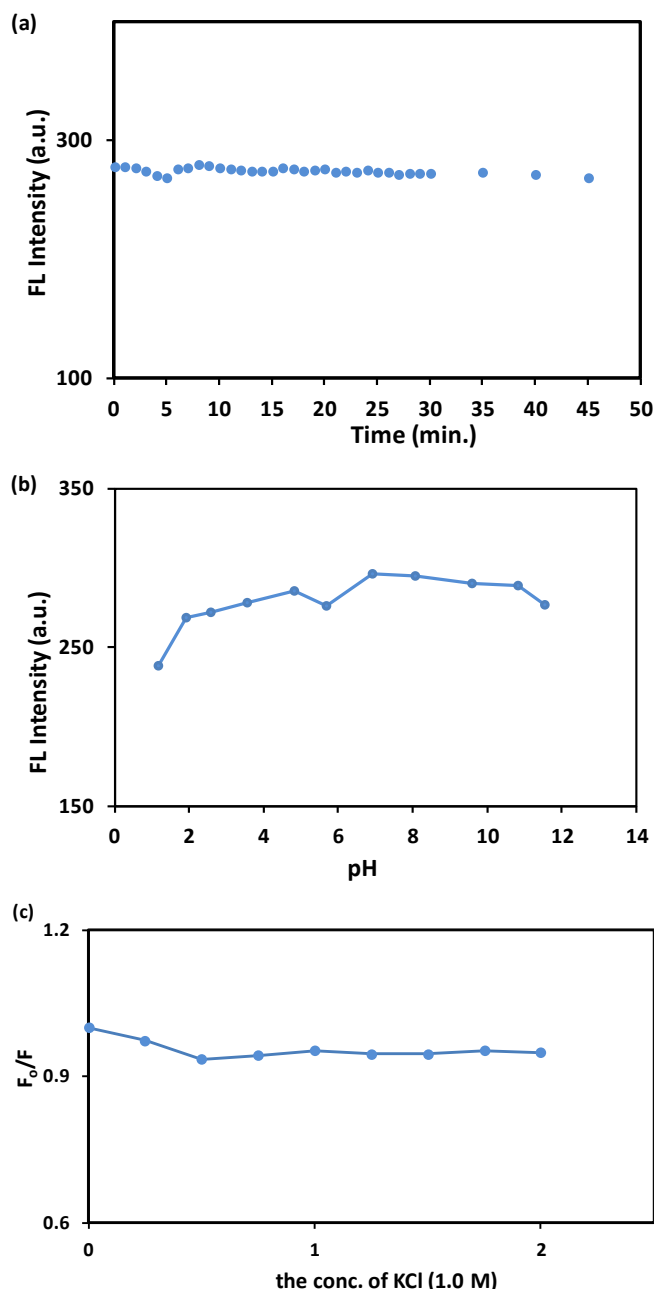


Figure 5. Fluorescence stability of CQDs under different conditions. Effect of (a) daylight illumination time, (b) pH, and (c) ionic strength (KCl concentration) on the FL intensity of the CQDs

Upon examining the graph, irregular fluctuations were observed between the 2nd and 6th minutes, while no significant change was noted between the 6th and 20th minutes (ranging from 0.62% to 0.71%). This indicates that the activation of CQDs under daylight at room temperature is minimal between the 6th and 20th minutes. Therefore, the 6th minute, when daylight-induced activation was lowest, was selected as the incubation period.

As depicted in Fig. 5b, the influence of pH on the fluorescence intensity of CQDs was studied over a pH range of 1 to 12. At the strongly acidic pH of 1, the fluorescence intensity of CQDs was relatively low. However, it gradually increased as the pH approached neutrality (from pH 1 to pH 7, excluding pH 6),

reaching a maximum at pH 7. At pH 12, a substantial decline in fluorescence was observed, while under moderately alkaline conditions, the decrease was less pronounced. Thus, significant fluorescence quenching was noted under strongly acidic and highly alkaline (pH > 11) conditions. This can be attributed to protonation and deprotonation of surface functional groups (e.g. COOH, OH, and amino groups) on the CQDs. Between pH 7 and 11, the fluorescence intensity remained relatively stable. Consequently, pH 7 was selected as the optimal condition for further experiments. As shown in Fig. 5c, the fluorescence intensity of CQDs remained nearly unchanged across varying ionic strengths (0–2.0 M KCl). This stability under high ionic strength conditions demonstrates the excellent salt resistance of the CQDs.

3.4. Detection of Pd²⁺ Ions

Initially, the effect of various metal ions at a concentration of 50 μ M on the fluorescence properties of CQDs was investigated. Fluorescence spectra were recorded for aqueous CQD solutions containing different metal ions, including Li⁺, Na⁺, K⁺, NH₄⁺, Mg²⁺, Ca²⁺, Ba²⁺, Be²⁺, Se²⁺, Cr³⁺, Mn²⁺, Al³⁺, Co²⁺, Ni²⁺, Cu²⁺, Zn²⁺, Ag⁺, Cd²⁺, Sr²⁺, Sn²⁺, Sb²⁺, As²⁺, Y³⁺, Sc³⁺, Mo²⁺, W³⁺, Tl³⁺, Ti⁴⁺, and Pd²⁺ using an excitation wavelength of 340 nm (Fig. 6). The free CQDs, without any metal ions, exhibited a maximum emission at 420 nm. Almost all the tested metal ions induced a certain degree of fluorescence quenching in the CQDs. Notably, Pd²⁺ ions led to a pronounced decrease in fluorescence intensity. As illustrated in Fig. 6, Pd²⁺ exhibited the strongest quenching effect among all the metal ions tested, indicating its potential for selective detection using the synthesized CQDs.

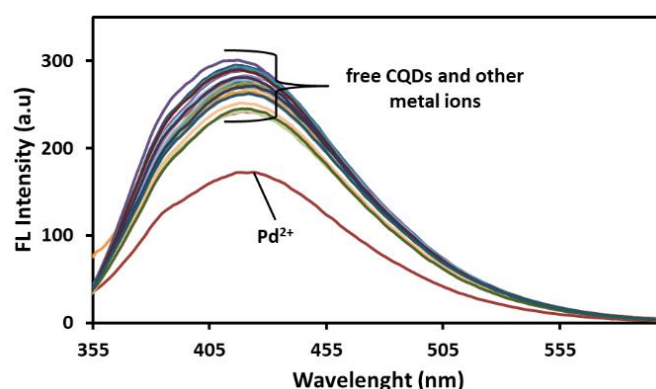


Figure 6. Fluorescence emission spectra of CQDs in the presence of various metal ions (50 μ M each).

The interaction between carbon quantum dots (CQDs) with Pd²⁺ ions was investigated through fluorescence titration, which revealed a concentration-dependent quenching effect. As shown in Fig 7a, the fluorescence intensity of CQDs (recorded between 355

and 600 nm) progressively decreased with increasing concentrations of Pd^{2+} ions. Based on the quenching observed at 420 nm, an external calibration curve was constructed, as illustrated in Fig. 7b. However, deviations from *Beer's law* were noted at Pd^{2+} concentrations above 15.0 μM . The inset in Fig. 7b reveals a strong linear relationship in the concentration range of 1.5–15.0 μM , described by the linear equation $y = -41210x + 3\text{E}+00$ with a correlation coefficient (R^2) of 0.9857. The limit of detection (LOD) for Pd^{2+} was calculated to be 50.2 nM, based on the IUPAC 3σ criterion: $\text{LOD} = (3 \cdot \text{SD})/S$, where SD is the standard deviation of the intercept and S is the slope of the calibration curve. Furthermore, the limit of quantification (LOQ), defined as nine times the standard deviation of the blank signal divided by the slope, was found to be 150.6 nM. For real sample analysis, tap water was spiked with Pd^{2+} at concentrations of 1.5 μM , 1.75 μM , 2.0 μM , and 2.5 μM . A modified standard addition method (described in Scheme S1, Supplemental Information) was employed to enhance the accuracy of Pd^{2+} quantification. Additional experimental details are provided in Fig. S1 (in the Supplemental Information). This calibration strategy has been previously adopted in fluorometric methods [21].

3.5. Pd^{2+} detection mechanism of CQDs

The detection of Pd^{2+} using CQDs was achieved through a fluorescence quenching mechanism. A linear relationship was established between the quenching intensity and Pd^{2+} concentrations in the range of 0.5–15.0 μM , with a limit of detection (LOD) of 50.2 nM, as shown in the inset of Fig. 7b. Numerous studies have investigated the fluorescence quenching interaction between CQDs and Pd^{2+} ions. As depicted in Fig. 8a, significant spectral overlap between the absorption spectrum of Pd^{2+} (peaks at 288 nm and 382 nm) and the excitation spectrum of CQDs suggests the involvement of two possible mechanisms: the inner filter effect (IFE) and Förster resonance energy transfer (FRET). FRET involves energy transfer from the excited state of the CQDs to the ground state of the Pd^{2+} ions, whereas IFE occurs when a secondary absorber reduces the intensity of the excitation light, resulting in apparent fluorescence quenching [31].

Notable changes were observed in the absorbance peaks at 278 nm and 326 nm upon the addition of Pd^{2+} ions to the CQD solution. To investigate this, a photometric titration was performed by gradually increasing the concentrations of Pd^{2+} ions from 12.5 μM to 500 μM (Fig. 8b). With increasing Pd^{2+} concentrations, the initial absorbance peak at ~278 nm red-shifted to ~289 nm and increased in intensity.

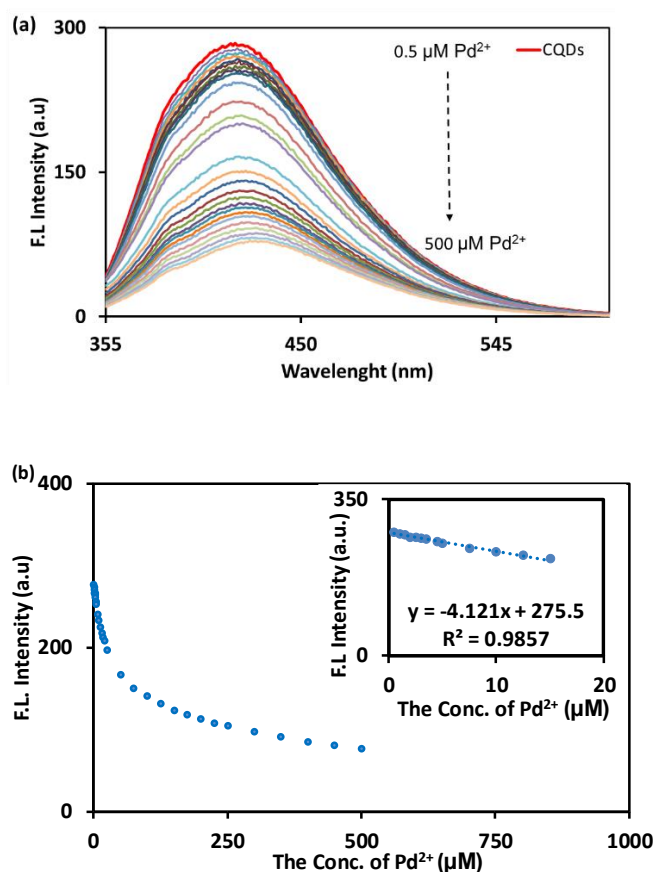


Figure 7. (a) Fluorescence response of CQDs in the presence of Pd^{2+} (0.5–500 μM Pd^{2+}). (b) Relationship between F.L intensity and different concentrations of Pd^{2+} (0.5–500 μM Pd^{2+}). Inset: Calibration graph for Pd^{2+} determination (0.5–15.0 μM Pd^{2+})

Additionally, a broad peak appeared between 330 and 450 nm, with a maximum around 383 nm. The enhancement in absorbance at ~289 nm and ~383 nm likely indicates strong electrostatic interactions and complex formation between CQDs and Pd^{2+} ions. Fig. 8b clearly shows a consistent increase in absorbance at these wavelengths as Pd^{2+} concentration increases, supporting the formation of ground-state complexes between CQDs and Pd^{2+} ions [32].

To evaluate the stability of these potential complexes, a plot of $1/(A_0 - A)$ versus $1/[\text{Pd}^{2+}]$ yielded a linear relationship ($R^2 = 0.9933$) at 383 nm, as shown in Fig. S2. Here, A_0 represents the absorbance of CQDs alone, and A is the absorbance of the CQDs- Pd^{2+} complex. The intercept-to-slope ratio provided a stability constant of $K = 1.57\text{E}+03$ ($\text{Log}K: 3.12$), suggesting the formation of relatively stable complexes, likely involving –OH- and –COO- groups on the CQDs surface.

The CQDs display distinct absorption peaks at 278 nm and 326 nm. Upon the addition of Pd^{2+} ions to the CQD solution, noticeable modifications in the UV-vis absorption spectra were observed. The shift in the absorption peaks following Pd^{2+} introduction suggests a significant interaction between Pd^{2+} ions and the CQDs, likely due to strong electrostatic forces, which result in fluorescence quenching.

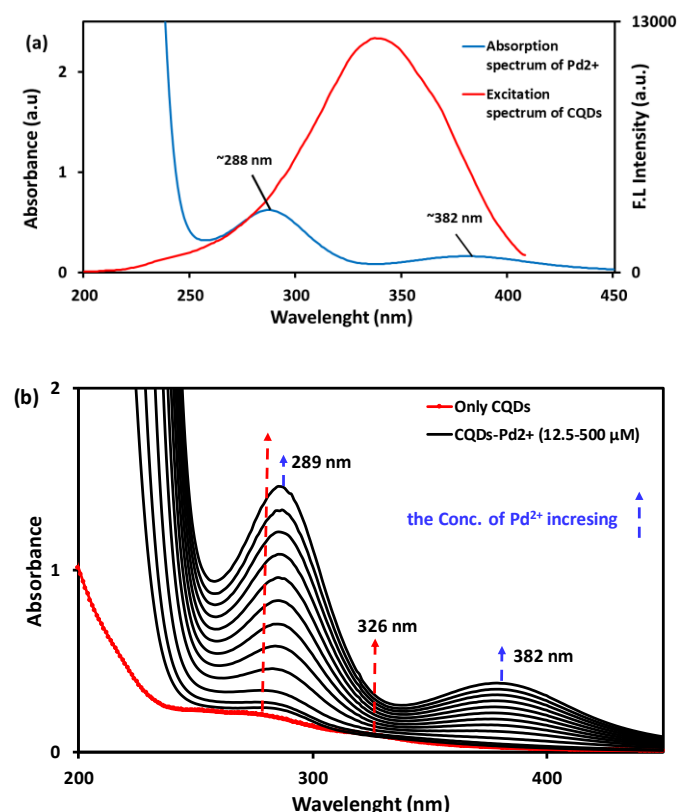


Figure 8. (a) Absorption spectrum of Pd^{2+} and excitation spectrum of CQDs. (b) Absorption spectra for the spectrophotometric titration of the CQDs with Pd^{2+} ions. $[\text{Pd}^{2+}] = 12.5 \mu\text{M} - 500 \mu\text{M}$.

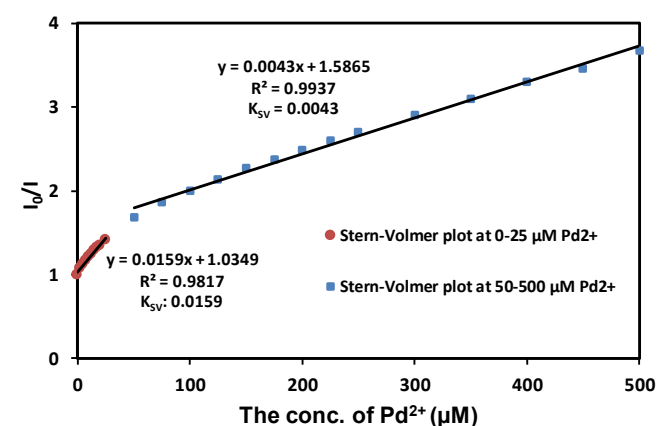


Figure 9. Stern-Volmer plots at different Pd^{2+} concentration ranges (0–25 μM Pd^{2+} and 50–500 μM Pd^{2+})

K_{SV} is the Stern-Volmer quenching constant, indicating the efficiency of the quenching process, and $[Q]$ is the concentration of the quencher (Pd^{2+}). A linear relationship between fluorescence quenching and Pd^{2+} concentrations was observed within two separate ranges: 0–25 μM and 50–500 μM , with K_{SV} values of 0.0159 and 0.0043, respectively. This suggests a concentration-

dependent quenching mechanism, wherein the quenching efficiency decreases at higher Pd^{2+} concentrations. At lower concentrations, the quenching mechanism is attributed to dynamic quenching, where rapid interactions between CQDs and Pd^{2+} lead to a reduction in fluorescence. The lower K_{SV} value at a higher concentration range may suggest the saturation of binding sites or a possible shift in the quenching mechanism, where secondary effects like Inner filter effects (IFE) or Förster resonance energy transfer (FRET) may become significant. These findings underscore the important role of electrostatic interactions, dynamic quenching at low concentrations, and the contribution of secondary mechanisms at elevated concentrations in the fluorescence quenching process, as reported in similar systems [33,34].

3.6. Application to tap water sample

To assess the accuracy of the method, spiked tap water samples were analyzed at various concentrations. A modified standard addition method was applied at four concentration levels within the linear range. Each recovery test was conducted in triplicate ($N = 3$) on the same day. The recovery rates ranged from 96.9% to 99.8% as shown in Table 1. These results demonstrate that the proposed method is reliable and suitable for the quantification of Pd^{2+} ions in water samples.

3.7. Comparison with previous studies

To highlight the advantages of the present method, its analytical performance was compared with previously reported Pd^{2+} detection sensors based on carbon quantum dots (CQDs). Key parameters such as the limit of detection (LOD), linear range, synthesis procedure, environmental compatibility, and real sample applicability were evaluated. Detailed data are summarized in Table S1 (Supporting Information). Kang et al. [35] developed a multi-step system using grape skin powder along with $\text{C}_2\text{H}_4\text{O}_3$ and $\text{C}_5\text{H}_5\text{NO}_2$, relying on chemical additives; however, the use of ionic liquids and organic solvents (e.g., n-heptane) poses limitations in terms of environmental sustainability. Their sensor exhibited a LOD of 360 nM and a linear range of 0–40 μM , and it was tested in real tap and river water samples. Dong et al. [36] reported a sensor based on hydrothermally synthesized CQDs from *Momordica charantia*, achieving a LOD of 348 nM and a linear range

Table 1. Application of the developed method with the modified standard addition method for the determination of Pd^{2+} in tap water samples

Sample	Added (μM)	^a Found (μM) $\pm s$	^b Recovery%	RSD%
Tap Water	1.50	1.50 ± 0.01	100.2	0.6
	1.75	1.71 ± 0.02	98.4	1.2
	2.00	1.99 ± 0.05	99.6	2.3
	2.50	2.50 ± 0.05	100.1	2.1

^a: mean of three replicates; s : standard deviation; ^b: intraday precision; RSD: relative standard deviation

of 0–325 μM ; however, its response to Fe^{3+} ions alongside Pd^{2+} limited its selectivity. Gao et al. [37] prepared sulfur-chlorine doped CQDs from humic acid using environmentally questionable starting materials (landfill leachate concentrate, polyethylene glycol), obtaining a LOD of 100 nM and a linear range of 5–40 μM . However, their method was not validated in real water samples. Nitrogen-doped red-emitting CQDs synthesized from p-phenylenediamine, aminobenzoic acid, and nitric acid exhibited an LOD of 60 nM and a linear range of 0–33 μM , but were applied only in confocal imaging and niosome systems without Pd^{2+} detection or environmental analysis. Furthermore, red fluorescence is susceptible to photobleaching and background interference [38]. Carbon dots synthesized via microwave-assisted pyrolysis of *Pithecellobium dulce* seed pods (LOD: 370 nM, linear range: 2–50.2 μM) were used for Pd^{2+} detection in well and pond water but showed a significantly higher LOD than the 50.2 nM obtained in our study [39]. Additionally, microwave pyrolysis requires specialized equipment and poses challenges in terms of laboratory accessibility and reproducibility. Despite these limitations, our hydrothermal synthesis of carbon quantum dots from *Equisetum arvense* without the use of chemical additives provides a more sensitive, selective, and environmentally friendly alternative for Pd^{2+} detection in environmental samples.

4. Conclusions

In this study, water-soluble fluorescent carbon quantum dots (CQDs) were successfully synthesized for the first time from field horsetail (*Equisetum arvense* L.) via a simple hydrothermal method. To the best of our knowledge, this plant source has not been previously employed for CQD synthesis, with the exception of its use in silicon nanoparticle production by Adinarayana et al. in 2020. The as-prepared exhibited strong blue fluorescence with excitation-dependent emission behavior in aqueous solutions. Among 32 metal ions tested, Pd^{2+} induced the most pronounced fluorescence quenching. A fluorimetric method for the selective and sensitive detection of Pd^{2+} ions were developed, offering a linear response in the range of 0.5–15.0 μM and a low detection limit of 50.2 nM. The limit of quantification (LOQ) was determined to be 150.6 nM. Method validation using spiked tap water samples yielded excellent recovery values between 96.9% and 99.8%, confirming the method's accuracy and reliability. The Stern–Volmer analysis confirmed that fluorescence quenching followed a dynamic quenching mechanism, with potential contributions from inner filter effect (IFE) and Förster resonance energy transfer (FRET).

Although the current study focused on spiked tap water, future research will aim to expand the applicability of this method to diverse environmental water matrices, such as river and industrial wastewater, to further assess its robustness and practical utility.

Funding

This study was conducted without the support of any specific funding from governmental, commercial, or non-profit organizations.

Ethical compliance statement:

The authors confirm that there are no conflicts of interest related to this publication.

Ethical approval:

No experiments involving human or animal subjects were conducted by the author in the scope of this article.

Conflict of interest statement:

The author states that there are no known financial or personal conflicts of interest that could have influenced the content or outcomes of this work.

Data availability statement:

No datasets were generated or analyzed during the preparation of this article.

Author contributions:

All experimental work, including the green synthesis of carbon quantum dots (CQDs) from field horsetail (*Equisetum arvense* L.), structural characterization, and the fluorometric detection of Pd^{2+} ions, was carried out by Aysel Başoğlu. The manuscript was also solely written by Aysel Başoğlu. TEM and XRD measurements were performed by authorized technical staff at the Bayburt University Research Laboratory.

References

- [1] X. Xu, R. Ray, Y. Gu, H.J. Ploehn, L. Gearheart, K. Raker, W.A. Scrivens, Electrophoretic Analysis and Purification of Fluorescent Single-Walled Carbon Nanotube Fragments, *J Am Chem Soc* 126 (2004) 12736–12737.
- [2] Y.-P. Sun, B. Zhou, Y. Lin, W. Wang, K.A.S. Fernando, P. Pathak, M.J. Meziani, B.A. Harruff, X. Wang, H. Wang, P.G. Luo, H. Yang, M.E. Kose, B. Chen, L.M. Veca, S.-Y. Xie, Quantum-Sized Carbon Dots for Bright and Colorful Photoluminescence, *J Am Chem Soc* 128 (2006) 7756–7757.

- [3] J.T. Margraf, V. Strauss, D.M. Guldi, T. Clark, The Electronic Structure of Amorphous Carbon Nanodots, *J Phys Chem B*, 119, (2015), 7258–7265.
- [4] A.B. Siddique, V.P. Singh, A.K. Pramanick, M. Ray, Amorphous carbon dot and chitosan based composites as fluorescent inks and luminescent films, *Mater Chem Phys*, 249, (2020), 122984.
- [5] L. Wang, W. Li, L. Yin, Y. Liu, H. Guo, J. Lai, Y. Han, G. Li, M. Li, J. Zhang, R. Vajtai, P.M. Ajayan, M. Wu, Full-color fluorescent carbon quantum dots, *Sci. Adv.* 6 (2020) eabb6772.
- [6] F. Yuan, T. Yuan, L. Sui, Z. Wang, Z. Xi, Y. Li, X. Li, L. Fan, Z. Tan, A. Chen, M. Jin, S. Yang, Engineering triangular carbon quantum dots with unprecedented narrow bandwidth emission for multicolored LEDs, *Nat Commun*, 9, (2018) 2249.
- [7] M.J. Krysmann, A. Kelarakis, P. Dallas, E.P. Giannelis, Formation Mechanism of Carbogenic Nanoparticles with Dual Photoluminescence Emission, *J Am Chem Soc* 134 (2012) 747–750.
- [8] H. Ding, J.-S. Wei, P. Zhang, Z.-Y. Zhou, Q.-Y. Gao, H.-M. Xiong, Solvent-Controlled Synthesis of Highly Luminescent Carbon Dots with a Wide Color Gamut and Narrowed Emission Peak Widths, *Small* 14 (2018) 1–10.
- [9] D.-W. Wang, D. Su, Heterogeneous nanocarbon materials for oxygen reduction reaction, *Energy Environ. Sci.* 7 (2014) 576–591.
- [10] J. Schneider, C.J. Reckmeier, Y. Xiong, M. Von Seckendorff, A.S. Susha, P. Kasak, A.L. Rogach, Molecular fluorescence in citric acid-based carbon dots, *J Phys Chem C* 121 (2017) 2014–2022.
- [11] W. Hong, Y. Zhang, L. Yang, Y. Tian, P. Ge, J. Hu, W. Wei, G. Zou, H. Hou, X. Ji, Carbon quantum dot micelles tailored hollow carbon anode for fast potassium and sodium storage, *Nano Energy* 65 (2019) 104038.
- [12] M.L. Sall, A.K.D. Diaw, D. Gningue-Sall, S. Efremova Aaron, J. Aaron, Toxic heavy metals: impact on the environment and human health, and treatment with conducting organic polymers, a review, *Environ Sci Pollut Res.* 27 (2020) 29927–29942.
- [13] T.V.S. Adinarayana, A. Mishra, I. Singhal, D.V.R.R. Koti, Facile green synthesis of silicon nanoparticles from: *Equisetum arvense* for fluorescence based detection of Fe(III) ions, *Nanoscale Adv.* 2 (2020) 4125–4132.
- [14] J. Kielhorn, C. Melber, D. Keller, I. Mangelsdorf, Palladium - A review of exposure and effects to human health, *Int. J. Hyg. Environ. Health* 205 (2002) 417–432.
- [15] J. Wataha, Palladium, Biological Effects, in: *Encycl. Met.*, Springer New York, New York, NY, 2013: pp. 1628–1635.
- [16] L. Savignan, S. Faucher, P. Chéry, G. Lespes, Platinum group elements contamination in soils: Review of the current state, *Chemosphere* 271 (2021) 129517.
- [17] G.O. Conti, S. Giordanella, P. Rapisarda, G. Leotta, A. Cristaldi, C. Favara, M. Ferrante, Toxicological Implications of Platinum Group Elements (PGEs): A Systematic Review of In Vivo and In Vitro Studies Using Mammalian Models, *Front Biosci. - Landmark* 29 (2024) 304.
- [18] E.S. Koçoğlu, Ö. Yılmaz, E.G. Bakırdere, S. Bakırdere, Quantification of palladium in wastewater samples by matrix-matching calibration strategy assisted deep eutectic solvent based microextraction, *Environ. Monit. Assess.* 193 (2021) 1–7.
- [19] WHO, Lead in drinking-water: Health risks, monitoring and corrective actions, (2022) 1–26.
- [20] A. Gümrükçüoğlu, A. Başoğlu, S. Kolaylı, S. Dinç, M. Kara, M. Ocak, Ü. Ocak, Highly sensitive fluorometric method based on nitrogen-doped carbon dot clusters for tartrazine determination in cookies samples, *Turkish J Chem* 44 (2020) 99–111.
- [21] A. Başoğlu, G. Tosun, M. Ocak, H. Alp, N. Yaylı, Ü. Ocak, Simple Time-Saving Method for Iron Determination Based on Fluorescence Quenching of an Azaflavanon-3-ol Compound, *J. Agric Food Chem* 63 (2015) 2654–2659.
- [22] F.S. Salim, İ. Sargin, G. Arslan, Carbon quantum dots and chitosan-based heterogeneous silver catalyst for reduction of nitroaromatic compounds, *Turkish J Chem* 47 (2023) 148–163.
- [23] H. Shabbir, E. Csapó, M. Wojnicki, Carbon Quantum Dots: The Role of Surface Functional Groups and Proposed Mechanisms for Metal Ion Sensing, *Inorganics* 11 (2023).
- [24] H. Sun, L. Wu, W. Wei, X. Qu, Recent advances in graphene quantum dots for sensing, *Mater Today* 16 (2013) 433–442.
- [25] H. Wang, H. Luo, Y. Liu, F. Wang, B. Peng, X. Li, D. Hu, G. He, D. Zhang, Improved Energy Density at High Temperatures of FPE Dielectrics by Extreme Low Loading of CQDs, *Materials (Basel)*. 17 (2024) 3625.
- [26] X.-W. Hua, Y.-W. Bao, H.-Y. Wang, Z. Chen, F.-G. Wu, Bacteria-derived fluorescent carbon dots for microbial live/dead differentiation, *Nanoscale* 9 (2017) 2150–2161.
- [27] F.N. Ajjan, M.J. Jafari, T. Rebiş, T. Ederth, O. Inganäs, Spectroelectrochemical investigation of redox states in a polypyrrole/lignin composite electrode material, *J. Mater. Chem. A* 3 (2015) 12927–12937.
- [28] S. Devi, A. Kaur, S. Sarkar, S. Vohra, S. Tyagi, Synthesis and characterization of highly luminescent N-doped carbon quantum dots for metal ion sensing, *Integr Ferroelectr* 186 (2018) 32–39.
- [29] S.J. Phang, J. Lee, V.-L. Wong, L.-L. Tan, S.-P. Chai, Synergistic effects of the hybridization between boron-doped carbon quantum dots and n/n-type g-C₃N₄ homojunction for boosted visible-light photocatalytic activity, *Environ Sci Pollut Res* 29 (2022) 41272–41292.
- [30] A. Kumari, A. Kumar, S.K. Sahu, S. Kumar, Synthesis of green fluorescent carbon quantum dots using waste polyolefins residue for Cu²⁺ ion sensing and live cell imaging, *Sensors Actuators B Chem* 254 (2018) 197–205.
- [31] J.-W. Zhou, X.-M. Zou, S.-H. Song, G.-H. Chen, Quantum Dots Applied to Methodology on Detection of Pesticide and Veterinary Drug Residues, *J Agric Food Chem* 66 (2018) 1307–1319.
- [32] S. Erdemir, D. Aydın, M. Oguz, O. Kocyigit, S. Malkondu, Building an eco-friendly, biocompatible, and ratiometric NIR fluorescent sensor for the rapid detection of trace Pd²⁺ in real samples and living cells, *J Hazard Mater*, 488 (2025) 137463.
- [33] A.S.G.T. Lawson, M.G. Ellis, M. Davis, J. Turner-Dore, A.S.H. Ryder, M.H. Frosz, M. Ciaccia, E. Reisner, A.J. Cresswell, T.G. Euser, Stern-Volmer analysis of photocatalyst fluorescence quenching within hollow-core photonic crystal fibre microreactors, *Chem Commun* 58 (2022) 10548–10551.
- [34] T. Kohlmann, M. Goez, Combined static and dynamic intracellular fluorescence quenching: effects on stationary and time-resolved Stern–Volmer experiments, *Phys Chem Chem Phys*, 21, (2019), 10075–10085..
- [35] K. Kang, B. Liu, G. Yue, H. Ren, K. Zheng, L. Wang, Z. Wang, Preparation of carbon quantum dots from ionic liquid modified biomass for the detection of Fe³⁺ and Pd²⁺ in environmental water, *Ecotoxicol Environ Saf*, 255, (2023), 114795.
- [36] Y. Dong, Y. Zhang, S. Zhi, X. Yang, C. Yao, Green Synthesized Fluorescent Carbon Dots from *Momordica charantia* for Selective and Sensitive Detection of Pd²⁺ and Fe³⁺, *ChemistrySelect*, 6, (2021), 123–130.
- [37] S. Gao, H. Zhang, H. Li, Y. Pei, Synthesis of sulfur-chlorine-doped fluorescent carbon quantum dots from leachate membrane concentrate as a selective probe for Pd²⁺ detection, *Opt Mater (Amst)*, 139, (2023), 113746.
- [38] S. Pawar, S. Kaja, A. Nag, Red-Emitting Carbon Dots as a Dual Sensor for In³⁺ and Pd²⁺ in Water, *ACS Omega*, 5, (2020), 8362–8372.
- [39] R. Swathi, G.B. Reddy, B. Rajkumar, G. Yaku, S. Kondaiah, P.Y. Swamy, Microwave-assisted green synthesis of *Pithecellobium dulce* seed pods derived fluorescent carbon dots for Pd²⁺ detection, *Emergent Mater*, 6, (2023), 1207–1215.

Supplementary materials

1. The content of figures, scheme and, table:

Figure S1. Modified standard addition graph for Pd²⁺ determination (Spiked Pd²⁺ = 1.5 μM) in tab water sample.

Scheme S1. The procedure of modified standard addition method.

Figure S2. A plot of $1/(A_0 - A)$ versus $1/[Pd^{2+}]$ to explore the stability of these potential Pd- CQDs complex.

Table S1. The analytical performance metrics of the developed method for Au³⁺ determination.

Table S2. Comparison of recent CQD-based fluorescent sensors for Pd²⁺ detection.

Figure S1.

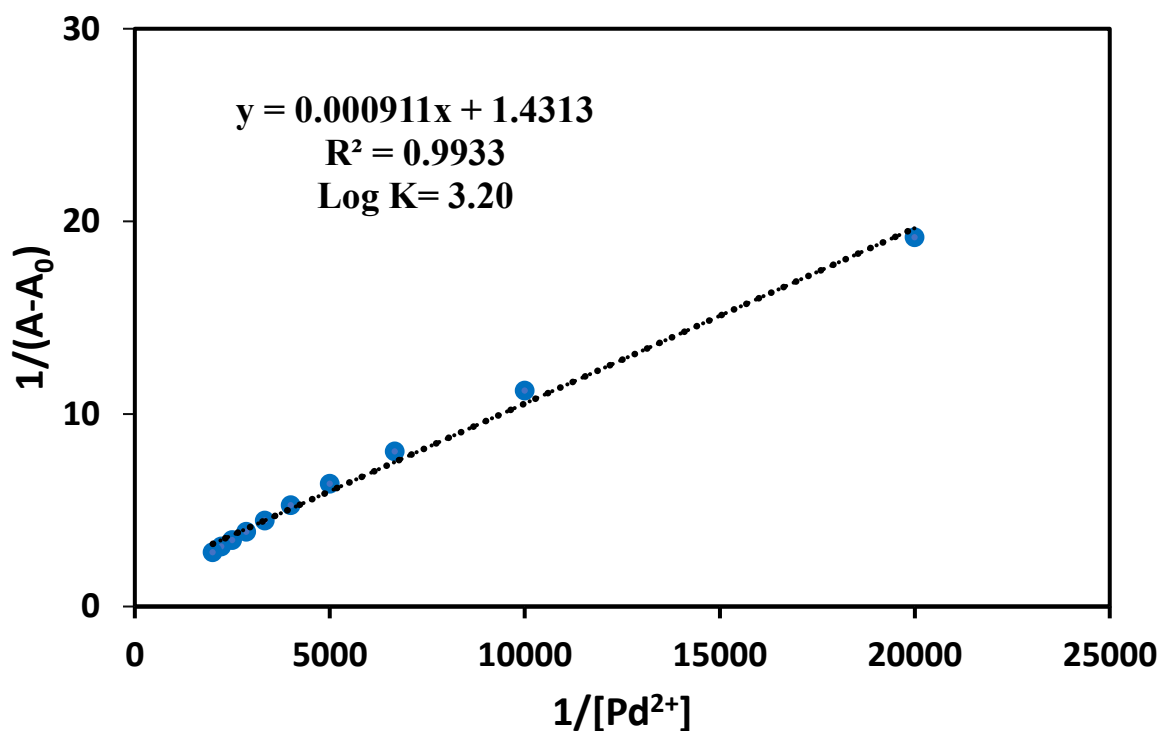


Figure S1. A plot of $1/(A_0 - A)$ versus $1/[Pd^{2+}]$ to explore the stability of these potential Pd- CQDs complex

2. The procedure of modified standard addition method

Tubes for a Standard Addition Methods	F0	F1	F2	F3	F4	F5	F6	F7	F8
Substances Added (mL)									
CQDs	2	2	2	2	2	2	2	2	2
pH citrate buffer (PH=7)	0.5	0.5	0.5	0.5	0.5	0.5	0.5	0.5	0.5
Tap water Sample (spiked 1.5 µM)	-	0.06	0.06	0.06	0.06	0.06	0.06	0.06	0.06
Standard Pd ²⁺ for graph	-	-	0.06	0.1	0.2	0.3	0.4	0.5	0.6

Scheme S1. The procedure of modified standard addition method

2 mL of carbon quantum dots (CQDs) were added to all tubes. A defined volume of sample was added to all tubes except the first one. Increasing amounts of Pd²⁺ (ranging from 1.5 to 15.0 µM) were sequentially added to the third tube and subsequent tubes. The pH of the solutions was adjusted to 7.0 using 0.5 mL of citrate buffer and, the final volume was brought to 4 mL. The difference between the FL intensity of the first and the second tubes was related to the Pd²⁺ amount in the tap water sample solution. The fluorescence spectra of all solutions were recorded at an emission wavelength of 420 nm, with excitation at 340 nm. The concentration of Pd²⁺ was calculated using Eq. (S1):

$$C_x = \frac{F_0 - F_1}{m}$$

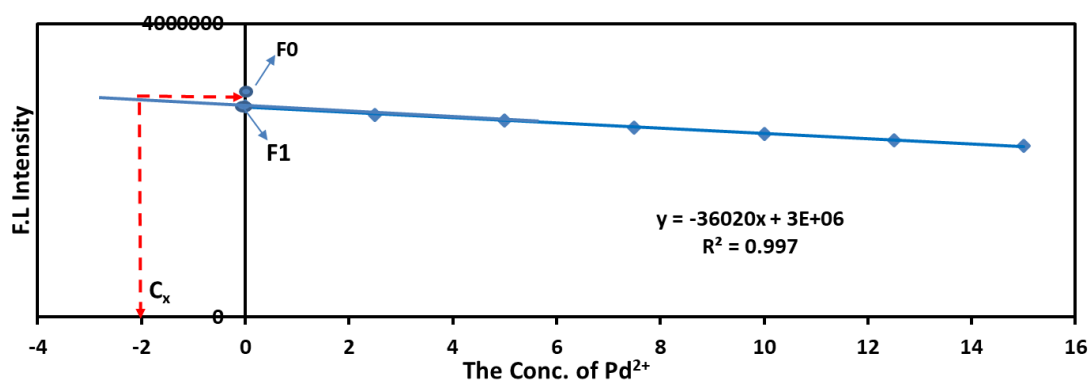


Figure S2. Modified standard addition graph for Pd²⁺ determination in tap water sample (for the spiked conc. of 1.5 µM Pd²⁺)

Table S1.

Excitation wavelength (nm)	340
Emission wavelength (nm)	420
LOD (nM)	50.2
LOQ (nM)	150.6
Linear range (μM)	0.5–15.0
Solvent	water
Time before measurement (minutes)	6
The correlation coefficient (R^2)	0.9857
Intraday precision (RSD%, N = 3, for 1.5 μM ; 1.75 μM ; 2.0 μM ; 2.5 μM Pd ²⁺)	0.6 - 2.3

LOD: limit of detection; LOQ: limit of quantification; RSD: Relative standard deviation

Table S2. Comparison of recent CQD-based fluorescent sensors for Pd²⁺ detection

Fluorescent probes	Precursor	Synthesis method/Temp.	LOD (μM)	Linear range (μM)	Application/Sample	Ref.
CQDs	Grape skin powder/C ₂ H ₄ O ₃ :C ₅ H ₉ NO ₂	hydrothermal treatment/210°C	0.36	0–40	Determination/Tap water and river water	[35]
CQDs	Momordica charantia (bitter gourd)	hydrothermal treatment/210°C	0.348	0–325	Determination Tap and lake water	[36]
L-CQDs	polyethylene glycol/ landfill leachate concentrate	hydrothermal technique /200°C	0.1	5–40	Sensor/No application	[37]
NRCDs	p-Phenylenediamine/amino benzoic acid/ nitric acid	Hydrothermal treatment/180°C	0.060	0–33	confocal imaging/ niosomes	[38]
CDs	Pithecellobium dulce seed pods	microwave-aided pyrolysis/ 500 watts	0.37	2 -50.2	Determination/Bore water and Pond water	[39]
CQDs	field horsetail (Equisetum arvense L.)	Hydrothermal treatment/180°C	0.050	0.5–15	Determination/tap water	This work

CQDs:carbon quantum dots; CDs: carbon dots; NRCDs: nitrogen-doped red-emitting carbon dots; L-CQDs: humic acid-based sulfur-chlorine-doped carbon quantum dots.

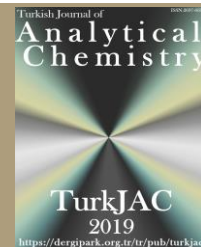
References:

- [35] K. Kang, B. Liu, G. Yue, H. Ren, K. Zheng, L. Wang, Z. Wang, Preparation of carbon quantum dots from ionic liquid modified biomass for the detection of Fe³⁺ and Pd²⁺ in environmental water, *Ecotoxicol Environ Saf*, 255, (2023), 114795.
- [36] Y. Dong, Y. Zhang, S. Zhi, X. Yang, C. Yao, Green Synthesized Fluorescent Carbon Dots from Momordica charantia for Selective and Sensitive Detection of Pd²⁺ and Fe³⁺, *ChemistrySelect*, 6, (2021), 123–130.
- [37] S. Gao, H. Zhang, H. Li, Y. Pei, Synthesis of sulfur-chlorine-doped fluorescent carbon quantum dots from leachate membrane concentrate as a selective probe for Pd²⁺ detection, *Opt Mater (Amst)*, 139, (2023), 113746.
- [38] S. Pawar, S. Kaja, A. Nag, Red-Emitting Carbon Dots as a Dual Sensor for In 3+ and Pd 2+ in Water, *ACS Omega*, 5, (2020), 8362–8372.
- [39] R. Swathi, G.B. Reddy, B. Rajkumar, G. Yaku, S. Kondaiah, P.Y. Swamy, Microwave-assisted green synthesis of Pithecellobium dulce seed pods derived fluorescent carbon dots for Pd²⁺ detection, *Emergent Mater*, 6, (2023), 1207–1215.



TurkJAC

Turkish Journal of Analytical Chemistry

<https://dergipark.org.tr/tr/pub/turkjac>TurkJAC
2019<https://dergipark.org.tr/tr/pub/turkjac>

Treatment of Silicate Ion with *Bacillus subtilis* Bacteria in Demineralization-Water/Steam Cycles in Power Plants

Deniz Bozkurt¹ , Aslıhan Dalmaz² , Sefa Durmuş^{2,*} ¹ Düzce University, Graduate Education Institute, Department of Chemistry, 81620, Düzce, Türkiye² Düzce University, Faculty of Art and Science, Department of Chemistry, 81620, Düzce, Türkiye

Abstract

Inorganic silica and various mineral deposits are particularly important in the process waters of power plants. The presence of these inorganic species, especially silica, poses many challenges for process water applications in power plants. If silica in process waters is not controlled, it forms hard, difficult, and dangerous deposits in the process water. Silica formation and accumulation cannot be prevented by many conventional methods and scale inhibitors. In this study, *Bacillus subtilis* bacteria were used to minimize silica formation in the process water of power plants. For this purpose, many different parameters were optimized in the system steps. Under the optimum experimental conditions, the detection limit for SiO₂ was determined as 0.0375 mg/mL, the quantitation limit as 0.1136 mg/mL, and the correlation coefficient as 0.9997. Additionally, recovery values range between 96.5% and 103.2%, indicating the accuracy of the method. The results obtained are promising for the use of silica removal in process water applications. In addition, the use of *Bacillus subtilis* bacteria for the treatment of process water will provide significant economic benefits. Therefore, this study will make an important contribution to the literature and will be very advantageous in terms of cost for various industrial organizations that face silica problems in process waters.

Keywords: SiO₂, *Bacillus subtilis*, energy, water treatment, demineralization

1. Introduction

An ideal boiler water treatment system consists of a reverse osmosis unit, thermal degasser, pressure filter, and softening unit to ensure the flow of high-purity feed water. If normal hard tap water is used as additional water in steam boilers, silica begins to accumulate on the heating surface of the boiler after a while. This consumes more energy and requires the use of more chemicals and large amounts of acid to clean the inside of the boiler. Although the water softening in the system helps to prevent scaling, after a while, it becomes insufficient, and more systemic problems arise. This is undesirable in terms of both time and cost [1,2]. Good pre-treatment, which is the building block of every system, is very important in terms of providing high standards of feed water to the system [3]. A schematic representation of feed water pretreatment for boilers is given in Fig. 1.

Silica and mineral deposits can become serious operational problems for untreated or poorly treated process waters [4,5]. Poorly soluble electrolytes found in

process water include calcium oxalate, silica, strontium sulfate, barium, carbonate, phosphate, calcium, and others. The constituents of these electrolytes vary depending on many variables such as pH, temperature, water chemistry, conductivity, etc. Among these mineral deposits, magnesium silicate and silica are particularly problematic. Since they cause excessive amounts of sediment formation, they cause operational failures that cause catastrophic damage in process water systems [6]. In industrial water systems, especially silica causes serious problems that cannot be solved. Uncontrolled silica will accumulate in significant quantities throughout the process, resulting in the formation of hard and challenging deposits that are difficult to clean. Conventional cleaners cannot counteract the silica build-up and are also dangerous as they try to get rid of the silica by chemical treatment. It will also cause significant corrosion over time. This will reveal another problem that silica will create [5].

Citation: D. Bozkurt, A. Dalmaz, S. Durmuş, Treatment of silicate ion with *Bacillus subtilis* bacteria in demineralization-water/steam cycles in power plants, 7(2), 2025, 220–227.

***Author of correspondence:** sefadurmus@duzce.edu.tr

Tel: +90 (380) 541 24 04

Fax: +90 (380) 541 24 03

Received: March 28, 2025

Accepted: May 29, 2025

doi <https://doi.org/10.51435/turkjac.1667603>

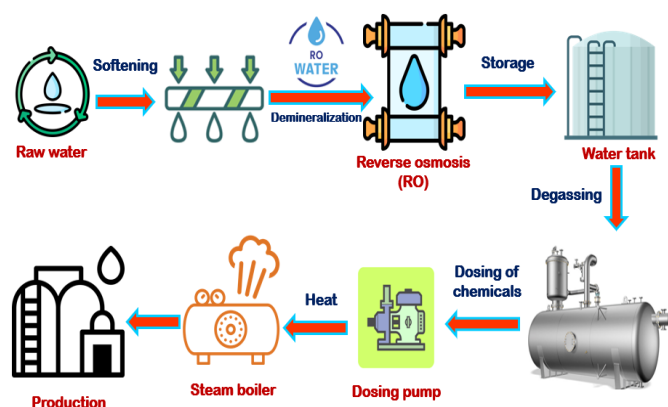


Figure 1. Schematic representation of feedwater pretreatment for boilers

Silica deposits accumulating in equipment such as distillation units, engine jackets, boilers, cooling tower fillings, steam generators, heat exchangers, evaporators, etc. cause inefficient heat transfer and a significant decrease in heat transfer rates. Failure in one or more of the successive steps will greatly affect the other steps. One of them is that organic and inorganic deposits in paper and pulp mills cause significant losses in production. Another is the accumulation in boiler pipes in industrial water systems. A visual of the accumulation of silica and mineral deposits is shown in Fig. 2 [7]. This buildup in boiler tubes reduces equipment efficiency, leading to increased fuel consumption and overheating in the system. In parallel, the accumulation of poorly soluble silica in the system creates a complex matrix environment. This will directly affect corrosion exposure, creating negative consequences for the system [8].

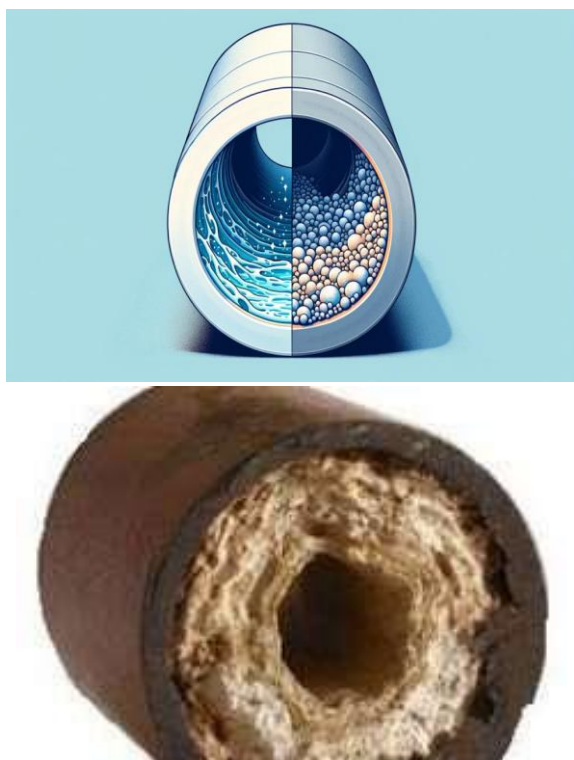


Figure 2. Silica and mineral deposits

Many methods have been proposed to improve the quality of process water and, furthermore, to ensure that wastewater is purified and reused. In addition, with the advancement of technology, many different systems have been developed and used [9–11]. These include bio-floc technology, recirculating aquaculture systems, and aquaponics [12,14]. These methods are generally expensive, can cause contamination by introducing different pathogens into the system, and are laborious. Other disadvantages include the fact that they often cause confusion in systems and also pose a threat to human health through accumulation. For this reason, the method that has been used more popularly in recent times to improve wastewater quality and provide treatment of process water is to use *Bacillus subtilis* bacteria. The method using *Bacillus subtilis*, which also has probiotic properties, is quite remarkable in that it is effective against a wide range of pathogens and has more advantages than others in improving the quality of process water [15,16]. In this study, experiments are presented to see what kind of change occurs when *Bacillus subtilis* bacteria are applied to all steps of the system to improve process water quality and reduce silica accumulation.

2. Materials and methods

2.1. Chemicals and reagents

All chemicals used in this study were of analytical grade and used without further purification. Molybdic acid ($\text{MoO}_3 \cdot (\text{H}_2\text{O})_2$), hydrochloric acid (HCl), sodium hydroxide (NaOH), oxalic acid ($\text{H}_2\text{C}_2\text{O}_4$), and 4-(methylamino)phenol sulfate were used to form the reducing solution, and sodium disulfite chemicals were obtained from Merck. Silica stock solutions at a concentration of 100 mg mL^{-1} were prepared with sodium metasilicate (Na_2SiO_3) in deionized water. Working solutions of silica at different concentrations were prepared by diluting the main stock solution to appropriate concentrations. *Bacillus subtilis*, the biosorbent used in this study, was isolated from thermal water deposits in the lower region of Pamukkale travertines in Türkiye. 250 mL of Nutrient Broth (NB) medium was used to grow *Bacillus subtilis* bacteria. The pH of the medium was adjusted with 0.1 mol/L HCl or NaOH to ensure fermentation and then autoclaved. After the autoclaving step, 2.5 mL (3.6×10^7) of cell suspension was inoculated into each glass vial. Then, it was shaken at 120 rpm at 35 °C.

2.2. Instruments

The Water Story brand Dream Plus I Finesta model deionized water device was used to prepare the solutions required for the experimental studies. The Shin

Saeng brand SHPM-10 model magnetic stirrer was used to adjust the sample temperature. The WTW brand Inolab Multi 9630 IDS model pH meter was used to measure the instantaneous pH of the samples taken from each step of the demineralization system. Weighing of the chemical materials used to prepare the solutions during the study was carried out using the Mettler Toledo brand ML204T model precision balance. The measurements of the samples taken from each step of the water-vapor cycle were performed on a WTW brand AE-S60-2U model spectrophotometer. Specific conductivity measurements of the samples taken in the water-steam cycle were carried out on the WTW brand Cond 3110 model device. The determination of silica was carried out at a wavelength of 800 nm.

2.3. Procedure

This method was based on the measurement of biosorption of silica on *Bacillus subtilis*. To investigate the effectiveness of bacteria on silica accumulated in the system, a 50 mL water sample taken from the process was placed in a polypropylene volumetric flask. Before the addition of *Bacillus subtilis*, the process water sample had a total silica concentration of 41.8 mg/L, with 37.6 mg/L in dissolved form and 4.2 mg/L as suspended silica. Other physical and chemical characteristics of the raw water sample were as follows: pH 7.3, electrical conductivity 1560 $\mu\text{S}/\text{cm}$, total dissolved solids (TDS) 1648 mg/L, total hardness 90.1 $^{\circ}\text{Fr}$, calcium 185.8 mg/L, magnesium 106.1 mg/L, bicarbonate 413 mg/L as CaCO_3 , sulfate 550 mg/L, and total organic carbon (TOC) 5.7 mg/L. Then, 3 mL volume of *Bacillus subtilis* suspension (corresponding to a concentration of 3×10^8 CFU/mL) was applied to determine the amount of silica. Silica analysis was performed according to the Advancing Standards Transforming Markets (ASTM) standards [17,18]. First of all, a sample with a 3 mL concentration of *Bacillus subtilis* suspension was taken, and optimum conditions for the

process were pH 8.7 and room temperature. And the preliminary step required for silica determination was completed. Then, a 10 mL volume of this sample with optimum conditions was taken into a polypropylene volumetric flask, and 2 mL of 10% (w/v) molybdic acid solution was added. Then, this mixture was stirred in a magnetic stirrer for 10 minutes. After this step, a 2 mL volume of 4-(methylamino)phenol sulfate ($\text{C}_{14}\text{H}_{20}\text{N}_2\text{O}_6\text{S}$) reducing solution was added to the volumetric flask, and the stirring process was continued for another 10 minutes. After the reaction, the sample prepared for measurement was transferred to the UV cuvette, and analysis was performed using the UV-Vis spectrophotometer. All experiments were performed in three replicates. A schematic representation of the procedure in the study is given in Fig. 3.

3. Results and discussion

3.1. Effect of waiting time on *Bacillus subtilis* activity

Samples taken from each step of the demineralization and boiler water systems to which *Bacillus subtilis* was added were kept for 0-72 hours, and the change in SiO_2 content was examined. The procedure in the study was applied to samples taken from each step of the system, and when the values obtained as a result of the analysis were examined, it was determined that very small decreases occurred in the amount of silica with *Bacillus subtilis* bacteria up to 48 hours of waiting and that silica removal was fixed after 48 hours. This result showed that the *Bacillus subtilis* activity and removal were still at high levels up to 48 hours to perform silica analysis in water samples taken from all steps of the process. When the same procedure was applied to water samples taken from the process steps at the end of the 48 hours, the analysis result showed that the activity of *Bacillus subtilis* decreased. What is intended to be explained in this section is that the conditioning with *Bacillus subtilis*

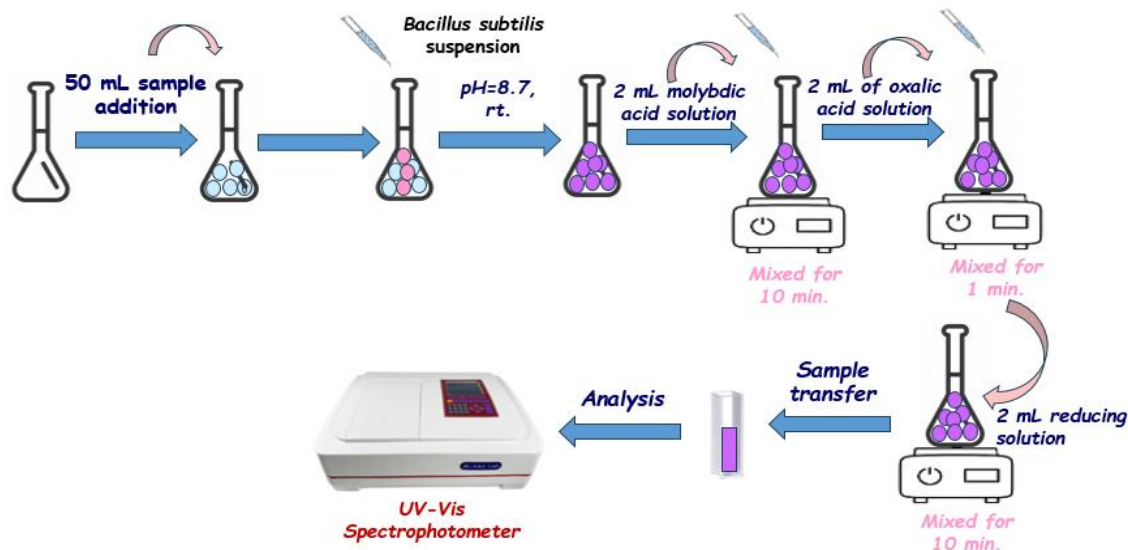


Figure 3. Schematic representation of the procedure

bacteria can be applied immediately without waiting for any period of time in water samples taken from process steps. The procedure was applied to determine the direction of its effectiveness both as soon as the sample is taken from the process steps and when it is incubated with *Bacillus subtilis* for the specified periods. As a result, the optimization made in the 0-72 hour range is to check whether the effectiveness of *Bacillus subtilis* bacteria continues after how many hours the sample is left. It was shown that this value was fixed at the end of the 48 hours, and the removal value decreased. The effect of waiting time on *Bacillus subtilis* activity is shown in Fig. 4.

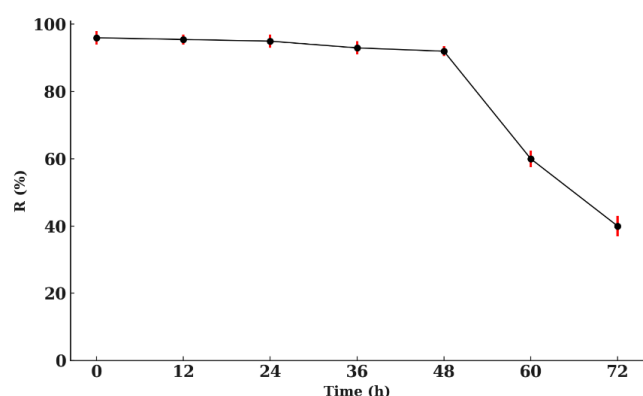


Figure 4. Effect of waiting time on *Bacillus subtilis* activity

3.2. Effect of pH on *Bacillus subtilis* activity

The aim of pH optimization is to control the system's operation in the ideal pH range when the *Bacillus subtilis* suspension is added. The pH change was controlled at different stages of the process, and optimization was carried out at certain pH ranges to determine the required value for all stages of the process. According to the results obtained from all stages of the process, pH control provides a more reliable assessment of bacterial activity under changing conditions. For this purpose, a procedure was applied between pH 5-11 values to determine the effect of pH on silica removal in all stages of the process. The optimum pH value at which silica removal was achieved for all process steps was determined as 8.7 [19,20]. The effect of pH on *Bacillus subtilis* activity is shown in Fig. 5.

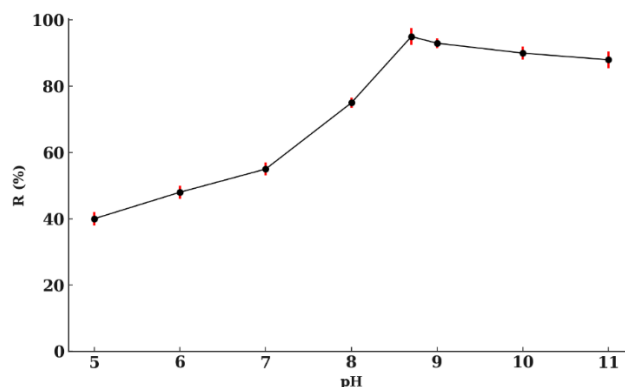


Figure 5. Effect of pH on *Bacillus subtilis* activity

The values obtained after applying the procedure to perform SiO₂ analysis in raw water are given in Fig. 6. When Fig. 6 is examined, the effect of mixing time on the effect of *Bacillus subtilis* bacteria in raw water is examined. As a result of the examinations, it was seen that there was an increase in removal up to 10 minutes, but there was no difference in removal after 10 minutes. For this reason, it was seen that 10 minutes of mixing time was sufficient for the analysis in raw water.

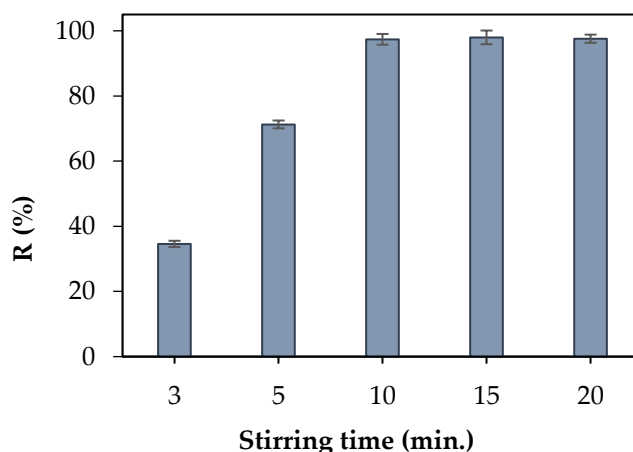


Figure 6. Effect of mixing time on removal in raw water.

3.3. Demineralization system

3.3.1. Effect of *Bacillus subtilis* on silica concentration in raw water

In the study, the specific environmental conditions of the sample to be analyzed for raw water when it is first taken are important. Therefore, the initial temperature, pH, and conductivity values at the point where the raw water sample was taken were measured. It was determined that the initial temperature at the point where the raw water sample was taken was 15 °C, the pH was 7.23, and the conductivity was 1726 µS/cm.

3.3.2. Effect of *Bacillus subtilis* on the pretreatment plant

The pre-treatment process takes feed water from raw water. The ideal operating temperature of the pre-treatment and subsequent demineralization process is 15-35 °C. In addition, the ideal operating temperature varies seasonally between 15-35 °C. For this reason, *Bacillus subtilis* activity was examined at these temperatures, and its effect was evaluated (Fig. 7). The activity of *Bacillus subtilis* was examined by pre-conditioning with *Bacillus subtilis* in the mentioned temperature range. It was observed that there was very little change in the amount of SiO₂ as the temperature increased. It was also found that *Bacillus subtilis* bacteria worked effectively at 30 °C.

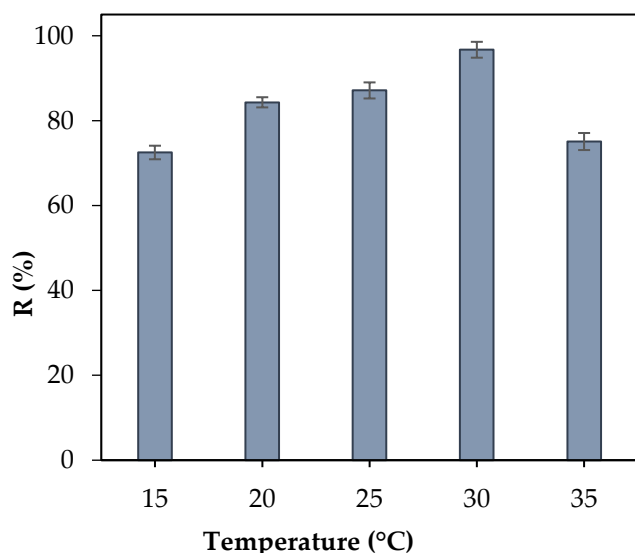


Figure 7. Effect of temperature on removal in the pretreatment plant.

3.3.3. Effect of *Bacillus subtilis* on reverse osmosis system

The formation of insoluble metal silicates in reverse osmosis is another problem. To prevent this situation, the softening process must be carried out appropriately. Therefore, samples taken from the feed water were examined in detail in the laboratory. First of all, specific environmental conditions in the field were determined to determine the conditioning rates in the process. Then, the initial temperature, pH, and conductivity values at the points where the sample was taken before reverse osmosis were measured. From the on-site measurement values of the water sample before reverse osmosis, it was found that the temperature was 20 °C, the pH was 7.20, and the conductivity was 1510 $\mu\text{S}/\text{cm}$. Among the chemicals dosed before reverse osmosis, silica-based antiscalant was used for membrane protection, and NaOH and HCl were used to balance the pH of the system. The effect of *Bacillus subtilis* on SiO_2 in the presence of these chemicals used in the treatment before reverse osmosis was also investigated. The process was carried out by adding 0-10 mL of *Bacillus subtilis* bacteria to the raw water for analysis. As a result of SiO_2 analysis, while the amount of SiO_2 in the raw water sample without *Bacillus subtilis* bacteria was quite high, it was found that the SiO_2 removal in the raw water sample with 3 mL of *Bacillus subtilis* bacteria was high. It was determined that the value remained constant when more was added. For this reason, the study was continued with the optimum value of 3 mL of bacteria.

3.3.4. Effect of *Bacillus subtilis* on reverse osmosis membrane and effluent SiO_2 concentration

Biofilm growth in reverse osmosis membranes significantly reduces the water velocity inside the membrane. For this reason, when microbiological organisms enter the membrane, they reproduce here and

form a biofilm. As a result, the pressure loss in the membranes increases, the production flow rate decreases, and as a result, the production efficiency of the system decreases, and causing production losses. However, instead of the antiscalant given before the membrane, the solution created with the addition of 5-10-15-20-30% *Bacillus subtilis* bacteria for about one month was dosed into the system to condition the system. Determination of these dosage rates was preferred to be the same as the dosage rate of the existing antiscalant chemical to facilitate performance-cost comparison. Membrane efficiency was kept under observation during the one-month trial period. It has been determined that high efficiency is achieved in removing the amount of silica when the same amount of *Bacillus subtilis* bacteria is used instead of the existing antiscalant chemical. This led to the conclusion that the bacteria used are beneficial to the system, do not form a biofilm, reduce the amount of flux passing through the membranes, increase the membrane permeability, and are effective in the treatment of other impurities in the water, such as SiO_2 . High-pressure pumps are used for the effective operation of the reverse osmosis system. The operating pressure of the sample plant is 16-32 bar max, 50 Hz. The analysis results of the study showed that *Bacillus subtilis* was not affected by the operating pressure in this range. No additional chemical treatment was applied during the study period.

3.3.5. Effect of *Bacillus subtilis* on electro-deionization system efficiency and product water SiO_2 concentration

Pretreatment with *Bacillus subtilis* increased the permeability of the Electro-Deionization (EDI) system and improved the water quality of the system. In the study conducted on the EDI product water according to the procedure, it was observed that positive improvements were experienced as the amount of wastewater decreased and the product capacity increased. In addition, this process maintained the stability of ideal pH (8.7) and pressure conditions (2 bar). It was determined that it did not affect the pH, which is one of the important parameters for the process of the system in this study, during the flow, and stabilized the system operating pressure. In addition, *Bacillus subtilis* conditioning was performed before EDI, and from the analysis results, it was seen that it provided an improvement equal to the amount of chemical used in the system, corresponding to 30%. In addition, the increase in membrane permeability of the EDI module is understood from the stability of pH and pressure, the stability of wastewater pressure, wastewater amount, and the stability of product water amount (maximum product water amount determined by the EDI manufacturer = 10 tons). It has also been observed that membrane life can be extended and used beyond 2 years

when *Bacillus subtilis* conditioning is applied instead of chemical conditioning.

3.4. Boiler system

3.4.1. Effect of *Bacillus subtilis* on boiler feed water

Since silicates form highly persistent deposits in boiler tubes, their volatile carryover to turbine components is a critical issue. The composition of boiler feedwater must allow impurities to concentrate within reasonable levels without exceeding the tolerance limits of the specific boiler design. If the feedwater does not meet these requirements, pretreatment is necessary to remove impurities. However, complete removal of impurities is not always required, as chemical treatment within the boiler can effectively and economically eliminate them. The quantity and nature of impurities affect system purity, with certain impurities, particularly silica, being of greater concern. The impurity requirements for any given feedwater depend on the feedwater usage rate and the specific boiler design (pressure, heat transfer rate, etc.). Consequently, feedwater purity requirements can vary significantly [16].

Boiler water softening chemicals are added continuously or intermittently depending on the hardness of the water and other factors, and the chemicals added to react with dissolved oxygen and the chemicals used to prevent scale formation and corrosion in the water supply system are continuously supplied to the water supply system during the process. A sample was taken from the boiler for analysis at 45 °C. It was left to cool in the cooler, and the sample was processed after the temperature was brought to normal. This situation represents the desired situation for the boiler system. According to the ABMA (American Boiler Manufacturers Association) standard, the system operates under ideal conditions. 0-30 mL of *Bacillus subtilis* bacteria was added to the boiler feed water. This value was determined according to the chemical ratio used in boiler feed water conditioning. Maximum silica removal was obtained as a result of using 20 mL of bacteria. The obtained result is given in Fig. 8.

3.4.2. Importance of conditioning for turbine

Direct steam conditioning is not applied under any circumstances, and therefore, the chemical quality of the steam depends on the measures applied to control the feedwater and boiler water. Therefore, feedwater and boiler water conditioning are very important. Because one of the most important objectives is to prevent deposits and corrosion in the steam path, for example, in pipes, valves, and turbine parts. The purity of the steam must be high. Silica is the most soluble of the common boiler water contaminants in high-pressure steam and has a high volatility. It can become supersaturated

during expansion in the turbine. Its deposits on the blades cause loss of turbine efficiency and serious damage. Salts deposited in the steam pipe under load cause the development of concentrated solutions on unloading, following the entry of significant air or condensation of residual steam (Fig. 9) [21]. This effect is a situation that should be taken into consideration, especially for reheaters, turbines, and some feed heaters. In addition to causing mechanical failure, the stress occurring during turbine operation can initiate other forms of corrosion, such as corrosion cracking.

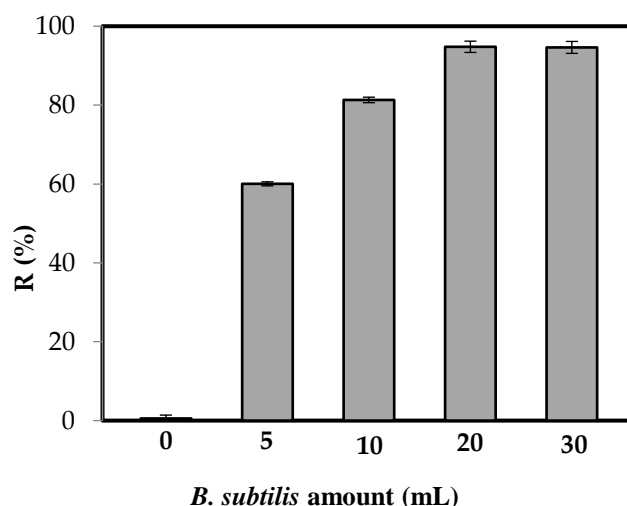


Figure 8. Effect of *Bacillus subtilis* on boiler feed water

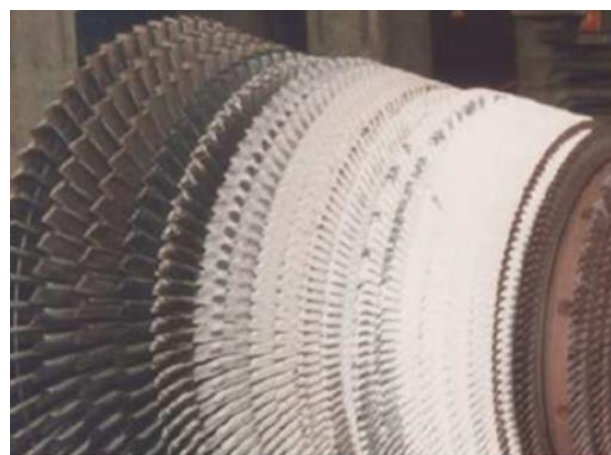


Figure 9. Damage caused by silica on turbine blades.

During the periodic maintenance after conditioning, it was observed that the turbine blades were not fouled and were clean after long-term use without much need for a suitable stabilizer. This indicated that the steam carried in the system was adequately conditioned in the feed and boiler water and that the *Bacillus subtilis* conditioning also reduced silica and other impurities in the feed water.

3.5. Method validation

Some validation parameters, such as the calibration equation, detection limit, recovery values, correlation

coefficient, and quantitation limit of the method used for the analysis of SiO₂, were investigated. All analyses were performed at 25°C. Each solution was prepared in triplicate to ensure calibration accuracy and validate the analytical method. A calibration graph was created by evaluating the data obtained as a result of the analysis in the study. To determine repeatability, intraday and interday standard deviations were examined. The relative standard deviation (%RSD) value between the outcomes of five distinct sample solutions generated at the same concentration was less than 2%, indicating the analytical method's precision. In this study, the lowest analyte concentration (LOD) and the lowest analyte concentration values that can be determined with acceptable repeatability and accuracy (LOQ) were determined using the values of 3Sb/m and 10Sb/m. Where Sb is the standard deviation and m is the slope of the calibration equation. Under the optimum experimental conditions, the detection limit for SiO₂ was determined as 0.0375 mg/mL, the quantitation limit as 0.1136 mg/mL, and the correlation coefficient as 0.9997. Additionally, the calibration equation is $y = 0.0253x + 0.0032$, and the recovery values vary between 96.5% and 103.2%, demonstrating the accuracy of the method.

4. Conclusion

Chemical pollution in water, air, and soil is becoming more and more alarming day by day. This study aims to replace chemical treatment in power plants or all processes that require a water/steam cycle with an economical and environmentally beneficial one. For this reason, some preliminary research has been carried out on the silica problem, one of the biggest problems in closed cycles. While the field application of this study was carried out, preliminary tests were carried out to see what effect it has on the removal of silicate-induced pollution in water and steam cycles in industry. To investigate the effect of the parameters taken from different steps, such as temperature and mixing time in the water and steam cycles of a private industrial establishment, and which are more important for each step, *Bacillus subtilis* bacteria were added to samples containing silica, and the results obtained were examined. The biosorption of silica on the *Bacillus subtilis* bacterium largely depends on the active sites of the biomass. Since they have both a live and active metabolism, resistance and biosorption mechanisms act as a whole. Biosorption of silica was achieved effectively thanks to the active sites of the *Bacillus subtilis* bacterium. When the results obtained in the study were analyzed, a more environmentally friendly way was followed by using *Bacillus subtilis* bacteria instead of toxic chemicals to reduce the amount of silica. In addition, one of the

important results of the study is that *Bacillus subtilis* has been found to reduce not only silica but also the amount of impurities in the water. In addition to silica, this study revealed that *Bacillus subtilis* treatment effectively reduced other waterborne impurities. Specifically, in raw process water and boiler systems, notable reductions were observed in total hardness (from 1.76 to 0.88 mg/L), magnesium (from 106.1 to 54.8 mg/L), calcium (from 185.8 to 91.2 mg/L), and total dissolved solids (TDS). These reductions were achieved without the need for conventional chemical dosing, highlighting the dual benefit of this biological approach in both silica and secondary impurity control. At the same time, it creates a preliminary idea by providing a different dimension for many similar studies. Most importantly, by strongly affecting the needs in the field of wastewater treatment, added value will be provided on behalf of our country, especially in the economic sense, on an issue that exists in the industry and is a constant problem. In light of the information obtained as a result of this study, the fact that it will both protect the environment from tons of chemicals used for the steam water cycle and help to provide a great economic gain reveals the other advantageous aspects of the study. It will also be beneficial to extend the life of the process and provide ease of operation.

Conflict of interest

The authors declare that they have no conflict of interest.

Author contributions

Deniz Bozkurt: Material preparation, Formal analysis, Investigation, Writing—original draft.

Aslıhan Dalmaz: Data curation, Writing—original draft, Writing—review & editing, Conceptualization.

Sefa Durmuş: Conceptualization, Methodology, Writing—review & editing, Funding acquisition, Supervision.

References

- [1] S.B. Dalgaard, M.O. Sanford, Review of the hydrazine/oxygen reaction kinetics, Corrosion/81, April 6–10, Toronto, 1981, Canada, P15.
- [2] A.P. Akol'zin, V.G. Klochkova, A.E. Balabanov, Protection against corrosion of boiler steel with carbohydrazide, Therm Eng+, 35, 1988, 462–463.
- [3] V.V. Slesarenko, E.V. Kozlov, Application of combined water treatment systems at thermal power plants of the far east region, Thermal engineering, 53, 2006, 403–406.
- [4] K. Demadis, Scale formation and removal, Power, 148, 2004, 19–19.
- [5] K.D. Demadis, E. Mavredaki, A. Stathouloupoulou, E. Neofotistou, C. Mantzaridis, Industrial water systems: problems,

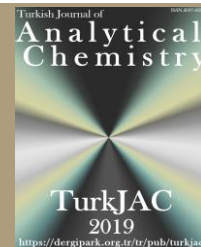
- challenges and solutions for the process industries, *Desalination*, 213, 2007, 38-46.
- [6] A.S. Abd Askar, Pretreatment of Water for Industrial Boilers Purposes, Alexandria, Texas Journal of Multidisciplinary Studies, 24, 2023, 120-133.
 - [7] Q. Cao, T. Pojtanabuntoeng, M. Esmaily, S. Thomas, M. Brameld, A.Amer, N. Biribilis, A review of corrosion under insulation: a critical issue in the oil and gas industry, *Metals*, 12, 2022, 561.
 - [8] A.N. Samodurov, S.E. Lysenko, S.L. Gromov, A.A. Panteleev, E.B. Fedosseva, The use of reverse osmosis technology for water treatment in power engineering, *Thermal engineering*, 53, 2006, 439-443.
 - [9] L. Jahangiri, M.A. Esteban, Administration of probiotics in the water in finfish aquaculture systems: a review, *Fishes*, 3, 2018, 30–33.
 - [10] C.I.M. Martins, E.H. Eding, M.C.J. Verdegem, L.T.N. Heinsbroek, O. Schneider, J.-P. Blancheton, E.R. d'Orbcastel, J.A.J. Verreth, New developments in recirculating aquaculture systems in Europe: a perspective on environmental sustainability, *Aquac. Eng.*, 43, 2010, 83–93.
 - [11] R. Crab, Y. Avnimelech, T. Defoirdt, P. Bossier, W. Verstraete, Nitrogen removal techniques in aquaculture for a sustainable production, *Aquaculture*, 270, 2007, 1–14.
 - [12] J. van Rijn, Waste treatment in recirculating aquaculture systems, *Aquac Eng.*, 53, 2013, 49–56.
 - [13] C. Maucieri, C. Nicoletto, R. Junge, Z. Schmautz, P. Sambo, M. Borin, Hydroponic systems and water management in aquaponics: A review, *Ital J Agron*, 13, 2018, 1-11.
 - [14] T. Devaraja, S. Banerjee, F. Yusoff, M. Shariff, H. Khatoon, A holistic approach for selection of *Bacillus* spp. as a bioremediator for shrimp postlarvae culture, *Turkish Journal of Biology*, 37, 2013, 92-100.
 - [15] F.K.A. Kuebutornye, E.D. Abarike, Y. Lu, A review on the application of *Bacillus* as probiotics in aquaculture, *Fish Shellfish Immunol*, 87, 2019, 820–828.
 - [16] M. Soltani, K. Ghosh, S.H. Hoseinifar, V. Kumar, A.J. Lymbery, S. Roy, E. Ringø, Genus *Bacillus*, promising probiotics in aquaculture: aquatic animal origin, bio-active components, bioremediation and efficacy in fish and shellfish, *Reviews in Fisheries Science & Aquaculture*, 27, 2019, 331-379.
 - [17] B.R. Manno, I.K. Abukhalaf, J.E. Manno, A simple spectrophotometric assay for the measurement of soluble silica in water, *Journal of Analytical Toxicology*, 21, 1997, 503-505.
 - [18] S. Faza, J. Kwok, O. Salah, Application of high-strength and corrosion-resistant ASTM A1035 steel reinforcing bar in concrete high-rise construction, *Des Sustain*, 211, 2007.
 - [19] A.W. Danial, F.M. Dardir, Copper biosorption by *Bacillus pumilus* OQ931870 and *Bacillus subtilis* OQ931871 isolated from Wadi Nakheil, Red Sea, Egypt, *Microb Cell Fact*, 22, 2023, 152.
 - [20] C. Thongchom, T. Laemthong, P. Sangkeaw, N. Yamasamit, S. Keawsawasvong, Evaluation of encapsulated *Bacillus subtilis* bio-mortars for use under acidic conditions, *Sci Rep*, 14, 2024, 25947.
 - [21] Powertech, Feed water, boiler water and steam quality for power plants/industrial plants. VGB PowerTech Service GmbH Essen, Germany, 2011.



TurkJAC

Turkish Journal of

Analytical Chemistry

<https://dergipark.org.tr/tr/pub/turkjac>TurkJAC
2019<https://dergipark.org.tr/tr/pub/turkjac>

Eco-friendly spectrofluorimetric determination of Hg²⁺ using green-synthesized carbon nanodots from apricot kernel shells

Najlaa Ayad Salahaldeen¹ , Nurhayat Özbek¹ , Miraç Ocak^{1*} , Ümmühan Turgut Ocak¹ ¹ Karadeniz Technical University, Faculty of Sciences, Department of Chemistry, 61080, Trabzon, Türkiye

Abstract

The green synthesis of blue fluorescent carbon nanodots (CNDs) from apricot kernel shells via a hydrothermal method was successfully executed. The interaction of the synthesized CNDs with various cations was systematically investigated using fluorescence spectroscopy. Fluorescence measurements were performed to evaluate the interaction of CNDs with 36 different cations, including Li⁺, Na⁺, K⁺, Be²⁺, Mg²⁺, Ca²⁺, Sr²⁺, Ba²⁺, Sc³⁺, Y³⁺, Ti⁴⁺, V⁵⁺, Cr³⁺, Mo⁶⁺, W⁶⁺, Mn²⁺, Fe³⁺, Co²⁺, Ni²⁺, Cu²⁺, Ag⁺, Zn²⁺, Cd²⁺, B³⁺, Al³⁺, Tl⁺, As⁵⁺, Se²⁺, NH₄⁺, Au³⁺, Sb³⁺, Sn⁴⁺, Bi³⁺, Hg²⁺, Pd²⁺, and Pb²⁺. Among these, the CNDs exhibited exceptional selectivity and sensitivity as a fluorescent probe for the detection of Hg²⁺ ions. The working range for Hg²⁺ detection was established as 35–95 µM, with a detection limit of 14.0 µM and a quantification limit of 41.4 µM. The method was validated and successfully applied to tap water and river water, demonstrating the practical utility of CNDs derived from apricot seed shells for environmental monitoring and analytical applications.

Keywords: Carbon nanodots (CNDs), hydrothermal method, apricot kernel shell, fluorescence spectroscopy, Hg²⁺ determination.

1. Introduction

CNDs, a class of carbon-based nanomaterials, have garnered significant attention in recent years due to their unique optical properties, biocompatibility, environmental friendliness, and cost-effective synthesis [1-2]. These nanomaterials exhibit high fluorescence quantum yields, excellent photostability, and versatile surface functionalization capabilities, making them ideal candidates for sensing applications, especially in fluorescence-based detection systems [3-4]. Among these, the detection of heavy metal ions, particularly Hg²⁺, has been a major focus due to its toxicological and environmental significance [5].

Mercury is a highly toxic heavy metal with severe impacts on human health and ecosystems even at trace levels [6]. It is well known for its bioaccumulation in the food chain and persistence in the environment [7]. Consequently, the development of efficient, sensitive, and selective methods for Hg²⁺ detection has become a pressing need. In this context, CNDs-based spectrofluorimetric techniques have emerged as promising tools, offering rapid, cost-effective, and

environmentally friendly solutions for mercury ion detection.

Numerous studies in the literature highlight the potential of CNDs for Hg²⁺ sensing, leveraging their remarkable fluorescence properties and unique interaction mechanisms [8]. The fluorescence quenching of CNDs in the presence of Hg²⁺ is a commonly employed detection strategy, attributed to processes such as static or dynamic quenching [9-12]. The strong affinity of Hg²⁺ ions for the functional groups on the surface of CNDs, such as carboxyl, hydroxyl, or amine groups, underpins the high sensitivity and selectivity of these systems [13].

Significant advancements have been reported in the development of CND-based sensors with ultra-low detection limits, often reaching nanomolar or even picomolar levels [14-15]. These sensors have demonstrated excellent selectivity for Hg²⁺ over other metal ions, making them suitable for applications in environmental water samples [16-17]. Additionally, the use of green synthesis approaches for producing CNDs from natural or waste-derived carbon sources has

Citation: N. A. Salahaldeen, N. Özbek, M. Ocak, Ü.T. Ocak, Eco-friendly spectrofluorimetric determination of Hg²⁺ using green-synthesized carbon nanodots from apricot kernel shells, Turk J Anal Chem, 7(2), 2025, 228–236.

***Author of correspondence:** mocak@ktu.edu.tr

Tel: +90 (462) 377 25 25

Fax: +90 (462) 325 31 96

Received: March 16, 2025

Accepted: April 23, 2025

doi <https://doi.org/10.51435/turkjac.1658256>

further enhanced their appeal as sustainable materials for analytical applications [18–19].

Recent studies have explored the synthesis of CNDs from apricot kernel shells, highlighting their potential in various applications. For instance, Xu et al. utilized a carbonization technique to produce greenish-yellow luminescent carbon quantum dots from apricot shells, demonstrating high photostability [20]. Another study focused on the preparation and characterization of biochar derived from apricot kernel shells using a hydrothermal method. The resulting biochar exhibited a uniform distribution of non-aggregated carbon microspheres and contained numerous oxygen-containing functional groups, indicating its potential for adsorption applications [21]. Additionally, research has been conducted on recycling lignocellulosic waste, including apricot kernels, to design advanced carbon material precursors. These precursors can be used to obtain nanopowders with high applicability in pollution abatement, showcasing the versatility of apricot kernel-derived carbon materials [22].

Although there is extensive research on the use of biomass-derived CNDs for the spectrofluorimetric detection of metal ions [23], studies specifically focused on metal ion determination using CNDs derived from apricot kernel shells remain highly limited in the literature [20]. In a recent study, greenish-yellow fluorescent carbon quantum dots synthesized from apricot kernel shells exhibited selective fluorescence quenching in the presence of Fe^{3+} ions, with the fluorescence being restored upon the addition of ascorbic acid [20]. This finding demonstrated the potential of these CNDs for the selective detection of ascorbic acid [20].

In the presented study, CNDs were synthesized using a simple and rapid hydrothermal method from apricot kernel shells, and their interactions with a series of cations were investigated through fluorescence measurements. Among the examined cations, selective fluorescence quenching was observed with Be^{2+} , V^{5+} , Fe^{3+} , Au^{3+} , Hg^{2+} , and Pd^{2+} ions. Notably, the fluorescence quenching of CNDs was found to be linearly dependent on Hg^{2+} ion concentration, making it possible to develop a new spectrofluorimetric method for the detection of Hg^{2+} . The applicability of this method to real samples was also demonstrated. Thus, the presented study addresses a gap in the literature by providing a simple, rapid, and cost-effective spectrofluorimetric method for the determination of Hg^{2+} using CNDs synthesized from apricot kernel shells.

2. Materials and Methods

2.1. Instrumentation, reagents, and samples

The instrumentation employed in this study included a Photon Technologies International Quanta Master

Spectrofluorimeter (QM-4-2006) for fluorescence measurements, a high-precision Sartorius Ed224s analytical balance for mass determination, and an Analytik Jena Specord 210 spectrophotometer for UV-Vis absorption spectroscopy. Sample preparation was conducted using a Vacuelli Eco Line vacuum oven, a HERMLE Z 326 K centrifuge, an IKA RCT magnetic stirrer, and a JSOF-050 forced convection oven. Sample mixing and volumetric handling were facilitated by a Labnet Model No. 50100-320 V vortex shaker and Nichiryo automatic pipettes (10–100–1000 μL). Deionized water used in the study was obtained from a Merck Millipore Direct-Q 8 UV system. Ultraviolet measurements were performed using a SPECTROLINE MODEL CM-10 UV device, while pH analyses were carried out with an Orion Research Model 601 Digital Ionalyzer pH meter. Dialysis bags (6000 Da) were obtained from Merck (Darmstadt, Germany). Single-use filters with a pore size of 0.45 microns were purchased from Sartorius. Standard aqueous solutions of cations (1000 mg/L) were supplied by Merck. The real water samples analyzed in this study were tap water from Karadeniz Technical University (KTU) and water from the Harşit River.

2.2. Preparation of the CNDs

The apricot kernels were carefully cleaned, dried, and finely ground using a laboratory grinder. A precisely measured 1.0 g of the powdered material was dispersed in 150 mL of deionized water. The resulting mixture underwent hydrothermal treatment in a stainless steel autoclave at 180°C for 3 hours. Upon completion of the reaction, the obtained solution was sequentially filtered through black and white band filter papers to eliminate solid residues. The filtrate was subsequently centrifuged at 10000 rpm for 10 minutes to further purify the suspension. The supernatant was then subjected to dialysis against 200 mL of deionized water under continuous stirring at 600 rpm for 3 days, utilizing a dialysis membrane with a molecular weight cut-off of 6000 Da. Following dialysis, the external solution was separately filtered through a 0.45-micron membrane filter to ensure the complete removal of any residual impurities. A 12.5 mL aliquot of the external solution was collected and diluted to a final volume of 100 mL with deionized water. The purified CND solution obtained after dialysis and filtration was subsequently diluted and utilized in spectrofluorimetric analyses for the detection of Hg^{2+} ions.

2.3. Determination of the quantum yield

The quantum yield of the synthesized CNDs (Φ_{CNDs}) was determined using a comparative method, as described in previous studies [24]. A 0.1 M solution of quinine sulfate in 0.1 M H_2SO_4 ($\Phi_{\text{R}} = 0.54$) with a refractive index (η) of

1.33 served as the reference fluorescence standard. The CND solutions were prepared in deionized water, also with a refractive index (η) of 1.33, to ensure consistency in optical properties. Fluorescence emission spectra were recorded for both the quinine sulfate reference and the CND solutions at varying concentrations, with an excitation wavelength (λ_{ex}) of 310 nm. The integrated fluorescence intensity values of the emission spectra were calculated. Corresponding absorbance values for each solution were measured under the same conditions as the emission spectra to maintain accuracy. A linear plot of integrated fluorescence intensity versus absorbance was generated for both the reference and the CND solutions. The slope (m) of the linear fit for the CNDs was compared to that of the reference solution, enabling calculation of the quantum yield for the CNDs using Eq. 1.

$$\Phi_{\text{CNDs}} = \Phi_Q \left(\frac{m_{\text{CNDs}}}{m_Q} \right) \left(\frac{\eta_{\text{CNDs}}^2}{\eta_Q^2} \right) \quad (1)$$

In Equation (1), the terms CNDs and Q represent the synthesized CNDs and quinine sulfate, respectively. The parameter m corresponds to the slope obtained from the linear plot of integrated fluorescence intensity versus absorbance for each solution. The refractive index, η , represents the optical property of the solvent used for each sample, accounting for variations in the medium's influence on fluorescence efficiency. These parameters collectively enable accurate determination of the quantum yield of CNDs relative to the reference standard.

2.4. pH effect on the fluorescence spectra of CNDs

To investigate the effect of pH on the fluorescence intensity of the CNDs, solutions were prepared across a pH range of 3 to 11 using appropriate buffer systems to maintain pH stability. Fluorescence measurements were performed by exciting the CND solutions at a wavelength of 310 nm, and the corresponding emission intensities were recorded. This systematic study was conducted to evaluate the impact of pH on the photophysical properties of the CNDs.

2.5. Interactions of cations with CNDs

2 mL of the CND solution was aliquoted into separate tubes. To achieve a final cation concentration of 1×10^{-3} M, appropriate volumes of the prepared intermediate stock solutions were added. The total volume in each tube was adjusted to 4 mL by adding deionized water. The fluorescence spectra of the prepared samples were then recorded, with excitation set at the wavelength corresponding to the maximum fluorescence intensity of the CNDs. The interactions of CNDs with cations such as Li^+ , Na^+ , K^+ , Be^{2+} , Mg^{2+} , Ca^{2+} , Sr^{2+} , Ba^{2+} , Sc^{3+} , Y^{3+} , Ti^{4+} , V^{5+} , Cr^{3+} , Mo^{6+} , W^{6+} , Mn^{2+} , Fe^{3+} , Co^{2+} , Ni^{2+} , Cu^{2+} , Ag^+ , Zn^{2+} , Cd^{2+} ,

B^{3+} , Al^{3+} , Tl^+ , As^{5+} , Se^{2+} , NH_4^+ , Au^{3+} , Sb^{3+} , Sn^{4+} , Bi^{3+} , Hg^{2+} , Pd^{2+} , and Pb^{2+} were investigated spectrofluorimetrically. Among these, a regular decrease in fluorescence intensity was observed during titrations with increasing concentrations of Hg^{2+} ions, indicating a selective quenching effect.

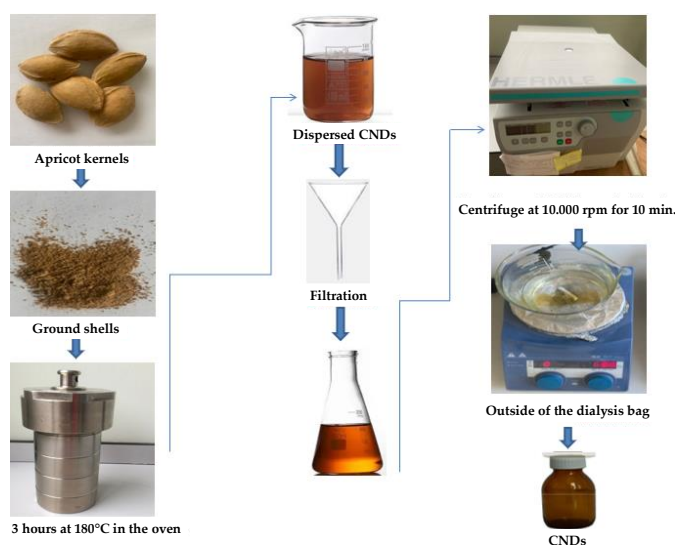
2.6. Determination of Hg^{2+} ions

A spectrofluorimetric method for the determination of Hg^{2+} was developed based on the regular fluorescence quenching exhibited by CNDs in the presence of Hg^{2+} . Initially, Hg^{2+} was added to pure water to calculate the recovery values. For this, a standard calibration curve was prepared and used to determine the concentration of Hg^{2+} . The fluorescence intensity measurements were carried out at an emission wavelength of 347 nm. The limits of detection (LOD) and quantification (LOQ) of the developed method were determined to be 14.0 μM and 41.4 mg/L, respectively. The working range of the method was established between 35 and 95 μM . The proposed method was successfully applied to tap water and river water samples.

3. Results and discussion

3.1. Synthesis and characterization of CNDs

The summary of the hydrothermal method used for the synthesis of CNDs is shown in Scheme 1. The morphology of the CNDs was examined using transmission electron microscopy (TEM), which revealed the formation of aggregated clusters with sizes smaller than 50 nm (Fig. 1a). In the HRTEM images of the CNDs (Fig. 1b), a 0.34 nm d-spacing corresponding to the (002) plane of hexagonal graphite was observed, indicating that the CNDs possess a hexagonal graphite structure [25–27].



Scheme 1. Schematic diagram of the synthesis of CNDs via hydrothermal method

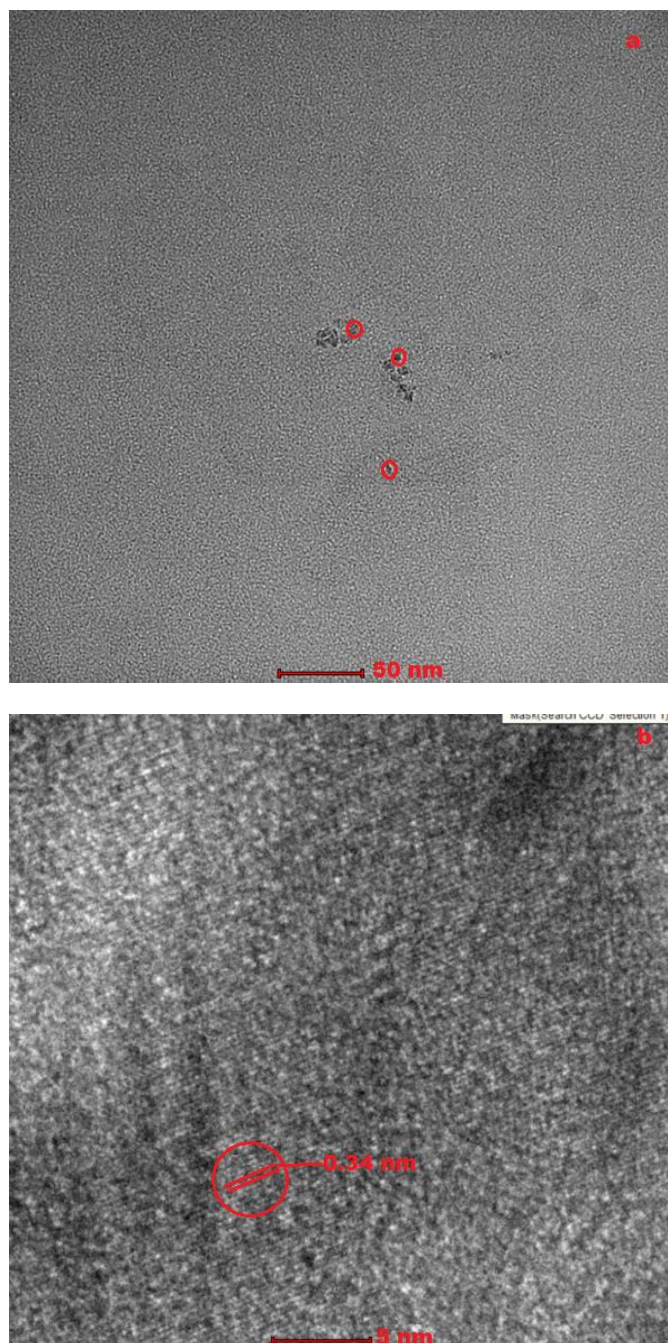


Figure 1. (a): TEM image of CNDs, (b): HRTEM image of CNDs

XRD analysis confirmed the presence of a graphite-like structure in CNDs (Fig. 2). The broad peak observed in the XRD pattern of the CNDs at approximately $2\theta = 22.3^\circ$ is characteristic of amorphous carbon structures [28]. This peak reflects the short-range ordering and partially crystalline nature of the CNDs. Additionally, this value corresponds to a d-spacing of around 0.4 nm, commonly observed in carbon materials such as amorphous carbon, carbon nanotubes, or graphene oxide [29]. This suggests that the CNDs do not exhibit a fully crystalline structure but instead display partial ordering and possess an amorphous character [30]. The peak observed at $2\theta = 34.0^\circ$ in the XRD pattern corresponds to the (112) planes of graphite, confirming that the CNDs possess a hexagonal graphite structure [31]. The crystallite size of the CNDs was approximately

calculated to be 32.2 nm using the Scherrer equation based on the XRD data.

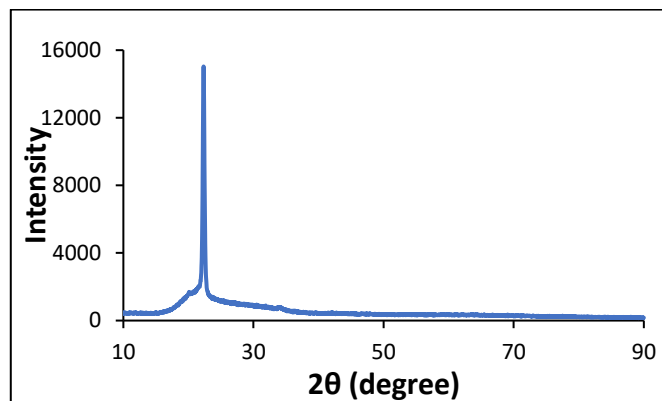


Figure 2. XRD diffractogram of CND

XPS analysis was employed to determine the elemental composition of the CNDs, identifying the presence of carbon, oxygen, and nitrogen atoms (Fig. 3a). A detailed deconvolution of the XPS spectra revealed that the C1s peak was associated with various carbon bonding environments, including C=C, C-C, C-O, and C-N bonds (Fig. 3b). The N1s peak was attributed to pyridinic C-N bonds, indicating the presence of nitrogen in a nitrogen-rich functional group (Fig. 3c). The O1s peak was assigned to a combination of oxygen-containing functional groups, including C=O, O-H, and C-O bonds (Fig. 3d), further confirming the presence of oxygen functionalities on the surface of the CNDs.

FTIR spectroscopy provided further evidence for the functional groups present within the structure of CNDs (Fig. 4). Substantial vibrational bands included the C-H stretching vibration at 2913 cm^{-1} , C=C stretching vibration at 1590 cm^{-1} , the O-H stretching vibration at 3311 cm^{-1} , the C=O stretching vibration at 1723 cm^{-1} , and the C-O/C-N stretching vibrations at 1029 cm^{-1} .

3.2. Optical and fluorescence properties of CNDs

The optical properties of CNDs were analyzed using UV-Vis absorption spectroscopy. The UV-Vis absorption spectrum of CNDs is presented in Fig. 5. A strong absorption peak observed around 200 nm is attributed to the $\pi \rightarrow \pi^*$ transitions of the C=C bonds, characteristic of sp^2 -hybridized carbon atoms within the graphite-like structure. Additionally, an absorption band near 250 nm corresponds to $n \rightarrow \pi^*$ transitions of C-O and C-N bonds. These findings align with previously reported UV-Vis absorption spectra of carbon-based nanomaterials [32].

The visual appearance of the aqueous CND solution was documented under both daylight and UV light at 365 nm, as illustrated in Fig. 5.

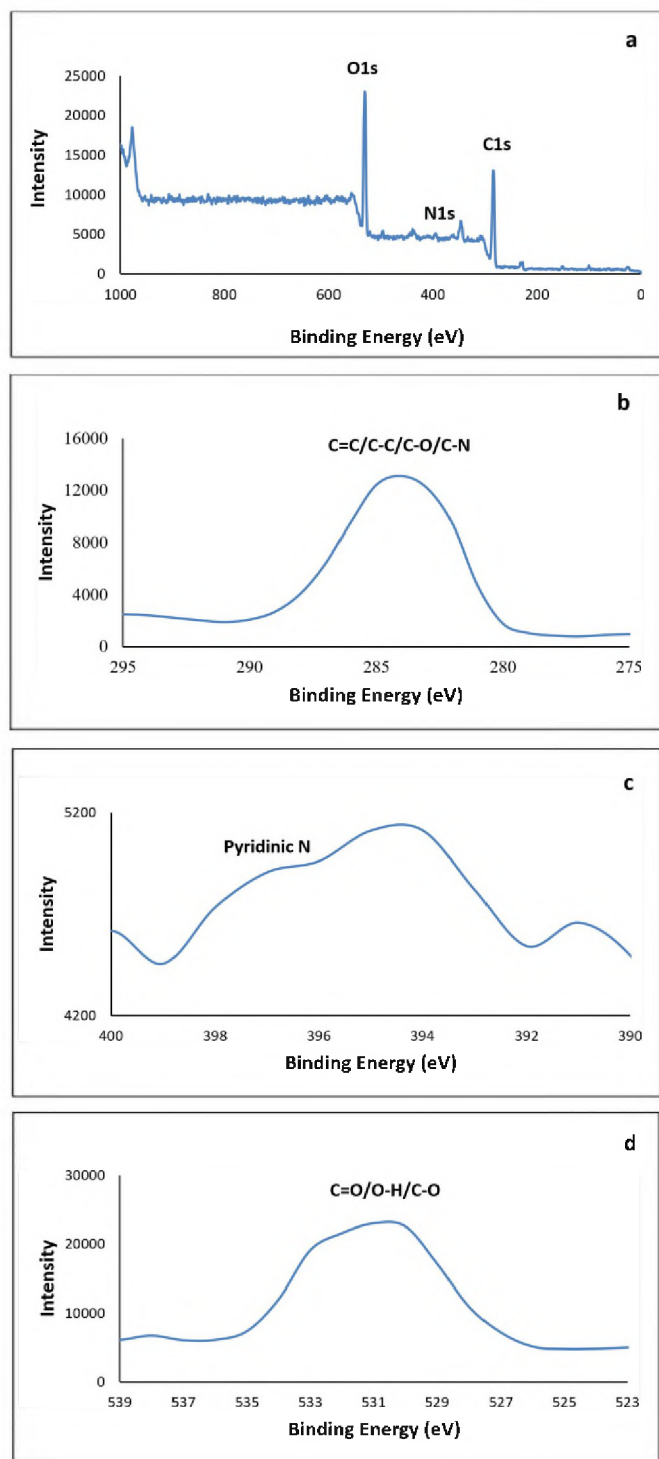


Figure 3. (a): XPS full spectra for the CNDs, (b): C1s, (c): N1s, (d): O1s spectra.

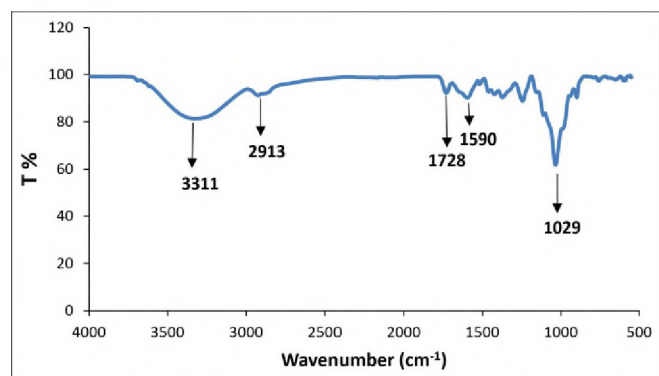


Figure 4. FTIR spectra of CNDs

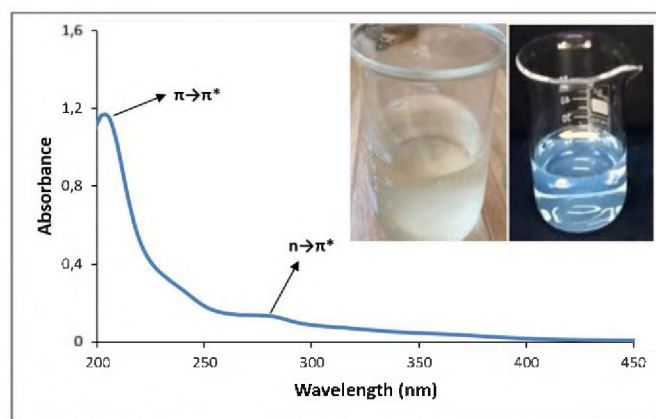


Figure 5. UV-Vis absorption spectrum of CNDs. Images of the CND solution under UV light (inset right) and daylight (inset left)

Under daylight conditions (Fig. 5 inset, left), the CND solution exhibited a pale yellow color, whereas under UV light (Fig. 5 inset, right), it displayed blue fluorescence. This observation confirms the fluorescent properties of the synthesized CNDs. The quantum yield of the CNDs was also determined using quinine sulfate as the standard reference. The quantum yield was found to be 0.27.

To further investigate the fluorescence properties of CNDs, fluorescence emission spectra of the aqueous CND solution were recorded at excitation wavelengths ranging from 300 to 400 nm in 10 nm intervals (Fig. 6). As depicted in Fig. 6, increasing the excitation wavelength resulted in a decrease in fluorescence emission intensity and a red shift in the emission peak maxima. This excitation-dependent fluorescence behavior demonstrates that the synthesized CNDs exhibit multicolor fluorescence characteristics, consistent with findings reported in the literature [32]. As shown in Fig. 6, the CNDs exhibited the highest fluorescence intensity when excited at 310 nm. Therefore, 310 nm was used as the excitation wavelength in subsequent studies.

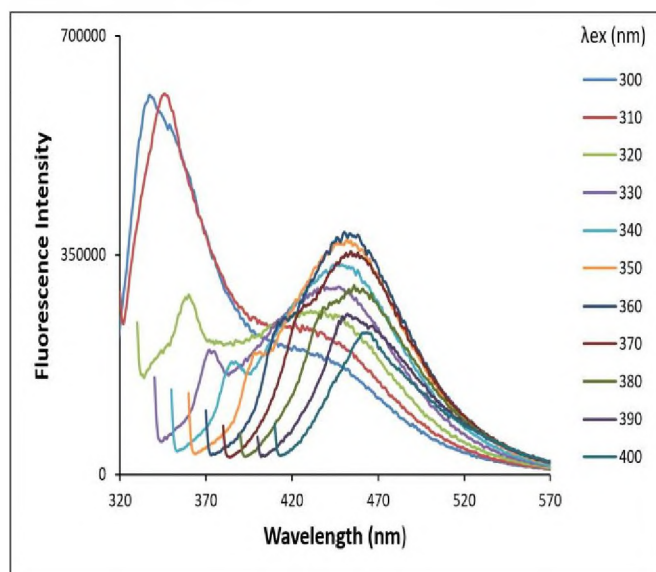


Figure 6. Emission spectra of CNDs at different excitation wavelengths

3.3. The effect of pH on the fluorescence intensity of CNDs

The fluorescence intensity of CNDs is highly influenced by pH, and this effect has been extensively studied in the literature [13]. To examine the effect of pH on the fluorescence intensity of prepared CNDs, solutions of CNDs were prepared across a pH range of 3 to 11 and excited at 310 nm. Fluorescence intensity at 347 nm was subsequently recorded, as shown in Fig. 7. As depicted, a significant reduction in fluorescence intensity is observed at pH 11, while no notable changes in fluorescence intensity occur at pH values of 3, 5, and 7. Considering that the pH of real samples typically ranges around 7, the experiments were conducted without the addition of any buffer solution. This approach, which eliminates the need for supplementary chemicals, provides several advantages, including cost-effectiveness, environmental sustainability, and a more efficient experimental procedure. These benefits make this method a more practical and efficient alternative compared to other Hg^{2+} detection techniques reported in the literature.

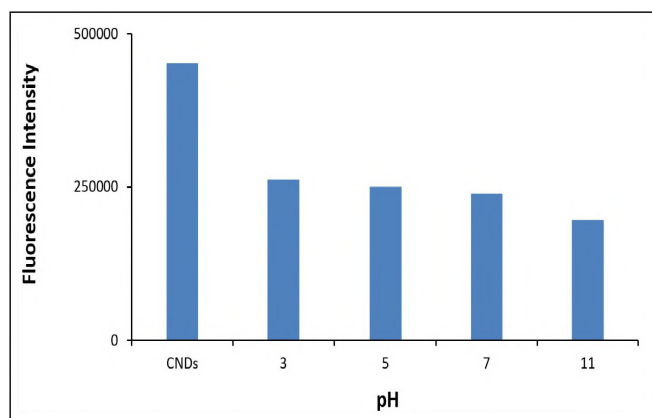


Figure 7. Variation of the fluorescence intensity of CNDs with pH (λ_{exc} :310 nm, λ_{em} :347 nm)

3.4. The effect of cations on the fluorescence of CNDs

The interactions between CNDs and a variety of cations were systematically investigated by monitoring the fluorescence response at an excitation wavelength of 310 nm. The effect of 36 different cations on the fluorescence spectra of CNDs was explored, including Li^+ , Na^+ , K^+ , Be^{2+} , Mg^{2+} , Ca^{2+} , Sr^{2+} , Ba^{2+} , Sc^{3+} , Y^{3+} , Ti^{4+} , V^{5+} , Cr^{3+} , Mo^{6+} , W^{6+} , Mn^{2+} , Fe^{3+} , Co^{2+} , Ni^{2+} , Cu^{2+} , Ag^+ , Zn^{2+} , Cd^{2+} , B^{3+} , Al^{3+} , Tl^+ , As^{5+} , Se^{2+} , NH_4^+ , Au^{3+} , Sb^{3+} , Sn^{4+} , Bi^{3+} , Hg^{2+} , Pd^{2+} , and Pb^{2+} (Fig. 8a). Changes in the fluorescence intensity of CNDs upon interaction with different cations were monitored to evaluate their binding affinity and selectivity. This analysis aimed to elucidate the selectivity of CNDs for particular cations, with a focus on those ions that induced the most pronounced changes in fluorescence behavior.

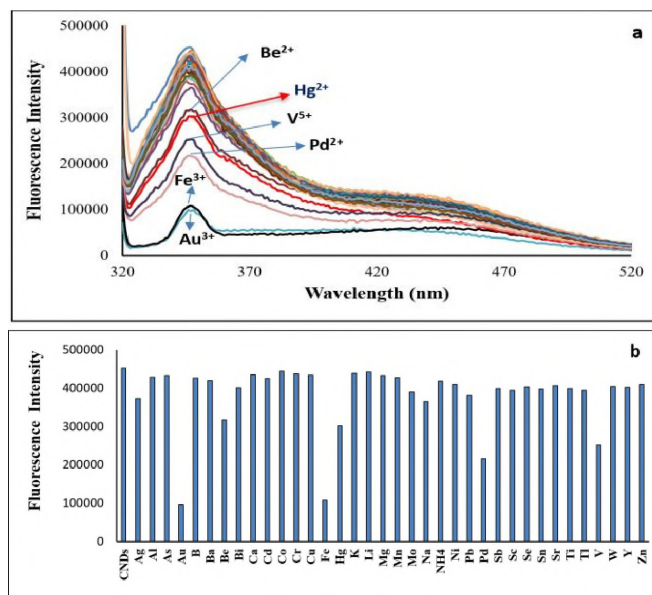


Figure 8. (a): Effect of cations on the fluorescence spectrum of CND, (b): The changes in fluorescence intensity at 347 nm with the effect of cations

Fig. 8a illustrates the effect of various cations on the fluorescence spectrum of CNDs. Upon analyzing the interaction results, notable quenching in fluorescence intensity was observed with Be^{2+} , V^{5+} , Fe^{3+} , Au^{3+} , Hg^{2+} , and Pd^{2+} cations (Fig. 8b). Spectrofluorimetric titrations were performed to determine whether the fluorescence quenching was related to the concentration of cation. However, there were no consistent and reproducible fluorescence responses with the increasing concentrations of Be^{2+} , V^{5+} , Fe^{3+} , Au^{3+} , and Pd^{2+} ions. The regular and predictable fluorescence quenching observed with only increasing Hg^{2+} concentrations provided a reliable basis for continued studies to develop a sensitive and selective determination method. Fig. 9 demonstrates the consistent fluorescence quenching in the spectra of CNDs as the concentration of Hg^{2+} increases. The inset of Fig. 9 illustrates the correlation between the fluorescence intensity at 347 nm and the Hg^{2+} concentration. A regular fluorescence quenching effect was observed within the Hg^{2+} concentration range of 35 to 95 μM (Fig. 9 inset).

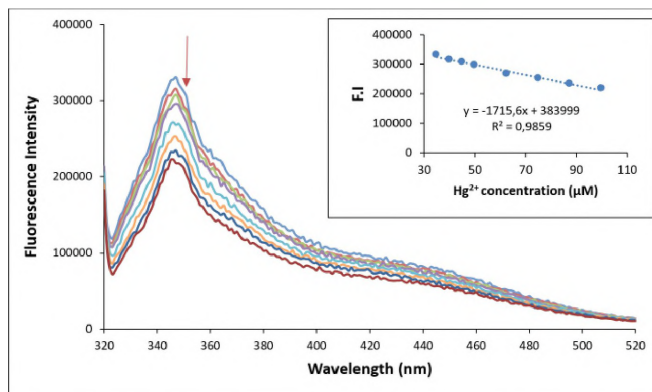


Figure 9. Spectrofluorimetric titration of CNDs with Hg^{2+} ions. Inset: Regular quenching in the fluorescence intensity of CNDs at 347 nm with increasing Hg^{2+} concentration (Hg^{2+} concentration: 35-95 μM)

3.5. Determination of Hg^{2+} ions

The determination of Hg^{2+} was performed using the standard calibration method. The analytical performance data of the proposed method is presented in Table 1. The LOD and LOQ values of the method were determined to be $14.0 \mu\text{M}$ and $41.4 \mu\text{M}$, respectively. The linear range (LR) was established to be $35\text{--}95 \mu\text{M}$. The accuracy of the method was demonstrated through spiking-recovery studies conducted on real water samples. The results are presented in Table 2. As shown in Table 1, the correlation coefficient was 0.9859, indicating a high degree of linearity. The LOD value was calculated by dividing three times the standard deviation by the slope of the calibration curve. Eleven blank measurements were performed to determine the standard deviation for these experiments. The LOQ value was determined as three times the LOD.

Table 1. Analytical performance data of the proposed method for Hg^{2+} determination

Excitation wavelength (nm)	310
Emission wavelength (nm)	347
LOD (μM)	14.0
LOQ (μM)	41.4
LR (mg/L)	35-95
Fluorescent reagent	(8/10) diluted CND solution
Volume of CND solution (mL)	2
Total volume (mL)	4
Solvent	water
Pre-measurement time	1-2 min
Correlation coefficient (R^2)	0.9859

Table 2. Results of spiked-recovery experiments for Hg^{2+} determination in water samples (N=3)

Sample	Spiked Hg^{2+} (mg/L)	R% (intra-day)	R% (inter-day)
Deionized water	9.0	96.2 \pm 1.2	95.1 \pm 1.5
Tap water	9.0	97.8 \pm 1.4	96.3 \pm 1.3
River water	9.0	97.8 \pm 0.9	95.9 \pm 1.1

3.6. Quenching mechanism

The Stern-Volmer relationship can be used to explain the fluorescence quenching of CNDs in the presence of Hg^{2+} . In the Stern-Volmer equation given by Eq. (2), K_{sv} represents the Stern-Volmer quenching constant, while I_0 and I denote the fluorescence intensities in the absence and presence of the quencher (Hg^{2+}), respectively. $[Q]$ symbolizes the molar concentration of the quencher.

$$I_0/I = 1 + K_{\text{sv}} [Q] \quad (2)$$

As expected from Eq. 2, plotting I_0/I versus the molar concentration of the quencher should yield a straight line with a y-axis intercept of 1 when the quenching mechanism follows the Stern-Volmer relationship. The slope of this line corresponds to K_{sv} . The static quenching mechanism is based on the complexation of the quencher

with the fluorophore in the ground state, while dynamic quenching is generally associated with collisions in the excited state [33]. The Stern-Volmer equation remains valid for both quenching processes, despite the differing mechanisms. Fig. 10a presents the Stern-Volmer plot for Hg^{2+} -induced fluorescence quenching of the CNDs. As seen in Fig. 10a, the intercept of the line on the y-axis is 1. This indicates that the Stern-Volmer relationship is valid for this system. However, to determine whether the quenching is dynamic or static, the effect of temperature was investigated. Fig. 10b shows the effect of temperature on I_0/I . As seen in Fig. 10b, the I_0/I value increases with increasing temperature. This result suggests that the quenching occurs through dynamic quenching [33].

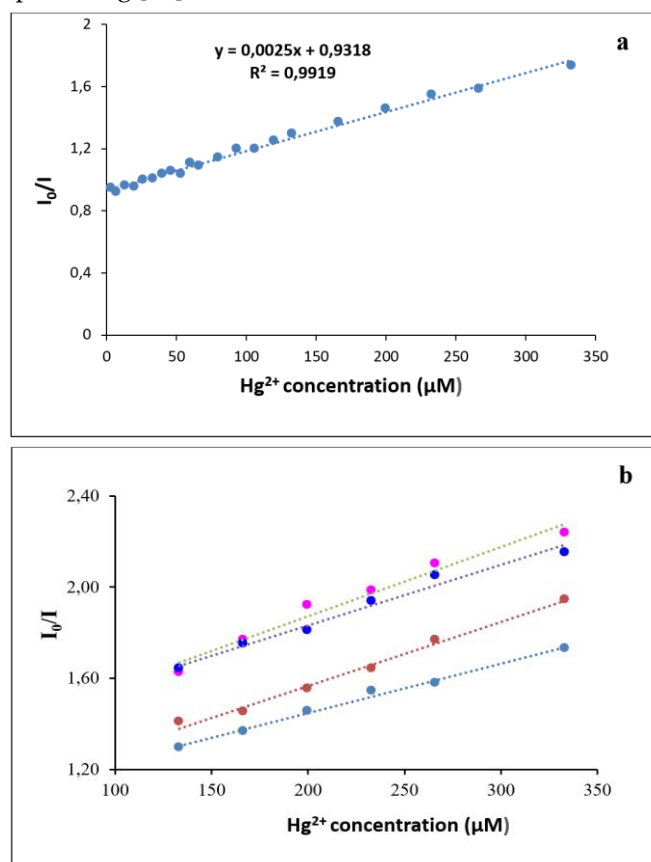


Figure 10. Stern-Volmer plot. The light blue: 297 K, the orange: 313 K, and the dark blue: 353 K

3.7. Comparison with other CNDs

Table 3 summarizes a comparison of several spectrofluorimetric Hg^{2+} detection methods in water samples based on CNDs reported in the literature. As shown in Table 3, although the LOD and LR values of these methods are more advantageous compared to the proposed work, the CNDs used as fluorescent probes in these studies were generally synthesized using chemical sources of carbon, such as ammonium citrate, citric acid, folic acid, ethylene glycol, and urea [18,34,36,37]. In contrast, in the presented study, apricot seed shells were utilized as a carbon source, making it a green synthesis approach compared to the methods in the literature.

Table 3. Comparison of CNDs-based methods for Hg²⁺ detection in water in the literature

Fluorescent reagent	Carbon source	Reaction temp. time	Chemicals	Sample	LOD (μM)	LR (μM)	Ref.
CDs	Folic acid, ethylene glycol	180 °C, 12h	—	Lake water, tap water	0.23	0-25	34
CDs	Carbon target	71h	HNO ₃ , PEG200, N-acetyl-L-cysteine, ethyl acetate	—	—	0-2.69	35
NSCNDs	Citric acid/urea/Lcysteine	MW, 5 min.	—	Lake water, tap water	2	0-40	36
CDs	Ethylene glycol	140 °C, 6h	H ₂ SO ₄	Tap water	0.035	0-1	37
FCDs	Citric acid	180 °C, 10h	NaOH, NaBH ₄	Tap water	0.02	0.1-1.2	13
NCDs	Ammonium citrate, urea	180 °C, 5h	—	Tap water	0.045	0.05-24.9	18
CQDs	Medlar Seed	300 °C, 2h	—	Tap, sea, and stream water	1.3	4.9-24.9	38
CNDs	Apricot kernel shells	180 °C, 3h	—	Tap water, river water	14	35-95	This work

Additionally, the methods in the literature involve relatively long reaction times [18,34,35, 37,13]. However, the reaction time in the proposed study is much shorter than most of the reaction times reported in the literature. Namely, the proposed synthesis method is a fast approach. As seen in Table 3, toxic chemicals such as NaOH and H₂SO₄ were used in some stages of the synthesis processes reported in the literature [37, 13]. In contrast, in the proposed study, only apricot seed shells, a natural waste product, were used as the carbon source in the hydrothermal synthesis of CNDs. Therefore, the proposed method is an environmentally friendly and cost-effective approach. The method was successfully applied to the determination of Hg²⁺ in tap water and river water samples. These results demonstrate that the proposed method is a rapid, economical, and environmentally friendly approach that can be effectively applied to water samples containing Hg²⁺ at concentrations within the detection limits of the method.

4. Conclusion

CNDs were efficiently synthesized from apricot kernel shells using a green hydrothermal synthesis method. The synthesized CNDs were characterized by TEM, XRD, XPS, and FTIR spectroscopy. The optical properties of the CNDs were analyzed using UV-vis absorption and fluorescence spectroscopy. The method demonstrated a linear range for Hg²⁺ detection between 35 and 95 μM. The LOD and LOQ values were determined to be 14 μM and 41.4 μM, respectively. The accuracy of the proposed method was successfully validated in tap water and river water samples.

In conclusion, the proposed spectrofluorimetric method provides a rapid, cost-effective, and highly selective approach for the detection of Hg²⁺ in water samples. By utilizing CNDs synthesized from apricot kernel powder, this method offers a significant improvement over existing techniques reported in the literature. It presents an eco-friendly and highly selective alternative for environmental monitoring and analytical applications, demonstrating both practical and environmental advantages.

Author contributions:

Najlaa Ayad Salahaldeen, Nurhayat Özbek, Ümmühan Turgut Ocak, and Miraç Ocak wrote the main manuscript text and prepared all figures. All authors reviewed the manuscript.

Funding:

No funding.

Data availability:

Datasets and materials used can be reached from Najlaa Ayad Salahaldeen.

Declarations

Competing interests:

The authors declare no competing interests.

Ethical approval:

An ethics approval is not legally required for the study.

References

- [1] D.S. Chauhan, M.A. Quraishi, C. Verma, Carbon nanodots: recent advances in synthesis and applications, *Carbon Lett*, 32, 2022, 1603–1629.
- [2] S. Dinç, M. Kara, Synthesis and applications of carbon dots from food and natural products: Review, *J Api Nat*, 1, 2018, 33–37.
- [3] M. Jabeen, I. Mutaza, A comprehensive review on carbon quantum dots, *Turk J Anal Chem* 6, 2024, 50–60.
- [4] X. Sun, Y. Lei, Fluorescent carbon dots and their sensing applications, *TrAC Trends Anal Chem*, 87, 2017, 163–180.
- [5] W.L. Zhong, J.Y. Yang, Fluorescent carbon quantum dots for heavy metal sensing, *Sci Total Environ*, 957, 2024, 177473.
- [6] G. Björklund, M. Dadar, J. Mutter, J. Aaseth, The toxicology of mercury: Current research and emerging trends. *Environ Res*, 159, 2017, 545–554.
- [7] A. Kumar, V. Kumar, P. Bakshi, R.D. Parihar, M. Radziemska, R. Kumar, Mercury in the natural environment: Biogeochemical

- cycles and associated health risks, *J Geochem Explor* 267, 2024, 107594.
- [8] M.V. Maia, WT. Suarez, V. Bezerra dos Santos, SC. Bezerra de Oliveira, JP. Barbosa de Almeida, A novel approach to Hg²⁺ determination in water samples using carbon dots based on paper and fluorescence digital image analysis, *J Chem Technol Biotechnol*, 99, 2024, 1157–1164.
 - [9] DJ. Dai, CY. Zhang, NT. Thi Dieu Thuy, G. Zhao, W. Lu, JY. Fan, Strong fluorescence quenching of carbon dots by mercury (II) ions: Ground-state electron transfer and diminished oscillator strength, *Diam Relat Mater*, 126, 2022, 109076.
 - [10] J.Y. Liang, L. Han, SG. Liu, YJ. Ju, NB. Li, HQ. Luo, Carbon dots-based fluorescent turn off/on sensor for highly selective and sensitive detection of Hg²⁺ and biothiols. *Spectrochim Acta A: Mol Biomol Spectrosc*, 222, 2019, 117260.
 - [11] E. Yahyazadeh, F. Shemirani, Easily synthesized carbon dots for determination of mercury (II) in water samples, *Heliyon* 5, 2019, e01596.
 - [12] PY. Yin, GX. Yao, TR. Zou, N. Na, WR. Yang, HB. Wang, W. Tan, Facile preparation of N, S co-doped carbon dots and their application to a novel off-on fluorescent probe for selective determination of Hg²⁺, *Dyes Pigments*, 206, 2022, 110668.
 - [13] ZH. Gao, ZZ. Lin, XM. Chen, ZZ. Lai, ZY. Huang, Carbon dots-based fluorescent probe for trace Hg²⁺ detection in water sample, *Sens Actuators B Chem*, 222, 2016, 965–971.
 - [14] S. Samota, P. Tewatia, R. Rani, S. Chakraverty, A. Kaushik, Carbon dot nanosensors for ultra-low level, rapid assay of mercury ions synthesized from an aquatic weed, *Typha angustata* Bory (Patera), *Diam Relat Mater*, 130, 2022, 109433.
 - [15] KHH. Aziz, KM. Omer, RF. Hamarawfa, Lowering the detection limit towards nanomolar mercury ion detection via surface modification of N-doped carbon quantum dots, *New J Chem*, 4, 2019, 8677–8683.
 - [16] L.K. Singh, S. Sharma, K.K. Ghosh, Spectroscopic detection of Hg²⁺ in water samples using fluorescent carbon quantum dots as sensing probe, *Main Group Chem*, 20, 2021, 1–18.
 - [17] D. Huang, CG. Niu, M. Ruan, X.Y. Wang, G.M. Zeng, C.H. Deng, Highly sensitive strategy for Hg²⁺ detection in environmental water samples using long lifetime fluorescence quantum dots and gold nanoparticles, *Environ Sci Technol*, 47, 2013, 4392–4398.
 - [18] Y. Zhang, N. Jing, JQ. Zhang, YT. Wang, Hydrothermal synthesis of nitrogen-doped carbon dots as a sensitive fluorescent probe for the rapid, selective determination of Hg²⁺, *Int J Environ Anal Chem*, 97, 2017, 841–853.
 - [19] H.H. Jing, F. Bardakci, S. Akgöl, K. Kusat, M. Adnan, M.J. Alam, R. Gupta, S. Sahreen, Y. Chen, S.C.B. Gopinath, S. Sasidharan, Green Carbon Dots: Synthesis, characterization, properties and biomedical applications, *J Funct Biomater*, 14, 2023, 27.
 - [20] H.B. Xu, S.H. Zhou, M.Y. Li, P.R. Zhang, Z.H. Wang, Y.M. Tian, X.Q. Wang, Preparation of biomass-waste-derived carbon dots from apricot shell for highly sensitive and selective detection of ascorbic acid, *Chinese J Anal Chem*, 50, 2022, 100168.
 - [21] Z.Q. Zhang, C.H. Zhou, J.M. Yang, B.J. Yan, J.H. Liu, S.N. Wang, Q. Li, M.M. Zhou, Preparation and characterization of apricot kernel shell biochar and its adsorption mechanism for atrazine, *Sustainability*, 14, 2022, 4082.
 - [22] G. Predeanu, V. Slăvescu, M.F. Drăgoescu, N.M. Bălănescu, A. Fiti, A. Meghea, P. Samoila, V. Harabagiu, M. Ignat, A.M. Manea-Saghin, BS. Vasile, N. Badea, Green synthesis of advanced carbon materials used as precursors for adsorbents applied in wastewater treatment, *Materials (Basel)*, 16, 2023, 1036.
 - [23] S.D. Torres Landa, N.K. Bogireddy, I. Kaur, V. Batra, V. Agarwal, Heavy metal ion detection using green precursor derived carbon dots, *iScience*, 25, 2022, 103816.
 - [24] F. Li, C.J. Liu, J. Yang, Z. Wang, W.G. Liu, F. Tian, Mg/N double doping strategy to fabricate extremely high luminescent carbon dots for bioimaging, *RSC Adv*, 4, 2014, 3201–3205.
 - [25] D. Ozyurt, M. Al Kobaisi, R.K. Hocking, B. Fox, Properties, synthesis, and applications of carbon dots: A review, *Carbon Trends*, 12, 2023, 100276.
 - [26] N.C. Verma, A. Yadav, C.K. Nandi, Paving the path to the future of carbogenic nanodots, *Nat Commun*, 10, 2019, 2391.
 - [27] C.J. Reckmeier, J. Schneider, A.S. Sussha, AL. Rogach, Luminescent colloidal carbon dots: optical properties and effects of doping, *Opt Express*, 24, 2016, A312–A340.
 - [28] B. Ramoğlu, A. Gümrükçüoğlu, E. Çekirge, M. Ocak, Ü. Ocak, One spot microwave synthesis and characterization of nitrogen doped carbon dots with high oxygen content for fluorometric determination of banned Sudan II dye in spice samples, *J Fluoresc*, 31, 2021, 1587–1598.
 - [29] A.B. Siddique, A.K. Pramanick, S. Chatterjee, M. Ray, Amorphous carbon dots and their remarkable ability to detect 2,4,6-trinitrophenol, *Sci Rep*, 8, 2018, 9770.
 - [30] M. Kavgacı, HV. Kalmış, H. Eskalen, Synthesis of fluorescent carbon quantum dots with hydrothermal and solvothermal method application for anticounterfeiting and encryption, *Int J Inn Eng Appl*, 7, 2023, 32–38.
 - [31] W.K. Zhang, Y.Q. Liu, X.R. Meng, T. Ding, Y.Q. Xu, H. Xu, Y.R. Ren, B.Y. Liu, J.J. Huang, J.H. Yang, XM. Fang, Graphenol defects induced blue emission enhancement in chemically reduced graphene quantum dots, *Phys Chem Chem Phys*, 17, 2015, 22361–22366.
 - [32] Y.P. Sun, B. Zhou, Y. Lin, W. Wang, K.A.S. Fernando, P. Pathak, M.J. Meziani, B.A. Harruff, X. Wang, P.G. Luo, H. Yang, M..E. Kose, B. Chen, LM. Veca, S.Y. Xie, Quantum-sized carbon dots for bright and colorful photoluminescence, *Am Chem Soc*, 128, 2006, 7756–7757.
 - [33] Y. Çağlar, E.T. Saka, H. Alp, H. Kantekin, M. Ocak, Ü. Ocak, A simple spectrofluorimetric method based on quenching of a Nickel(II)-phthalocyanine complex to determine iron (III), *J Fluoresc*, 26, 2016, 1381–1389.
 - [34] R. Zhang, W. Chen, Nitrogen-doped carbon quantum dots: Facile synthesis and application as a "turn-off" fluorescent probe for detection of Hg²⁺ ions, *Biosens Bioelectron*, 56, 2014, 83–90.
 - [35] H.M.R. Gonçalves, A.J. Duarte, J.C.G. Esteves Da Silva, Optical fiber sensor for Hg (II) based on carbon dots, *Biosens Bioelectron*, 4, 2010, 1302–1306.
 - [36] L. Li, B. Yu, T. You, Nitrogen and sulfur co-doped carbon dots for highly selective and sensitive detection of Hg (II) ions, *Biosens Bioelectron*, 74, 2015, 263–269.
 - [37] Y. Liu, C. Liu, Z. Zhang, Synthesis of highly luminescent graphitized carbon dots and the application in the Hg²⁺ detection, *Appl Surf Sci*, 258, 2012, 481–485.
 - [38] N. Özbek, E. Çekirge, M. Ocak, Ü. Ocak, Highly Blue-fluorescent Carbon Quantum Dots Obtained from Medlar Seed for Hg²⁺ Determination in Real Water Samples, *J Fluoresc*, 34, 2024, 2533–2542.

